A Laboratory Investigation of Load Transfer in Reinforced Soil

by

Douglas Gregory Larson

B.S. Civil Engineering, Carnegie Mellon University, 1987

S.M. Civil Engineering, Massachusetts Institute of Technology, 1989

Submitted to the Department of

Civil and Environmental Engineering

in partial fulfillment of the requirements for the degree of

Doctor of Philosophy in Civil Engineering

at the

Massachusetts Institute of Technology

August, 1992

Signature of Author _____
Department of Civil and Environmental Engineering

Certified by _____
Prof. Andrew J. Whittle
Thesis Co-Supervisor

Certified by _____
Dr. John T. Germaine
Thesis Co-Supervisor

Accepted by _____
Prof. Eduardo Kausel
Chairman, Departmental Committee on Graduate Studies

A Laboratory Investigation of Load Transfer in Reinforced Soil

by: Douglas Gregory Larson

Submitted to the Department of Civil and Environmental Engineering
on August 28, 1992 in partial fulfillment of the requirements for the degree of
Doctor of Philosophy in Civil Engineering

Abstract

This dissertation describes the development of a new laboratory device, referred to as the Automated Plane Strain Reinforcement (APSR) cell, which measures the tensile stresses induced in a planar reinforcement due to shearing of the surrounding soil. The APSR cell applies uniform boundary tractions (σ_1, σ_3) to deform the soil specimen in plane strain compression and can contain a single reinforcement with length, $L/2 \leq 0.45$m. The tensile force in the inclusion is measured by an external load cell at a location corresponding to the center of an inclusion of length, L. The device can impose axial strains of up to 10% on the specimen, while maintaining high quality plane strain conditions through a novel active control system which uses a pressurized water diaphragm within the sidewalls. The automation systems for the APSR cell include five computer control loops and three independent analog feedback circuits. Automation provides great flexibility in test procedures and enables tests to be performed under conditions of stress or displacement control. Radiography is used to evaluate deformations within the specimen while additional instrumentation measures the local strains and/or stresses at locations along the inclusion.

A series of proof tests were performed to evaluate the specimen preparation procedures, influence of boundary friction, uniformity of soil strains and control systems. All tests were performed on unreinforced specimens of dry Ticino sand, deposited by raining in a direction normal to the plane of shearing, at relative densities, $D_r = 30\%$ and 75%. The data are compared with sand behavior reported in other plane strain devices. The initial stiffness, peak strength, and volumetric behavior in the APSR cell are within the range of previous observations for sand sheared in the isotropic plane.

Measurements of load transfer are presented for instrumented steel sheet reinforcements in both dense and loose Ticino sand at a nominal confining pressure, $\sigma_3 = 31$ kPa. The results include complete distributions of tensile stress, from strain gauges located along the inclusion, for reinforcements of lengths $L/2 = 0.09$ to 0.45m. At all locations along the inclusion, the tensile stress is directly proportional to the applied stress ratio, σ_1/σ_3, while the maximum stress occurs at the centerline. The results show that maximum tensile stresses increase significantly with the length of the inclusion, but are less affected by the deposition density.

The measurements of load transfer are compared to predictions from a new shear lag analysis. The predictions are based on elastic properties of the unreinforced sand and steel reinforcement. The observed load transfer behavior in the APSR cell matches closely the shear lag predictions. The analysis describes reliably the effects of inclusion length.

Thesis Co-Supervisor: Dr. **Andrew J. Whittle**
Title: Assistant Professor of Civil Engineering

Thesis Co-Supervisor: Dr. **John T. Germaine**
Title: Principal Research Associate

Acknowledgements

This thesis was the product of support from many people. I thank the members of my thesis committee for their guidance in this work, namely:

Prof. Andrew Whittle, whose creativity sparked the APSR project. He taught me about patience in the midst of adversity.

Dr. John (Jack) Germaine, who provided many of the technical innovations during the course of this research and who kept a realistic perspective on our goals.

Prof. Charles C. Ladd, for his help in evaluating my work and for his excellent teaching.

I am also grateful to the Army Research Office, Program for Advanced Construction Technology, who sponsored the APSR project.

Credit for my sanity as a graduate student goes to many people within the MIT community. I thank: Youssef Hashash, who has been a good friend to me over the last five years, sharing commiseration, skating, ice cream breaks, and homemade falafel; the members of the "APSR team" including Mauricio Abramento, Samir Chauhan, Duncan Black, and Linda Roos, all of whom gave unique insights along the way and made the work much lighter; my office-mate Dante Legaspi for cheerfully tolerating the nightmare of my messy desk; Juan and Chuck (the older and wiser generation); and Arthur and Stephen Rudolph, who patiently showed me the ins and outs of basic machining. I also thank Scott Phelan, Ute Schran, and Mike Toole for making our weekly lunches a success.

Many people have made Boston a great place to call home, particularly Andy Altaner, Debbie MacDonald, and the Newton Presbyterian Sr. High Youth Group. I am also grateful to my good friends William (Bo) Steptoe and Bill Howell, who have stayed faithful over the long haul.

Thank you, Mom and Dad, for encouraging me to look ahead and for giving me the freedom to explore new things since I was very young. And thank you, Bruce, for teaching me about MIT, tempeh, and the guitar.

Out of everyone, I certainly owe the most to Kelly. Our last five years together in marriage have been the best years of my life. I dedicate this thesis to her, and hope that I can reflect to others the love she continually gives to me.

Ultimately, I thank God, Who through His Son taught me how to live and find contentment in all circumstances. Without Him our efforts are meaningless.

Douglas G. Larson

Proverbs 3: 5,6

Table of Contents

List of Tables

List of Figures

Chapter 1: Introduction

The use of geosynthetic materials for soil reinforcement in the construction of retaining walls, embankments, and foundations has been an area of rapid growth over the last fifteen years. Modern soil reinforcement was pioneered by Vidal (1966) through a patented system of retaining wall construction known as "terre armée" (or "reinforced earth"). Vidal's method originally used flat steel strips laid in the soil backfill to produce a composite material which reduced the lateral pressure against the wall face.

The term "geosynthetics" refers to a wide range of polymeric material products which are used in foundation engineering. Geosynthetics include woven and non-woven fabrics, high strength polymer strips and grids, impermeable membranes (geomembranes), and composite materials which are commonly used for filtration and drainage. The first uses of these materials for earth reinforcement are reported by Broms (1977) and Chang et al. (1977). Subsequent production of high strength and stiffness products, such as Tensar grids and Paraweb strips, has led to an increased use of geosynthetics for soil reinforcement applications.

Although geosynthetics have had a significant impact on foundation and earthwork construction practice, much of their success is due to aggressive marketing on the part of the geosynthetics manufacturers. Engineering design methods for reinforced soil systems are largely empirical. As a result, the foundation engineering community has been slow to use the new materials, particularly in critical applications. It has been widely appreciated that one of the most fundamentally important but least understood aspects of soil reinforcement is the mechanical interaction between the soil and

reinforcing inclusions (Mitchell and Schlosser, 1979), particularly at working loads. The mechanisms of interaction are especially complex for inclusions with non-planar surfaces (such as grids), and for materials such as geosynthetics which exhibit non-linear and time dependent behavior. Without this understanding, it is impossible to make reliable predictions of the loads carried by the reinforcement, which in turn controls the selection of material properties in design.

This thesis describes the design and development of a new laboratory apparatus, referred to as the Automated Plane Strain Reinforcement (APSR) cell, for measuring the load transfer between soil and a single planar reinforcement at working load levels. Chapter 2 reviews the measurement and interpretation of soil-reinforcement interaction from laboratory experiments described in the literature. This background study provides the rationale for this research. The chapter shows that the primary limitations of existing tests are due to a) the lack of direct measurements of loads carried by the reinforcing materials, and b) the complex boundary conditions imposed in the tests.

Chapter 3 describes the design of the APSR cell. The cell has the unique capability of measuring the maximum tensile load transferred to a planar inclusion due to plane strain compression shearing of the surrounding soil. The APSR cell imposes well defined boundary conditions (uniform tractions) and can be equipped with additional instrumentation to measure the load distribution within the inclusion. Internal soil strains are measured using radiography.

The APSR cell represents a major departure from pre-existing laboratory equipment used to evaluate soil-reinforcement interaction. Chapter 4 presents results of an extensive proof testing program which has examined: 1) the uniformity of APSR sand specimens (prepared by dry multiple sieve pluviation), 2) the accuracy and precision of

the application and measurement of boundary stresses, 3) the amount of boundary friction between soil specimens and the cell walls, and 4) the precision of an unique active control system for imposing plane strain conditions. The chapter describes the measurement and interpretation of stress-strain behavior for unreinforced Ticino sand which is used as a reference soil. The data are evaluated through comparison with measurements from other plane strain devices reported in the literature.

Load transfer measurements have been obtained for loose and dense Ticino sand reinforced with elastic, steel sheet inclusions. Chapter 5 describes the refinement of test procedures and instrumentation used to achieve reliable and repeatable measurements of the tensile reinforcement loads. The chapter presents results which evaluate how the load transfer is affected by the placement density of the sand and by the length of the reinforcement. The experiments include measurements of the load distribution within the reinforcement and the soil strain fields (based on radiographic measurements) which illustrate the underlying mechanisms of soil-reinforcement interaction.

A parallel research program has focused on the development of theoretical methods for interpreting the load transfer in the APSR cell. Abramento and Whittle (1992) present analytical solutions, based on shear lag approximations, for estimating the tensile loads in the reinforcement as functions of the APSR geometry and the elastic properties of the constituent materials (soil and reinforcement). Chapter 6 summarizes the proposed shear lag analysis and uses these solutions to interpret the APSR cell data.

Chapter 2: Previous Studies of Soil-Reinforcement Interaction

2.1. Introduction

It has been widely appreciated that the most fundamentally important but least understood aspect of soil reinforcement is the interaction between the soil and the reinforcing inclusions (Lee, 1978; Mitchell and Schlosser, 1979; TRB, 1985; NRC, 1989) which determines the magnitudes of the loads carried by the reinforcements and hence controls the selection of material properties. The mechanisms of interaction are particularly complex for inclusions with non-planar geometries, such as grids (e.g., Jewell et al., 1985), and for reinforcing materials such as geosynthetics which exhibit non-linear and time dependent behavior (e.g., McGown et al., 1985).

There are three basic approaches which have been used to represent soil-reinforcement interaction in analysis:

a) equivalent homogenization methods, in which the soil and reinforcement are treated (macroscopically) as a homogeneous, anisotropic composite material;

b) limit equilibrium methods, which evaluate the stability of the reinforced soil in simplified modes of interaction; and

c) explicit modelling of the deformation properties of the constituent materials (soil and reinforcement) and soil-reinforcement interface.

This chapter reviews laboratory experiments which have been used to define input parameters for characterizing soil-reinforcement interaction in each of these types of analysis. The main aim of this review is to identify the capabilities of the existing laboratory devices for estimating load-transfer characteristics (i.e. stresses which develop within the reinforcement) both at working stress levels and at failure. The need for improved studies of load transfer behavior provides the basis for the design of the Automated Plane Strain Reinforcement (APSR) cell, described in Chapter 3.

2.2. Homogenization Methods

2.2.1. Introduction

Homogenization methods typically assume that the soil mass is reinforced with uniform, closely-spaced inclusions ('periodically heterogeneous') such that explicit modelling of load transfer between the soil and reinforcement is not considered. For example, Harrison and Gerrard (1972) derive equivalent elastic moduli for a linear, isotropic soil reinforced with thin, extremely stiff elastic layers. Their formulation generalizes earlier solutions presented by Westergaard (1938) and is based on rules of mixtures for elastic properties of composites (Hill, 1963). The analyses have not been validated experimentally, but similar formulations have been applied in finite element simulations (e.g., Romstad et al., 1976). The strength of the reinforced soil composite was originally described by modifying the classical Mohr-Coulomb failure criterion to incorporate an 'apparent cohesion'[1] due to the reinforcements (e.g., Long et al., 1972; Hausmann, 1976). More recently, Sawicki (1983) and deBuhan et al. (1989) have

[1]Hausmann and Lee (1976) later modified this solution to incorporate soil-reinforcement slip at low confining stress levels.

developed generalized anisotropic failure criteria assuming concurrent frictional failure in the sand and tensile yield of the reinforcements. Homogenization has also been used to estimate the reinforcement stresses by equating tensile strains in the reinforcement with soil strains acting in the same direction. This 'strain compatibility' approach has been used in finite element simulations of reinforced earth as a composite materials (e.g., Romstad et al., 1976) and in the formulation of non-linear constitutive equations (e.g., Juran et al., 1988a,b).

2.2.2. Laboratory Investigations of "Reinforced-Soil Composites"

Measurements of loads (surface tractions) and displacements on the boundaries of soil specimens reinforced with several uniformly spaced inclusions correspond closely to the conditions assumed in homogenization methods. Table 2.1 summarizes experimental data reported in the literature for tests on these 'reinforced-soil composites' in three standard types of shear tests: triaxial (axisymmetric) compression, direct shear box and direct simple shear. In these experiments, properties of the composite are evaluated by comparing boundary measurements for different volume fractions, spacing, and types of reinforcements. The following paragraphs describe typical observations from these tests.

2.2.2.1. Triaxial Tests

The majority of the composite element studies are based on small scale triaxial tests (d = 36-100mm, h = 70-300mm; Table 2.1) performed on sands[2] reinforced with a variety of materials including aluminum foil disks (Schlosser and Long, 1972), fiberglass mesh (Yang, 1972), woven and non-woven geosynthetic fabrics (Broms, 1977), and

[2]Triaxial tests on reinforced cohesive soils were performed by Christie (1982).

brass strainer cloth (Gray et al., 1982). More recently, Fukushima et al. (1988) have presented results from an ultra-large triaxial device (height, h = 2.4m, diameter, d = 1.2m) using Toyoura sand reinforced with metal strips, geogrids, and non-woven fabrics. In most of the tests, the reinforced specimen is initially consolidated under hydrostatic stress conditions, and is sheared at constant cell pressure ($\sigma_3 = \sigma_c$).

Figure 2.1b shows typical results for tests on dry G12 sand, reinforced with a number of layers of fabric (Fodervävdader Teknisk Väv 600). The results show that when the fabric is placed at the ends of the specimen, there is virtually no effect on the externally measured soil response.[3] As additional reinforcements are added, there is a significant increase in the peak shear stress but little change in the apparent stiffness or volumetric strain response. The reinforced specimens fail either by bulging or lateral spreading between layers (Gray et al., 1982). Broms (1977) and Yang (1972) attribute this increase in shear strength to an equivalent increase in confining stress associated with the development of tensile stresses, σ_R, in the reinforcements.

Figure 2.2a illustrates the postulated stress changes in the triaxial test. As the soil is sheared, tensile stresses in the reinforcements, σ_R, cause an increase in apparent confinement, $\bar{\sigma}_3$, within the specimen and hence the measured boundary tractions show an increase in the shear strength of the composite material. Schlosser and Long (1972) report the shear strength envelope (i.e., strength as a function of confining stress) for Fontainbleau sand reinforced with thin aluminum sheets[4] (Fig. 2.2b). At high confining stress levels ($\bar{\sigma}_3 > 40$ kPa), failure occurs by breakage of the reinforcements

---

[3]This is likely due to the fabric being in the 'dead zone' near the frictional ends in the triaxial apparatus.

[4]The typical yield strain for aluminum is $\varepsilon_y = 0.4\%$.

and can be characterized by an equivalent Mohr-Coulomb criterion with friction angle, ϕ (similar to that of the unreinforced sand), and 'pseudo-cohesion,' c_R:

$$c_R = \frac{R_T \sqrt{K_p}}{2 S_R} \tag{2.1}$$

where: R_T is the tensile resistance per unit thickness,

S_R is the vertical spacing of the reinforcement, and

$K_p = \frac{1 + \sin \phi}{1 - \sin \phi}$ is the passive earth pressure coefficient mobilized at failure.

Schlosser and Long (1972) also found that the pseudo-cohesion (c_R) was directly proportional to the volume fraction and tensile strength of the reinforcements. However, similar experiments performed by Yang (1972) using glass fiber sheets gave smaller changes in pseudo-cohesion than were predicted based on tensile strength of the reinforcements.

At lower confining stresses, failure occurs when the soil slips relative to the reinforcement. Hausmann (1976) proposed an empirical expression to describe the transition between the two failure mechanisms (Fig. 2.2b):

$$\sin \phi_R = \frac{1 + f - K_a}{1 - f + K_a} \tag{2.2}$$

where K_a is the active earth pressure coefficient (at peak strength of the unreinforced sand), and f is an empirical 'friction factor' which relates the tensile stresses in the reinforcement to the major principal stress, σ_1.

Christie (1982) estimates the tensile stress which causes rupture of the reinforcement based on a simple analysis of stresses in an elastic disk. Figure 2.2c shows the in-plane tensile stresses σ_{rr} and $\sigma_{\theta\theta}$ for a disk element of outer radius, R, and half-thickness,

t/2, subject to a radial body force, T (equivalent to the shear stresses transferred from the soil). The equilibrium of the plate can be written:

$$r^2 \frac{d^2\sigma_{rr}}{dr^2} + 3r\frac{d\sigma_{rr}}{dr} + T\,t\,r\,(2+\nu) = 0 \qquad (2.3)$$

As a first approximation, Christie (1982) assumes T = constant and hence:

$$\sigma_{rr} = \frac{T\,t}{3}(2+\nu)\,(R-r), \text{ and}$$

$$\sigma_{\theta\theta} = \frac{T\,t}{3}(2+\nu)\,(R-r) + T\,t\,r$$

The maximum tensile stress, $\sigma_{max} = \frac{T\,t\,R}{3}(2+\nu)$ occurs at the center of the plate. Equating σ_{max} with the yield stress of the reinforcement, σ_y, the total load transfer for reinforcement rupture can be written:

$$f_R = \int_0^R \int_0^{2\pi} T\,t\,r\,dr\,d\theta = \frac{3\,\pi\,R\,\sigma_y}{(2+\nu)} \qquad (2.4)$$

For reinforcements with vertical spacing, S_R, this force can be equated to an equivalent reduction in the confining cell pressure, $\Delta\sigma_3$ (cf. eqn. 2.1, $\Delta\sigma_3 \equiv R_T/S_R$):

$$\Delta\sigma_3 = \frac{f_R}{2\,\pi\,R\,S_R} = \frac{3}{2}\frac{\sigma_y}{(2+\nu)\,S_R} \qquad (2.5)$$

One of the major limitations of the small scale tests is that the stresses transferred to the reinforcement are dependent on factors such as the inclusion length and spacing. Thus, the results of the laboratory tests cannot be scaled reliably for analysis of prototype field situations. Fukushima et al. (1988) addressed this problem by performing tests on reinforced Toyoura sand in an ultra-large triaxial apparatus (Table 2.1). Figure 2.3a summarizes the shear strengths for the composite material as functions of the inclusion

spacing (i.e. volume fraction) for geogrids[5], non-woven fabrics, and metal strip reinforcements tested at a confining pressure, σ_3 = 100 kPa. The results show the following:

1) The shear strengths of the geogrid reinforced composites are significantly larger than those measured using either non-woven or metal strip reinforcements, especially for small inclusion spacings, Δh = 30 cm. There is little improvement (< 10%) in the measured strength (for any of the three materials) for inclusion spacings, $\Delta h \geq 100$ cm.
2) The increase in shear strength is not linearly related to the geogrid inclusion spacing (cf. eqn. 2.1). However, changes in shear strength for the metal strip and non-woven fabric in loose Toyoura sand (Fig. 2.3a) are approximately linearly related to the spacing.

Figure 2.3b shows that for a given inclusion spacing, the geogrid reinforcement is especially effective in increasing the shear strength at confining stresses, $\sigma_3 < 100$ kPa. It is important to note that the measurements of shear strength in the large scale triaxial apparatus show much less pronounced effects of the reinforcements than those reported from small scale tests (e.g. Schlosser and Long, 1972; Fig. 2.2b). This reflects a number of factors, including: a) differences in the reinforcing materials and volume fraction of reinforcements, and b) the difficulty in applying homogenization techniques for soils reinforced with a (relatively) small number of tensile inclusions.[6]

---

[5]The authors report that the specimens failed by tensile breakage of the grids in these tests.

[6]Homogenization techniques can be applied with much greater confidence for soils reinforced with random fibers (e.g., McGown et al., 1985) or random continuous filaments (e.g., TEXSOL; John, 1987)

2.2.2.2. Plane Strain Tests

McGown et al. (1978) present similar results of boundary tractions and deformations from a plane strain shear device containing a single planar inclusion oriented in various directions to the major principal stress (θ, Fig. 2.4a).

The Strathclyde plane strain test device contains a specimen of dimensions 152 x 102 x 102mm which is confined by a constant vacuum pressure, $\sigma_3 = 70$ kPa. The major principal stress is applied through rigid top and bottom platens at a constant displacement rate, $\dot{\Delta} = 0.2$ mm/min. The side walls are lubricated and incorporate a 10mm thick glass plate to permit photographic measurements of internal deformations during the test (see section 2.4.1.1.). The walls provide a nominal plane strain constraint on lateral deformations.

McGown et al. (1978) present data for dry Leighton Buzzard sand deposited at three densities (Table 2.1) and reinforced with three different materials: 1) aluminum foil, 2) aluminum mesh, and 3) a melt-bonded, non-woven fabric (T140).

Figure 2.4b summarizes the effect of the inclusion orientation on the peak stress ratio, $\left(\frac{\sigma_1}{\sigma_3}\right)_{max}$, of specimens deposited at relative densities $D_r = 27$, 51, and 65% for non-woven fabric and aluminum foil, respectively. In all of these tests, the maximum strength increase is measured when the inclusion is oriented in the horizontal direction, which corresponds to the direction of principal tensile strains for the unreinforced soil (and confirms observations made by Basset and Last, 1978). For inclusions oriented at angles greater than 45° to 60° to the horizontal, the composite material exhibits a lower shear strength than the unreinforced sand. The authors attribute this loss of strength to the fact that the soil-inclusion interface has lower frictional resistance than the soil itself.

Figure 2.5a and b compares the stress ratio-axial strain measurements for tests with horizontal inclusions on medium dense (D_r = 58 to 65%) and loose (D_r = 11 to 18%) Leighton Buzzard sand, respectively. The unreinforced, dense sand reaches a peak stress ratio, R_{max} = 1.8, at an axial strain, $\varepsilon_{ap} \approx 2.3\%$, and then exhibits strain softening as the specimen slides along shear planes that develop in the specimen. The addition of horizontal inclusions clearly modifies the externally measured composite behavior of the specimen. The aluminum mesh gives rise to a large increase in the peak stress ratio ($R_{max} \approx 13$) and pre-peak soil stiffness. However, the grid has little influence on the strain at peak strength, and the measurements show a very brittle post-peak behavior associated with rupture of the grid. In contrast, the T140 fabric gives rise to a peak shear stress (R_{max} = 10.5) which is mobilized at $\varepsilon_{ap} \approx 4.0\%$, and inhibits the apparent post-peak strain softening of the specimen.[7] Figure 2.5b shows qualitatively similar behavior for reinforced, loose Leighton Buzzard sand.

Based on these results, McGown et al. (1978) characterize qualitative differences between 'inextensible' and 'extensible' reinforcing materials:[8]

1. Inextensible reinforcing materials have rupture strains which are less than the maximum tensile strains in the (unreinforced) soil under the same operational stress conditions. Although these materials can generate large

---

7The authors do not explain why the aluminum foil has such a small effect on the composite stress-strain behavior. Their data show similar in-isolation stiffness properties for both the aluminum grid and foil. One probable explanation is the difference in the interface bond between the inclusion and the soil.

8Gray and Ohashi (1983) identify $E_R/E_S > 3000$ for perfectly inextensible reinforcing materials, where E_R and E_S are the Young's moduli of the reinforcement (in-isolation) and the soil (at the imposed confining stress), respectively.

increases in the apparent shear strength of the composite soil, failure in the reinforcement causes a brittle post-peak loss of shear resistance.

2. Extensible reinforcing materials (e.g., T140 fabric) rupture only at very large tensile strains. These inclusions can increase the apparent shear strength and give the composite greater ductility.

Section 2.4.1.1 discusses internal observations of soil deformations within these tests.

2.2.2.3. Direct (Box) Shear Inclusion Tests

The most comprehensive studies of soil-reinforcement interaction are based on measurements from shear box tests on specimens of dry sand reinforced by inclusions which bisect the imposed horizontal failure plane at various orientations (and preserve symmetry between the two halves of the shear box) as shown in Figures 2.6a and 2.7a. Table 2.2 summarizes the device geometry and pertinent test conditions used in a number of these experimental programs. This section focuses on external measurements of the composite behavior of the reinforced soil, while sections 2.4.1 and 2.4.2 describe more detailed evaluation of reinforcement stresses and soil deformations (using the internal measurements listed in Table 2.2).

Figure 2.6a illustrates the geometry of the Direct Shear Apparatus (DSA) used by Jewell (1980). The cell has dimensions 254 x 152 x 152mm and contains a single plane of reinforcement oriented at an angle θ to the vertical direction. The specimen is consolidated under a vertical load, N, which is applied through a rigid platen. During shear, the platen is locked to the top half of the shear box to prevent rotation and ensure symmetry about the mid-plane of the specimen. Jewell and Wroth (1987) report boundary tractions and displacements for tests performed using dense Leighton Buzzard sand (D_r = 100%) reinforced with close-coiled steel tension springs of length,

L = 127mm. Figure 2.6b compares the effects of axial stiffness[9] for inclusions oriented at $\theta = 25^{\circ}$ to the vertical:

1. The presence of reinforcement does not affect the initial stiffness of the composite material. However, there is a significant improvement (up to 50%) in the shear resistance at relatively small lateral displacements, $\bar{x}$ = 1.3mm (which corresponds to the peak strength of the unreinforced sand).
2. For the stiff, inextensible reinforcement, the peak shear resistance is mobilized at a displacement $\bar{x} \approx$ 2mm (F, Fig. 2.6b). Continued shearing causes a post-peak reduction in shear resistance which is parallel to that of the unreinforced sand (there is no failure of the reinforcement in these tests).
3. For the 'extensible', low stiffness inclusion, the peak shear resistance is mobilized at a much larger displacement ($\bar{x} \approx$ 4.7mm; i.e., G in Fig. 2.6b). The post peak shear resistance is independent of the axial stiffness of the inclusion.

The underlying mechanism of soil reinforcement in these tests can be readily appreciated by considering the force equilibrium for one half of the shear box (Fig. 2.6c). When a tensile force, P_R, develops at the center of the inclusion, there are two mechanisms which give rise to an apparent increase in the shear resistance:

1. The component of reinforcement force in the horizontal direction reduces the shear force which the sand must support by an amount, $P_R \sin \theta$.
2. The vertical component ($P_R \cos \theta$) increases the normal force acting on the imposed shear plane, thereby increasing the available shear resistance of the sand.

---

[9]The axial stiffness of the steel spring was increased by inserting a steel rod inside the spring.

The average horizontal shear stress which the sand must support along the horizontal plane then becomes:

$$\tau = \tau_{yx} - \frac{P_R}{A_s} \sin \theta \tag{2.6}$$

and hence the apparent reduction in applied shear stress is:

$$\Delta\tau_{applied} = \tau_{yx} - \tau = \frac{P_R}{A_s} \sin \theta \tag{2.7}$$

Similarly, the vertical component of the tensile force in the reinforcement causes an increase in the vertical stress acting on the shear plane:

$$\Delta\sigma_{yy} = \frac{P_R}{A_s} \cos \theta \tag{2.8}$$

where A_s is the cross-sectional area of the central plane in the DSA. Hence, the change in available shear resistance due to the increased normal stress is:

$$\Delta\tau_{avail} = \frac{P_R}{A_s} \cos \theta \ \tan \phi' \tag{2.9}$$

where ϕ' is the average mobilized friction angle in the soil.

Combining equations 2.7 and 2.9, the overall change in shear resistance is:

$$\tau_{ext} = \frac{P_R}{A_s} (\cos \theta \ \tan \phi' + \sin \theta) \tag{2.10}$$

Gray and Ohashi (1983) describe a set of direct shear tests on Muskegon beach sand (D_{50} = 0.23 mm, C_u = 1.5) reinforced with various fibers (with diameter 1 to 2.2mm, length, L = 2 to 25cm; Table 2.2). The purpose of these tests was to study how the density and orientation of the fibers affect the strength of the reinforced soil composite in direct shear. The tests were performed in a standard shear box, in which the normal

load, N, is applied through a rigid top platen and the horizontal shear force, T, by a hand crank.

The authors interpret their results based on the model shown in Figure 2.7a. The model assumes that the reinforcing fibers extend through a well defined shear zone of width, z. As the soil deforms, the inclusions develop a tensile stress, σ_t, which can be divided into a component normal and tangential to the shear plane (cf. Jewell and Wroth, 1987). The normal component ($\sigma_t \cos \hat{\theta}$) increases the confining stress on the failure plane, while the horizontal component ($\sigma_t \sin \hat{\theta}$) reduces the applied shear stress in the same plane. For fibers which are initially vertical, the net change in shear resistance can be written:[10]

$$\Delta S = \frac{A_r}{A_s} \sigma_t [\sin \hat{\theta} + \cos \hat{\theta} \tan \phi'] \qquad (2.11)$$

where: $\hat{\theta}$ is the angle of shear distortion in the failure zone (Fig. 2.7b),
$\frac{A_r}{A_s}$ is the cross-sectional area ratio of fibers to soil in the central plane of the soil, and
σ_t is the mobilized tensile stress in the fibers.

For fibers which are initially oriented at θ^o to the vertical, the increase in shear resistance is given by:

$$\Delta S = \frac{A_r}{A_s} \sigma_t [\sin (90 - \psi) + \cos (90 - \psi) \tan \phi'] \qquad (2.12)$$

where ψ is the distortion angle for a horizontal displacement x across the shear zone.(Fig. 2.7b).

---

[10]It is assumed that the fibers are thin and have negligible bending resistance.

Assuming that the width of the shear zone is independent of the reinforcement area ratio, then the model of Gray and Ohashi shows that the increase in shear strength of the soil is proportional to A_r/A_S.

Figure 2.8 shows typical results of the external stress-displacement for a reed fiber reinforced soil composite with different area ratios of reinforcement. The fibers do not affect the initial stiffness of the composite. However, the peak shear resistance and displacement at peak resistance both increase with fiber area ratio. Gray and Ohashi (1983) report that the increase in shear resistance is proportional to the cross-sectional area ratio for $A_r/A_S \leq 1.7\%$, using a variety of reinforcing materials. The composite strength envelope (Fig. 2.8b) is qualitatively similar to the behavior measured in triaxial tests (cf. Fig. 2.2b).

Figure 2.9 summarizes measurements of the peak shear resistance in direct shear box tests as a functions of the inclusion orientation, θ, for close-coiled steel tension springs (Jewell and Wroth, 1987) and reed fiber reinforcements (Gray and Ohashi, 1983). Both sets of data show that the greatest improvement in shear resistance occurs when the inclusions are oriented at approximately $\theta = 30^o$ to the vertical. Detailed measurements of internal deformations (by radiographic and photographic methods, section 2.4.1) show that the principal tensile strains in the unreinforced soil are oriented at approximately 30^o to the vertical[11] (at locations along the central plane of the shear box). Thus, the observations of composite behavior are consistent with earlier observations (McGown et al., 1978; Basset and Last, 1978) that the tensile

---

[11]For slender fibers, the shear strength is minimized when fibers are oriented orthogonal to the principal tensile strains (i.e., at $\theta = 120^o$). In comparison, the rough steel sheet gives a small strength increase at $\theta = 120^o$ which is not explained by Jewell and Wroth (1987).

reinforcements are most effective when they are oriented parallel to the direction of principal tensile soil strains.

Palmeira (1987) presents a detailed comparison of the reinforcing capabilities of typical materials used in earthwork construction, using a large scale direct shear apparatus (Fig. 2.10a). This device overcomes some of the limitations of small scale laboratory tests. It contains a soil specimen 1 x 1 x 1m, which is sheared by a 600 kN hydraulic jack at a horizontal displacement rate, $\dot{\Delta} = 0.5$ mm/min. Uniform vertical stresses are applied to the top of the specimen through a water bag, up to a maximum pressure, σ_y = 150 kPa. The specimen boundaries are lubricated with a double layer of Castor grease, oil, and polyethylene sheet. Table 2.2 summarizes the extensive internal instrumentation used in the device, which is discussed later in section 2.4.1.2.

Palmeira (1987) performed extensive verification tests on unreinforced sand (Fig. 2.10b) which show that the large shear box measures similar peak shear resistance to that obtained using standard devices with much smaller dimensions, 60 x 60 x 32mm. However, there are significant differences in the pre-peak stiffness, shear band thickness, and post-peak strain softening response obtained in the two shear boxes.

Figure 2.11a and b compares the shear stress vs. displacement measured for the composite soil reinforced with:

- smooth and rough (mild) steel sheet,
- metal grids of varying axial stiffness and geometry (Fig. 2.11a),
- two polyethylene geogrids, and
- two woven polyester geotextiles.

All of the tests were performed using dense Leighton Buzzard sand ($D_r \approx 87\%$) under a vertical confining pressure, σ_y = 30 kPa, with a single vertical ($\theta = 0^o$) plane of

inclusions of length, L = 600mm. The composite behavior measured for the roughened steel sheet corresponds to the maximum reinforcing effect which can be obtained for a planar inclusion in which the load transfer occurs solely due to interface friction. Similar reinforcing behavior is measured (Fig. 2.11a) for steel grids of comparable axial stiffness (but dissimilar surface contact area). For all of the steel reinforcements, the peak shear resistance is mobilized at lateral displacements, $\bar{x}$ = 12 to 20 mm. The measurements for typical polymeric geogrid and geotextile materials (whose axial stiffness is up to two orders of magnitude smaller than the steel sheet) show that the maximum reinforcing effect occurs at large shear displacements ($\bar{x}$ > 40 mm). The peak shear stress ratio is not affected significantly by the axial stiffness of the metal grids. The two synthetics generate smaller shear resistance over the range of displacements measured in the tests ($\bar{x} \leq$ 50 mm). However, the shear resistance at large displacements is generally greater or equal in magnitude to that measured for the roughened steel sheet (whose axial stiffness is up to two orders of magnitude larger).

2.2.2.4. Direct Simple Shear Tests

The direct shear box apparatus imposes highly non-uniform stress and strain conditions and generates large shear distortions within a relatively small volume of the soil. These factors can affect the scaling of results from shear box inclusion tests, and complicate significantly the rational interpretation of soil-reinforcement interaction. Hayashi et al. (1988) constructed a direct simple shear device (Fig. 2.12a) which eliminates some of the non-uniformity problems created by direct shear box tests. The apparatus contains a 20 x 20 x 20cm cubical specimen inside a thin (0.3mm) latex rubber membrane. The side walls comprise a stack of 20 thin aluminum frames with a system of bearings and guide rods which allows the frames to slide freely past one another in a horizontal plane. A rigid frame holds the top of the shear cell fixed while the loading is imposed

by displacing the bottom of the cell. A rubber pressure bag at the top of the specimen imposes a uniform vertical stress. The deformed shape of the specimen can be changed by locking some of the shear frames together (Fig. 2.12b) and can reproduce a variety of shear modes ranging from a rigid walled shear box to a 'zone simple shear' similar to that analyzed by Gray and Ohashi (1983) (Fig. 2.7).

Hayashi et al. (1988) present preliminary results for dense Toyoura sand (D_r = 82%, σ_v = 75 kPa) reinforced with a set of 12 evenly spaced phosphor bronze bars[12] made fully rough by gluing sand to their surfaces. Figure 2.12c summarizes the reinforcement performance[13] of the composite in direct simple shear as a function of the inclusion orientation, θ, at three shear strains, γ = 5, 10, and 15%. The results show the following:

1. The composite provides maximum shear resistance for θ = 5 to 10°, at all strain levels.
2. The reinforcement increases the shear resistance of the sand by 10 to 50% for $-15° \leq \theta \leq 20°$.

More comprehensive studies of composite behavior are currently in progress at Kyushu University (Ohiai, 1992).

2.3. Parameters for Limit Equilibrium Analyses

Current design methods for reinforced soil masses, including retaining walls (e.g., Bonaparte and Schmertmann, 1987; Jewell, 1990; Gourc et al., 1986), embankments

---

[12]The inclusions were instrumented with strain gages to measure the local tensile strains.

[13]The reinforcing effect is shown by $R = \tau_{reinf}/\tau_{unreinf}$, where $\tau_{unreinf}$ is the strength of unreinforced Toyoura sand. Note: $\tau_{ext} = (R - 1)\,\tau_{reinf}$.

(e.g., Koerner et al., 1987) and slopes (e.g., Leshchinsky and Volk, 1985), are all based on limit equilibrium analyses which treat the soil-reinforcement interaction in a highly simplistic fashion. For example, Figure 2.13 shows two possible failure mechanisms for a reinforced earth wall. Stability of the structure is maintained either

a) through shear resistance along the soil-reinforcement interface (A; Fig. 2.13), or

b) through tensile (and bending) stresses generated in the reinforcement, which are resisted by a bond or anchor length in the stable soil mass (i.e., pullout mode B, Fig. 2.13).

At locations where the (assumed) failure plane in the soil intersects the reinforcement (e.g., C; Fig. 2.13), the interaction can be simulated by reinforced direct shear box or direct simple shear tests (sections 2.2.1.3 and 2.2.1.4). Input parameters for characterizing the soil-reinforcement interaction mechanisms A and B are conventionally obtained from direct shear box interface and pullout tests. The following paragraphs describe these measurements.

2.3.1. Direct Shear Interface Tests

In a classic paper, Potyondy (1961) describes shear box tests to measure interface friction, δ, between sands and various construction materials[14] (timber, concrete, and steel). In these experiments, the lower half of the standard shear box is replaced by solid material. The interface friction angle is measured directly:

---

[14]Similar measurements have been made more recently by Uesugi and Kishida (1986a, b) using a direct simple shear apparatus. This equipment permits reliable measurements of interface friction at large shear strains.

$$\tan \delta = \tau / \sigma_n \qquad (2.13)$$

with $\sigma_n = N / A_S$ and $\tau = T / A_S$, where N and T are the applied vertical and shear forces and A_S is the initial cross sectional area of the contact.

Reliable measurements of interface friction are more difficult to achieve for extensible reinforcing materials such as geosynthetics, and for materials with irregular surface profiles such as grids. Figure 2.14 illustrates typical designs of shear boxes used to measure interface friction for geosynthetic reinforcements. There are two basic designs:

a) fixed boxes, in which a 'conformable' reinforcement is wrapped around a dummy block in the lower part of the cell, and
b) free boxes, in which the inclusion is sandwiched between soil layers.

Neither design is completely satisfactory. The clamping arrangement suppresses the deformation of the reinforcing material (e.g., Richards and Scott, 1985) and the vertical stress distribution acting on the central plane of the shear box is non-uniform due to the boundary friction.[15]

For planar reinforcements with flat surface profiles, the shear resistance is due almost exclusively to interface friction. Figure 2.15 summarizes measurements of the interface friction angle, δ', and the peak friction angle, ϕ'_{DS}, measured in unreinforced direct shear tests for a variety of reinforcing materials. The great majority of the data show interface friction angles, δ', in the range of $0.7\,\phi' \le \delta' \le \phi'$, and are consistent with data reported previously by Potyondy (1961). Much lower interface friction is measured for metal reinforcement with smooth surfaces.

---

[15]Jewell (1980) proposes a trapezoidal normal stress distribution for interpreting direct shear box interface tests.

2.3.2. Pullout Tests

Pullout tests, which simulate the action of the reinforcing inclusion as an anchorage, have been investigated in laboratory (e.g., Chang et al., 1977; Juran et al., 1988) and field tests (e.g., Schlosser and Elias, 1978) at a variety of scales (Fig. 2.16). In the standard interpretation of these tests, it is assumed that:

a) the full shear resistance is mobilized over the embedded surface area of the inclusion at the pullout load, and

b) the normal traction acting at the interface is equal in magnitude to the vertical boundary stress applied on the specimen.

The average shear resistance, τ_b, at peak pullout force, P_p, is given by:

$$\tau_b = \frac{P_p}{A_r} \tag{2.14}$$

where A_r is the embedded surface area of the reinforcement and τ_b is a measure of the 'bond' between the soil and reinforcement. Thus, the apparent friction $\hat{\delta}$ can be reported as:

$$\tan \hat{\delta} = \frac{\tau_b}{\sigma_v'} \tag{2.15}$$

where $\sigma_v' = N / A_s$ is the average vertical stress applied to the soil.

In practice, this interpretation is overly simplistic and there are a number of severe limitations associated with pullout tests:

1. The measurements can be affected significantly by the boundary conditions of the test.

2. Deformation of extensible reinforcing materials can introduce a progressive failure mechanism, and hence test results are affected by the length of the inclusion.[16]
3. The pullout capacity of grid reinforcements is controlled by mechanisms of bearing resistance between the soil and transverse elements of the grid.

Figure 2.17 illustrates the complex mechanism of grid pullout resistance from photoelastic measurements (Dyer, 1985). Jewell et al. (1984) and Palmeira and Milligan (1989) proposed semi-empirical methods for interpreting the bond resistance due to interference between bearing members of the reinforcing grid.

Figure 2.16 illustrates the variety of designs used in laboratory and field pullout tests to overcome intrinsic limitations associated with boundary conditions. The designs focus on three issues:

1. the uniformity of vertical stresses imposed externally on the soil,
2. the design of the slot where the reinforcement exits from the shear box, and
3. control of the embedded length of the inclusion.

Recent data from test devices using rigid top platens and flexible pressure bags (e.g., Palmeira, 1987; Fig. 2.16) suggest that the vertical boundary condition does not affect significantly the pullout measurements.[17] Similarly, the inclusion length is only an important factor for estimating the large displacement anchor resistance and has little influence on the peak bond capacity for reinforcing materials of practical interest.

---

[16]This factor explains, in large part, recent designs of large scale laboratory pullout tests (e.g., Koerner and Wayne, 1990).

[17]These results apply for pullout boxes with height to length aspect ratios, $h/L \geq 0.6$.

The boundary condition at the front wall, however, can affect significantly the measured data. In conventional pullout tests, there are large shear stresses acting at the soil-reinforcement interface, close to the front wall of the cell. Thus, boundary 'friction' between the soil and the cell wall can affect the pullout measurements. Figure 2.18 shows that wall lubrication can cause a 100% change in the measured bond capacity for a pullout test performed on a steel grid reinforcement in dense Leighton Buzzard sand (Palmeira and Milligan, 1989). Due to the practical difficulty in lubricating the front face, many pullout tests use an intruded slot (Fig. 2.16; Juran and Christopher, 1989) which separates the inclusion from the front face. Although this approach is more consistent with conditions assumed in limit equilibrium analyses, there have been no systematic studies to compare results from different pullout box designs.

Figure 2.15b compares measurements of the apparent interface friction angle, $\hat{\delta}$, from pullout tests with the reference direct shear friction angle of the soil, ϕ'_{DS}, for a variety of reinforcing materials with planar surface profiles. The data show greater scatter than similar comparisons from shear box interface tests, especially for geotextile reinforcements pulled out at low confining pressures. However, overall there is reasonable agreement in the measurements of interface friction from the direct shear and pullout tests. For grid reinforcements, there are large differences in the bond capacity for these two modes of interaction (e.g., Ingold, 1982; Jewell et al., 1984), as demonstrated in Figure 2.19 which compares interface friction measurements from several direct shear and pullout tests over a range of confining pressures. The tests highlight the difficulty of determining $\hat{\delta}$ accurately for grid reinforcements.

2.4. Local Measurement of Soil-Reinforcement Interaction

The previous sections described global interpretations of the strength of reinforced soil composites in various modes of shearing, and laboratory measurements for estimating parameters in limit equilibrium analyses. This section describes measurements which provide more detailed insights on soil-reinforcement interaction, including: a) qualitative observations of mechanisms, and b) quantitative evaluation of tensile stresses in the reinforcement.

2.4.1. Deformations, Strains, and Stresses within the Soil

2.4.1.1. Plane Strain Device

McGown et al. (1978) present measurements of the internal soil strains for plane strain compression of Leighton Buzzard sand reinforced with a single, horizontal layer of aluminum mesh and non-woven geotextile fabric. The strains are interpreted from photographic measurements[18] of the displacements of a grid of markers placed within the soil mass using a stereo-viewing photogrammetric technique (Butterfield et al., 1970).

Figure 2.20 shows contours of the volumetric (ε_{vol}) and maximum shear strain ($\gamma_{max} = \varepsilon_1 - \varepsilon_3$) components for a reference test on dense, unreinforced Leighton Buzzard sand at applied axial strains, $\varepsilon_a = 2.8\%$ and 5%. These results correspond to conditions at peak shear resistance and in the post peak regime, respectively (cf. Fig. 2.5). At peak shear strength, there are significant non-uniformities in both ε_{vol} and γ_{max}, which

[18]The side walls of the device were made of 10mm thick glass plate.

ranges from 4% near the specimen corners to 10% at the center of the top and left faces. This behavior is probably due to boundary conditions including friction mobilized on the plane strain walls and loading platens. The data show a dramatic localization of shear strain at $\varepsilon_a = 5\%$, which indicates the formation of a failure plane through the specimen,[19] parallel to the plane strain direction.

Figure 2.21 summarizes similar results for the aluminum mesh and non-woven fabric reinforcements. At peak shear resistance, the reinforcement reduces significantly the volumetric strains occurring at the center of the specimen while inducing large shear strains at the same location. These results indicate that the reinforcement reduces the tendency of the soil to dilate and causes a significant rotation of principal strain directions locally within the specimen. The aluminum mesh reinforcement fails in tension and there is a large post-peak softening associated with shear band formation through the plane of the inclusion (Figure 2.21a). In comparison, the non-woven fabric continues to reinforce the soil at large strain conditions where failure initiates in the soil away from the plane of reinforcement. McGown et al. (1978) summarize these results qualitatively by concluding that the reinforcement inhibits lateral deformation in the soil.

2.4.1.2. Direct Shear Box Inclusion Tests

More comprehensive studies of soil deformations and stress conditions have been investigated in direct shear box inclusion tests using techniques of radiography (Jewell, 1980), photoelasticity (Dyer, 1985; Table 2.2), and photographic measurement

---

[19]The failure plane is oriented at approximately 66^o to the horizontal, corresponding to an apparent angle of friction, $\phi' = 2\,(66^o - 45^o) = 42^o$ which is actually less than the mobilized friction based on boundary tractions: $\phi' = \sin^{-1}\frac{\sigma_1' - \sigma_3'}{\sigma_1' + \sigma_3'} = 51^o$.

(Palmeira, 1987). Figure 2.22 shows typical photoelastic measurements reported by Dyer and Milligan (1986) for direct shear box tests on a specimen of crushed glass[20] reinforced with a single perforated brass inclusion placed at three different orientations ($\theta = 40°$, $0°$, and $-15°$) to the direction of applied shear traction. The light stripes indicate the principal stress trajectory in the soil, while the magnitude of the stress is shown by the intensity of the stripes. The results show the following:

1. The reinforcement has the greatest strengthening effect at $\theta = 40°$, where it is oriented normal to the direction of major principal stress in the soil (σ_1 acts at $\theta = -53°$ in tests without reinforcement). At this orientation, there is a concentration of large compressive stresses acting normal to the reinforcement (Fig. 2.22a).
2. The reinforcement has virtually no effect on the soil stress distribution at $\theta = -45°$. In this orientation, the reinforcement undergoes primarily axial compression.
3. The reinforcement acts in both shear and bending when placed perpendicular to the failure surface ($\theta = 0°$, Fig. 2.22c), resulting in complex modification of stresses in the soil.

Figure 2.23 shows the directions and magnitude of principal strains (ε_1, ε_3) interpreted from photographic measurements of soil deformations at peak stress ratio for large shear box tests on dense Leighton Buzzard sand (Palmeira and Milligan, 1989). The results for the unreinforced sand (Fig. 2.23a) give an indication of the vertical

---

[20]Photoelasticity (Wakabayashi, 1957) requires that the solid material and pore space have the same refractive index. Dyer used crushed glass to simulate a granular soil, while the pore spaces were filled with clear liquid paraffin. The shear box was fitted with perspex sidewalls to allow light to pass through the entire assembly, enabling photoelastic observations of the stress fields in the glass.

dimension of the failure zone[21] in which the principal tensile strain acts at $\theta = +32 \pm 5^{o}$ to the vertical direction.[22] When the specimen is reinforced with a metal grid inclusion oriented at $\theta = +30^{o}$ to the vertical, there is a dramatic reduction in the soil strains in the vicinity of the inclusion and there is no well defined failure plane passing through the specimen. These results confirm the role of the tensile reinforcement in suppressing tensile strains in the soil.

Palmeira (1987) also measured normal stress components acting locally at a number of locations within the large shear box. Figure 2.24a shows measurements of the incremental horizontal stress, $\Delta\sigma_x$, acting on the cell wall at peak shear resistance for tests using a variety of reinforcing materials oriented at $\theta = 0^{o}$ and 30^{o} to the vertical direction. The results show that the horizontal stress is non-uniform and decreases with elevation relative to the center plane of the specimen. The stress distribution is similar for both the unreinforced and reinforced specimens, which indicates that these non-uniformities are controlled by the boundary conditions and geometry of the shear box itself.

Equilibrium considerations show that if the horizontal stresses vary in a vertical plane (as in Fig. 2.24a), then the vertical stresses acting along the center plane of the specimen must also be non-uniform. Figure 2.24b shows an assumed trapezoidal distribution of vertical stresses for the unreinforced sand which satisfy equilibrium requirements for the upper half of the shear box (based on the measured horizontal stress distribution, Fig. 2.24a, and applied vertical stress $\sigma_y = 30$ kPa). Local

---

[21]The authors show that the size of the shear zone, z, depends on the dimensions of the shear box. Palmeira (1987) reports z/H = 0.05 to 0.15, where H is the height of the specimen.

[22]Note the difference in displacement direction in Figures 2.22 and 2.23.

measurements of vertical stress close to the central plane, σ_{yr} (located approximately 20mm from the central plane), show that the reinforcement causes a large increase in the vertical stress (up to a factor of 3) along the centerline. This result confirms that the primary effect of the reinforcement is to increase the available shear resistance along the imposed failure plane due to tensile stresses in the reinforcement. The local measurements of the stress component σ_{yr} confirm that the available shear resistance is not uniform across the central plane of the shear box.

Finally, Figure 2.24c presents measurements of the local stress acting normal to the surface of the reinforcement. These results illustrate the amplification of confining stress observed in photoelastic measurements (cf. Fig. 2.22a) which prevent bond failure between the soil and reinforcement.[23]

2.4.2. Deformations of the Reinforcement

Deformations of the reinforcement in direct shear box inclusion tests have been reported by a number of authors, notably Shewbridge and Sitar (1989), and Palmeira and Milligan (1989). Figure 2.25 summarizes the deformed shapes of reinforcements measured by a photographic technique at peak stress ratio in large shear box tests (Palmeira, 1987). The results show that flexible reinforcements tend to conform to the deformed shape of vertical planes in the unreinforced sand, while grid reinforcements with higher bending stiffness show smaller deformations. The distortion of the

---

[23]The limiting frictional bond force for a planar reinforcement can be written:

$$F_R = \int_0^{L_r} 2\, \sigma_n'(x) \tan \delta'\, dx \quad \text{per unit width.}$$

reinforcement from its original alignment, β (Fig. 2.25), is relatively small ($\leq 5^{o}$) at peak shear resistance.

Shewbridge and Sitar (1989) made detailed studies of the deformed shapes of fiber-type reinforcements as a function of the area fraction A_r/A. Their tests (see Table 2.2) were performed on compacted, dense Monterey sand using various reinforcing materials including bungy and parachute cords, wooden dowels, and metal rods. The test apparatus comprises a medium size box (0.76 x 0.40 x 0.14m; Fig. 2.26a) containing inclusions of length, L = 0.75m, which shears the sample in a horizontal plane.[24] A uniform layer of lead shot applies the vertical confining stress (σ_y = 10.25 kPa in all tests) while the shear force is controlled by a hand operated hydraulic hack and measured by a proving ring. The apparatus has a glass bottom to allow direct observation of the deformed shape of the reinforcements.

The authors find that the deformed shape of the inclusions can be characterized by an exponential decay function:

$$\Delta_x = \frac{1}{2}\delta_x (1 - e^{b/y}) \qquad (2.16)$$

where: Δ_x is the lateral deformation of the fiber,
δ_x is the shear displacement applied externally,
y is the dimension normal to the shear plane (Fig. 2.26b), and
b is an empirical constant.

The parameter b gives an indication of the thickness of the shear zone and the distribution of shear strains within it (Shewbridge and Sitar, 1989). Figure 2.26c

---

[24]The specimen is not perfectly symmetrical about the central plane (Fig. 2.26a).

shows that b depends on the axial stiffness of the reinforcements and the density of the fiber reinforcement. In general, the size of the shear zone increases (i.e., b reduces) with increasing stiffness and density of reinforcements. Thus, the authors show that the increase in shear resistance, ΔS (eqn. 2.12) is not linearly related to the fiber density (Fig. 2.26c). This result contradicts earlier studies by Gray and Ohashi (1983) which assumed a constant shear zone thickness.

2.4.3. Evaluation of Tensile Force in the Reinforcement

There are currently no direct measurements of tensile forces which develop in the reinforcement due to shearing of the surrounding soil.[25] Jewell and Wroth (1987) report maximum tensile stresses (at peak shear resistance) based on radiographic measurements of the elongations of steel spring reinforcements. Similarly, Palmeira and Milligan (1989) estimate tensile stress from photographic measurements of markers placed on polymeric grid reinforcements (and from yield strains of metal grids). The authors do not explain the accuracy of these measurements and the results must be viewed with caution, especially for stiff reinforcements where axial strains are very small.

Maximum tensile stresses can be interpreted with reasonable reliability at the peak shear resistance in shear box inclusion tests using limit equilibrium analysis (e.g., Palmeira, 1987). Figure 2.27 shows that the maximum reinforcement force, P_r, can be obtained as follows:

---

[25]Hayashi et al. (1988) do report stresses based on strain gage measurements for phosphor bronze inclusions.

$$\frac{P_r}{A_s \sigma_y'} = \frac{\frac{\bar{\tau}_{yx}}{\sigma_y'} - \tan \phi_{ds}'}{\sin (\theta + \beta) + \cos (\theta + \beta) \tan \phi_{ds}'} \qquad (2.17)$$

where: σ_y' and $\bar{\tau}_{yx}$ are the average applied vertical and shear stresses,

ϕ_{ds}' is the mobilized friction angle in the unreinforced sand,

θ is the initial orientation of the inclusion, and

β is the centerline distortion of the reinforcement at peak shear resistance (cf. Fig. 2.25).

In order to apply this equation, the average vertical stress on the central plane, σ_{yr}', must also be estimated:

$$\frac{\sigma_{yr}'}{\sigma_y'} = \frac{\tan (\theta + \beta) + \bar{\tau}_{yx}/\sigma_y'}{\tan (\theta + \beta) + \tan \phi_{ds}'} \qquad (2.18)$$

In general, $\tan \phi_{ds}'$ depends on the confining pressure σ_{yv}', and therefore equations (2.17) and (2.18) must be solved iteratively.

Jewell and Wroth (1987) develop a more comprehensive prediction of the maximum frictional bond[26], P_{rl}, that can develop between the reinforcement and soil in a direct shear box inclusion test. They assume that, at peak shear resistance, the principal stress directions in the soil are co-axial with the strain increments. The stress component normal to the reinforcement (in its undeformed configuration) can then be computed from the Mohr circle of stress:

---

[26]This analysis applies only for frictional reinforcements, whose bond strength is controlled by the interface friction angle, δ' (section 2.3.1).

$$\sigma_n'(\theta) = \sigma_y' \left\{ \frac{1 + \sin \phi_{ps}' \sin (\phi_{ps}' + 2\theta)}{\cos^2 \phi_{ps}'} \right\} \qquad (2.19)$$

where ϕ_{ps}' is the peak friction angle measured in a plane strain shear test.[27] Assuming that the maximum shear resistance of the reinforced composite occurs when the interface bond resistance is mobilized, then $P_r \rightarrow P_{rl}$. Figure 5.27c compares predictions of the increase in shear resistance for the composite with measurements obtained for dense Leighton Buzzard sand reinforced with a single, rough steel sheet. The predictions are in good agreement with the measured data for $-10^o \leq \theta \leq 90^o$ for the selected values of ϕ_{ps}' and δ'.

The above interpretations can only be used reliably in cases where the full frictional resistance of the soil is mobilized. In contrast, Shewbridge and Sitar (1989) have developed an analysis for interpreting development of tensile stresses based on the measured deformations of the reinforcing fibers. The authors assume that the maximum tensile stress at the center of the fiber reinforcement can be written:

$$P_r = 2 \pi r \tau_s \hat{1} \qquad (2.20)$$

where: $\tau_s = \frac{1}{2}(1 - K)\, \sigma_1 \tan \delta'$ is the maximum shear resistance acting along the reinforcement-soil interface,

δ' is the interface friction angle,

K is a constant controlling the normal stress on the reinforcement (equivalent to $\sigma_n'(\theta)$ in eqn. 2.19), and

---

[27]For unreinforced sand, Rowe (1969) relates ϕ_{ps}' and ϕ_{ds}' by:

$$\tan \phi_{ds}' = \tan \phi_{ps}' \cos \phi_{cv}'$$

where ϕ_{cv}' is the constant volume friction angle which is typically $\phi_{cv}' = 32 \pm 3^o$.

$\hat{l}$ is the length of the reinforcement in tension.

For elastic reinforcements, $\hat{l}$ is obtained numerically by matching the elongation of the fiber with the observed deformation (using eqn. 2.16). Although the authors present comparisons with measured data, they do not state a clear rationale for selecting K, and use assumed values of δ. As a result, it is not possible to establish the reliability of this method for estimating stresses in the reinforcement.

2.5. Conclusions

This chapter reviews existing laboratory measurements of soil-reinforcement interaction grouped in three main categories:

1. deformation and shear strength properties of reinforced soil composites, interpreted using homogenization methods,
2. parameters of soil-reinforcement 'bond' resistance (from interface shear and pullout tests) used in limit equilibrium analyses, and
3. more detailed observations of mechanisms of soil-reinforcement interaction from local measurements of deformations, stresses, and strains.

Composite material behavior has been reported for a variety of shear modes including triaxial and plane strain compression, direct shear (in shear box) and direct simple shear. The test data include results for a wide range of reinforcing materials using single and multiple inclusions with various geometries (fibers, planar sheets, grids, bars, dowels, etc.). In all cases, the reinforcements exhibit relatively high tensile stiffness and strength, and relatively low bending stiffness. The main results of these studies can be summarized as follows:

1. The reinforcements can increase the apparent shear strength of the composite most significantly when they are oriented in the direction of principal tensile strains for the unreinforced soil.
2. The data show consistent trends in the stress-strain response of the composite as a function of the axial stiffness and strength of the reinforcing materials for stiff reinforcements with well defined yield. Peak shear resistance of the composite occurs at similar strain levels to the unreinforced soil, while brittle post-peak behavior can occur if the reinforcements rupture. For most extensible reinforcements, the peak strength of the composite is mobilized at large shear strains corresponding to more ductile behavior.
3. The shear strength of the composite increases with the density of the reinforcing inclusions. However, there is no underlying framework for estimating the strength properties as a function of the properties of the constituent components (soil and reinforcing material) and geometry. This result reflects a major limitation in applying homogenization methods for soils reinforced with a relatively small number of tensile reinforcements.[28] As a result, measurements of composite behavior in small scale laboratory tests can't be reliably used to estimate the performance of prototype reinforced soil structures (i.e., at field scale). Scale effects in the laboratory tests include the size of the shear apparatus, non-uniformities associated with boundary conditions, reinforcement length (and other characteristic dimensions such as grid aperture) and spacing (density).

---

[28]As compared to systems where soil is mixed with random fibers or continuous filament systems (e.g., TEXSOL; John, 1987).

In practice, limit equilibrium analyses are widely used to estimate the stability of reinforced soil structures. These calculations require input parameters to characterize the bond resistance[29] between the soil and reinforcement in two modes: 1) direct shearing along the soil-reinforcement interface, and 2) tensile anchorage within the stable soil mass. In practice, these parameters are obtained from direct shear box interface tests and pullout tests. These tests provide consistent measurements of interface friction for stiff frictional reinforcing materials. However, it is particularly difficult to estimate the bond resistance for extensible reinforcements (such as geosynthetics) and materials with non-planar surface profiles (such as grids). The interface shear box tests restrict deformations of the reinforcing material, while boundary conditions and other scale effects create difficulties in interpreting pullout data.

The most comprehensive studies of soil-reinforcement interaction have been conducted in conjunction with direct shear box inclusion tests. These data have included a) deformation (and strain) patterns in the soil and reinforcement using radiographic and photographic methods, b) photoelastic stress distributions and c) local stress measurements using miniature earth pressure cells. The results provide detailed insights into the mechanisms of load transfer for inclusions oriented at different angles to the imposed failure plane in the soil. Tensile stresses in the reinforcements are interpreted from the measured deformations of markers located on the inclusions. These results are in good agreement with calculations of the maximum reinforcement force obtained from limit equilibrium analysis of forces mobilized at peak shear resistance.

---

[29]'Bond' describes interface friction and other mechanisms such as bearing on transverse grid elements.

Overall, these shear box experiments represent a major contribution in understanding the complex interactions between the soil and reinforcement. However, the tests have a number of intrinsic limitations:

1. The stress and strain conditions are highly non-uniform. The device imposes a relatively narrow, horizontal failure plane within the soil mass where deformations and strains are localized. The presence of inclusions, which intersect the failure plane, introduces further non-uniformities that prevent more systematic interpretation of soil-reinforcement interaction.
2. There are scale effects associated with the length of the inclusions and size of the shear zone. As a result, there is no reliable procedure for scaling the results to the prototype field situation.
3. The interpretation of tensile stresses in the reinforcement can only be achieved at peak shear resistance where it is assumed that the full shear strength of the soil is mobilized along a horizontal shear plane.

It can be concluded from this study that, although existing laboratory tests provide design parameters describing soil-reinforcement interaction in limit equilibrium analyses, they are not well suited for estimating load transfer characteristics (i.e., stresses which develop within the reinforcement), especially at working stress levels. Primary limitations of existing tests are due to: a) non-uniformity of stress and strain within the soil, and b) lack of direct measurement of loads carried by the reinforcing materials.

Subsequent chapters of this thesis describe the design, development, and application of a new laboratory device which has the unique capability of measuring the tensile stresses that develop in the reinforcement due to shearing of the surrounding soil.

Apparatus	References	Dimensions	Sand	Reinforcing Materials[1]	σ_c (kPa)	D_r (%)	Notes
Triaxial Cell 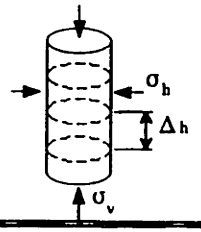	Broms (1977)	d=69mm, h=137mm	G12	FTV 600 Fabric	20-200	Not given	
	Fukushima (1988)	d=1.2m, h=2.4m	Toyoura	GG, NW, metal strip	50-400	34, 70	Very large scale test
	Gray et al. (1982)	d=61mm, h=127mm	Muskegon	NW, WF, brass cloth	20-400	Not given	
	Holtz et al. (1982)	d=36mm, h=73mm	Lafayette	NW, WF	35-276	90	Long-term creep tests
	Schlosser & Long (1972)	d=10cm, h=20-30cm	Fontaine-bleau	aluminum foil	10-700	90	Δh = 2-4cm
Direct (Box) Shear 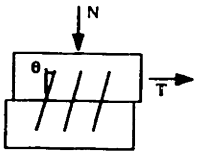	Gray & Ohashi (1983)	Not given	Muskegon	reed/PVC fibers copper wire	34-68	20, 100	Varied fiber length, diameter, and concentration
	Jewell & Wroth (1987)	254x152x152mm	LBS[2]	tension springs	25-85	90	Varied spring stiffness and orientation
	Palmeira et al. (1989)	1x1x1m	LBS	GG, WF, metal strip	30	87	Varied grid type and orientation
	Shewbridge et al. (1989)	761x402x135mm	Monterey	nylon cord, wood/metal rods	10.25	71	Sheared on a vertical plane
Direct Simple Shear 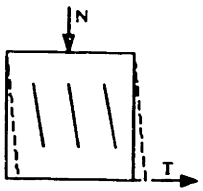	Hayashi et al. (1988)	200x200x200mm	Toyoura	GG, bronze bars	25-150	82	θ = -20 to +20°
Plane Strain Unit Cell 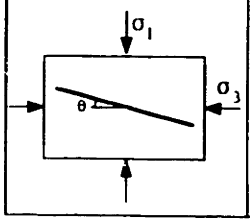	McGown et al. (1978)	152x102x102mm	LBS	NW, Al foil, Al mesh	70	11-70	θ = 0 to 90°

[1]GG = Geogrid NW = non-woven fabric WF = woven fabric

[2]LBS = Leighton Buzzard sand

Table 2.1: Laboratory Investigations of Reinforced Soil Composites

Reference	Specimen Dimensions	Sand	Formation Densities D_r (%), e	Confining Stress σ_n (kPa)	Inclusion Materials	#	Orien-tation (θ°)	Internal Measurements
Jewell (1980) Jewell and Wroth (1987)	254x152x152mm	Leighton Buzzard	90 (0.52)	25-85	Close-coiled steel tension springs	1-6	0-180	Radiography of markers in soil and on inclusion
Dyer (1985) Dyer and Milligan (1984)	204x52x150mm	Crushed glass	Not given		Perforated brass sheet Steel wire mesh Steel plate	1	40, 0, -45	Photoelastic stresses Soil strains from displace-ments of opaque markers
Palmeira (1987) Palmeira and Milligan (1989)	1x1x1m	Leighton Buzzard	87 (0.53)	30	8 metal grids, varying apertures 2 polyethylene geogrids 2 woven geotextiles Smooth and rough metal sheets	1	0, 30	Total stress cells on inside wall Total pressure cells in soil 70mm above shear plane 3 pressure cells along reinforcement
Gray and Ohashi (1983)	Not given	Muskegon	100 (0.50) 20 (0.73)	34-68	Basket reeds (1.8mm diameter) Palmyra palm fibers (1.2mm diameter) PVC fibers (2.2mm diameter) Copper wire (1.0mm diameter)	3-22	-60 to 30	None
Shewbridge and Sitar (1989)	760x400x135mm (Sheared in horizontal plane)	Monterey	71 (0.67)	10.25	Bungy and parachute cord Wood rod and wood dowel Aluminum rod and steel rod	12-100	0	Hand sketching of observed deformations

Table 2.2: Summary of Direct Shear Inclusion Tests

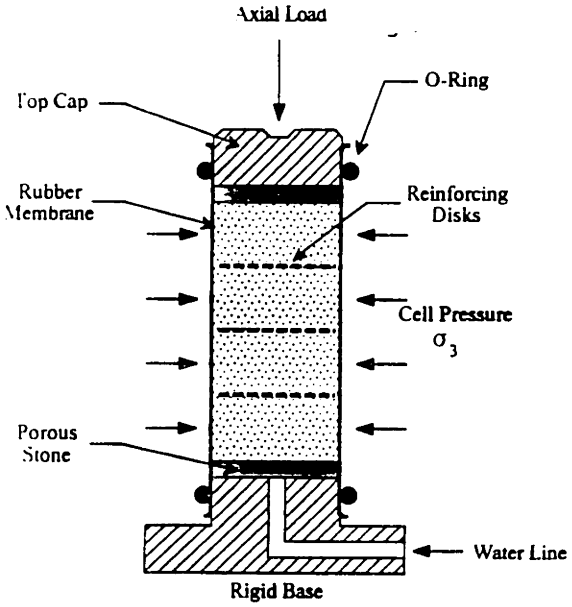

(a) Schematic of a reinforced soil triaxial test

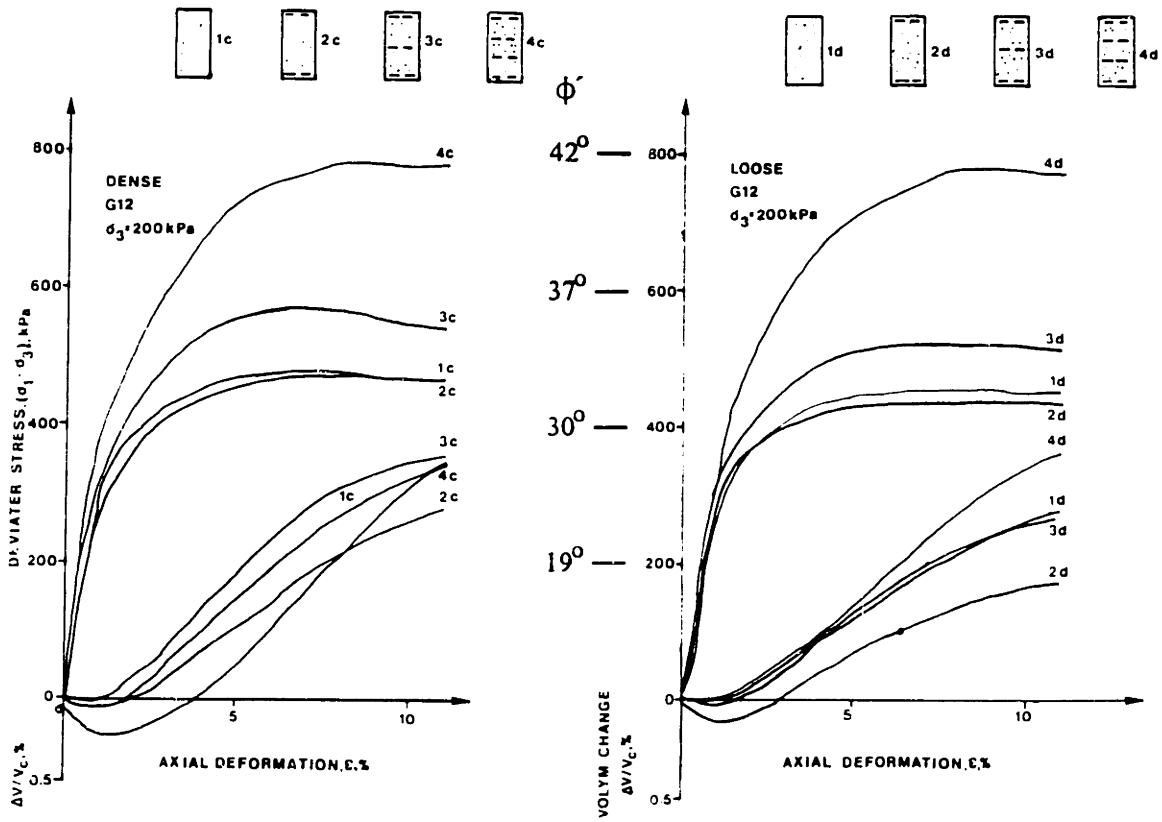

(b) Results for dense and loose sand with fabric inclusions

Figure 2.1: Reinforced Soil Triaxial Tests (After Broms, 1977)

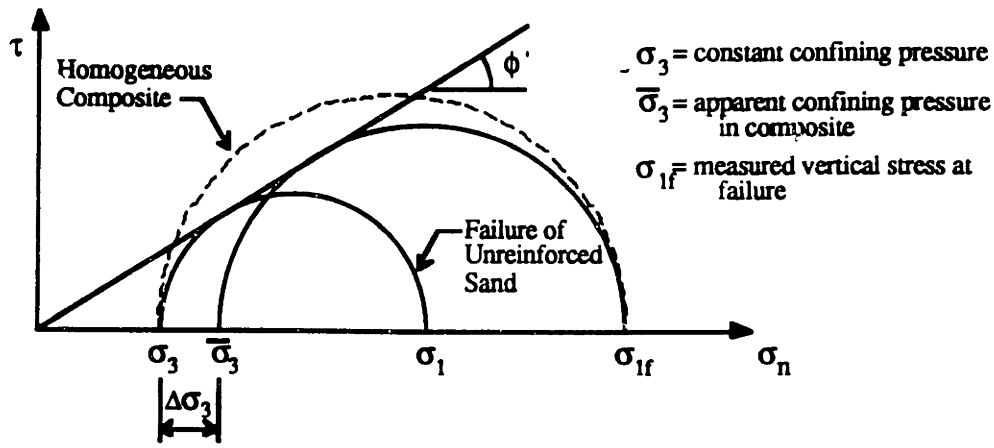

(a) Apparent confining stress caused by reinforcement in a triaxial specimen

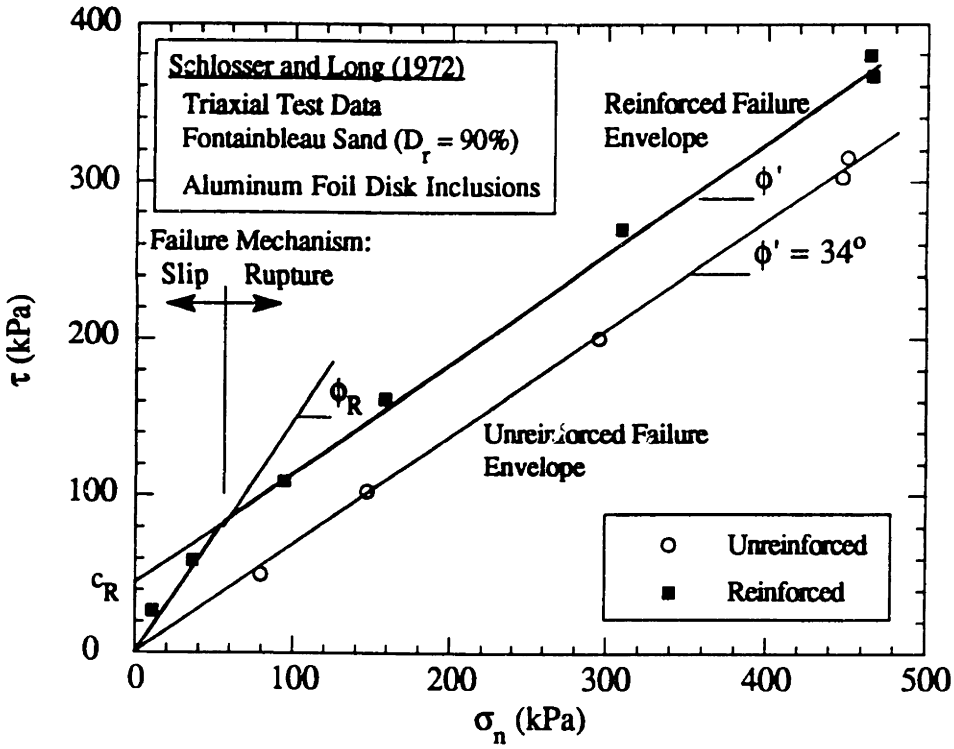

(b) Bi-linear failure envelope for triaxial tests on sand with inextensible disk inclusions

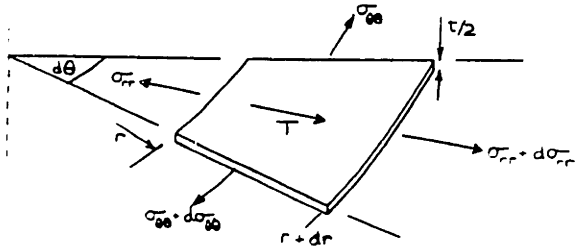

(c) Disk element subjected to radial body force R (After Christie, 1982)

Figure 2.2: Strength Analyses of Reinforced Soil Based on Homogenization Assumptions

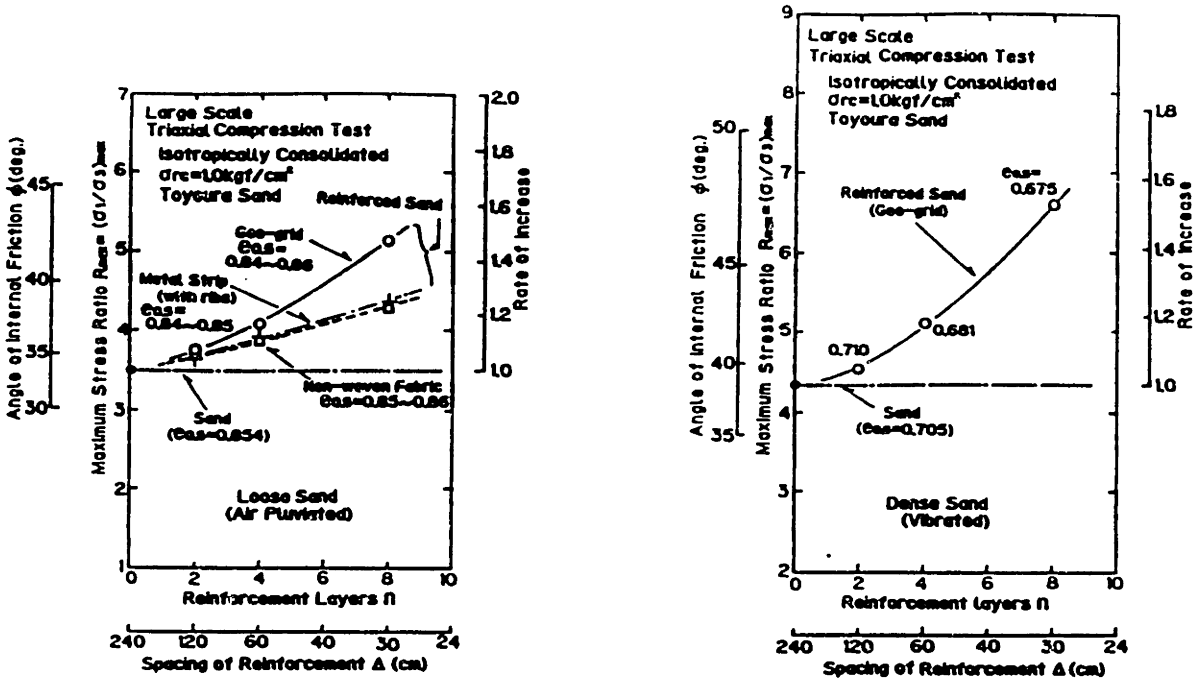

Loose sand Dense sand

(a) Relation between the number of reinforcing layers and their effect

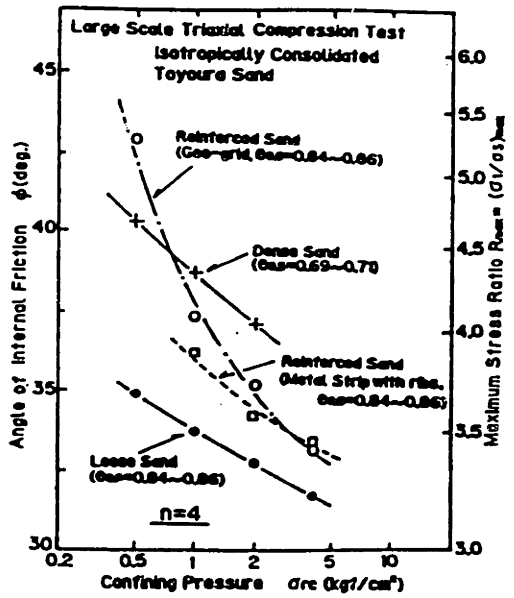

(b) Relation between reinforcing effect and confining pressure

Figure 2.3: Results from Large Scale Triaxial Apparatus
(After Fukushima et al., 1988)

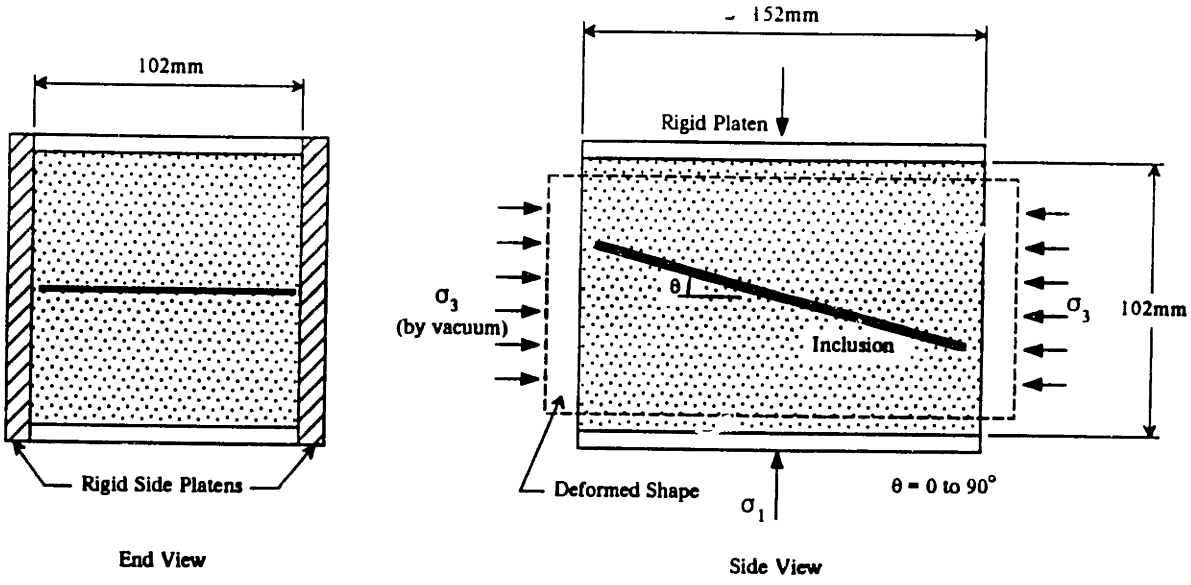

(a) Boundary conditions in the unit cell

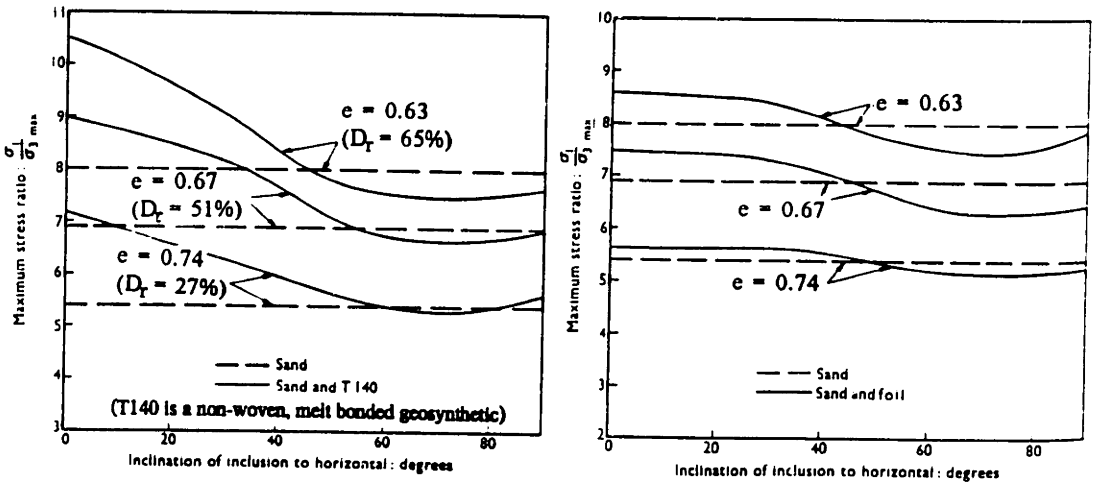

(b) Effect of inclusion orientation on peak stress ratio for non-woven and aluminum foil inclusions

Figure 2.4: Plane Strain Tests on Reinforced Leighton Buzzard Sand (McGown et al., 1978)

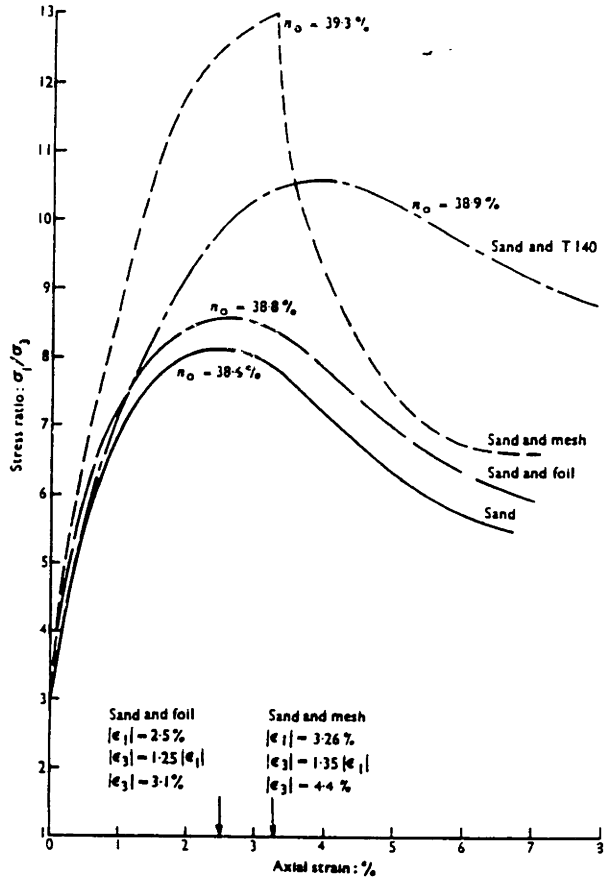

(a) Dense Leighton Buzzard sand

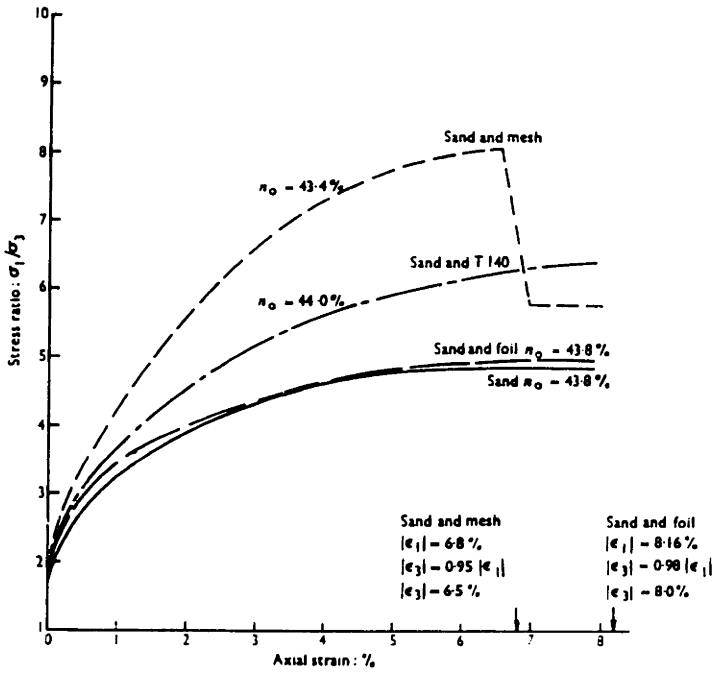

(b) Loose Leigton Buzzard sand

Figure 2.5: Effect of Reinforcements on External Stress-Strain Behavior Measured in Plane Strain Shear Tests (McGown et al., 1978)

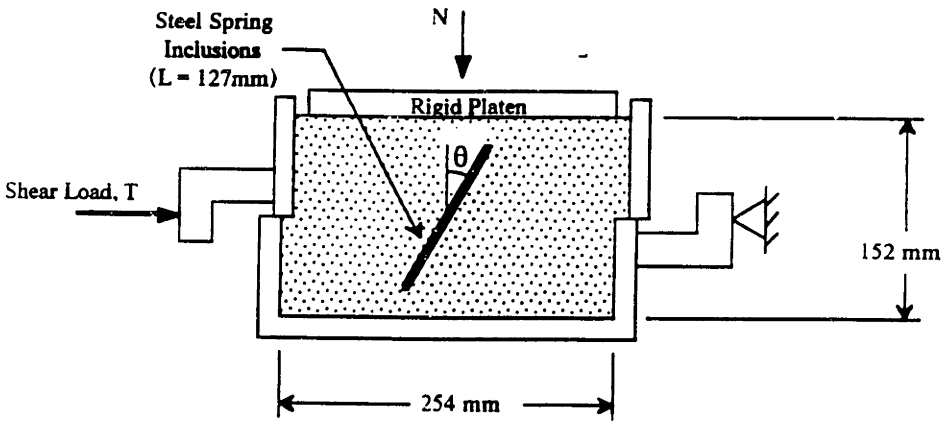

(a) Schematic of reinforced direct shear box test (after Jewell, 1980)

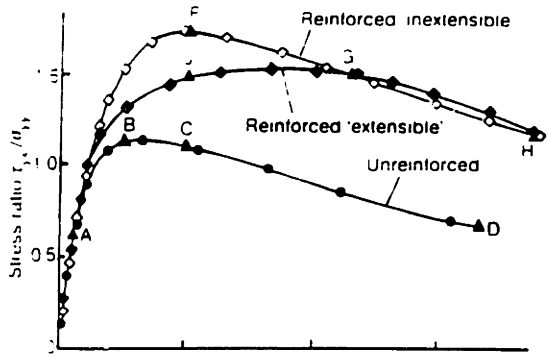

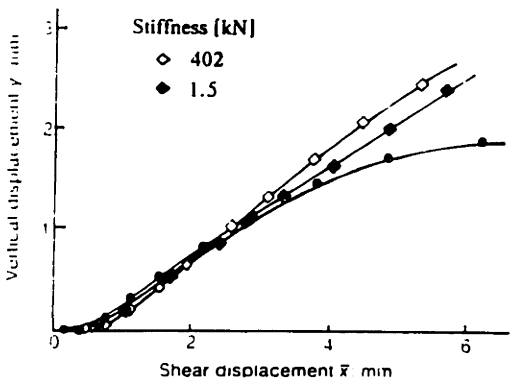

(b) Externally measured shear behavior, $\theta = 25^{\circ}$

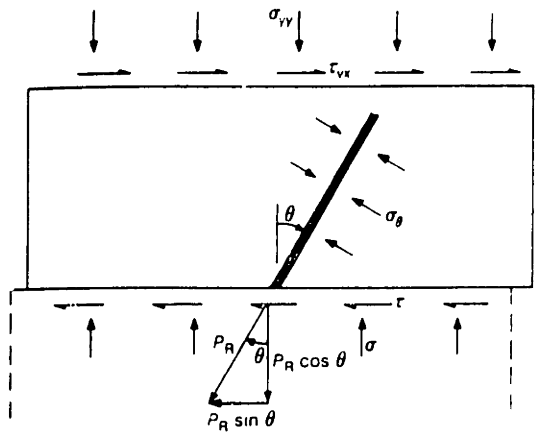

(c) Equilibrium conditions for top half of the shear box

Figure 2.6: Direct Shear Box Tests with Single Plane of Inclusions (after Jewell, 1980)

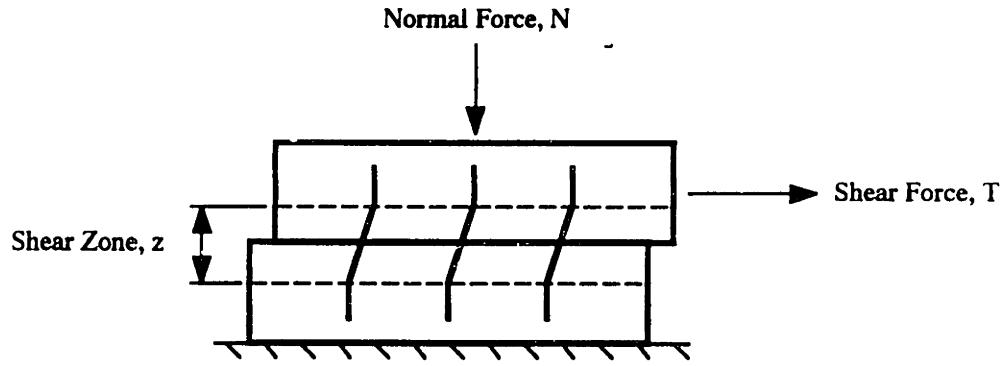

(a) Schematic diagram of deformed geometry

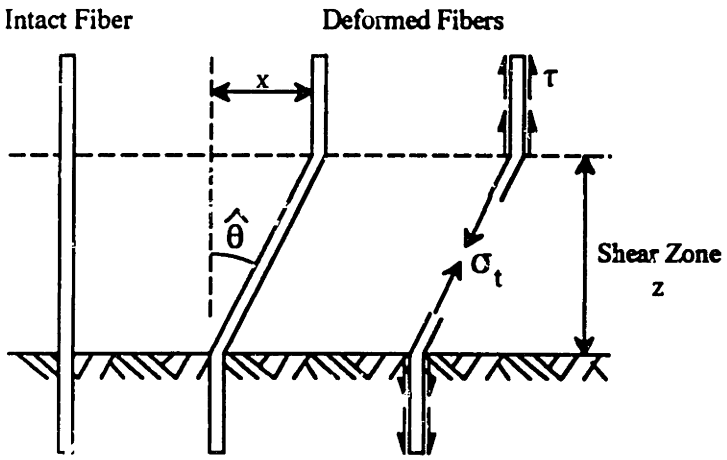

Fiber perpendicular to shear surface

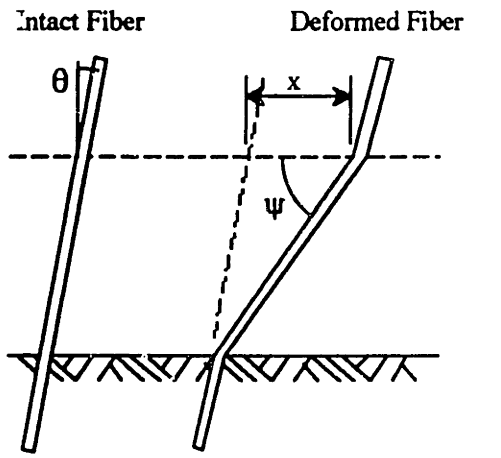

Fiber oriented at angle θ to shear surface

(b) Fiber reinforcement models

Figure 2.7: Direct Shear Box Tests with Multiple Inclusions
(after Gray and Ohashi, 1983)

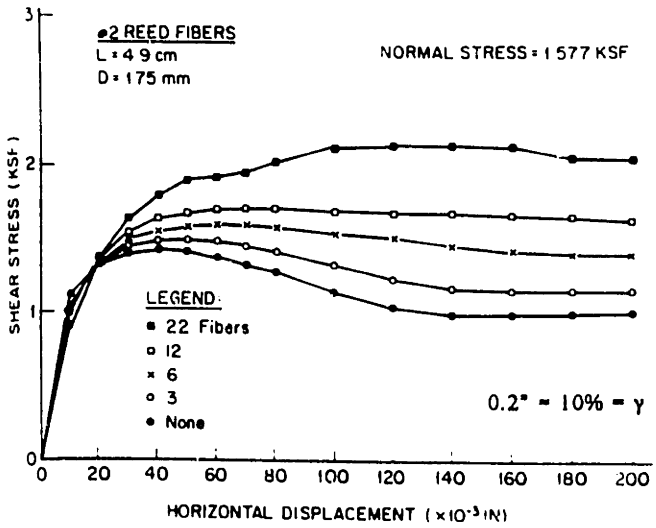

(a) Influence of area ratio on direct shear behavior

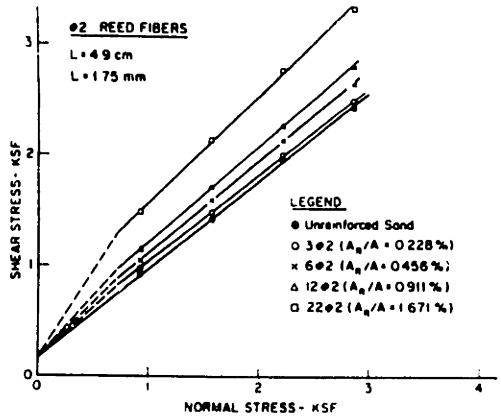

(b) Bi-linear strength envelopes for different area ratios

Figure 2.8: Results from Direct Shear Inclusions Tests by Gray and Ohashi (1983)

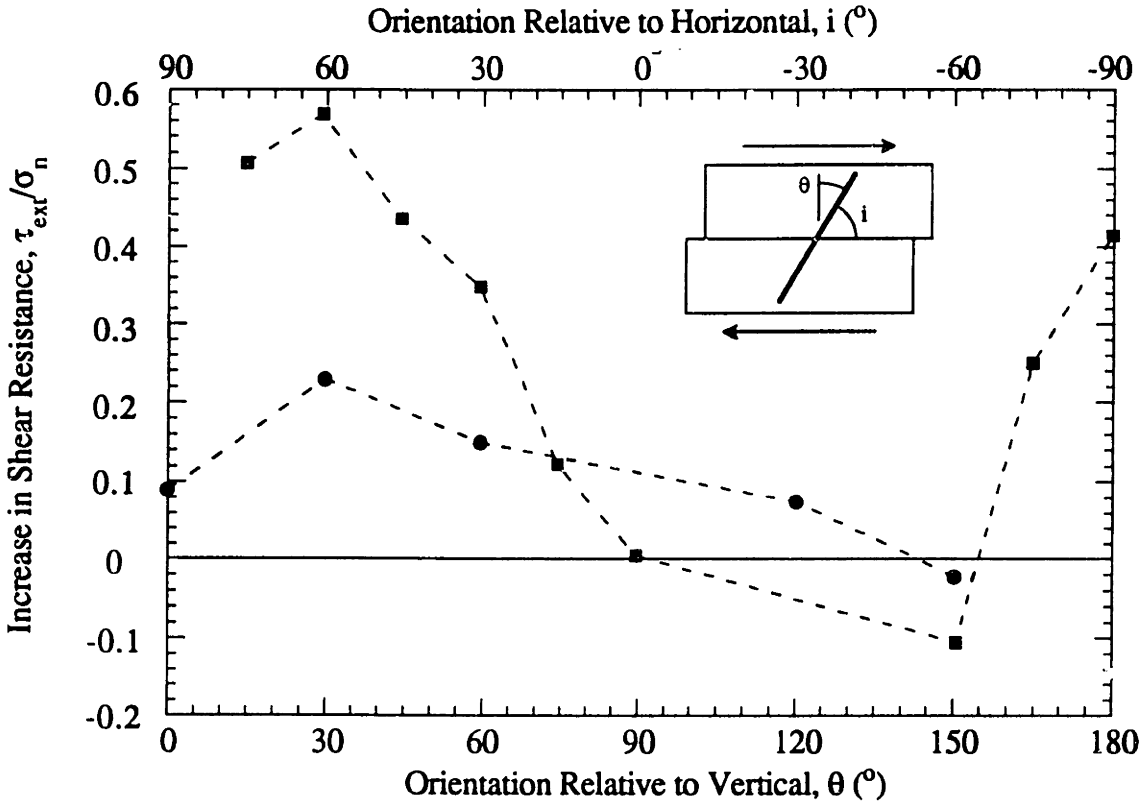

Symbol	Reference	Sand	D_r (%)	σ_n (kPa)	Reinforing Material
■	Jewell, 1980 Jewell and Wroth, 1987	Leighton Buzzard	90	30	Close coiled steel tension springs
●	Gray and Al-Refeai, 1986	Muskegon Dune Sand	100	76	reed fibers

Figure 2.9: Effect of Reinforcement Orientation on Direct Shear Resistance

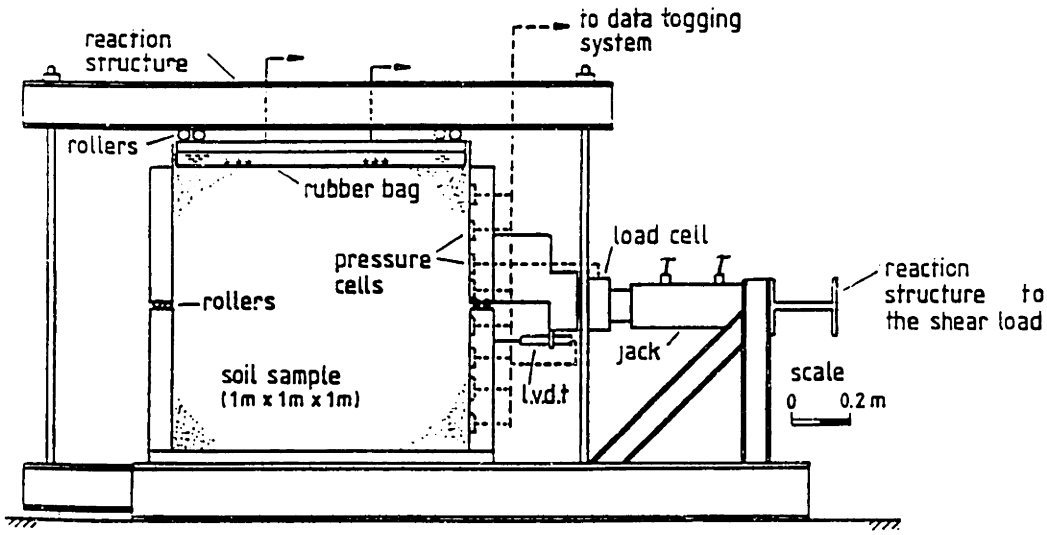

(a) Apparatus schematic

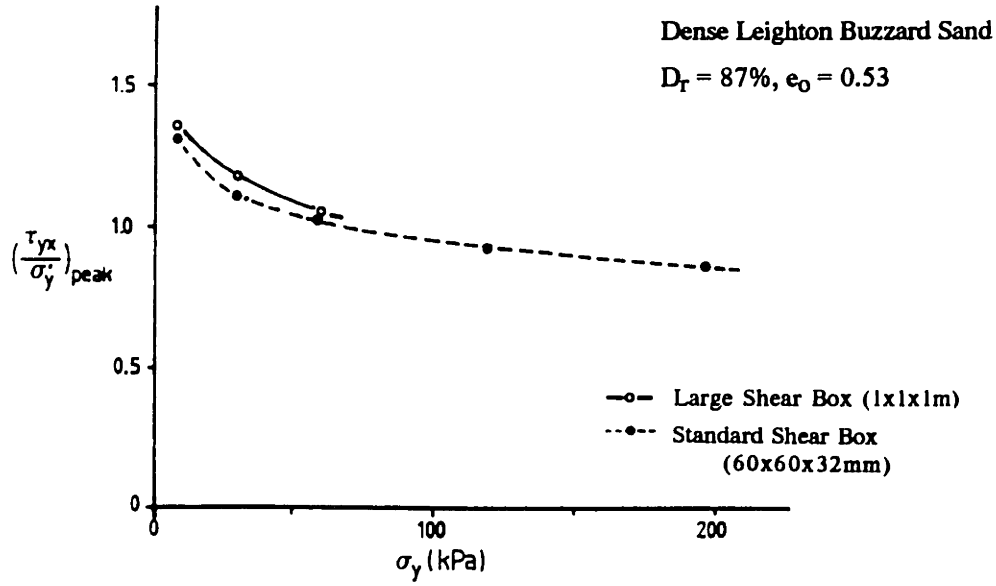

(b) Variation in direct shear friction angle for different normal stresses

Figure 2.10: The Large Scale Direct Shear Apparatus (after Palmeira, 1987)

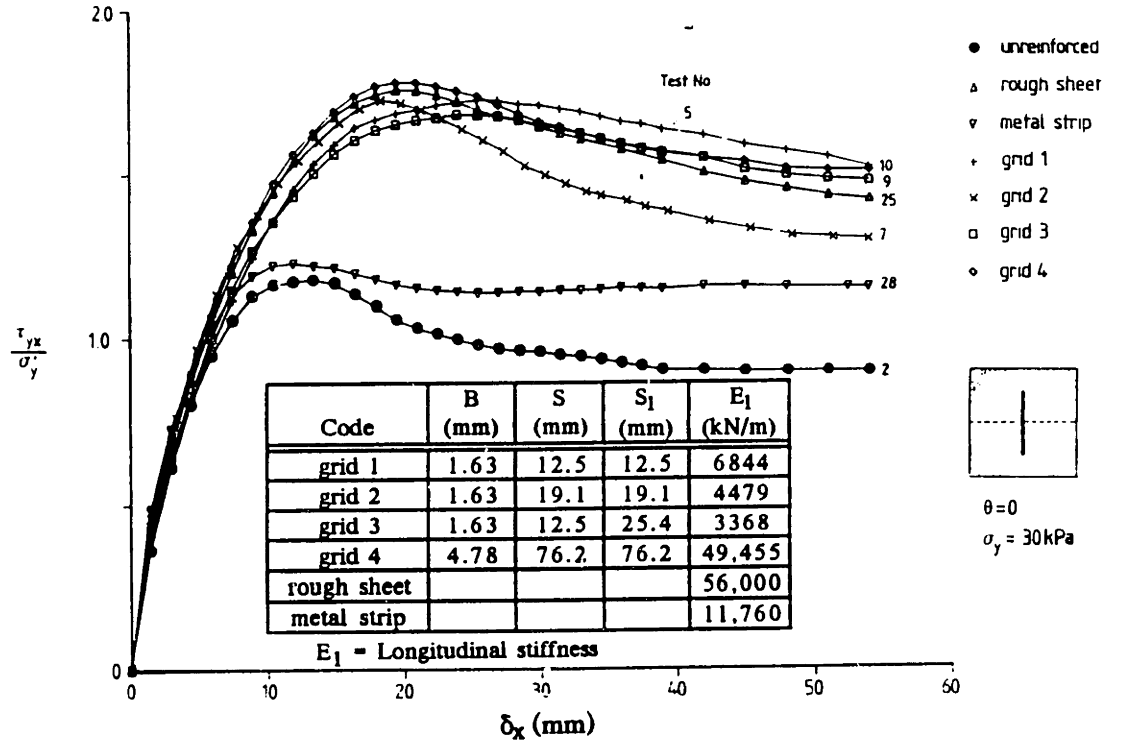

(a) Results for samples reinforced with metal inclusions oriented at $\theta = 0^{o}$

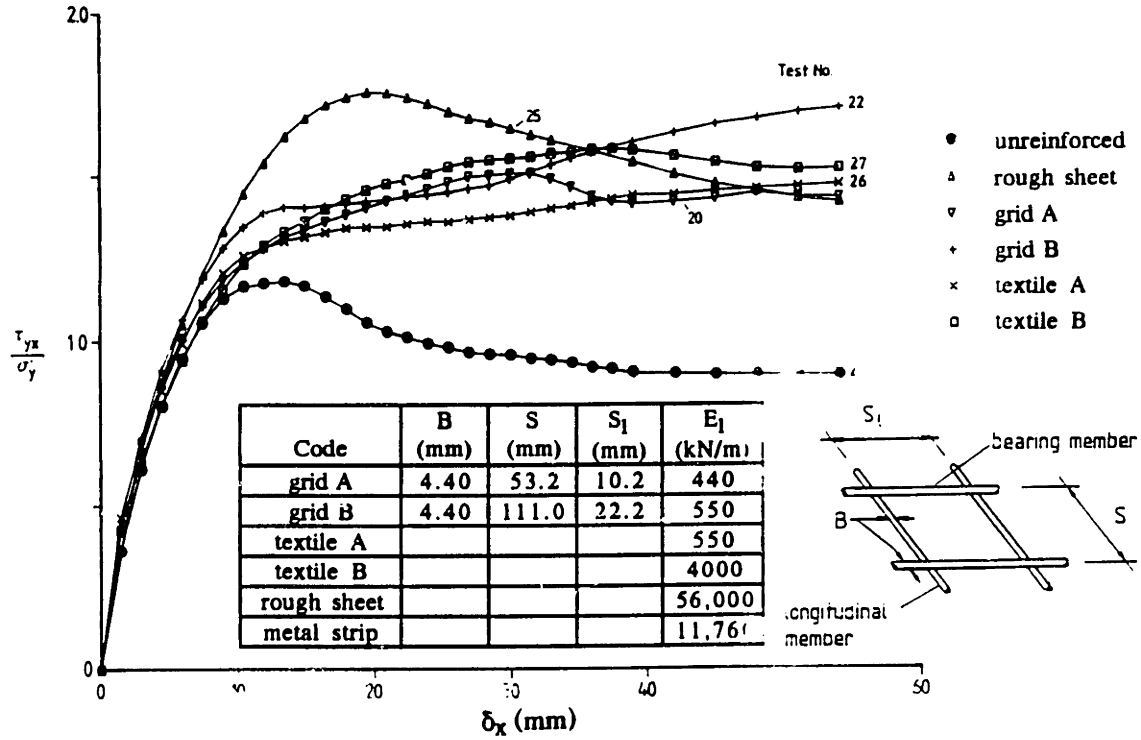

(b) Results for samples reinforced with polymeric inclusions oriented at $\theta = 0^{o}$

Figure 2.11: Externally Measured Behavior in the Large Scale Direct Shear Apparatus (after Palmeira, 1987)

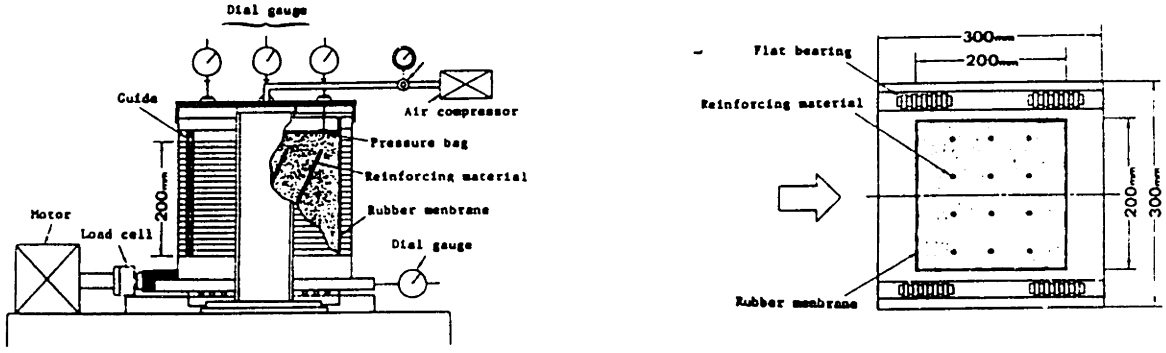

Side View

Plan View

(a) Schematic of the direct simple shear apparatus

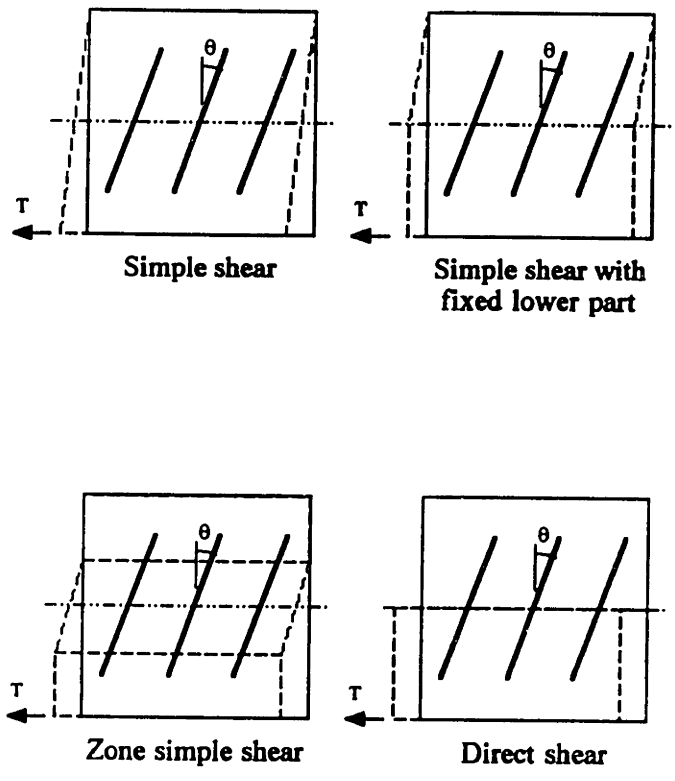

(b) Available modes of shearing in the direct simple shear apparatus

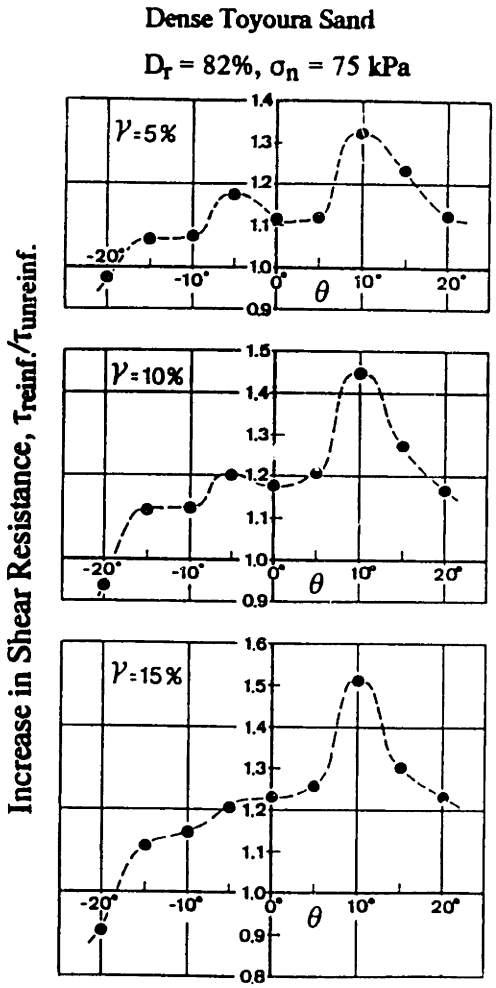

(c) Influence of reinforcement orientation on the behavior of sand reinforced with phosphor bronze bars

Figure 2.12: Direct Simple Shear Device Reported by Hayashi et al. (1988)

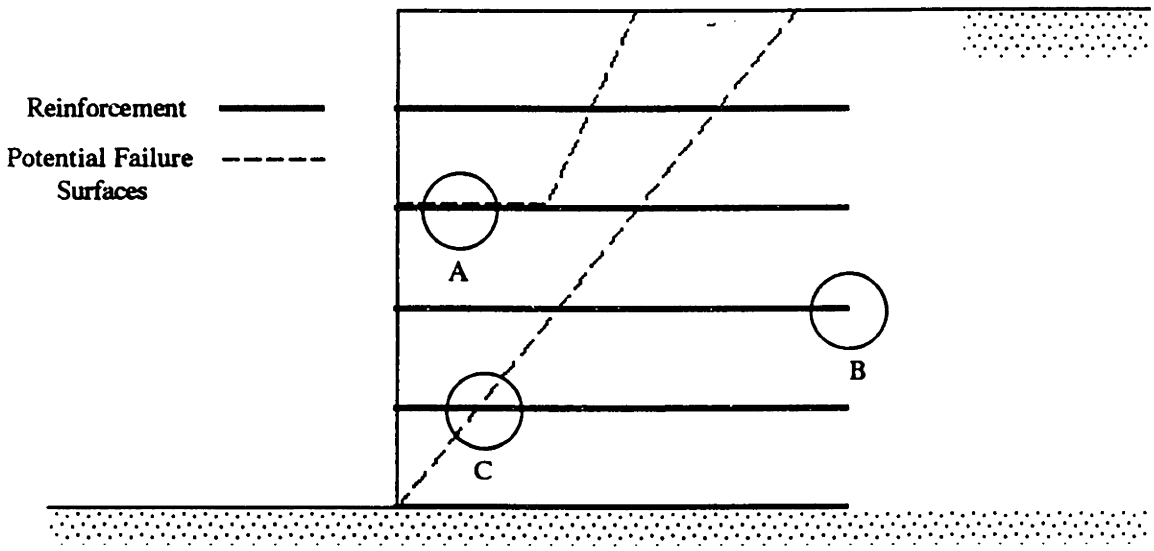

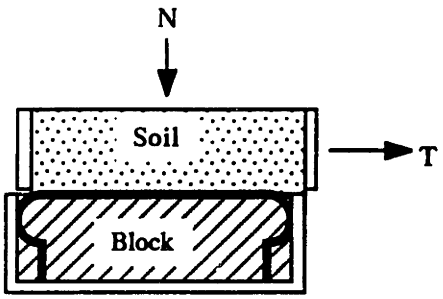

Mechanism A: Interface Shear Test

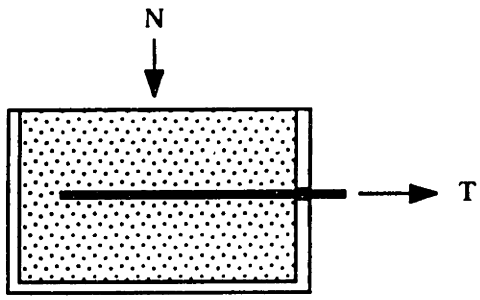

Mechanism B: Pullout Test

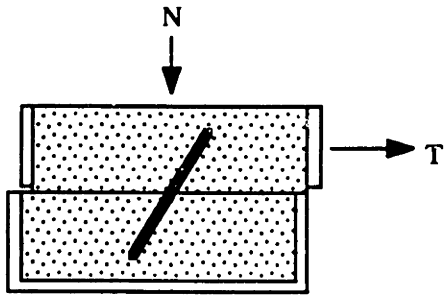

Mechanism C: Direct Shear Inclusion Test

Figure 2.13: Assumed Failure Mechanisms in a Reinforced Soil Structure (after Palmeira, 1987)

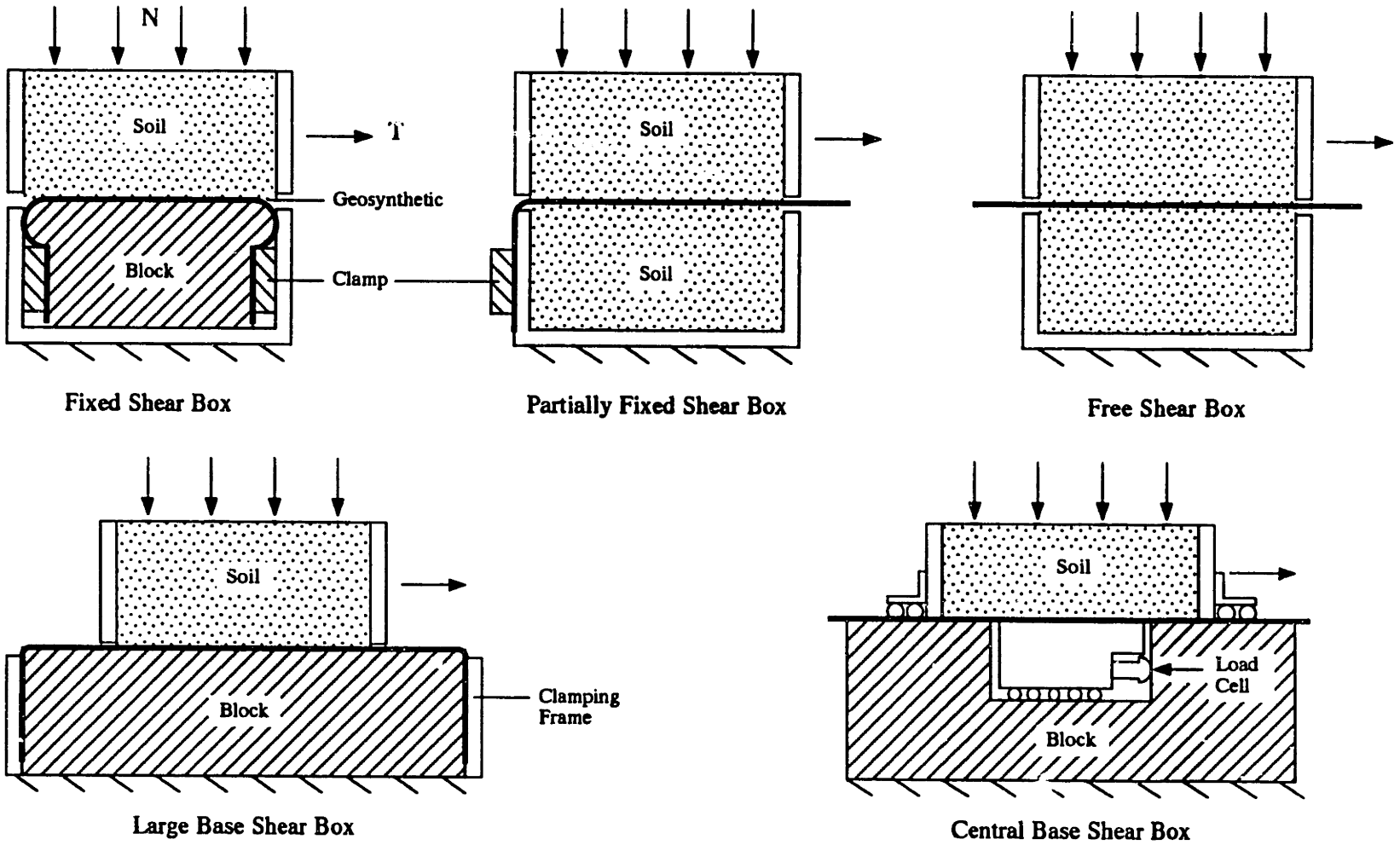

Figure 2.14: Boundary Conditions in Direct Shear Interface Tests (After Richards and Scott, 1985)

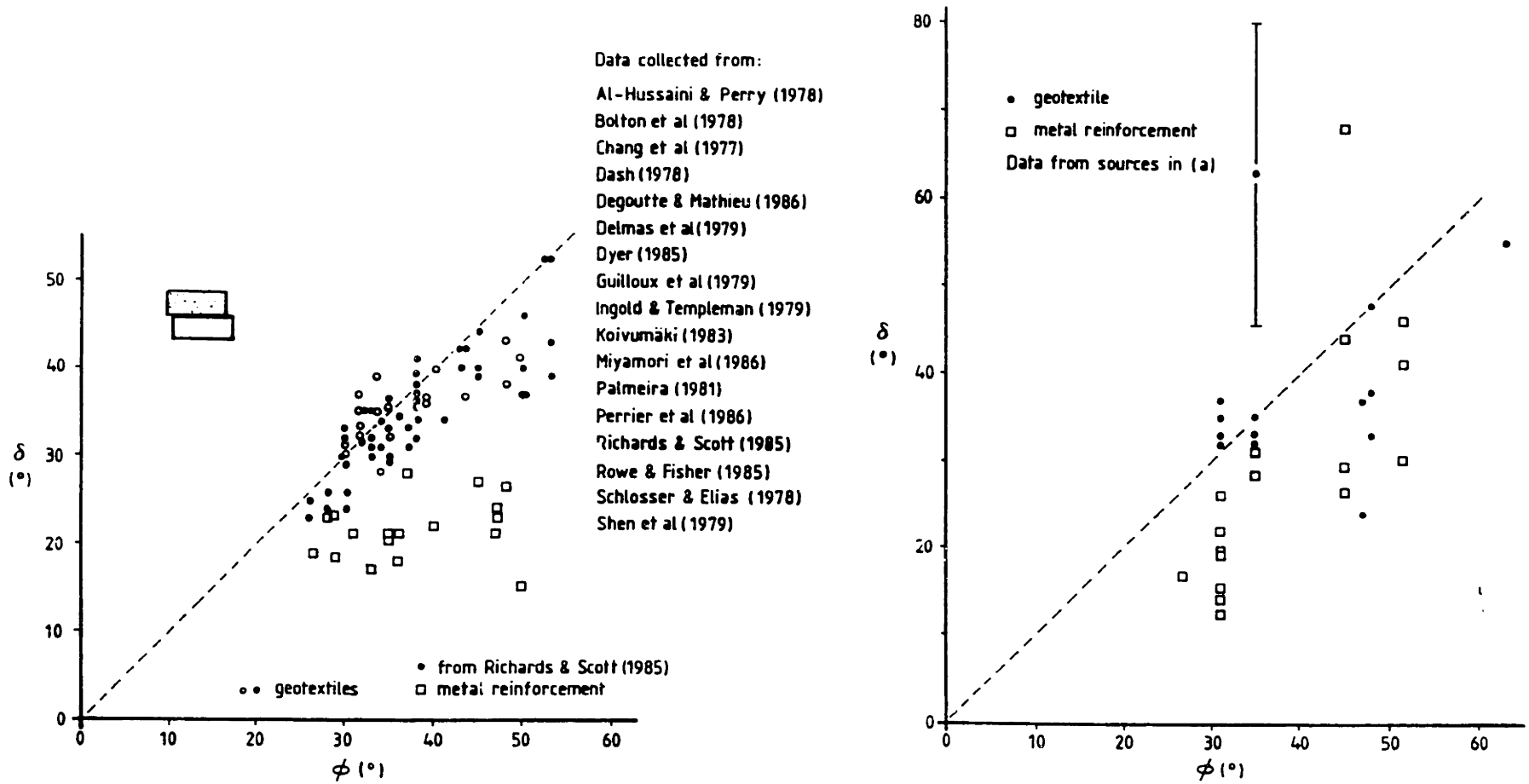

(a) Interface shear test results

(b) Pullout test results

Figure 2.15: Interface Shear and Pullout Test Data
(after Palmeira, 1987)

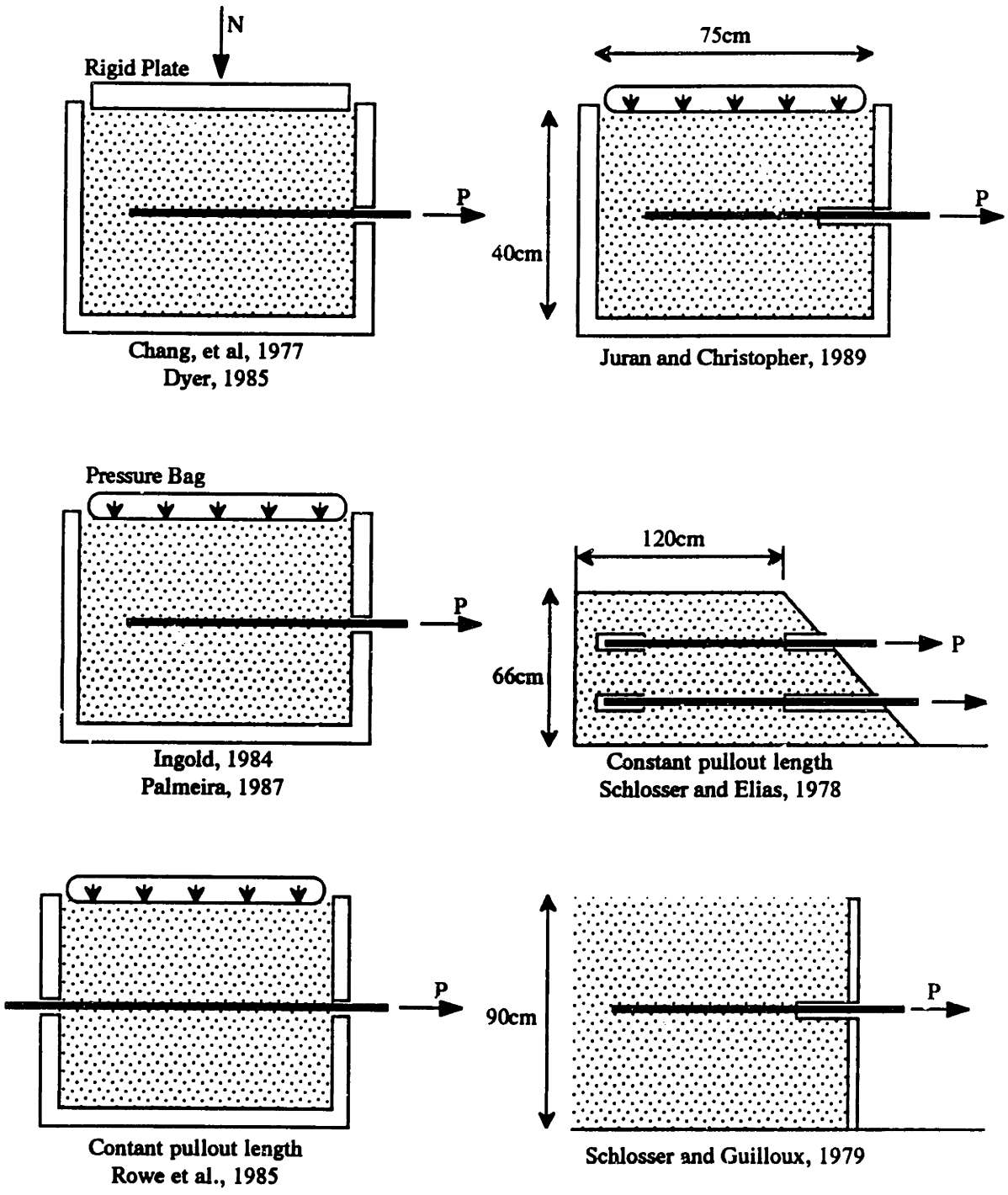

Figure 2.16: Boundary Conditions in Pullout Tests

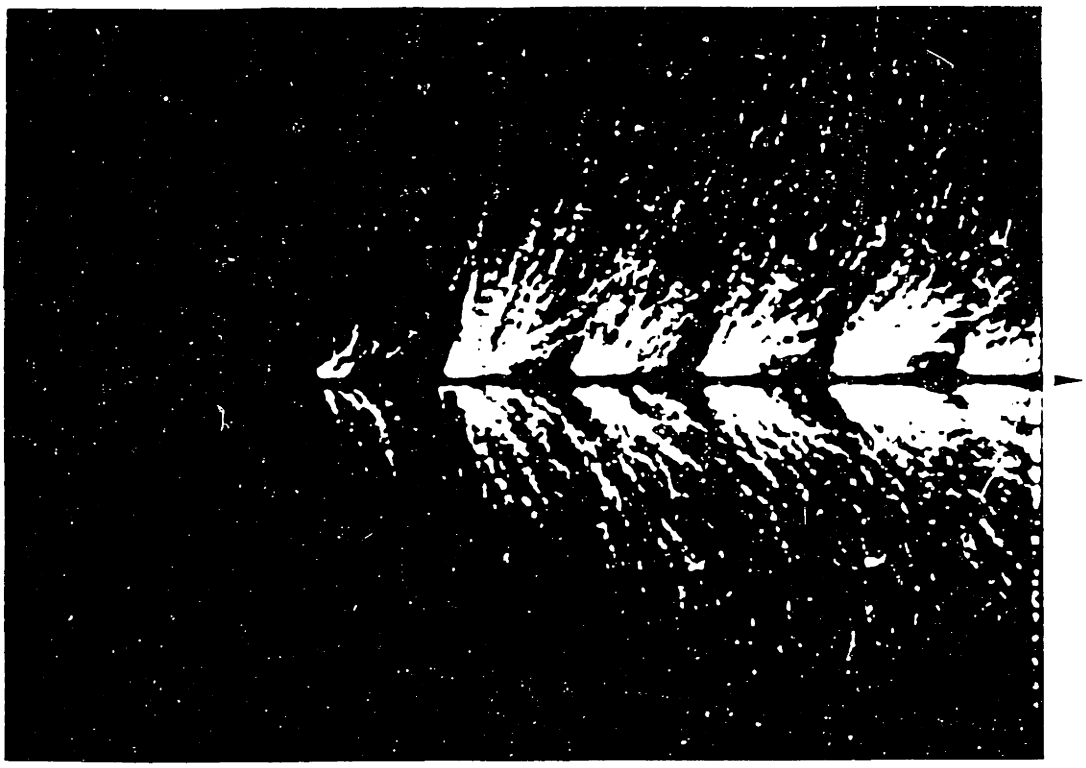

(a) Photoelastic observations of stresses

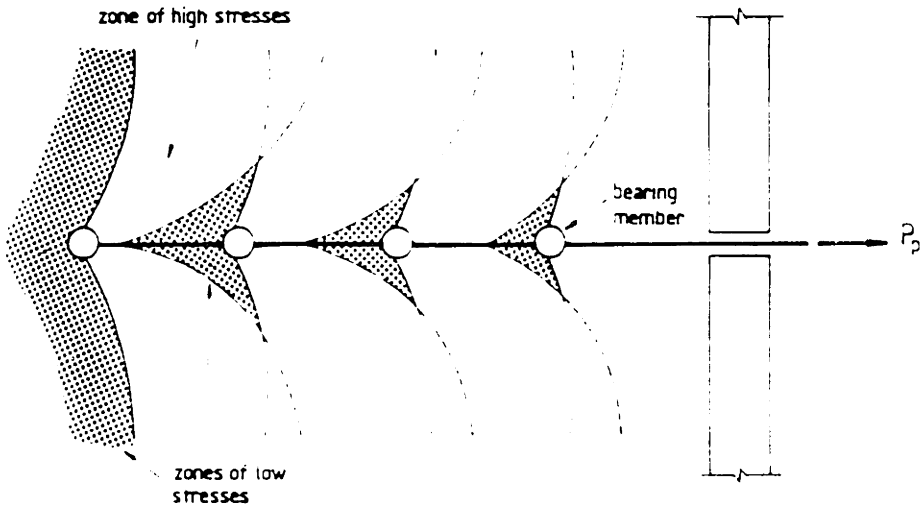

(b) Schematic illustration of the effect of interference between bearing members

Figure 2.17: Stresses around a Grid in a Pullout Test (after Dyer, 1985)

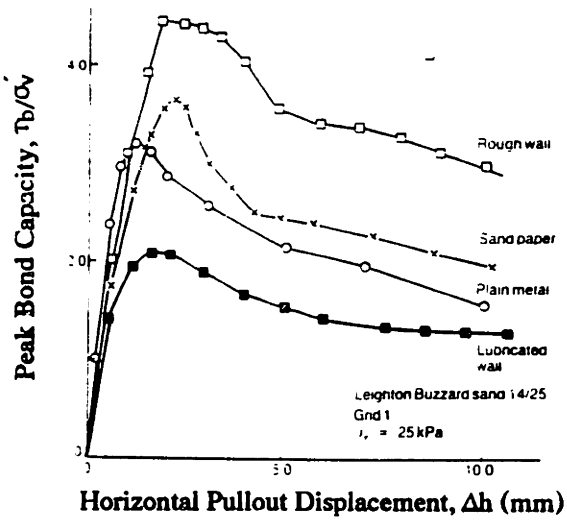

(a) Normalized bond stress vs. pull-out displacement for different front wall conditions (Palmeira and Milligan, 1989b)

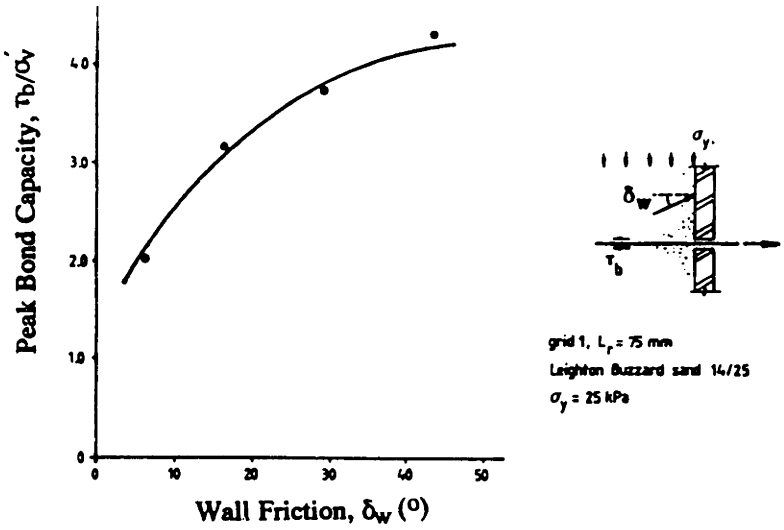

(b) Influence of front wall roughness on peak bond capacity (Palmeira, 1987)

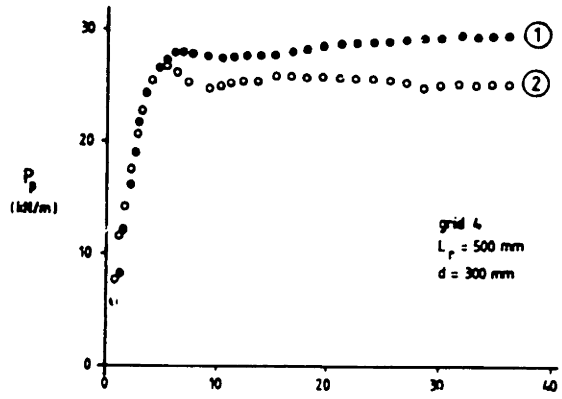

(c) Influence of the proximity of the front wall

Figure 2.18: Influence of Boundary Conditions in a Pullout Test

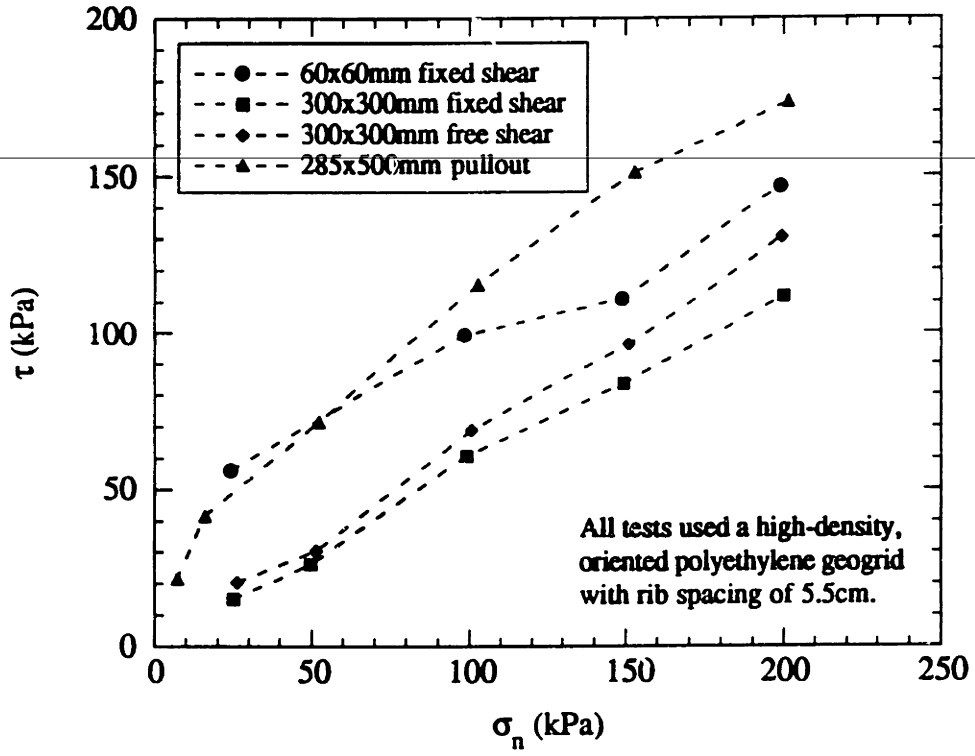

Figure 2.19: Comparison of Results from Direct Shear and Pullout Tests (after Ingold, 1982)

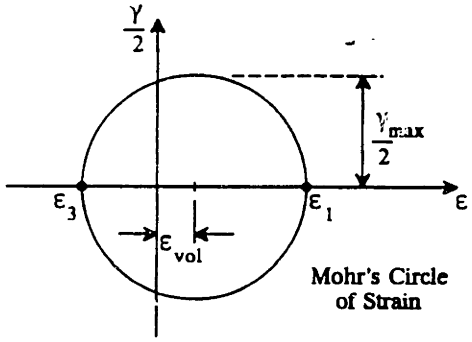

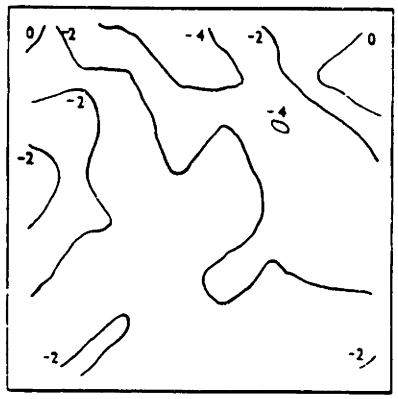

εvol contours

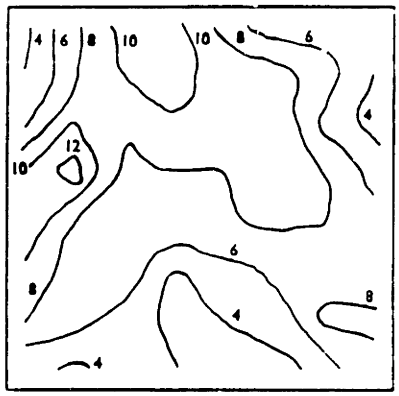

γmax contours

(a) Contours of γ_{max} and ε_{vol} at an applied axial strain of 2.8%

εvol contours

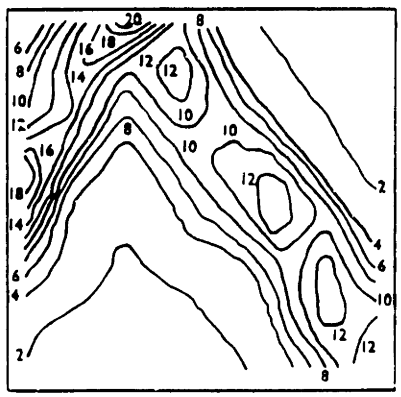

γmax contours

(b) Contours of γ_{max} and ε_{vol} at an applied axial strain of 5%

Figure 2.20: Computed Strain Fields for Unreinforced Dense Sand in the Unit Cell (after McGown et al., 1978)

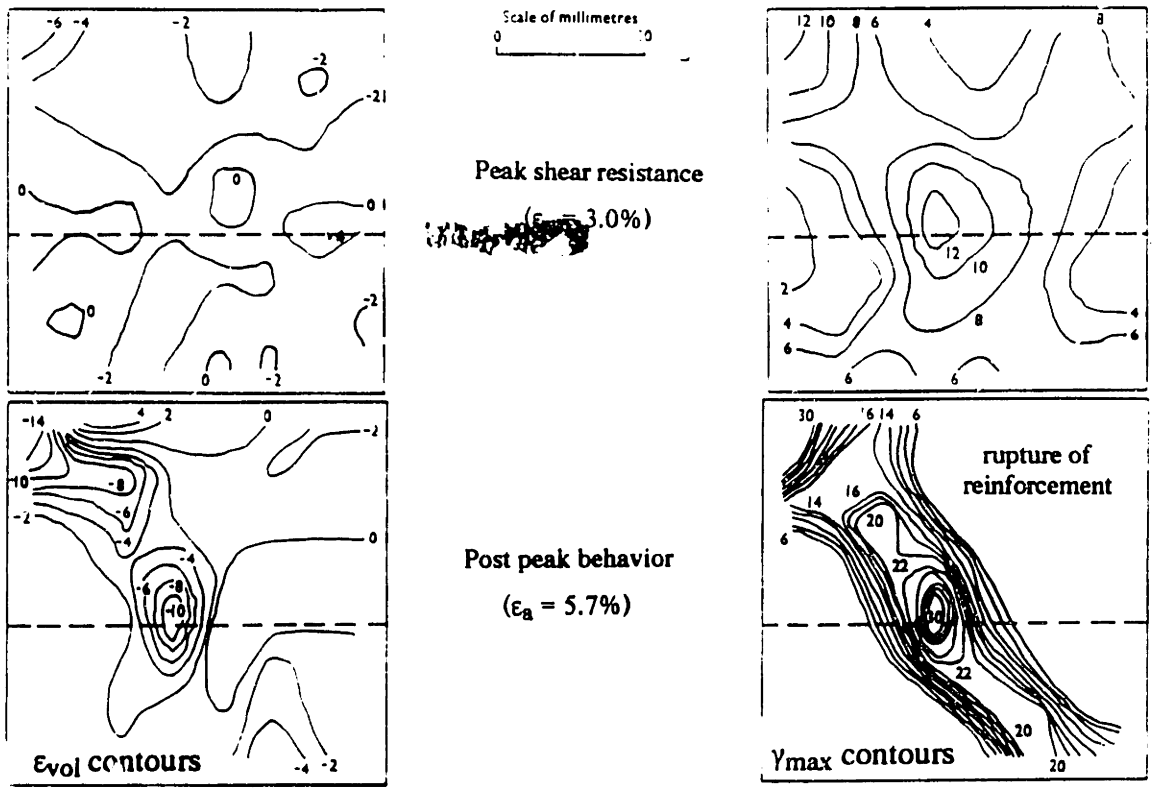

(a) Specimen with a horizontal aluminum wire mesh inclusion

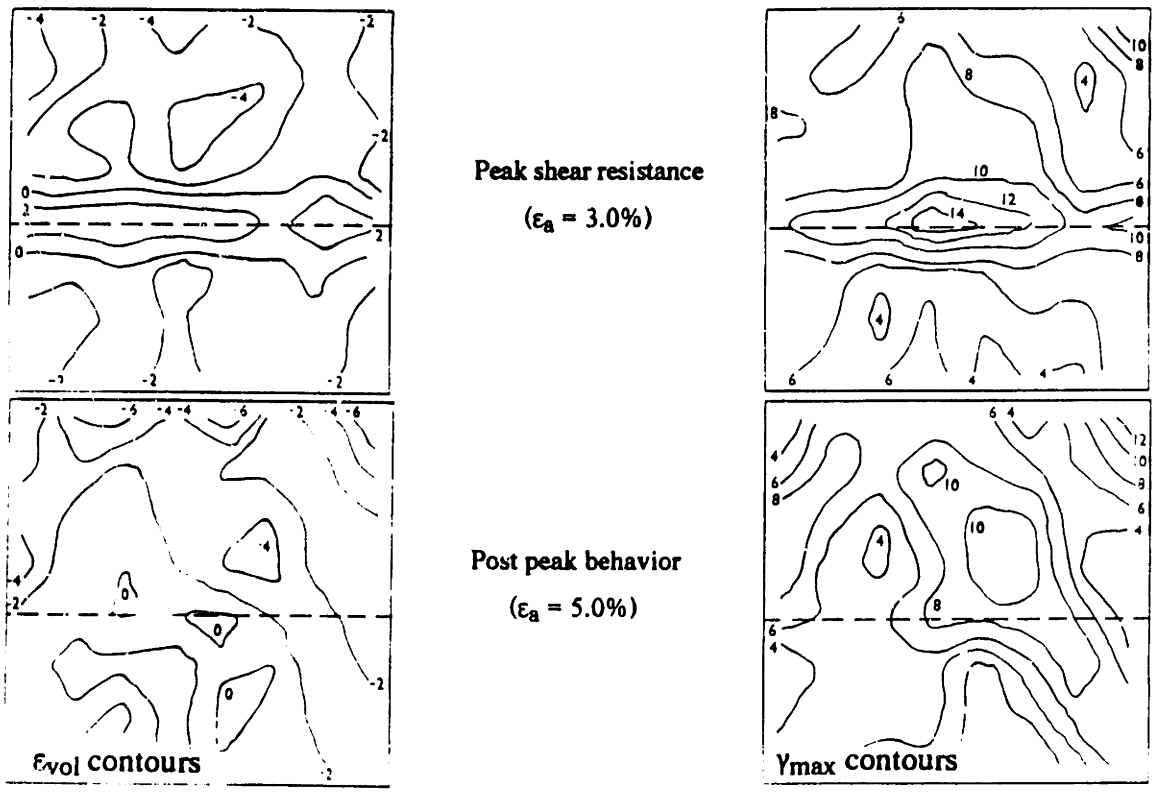

(b) Specimen with a horizontal non-woven fabric inclusion

Figure 2.21: Computed Strain Fields for Reinforced Dense Sand in the Unit Cell (after McGown et al., 1978)

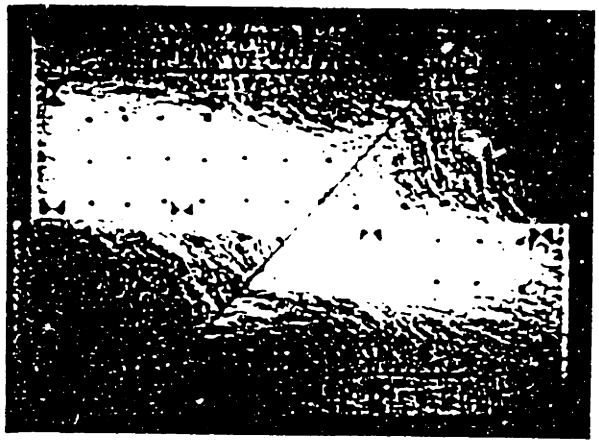

a) Reinforcement at $\theta=40^0$

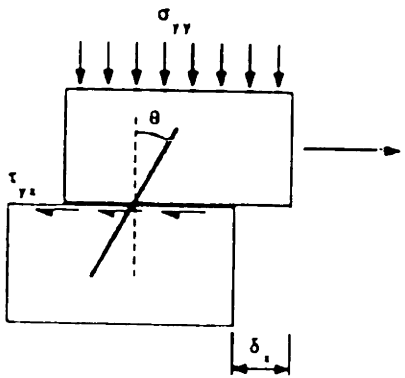

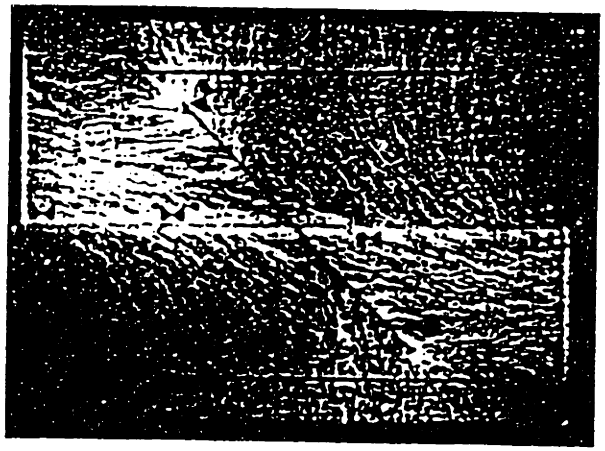

b) Reinforcement at $\theta=-45^0$

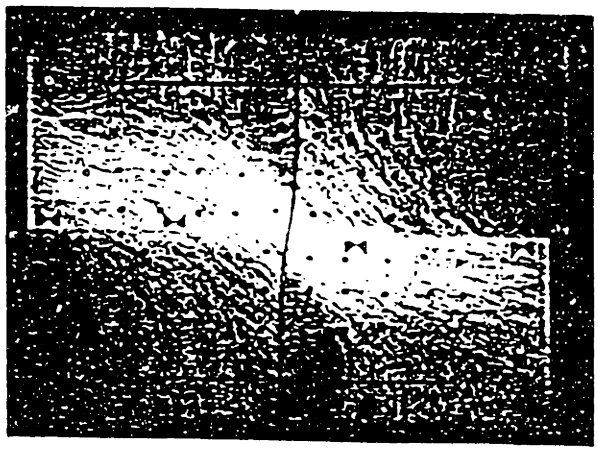

c) Reinforcement at $\theta=0^0$

Figure 2.22: Photoelastic Measurements of the Effect of Reinforcement Orientation in Direct Shear Box Inclusion Tests (Dyer and Milligan, 1986)

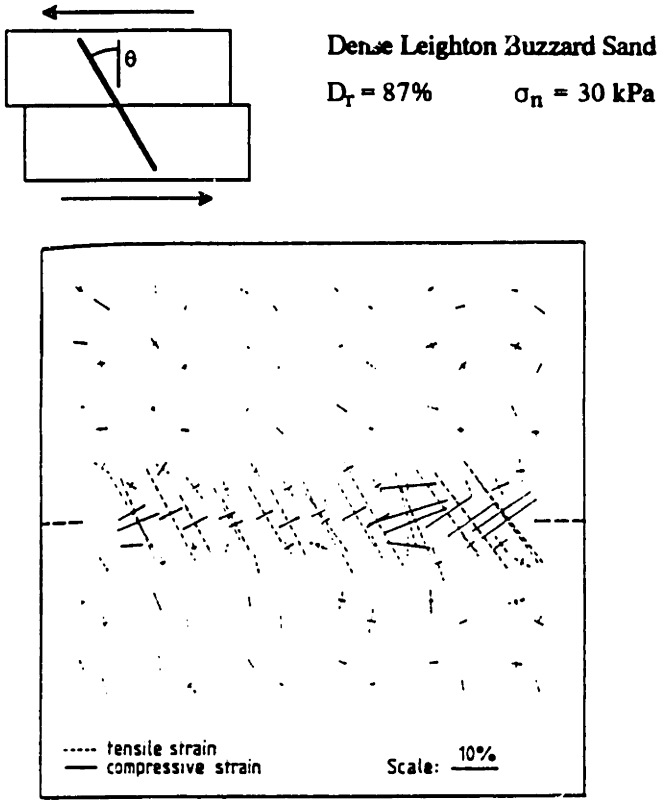

(a) Unreinforced sand

(b) Sand reinforced with a metal grid ($\theta = +30^o$)

Figure 2.23: Internal Soil Strains in the Large Scale Direct Shear Apparatus (after Palmeira and Milligan, 1989)

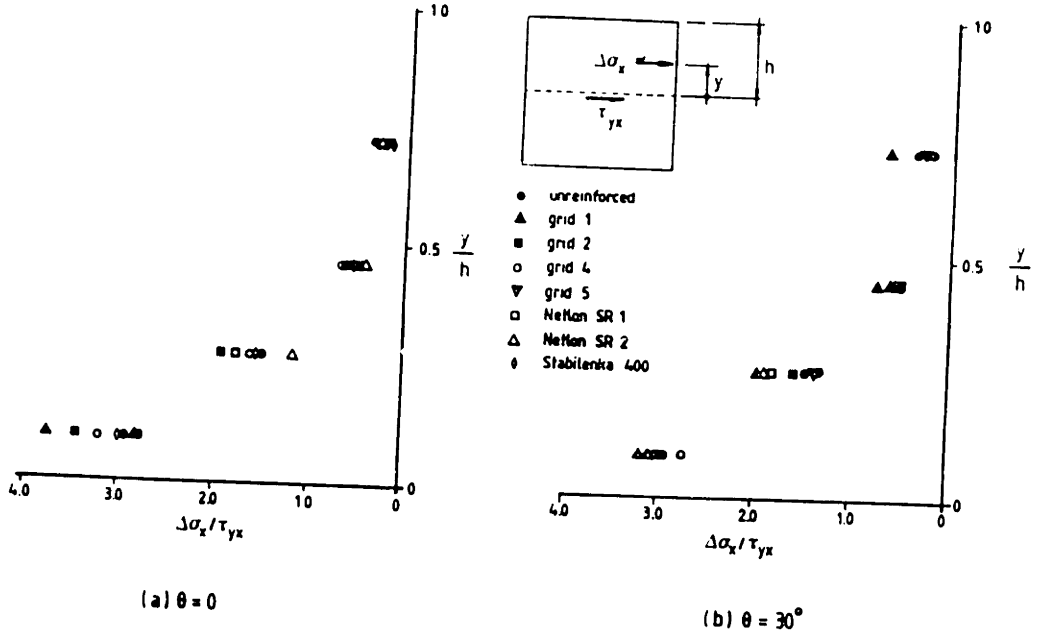

(a) Increments of horizontal stress along the end wall

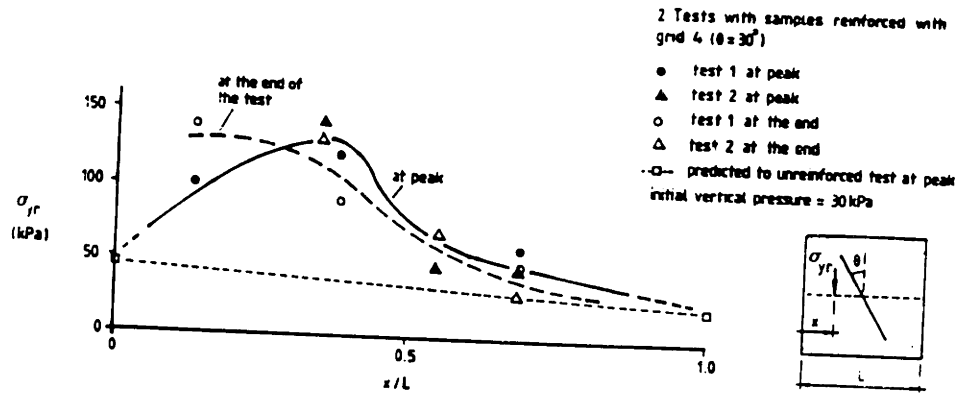

(b) Vertical pressure along central plane

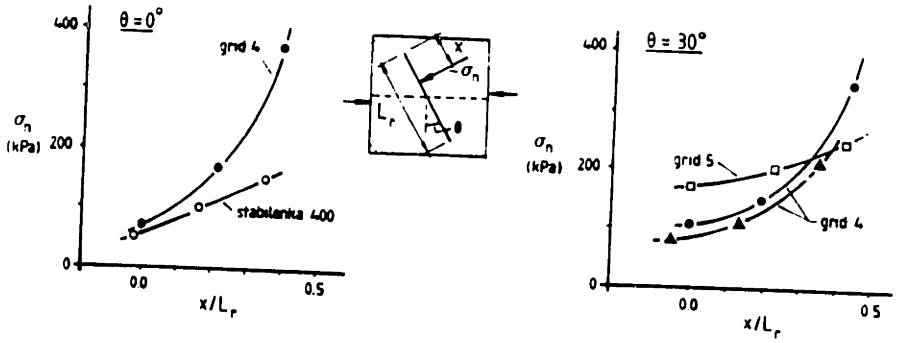

(c) Normal pressure against the reinforcement

Figure 2.24: Internally Measured Soil Pressures in the Large Scale Direct Shear Apparatus (after Palmeira, 1987)

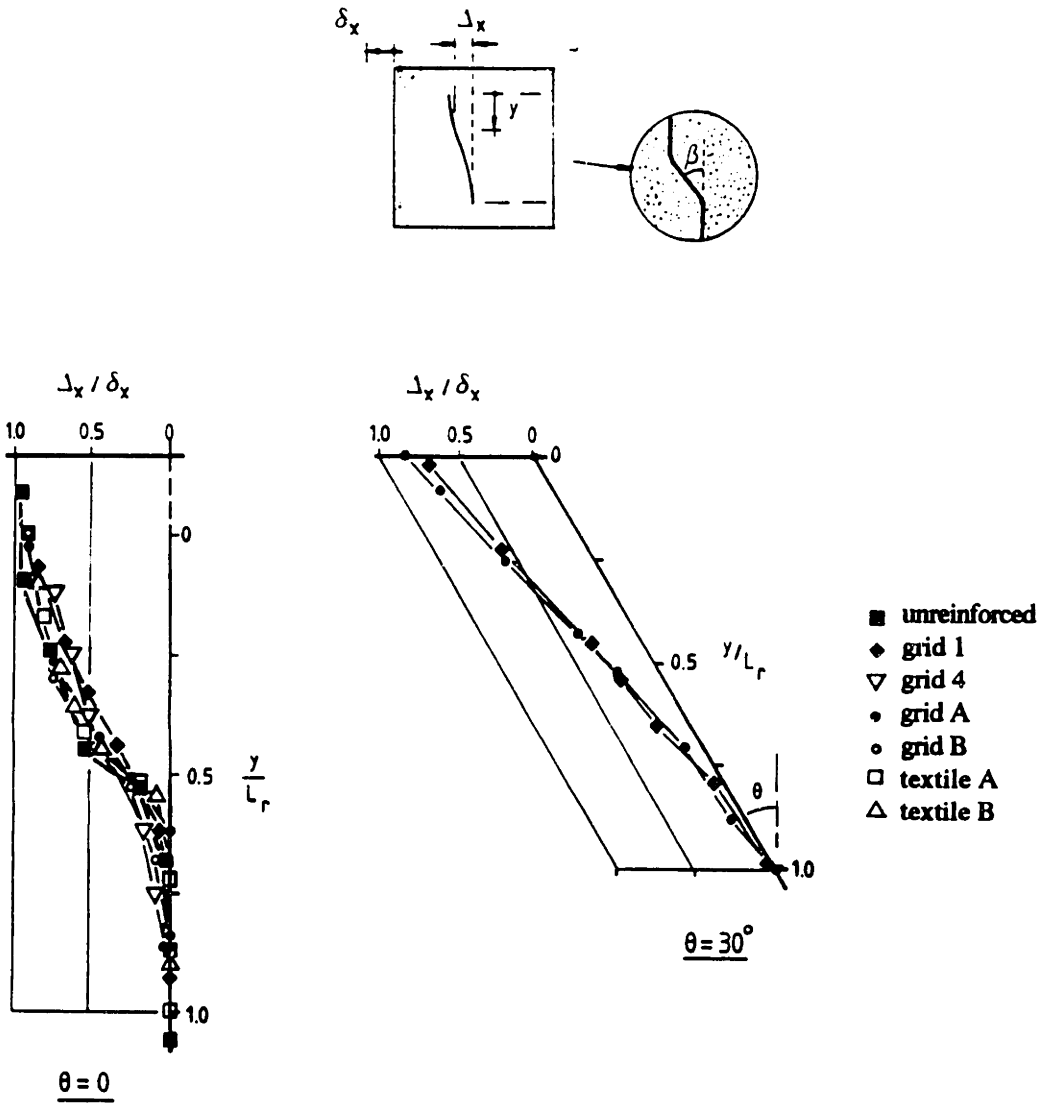

Code	B (mm)	S (mm)	S_l (mm)	E_l (kN/m)	β (°) Peak	β (°) End of Test
grid 1	1.63	12.5	12.5	6844	0.9	1.4
grid 4	4.78	76.2	76.2	49,455	2.7	8.7
grid A	4.40	53.2	10.2	440	5.4	22.4
grid B	4.40	111.0	22.2	550	4.0	20.3
textile A				550		
textile B				4000		

E_l = Longitudinal stiffness

Reinforcement Properties

Figure 2.25: Profiles of Reinforcements at Peak Stress Ratio in the Large Scale Direct Shear Box (after Palmeira and Milligan, 1989)

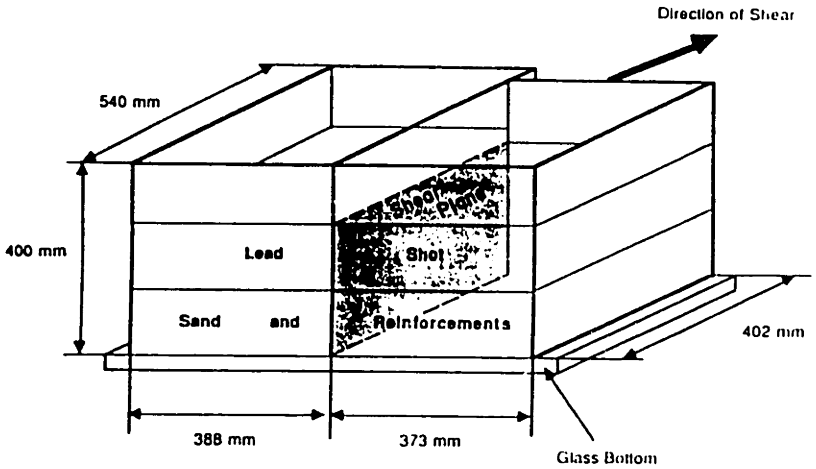

(a) Schematic of the direct shear box

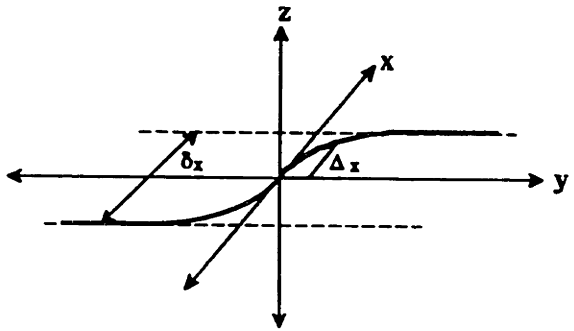

(b) Geometry of deformed fibers

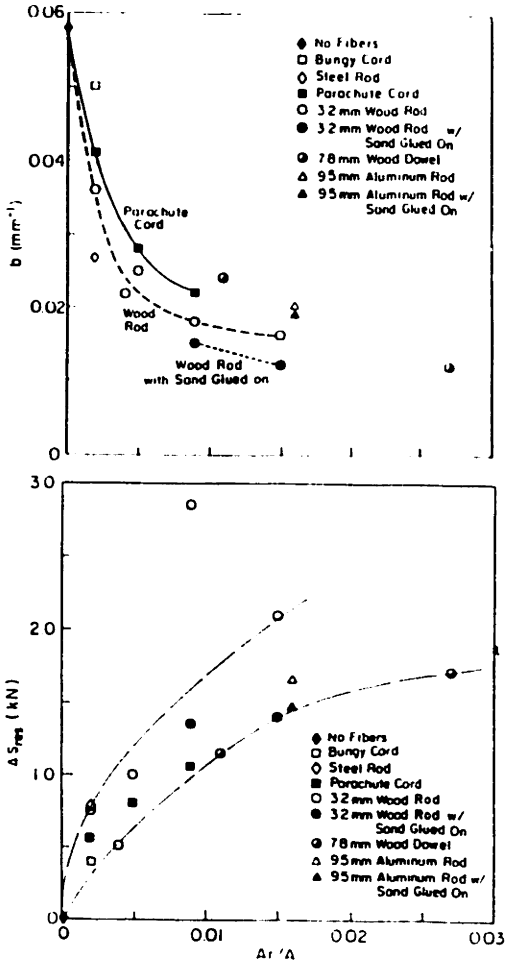

(c) Influence of reinforcement area ratio on direct shear strength and deformation decay constant

Figure 2.26: Direct Shear Box Results Reported by Shewbridge and Sitar (1989)

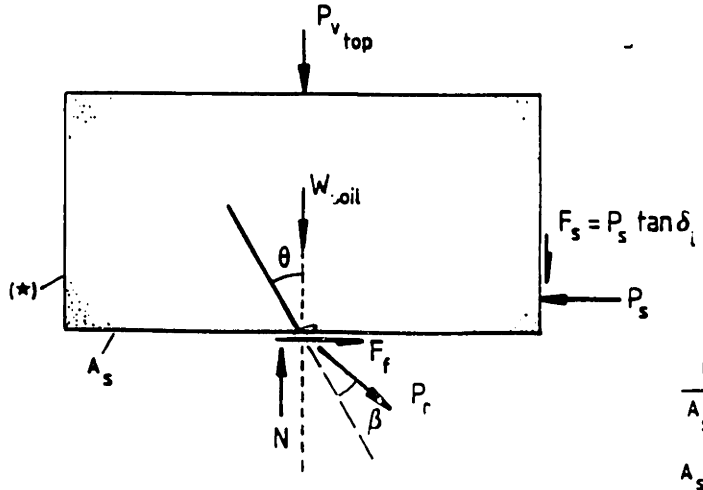

$$P_s = F_f + P_r \sin(\theta+\beta)$$

$$N = P_{v\,top} + W_{soil} + P_r\cos(\theta+\beta) + F_s$$

$$F_f = N\tan\phi_{ds} \qquad \bar{\sigma}_{yr} = N/A_s$$

$$P_v = P_{v\,top} + W_{soil} + F_s \qquad \sigma'_y = P_v/A_s$$

$$\bar{\tau}_{yx} = P_s/A_s$$

$$\frac{P_r}{A_s\,\sigma'_y} = \frac{\bar{\tau}_{yx}/\sigma'_y - \tan\phi_{ds}}{\sin(\theta+\beta) + \cos(\theta+\beta)\tan\phi_{ds}}$$

(★) – forces are negligible on this face

A_s - sample area W_{soil} - sample weight

$\bar{\sigma}_{yr}$ - mean vertical pressure on the central plane in reinforced tests.

(a) Forces acting on the top half of the specimen in a direct shear inclusion test (after Palmeira, 1987)

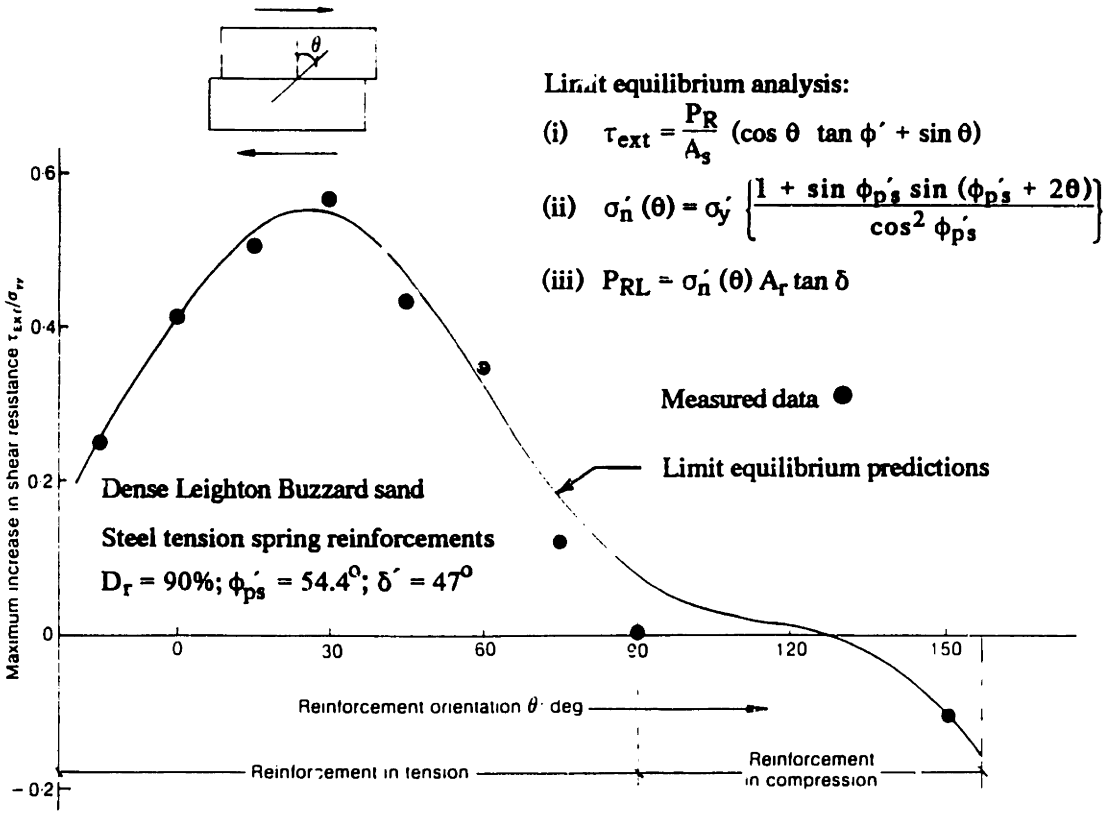

(b) Comparison of predicted vs. measured strength increase for reinforced direct shear tests (after Jewell and Wroth, 1987)

Figure 2.27: Limit Equilibrium Predictions of Loads in Inclusions at Different Orientations in a Direct Shear Test

Chapter 3: The APSR Cell

3.1. Introduction

This chapter describes the design and construction of a new laboratory device, referred to as the Automated Plane Strain Reinforcement (APSR) cell, which can measure the tensile force transferred to a planar reinforcing inclusion due to plane strain shearing of the surrounding soil matrix. The APSR cell simulates the mechanical interaction that occurs in a reinforced soil at working load levels under realistic and interpretable boundary conditions, and hence represents a significant advance over existing measurements of load-transfer characteristics (cf. Chapter 2).

Figure 3.1 shows the idealized geometry for a composite plane strain element of soil reinforced by a planar inclusion of length, L, which is oriented parallel to the direction of the external minor principal stress, σ_3. As the soil is sheared in a plane strain compression mode (by increasing the major principal stress, σ_1), tensile stresses are transferred to the inclusion. The plane of symmetry, $x = 0$ (Fig. 3.1) has well defined, mixed boundary conditions specified by: 1) no lateral displacement, $u_x = 0$, and 2) no shear stress acting along the plane, $\sigma_{xy} = 0$. These conditions are simulated in the design of the APSR cell, which corresponds to one-half of the unit element containing an inclusion of length, L/2, as shown in Figure 3.2. The rear wall of the cell ($x = 0$ plane, Fig. 3.2a) is rigid and lubricated to minimize friction. The key design feature of the APSR cell is that the inclusion is clamped externally to a load cell which measures the force in the reinforcement at a location equivalent to the centerline of an inclusion with length, L. In order to maintain the symmetry along the rear wall, a hydraulic

piston controls the position of the reinforcement such that there is no displacement of the inclusion at the reference entry point (X in Fig. 3.2).

Figure 3.3 shows the actual cross section through the APSR cell. It contains a soil specimen measuring 570mm high by 450mm wide by 152mm deep (plane strain direction) enclosed in a thin rubber membrane. The inclusion passes through a slot in the rear wall of the cell and is supported by jacking against an external support arch. In practice, the inclusion can be inclined at angles up to 50° to the major principal stress direction (θ, Fig. 3.2).[1]

The cell applies air pressure to the outside of the specimen to control the confining stress ($\sigma_3 \leq 50$ kPa), while the major principal stress is imposed by moving two end platforms into the specimen. Waterbags on top of these platforms provide uniform boundary pressures ($\sigma_1 \leq 400$ kPa). The specimen can deform freely in the lateral direction into the air void at the front of the cell. The cell imposes axial strains up to 10% on the specimen. These relatively large strain levels are necessary for investigating load transfer using relatively extensible reinforcing materials (e.g., Palmeira and Milligan, 1989; Section 2.2.1.3). The plane strain walls of the APSR cell have a unique active control system which ensures that $\varepsilon_{zz} \leq 0.02\%$ throughout the test.

Uniform specimens of dry sand are prepared using a custom-built raining apparatus. The sand can be deposited along either the z or y axes (Fig. 3.2). Sand specimens deposited in the z direction initially exhibit isotropic properties for plane strain shearing

---

[1]However, boundary conditions on the rear wall do not represent accurately the conditions on the central plane of the reinforced composite when the inclusion is rotated relative to the directions of σ_1 and σ_3.

in the x-y plane, while those formed in the y-direction will have cross-anisotropic properties (Arthur et al., 1972). Deposition in the z-direction permits load-transfer behavior to be examined independent of the effects of soil anisotropy.

Figure 3.4 shows the external instrumentation used in the APSR cell. Displacement transducers measure movements of the specimen boundaries and pressure transducers measure the applied major, minor and intermediate principal stresses. Radiography provides a record of internal soil displacements. Additional instrumentation can be designed to measure the local strains and/or stresses at locations along the inclusion for different types of reinforcing materials.

The APSR cell is fully automated with eight closed feedback control loops for the displacements of the platform and arch jacks, the positions of the plane strain walls, and the confining air pressure. These are controlled by a microcomputer and three custom-built analog feedback circuits. Two separate carts house the APSR cell and the test control electronics (Fig. 3.5). Connections between the two are quickly and easily removed and reattached so both carts can be transported separately.

This chapter discusses, in detail, the design considerations behind the APSR cell and the instrumentation required to provide interpretable results. The last part of the chapter describes the control systems that maintain the necessary boundary conditions in the cell.

3.2. Design of the APSR Cell

3.2.1. General Design Requirements

The previous section outlined the conceptual design and summarized the final configuration of the APSR cell based on the concept of a composite reinforced soil element. The overall goal of the design was to develop a laboratory device capable of measuring load transfer characteristics for a variety of candidate reinforcing materials (ranging from metal strips to polymeric grids and fabrics). The key design requirements for the device were originally identified as follows:

1. Cell dimensions were controlled by a) the representative size of reinforcing materials (such as grids) used in practice, b) predictions of the inclusion length necessary to achieve full load transfer, and c) stress levels comparable to field situations.
2. Uniform exterior stress fields (i.e., uniform boundary tractions) should be provided to allow a rational interpretation of the test data.
3. The cell must be able to subject the soil and reinforcement to relatively large strain levels (~10% axial strain) in order to study load-transfer for relatively extensible reinforcing materials.
4. Instrumentation should include direct measurements of forces and/or deformations in the reinforcement. The measurements of deformations in the surrounding soil provide important information for interpreting the mechanisms of load-transfer.

This section describes the development of the APSR cell, and shows how these considerations were incorporated into the final design.

3.2.2. Size Considerations

Selection of a general specimen size was the first step in the design process. Several factors played into the selection of the specimen size, and the final design was a compromise between the need to obtain interpretable results representative of field situations and the conditions that could be achieved practically in a laboratory scale test.

Four factors determined the size of the APSR cell sand specimens:

1. The characteristic dimensions of inclusion materials of interest (especially grids) controls the minimum acceptable specimen size in the x- and z-directions.
2. The length of the reinforcement required to achieve maximum load transfer determines how the measured data must be scaled to the prototype field situation.
3. The need to apply stress levels representative of field situations controls the magnitude of forces in the structural design. Practical considerations limit the magnitude of these forces.
4. The device was designed for an inclusion which can be rotated relative to the x-axis (Fig. 3.2). This determined the necessary specimen size in the y-direction.

This section describes the evaluation of these factors and the selection of the final cell dimensions.

3.2.2.1. Representative Size of Inclusion Materials

The APSR cell is designed to contain reinforcing inclusions representative of those used in actual construction applications. These include geosynthetic materials such as

polymer grids, woven and non-woven fabrics. The characteristic dimensions of such inclusion materials helped determine the necessary size of the APSR cell. Non-planar inclusions such as grids are of particular concern, since the grid aperture is a characteristic dimension affecting the load transfer.

Existing grid reinforcements come in a wide variety of aperture sizes and are manufactured using many different methods. The most commonly used geogrids were developed by Netlon Ltd. (Wrigley, 1987) and are formed from a punched polymer sheet (1 to 6mm thick) which is drawn under controlled temperature to produce a uniaxially strengthened grid (i.e., cold working aligns the polymer chains, producing a high tensile modulus in the direction of drawing). Ideally the inclusion specimen used in the APSR cell should have enough grid 'cells' to approximate the behavior of an infinite sheet. McGown et al. (1985) performed a set of uniaxial tensile tests on uniaxially and biaxially drawn Tensar geogrids, at constant rate of strain, to determine the necessary specimen size which approximates an infinite sheet. For a uniaxial grid (Tensar SR2), the critical specimen dimensions were 14 cells wide by 4 cells long (32cm wide x 41cm long), while the minimum biaxial specimen (Tensar SS2) had dimensions 11cm wide x 18cm long. Tensar SS2 is representative of many geogrids commonly used in reinforced earth construction. The width of the APSR cell (in the plane strain direction), z = 15.2cm was based on these findings.

3.2.2.2. Pick-up length

Chapter 6 compares predictions of tensile stresses in a planar reinforcement using a proposed shear lag analysis (Abramento and Whittle, 1992) with measurements for a steel sheet inclusion in the APSR cell. Prior to the development of the new shear lag analysis, preliminary estimates of the inclusion length required to achieve load transfer

were necessary for the design of the APSR cell. A significant amount of research has been performed in the field of composite materials to determine the distribution of stress in a cylindrical fiber embedded in an elastic matrix (Fig. 3.6a), based on an approximate analysis proposed by Cox (1952)[2]. Cox's derivation leads to a solution for the tensile stress in the fiber, σ^f, as a function of x of the form:

$$\sigma^f = E_f e \left[1 - \frac{\cosh \beta \left(\frac{L}{2} - x \right)}{\cosh \beta \frac{L}{2}} \right] \tag{3.1}$$

where E_f is the Young's modulus of the elastic fiber, L/2 is the half-length of the fiber, and e is the axial tensile strain in the surrounding matrix (positive in tension). The dimensionless shear lag parameter, β, is a function of the volume fraction of the fiber and the relative stiffness of the fiber and matrix materials:

$$\beta = \sqrt{\left[\left(\frac{G_m}{E_f} \right) \left(\frac{2 \pi}{A_f \ln(R/r_o)} \right) \right]} \tag{3.2}$$

where G_m is the shear modulus of the matrix, A_f is the cross-sectional area of the fiber, and R, r_o are the radius of the composite element and fiber, respectively.

The shear stress, τ, at the fiber-matrix interface can be obtained from the stress equilibrium of the fiber:

$$\tau = - \frac{r_o}{2} \frac{\partial \sigma^f}{\partial x} = E_f e \sqrt{\left(\frac{G_m}{2 E_f \ln(R/r_o)} \right)} \frac{\sinh \beta \left((L / 2) - x \right)}{\cosh \beta (L / 2)} \tag{3.3}$$

---

[2]This paper presents the original 'shear lag' analysis which has been subsequently modified by numerous authors. For review, see Hollister and Thomas (1969).

Estimates of the critical length of reinforcement required in the APSR cell were based on a parametric study of this solution. The parametric study examined the effects of varying fiber length and fiber-matrix stiffness ratio. Figures 3.6b and c summarize these results. Figure 3.6b shows the relative strain in a fiber of half length, L/2 = 0.4m as a function of distance from the centerline for three values of fiber-matrix stiffness ratio, E_f/G_m = 1, 2100, and 6000[3]. The examples use a ratio, R/r_o = 100, corresponding to a cell with radius R = 0.25m, and a thin reinforcing inclusion, r_o = 0.25cm (A_f = 0.2cm^2) (Table 3.1). For E_f/G_m = 1, the fiber and inclusion have equal axial strains. However, as the relative stiffness of the fiber increases, there is a lag between the strains in the matrix and the fiber, and hence less tensile stress is transferred at any point along the inclusion. Figure 3.6c shows the variation in the maximum tensile stress at the center of the inclusion for a very stiff reinforcement (E_f/G_m = 6000) as a function of the half-length, L/2. The inclusion stress is normalized by the maximum tensile stress that would develop in an infinitely long inclusion, σ_∞^f. The results show that relatively large dimensions (L/2 > 1m) are required to achieve the full load transfer expected at the prototype scale. Figure 3.6c also presents results from the recent shear lag analysis of the plane strain composite element (Fig. 3.1) developed by Abramento and Whittle (1992), with input parameters listed in Table 3.1. These results are qualitatively similar to the solutions of Cox, but show that full load transfer can be obtained for slightly shorter inclusions.

---

[3]These ratios correspond to a steel fiber, E_f = 2.1 x 10^5 MPa, embedded in a typical soil matrix with stiffness G_m/σ_c' = 350 to 1000 and a confining stress σ_c' = 100 kPa.

These analyses were used to guide the final selection of the maximum inclusion half length, $L/2 \leq 0.45$m used in the APSR design.[4] Measurements of tensile stresses for inclusions of different lengths in the APSR cell can define the maximum load transfer ratio (Fig. 3.6c) and hence permit reliable scaling of prototype stresses.

3.2.2.3. Structural Design Considerations

The structural design of the APSR cell was a compromise between the requirements to apply stresses representative of in situ conditions and the strong box dimensions necessary to support the resulting forces. The design was an iterative process, based on the selection of a reference confining stress. For a given confining stress, σ_3, the maximum principal stress, σ_1, required to induce failure in the specimen was calculated assuming a plane strain friction angle, $\phi'_{ps} = 50^{\circ}$. This led to the plate thicknesses required to keep the stresses in the walls to less than 7000 kPa.

The final design of the APSR cell assumes a maximum confining stress, $\sigma_3 \leq 50$ kPa, which is roughly equivalent to 3m of overburden pressure and is comparable to in situ confining stresses in actual reinforced earth structures. At this confining stress, the major principal stress at failure is:

$$\sigma_{1f} = \sigma_3 K_p = 380 \text{ kPa} \qquad (3.4)$$

where $K_p = \dfrac{1 + \sin \phi}{1 - \sin \phi}$ is the passive earth pressure coefficient. The stresses against the sidewalls (the intermediate principal stress, σ_2) to achieve the plane strain condition

---

[4]The resulting overall width of the APSR cell is 54.3cm, which is small enough to pass though a standard doorway, an important consideration since the cell must be moved into the MIT X-Ray room during testing.

were estimated using b = 0.5, where $b = \frac{\sigma_2 - \sigma_3}{\sigma_1 - \sigma_3}$. This maximum intermediate principal stress, σ_{2f} = 215 kPa, is a conservative estimate, as data from other plane strain devices show b = 0.35 to 0.45 (e.g., Green et al., 1975; Deterling, 1984).

The cell was designed as a strong-box made from aluminum plate. The sidewalls not only maintain the plane strain condition, they also provide the tensile support required to resist the compressive forces against the specimen. The end plates (Fig. 3.3) of the APSR cell are 13mm thick, and the front and back plates are 16mm thick. These thicknesses were selected to keep the maximum tensile stresses, $\sigma_t \leq 7000$ kPa, for an overall factor of safety, F_S = 35, against yield of the aluminum. The design of the plane strain sidewalls is described in section 3.2.4.3. The four walls of the cell stand 15.2cm high. Six 1/4-20 steel bolts attach each end plate to the front and back plates, and 53 1/4-20 bolts attach each sidewall onto the cell. The bolts are designed to resist shear and tension generated by the internal pressure forces in the cell. The number of bolts and the bolt sizes were selected using a factor of safety, F_S = 2.

3.2.3. Application of Boundary Stresses

The APSR cell is designed to apply uniform boundary tractions to the soil specimen and therefore cannot control the deformations and strains within the specimen. This is a common problem encountered in the design of laboratory element tests in soils (Arthur, 1988). Measurements of the uniformity of strains and deformations in unreinforced specimens provide a method for assessing the capability of the APSR cell to represent ideal elemental behavior.[5]

---

[5]In an ideal soil element, the state of both stress and strain is uniform.

The confining stress, σ_3, is applied via air pressure against the rubber membrane which envelopes the soil specimen. The major principal stress is applied through two platforms which move in unison to maintain the symmetry of the test and have a maximum displacement of 3.5cm. When fully extended, the platforms can impose an axial strain, $\varepsilon_{yy} = 10\%$ on the specimen (Fig. 3.3). As the specimen shears, it deforms into the air void at the front of the cell. This void is 5cm wide to allow up to 10% lateral strain (ε_{xx}). Such strain levels are believed necessary for a complete investigation of load-transfer behavior, especially for extensible materials such as geosynthetics which can greatly increase the strain to failure in the soil composite (Palmeira and Milligan, 1989).

3.2.3.1. Confining Stress

Compressed air applies the minor principal stress (or confining pressure) to the soil specimen. The advantage of compressed air is that there is no need to separate the systems that apply the major and minor principal stresses. The cell is made air tight using a bead of RTV[6] placed along all joints.

The air pressure is controlled by a voltage-pneumatic regulator, manufactured by Fairchild, Inc. The regulator scales the amount of pressure it supplies to the cell according to a signal voltage that it receives from a control source. The regulator accepts an input signal between 0 to 10V and scales its output between 0 to 100 kPa. The regulator requires a supply of air at high pressure (the laboratory compressor provides air at 1100 kPa) which it scales down to the proper output pressure.

---

[6]RTV is a silicone rubber adhesive sealant, manufactured by General Electric.

A 6.4mm diameter tube runs from the regulator to a Swagelok fitting that threads into a hole in the front wall of the cell. The air pressure fills the entire cell and provides a hydrostatic confining stress against the specimen. A pressure transducer mounted to the front wall (Transducer P3, Fig. 3.4a) monitors this cell pressure.

3.2.3.2. Major Principal Stress

Two pairs of hydraulic jacks (Fig. 3.3) apply a uniform major principal stress to the specimen via two pressurized water bags. Figure 3.7 shows a detailed view of the jack and platform assembly. The platforms comprise 1.57cm thick aluminum plates with an all-around clearance of 0.8mm to prevent the plates from binding against the outer walls of the cell. The platforms are attached to the hydraulic jacks with eight 6-32 socket head screws, four through each jack. A thin sheet metal cover fits over the entire platform assembly to cover the platform mounting holes. On top of this cover is a flexible, water-filled pressure bag. The bag provides a uniform axial pressure against the specimen. A pressure transducer measures the water pressure inside the bag (transducers P1 and P2; Fig. 3.4).

The four hydraulic jacks were custom designed for the APSR cell. Each jack consists of two concentric brass cylinders with outer diameter 14cm. The cylinder walls are 6.1mm thick. An O-ring fits inside a groove near the open end of the smaller cylinder to provide a water-tight seal. The bottom of each jack has a threaded hole to accommodate a 1/4 inch Swagelok tube fitting. The jacks are extended and retracted by pumping water into or out of this hole. They have a maximum design stroke of 3.5cm.

Each jack attaches to the end plates of the cell with four 6-32 socket head screws. The end plates have 2.5cm diameter holes to accommodate the tube fittings that protrude

from the base of the jacks. There is an O-ring seal around the base of each jack to prevent air from leaking under the jacks and out through the holes in the end plates.

The hydraulic jacks have several advantages over direct motor control of the two platforms. They are relatively inexpensive, very compact, and can easily be replaced to permit either increased load or extension capacity. The hydraulic control doesn't transmit mechanical vibrations to the soil specimen, and the motors which control the flow into and out of the jacks are external to the cell so they can be serviced or replaced even if a test is in progress.

The platform waterbags were custom manufactured by Aero Tec Industries for the APSR cell. They are made from a smooth, high-strength elastomer and have a maximum design pressure of 690 kPa. The waterbags have an overall thickness of approximately 1.5cm. They are each filled with water through a 1/4 inch pipe fitting which protrudes out of the rear face of the bag through a hole in the jack platform. Displacement transducers (D8 and D9, Fig. 3.4) measure the positions of the front faces of the pressure bags (the faces in contact with the soil). The transducer rods pass through 3.2mm diameter tubes across the thickness of the bags.

The water bags have the same width as the undeformed the soil specimen (45cm). Rubber blocks immediately adjacent to the water bags (Fig. 3.7) cover the rest of the platform over the width of the air void. As shearing proceeds, the soil specimen deforms laterally over these rubber end blocks, which keep the pressure against the axial faces of the specimen as uniform as possible. In some APSR tests, a thin aluminum sheet (1.5mm thick) was placed over the entire width of the cell to cover both the water bag and the rubber end block on each platform. The aluminum sheets were a

late addition, but were found necessary to reduce nonuniform specimen deformations and are now part of the final design (cf. section 4.6.1).

3.2.4. Boundary Constraints

3.2.4.1. The Rear Wall

Boundary conditions on the rear face of the APSR cell (x = 0 plane, Fig. 3.2) are an essential feature of the design concept. Ideally the wall is rigid and frictionless. In practice, the rear wall is made of 1.6cm aluminum plate and the inside surface is lubricated with two thin layers of grease, separated by a sheet of 0.25mm thick natural rubber. The grease is a 50-50 mixture of Dow-Corning high vacuum grease and Compound 7. The Compound 7 is a release agent which reduces the viscosity and shear strength of the vacuum grease. Section 4.4 describes several tests to determine the amount of friction transmitted across the lubricated specimen boundaries. The results show that this combination of rubber and grease produces a very low friction surface.

3.2.4.2. Reinforcement Position Control

One of the key design features incorporated into the APSR cell is the restraint of the reinforcement at the reference entry location (X, Fig. 3.2). For the rear wall of the cell to be a plane of symmetry, there must be negligible movement of the reinforcement at its point of entry perpendicular to the rear wall. The entry point corresponds to a location at the center of an inclusion of length, L, where the maximum load transfer occurs (e.g., Fig. 3.6b). Any displacement of the reinforcement into the specimen will result in a decrease of the load measured at the reference point.

Figure 3.8 shows the mechanism that references the position of the entry point on the reinforcement to the rear surface of the specimen. A proximity sensor, fixed to the entry point on the inclusion, monitors the position of a steel target embedded at the rear face of the specimen. The target consists of two 3mm thick steel squares, one inside the specimen and one outside the cell, connected by a shaft which passes through a small hole in the rear wall of the cell. The target shaft is coated with a lubricant (WD40) so it slides freely through this hole. Any movement of the specimen perpendicular to the wall due to compression of the grease or rubber against that surface is accompanied by an outward movement of the target, so that the reinforcement position is referenced to the true rear-most boundary of the soil specimen.

The proximity sensor fits into a thin plexiglas plate that is attached by a hinge to the outside of the cell. The other end of the plexiglas has a pin protruding from it. A hook passes through a hole in the inclusion and over the end of this pin. The plexiglas plate is spring-loaded to maintain pressure against the hook. In this way, the proximity sensor measures the position of the entry point on the reinforcement relative to the steel target. The position of the reference point is controlled by a feedback control loop (section 3.4.4) which adjusts the pressure in the arch jack according to displacements measured by the proximity sensor. This system can control the position of the reinforcement to within 1 μm of its target position.

3.2.4.3. Plane Strain Control

Most reinforced soil structures, including embankments and walls, can be characterized as satisfying kinematic conditions of plane strain wherein there are no strains in the direction normal to the applied stresses (i.e., the z-direction; Fig. 3.2). The APSR cell

has a unique active control system capable of keeping the out-of-plane strain, $\varepsilon_{zz} \leq \pm 0.02\%$.

There are many plane strain laboratory devices described in the literature (Seah, 1990; Tatsuoka et al., 1986; McGown and Andrawes, 1977; Green and Reades, 1975). All of these devices rely on the high bending stiffness of the side platens to approximate plane strain conditions. The large surface area of the APSR cell ($A_s = 0.26m^2$) and range of design pressures ($\sigma_2 \leq 215$ kPa) impose a serious constraint on the size of the sidewalls. An active control system was developed in order: a) to reduce the size and weight of the sidewalls, and b) to enable measurements of the intermediate principal stress, σ_2. This design has the added benefit that soil deformations can then be measured by radiography.

Radiography is important in the design of the APSR cell as it provides a method for establishing the uniformity of strains inside the unreinforced soil, and can monitor mechanisms of soil reinforcement interaction (cf. section 3.3.3). With the equipment available in the MIT geotechnical laboratory, the strains in the plane of the X-Ray film can be measured to the nearest 0.2% for a marker spacing of 2cm (section 3.2.6.3) as is used in the APSR soil specimens. Out-of-plane strain should therefore be kept to a fraction of that precision, ideally to less than 0.05%.

The first step in designing the plane strain sidewalls for the cell was to determine the required thickness of the sidewalls for a maximum deformation, $\delta_z \leq 38\mu m$ (corresponding to $\varepsilon_{zz} \leq 0.05\%$). In the preliminary design phase, solutions for the

bending of a thin elastic plate were used (Roark and Young, 1975)[7], based on finite difference approximations for the plate differential equations.

For a uniformly loaded, rectangular plate with all edges fixed, the maximum deflection, δ, is given by:

$$\delta = \frac{\alpha\, q\, w^4}{E\, t^3} \tag{3.5}$$

where q is the normal pressure against the plate, E is the Young's modulus of the plate, w is the plate width, t is the plate thickness, and α is a tabulated function of the length/width aspect ratio of the plate. For the APSR sidewalls, $w \approx 51$cm, and $\alpha \approx 1.55$. For a maximum stress, $\sigma_2 = 215$ kPa (section 3.2.2.3), the normal load over the entire plate is approximately 57 kN. For steel plate ($E = 207 \times 10^6$ kPa) the required thickness, t = 3.6cm.

In comparison, the active control system (shown schematically in Fig. 3.4b) uses a sidewall which comprises two aluminum plates (inner plate t = 6mm, outer plate t = 19mm), separated by a pressurized water diaphragm. Movements of the inner wall are monitored by centrally located displacement transducers (D10 and D11, Fig. 3.4b), which are mounted to an external reference frame. As the inner wall starts to deform, a feedback control loop (identical to that used for the reinforcement position) pumps water into the cavity between the inner and outer walls. The increase in water pressure returns the inner wall to its initial position, transferring the required strain energy to the heavy outer wall. The water pressure in the sidewall corresponds to the intermediate

---

[7]Roark and Young (1975) state for elastic materials with Poisson's ratio in the range of 0.15 to 0.30, errors in computed deflections should not exceed 8 percent.

principal stress for plane strain shearing and is monitored by pressure transducers P4 and P5 (Fig. 3.4b).

Figure 3.9 illustrates the construction of the plane strain walls. The outer wall is actually composed of three pieces: a heavy outer plate, a shim, and a sheet metal liner to contain the water layer. The water diaphragm is sealed by an O-ring in the outer plate. The shim is made from 1.6mm thick aluminum sheet with a cut-out to fit around the O-ring in the outer wall. The sheet metal liner sits on top of the shim. A series of flat-head screws pass through the liner and the shim and thread into the outer plate to squeeze the liner against the O-ring. This forms a tight seal to hold the water inside the wall. The outer plate has a threaded hole to accommodate a 1/4" Swagelok tube fitting. The water pressure inside the wall is adjusted by pumping water into this hole.

Each sidewall attaches to the other cell walls with 53 1/4-20 bolts spaced every 5.07cm. Assuming a maximum sidewall pressure of 215 kPa, the maximum load in each bolt is 7.48 kN, resulting in a stress of 236,000 kPa. This is approximately half the yield stress of the bolts.

3.2.5. Accommodation of Various Reinforcement Geometries

The APSR cell has been designed to accommodate a wide variety of reinforcing materials with different thicknesses and geometries. The cell has an adjustable slot where the inclusion enters the soil specimen. This slot can accommodate reinforcement widths up to 130mm. The linkage which connects the reinforcement to the load cell on the support arch (Figs. 3.8 and 3.10) can accommodate grips designed specifically for a given reinforcement material. The linkage can rotate around the support arch by $\theta = \pm 50^{\circ}$ (Fig. 3.2) to the centerline for studying the effects of reinforcement orientation in the APSR cell.

3.2.5.1. Entry Slot

The APSR cell has a slot in the rear wall to allow a reinforcing inclusion to pass from the inside to the outside of the cell. The clearance between the edges of this slot and the reinforcement must be of the same order as the grain size of the soil to prevent particles from squeezing out of the cell. Figure 3.8 shows a detail of the entry slot. The rear wall of the cell contains a 12.7cm gap, into which are fitted two wedge shaped pieces that form a tight fitting slot around the inclusion. The wedges can be custom machined for any reinforcement width up to 12.7cm. The wedges bolt into place between the plane strain sidewalls.

3.2.5.2. Reinforcement Clamping Mechanism

The first set of grips used in the APSR cell were designed for testing steel sheet inclusions (Fig. 3.10). The grips consist of two 12.7mm thick steel plates measuring 152mm x 79mm. They fasten to the end of the steel sheet inclusion with seven 3/8-inch bolts. Two 3.2mm rubber pads placed between the grips and the inclusion maximize the interface friction, while Belleville 'spring' washers on the bolts ensure a minimal loss of normal load for slight changes in the thickness of the rubber pads.

The linkage from the grips to the arch piston is shown in Figure 3.10. The pieces are adjustable to accommodate various grip geometries. The linkage attaches to a yoke which is connected through a ball joint to the load cell on the support arch. This ball joint acts as a moment break so that no bending moment is transmitted to the load cell. The other end of the load cell threads into the arch jack which is fitted via two 3.2mm thick aluminum plates to the curvature of the semi-circular support arch. Thus, the tensile force in the reinforcement is transmitted over a relatively large surface area of the support arch.

3.2.5.3. Orientation of Inclusion to Principal Stress Directions

The arch and entry slot allow the reinforcement clamping mechanism to be rotated by $\pm 50^{\circ}$ from the centerline. The arch fits against the rear wall of the cell where it is held in place by four angles (Fig. 3.8). Each angle bolts onto the arch with three 3/8-inch diameter bolts. Three more bolts hold each angle fixed to the cell wall. Two set screws (Fig. 3.10) prevent the jack assembly from sliding along the arch. The jack can be repositioned by releasing the set screws, sliding the jack to the desired orientation along the arch, and retightening the screws.

3.2.6. Sand Deposition

An important design consideration is the method of specimen preparation. The APSR cell is initially designed to test dry sand, and all of the tests performed to date have been on an uniform, medium grained sand. The sand specimens are contained in a thin, rubber membrane that is custom made for each test. Prior to placing the sand, the cell is cleaned and greased to ensure the proper boundary conditions during shearing.

The method of depositing the sand is critical to the reliability of the test results as it controls the specimen uniformity (of density), repeatability (consistency from one specimen to the next), and preparation time. Specimens are prepared in the APSR cell by means of multiple sieve dry pluviation, a method in which the sand is dropped from a controlled height through a set of sieves configured to achieve a desired density (Miura and Toki, 1983). The specimen uniformity and repeatability obtained by this method are evaluated in Chapter 4.

The direction of deposition relative to the plane of shearing affects the measured soil behavior (Arthur et al., 1972). During deposition, irregularly shaped particles come to

rest with a preferred orientation in which the long axes of the particles are inclined towards the horizontal plane (Oda, 1972), and the sand develops a cross-anisotropic fabric. Figure 3.11 illustrates two angles used to identify the direction of shearing relative to the direction of sand deposition:

1. If the sand is sheared in the plane perpendicular to the direction of deposition (the horizontal x-y plane, Fig. 3.11a), it exhibits isotropic stress-strain properties because there is no preferred particle orientation in this plane. Thus, the measured stress-strain behavior is independent of the direction of loading (ψ) in this plane.
2. If the specimen is sheared, in a plane strain mode, at an angle $\delta < 90^{o}$ to the direction of deposition (i.e., in the z-x plane, Fig. 3.11b), then the measured stress-strain behavior is affected significantly by the direction of σ_1.

The APSR cell is designed so that sand is most easily rained perpendicular to the plane of shearing (i.e., Case 1 above). Thus, shearing takes place in the isotropic plane and the measurements are not affected by issues of depositional anisotropy. The sand can also be rained parallel to the plane of shearing in order to investigate the effects of anisotropy, although procedures have not yet been refined for raining in this direction. All tests described in this thesis were deposited in the x-direction (Figs. 3.2, 3.11), and hence are sheared in the plane of isotropic soil properties.

The following paragraphs describe the procedure for preparing unreinforced sand specimens in the APSR cell. Specimen membrane preparation will vary depending on the geometry of the inclusion for reinforced tests. Preparation procedures for tests with steel inclusions are discussed in Chapter 5. The raining technique is the same for tests with and without inclusions.

3.2.6.1. Specimen Membrane Preparation

The APSR specimen membranes are cut from a standard roll of 0.38mm thick natural rubber, sold under the trade name "dental dam." The membrane contains the sand during deposition and allows the specimen to support a vacuum so that the specimen mold can be removed and the top cover bolted in place. The membrane must be completely air tight to ensure a uniform effective confining stress during shearing.

In the initial series of APSR tests, membranes were 0.25mm thick. These thinner membranes frequently ruptured prematurely. Figure 3.12 shows the dimensions of the pieces that make up a membrane. To obtain the maximum utility from a standard roll of rubber, the pieces should be cut according to the pattern shown in Figure 3.12b. The three pieces are bonded together with P7865 latex contact adhesive, manufactured by the American Finish and Chemical Company. To assemble the membrane, the three pieces are laid on a large, smooth surface such as a clean floor or large table top. The side flaps are first bonded to the primary sheet (Fig. 3.13a). Then the corner seams are made as shown in Figure 3.13b and c to create a rectangular prism. After all the seams are finished, a narrow bead of RTV (a silicone rubber adhesive sealant) seals the inside and outside of the corners. The membrane is inserted into a wire mesh frame and filled with water to check for leaks.

3.2.6.2. APSR Cell Preparation

Before setting up a membrane to rain a specimen, the inside surfaces of the APSR cell must be free of sand and dirt. The most critical surfaces are the rear wall of the cell, the surfaces of the water bags, and the floor of the cell. Next, a thin layer of grease is applied to these areas. The grease is a 50-50 mixture of Dow-Corning high vacuum grease and Compound 7. The grease is spread using a paint roller which creates a

uniform layer over the floor and rear wall of the cell. Rubber sheets (0.25 mm thick) are then placed on these walls and covered with another layer of grease. The paint roller is used again to squeeze out any occluded air bubbles.

The specimen mold is then inserted into the APSR cell (Fig. 3.14a) and is attached to the rim of the cell with seven 1/4-20 bolts. The membrane fits inside, with the top flaps laying over the edge of the mold.[8] A light layer of grease inside the mold causes the rubber to adhere to the metal surface, which facilitates setting up the membrane. After the air bubbles have been removed, the top edge of the membrane is taped to the side of the mold to prevent sand particles from falling between the two. The tape must be continuous around this top edge. Finally, the membrane is punctured with an awl or a nail through the vacuum port, and the vacuum tube is inserted through the membrane. The vacuum tube attaches to a Swagelok fitting that screws into the rear wall of the cell. A piece of filter paper is fitted over the end of the tube and held in place by an O-ring to prevent sand from being sucked into the tube when the vacuum is applied.

Two wooden triangular inserts are placed at the two front corners of the specimen.[9] These inserts prevent the development of a premature failure plane from one of these two corners. A similar technique has been used in the Directional Shear Cell (Wong, 1985).

---

[8]It is important to massage out any air bubbles trapped under the membrane.

[9]The inserts have dimensions 23mm x 16mm x 145mm, cut at a 35° angle. They are bonded to the membrane corner using latex adhesive.

3.2.6.3. Sand Deposition

There are several common methods for preparing sand specimens in the laboratory. These include moist and dry tamping, vibration, and pluviation (or raining). Each method has advantages and disadvantages, and results in different soil fabric. For uniform soils (poorly graded), pluviation creates homogeneous specimens with controlled relative densities, and simulates a soil fabric most similar to natural, sedimentary deposits (Oda et al., 1978). There are several factors to consider when designing a sand raining device. These include the height of the fall (the distance from the bottom of the sieves to the top of the specimen), shutter porosity (or deposition intensity), and the number and size of diffuser sieves (Rad and Tumay, 1987).

Figure 3.15 shows the raining configuration for preparing dense APSR specimens. It consists of a sand hopper perched on top of a 1.4m high chimney. The hopper has a perforated floor, with a shutter porosity of 6.7%. The hole pattern is the same as that used by Sweeney (1987) for preparing dense sand specimens. A sliding plate covers the holes in the floor so the hopper can be filled with sand. Inside the chimney are two wire mesh screens with 6.3mm square openings. The screens are mounted on a frame and can be removed as a unit. There is a slight gap (approximately 3mm) between the sieves and the chimney wall. This is covered with tape prior to raining so that sand does not fall through the gap and into the cell. The two sieve patterns are rotated at 45° with respect to each other at a distance 200mm apart. The lowest sieve is 430mm above the floor of the cell such that the fall height of the sand varies from 430mm to 280mm as the specimen forms.

The raining configuration for depositing a loose specimen involves removing the diffuser screens from the chimney (after Rad and Tumay, 1987). The specimen is then

deposited at a higher velocity with a reasonable uniformity and an average relative density, $D_r = 31\%$ (for Ticino sand). Chapter 4 describes the procedure used to check the uniformity and repeatability of the rainer for preparing dense and loose specimens.

The top of the specimen mold has a frame made out of aluminum angle pieces. A sheet metal deflection shield sits on top of this frame to prevent sand from depositing on the rim of the mold and dropping into the cell at an uncontrolled velocity, which might result in nonuniform sand densities near the walls of the cell. The inside dimensions of the deflection shield match those of the final specimen length and width. The shield rests on top of the flaps of the rubber membrane which are draped outside of the specimen mold. The flaps later fold and seal over the top of the sand specimen. The complete specimen preparation procedure is as follows:

1. The raining chimney sits inside the frame on the top of the specimen mold. It is lifted onto this frame by means of two aluminum rods that pass through the width of the chimney near its base.
2. The hopper at the top of the chimney is filled with sand which is then rained by removing the sliding aluminum cover from the bottom of the hopper, allowing the sand to pour through the perforated hopper floor.
3. Internal soil strains are determined in the APSR cell using radiography. A regular grid of tungsten carbide spheres, 2.4mm in diameter, is placed at the mid-height of the specimen. Each marker produces a clear, perfectly circular image on the X-ray film from which the sand displacements can be estimated. In order to place the markers, the sand hopper is filled to the half-way mark, then the sliding door is removed to deposit the sand. The cover is replaced so that no further sand particles rain down the chimney. The surplus sand is scooped from the floor of the hopper and the hopper and

chimney are lifted off of the specimen mold. Some sand that was caught between the wall of the chimney and the deflector shield spills out when the chimney is removed. Sand deposited in the frame around the mold is vacuumed out, then the deflector shield is removed. The tungsten carbide balls are placed with a plexiglas positioning template that has 100 holes spaced on a 2cm square grid. A small diameter clear tube is used to drop the balls into the template holes.

4. The second half of the specimen rains into the cell in much the same way, except that now the hopper is filled to approximately 2cm above the half-way mark. This ensures that the height of the rained specimen is higher than the desired final configuration. After most of the sand falls from the hopper, any leftover particles are swept down the chimney (since the top of the specimen will be screeded off). The hopper and chimney are again removed, and excess sand vacuumed out of the specimen mold frame. Then the deflector shield is removed.

5. The sand specimens are rained to approximately 2 cm above the final specimen height. A screeder removes the excess sand to produce a flat surface (Fig. 3.14b). The screeder is a 3.2mm thick aluminum plate measuring 44.5 x 12.5cm, mounted to an aluminum angle with two screws. The angle slides along the top of the mold frame so that the bottom of the plate scrapes the sand off at a controlled height. The final height of the specimen can be altered by loosening the mounting screws and readjusting the plate position. The sand pushed from the top of the specimen is initially removed with a scoop. After a number of passes, the amount of sand displaced by the screeder decreases and the excess must be removed carefully with a shop vacuum to avoid disturbing the top of the specimen.

6. In order to seal the membrane, the two side flaps are folded back over the top of the specimen. The line of overlap is lightly marked with a soft-point pen, taking care not to disturb the specimen surface. The flaps are then lifted back again, cleaned with a degreasing solvent, such as acetone, and a band of latex adhesive is applied to the overlapping surfaces. When this joint is complete, the edge flaps are cleaned and sealed to the side flaps.
7. The specimen membrane rarely seals properly with the latex adhesive alone, and so additional RTV must be applied at the corner. Once the RTV has cured, a vacuum can be applied to the specimen. Leaks in the top seams usually make a hissing sound and can be sealed with more RTV. If the specimen doesn't hold an adequate vacuum and makes no hissing sound, a bead of RTV placed across every latex adhesive seam usually solves the problem.

3.3. Instrumentation

The APSR cell is instrumented to measure boundary stresses and displacements as well as internal strains in the sand and along the reinforcing inclusion. The instrument package provides both test control information and response data. A total of 16 electronic transducers record the external measurements of boundary stresses and displacements, while X-rays of the specimen, taken at regular intervals during shear, measure the internal soil displacements. A computer program interprets the average and local strain fields from the radiographic images. Additional instrumentation measures the force and strain distribution in the inclusion. All of the response data is collected by the central data acquisition system of the MIT Geotechnical Laboratory (section 3.3.1.5).

3.3.1. Boundary Measurements

Figure 3.4 shows the locations of the boundary pressure and displacement transducers. Direct current, linear voltage displacement transformers (LVDTs) measure directly the boundary displacements on the specimen. Boundary stresses applied by the water bags, sidewalls, and confining air pressure are all measured by pressure transducers. The load cell on the support arch measures the external load in the inclusion, and an electromagnetic proximity sensor detects the movement of the inclusion. All of these transducers receive their power from two Hewlett Packard dual DC power supplies (model 6205C). The central data acquisition system monitors the output for most of the transducers. Transducer output is also read manually with Keithley Model 177 digital multimeters.

3.3.1.1. Boundary Displacements

The APSR cell has eleven LVDTs to measure specimen boundary displacements. These include the axial displacement of the specimen imposed by the waterbags (D8, D9; Fig. 3.4), the lateral deformation of the specimen against the confining air pressure (D5, D6, D7), and the out-of-plane deformation in the plane strain sidewalls (D10, D11). The LVDTs used in this project are manufactured by Trans-Tek, Inc. and comprise two parts: a barrel and a core assembly. The barrel contains an oscillator, a demodulator, and a differential transformer. The oscillator converts the DC input voltage to AC. The AC current excites the primary winding of the differential transformer which induces a voltage in the secondary windings. The core moves through the electrical field produced by the primary winding, altering the amount of voltage generated in the secondary winding. The demodulator converts the output back to a DC signal. The

resulting output is a DC voltage that is linearly proportional to core displacement inside the barrel.

All of the LVDTs used in the APSR cell have a displacement range ±1.3 or ±2.5cm. The LVDTs accept any input voltage between 6 and 30V. However, because most of the other transducers used in the cell require 5 to 6V input, a standard of 6V was used for all transducers. At this input voltage, the LVDTs have an output range of ±3.0V for the ±1.3cm capacity and ±4.3V for the ±2.5cm capacity transducers.

Two LVDTs (D8, D9; Fig. 3.4) measure the axial strain, ε_{yy}, in the specimen by monitoring the front face of each waterbag (Fig. 3.7). They are each seated in a fitting that threads into the outer wall of the APSR cell. The core extension rod in the LVDT passes through a hole in the bottom of this fitting and into a hole in the cell wall. An O-ring squeezed between the threaded fitting and the cell wall surrounds the LVDT rod and prevents air from leaking out of the cell. Inside the cavity, between the outer cell wall and the axial platforms, the end of the LVDT rod is soldered to a 20-gage copper wire. This wire passes through a hole in the load platform, and through the tube in the center of the waterbag. A #2 brass washer is soldered to the end of the copper wire. The washer rests directly on the rubber membrane, so that any deformations of the specimen at this point are detected.

Four LVDTs (D1, D2, D3, D4; Fig. 3.4) measure the displacements of the two load platforms. These transducers are held outside the cell by the same type of fitting described for D8 and D9. The LVDT rods thread into 1.27cm diameter posts, which in turn thread into tapped holes in the platforms to form a rigid connection. These data are used to match the displacements of the two jacks on each platform and hence prevent platform rotation. The test control matches the two readings for each platform to the

nearest 0.01mm. Although the platform readings do not measure the true boundary displacement as accurately as the centerpoint transducers (D8, D9), they provide a reasonable backup in case of device malfunction.

The lateral strain in the specimen, ε_{xx}, is measured by three LVDTs spaced 15.2cm apart along free face of specimen (D5, D6, D7; Fig. 3.4). These are also held by fittings that thread into the outside wall of the cell. Inside the cell, the end of each LVDT threads into curved plexiglas feet that are in direct contact with the specimen membrane. Very low stiffness springs between the plexiglas feet and the cell wall maintain contact against the specimen.

Two LVDTs (D10, D11; Fig. 3.4) monitor the movement of the inner plane strain walls as shown in Figure 3.16. The LVDTs clamp to an external reference system that balances on three points on top of the APSR cell. This floating reference frame ensures that the two LVDTs remain a fixed distance apart. The frame consists of heavy steel angles bolted together around the cell. A 2.1mm diameter machined brass pin passes through a hole in each of the outer side walls and rests against the inner wall (Fig. 3.16). An O-ring around the pin forms a seal to prevent the pressurized water between the inner and outer walls from leaking out. A plug threaded into the outer wall presses against the seal to ensure that it presses firmly around the pin. There is a slot on top of this plug so the amount of force against the O-ring can be adjusted with a screwdriver. The seal must be snug enough to prevent leaks, but not so tight that the brass pin cannot move freely. The top of the brass pin threads into an aluminum foot. The sidewall LVDT core rod threads into the opposite side of the foot, in line with the brass pin (Fig. 3.16). A spring between the foot and the barrel of the LVDT presses the foot toward the sidewall, keeping the end of the brass pin in firm contact with the inner sidewall.

Using an input voltage of 6V, the sidewall LVDTs have a nominal output range of ±3.0V, corresponding to ±1.3cm displacements. The output of the LVDTs is, therefore, approximately 0.43 cm/V. The resolution on the voltmeters is 0.1 mV when reading on the ±2 V scale. 0.1mV corresponds to 0.43μm of displacement in the LVDTs. The specimen is 15.2cm wide in the plane strain direction, so this configuration is capable of measuring the out-of-plane strain to a precision of 0.0006%.

3.3.1.2. Boundary Stresses

Five pressure transducers, manufactured by Data Instruments, Inc., measure the boundary stresses in the APSR cell. They consist of a sealed chamber with a stainless steel diaphragm that deforms under an external pressure. Two semi-conductor strain gages coupled to the diaphragm are put in tension and compression, unbalancing a Wheatstone bridge circuit[10]. The resulting output is a small voltage that is linearly proportional to the pressure against the diaphragm. The pressure transducers require an input voltage of 5 to 6V DC, and produce an output signal of 0 to 100mV.

Two transducers measure the axial stress, σ_{yy}, applied to the specimen by the two waterbags (P1, P2; Fig. 3.4). The transducers have a capacity of 690 kPa and are housed in a stainless steel fitting that connects to the waterbag extension tube (Fig. 3.7), plugging the waterbag with the pressure transducer in direct contact with the water in the bag. The electrical lines to the transducer are linked to the outside of the cell through an amphenol connector sealed into the end wall.

---

[10] Chapter 5 provides a more complete description of the principles underlying the Wheatstone bridge circuit.

Pressure transducer P3 (Fig. 3.4) is mounted to the front wall and measures the air pressure inside the cell. This transducer has a capacity of 172 kPa and is housed in a fitting like the ones attached to the waterbags. It threads into an adapter which converts the male pipe thread on the fitting to a 1/4-inch straight thread with an O-ring seal. The adapter fits into a 1/4 inch tapped hole in the front wall of the cell. When tightened down, the O-ring at the base of the thread presses against the cell wall and seals off any gaps around the threads through which air might escape.

The pressures in the plane strain walls are applied by two pressure actuators (section 3.4.2), one for each wall. Pressure transducers (P4, P5, with capacities of 690 kPa; Fig. 3.4) are mounted to the lines that feed the sidewalls. As there is very low flow in the sidewall system, measuring the pressure at the source reflects accurately the pressure between the inner and outer sidewalls.

3.3.1.3. Inclusion Position

The relative position of the reference point on the inclusion and the rear wall of the cell is monitored by an electromagnetic proximity sensor using the mechanism shown in Figure 3.8. The sensor is marketed under the name EMDT, short for Electro-Mike Displacement Transducer, manufactured by the Electro Corporation. It consists of two parts: a converter module and a sensor. The converter module sends power to the sensor, which projects a 200 kHz electrical field in front of its tip. This field generates eddy currents in any metal target which the field intercepts. These eddy currents remove energy from the field. The amount of energy returned from the sensor to the converter module decreases in proportion to the distance between the tip of the sensor and the metal target.

The feedback loop controlling the position of the reinforcement uses the signal from the proximity sensor to keep the reinforcement fixed with respect to the rear surface of the specimen. If the signal changes, the feedback loop senses the change in voltage and activates the arch piston until the proximity sensor reading returns to its initial value.

3.3.1.4. Inclusion Load

A load cell mounted on top of the arch piston measures the force applied by the piston on the inclusion. The tests described in this thesis used a JP-2000 load cell with a capacity of 8.9 kN, manufactured by Data Instruments, Inc. The load cell measures the axial force exerted by two threaded rods that fit into tapped holes (1/2-20) on either side of the cell and connect on one side to the top of the arch piston and on the other to the loading yoke (Fig. 3.10). The load cell is of the shear beam design, and, like the pressure transducers described earlier, relies on a strain gage circuit to produce output as a linear function of applied load. The JP-2000 load cell has two germanium strain gages connected in a wheatstone bridge. It has a maximum deflection of 0.05mm, and an output of approximately 150mV at its maximum load.

3.3.1.5. Data Acquisition

A central data acquisition system serves all of the equipment in the MIT geotechnical laboratories. The system consists of a Hewlett Packard 3497A Data Acquisition Control Unit interfaced to an AT compatible microcomputer. The control unit receives a voltage and converts it to a digital signal which is stored in a format compatible with Lotus 123. The computer can take a complete set of readings at time intervals, $\Delta t \geq 1$ sec., specified by the user.

The APSR cell has access to 15 lines on the central data acquisition computer. Table 3.2 summarizes all of the transducer lines required by the cell, and shows which are monitored by the data acquisition system and which are required for feedback control loops. The APSR channels not recorded by the data acquisition system are usually read by hand at regular intervals during a test. Table 3.2 also shows the precision with which each measurement can be made by both the data acquisition system and the APSR control computer.

All of the transducers in the APSR cell, except for the proximity sensor, receive their power from two junction boxes. The main junction box (Fig. 3.17) serves most of the transducers in the APSR cell, while a secondary junction box serves the transducers for the plane strain sidewalls (D10, D11, P4, and P5; Fig. 3.4) and the proximity sensor. Both boxes reside on the control cart with the test control electronics (Fig. 3.5)

The junction boxes are made from aluminum sheet metal and fitted with a set of 5 pin male amphenol connectors. The power to the boxes goes into the lower two pins (pins D and E) of the connector labelled "Power" (Fig. 3.17). The two lower pins of the "Input Voltage" connector are wired to the power supply so that the voltage into the junction box can be checked with a voltmeter. The power is connected to the lower two pins on all of the connectors labelled "To Transducer"; pin D connects to the low end and pin E to the high end of the input voltage.

The transducers transmit return signals to the junction boxes through pins A and B (on the transducer amphenols). At the junction box, pins A and B are wired to the amphenol connectors labelled "To Voltmeter". Wires from some of these connectors are

attached to the APSR cell microcomputer, allowing the computer to monitor the transducer signals.[11]

In the main junction box, the transducer output is also wired to one of two 14 pin cable connectors located in the side of the box. Two cables containing wires to the central data acquisition system hook into the cable connectors. Transducer lines 1 through 5 connect to Cable Connector 1 and lines 7 through 11 to Cable Connector 2. Lines 6 and 12 are not monitored by the data acquisition system and are used solely for the computer control of the APSR cell described in section 3.4.3.

All of the tests on reinforced soil conducted to-date in the APSR cell have used steel sheets instrumented with strain gages. An additional junction box accommodates the instrumentation for the reinforcement, which includes the strain gages and JP-2000 load cell. The electronics inside this junction box are described in detail in Chapter 5. The box has a 25 pin connector that connects four strain gage output signals and the load cell signal to the central data acquisition system.

3.3.2. Transducer Data Reduction

The central data acquisition computer records voltages in a format compatible with the Lotus 123 spreadsheet program. The data reduction process for APSR tests has been largely automated with the use of two template spreadsheets. These spreadsheets are programmed to retrieve the raw data taken during a test, convert it to engineering units, and generate a series of data plots. The names of the two template spreadsheets are

---

[11]Transducer signals can also be read by hooking up a voltmeter to the amphenol connector next to the rotary switch at the bottom of the junction box (Fig. 3.17) and switching to the appropriate channel.

APSRTEMP.WK3 and LOADTEMP.WK3. APSRTEMP.WK3 reduces the data for the boundary stresses and displacements and generates standardized plots reported in subsequent chapters. LOADTEMP.WK3 processes the reinforcement force measurements from the strain gages and the load cell and generates plots of reinforcement loads as functions of the external stresses and strains in the reinforced soil composite. Appendix C presents the computations used to reduce the transducer data.

3.3.3. Internal Strain Measurements

Internal soil deformations in the APSR cell are measured using radiography. The technique is similar to that used by Bekenstein (1981) for studying soil strains in the directional shear cell (DSC). During a typical test, five X-rays are taken to record successive displacements of a grid of tungsten carbide markers located at the midplane of the specimen (section 3.2.6.3). After developing the film, the marker positions are digitized using an optical comparator and stored on a microcomputer. A FORTRAN computer program called "STRAIN" reduces the digitized coordinate data to compute the global strains and the local strain fields within the radiographed portion of the specimen. Appendix B gives a description and listing of "STRAIN".

3.3.3.1. X-Ray Procedure

The MIT Geotechnical X-Ray facility consists of two Phillips 160 kV metal-ceramic X-ray guns housed in a lead-lined room and controlled by a Phillips MG-160 constant potential X-Ray system.

The APSR specimens are prepared outside of the X-ray room (following the procedure in section 3.2.6). After the specimen is sealed, a vacuum of 83 kPa is applied and the

cell is wheeled into the room. The vacuum minimizes specimen disturbance during transportation. The transducer, water and air pressure lines that feed the cell run up and over the wall of the X-ray room so they can be controlled safely from outside.

Radiographic measurements are made vertically. The carbide markers are located approximately 85cm beneath the window of the radiation gun, while the film cartridge is housed beneath the cell (approximately 99cm below the radiation source). The APSR cart is equipped with a frame to hold the film cartridges such that successive radiographs are obtained in identical positions. Lead sheets are placed on the top surface of the cell to frame the radiographed portion of the specimen and to minimize scattered radiation (this improves the quality of the image).

The first exposure is taken immediately before shearing the specimen, when the confining pressure is established and the vacuum released. Exposures require approximately 10 minutes when operating the X-ray gun at a current of 3.8 mA. Further X-rays are performed at specified stress levels and immediately after failure of the specimen.

3.3.3.2. Analysis of Radiographs

After the films are developed, a digitizing system (Fig. 3.18) records the positions of the tungsten carbide markers on each image. The digitizing system comprises three components: an optical comparator, a digital position readout system (DPRS) and a personal computer to store data. The optical comparator consists of a light source, a moving platform (or stage) on which to mount the radiographs, and a viewing screen which displays the image (at 20x magnification). The stage has adjustment screws for fine motion control in the X and Y directions to allow precise positioning on the viewing screen. Two electronic position sensors (Sony Magnescales) measure the X

and Y positions of the platform to a resolution of 2μm; these are transmitted to the DPRS, which displays coordinate measurements in either inches or millimeters. The coordinates of a marker image are obtained by aligning the image so it is centered on the comparator screen. The screen has a series of concentric circles marked on it to facilitate this process.

The DPRS has an RS232 communication port on its rear panel which connects to the serial port of the microcomputer. It sends the (x, y) coordinate data to the computer in the form of an 18 byte 'word' whenever the user presses a foot pedal connected to the device.

A BASIC program called "POINTS" records the incoming coordinates on the computer. The program stores the data in a disk file and references the coordinates from the first radiograph. For all subsequent radiographs, it computes the displacements of the tungsten markers from their initial positions. This displacement data is stored in a separate file. A second program, called "STRAIN", computes global and local strains from the displacement data file. Appendix B describes both programs in greater detail.

The precision of this measuring technique depends upon several factors, including the quality of the X-ray image, the amount of movement of the film on the comparator platform, and the diligence of the operator. The measuring precision was checked by taking one X-ray film and digitizing it twice. "STRAIN" was then used to compute the 'apparent' displacements of the markers between the digitizing runs. If the system is error-free, the apparent displacements (or strains) should be zero. The standard deviation of the strain measurement computed with the STRAIN analysis program was 0.10%. This corresponds to the precision of the digitizing technique for measuring internal soil strains.

3.3.3.3. Strain Reduction Software

The strain analysis used in this research is based on the work of Seah (1990), using multiple linear regression to estimate strains from the measured displacement field. Appendix B summarizes the derivation of the analysis given in Seah (1990). For a global analysis, the strains are averaged over the entire field of interest by fitting a plane through the calculated strains at each known displacement point. In the local analysis, a uniform grid is defined over the displacement field. At each node on this grid, a specified number of displacement points within a 'weighting window' are used to compute the average strains at that node. The influence of a known displacement point on this average is weighted according to its distance from the node. The greater the number of known displacement points taken into account at each grid node, the smoother the fit from one grid point to the next. If all points are used, the local analysis yields a single average strain for the whole field (identical to the global analysis).

The program STRAIN is based on a program developed by Seah (1990), but with significant modifications. The program uses input displacement data (from POINTS) to compute global strains and local strain fields. The program is generalized for any number of displacement points and specified dimensions of the weighting window. The program generates two output files:

1) the global strain analysis, including rigid body rotations of the displacement field, magnitudes of the component, principal, volumetric and maximum shear strains, and
2) similar data for each node (on a 19x19 node imaginary grid) within the displacement field.

The output from the local strain analysis is reported in the form of strain contour plots (e.g., Fig. 3.19) using the commercially available SYSTAT statistics and graphics package on a Macintosh computer. Figure 3.19 shows the internal strains for two small viewing windows whose location is discussed in section 4.6.1.2.

3.4. APSR Cell Control Systems

3.4.1. Overview of Test Control

The APSR cell has eight control loops to maintain and update the boundary conditions required during a test. These control loops regulate the air pressure in the cell, the movements of the four platform jacks, and the positioning of the sidewalls and reinforcement. They can be divided into dynamic and static control loops. The dynamic loops follow a variable time history during a test and control the axial platform positions and the confining air pressure. They are regulated by a computer-controlled feedback loop that adjusts positions and pressures to corresponding time dependent target values.

The static control loops remain fixed throughout a test and control the sidewall positions and the reinforcement position. They are maintained by independent analog feedback loops which seek to match the readings in the appropriate transducers to their initial reference values (at the start of a test).

Overall, the APSR control hardware includes: 1) seven pressure actuators with seven corresponding motor control panels, 2) one voltage-pneumatic air pressure regulator, 3) a Hyundai 286C microcomputer to run the computer controlled feedback loops and reduce the test data, 4) three junction boxes to send power to and read the signals from

all of the transducers, and 5) a set of power supplies and voltmeters. The control hardware is mounted on a heavy-duty pushcart for ease of transportation and operation.

3.4.2. Pressure-Volume Actuators

All of the water pressures in the APSR cell are applied by custom-designed pressure-volume actuators. The actuators feed the four platform jacks, the arch piston, and the two plane strain walls. Figure 3.20 shows a schematic diagram of one of these actuators and Table 3.3 outlines the technical specifications of each actuator. They are based on an original design by Germaine and Andersen (Andersen, 1991).

Each actuator consists of a water chamber and a piston. The piston is driven by a ball screw actuator (Duff Norton Model 2625) into the water chamber, causing an increase in the water pressure. The ball screw actuator converts a small amount of applied torque, supplied by an electric motor, into a linear thrust. Given an input torque of 2.37 N-m, these ball screw actuators can supply up to 4 kN of thrust with a stroke of 15.2cm.

The water chamber and piston are made of brass. The chamber consists of a hollow cylinder with two end plates. The end plates have circular grooves that fit over the cylinder with an O-ring seated at the bottom of the groove. The end plates are squeezed together against the edges of the cylinder by a set of six stainless steel rods with nuts at either end (Figure 3.20). The piston passes through a hole in one of the end plates with a clearance of 0.03mm. This hole has a double O-ring seal to prevent the water in the chamber from leaking out around the piston. The other end of the chamber has a small threaded hole to accommodate a Swagelok tube fitting. The pressure-volume controllers are connected to the APSR cell via 6.35mm diameter plastic tubes. The end of each tube has a valve which can be closed to prevent air from entering the line when it is detached

from the cell. Swagelok Quick-Connect fittings are used to attach the waterlines to the cell to facilitate disconnection and reconnection.

The piston dimensions were selected based on:

a) the maximum design pressure (given the capacity of the ball screw actuator), and

b) the required volume of fluid used for the various components of the APSR cell.

The ball screw actuator connects to an aluminum plate with two bolts. The reaction force for the actuator comes from four stainless steel rods which tie this plate to the end plate of the pressure chamber (Fig. 3.20). The whole assembly is mounted to a 12.7cm wide aluminum channel.

Electrocraft 352 motors drive the pressure actuators. Each is fitted with a 100:1 gear box to provide a hundredfold increase its maximum output torque, for a total of 2.47 N-m. Electrocraft E352BU control cards regulate the rate of rotation of these motors. The rate of rotation is scaled according to an input signal voltage, $-15V \leq V_{in} \leq +15V$.[12]

3.4.3. Microcomputer Control

The confining pressure and the platform positions are controlled by a Hyundai 286C microcomputer which contains two analog-to-digital (A/D) converter cards that enable it to read transducer signals coming from the APSR cell. From these signals, the

---

[12]An input signal of -15V runs the motor full speed clockwise, while +15V runs it counterclockwise. A signal of 0V causes the card to hold the motor motionless.

computer calculates the platform and sidewall displacements, waterbag and sidewall pressures, and the confining air pressure and attempts to match these values to targets set by the user. It does this by sending voltage signals through a D/A converter to the Fairchild air regulator and pressure actuators (controlling the platform jacks and sidewalls). After sending a set of signals, the control loops again check the transducer readings.

3.4.3.1. Hardware Requirements

The hardware required for computer control of the APSR cell is illustrated in Figure 3.21. The components include: 1) a microcomputer with nine A/D channels and six D/A channels; 2) a terminal panel for the D/A channels; and 3) motor control panels for the platform and sidewall pressure actuators.

The two analog-to-digital converter cards (A/D) used in this project were developed by Sheahan (1991) and cost approximately one tenth the price of comparable commercially available circuits. The cards are built around the Analog Devices AD1170 chip, which is a programmable integrating A/D converter with a maximum conversion of 22 bits and variable integration time. This allows high precision without signal conditioning. The A/D cards have eight channels and are capable of taking up to 50 readings per second (Werner, 1990), which is more than sufficient for the feedback loops in the APSR cell. They fit into expansion slots in the computer, and reside at addresses 768 and 800 on the Hyundai 286 computer. A standard 25 pin connector on each card receives the lines that carry the transducer signals to the computer from the transducer junction boxes.

The digital-to-analog (D/A) converter was manufactured by Strawberry Tree, Inc., and resides at address 6960 in the computer. Each channel on the card has a switch to define its output range. In the APSR computer, channels 1-4 are set to ±5V (for the

platform jack pressure actuators), channel 5 to 0-10V (the Fairchild air regulator) and channel 6 to ±5V (the sidewall pressure actuators). The computer communicates to the card through 3 of 8 I/O addresses. The computer sends 8 bit words to these I/O addresses to specify a desired output voltage and a desired channel or channels to which to send that voltage. The magnitude of the voltage is set with 12 bits (or 1.5 'words'). This means that the output range (either ±5V or 0-10V) is divided into $2^{12} - 1$ (or 4095) parts for each channel. The card's output voltage is scaled according to how many bits the computer sends to the appropriate I/O addresses. The number 0 (all 12 bits set to 0) corresponds to the minimum voltage in the output range, and the number 4095 (all 12 bits set to 1) corresponds to the maximum. Each number in this scale corresponds to an increment of 2.4mV of output.

The I/O addresses on the Strawberry Tree card have the following functions:

I/O Address	Function
Base Address + 0	Set the first 8 bits (low bits) of analog output
Base Address + 1	Sets the last 4 bits (high bits) of analog output
Base Address + 2	Selects the channels to send the analog output

Strawberry Tree also manufactures a terminal panel which connects to the D/A card through a ribbon cable. The output voltages from the card travel to positive and negative screw connections on the terminal panel. Each device which receives output voltages from the computer connects to one of the channels on the terminal panel.

The four platform jack pressure actuators are controlled by the motor control panel shown in Figure 3.21. The panel contains the electric motor control cards for the pressure actuators, each with four modes: advance, stop, retract, and external signal. "Advance" sends a 15V signal to the motor control board, which runs the motor full speed forward. "Stop" shorts the two leads to the motor board, resulting in a 0 V signal. "Retract" sends a -15V signal, which runs the motor full speed reverse. The "External Signal" mode sends the voltage from the signal leads to the motor board, allowing direct computer control over the speed of the motor.

3.4.3.2. Control Algorithms

The computer program APSR, written in BASIC programming language, coordinates the microcomputer control of the APSR cell. The program reads the relevant transducer signals from the A/D card, and sends the necessary output voltages through the D/A card to match the target boundary conditions set by the user. A user's guide and program listing appears in Appendix A.

The program opens with the Main Menu screen shown in Figure 3.22. The command options are all menu driven. To select a command, the user moves a cursor up and down the menu on the left side of the screen and hits the [RETURN] key at the appropriate choice. These commands set target values for the air pressure, platform position or pressure, and sidewall pressure. Under the RUN command, the program continuously displays all of the relevant transducer readings in Volts and engineering units, and seeks to maintain the selected target conditions. The control algorithm cycle proceeds according to the flowchart in Figure 3.23. First the program checks and adjusts the air pressure until it matches the target value. If the user has specified computer sidewall control, the program adjusts the sidewall pressures until they reach

either the target pressure or displacement. Between each voltage pulse to the sidewall motors, the program rechecks and adjusts the air pressure if necessary. The final step in the cycle is to adjust the two platform positions. Between each voltage pulse sent to the platform motors, the program rechecks and, if necessary, adjusts the sidewall pressures and the air pressure. The user can interrupt this loop at any time to change the specified target conditions.

3.4.4. Independent Feedback Control

There are three analog feedback controllers that maintain the fixed boundary conditions in the APSR cell. These include the two sidewall positions and the reinforcement position. Figure 3.24 illustrates the control panel for operating these three feedback loops. The electronics behind the panel are based on a design by Andersen (1991).

Each controller can operate in one of four modes: Error Amplifier, External Signal, Advance, and Retract. Advance and Retract run the pressure actuator motors full speed forward and full speed backward, respectively. The External Signal option sends an external voltage directly to the motor, operating the controller identically to the direct computer control panel described previously. This mode is used in the sidewall controllers when the computer controls the sidewall pressures.

The Error Amplifier mode operates the panel as an independent analog feedback controller. The controller receives an analog input from a transducer and compares this input to a reference voltage. It then sends an output voltage to the motor influencing the transducer reading. The magnitude of the output voltage is directly proportional to the difference between the transducer signal and the reference voltage. Adjusting the reference voltage (also called the set point) is known as "tuning the loop." Typically this is done at the start of a test. The loop is tuned until there is no error; the transducer

signal and the reference voltage match each other. Over a period of time, the transducer reading will change slightly. When this happens, the error signal is sent to the motor controlling the condition measured by the transducer until the error signal returns to zero. The panel can amplify the error signal to increase the sensitivity at which the loop rebalances itself. It has selectable gains of 1, 10, 50, 100, and 200.

There are two options for providing a reference voltage.

1. The panel has a potentiometer that sets an internal reference voltage, with selectable ranges of ±0.5 V, ±1 V, ±3 V, or ±7 V. The loop is then tuned by adjusting the potentiometer until there is no movement in the corresponding motor.
2. The panel also has a pair of leads to hook up an external reference voltage. The loop is then tuned by adjusting this external voltage.

The feedback controllers have a more rapid response time than direct computer control because they respond continuously to any change in transducer output. The feedback loop maintains the measured sidewall positions to within ±8 μm of their target value. The total out-of-plane strain is therefore within ±0.01%. The loop controlling the reinforcement position keeps the proximity sensor reading to within 1 μm of its target value.

Steel Fiber in Axial Tension (Cox, 1952)	
Inclusion Properties	
Elastic Modulus	$E_f = 2.1 \times 10^8$ kPa
Fiber Radius	$r_o = 2.5$ mm
Fiber Area	$A_f = 20$ mm^2
Matrix (Soil) Properties	
Shear Modulus	$G_m = 35{,}000$ kPa
Matrix Radius	R = 25 cm

Planar Steel Reinforcement in Soil Under Plane Strain Compression (Abramento and Whittle, 1992)	
Inclusion Properties	
Elastic Modulus	$E_f = 2.1 \times 10^8$ kPa
Poisson's Ratio	$\upsilon_f = 0.2$
Fiber Thickness	f = 2.5 mm
Matrix (Soil) Properties	
Shear Modulus	$G_m = 35{,}000$ kPa
Poisson's Ratio	$\upsilon_m = 0.4$
Matrix Thickness	m = 25 cm
Confining Stress	$\sigma_3 = 100$ kPa
Strain in Matrix	$\varepsilon_{xx} = 0.05$ (5%)

Table 3.1: Input Parameters Used to Evaluate Inclusion Load Transfer Using Shear Lag Analyses

Channel	Transducer[1]	Calibration Factor	Data Acq. Channel[2]	Measurement Precision			
				Data Acq.		Feedback/Computer Control	
				Volts	Eng. Units	Volts	Eng. Units
Main 1	D1	3.405 cm/V/V_{in}	70	0.1 mV	0.6 μm	0.1 mV	0.6 μm
Main 2	D8	3.239 cm/V/V_{in}	71	0.1 mV	0.6 μm		
Main 3	D3	3.337 cm/V/V_{in}	72	0.1 mV	0.6 μm	0.1 mV	0.6 μm
Main 4	D9	3.237 cm/V/V_{in}	73	0.1 mV	0.6 μm		
Main 5	P3	8.548 kPa/mV/V	74	1 μV	1 Pa	0.1 mV	0.1 kPa
Main 6	D2	3.246 cm/V/V_{in}	N/A			0.1 mV	0.6 μm
Main 7	P1	34.42 kPa/mV/V	75	1 μV	6 Pa	0.1 mV	0.6 kPa
Main 8	P2	34.37 kPa/mV/V	76	1 μV	6 Pa	0.1 mV	0.6 kPa
Main 9	D5	3.350 cm/V/V_{in}	77	0.1 mV	0.6 μm		
Main 10	D6	3.256 cm/V/V_{in}	78	0.1 mV	0.6 μm		
Main 11	D7	3.321 cm/V/V_{in}	79	0.1 mV	0.6 μm		
Main 12	D4	3.266 cm/V/V_{in}	N/A	0.1 mV	0.6 μm	0.1 mV	0.6 μm
Secondary 1	P4	33.96 kPa/mV/V	N/A	1 μV	6 Pa	0.1 mV	0.6 kPa
Secondary 2	P5	34.49 kPa/mV/V	N/A	1 μV	6 Pa	0.1 mV	0.6 kPa
Secondary 3	Proximity Sensor		N/A				
Secondary 4	D10	2.485 cm/V/V_{in}	N/A	0.1 mV	0.4 μm	0.1 mV	0.4 μm
Secondary 5	D11	2.439 cm/V/V_{in}	N/A	0.1 mV	0.4 μm	0.1 mV	0.4 μm
Secondary 6	Load Cell	0.363 kN/mV/V	N/A	1 μV	0.06 N		
Inclusion Box 1	Inclusion Strain		45	1 μV	1x10^{-4}%		
Inclusion Box 2	Inclusion Strain		46	1 μV	1x10^{-4}%		
Inclusion Box 3	Inclusion Strain		47	1 μV	1x10^{-4}%		
Inclusion Box 4	Inclusion Strain		48	1 μV	1x10^{-4}%		
Inclusion Box 5	Load Cell	0.363 kN/mV/V	49	1 μV	0.06 N		

Notes: 1. Refer to Figure 3.4.

2. N/A means that channel is not read by data acquisition system and must be hand read.

Table 3.2: APSR Cell Transducer Lines

Pressure Actuator Components

1. Ball Screw Actuators:

Manufacturer:	Duff-Norton, Charlotte, NC
Model:	M28630-8 Inverted Ball Screw Actuator
Rated Load:	1000 lbs
Turns of Worm Gear for 1" Raise:	40
Torque at Full Load:	21 in-lbs
Actuator Efficiency Rating:	20%

2. Analog Motors:

Manufacturer:	Electro-Craft Corporation
Model:	E352-MGHD Gear Motor
Max. Speed:	50 rpm
Max. Torque:	14 in-lbs
Rated Voltage:	28 V
Torque Constant:	4.8 oz-in per Amp
Voltage Constant:	3.6 oz-in per krpm
Linearity:	0.2%
Temperature Coeff:	-0.02% per degree Centigrade

Pressure Actuator Specifications

Actuator No.	APSR Device	Actuator Volume (cm^3)	Maximum Pressure (kPa)
1-4	Platform Jacks	350	1550
5, 6	Sidewalls	480	1120
7	Arch Jack	146	3700

Table 3.3: Specifications for the APSR Cell Pressure Actuators

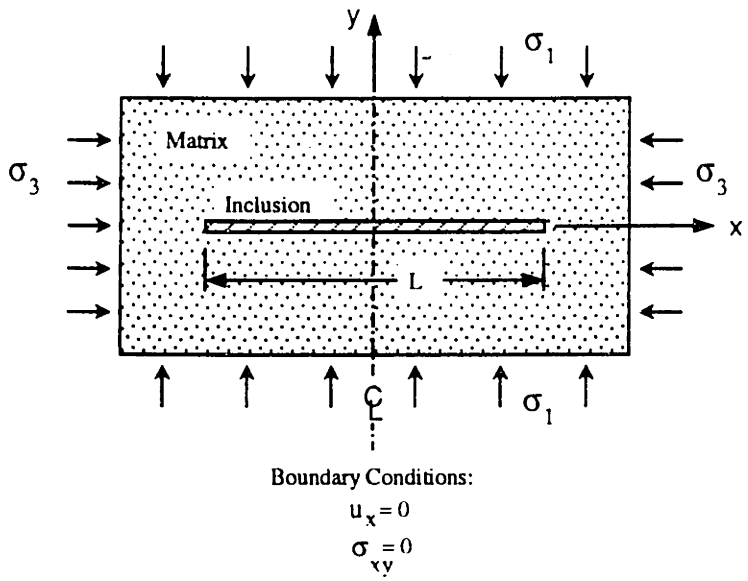

Figure 3.1: Geometry of the APSR Ideal Plane Strain Reinforced Composite Soil Element

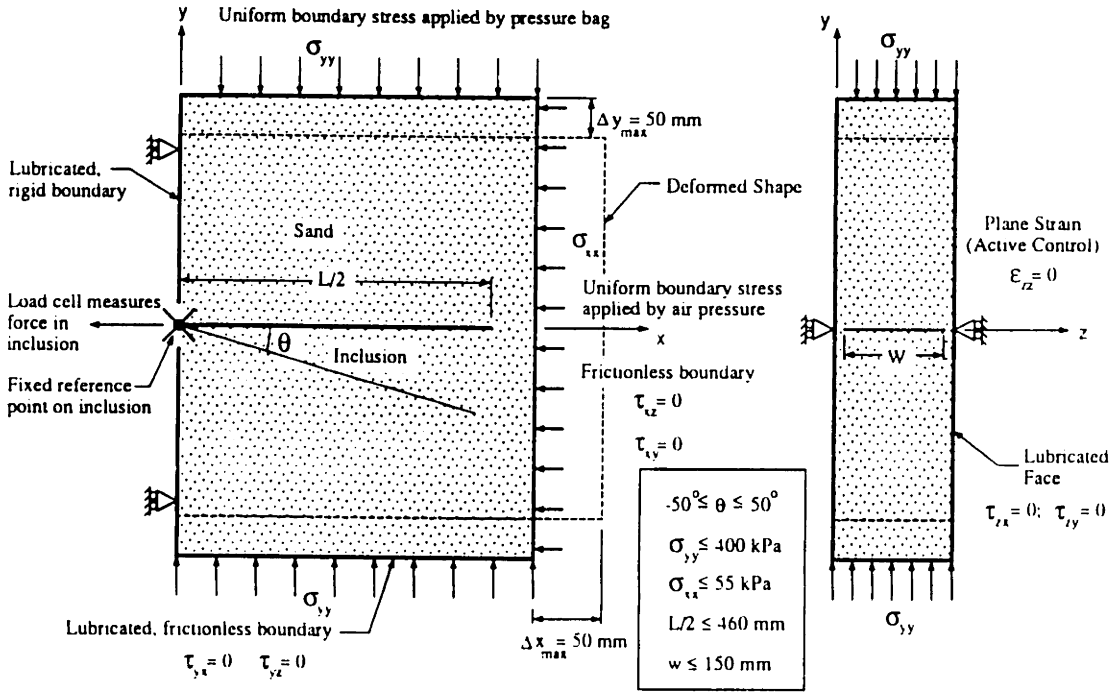

Figure 3.2: Conceptual Design of the APSR Cell

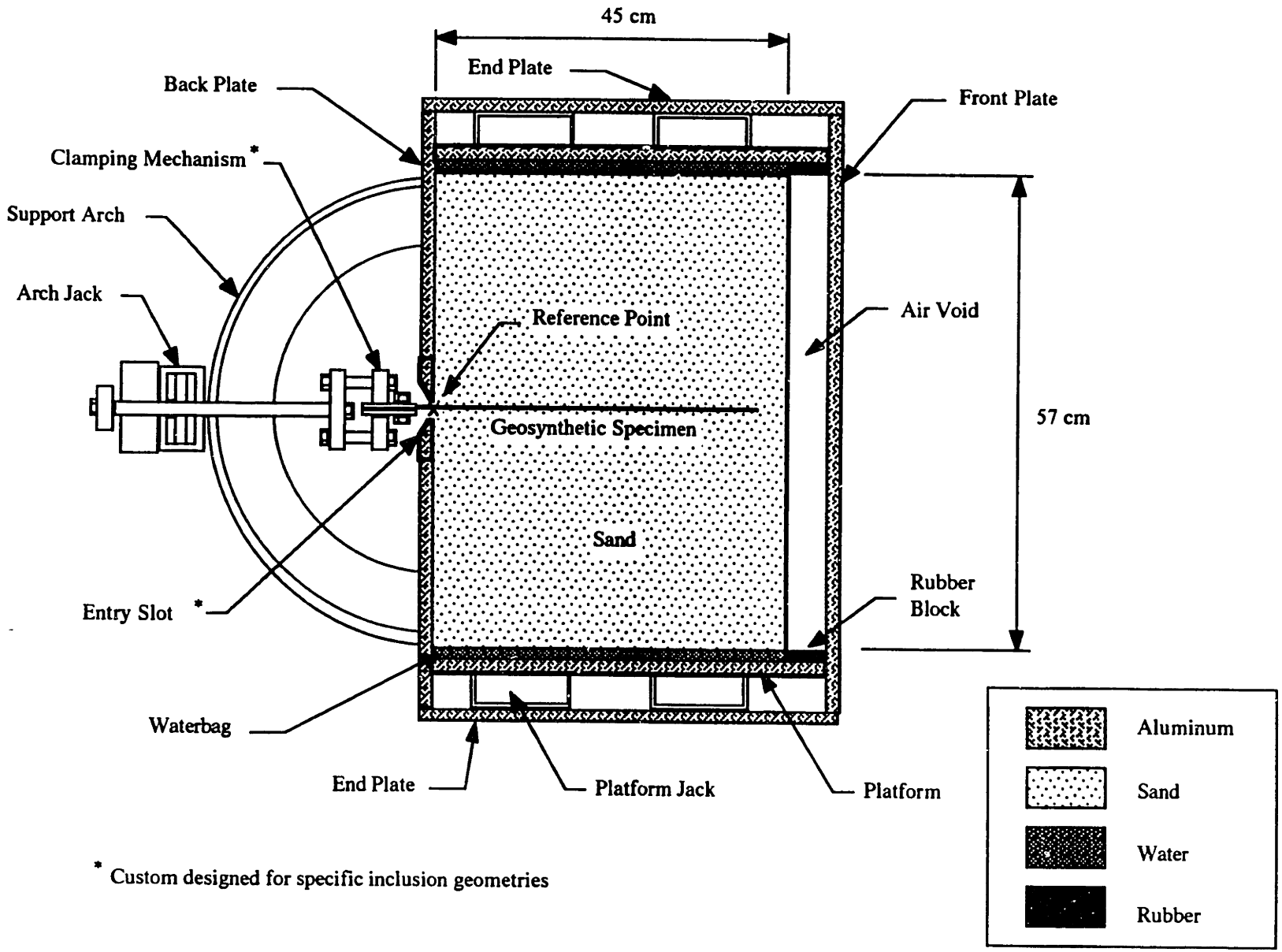

* Custom designed for specific inclusion geometries

Figure 3.3: Cross Section Through the APSR Cell

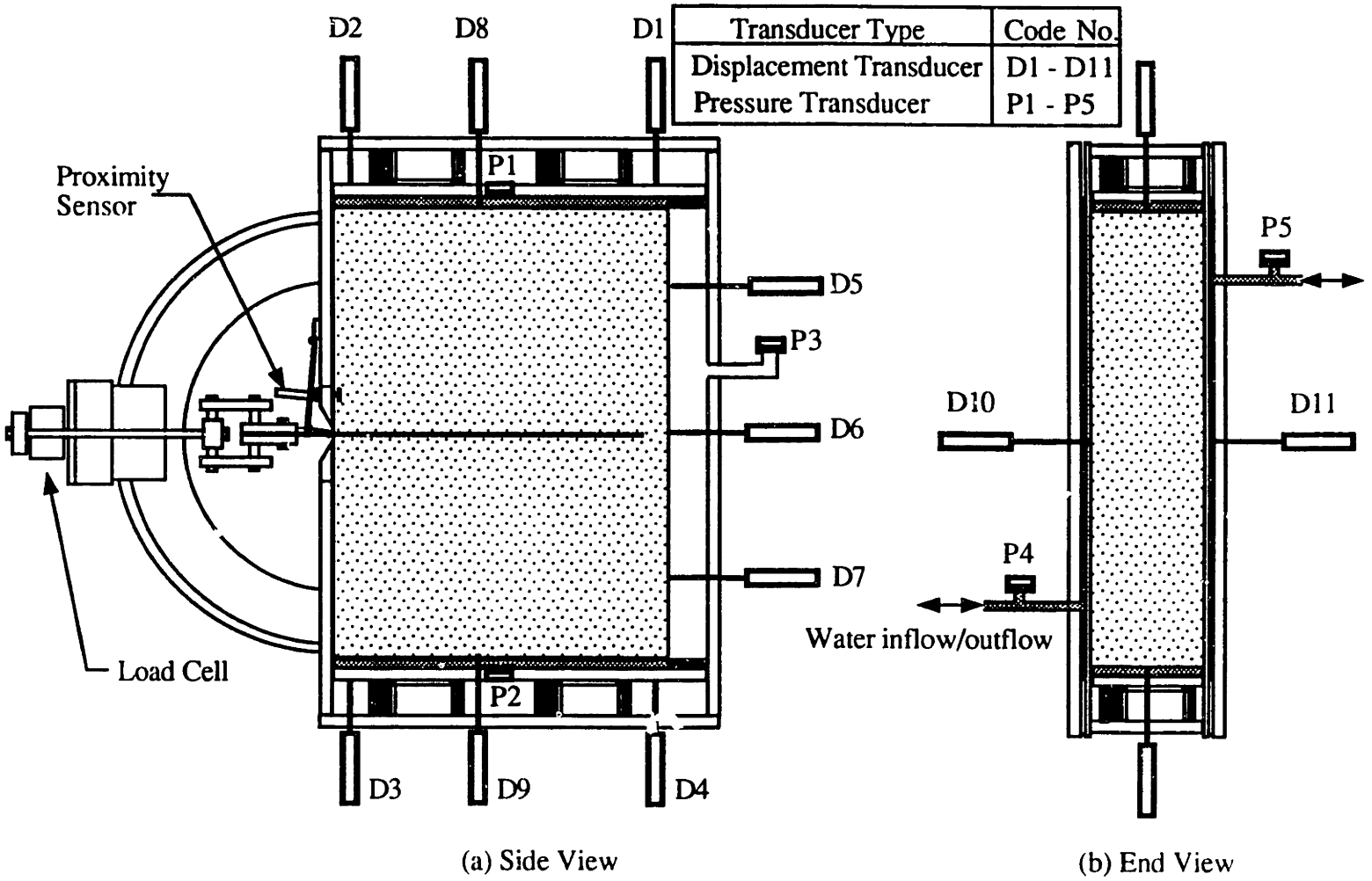

Figure 3.4: APSR Cell Instrumentation

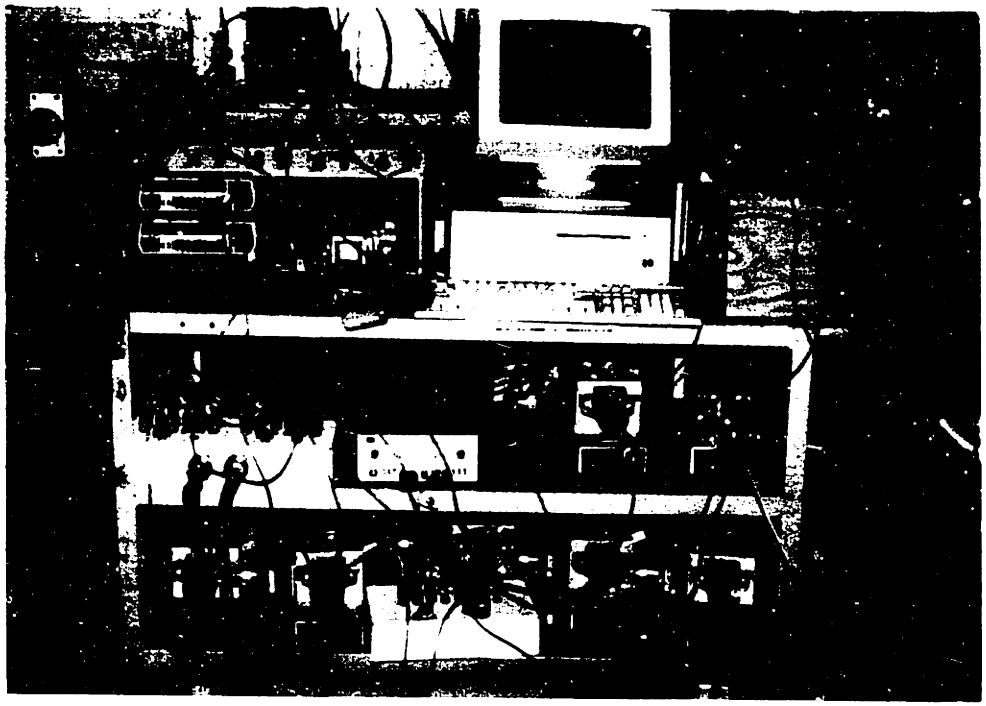

(a) Control Cart

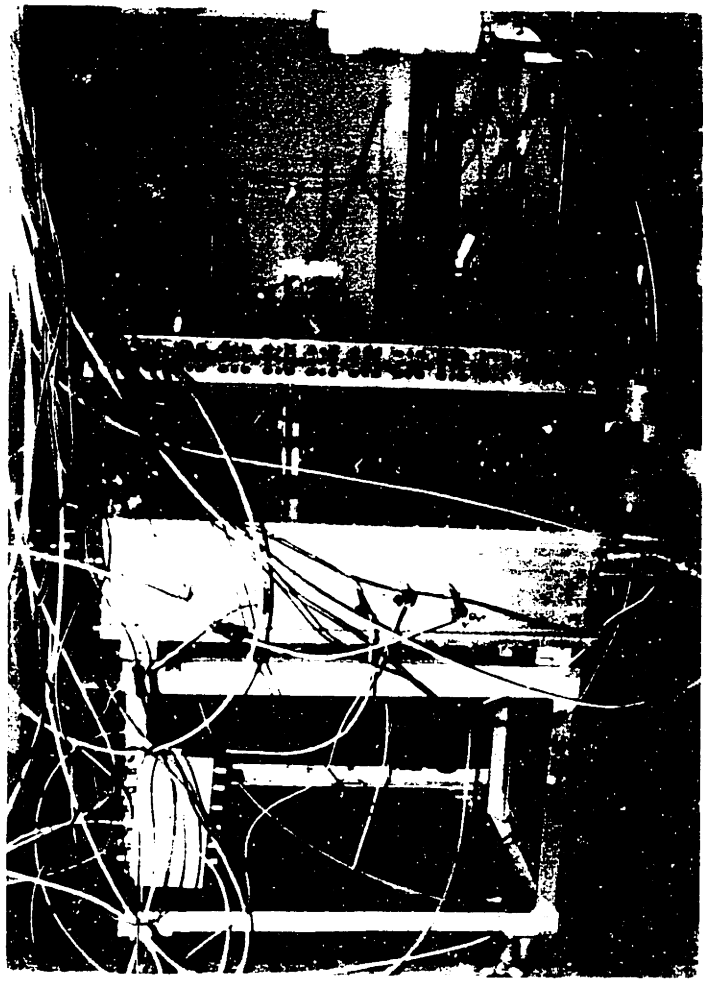

(b) The APSR Cell

Figure 3.5: Photographs of the APSR Cell and Control Cart

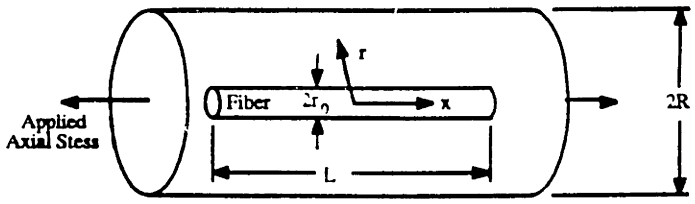

(a) Schematic diagram of the Cox solution for load pickup in a fiber

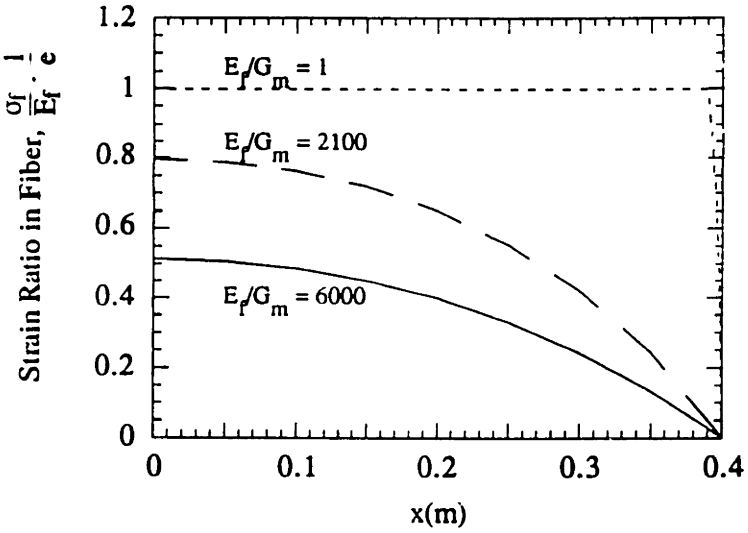

(b) Parametric study of load pickup in a cylindrical fiber of half-length L/2 = 0.4 m

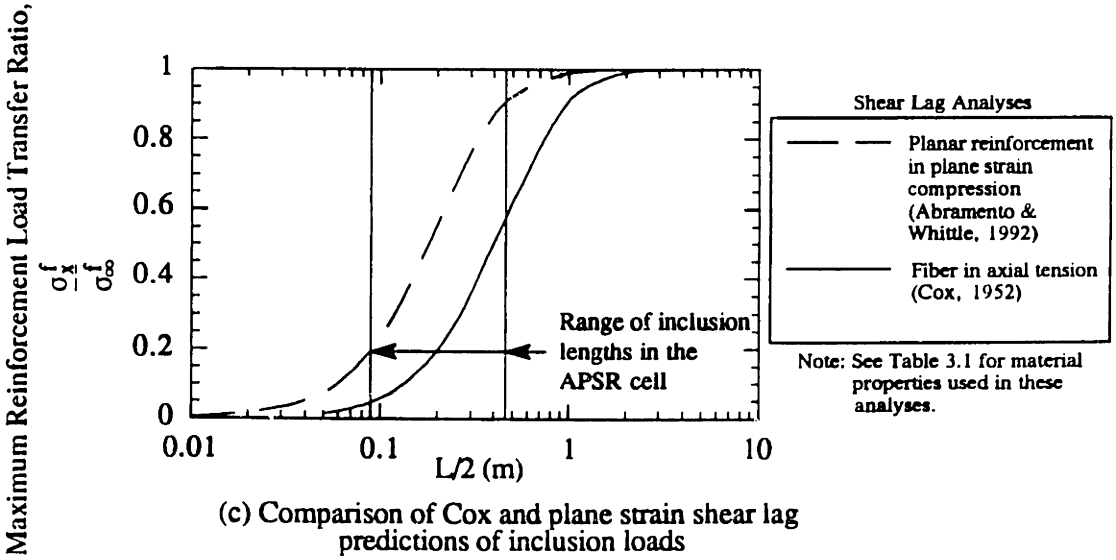

(c) Comparison of Cox and plane strain shear lag predictions of inclusion loads

Figure 3.6: Parametric Study of Inclusion Load Pickup

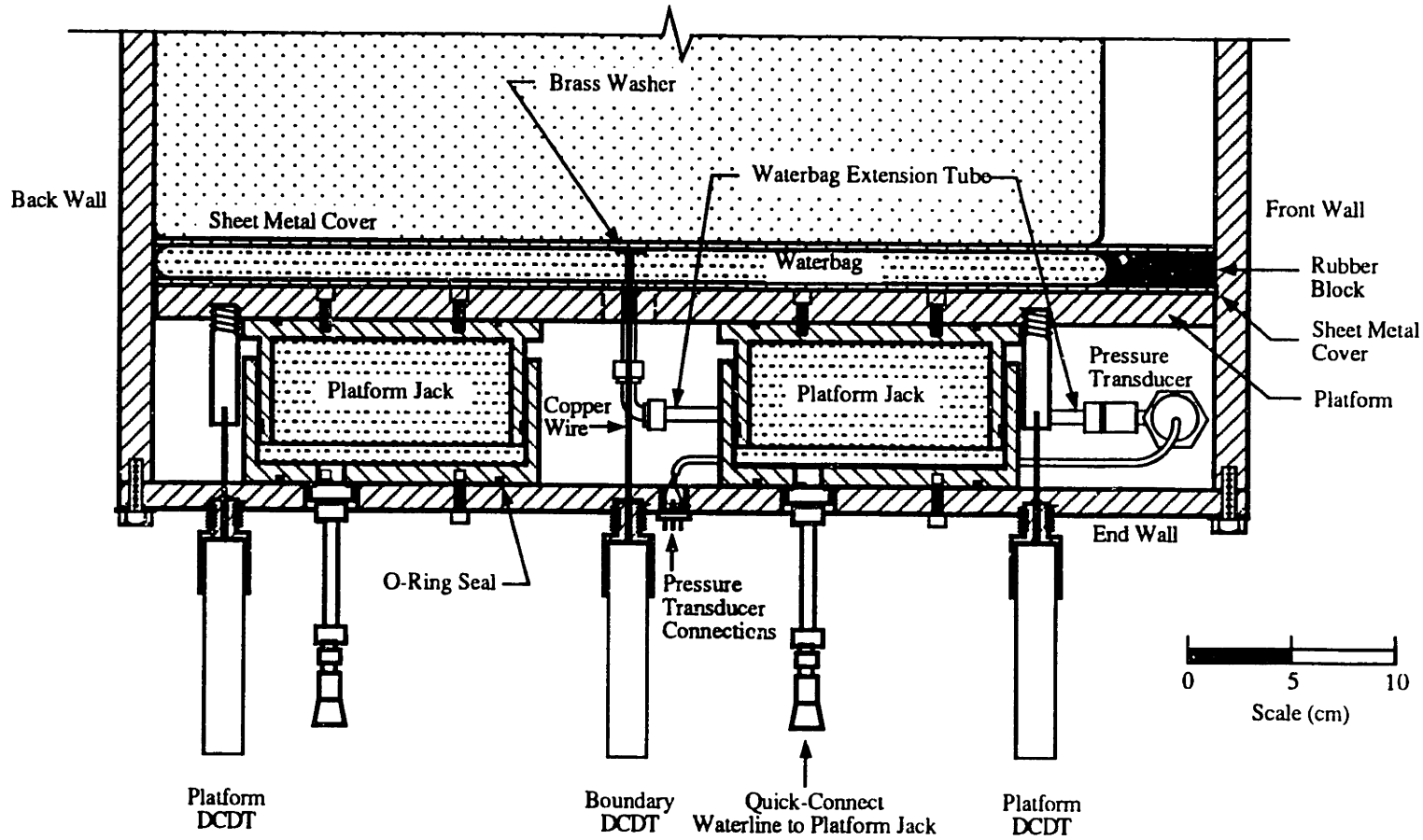

Figure 3.7: The APSR Cell Platform Assembly

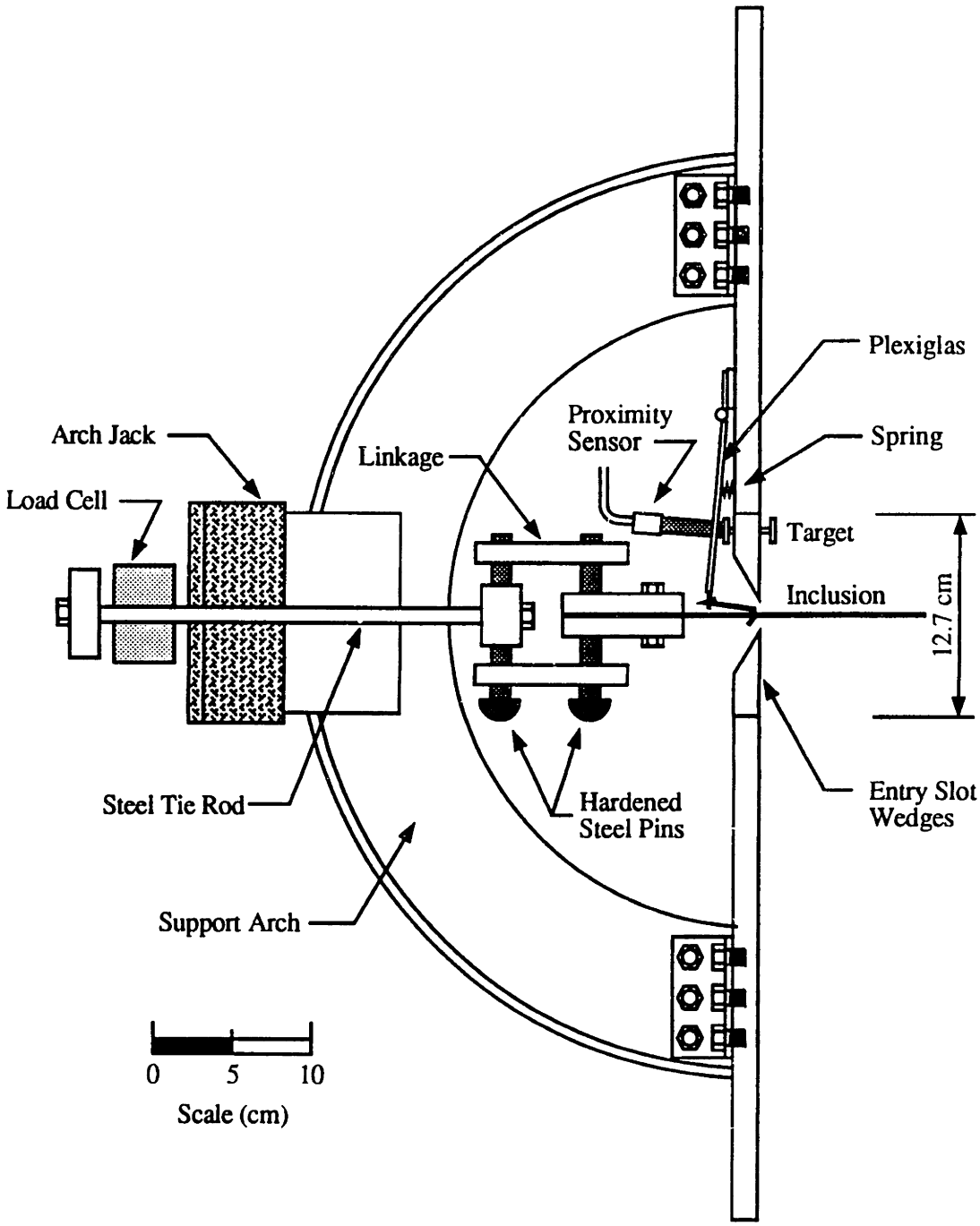

Figure 3.8: Inclusion Positioning Mechanism

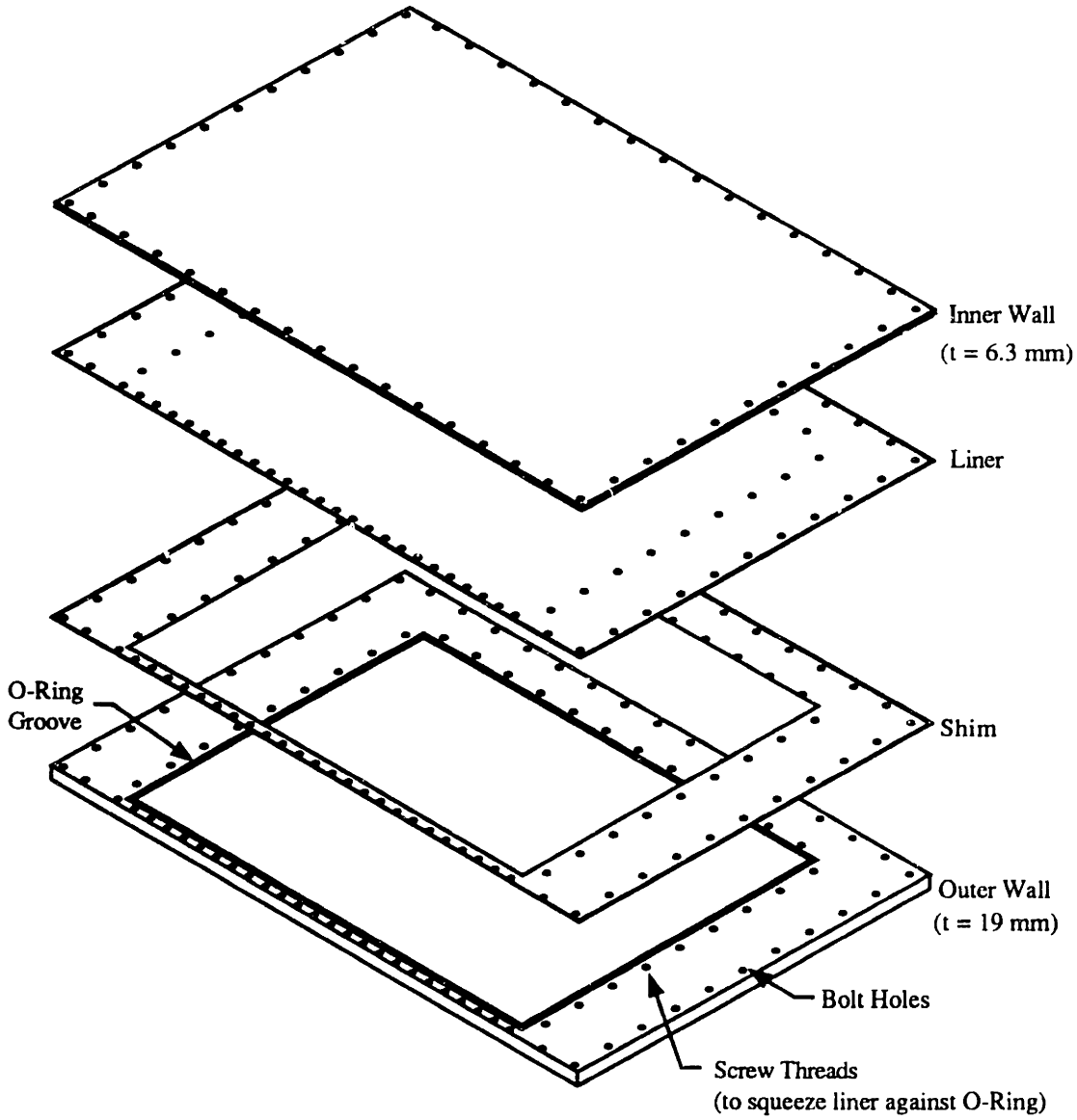

Figure 3.9: Exploded View of Plane Strain Sidewalls

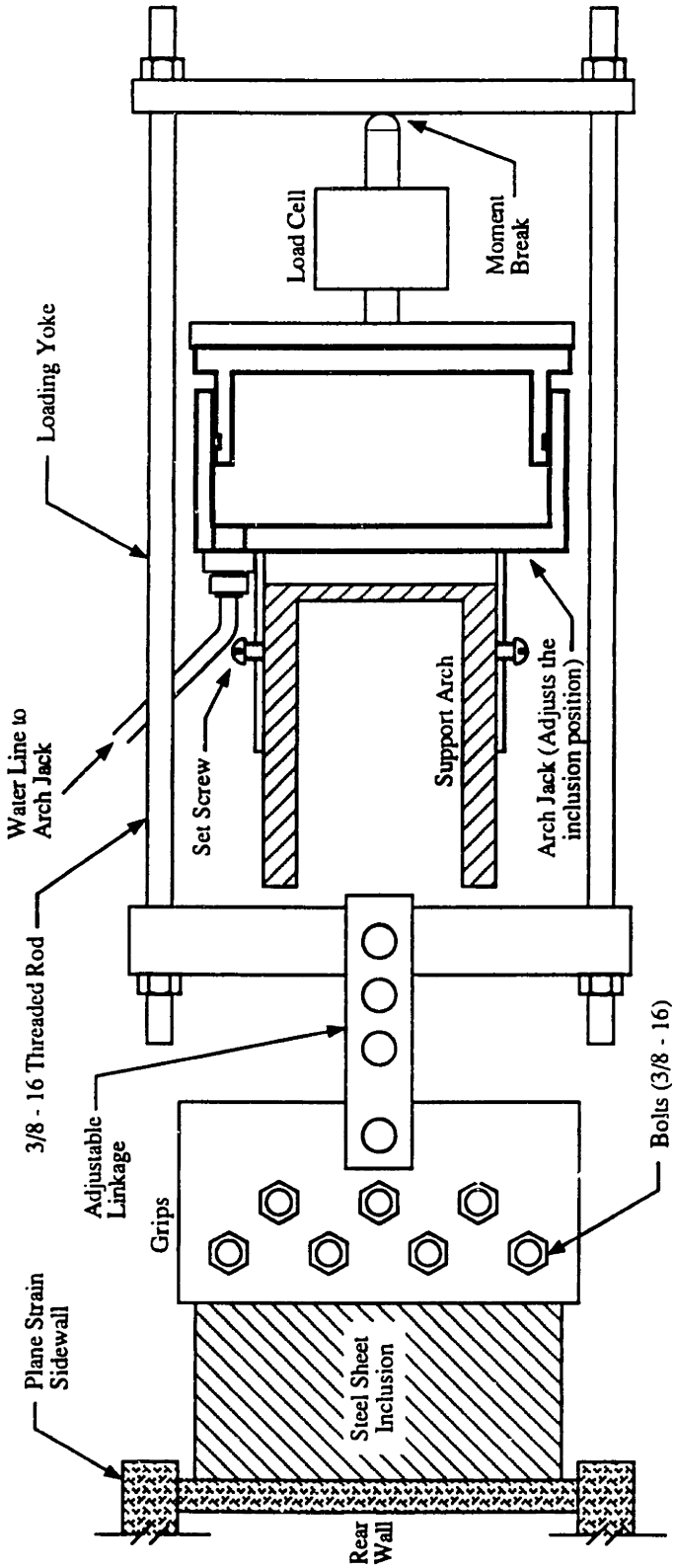

Figure 3.10: Connection from Arch to Reinforcement Grips

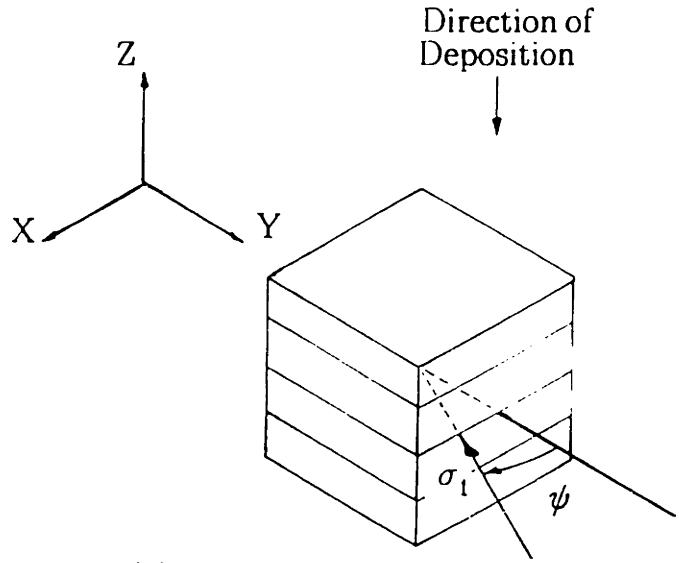

(a) Tests in X-Y Plane (Isotropic Test)

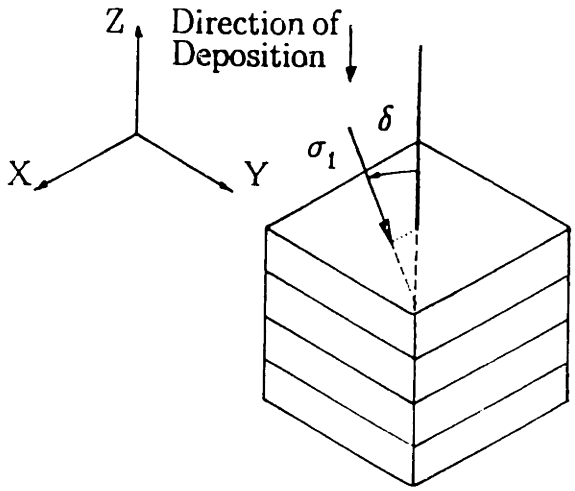

(b) Tests in X-Z Plane (with Inherent Anisotropy)

Figure 3.11: Definitions of the ψ and δ Angles (After Seah, 1990)

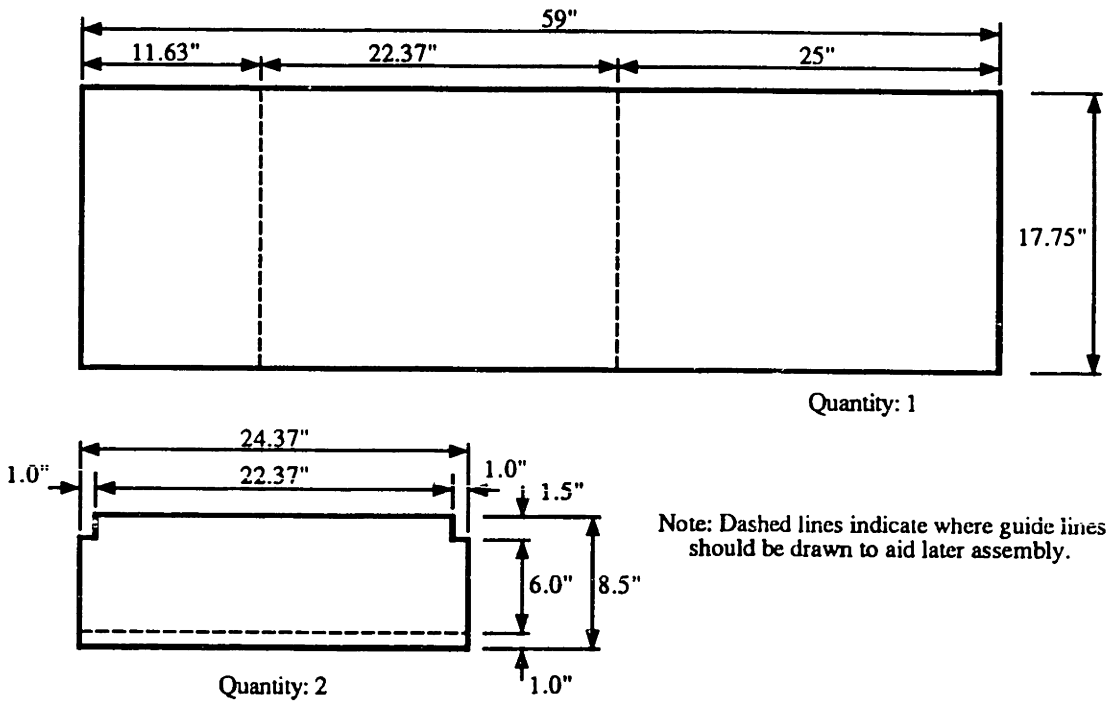

(a) Membrane Dimensions

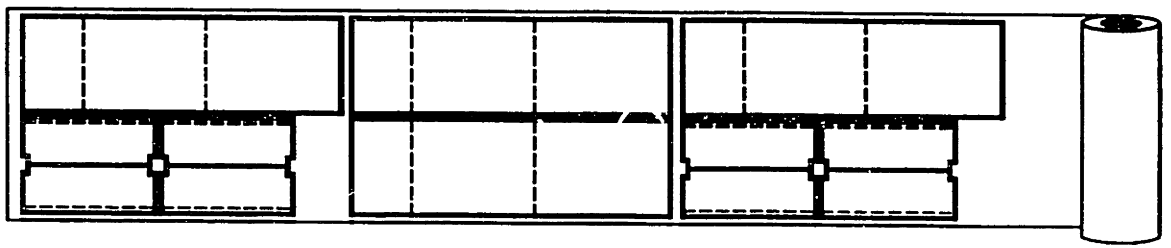

(b) Optimal Layout of Membrane Parts

Figure 3.12: APSR Specimen Membrane Parts

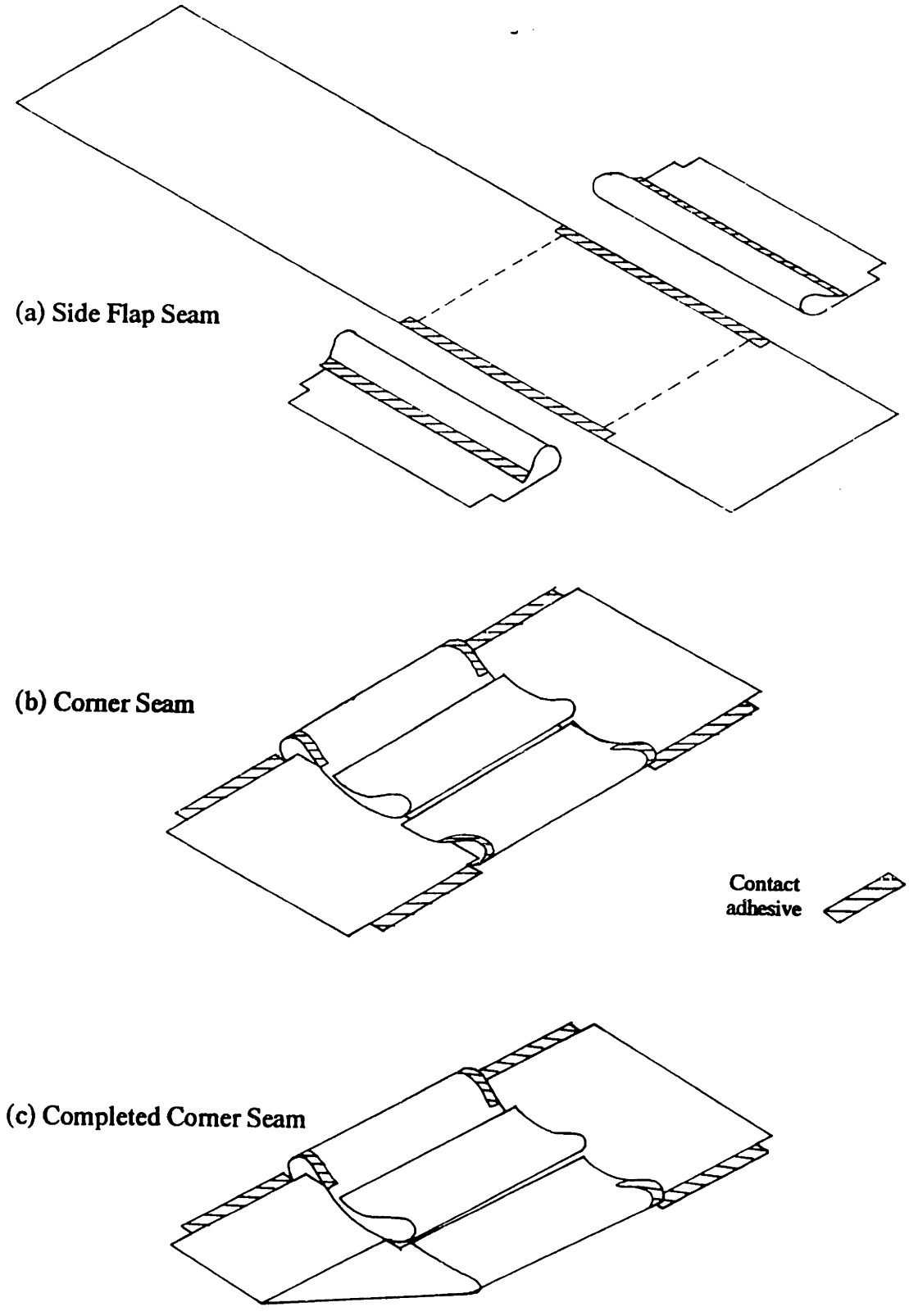

Figure 3.13: Membrane Assembly

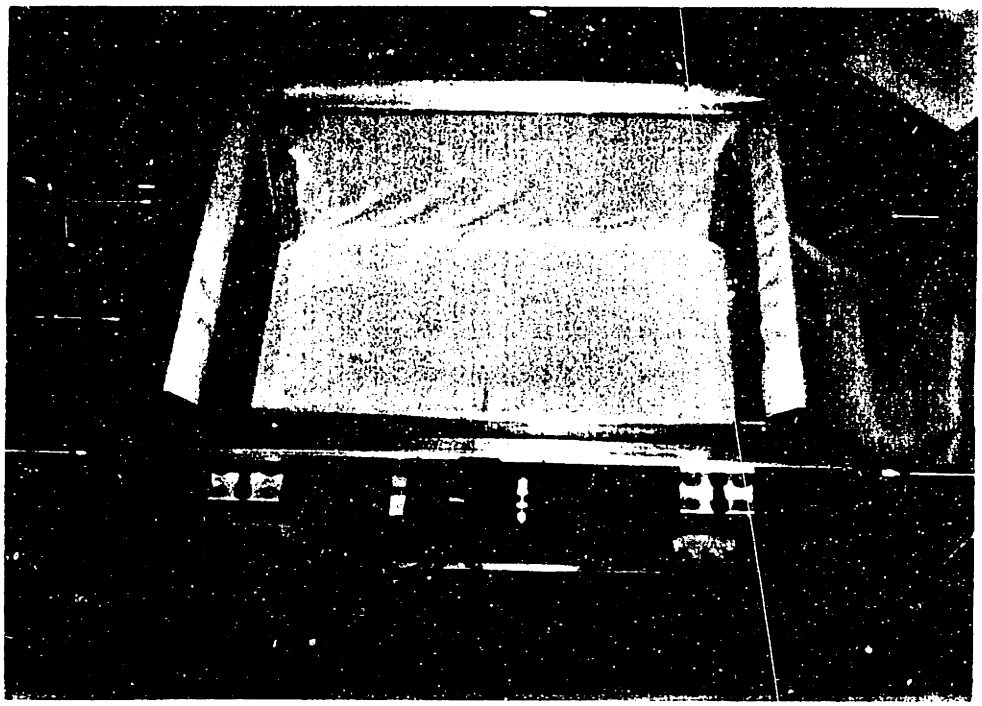

(a) Sample mold with rubber membrane in place

(b) Screeding the surface of the sample

Figure 3.14: Specimen Set-up Procedures

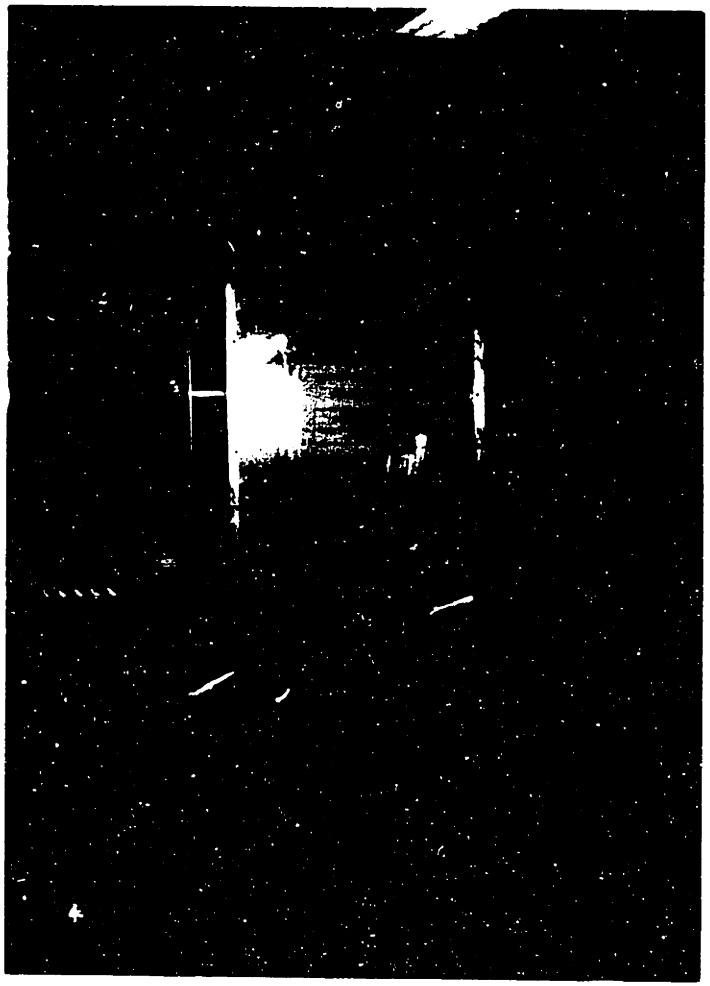

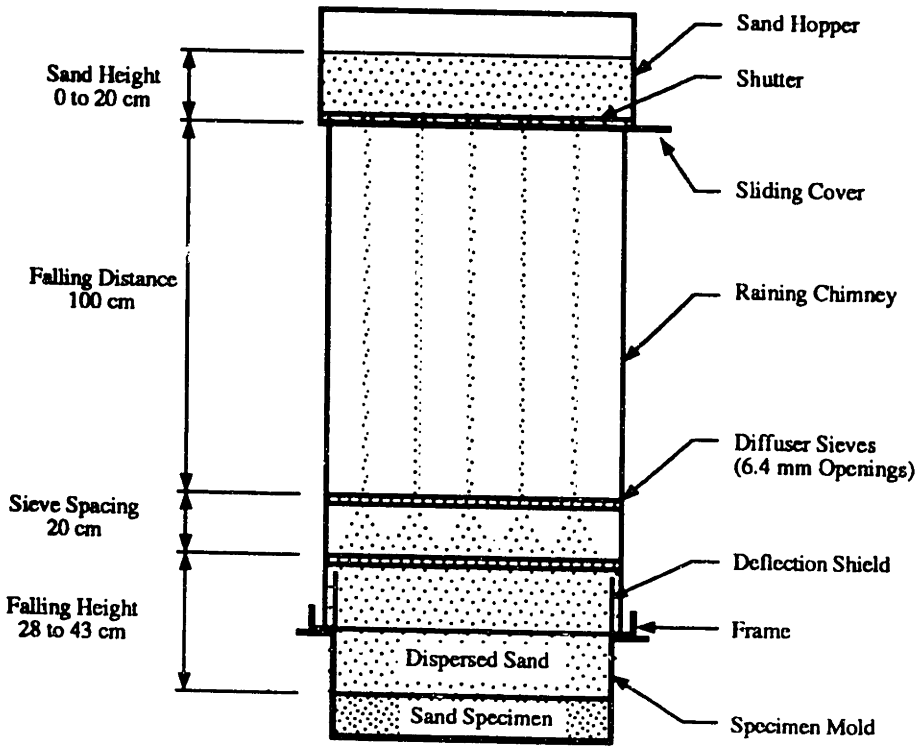

Figure 3.15: The APSR Cell Raining Apparatus

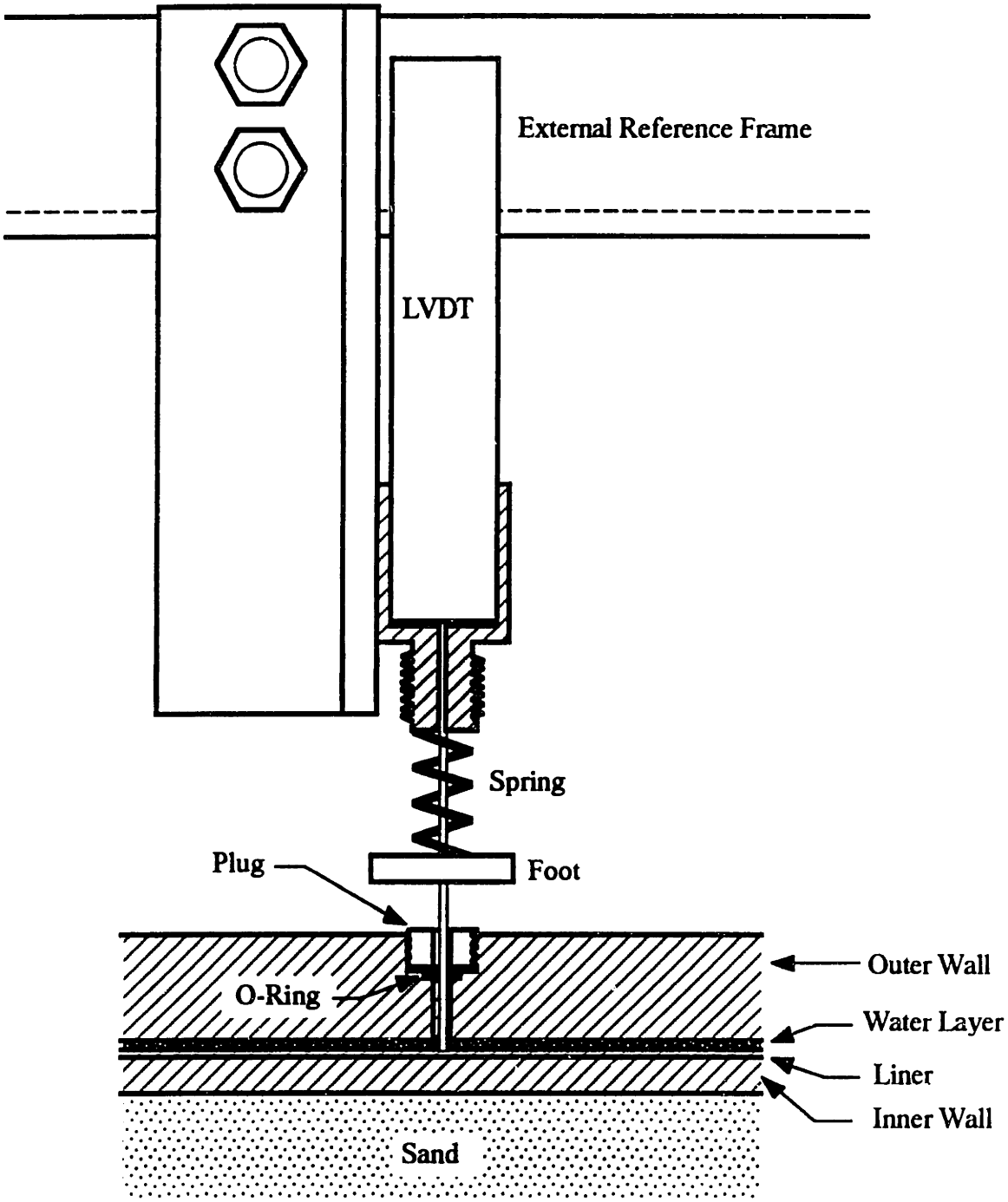

Figure 3.16: Detailed View of the Sidewall Position Measuring System

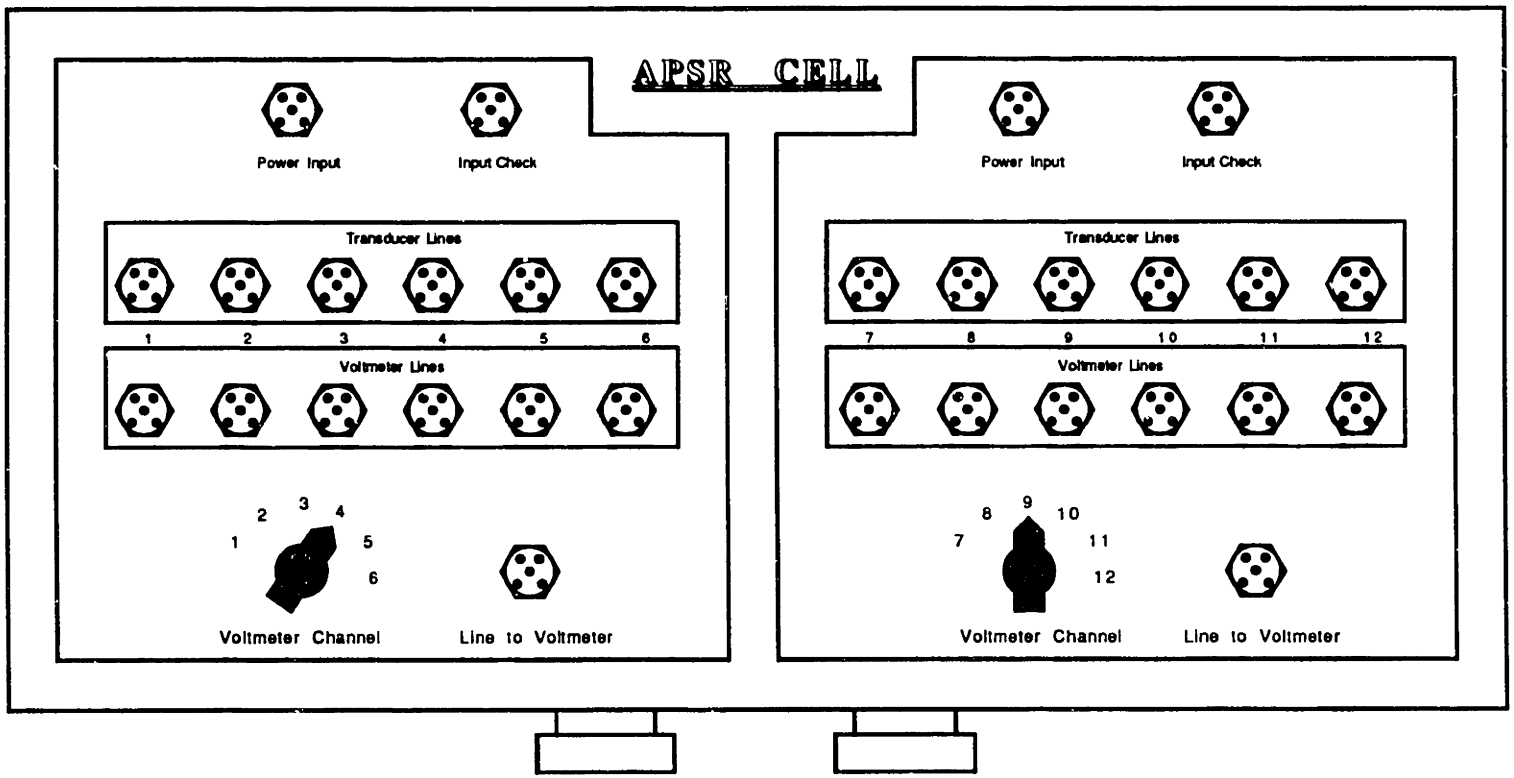

Figure 3.17: The Main Junction Box

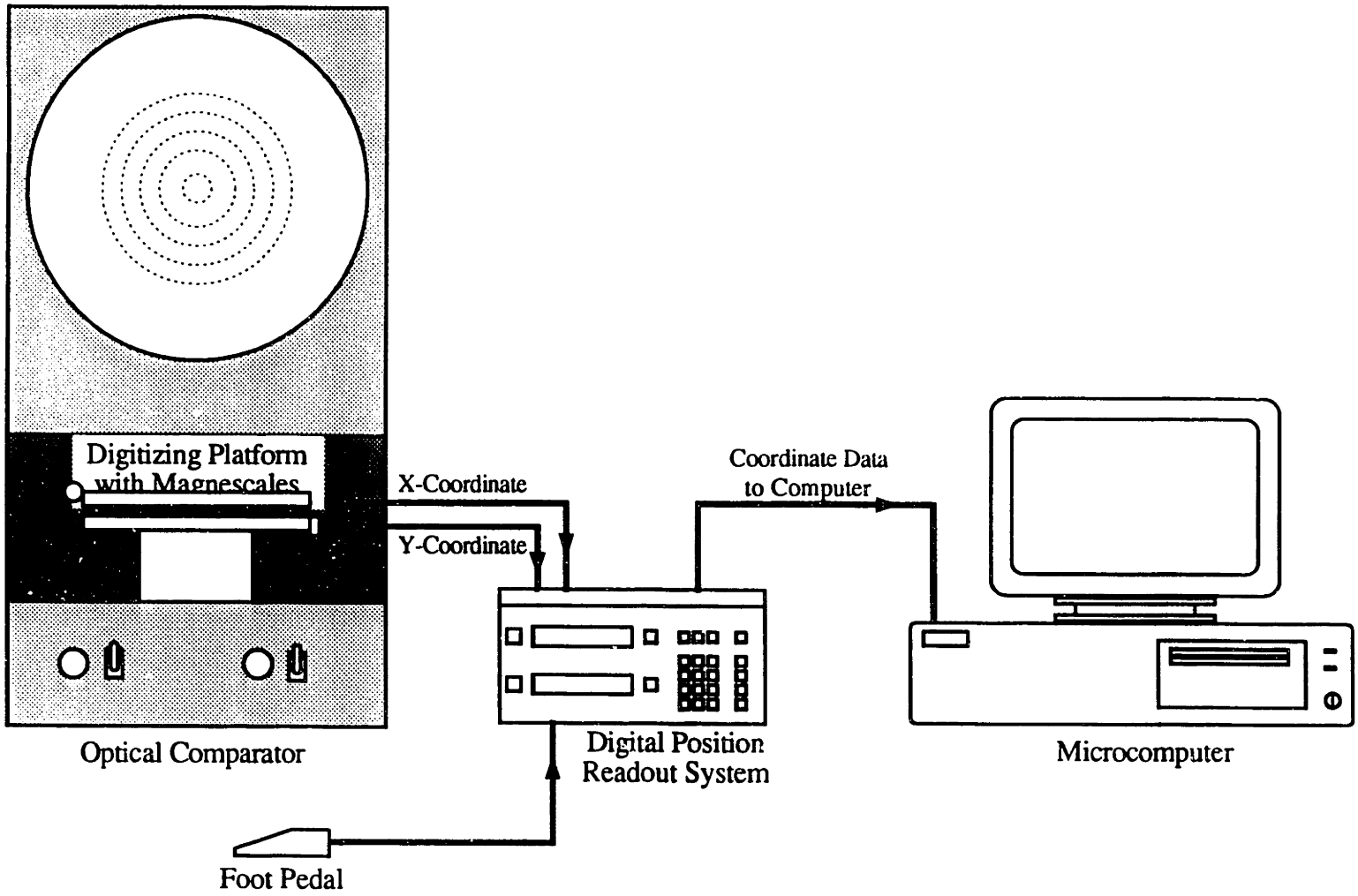

Figure 3.18: Schematic of Digitizing Equipment

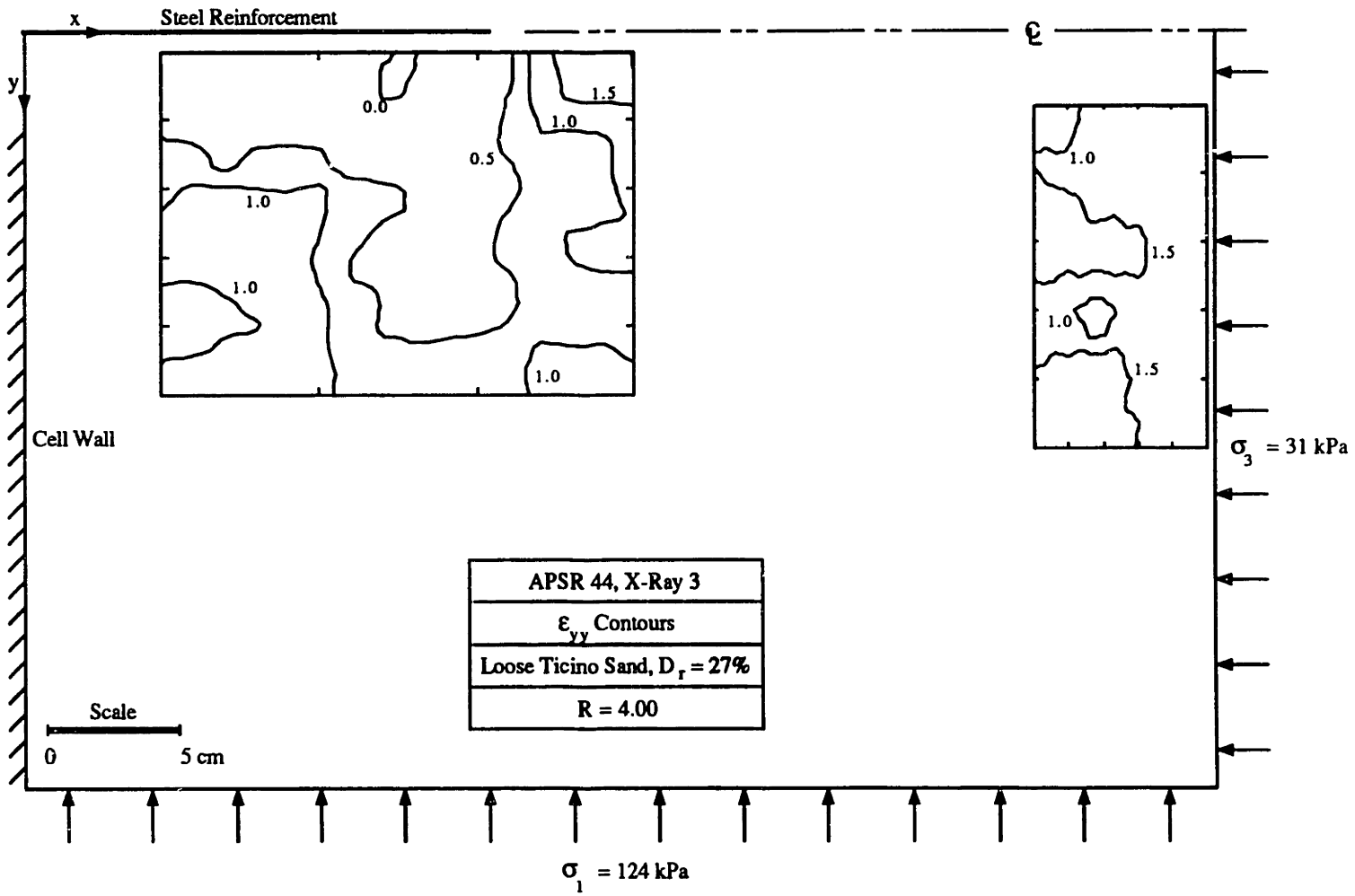

Figure 3.19: Example of a Strain Contour Plot

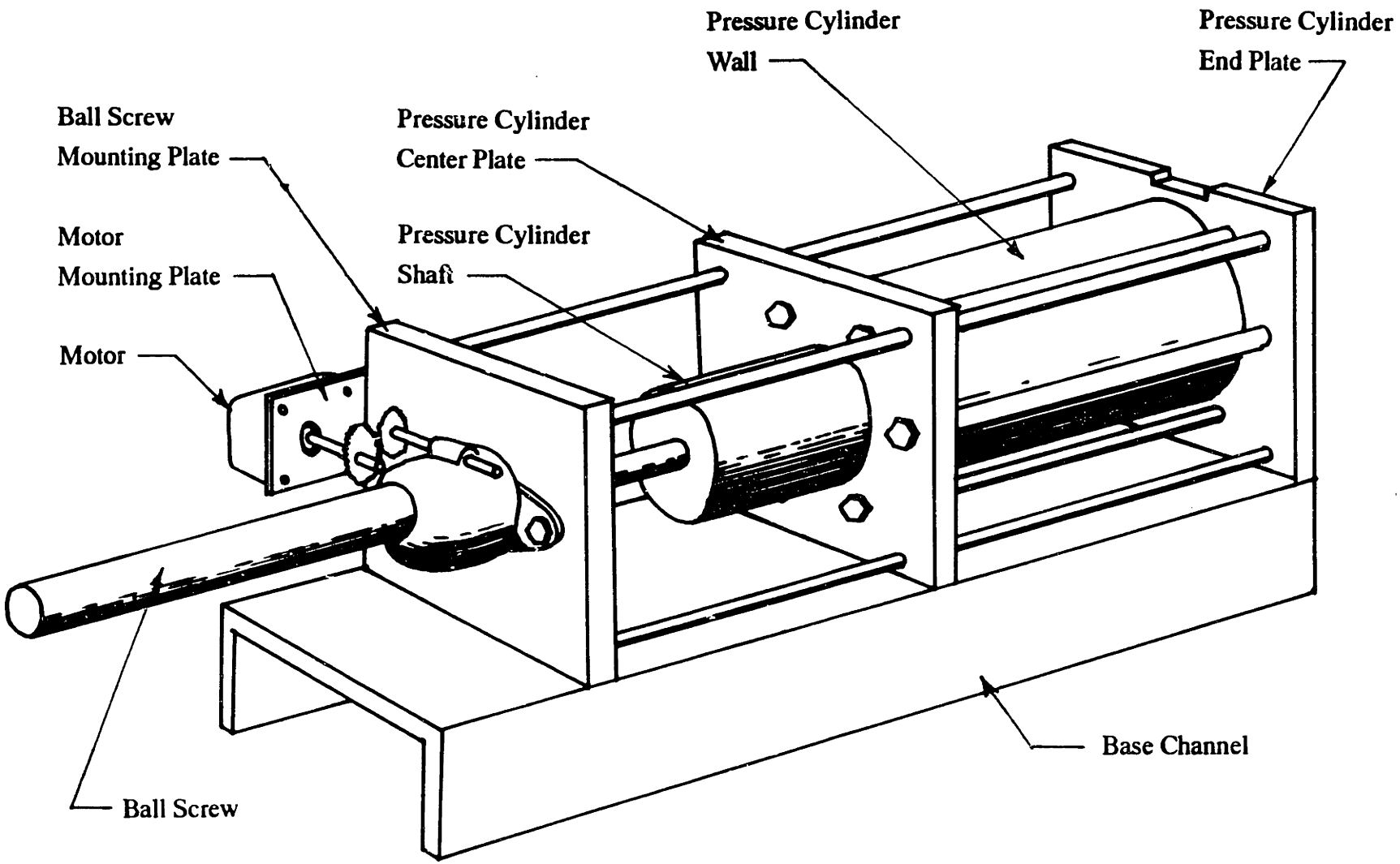

Figure 3.20: Illustration of a Pressure-Volume Controller

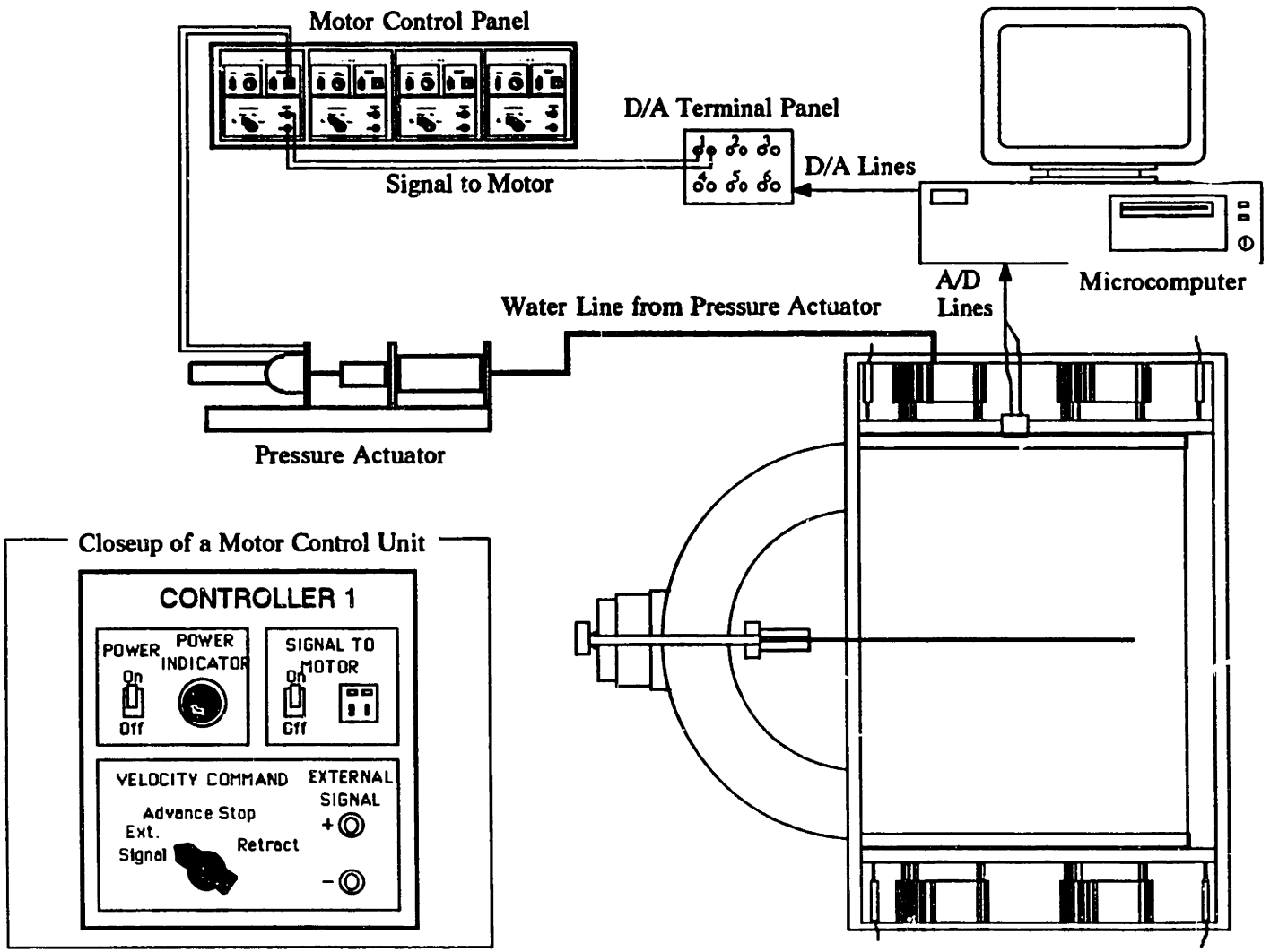

Figure 3.21: Computer-Controlled Feedback Loop

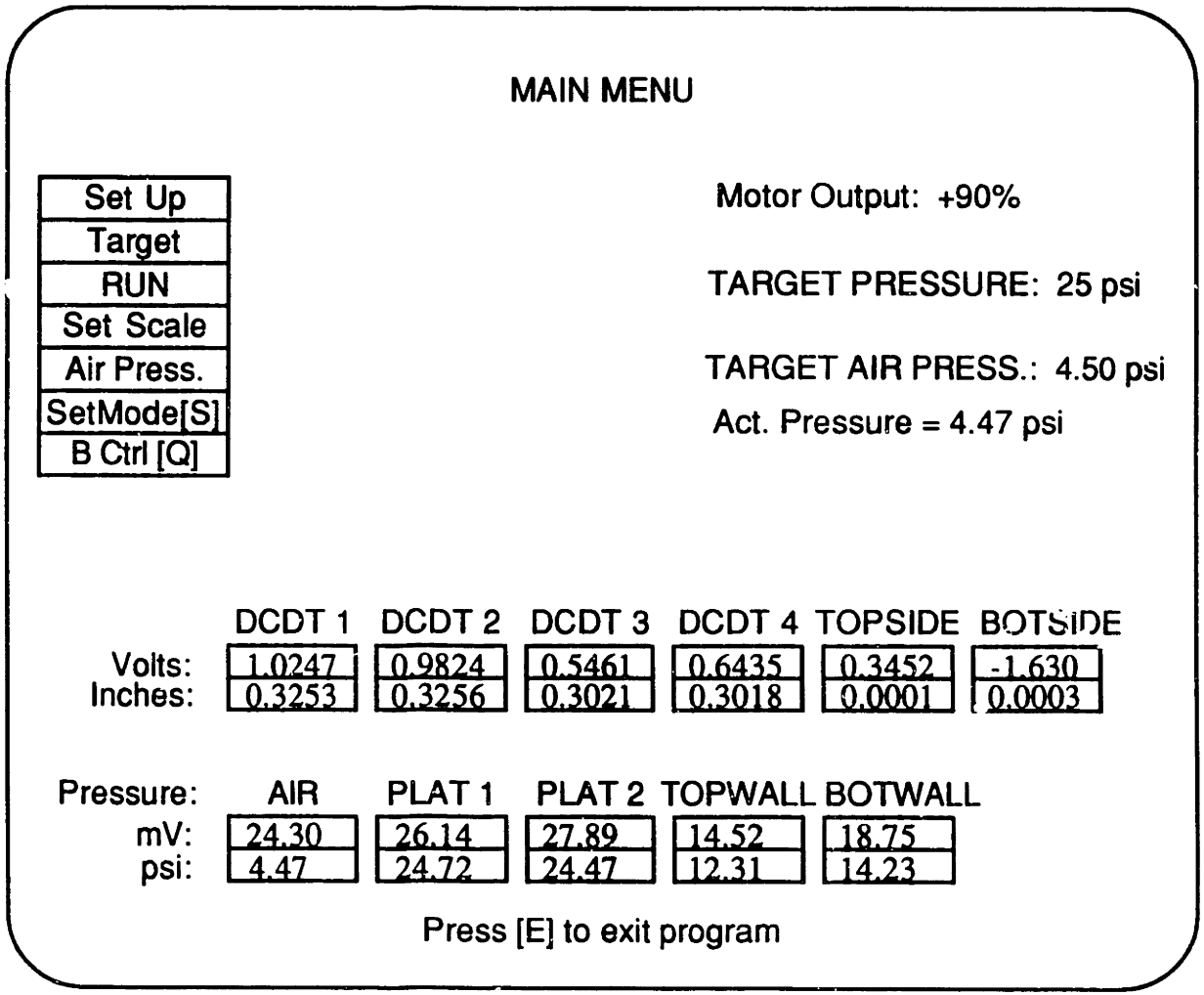

Figure 3.22: Main Menu Screen of the APSR Cell Control Program

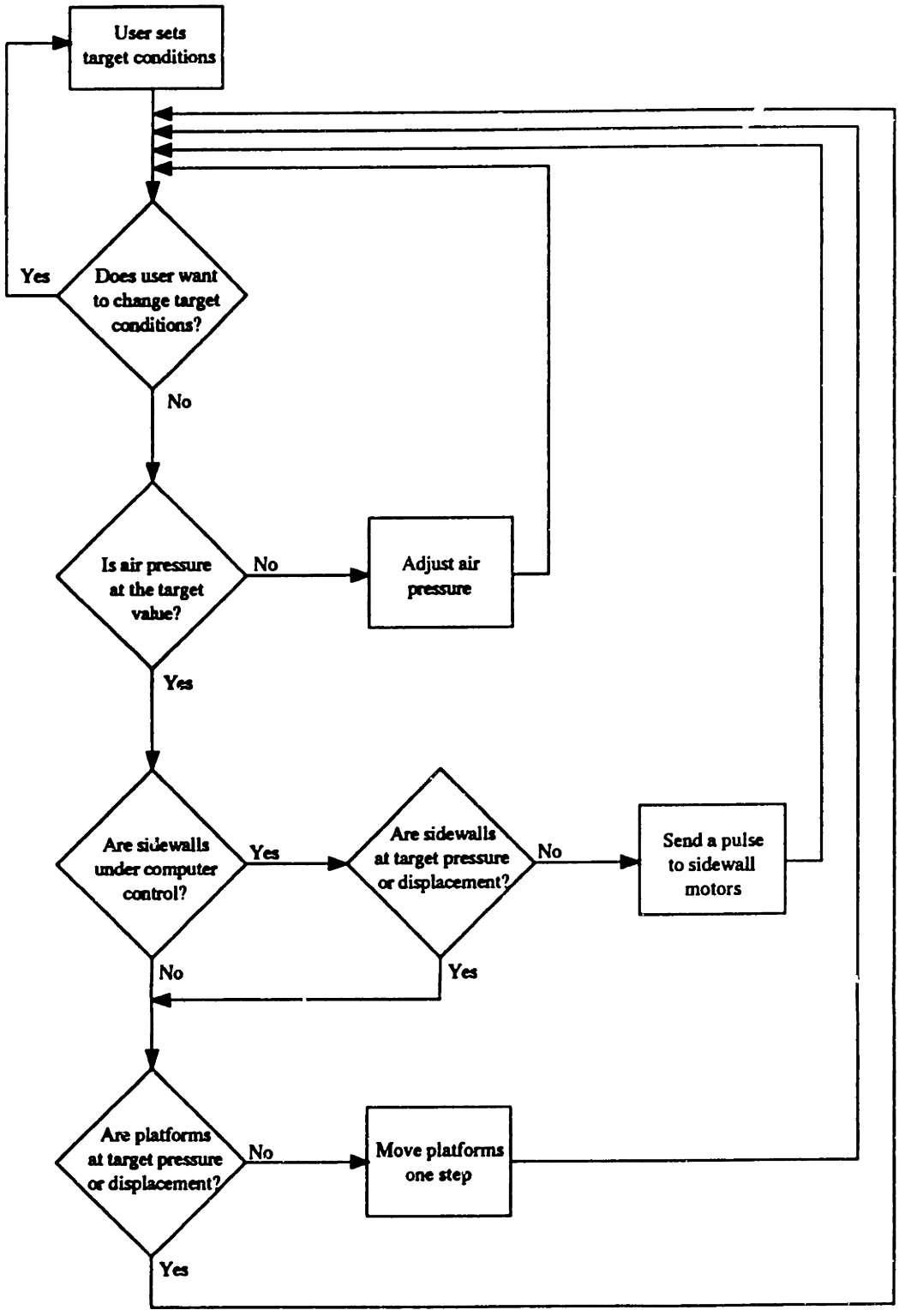

Figure 3.23: Flowchart for the APSR Control Program

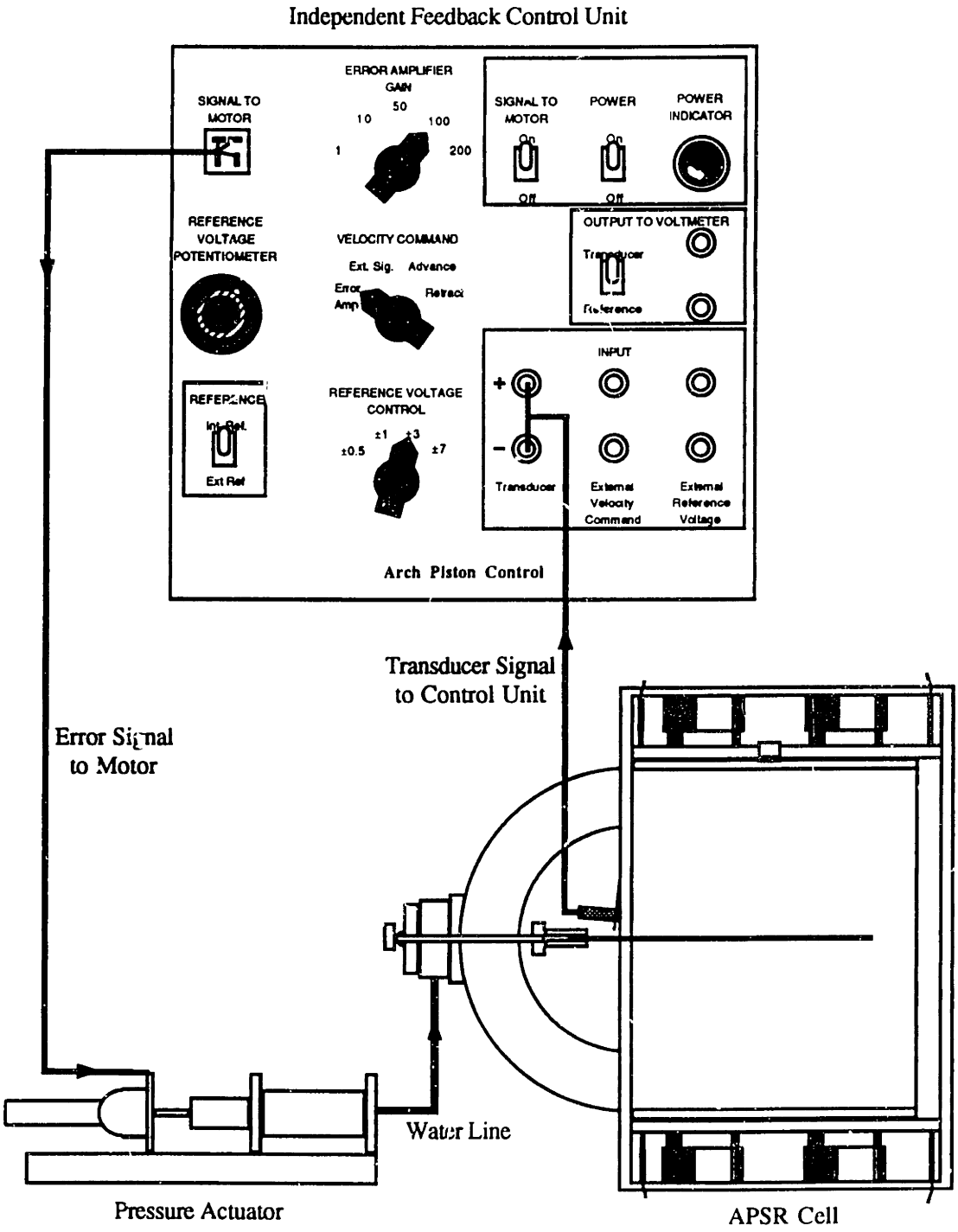

Figure 3.24: Independent Feedback Control Schematic

Chapter 4: Proof Tests of the APSR Cell

4.1. Introduction

The APSR cell represents a major departure from pre-existing laboratory equipment for evaluating the interaction between sand and reinforcing inclusions. Thus, proof testing of the APSR cell is an essential part of the development process and has the following main objectives:

1. Evaluation of the control (hardware and software) systems. Test procedures in the APSR cell are fully computer controlled, thus proof testing is used to debug the control software and evaluate the performance of the custom-designed hardware. Proof tests are also used to develop and refine procedures for reducing and interpreting the test data. For the APSR cell, this has included the development of software to compute distributions of internal strains within the specimen from radiographic measurements (see Appendix B).
2. Conduct tests to establish whether the design parameters of the cell can be achieved in practice. The design of the cell assumes that a) true plane strain conditions (zero lateral deformation) can be maintained during shearing, b) the wall friction is negligible on the plane strain faces and rear wall of the cell, and c) shearing of the unreinforced sand can be accomplished under conditions of relatively uniform stress and strain in the specimen. Proof testing is also used to evaluate the repeatability of data measured in the cell.

3. Compare measured data for unreinforced sand with behavior reported previously in other shear devices in order to establish the reliability of material properties measured by the APSR cell. Ticino sand has been selected as the standard soil used in the tests. It is a clean, multicolored sand with medium grained (less than 0.3% fines), sub-rounded particles with a specific gravity, $G_s = 2.67$. The physical and engineering properties of Ticino sand[1] are typical of many natural sands and have been extensively reported in the literature (Baldi et al., 1985). Figure 4.1 shows the grain size distribution of Ticino sand, with a mean grain size, $D_{50} = 0.5$mm, and a coefficient of uniformity, $C_u = 1.5$. The maximum and minimum dry densities are $\gamma_{d,max} = 1.70$ g/cm^3 and $\gamma_{d,min} = 1.38$ g/cm^3.

This chapter describes the results from an extensive program of proof tests and explains the evolution of the final test procedures and hardware configuration of the APSR cell. Table 4.1 summarizes the complete program of proof tests discussed in this chapter which are numbered chronologically (APSR 1 through APSR 35). It is apparent from this table that the proof tests fall into three primary categories:

1. evaluation of the pressure control and specimen preparation procedures,
2. evaluation of the influence of boundary friction on the stress distribution in the specimen, and
3. refinement of controls for active plane strain shearing.

---

[1]Some of the first proof tests used Leighton Buzzard and Ottawa sand (as noted in Table 4.1), prior to the availability of a supply of Ticino sand.

Further proof tests to refine the control of the reinforcement positioning are described in Chapter 5.

4.2. Evaluation of Boundary Condition Controls

4.2.1. Axial and Lateral Pressures

The first six tests (APSR 1 through 6, Table 4.1) evaluated the control systems for the confining air pressure and platform pressures and led to a number of hardware modifications. The design requirements include: a) control of the air pressure to a tolerance ±0.25 kPa, and b) maximum differential displacements of the end platforms to within 0.005mm of the target position.

Figure 4.2a shows the stability of the air pressure control measured by the transducer (P3, Fig. 3.4) attached to the front wall of the cell.[2] The pressure fluctuates by less than 0.5 kPa over the duration of the test (approximately 4 hours). Further validation of the cell pressure controls were obtained in test APSR 9: the cell was pressurized in 10.3 kPa increments with the axial load platforms out of contact with the specimen. After each increment, the water pressures were measured in the pressure bags (P1, P2, Fig. 3.4) . Figure 4.2b shows that the water pressures match the imposed air pressure (measured by transducer P3) to within 2 kPa, indicating that the air pressure is uniform throughout the cell.

---

[2]In the first test, this transducer was attached to the outlet port on the air regulator. However, flow losses in the line from the pressure regulator to the cell made the air pressure measurements unreliable at this location.

4.2.2. Evaluation of Lubrication

In order to achieve the ideal design concept of the APSR cell (section 3.1), the rear wall, loading platens, and plane strain surfaces must be all be frictionless. This condition is practically impossible to achieve and thus, an evaluation of the lubrication is necessary to determine how the contact resistance affects the stress distribution in the specimen. Boundary friction is of particular concern in the APSR design as the specimen has a large contact to loaded surface area ratio. Boundary resistance can therefore reduce significantly the amount of stress transmitted to the center of the specimen.

Figure 4.3 shows the scheme used to measure the amount of boundary resistance in the APSR cell. The specimen is first compressed by an amount $\Delta/2$ under hydrostatic conditions (i.e., R = 1 with confining stress, σ_c).[3] It is then translated through a displacement cycle of stroke, Δ, with no relative displacement between the two platforms. The transducers P1 and P2 (Fig. 4.3) measure the waterbag pressures at either end of the specimen throughout this displacement controlled test. Prior to translating the specimen, the computer control system adjusts the platform positions such that $P_1 = P_2$ at the start of the first displacement cycle. The difference in pressure ($|P_1 - P_2|$) during translation is a measure of the resistance acting on the specimen boundaries.

---

[3]In the initial tests, APSR 7 and 8 (Table 4.1), R = 4 was used due to misfit between the specimen mold and the waterbags. This problem was resolved in APSR 0 by re-machining the mold to achieve the design clearance between the waterbags and the specimen with the platform jacks in their fully retracted position.

A series of these tests[4] was performed in order to evaluate the influence of confining stress level (σ_3) and specimen displacement on the boundary resistance (Table 4.1). The lubrication used in all of the APSR tests is an equal mixture of Dow-Corning No. 7 Compound and Dow-Corning High Vacuum Grease. Figure 4.4 shows typical results from tests APSR 7 and 9:

1. As the specimen translates within the APSR cell, there is an increase in the water pressure in one platform necessary to drive the movement, and a corresponding decrease in pressure witnessed at the other end of the cell.
2. In all cases, the maximum average pressure difference, ΔP = 11 to 15 kPa, which develops within a displacement Δ = 1cm, regardless of confining stress conditions or number of stroke cycles.

Figure 4.5 shows the pressure difference (ΔP) as a function of confining stress and direction of translation. When platform 1 pushes the specimen, ΔP = 7.5 to 10 kPa for σ_c = 10 to 45 kPa. When platform 2 pushes the specimen, ΔP = 21 to 23 kPa for σ_c = 20 to 45 kPa.

If the resistance is due to a frictional mechanism, the pressure difference should be a function of the normal stress, σ_3.[5] The data show relatively small changes in pressure difference over the range of imposed confining stresses. The boundary resistance can be interpreted in terms of an equivalent friction angle of the grease or an average

---

[4]Note that all of the tests were performed using dense Ottawa sand because the Ticino sand was not yet available.

[5]And σ_1, σ_2 for $R \neq 1$.

apparent cohesion of the grease. The results from tests APSR 7-9 show that $\phi_g \approx 0.45^o$ (Fig. 4.5) or $\bar{c}_g \approx 1.4$ kPa (Fig. 4.4).

Seah (1990) evaluated the strength of the grease he used for performing tests in the Directional Shear Cell (DSC).[6] He found that the cohesion of the grease, c_g, is a function of the grease thickness which, in turn, is a function of the maximum applied normal stress, $\sigma_{n,max}$:

$$c_g = 0.025\ \sigma_{n,max} \tag{4.1}$$

In the APSR cell, the largest contact surface areas are on the plane strain sidewalls. For the lubrication tests described above, $\sigma_{n,max}$ on these surfaces varied between 30 to 100 kPa. According to eqn. 4.1, $c_g = 0.8$ to 2.5 kPa, which brackets the apparent cohesion, $\bar{c}_g = 1.4$ kPa interpreted from the APSR boundary resistance tests. Section 4.3.4 describes how later APSR test data were interpreted to account for this boundary resistance.

4.2.3. Plane Strain Shear Tests

One of the most innovative features of the APSR cell is the design of the sidewalls and active control of plane strain conditions. An extensive set of proof tests were conducted to fine tune the test procedure and hardware for performing plane strain shear tests. These proof tests can be subdivided into three groups:

1. Tests in which no attempt was made to control deformations in the plane strain direction.

---

[6]Seah (1990) used a mixture consisting of 30% Dow Corning No. 7 Compound and 70% Dow Corning Molykote III.

2. Tests to debug plane strain control.
3. Well-controlled plane strain shear tests ($\varepsilon_2 \leq \pm 0.02\%$).

All of the tests applied a confining stress, $\sigma_c = 31$ kPa to provide a common basis for comparing their results. The following paragraphs describes the lessons learned from these tests which led to the final plane strain shearing procedures.

4.2.3.1. Shear Tests without Active Plane Strain Control

In the first set of shear tests, out-of-plane deformations were resisted only by the bending stiffness of the 20.6mm sidewalls (i.e., with the shim removed, Fig. 3.9). The purpose of these tests was to obtain preliminary measurements of the shear behavior of sand in the APSR cell before addressing the complexities associated with active plane strain control of the sidewalls.

The specimen setup procedure was the same as described in Chapter 3. After the specimen held a vacuum ($\sigma_v \approx 90$ kPa), the top liner and outer plates were bolted into place. Once the confining air pressure ($\sigma_3 = 31$ kPa) was applied, the vacuum was released and the specimen was sheared. Two methods of platform motion control were used in these tests. In APSR 10, the computer applied uniform displacement control (i.e., both platforms moved into the specimen by an equal amount), while in APSR 12, the specimen was sheared with uniform pressure control (i.e., identical water pressures were imposed at both platforms).

Figure 4.6 shows the externally measured stress-strain properties for APSR 10. The plots present the applied stress ratio, $R = \sigma_1/\sigma_3$, and the lateral strain, ε_{xx}, as functions of the measured axial strain, ε_{yy}, imposed on the specimen. It should be noted that in tests prior to APSR 19, the axial strain was not measured directly on the specimen

surface. Instead, ε_{yy} was computed from the platform displacements, assuming that the waterbags are incompressible and the average axial strain in the specimen corresponds to the average displacement of the two platforms divided by the initial specimen length. The zero position of axial strain is discussed below.

The three LVDTs (D5-D7, Fig. 3.4) along the front wall of the cell measure the distribution of lateral displacements across the specimen. The external lateral strain is estimated directly from the lateral displacements and the initial specimen width (45cm).[7] The point of zero lateral displacement is equated with the conditions immediately after the confining air pressure has been applied (and the specimen vacuum released). Since the LVDTs rest directly on the front specimen surface, there are no errors in the measured lateral displacements. Figure 4.6 shows that the lateral strains measured by the three LVDTs are in very close agreement throughout the test, and hence, the front face of the specimen deforms uniformly.

Figure 4.7 shows the platform displacements and corresponding water pressures for APSR 10. The curves for the platform movements appear as a single line as the control matches the platform displacement to within 0.025mm. The plateaus in the curve are points where shearing was halted for approximately 10 minutes in order to radiograph the specimen. The water pressure in platform 2 is consistently higher than that of platform 1. This is due to a slight misalignment of the specimen mold during test setup, such that the specimen was initially closer to platform 2 than platform 1. At the start of the test, platform 2 was the first to make contact with the specimen. The pressure in

---

[7]Movements into the air void (i.e., lateral expansion) are considered negative, in accordance with standard soil mechanics convention.

platform 2 built up until it overcame the boundary cohesion of the grease around the specimen. Even after platform 1 made contact, the pressure difference remained at approximately $\Delta P = 9$ to 16 kPa. This is similar to the pressure difference measured in the lubrication tests (section 4.2.2), and can be attributed to the shear resistance along the lubricated cell surfaces. There is a slight drop in the waterbag pressures during the X-ray procedures which reflects a small amount of stress relaxation in the specimen (see also Fig. 4.6a). The major principal stress, σ_1 (R, Fig. 4.6a), is interpreted as the average of the two measured waterbag pressures (i.e., $\sigma_1 = [P_1 + P_2]/2$).

The shear stress-strain behavior (Fig. 4.6a) shows an initial region of system stiffening (i.e., secant stiffness increases with strain level) followed by a fairly linear response with a peak shear resistance at R = 8.1 (Point B) followed by post-peak strain softening. The initial stiffening of the soil is clearly not a true measurement of soil behavior, but can be attributed to a number of possible factors including: a) the compressibility of the load system, b) non-uniformity of strains within the soil specimen (due to sidewall friction), or c) inaccuracies in the externally measured strains.

The zero position of axial strain must account for the pickup region of the stress-strain curve. For the plots in Figure 4.6, the zero strain position is estimated from radiographs of internal soil strains. Later tests on Ticino sand show that the average axial strain within the sand at R = 3.33 is $\varepsilon_{yy} = 0.15$ to 0.3%. The point of zero axial strain in Figure 4.6 is adjusted so that, at R = 3.33, $\varepsilon_{yy} = 0.3\%$. This procedure is explained in more detail in section 4.3.3.1.

The measured peak deviatoric stress in APSR 10 occurred at R = 8.16, corresponding to a peak friction angle, $\phi_p = 51.4^o$. The axial strain at peak resistance $\epsilon_{yy} = 2.25\%$. The secant modulus[8] for this test, $E_{50} = 15{,}000$ kPa.

In test APSR 12, the computer control program adjusted the platform positions to maintain equal pressures in the waterbags. Figure 4.8 shows plots of the platform displacements and pressures during shear. The platform pressures are essentially identical (Fig. 4.8b) until a failure surface forms during post-peak strain softening. However, platform 2 displaced significantly less than platform 1 at the same pressure. This is due to the control sequence in which platform 1 is moved first, the pressures in both bags are then checked, and platform 2 is moved if a pressure difference is measured. Usually the waterbag pressures equalized fairly quickly, so instead of moving platform 2, the algorithm performed another adjustment of platform 1. The program was altered in subsequent tests to alternate between platforms 1 and 2 at the start of a load step cycle. This resulted in more uniform platform displacements, as shown in Figure 4.9a for test APSR 45. This procedure was adopted as the standard method of test control.

Figure 4.10 shows the stress-strain results for APSR 12 superimposed on those for APSR 10. The plots show that, in spite of different boundary displacement control methods, the two tests yielded very similar results (i.e., the system is very reproducible). Table 4.3 provides a summary of the externally measured stress-strain properties obtained from unreinforced tests on Ticino sand (these are discussed in detail

---

[8]The secant modulus is based on the slope of a straight line from the origin through the stress-strain curve at half of the peak deviator stress (i.e., at $(\sigma_1 - \sigma_3) = 0.5\ (\sigma_1 - \sigma_3)_f$).

in section 4.3). In all tests after APSR 12, the computer imposed the condition of uniform waterbag pressures, adjusting the platform positions using the refined control method. The principal advantage of boundary pressure control is that it prevents stress relaxation during radiographic measurements. The imposed boundary stresses during an X-ray remain constant, although the specimen tends to creep slightly. The shear stress response in Figure 4.10 shows small plateaus that occur during the X-ray intervals. The deviatoric stress remains approximately constant, but the curve shifts to a slightly higher axial strain.

4.2.3.2. Refinement of Active Plane Strain Control

The next series of tests addressed problems with the active plane strain control. These were resolved by changing the sidewall geometry and the reference frame for measuring sidewall displacements. The refinement of active plane strain controls proved to be particularly elusive and absorbed substantial research efforts over a period of seven months and 20 tests. Tests APSR 15 through 20 were performed on dense, unreinforced Ticino sand. These were the first tests to use the active plane strain control described in section 3.2.4.3. At this point, the sidewall design did not include the inner aluminum plate (cf. Fig. 3.9) and the 'liner plate' was in direct contact with the specimen. Also, the boundary of the pressurized diaphragm extended over the full lateral surface of the APSR cell (cf. Fig. 3.9; in the final design the diaphragm covers only the initial specimen area). The sidewall displacement transducers (D10, D11, Fig. 3.4) were held fixed in a set of angle brackets, bolted to the cell as shown in Figure 4.11.

In APSR 15, the independent feedback controllers were unable to prevent out-of-plane displacements in the sidewalls. At several points during shear, the pressure actuator

motors controlling the sidewall pressures lost control and were unable to return the sidewalls to their zero position. Test 16 suffered the same problem as test 15, but pressure transducers (P4, P5, Fig. 3.4) were added to measured the sidewall pressures. The average strain rate in APSR 15 and 16 was approximately 2% per hour. The strain rate was reduced to approximately 0.5% per hour in tests 17 through 20. This resulted in better plane strain control, although the sidewall controllers were still prone to occasional instabilities which were compensated by manual monitoring and re-zeroing of the system during each test.[9] Although these procedures are inherently not satisfactory, the data from tests APSR 19 and 20 did achieve consistent results. The addition of pressure transducers to the sidewall waterlines in APSR 16 provided measurements of the intermediate principal stress, σ_2, acting on the specimen. The magnitude of σ_2 relative to the other two principal stresses is commonly described by the parameter, b (Bishop, 1966):

$$b = \frac{\sigma_2 - \sigma_3}{\sigma_1 - \sigma_3} \tag{4.2}$$

Figure 4.12 shows measured values of ε_2 and b for APSR 19. Although the re-zeroing procedure permitted some residual out-of-plane strain in tests 19 and 20, the measured $\varepsilon_2 \leq \pm 0.1\%$ until failure. The b-values ranged between 0.4 and 0.6.

The next series of tests (APSR 20-35) was performed on dense Ticino sand containing a 0.025mm thick steel sheet inclusion (Table 4.1) of width 13.3cm and embedded length, L = 36cm. Unfortunately, the addition of the inclusion introduced further sidewall control problems in APSR 21 which could not be solved by adjusting the rate

---

[9]A time consuming and stressful procedure.

of shearing or re-zeroing the controllers. Further tests (APSR 22-31) attempted to diagnose and address the plane strain control problems. Table 4.2 summarizes the changes to the cell geometry and sidewall control that were made to try to reduce the amount of measured out-of-plane strain. These changes included:

1. Replacing the independent feedback controllers with a computer controlled loop to maintain either constant b-value or zero sidewall displacement;
2. Adding plates of different thicknesses to the inside of the plane strain walls;
3. Reducing the size of the pressurized water diaphragm within the sidewalls.

APSR 22 through 24 tested the computer sidewall control. The control program was able to impose a constant b-value during a test quite accurately, but this unfortunately did not bring the level of plane strain below the target value, $\varepsilon_2 \leq \pm 0.05\%$. Test 22 imposed $b = 0.44$ (chosen to match the average value from APSR 20) and led to measured intermediate strains approximately $\varepsilon_2 = \pm 0.8\%$. The next test used $b = 0.65$, and consequently reduced the measured out-of-plane strain ($\varepsilon_2 = \pm 0.3\%$), but did not achieve the target design conditions.

The computer controlled displacement feedback loop was no more effective than the independent analog loop in containing the out-of-plane displacements, although it did prevent the sidewall motors from running out of control. Even at $b > 1$ (i.e., sidewall pressure greater than waterbag pressure, APSR 24), the sidewalls still exhibited an outward movement.

The reinforced specimens have a non-uniform stiffness. A uniform pressure in the sidewalls will not maintain a uniform plane surface on the specimen and hence, one possible explanation for the control problems is due to the flexibility of the sidewalls. This hypothesis was checked by adding an inner sidewall plate to increase the bending

stiffness of the wall against the soil. A 1.9cm thick Lexan plate was bolted between the bottom sidewall and the rest of the cell in test APSR 25. The independent feedback controllers were used to apply the sidewall pressures. Although the specimen failed prematurely, prior to failure the bottom sidewall remained nearly motionless. All of the outward movements occurred in the top wall.

In APSR 26, a 0.64cm plexiglas plate was bolted between the top sidewall and the rest of the cell to increase the top wall stiffness. This time both sidewalls behaved erratically. Measurements of the top of the specimen taken after the test made it possible to construct a contour map of this surface. The measurements were taken after the top sidewall was removed at the end of the test. A vacuum on the specimen applied an effective stress to maintain the final geometry. A bar was laid across the top of the cell and a depth gauge used to measure the distance to the top of the specimen. Figure 4.13 shows the surface contours developed from 9 readings.[10] The key feature of the specimen surface is the depression along the front face of the specimen. Apparently the sidewall was collapsing into the air void at the front of the cell, causing the mode shape exhibited by the specimen surface. As water was pumped into the sidewalls, it pressed the inner walls further into the air void and caused the displacement reference points to move away from the specimen. The result was a negative feedback loop which made it impossible to control the sidewall displacements.

Further stiffening of the sidewall in test APSR 27 was achieved using a 1/4" aluminum plate in order to prevent collapse of the front edge of the specimen. The final surface contour map for this test is shown in Figure 4.13b. Although the tendency for the front

---

[10]Plotted using the commercial statistics package SYSTAT.

edge of the specimen to collapse was reduced, the specimen still exhibited a mode shape which indicated that the plane strain condition could not be adequately imposed by the sidewalls.

The final modification to the sidewall geometry was to reduce the area over which the water pressure acted. In the original wall design, the water layer extended over the entire sidewall surface, including the space between the specimen and the front wall of the cell. In APSR 28, a new O-ring groove in the outer plate eliminated the sidewall pressure over the air void. The new groove reduced the pressurized area so that it only covered the initial specimen surface. The intention was to eliminate the tendency for the sidewall to collapse into the air void.

Figure 4.13c shows that this modification worked. The specimen height readings were within 0.2 mm of each other. The sidewalls were now capable of keeping the plane strain surfaces of the specimen uniform. Unfortunately, the sidewall LVDTs showed excessive out-of-plane displacements. In APSR 29, the independent feedback controllers still behaved erratically, while tests at constant b-value (tests APSR 30 and 31) exhibited high out-of-plane displacements. The conclusion from these results was that the sidewall LVDTs were not accurately measuring the positions of the inner sidewalls, possibly due to bending in the clamps that connected the LVDTs to the cell (Fig. 4.11).

Tests APSR 32 and 33 monitored the positions of the sidewall LVDTs using an external reference frame around the entire cell. The frame balanced on the top of the cell at three points and dial gauges mounted to the frame measured the relative displacements of the LVDT brackets (Fig. 4.11) and the outward movements of the two end plates. In both tests, the computer imposed constant b-value control. The dial

gauge measurements revealed that, as the sidewall pressures increased, the brackets holding the LVDTs bowed slightly inward toward the cell. As a result, the LVDTs measure an apparent outward movement of the sidewalls due to an unreliable datum. This design flaw appears to account for the instability problems associated with the sidewall controllers. In test 33, the computer kept the b-value between 0.45 and 0.50. At failure the brackets had bowed in toward the cell a total 0.22mm, resulting in an apparent out-of-plane strain, $\varepsilon_2 = 0.28\%$.

In all subsequent tests, the sidewall LVDTs (D10, D11, Fig. 3.4) are mounted directly to the external reference frame. This system worked perfectly in test APSR 35[11] and there have been no subsequent stability problems in the active plane strain control. Figure 4.14 shows results of the stress-strain behavior, b-value, and measured out-of-plane strain, ε_2, for APSR 35. The b-value was between 0.42 and 0.56 for the entire loading portion of the test. The plane strain condition was accurately controlled with $\varepsilon_2 \leq \pm 0.01\%$ until the end of the test, at which point a failure surface formed in the specimen.

4.2.3.3. Effect of Plane Strain Control on Measured Sand Behavior

The previous sections described three groups of APSR cell tests on dense, unreinforced sand:

1. tests with passive plane strain control (and hence low b-values),

---

[11]Test APSR 34 demonstrated the performance of this referencing system for loose unreinforced Ticino sand. The maximum measured out-of-plane strain was 0.05%. The independent feedback controllers maintained continuous control with perfect stability, and b-values during loading in the range, b = 0.21 to 0.43.

2. tests with active, but inaccurate, plane strain control
3. tests with active control and very low ε_2 (true plane strain shear tests).

Table 4.3 summarizes conditions measured at peak and zero dilation rates in the proof tests. Figure 4.15 shows significant differences between the typical observed shear behavior for each type of test. Test APSR 12 represents the passive control case, test 19 the inaccurate active control, and APSR 45 the "true" plane strain case. Test APSR 19 measures a significant increase in the soil stiffness and peak strength which is mobilized at much smaller axial strains, ε_{yy}. However, the stress-strain behavior for the passive and true plane strain conditions are in fairly close agreement with peak resistance, R_{max} = 8.7 to 8.8 at ε_{yy} = 1.8 to 2.3%. The passive and the true plane strain tests also show close agreement in measurements of lateral strain, while APSR 19 exhibits much more dilative behavior.

4.3. Evaluation of Ticino Sand Behavior in the APSR Cell

4.3.1. Specimen Uniformity

The raining apparatus described in section 3.2.6.3 rains dense and loose sand specimens whose uniformity was evaluated by measuring the formation densities locally at several locations in the APSR cell. First the specimen mold and membrane are set up. Then tares of known volumes and various heights and diameters are placed on

the floor of the cell.[12] After raining the specimen, the full tares are carefully retrieved, levelled with a straight-edged spatula, and weighed. By varying the heights and diameters of the tares, local variations in sand density can be estimated. Repeatability of specimen placement density is checked by weighing the APSR specimens after shearing.

The material tested in the APSR cell is Ticino sand, a typical, multi-colored, clean river sand imported from Italy with physical properties summarized in Table 4.4. It has medium grained, sub-rounded particles, with less than 0.3% fines. Figure 4.1 shows two sets of sieve analysis results which are essentially identical. Ticino sand has a uniformity coefficient, $C_u = 1.5$, and maximum and minimum dry densities, $\gamma_{max} = 1.70$ and $\gamma_{min} = 1.38$ g/cm^3 (Franco, 1989).

The uniformity check on dense Ticino sand (Table 4.5) shows that the average specimen density, $\gamma = 1.63$ g/cm^3 with a standard deviation of 0.009 g/cm^3, which is below the precision of the density measurements. This corresponds to a relative density, $D_r = 78\%$, according to the maximum and minimum densities reported by Franco (1989) (Table 4.4). There is no noticeable variation in density with tare height or diameter. Table 4.6 shows the measurements of the global specimen densities from six dense APSR specimens. Each specimen has a volume of approximately 38.8 liters, based on measurements of a specimen under a vacuum after removal of the specimen mold. The densities range from 1.61 to 1.63 g/cm^3 ($D_r = 73$-79%). The mean density

---

[12]The tare volumes are determined by filling them with water, covering the top with a glass plate, and weighing them to determine the mass of the water. This provides a measure of the tare volume which is accurate to the nearest mL.

is 1.62 g/cm^3 (D_r = 75%), with a standard deviation of 0.009 g/cm^3. These results are in excellent agreement with the local measurements from the uniformity check.

Table 4.7 presents the results of the uniformity check on a loose Ticino sand specimen. The measured densities show more scatter than for the dense specimen; the values range from 1.45 to 1.51 g/cm^3 (D_r = 22-41%). The mean value is 1.48 g/cm^3 (D_r = 31%), with a standard deviation of 0.02 g/cm^3. The global measurements (Table 4.8) have a mean density of 1.47 g/cm^3 (D_r = 28%); quite close to the local density measurements. The standard deviation of the four global measurements is 0.022 g/cm^3.

4.3.2. Repeatability of External Measurements

Section 4.2 described the refinement of the APSR cell to achieve high quality plane strain shear measurements. Several tests were performed on unreinforced Ticino sand to evaluate its behavior in the isotropic plane. Three of these tests, APSR 36, 38, and 45, were performed on dense Ticino sand, and two (APSR 34 and 37) on loose Ticino sand. This section summarizes the external measurements from these tests in order to demonstrate the repeatability of experimental observations in the APSR cell.

4.3.2.1. Dense Ticino Sand

Figure 4.16 presents the externally measured behavior for APSR 45 (D_r = 74%). Points A and B correspond to the states of zero dilation rate and peak strength, respectively. The measured out-of-plane strain, $\varepsilon_2 \leq \pm 0.02\%$ throughout this test. The shear stress-strain response (Fig. 4.16a) exhibits an initial system stiffening region as the platforms contact the specimen surface. Improved experimental procedures have reduced this effect compared to data obtained previously in APSR 10 and 12 (cf. Fig. 4.10). The strains in APSR 45 are computed from direct measurements of surface

displacements (using transducers D8 and D9, Fig. 3.4), rather than from the average platform movement (used in all tests prior to APSR 19). The lateral strains show good agreement up to $\varepsilon_{yy} = 1\%$, beyond which transducer D5 (Fig. 3.4) measures greater deformations than D7 or D6 (centerline). A failure surface observed at the end of shearing cut through the free face of the specimen near D5. The formation of this failure surface is probably the source of a break which occurs in all three lateral strain curves at an axial strain $\varepsilon_{yy} \approx 2.4\%$. The higher lateral displacements measured by D5 (for $\varepsilon_{yy} >$ 1%) indicate that the failure plane developed gradually and hence, failure was not a sudden event. The breaks in the lateral strain curves may represent the point at which the specimen slides preferentially along a set of failure planes.

Figure 4.16b shows that the b-values in test 45 are generally in the range, b = 0.30 to 0.45, with the higher values occurring at failure as the specimen starts to dilate. The dilation causes a more rapid increase in the pressure exerted against the sidewalls. Similar values of b (0.35 to 0.4) are reported by Wong (1985) for shearing of dense Leighton Buzzard sand ($D_r = 90\%$, $\sigma_c = 14$ kPa) in the Directional Shear Cell (DSC) in the isotropic plane.

Figure 4.17 compares the shear behavior of dense Ticino sand in tests APSR 36, 38 and 45. The stress-strain curves are virtually identical up to $\varepsilon_{yy} = 1\%$ (R = 6) with an average secant modulus, $E_{50} \approx 18{,}700$ kPa. Beyond this point, APSR 36 diverges from the other two tests and exhibits a slightly lower peak strength (R = 8.2) as shown in Table 4.9. At failure, there is excellent agreement between the externally measured axial strains, $\varepsilon_f = 1.7$ to 1.9%, mobilized friction angles, $\phi' = 52^\circ$ to 53°, and lateral stress ratio, b = 0.44 to 0.47. The lateral and volumetric strains from the three tests also show close agreement, although APSR 45 is somewhat less dilative than the other two

tests. Overall , these results demonstrate the high degree of repeatability which can be achieved for shear tests performed on dense Ticino sand.

4.3.2.2. Loose Ticino Sand

Figure 4.18 shows the externally measured shear behavior for APSR 37, a test on loose Ticino sand (D_r = 36%). The shear stress-strain response shows that the loose sand is significantly less stiff than dense sand (E_{50} = 8300 kPa compared to 18,700 kPa for the dense sand). The peak stress ratio, R_{max} = 5.65, corresponds to a mobilized friction angle, $\phi' = 44^o$ at an axial strain ε_{yy} = 3%. Table 4.9 compares the externally measured stress-strain properties for the dense and loose specimens at peak shear resistance.

The externally measured lateral strains (Fig. 4.18c) again show good agreement from all three displacement transducers D5, D6, and D7 (Fig. 3.4), with the lateral strain at D7 somewhat lower than the other two readings throughout the test. The volumetric strains also show fairly close agreement, with a maximum value of $\varepsilon_{vol} \approx 0.60\%$ along the centerline of the specimen at ε_{yy} = 1.7%. For continued shearing beyond peak resistance, the specimen did not develop well defined failure planes. The intermediate principal stress ratio, b = 0.25 to 0.35 throughout the test, a range approximately 25% lower than observed for dense Ticino sand. This result is physically reasonable in view of the less dilative behavior of the loose sand. Wong (1985), also reports b-values between 0.25 and 0.35 for loose Leighton Buzzard sand (D_r = 20%) tested in the Directional Shear Cell (DSC).

Figure 4.19 summarizes the externally measured shear behavior from two tests on loose Ticino sand, APSR 34 and 37. The relative densities of the two test specimens are D_r = 28% and 36%, respectively. The stress-strain and volumetric strain plots are

not as repeatable as for dense Ticino sand. Although there are differences in the secant modulus (E_{50} = 6100 and 8300 kPa for tests 34 and 37, respectively), the mobilized friction angle, $\phi' = 44^{\circ}$ in both tests. The peak shear strength is mobilized at relatively large axial strains (ε_{yy} = 3.0 to 4.5%, Table 4.9) with significantly lower b values than for dense Ticino sand (b_f = 0.35 to 0.41). The differences in stiffness may be due to the lower relative density of the APSR 34 specimen. The volumetric behavior of the two specimens is very similar up to ε_{yy} = 1%. After this point, APSR 34 exhibits significantly more contraction than APSR 37. This may again be due to the difference in the initial densities of the two specimens.

4.3.3. Internal Soil Strains

Radiographic measurements of soil deformations within the APSR specimens provide essential information for evaluating the uniformity of strain conditions in the new device. Typically, radiographs are taken at five stages during a test. Figure 4.20 shows the layout of the tungsten carbide markers which are placed at the mid-height of the specimens. Two fields of markers, each consisting of 100 spheres spaced on a 2.0 cm grid, are designated 'near field' and 'far field'. The near field markers measure soil deformations close to the rear wall of the cell while the far field markers are located near the free face of the specimen. The first radiograph is taken just after the waterbags are brought into contact with the soil specimen, at a stress ratio, R ≈ 1. Successive radiographs then record the marker positions at three points during shearing, with an additional X-ray taken shortly after the peak shear resistance in order to record post-failure soil deformations. After completion of the test, the X-rays are developed and digitized using the procedures described in section 3.3.3.2.

Figure 4.20 also shows the digitized areas from the near and far field X-rays. Only portions of the marker fields could be digitized. The area digitized in the near field corresponds to the approximate size of the X-ray film. The markers outside of this area were therefore not recorded on film.

Only a small portion of the far field was digitized due to a shadow cast by the external reference frame which holds the sidewall LVDTs. This frame is made of steel angle stock and forms a ring around the cell as shown in Figure 4.21. The frame comes between the far field markers and the X-ray tube. When the X-rays are developed, there is an 8cm wide unexposed band across the far field image. The markers within this unexposed zone are not visible on the film and therefore can't be digitized. Further refinement of the referencing system can be undertaken in future APSR tests to eliminate this problem.

4.3.3.1. Global Strain Analysis

Table 4.10 provides a summary of the global strain analysis provided by program STRAIN (section 3.3.3.3; Appendix B). The multiple linear regression technique provides a complete description of the "average" Mohr's circle of strain for each digitized area. Table 4.10 presents the lateral and axial strains (ε_{xx} and ε_{yy}) and their standard deviations computed by the program, and compares these values with those obtained by the boundary displacement LVDTs. The results show the following:

1. The mean values for the far field strains are significantly greater than the mean values for the near field axial and lateral strains.
2. The standard deviations of the strain measurements in the near field are generally within 0.2%, corresponding to the measurement precision of the

digitizing system. In the far field, standard deviations of lateral strains are up to 0.31%.

3. The external measurements of axial strain agree quite closely with the far field axial strains, while the external lateral strains are bounded by the near and far field values.

The above observations indicate that although the strains within each field are fairly uniform, strain magnitudes tend to increase with distance from the rear wall of the cell. Thus, although the cell imposes uniform stresses through the waterbags, the resulting soil strains are non-uniform across the width of the specimen.

Figure 4.22 shows the results from the global analysis superimposed on the externally measured shear behavior. The lengths of the error bars correspond to ±1 standard deviation. In the shear stress-strain response, the R values for the internal measurement points are computed from the applied boundary stresses at the time each X-ray. The zero value used to compute the external axial strain measurements are shifted so that the internal and external stress-strain curves coincide at the stress level of the first X-ray (R = 3.33) (cf. Appendix C). The lateral and volumetric strains (Fig. 4.22b, c) are based on the internally averaged lateral strains and axial strains in the near and far fields. These results show the following:

1. The externally measured shear stress-strain behavior (Fig. 4.22a) matches closely the behavior observed in the far field. However, the near field stress-strain response is much stiffer and reaches peak strength conditions at smaller axial strain levels.
2. The internal lateral strains are greater than the externally measured lateral strains, especially in the far field near failure.

3. The near and far field strain measurements follow the same strain history. However, the near field experiences much smaller axial and lateral strains at the same applied stress ratio, R.
4. The internally measured volumetric behavior is much more dilative than the external measurements indicate. Results obtained in the far field show significant net increases in specimen volume at $\varepsilon_{yy} = 2.0\%$ while the external measurements suggest negligible dilation throughout the test.

4.3.3.2. Local Strain Analysis

Figures 4.23 through 4.28 present strain contour plots based on the local strain analysis described in section 3.3.3.3. The figures show the axial strains, ε_{yy}, lateral strains, ε_{xx}, and principal strain rotations[13], θ, within the digitized portions of the specimen at R = 3.33, 5.56, 7.78 (all pre-peak) and 8.67 (post-peak). The axial strains (Figs. 4.23-24) are fairly uniform within the near and far field windows for $R \leq 5.56$. At R = 5.56, the smallest strains are measured at locations near the rear wall of the cell ($\varepsilon_{yy} \approx 0$) while in the far field $\varepsilon_{yy} \approx 0.7$ to 0.8%. After failure, the strain magnitudes in the near field are only slightly higher than at R = 5.56 and most of the incremental strain is concentrated in the far field.

Figure 4.29 shows the distribution of axial strains, ε_{yy}, across the width of the specimen at two values of y (y = 10mm and 96mm). The plots were obtained by taking the axial strain measurements at five points from the local strain analysis (Figs. 4.23-24) along the y-line of interest. These results show clearly that axial strains are uniform

---

[13] θ is the orientation of ε_1 with respect to the y-axis.

across the specimen at R = 3.33. However, at higher R values, the strain magnitudes generally increase with distance from the rear cell wall.

The lateral strain (ε_{xx}) contours in Figures 4.25-26 reveal a pattern similar to the axial strains, although there is less variation in strain magnitudes with distance from the rear wall. The lateral strain contours up to R = 5.56 are fairly uniform, even between the near and far field zones. From this point until failure, however, most of the continued straining again appears to be concentrated in the far field. After failure, lateral strains throughout most of the near field are similar in magnitude to the values at R = 5.56, while those in the far field are significantly higher (Fig. 4.30).

Figures 4.27-28 show the principal strain rotations in the specimen. These values reflect the amount of shear strain acting in the x and y directions, and provide a means for evaluating the influence of boundary friction on shear distortions within the soil. The principal strain rotation is monitored by the angle θ between the y-axis and the major principal strain direction at a point in the soil specimen. Positive rotations are counterclockwise. The rotation contours (Figs. 4.27-28) reveal that the major and minor principal strain directions lie very near the y- and x-axes with maximum rotations, $\theta \leq 10^{\circ}$ occurring at locations close to the rear wall of the cell for $R \geq 5.56$. It is therefore reasonable to equate the axial strains with the major principal compressive strain occurring at all points in the specimen in this test. At failure the amount of strain rotation is even smaller, generally $\theta \leq 5^{\circ}$. The magnitudes of the strain rotations indicate that rear wall boundary friction does not significantly affect the strain directions within the soil, and that the applied major principal stress directions correspond closely to the resulting major principal strain directions for dense Ticino sand.

Figure 4.31 shows a sketch of the failure surfaces in the specimen after the top sidewall was removed from the cell. A distinct failure wedge formed in the front part of the specimen. After this, the specimen slid along these failure lines, resulting in the post-peak "steady-state" shear resistance (Fig. 4.16). The boundary deformations reveal a pattern that agrees with the internally measured strains, in that most of the deformations occur near the free face of the specimen. The failure plane did not pass directly through the far field internal measurement zone, and thus doesn't appear on the radiographs.

4.3.4. Interpretation of Shear Behavior

4.3.4.1. Dense Ticino Sand

The previous discussion pointed out several inconsistencies between the externally and internally measured strain response of dense sand measured in the APSR cell, particularly at $R > 3.3$. These inconsistencies can be explained by the cohesion of the grease acting along the plane strain faces of the specimen. Restraint caused by the grease cohesion has two effects on the stresses in the specimen:

1. reduction of the major principal stress, σ_1, toward the center of the specimen, and
2. apparent increase in the minor principal stress, σ_3, with increasing distance from the free face of the specimen.

Both of these effects cause a decrease in the stress ratio, R, at points away from the specimen boundary. The stress-strain plots shown in Figure 4.22 need to be corrected to reflect the actual stress ratio acting locally within the specimen.

Figure 4.32 presents a method for correcting the internal stresses. The calculation is based on the boundary friction measurement (section 4.2.2) and is expressed by eqn.

4.1. The grease resistance is proportional to the normal stress, σ_2, (Seah, 1990) which is assumed to act uniformly over the plane strain faces of the specimen. Figure 4.32 shows computations of the corrected stress ratio, $\hat{R}$, at the centerpoints of the near and far fields (N and F, respectively). The computations assume that the changes in the local stresses are uniform over the depth of the specimen.

Figure 4.32 shows that the change in axial stress ($\Delta\sigma_1$) due to sidewall friction is relatively small ($\Delta\sigma_1/\sigma_1 \leq 5\%$), while the change in confining stress ($\Delta\sigma_3/\sigma_3$) can be up to 50% in the near field. In terms of impact on R-value, the primary effect of side friction is to increase the confining stress in the specimen. The strain contour plots show little variation in the y-direction, which confirms that sidewall friction on the plane strain faces affects σ_3 more significantly than σ_1.

Figure 4.33 presents the external and corrected internal measurements of the shear behavior of dense Ticino sand (test APSR 45). Using the proposed correction there is now excellent agreement in the shear stress-strain behavior for both internal (near and far field) and external measurements. The peak friction angle based on external measurements, $\phi_p = 53°$, while the corrected internal measurements give $\phi_p \approx 51°$. The axial strain at failure, $\varepsilon_{yy} = 1.9$ to 2.0% for both sets of measurements, although the near field portion of the specimen never reaches a failure condition. At all points in the stress-strain curve, the near field is subjected to higher confining stresses than the far field due to the sidewall friction. The specimen therefore strains preferentially toward the free face where there is less confinement.

Another discrepancy between the internal and external measurements is the amount of lateral strain that occurs for a given amount of axial strain. The near and far field internal measurements show good agreement, although the far field is strained to much

higher levels at a given applied stress ratio, R. The external measurements, however, exhibit less lateral strain at a given axial strain. Table 4.10 shows that at each R-value, the external axial strain measurements match the far field axial strains, while the externally measured lateral strains fall somewhere between the near and far field internal measurements. The externally measured strain-strain response does not represent a consistent average across the specimen, but rather a combination of the average lateral strain and the maximum axial strain at a given stress ratio. The internally measured strain-strain response therefore reflects more accurately the true material behavior of dense Ticino sand.

Based on these observations, Figure 4.34 presents the best estimate of the stress-strain behavior for dense Ticino sand (test APSR 45). The stress-strain plot (R vs. ε_{yy}) is based primarily on the externally measured stress strain response, which is corrected at small strain levels to compensate for the initial pickup portion of the externally measured curve. The strain response plots (ε_{xx} and ε_{vol} vs. ε_{yy}) are based on the internally measured strains, and follow the same curve fitting lines presented in Figure 4.33. Figure 4.34 describes the stress and strain states at the points of zero dilation rate and peak shear resistance.

Finally, Figure 4.35 compares the internally measured shear behavior for APSR 38 and 45. These data confirm that APSR measurements of the stress-strain response are highly repeatable for internal strains as well as external measurements (cf. Fig. 4.17).

4.3.4.2. Loose Ticino Sand

Table 4.11 compares the internal strains in the near and far field with the externally measured strains observed for loose Ticino sand (test APSR 37). The table shows much higher axial and lateral strains in the loose specimen than in the dense specimen at

a given stress ratio, R. The far field strains are significantly larger than those in the near field (similar to the dense specimen). The externally measured axial and lateral strains generally fall between the near field and far field values at a given R. The internal strains exhibit higher means and standard deviations than the dense sand at a given R value. However, the coefficient of variation (C.O.V.) for each radiograph (Table 4.11) generally reduces with strain level (typically in the range 0.10 to 0.15%) and is comparable for both dense and loose specimens. Figure 4.36 compares the externally and internally measured shear behavior for the loose Ticino sand and shows the following:

1. The externally measured stress-strain behavior closely matches the behavior observed in the far field.
2. All three measurements show similar agreement for the lateral strains, ε_{xx}.
3. The externally measured volumetric behavior closely matches the near field behavior, while the far field measurements indicate more dilation at large strains.
4. The internally measured volumetric behavior in the near and far fields are in reasonable agreement for $\varepsilon_{yy} \leq 1.0\%$, but tend to diverge at larger strain levels.

Contours of axial strain, ε_{yy}, lateral strain, ε_{xx}, and principal strain rotation, θ, for APSR 37 are shown in Figures 4.37-42. The axial strain contours show remarkable uniformity up to R = 4.0. However, at R = 5.33 and 5.84, ε_{yy} is much larger in the far field which may indicate the formation of a failure plane passing through this zone (Fig. 4.38). Unfortunately, the specimen membrane ruptured before the top sidewall could be removed, so the formation of a failure plane could not be verified by direct observation.

The lateral strain contours, ε_{xx} (Figs. 4.39-40), are fairly uniform up to R = 4.0, with higher values in the far field than in the near field. After the specimen reaches a maximum shear stress, the strains concentrate in the far field. The contours of principal strain rotation, θ (Figs. 4.41-42), show that the amount of rotation decreases as R increases. At higher R values, the strain measurement precision (approximately 0.2%, cf. Table 4.11) is small relative to the strain magnitudes, giving better definition to the principal strain directions than at low R values.

The best estimate for the stress-strain behavior of loose Ticino sand can be made by applying boundary friction corrections as described in Figure 4.43. The figure summarizes the calculations for loose sand at the mid-points of the near and far field radiographs (N and F, Fig. 4.43). Figure 4.44 shows the corrected internal measurements. The increase in the near field confining stress is not as significant for the loose sand (compared to the dense sand; Fig. 4.32) as less lateral stress (σ_2) develops on the sidewalls during shearing. However, the correction does bring the internal and external measurements of shear stress-strain response into very close agreement (Fig. 4.44a). The maximum friction angle based on external measurements, $\phi_p' = 44^\circ$, compares closely with $\phi_p' = 43^\circ$ based on the corrected internal measurements. There is still a discrepancy, however, between the near and far field measurements of the volumetric behavior which cannot be explained from the proposed corrections.

Figure 4.34 compares the proposed stress-strain curves for loose Ticino sand with those for dense sand (at the same confining stress, σ_c = 31 kPa). For the loose sand, the stress-strain response is based on external measurements, while the dilational behavior is based on an average of strains in the near and far fields.

4.4. Comparison of APSR Results with Other Shear Devices

This section compares the plane strain shear results obtained in the APSR cell with data from other laboratory devices. The purpose of the comparison is to show that the APSR cell provides reliable shear data for unreinforced sand before proceeding to tests on reinforced sand in the next chapter. The primary variables of concern in this comparison include:

1. The soil stiffness, expressed by E_{50}.
2. The mobilized friction, ϕ'_{cv}, and strains ε_{yy} and ε_{vol} at the zero dilation rate condition.
3. The stress and strain properties at peak shear resistance, including R, b, ϕ_p, ε_{yy}, ε_{vol}, and dilation rate $D = \frac{d\varepsilon_{vol}}{d\varepsilon_{yy}}$.

The most common shear device used in laboratory studies of sand behavior is the triaxial cell, which imposes stress conditions significantly different from plane strain compression (i.e., b = 0 in triaxial compression or b = 1 in triaxial extension). Results from triaxial tests on Ticino sand sheared in the anisotropic plane are first compared to APSR tests. The section also compares APSR results to data from other plane strain devices, including some in which the soil is sheared in the isotropic plane. These devices are summarized in Table 4.12, which provides information on the type of sand tested, the plane of shearing, and the imposed stress level for each test series. Most of the discussion in this section focuses on the dense sand results, since there is more data available in the literature for material deposited under these conditions.

4.4.1. Triaxial Cell Results on Dense Ticino Sand

A series of triaxial tests on dense Ticino sand were performed by Chauhan (1991) to compare the shear behavior for the plane strain (APSR) and triaxial compression modes of shearing. The results also provide a basis for comparing the shear behavior of Ticino sand with the behavior of other types of sand.

Table 4.13 presents a summary of the triaxial shear data for two series of tests. In the first series, the specimen was isotropically consolidated to 98 kPa, then unloaded to 31 kPa and sheared to failure. This series simulates the sequence of confining pressures in the APSR cell, where specimens are subjected a vacuum pressure of approximately 98 kPa during setup and subsequently sheared at σ_3 = 31 kPa. In the second triaxial series (tests TIC-04 and TIC-06), the specimens were normally consolidated to 31 kPa and sheared to failure. All of the specimens were prepared using the "shaker" method (Rad and Tumay, 1987) which resulted in a relative density, $D_r \approx 93\%$. This condition is denser than specimens prepared in the APSR cell (D_r = 73-79%).

Figure 4.45 shows plots of the stress-strain and volumetric strain behavior for all five tests. The secant moduli of the specimens, E_{50} = 12,300 to 64,600 kPa, with a mean value of 30,100 kPa. The specimens reach their peak strengths at axial strains, ε_{yy} = 2.9 to 5.7%. Although the strains to failure vary considerably, the peak strengths are reasonably repeatable (Table 4.13). The peak friction angles for the overconsolidated specimens, ϕ_p' = 43.4 to 44.8°, while ϕ_p' = 45.4 to 45.7° for the two normally consolidated specimens.

The triaxial compression strengths are considerably lower than the plane strain friction angles observed in the APSR cell. The mobilized friction angles observed in the well

controlled plane strain tests, $\phi_p' = 52^o$ to 53^o (Table 4.9), and are approximately 7^o to 8^o higher than for triaxial compression.

Another major difference between the behavior observed in plane strain and triaxial compression is the magnitude of the volumetric strains. In the triaxial tests, there is very little soil contraction. In the tests at OCR = 3 (Table 4.13), the rate of dilation is zero at an axial strain, $\varepsilon_{yy} = 0.13$ to 0.45%, with corresponding stress ratio R = 2.32 to 2.81 ($\phi' = 23^o$ to 28^o) and negligible compressive volumetric strains (0.005 to 0.025%). In general the behavior is highly dilative throughout shear. The peak dilation rate, $D_{max} = -0.93$ to -1.05, which occurs at $\varepsilon_{yy} = 2.5$ to 4.0%. In the APSR cell, the soil is contractive until it reaches an axial strain, $\varepsilon_{yy} = 0.5\%$, and the measured peak dilation rate, $D_{max} = -0.53$.

The observed volumetric and stress-strain behavior in these triaxial tests is consistent with the stress-dilatancy relation defined by Rowe (1962) in which the dilation rate, D_{max}, is related to the peak stress ratio (friction angle at peak shear resistance) and conditions at constant volume shearing by the expression:

$$R_p = R_{cv} (1 - D_{max}) \tag{4.3}$$

where R_p and R_{cv} are the stress ratios at peak and constant volume conditions, respectively. For triaxial tests at OCR = 3, the average value, $D_{max} = -0.96$ at $R_p = 5.57$. Substituting into equation 4.3, $R_{cv} = 2.84$, which is slightly higher than the observed range of $R_{cv} = 2.32$ to 2.81.

Oda et al. (1978) summarize comparisons of plane strain and triaxial shear strength and dilatancy as follows:

specimens were deposited through a funnel into an oversized mold from a height of 90cm to obtain a relative density, $D_r = 90\%$. The specimens were saturated and frozen, then trimmed to obtain any tilting angle, $\delta = 0^o$ to 90^o. The application of the confining pressure and vertical deviator stress was identical to a conventional triaxial test. Two rigid, polished side platens imposed the plane strain condition. Lubricated rubber membranes on the platens reduced the frictional interference.

An additional series of tests on inclined triaxial specimens, prepared in a similar manner, provided a basis for evaluating the plane strain data. Figure 4.46 shows the results from plane strain and triaxial tests at $\sigma_c = 49$ kPa. Both modes of shearing show a general decrease in strength, stiffness, and dilatancy with increasing δ (i.e., as specimen inclination changes from the vertical to the horizontal shearing direction). The test at $\delta = 0^o$ corresponds to a standard plane strain compression test, while $\delta = 90^o$ is a 'plane strain extension' mode of shearing. In the triaxial compression tests, the peak friction angle drops from $\phi_p' = 45.4^o$ to 40.9^o for $\delta = 0^o$ and 90^o, respectively, while the axial strain at peak increases from $\varepsilon_{yy} = 3.9$ to 5.2%. The peak rate of dilation, $D_{max} = -0.9$ for $\delta = 0^o$, while $D_{max} = -0.5$ for $\delta = 90^o$.

Tests in plane strain compression have a higher strength and stiffness, exhibit more dramatic post-peak strain softening, and are less dilative than the corresponding tests in triaxial compression. For the $\delta = 0^o$ test, the peak friction angle, $\phi_p' = 51.6^o$ at an axial strain, $\varepsilon_{yy} = 2.5\%$ and peak dilation rate, $D_{max} = -1.2$. In the $\delta = 90^o$ test, the peak friction angle, $\phi_p' = 47.4^o$ at an axial strain, $\varepsilon_{yy} = 3.83\%$, with a corresponding dilation rate $D_{max} = -0.7$.

Figure 4.47 compares the triaxial tests on Toyoura sand ($\delta = 0^o$; Fig. 4.46a) with similar experiments on Ticino sand. There is excellent agreement in the behavior of the

1. The friction angle in plane strain tests, ϕ'_{ps}, is usually 10 to 20% greater than that measured by the triaxial compression test, ϕ'_{tc}, when a dense sand is tested under a low confining pressure. No significant difference between ϕ'_{ps} and ϕ'_{tc} can be observed when a sand is loose or when a dense sand is tested at sufficiently high confining pressure.
2. A sand with a given void ratio fails at a smaller axial strain in the plane strain test than in the triaxial compression test.
3. A sand dilates more extensively in the triaxial compression test than in the plane strain test.

The difference in peak friction angles for these two modes of shearing has also been observed by Cornforth (1964) and other authors, who attribute the higher strengths to the greater confinement in the plane strain tests. This makes particle re-arrangement more difficult, resulting in higher peak strengths and lower strains at failure.

The lower dilatancy observed in the APSR cell may be attributed to two factors: a) increased confinement in plane strain, and b) the specimen is sheared in the isotropic plane. These factors are considered in the rest of this section by comparing APSR cell data with data from other plane strain devices.

4.4.2. Small Scale Plane Strain Compression Tests

Oda et al. (1978) conducted a series of 28 plane strain compression tests[14] on Toyoura sand specimens inclined at various angles, δ, to the direction of deposition. Toyoura sand is a clean, fine, quartz sand, with a coefficient of uniformity, $C_u = 1.5$. The

[14]The specimen size was 4.4 x 6.0 x 8.0cm.

two sands. The normalized results from test TIC-06 (Ticino sand) and the reported results for the Toyoura sand are virtually identical, with friction angles, $\phi_p' = 45.7^\circ$ and 45.4°, respectively. The secant modulus for Toyoura sand, $E_{50} = 22{,}000$ kPa and is close to the mean value, $E_{50} = 30{,}100$ kPa for Ticino sand. The axial strain at failure in the Ticino sand, $\varepsilon_{yy} = 3.65\%$, compared to $\varepsilon_{yy} = 3.90\%$ in the Toyoura sand. Both sands are highly dilative in triaxial compression. The rate of dilation at peak shear resistance ranges from $D_{max} = -0.9$ to -1.1 for the Ticino sand, while $D_{max} = -0.88$ for Toyoura sand.

Figure 4.48 compares results for plane strain compression ($\delta = 0^\circ$) and extension ($\delta = 90^\circ$) tests of Toyoura sand and APSR data for Ticino sand sheared in the isotropic plane. The initial stiffness of Ticino sand observed in the APSR cell is greater than in both of the Toyoura sand tests. The Ticino sand reaches peak shear resistance ($\phi_p' = 53^\circ$) at $\varepsilon_{yy} = 2.0\%$, compared to $\varepsilon_{yy} = 2.5\%$ ($\phi_p' = 52^\circ$) for the $\delta = 0^\circ$ test and $\varepsilon_{yy} = 4.0\%$ ($\phi_p' = 47^\circ$) for the $\delta = 90^\circ$ test on Toyoura sand. The initial volumetric behavior for the Ticino and both Toyoura tests agree closely up to $\varepsilon_{yy} = 0.6\%$, then the Ticino sand exhibits more dilative behavior. All three specimens reach a maximum volumetric compression, $\varepsilon_{vol} \approx 0.15\%$. The greater stiffness and dilatancy of the Ticino sand may be due, in part, to the lower confining stress ($\sigma_3 = 31$ kPa compared to $\sigma_3 = 49$ kPa in the Toyoura sand tests).

Marachi et al. (1981) present results for dense Monterey sand tested in plane strain and triaxial compression at a confining pressure, $\sigma_3 = 70$ kPa. Monterey sand is a uniform quartz sand with rounded to sub-rounded particles having a uniformity coefficient, $C_u = 1.25$. The reported maximum and minimum void ratios are $e_{max} = 0.83$ and $e_{min} = 0.53$, respectively. Test specimens were prepared at relative densities, $D_r = 27\%$ (loose), 60% (medium dense), and 90% (dense).

Marachi et al. (1981) found that the peak friction angle for plane strain compression of dense sand is 8° higher than for triaxial compression (see Fig. 4.49a). This is the same difference observed for dense Ticino sand sheared in triaxial compression (Chauhan, 1991) and in plane strain compression (in the APSR cell). The peak stress ratio for plane strain compression of dense Monterey sand, $R_p \approx 8.3$ ($\phi'_p = 52°$), compared to an average of $R = 8.7$ ($\phi'_p = 53°$) in the APSR cell for dense Ticino sand. The Marachi et al. test series also showed that both ϕ'_{ps} and ϕ'_{TC} increase with decreasing confining pressure. Their measured axial strain at failure for the plane strain case, $\varepsilon_f = 0.9\%$, was about half the value observed for the triaxial case. The APSR cell and triaxial results on dense Ticino sand reflect this same difference. Figure 4.49a shows that, for a loose sand, ϕ'_{ps} is approximately 4° higher than ϕ'_{TC}. This conflicts with Oda's observation quoted earlier that ϕ'_{ps} and ϕ'_{TC} are approximately equal for a loose sand.

Another conclusion reached by Marachi et al. (1981) is that the amount of out-of-plane deformation has little effect on the measured friction angle at failure. They conducted a test series in which they allowed known amounts of outward sidewall movement. The peak friction angles varied by less than one degree as long as $\varepsilon_2 < 0.4\ \varepsilon_1$ (Fig. 4.49b). This agrees with the trends observed in the APSR cell, in which the true plane strain behavior matches closely the behavior with passive sidewall control (Fig. 4.15). The APSR cell behavior changes significantly, however, for the case of inaccurate active plane strain control (Fig 4.15).

4.4.3. The True Triaxial Apparatus (TTA)

Several researchers have developed laboratory devices that apply three independent principal stresses to a soil. These 'true' triaxial tests provide data which show the influence of the relative magnitudes of the principal stresses on the stress-strain and

strength properties of soils. Deterling (1984) summarizes the development of true triaxial testing, and presents results from a test series performed at MIT to investigate the influence of the intermediate principal stress on the stress-strain properties of Leighton Buzzard sand. This sand consists of uniform, sub-rounded quartz particles with diameters in the range of 0.65 to 0.80mm, having a specific gravity, $G_s = 2.66$. The maximum and minimum void ratios, $e_{max} = 0.79$ and $e_{min} = 0.49$ (Wong, 1985).

Deterling used a flexible boundary apparatus developed at University College London (UCL), which tests a 10cm cubical specimen. He performed stress controlled tests at a confining pressure, $\sigma_c = 20$ kPa, in which he increased σ_2 and σ_3 in proportional amounts to maintain a constant b-value. Internal soil displacements were monitored by radiographic measurements similar to those described for the APSR cell using marker grids placed in two orthogonal planes.

Deterling performed tests to evaluate how the intermediate principal stress ratio, b, affects the stress-strain response of the soil. He found that as b increased from 0 to 1, the stiffness and strength of the soil increased. When b=0, the mode of shearing corresponds to triaxial compression. Figure 4.50 compares the triaxial compression results for the TTA and the triaxial cell data reported by Oda et al. (1978) and Chauhan (1991). All three specimens were loaded in the vertical plane ($\delta = 0^o$). The initial stiffness of the Leighton Buzzard sand is greater than that of the Toyoura and Ticino sand, due in part to the lower confining pressure in the TTA. The axial strains at peak are similar; $\varepsilon_{yy} = 4.3\%$ and 3.9% for Leighton Buzzard and Toyoura sand, respectively. The peak friction angle for the Leighton Buzzard sand, $\phi'_p = 43.8^o$, while $\phi'_p = 45.4^o$ for the Toyoura and Ticino sand.

Figure 4.51 compares the plane strain compression results reported by Deterling and Oda et al. (1978) for dense specimens sheared in the vertical plane, and APSR data for dense Ticino sand sheared in the isotropic plane. All three sands show a decrease in axial strain at peak and an increase in strength at peak when sheared in plane strain compression rather than triaxial compression. The peak friction angles are similar: $\phi_p' = 51.1^\circ$ for Leighton Buzzard sand, $\phi_p' = 51.6^\circ$ for Toyoura sand and $\phi_p' = 53^\circ$ for Ticino sand at axial strains, $\varepsilon_{yy} = 1.3\%$, 2.5% and 2.0%, respectively. The three sands exhibit less dilation at peak shear resistance in plane strain compression than in triaxial compression. Despite the differences between Deterling's tests and conditions in the APSR cell, the stress-strain behavior shows close agreement in the two tests. This may be due to the fact that the TTA imposed a nearly ideal plane strain condition at b = 0.4, rather than using passive plane strain walls as in Oda's tests.

Figure 4.52 shows the effects of b on the intermediate principal strain, ε_2, in the TTA. At a b = 0.4, $\varepsilon_2 \rightarrow 0$ for both dense ($D_r = 94\%$) and loose ($D_r = 47\%$) specimens. This corresponds closely with APSR data, which measure $b_f = 0.44$ and 0.35 for dense and loose sand, respectively.

Under plane strain conditions, Deterling observed a peak stress ratio, R = 8.0, compared to R = 5.5 in triaxial compression (b = 0, Fig. 4.52). The corresponding plane strain friction angle, ϕ_{ps}', was 7° higher than the friction angle for dense Leighton Buzzard sand in triaxial compression. Figure 4.53 compares Deterling's findings of ϕ' as a function of b with other TTA tests on dense Leighton Buzzard sand. These results agree with those observed in the APSR cell. Although the peak R values are slightly higher for Ticino sand than for Leighton Buzzard sand, the plane strain friction angle is 52° to 53° in the APSR cell, which is about 7° to 8° higher than the friction angle for Ticino sand in triaxial compression.

4.4.4. The Directional Shear Cell (DSC)

Bekenstein (1981) and Wong (1985) both performed plane strain tests on dense Leighton Buzzard sand with the Directional Shear Cell (DSC).[15] The device applies a major and minor principal stress to a cubical specimen by two sets of flexible pressure bags. Two parallel, rigid glass plates impose a passive plane strain condition. Strains are measured by radiography of tungsten markers at the mid-height of the specimen. All of the DSC tests were performed at confining pressures σ_c = 14 kPa.

Figure 4.54 compares data from Bekenstein (1981) and Wong (1985) to APSR cell data. All of these tests were performed on dense sand specimens sheared in the isotropic plane. Table 4.14 compares the stresses and strains at the points of zero dilation rate and at peak shear resistance.

The stress-strain curves in Figure 4.54 show that the initial stiffness of the APSR specimens is greater than observed in the two DSC specimens. For the specimens which exhibited a point of zero dilation rate (i.e., Bekenstein and APSR 45), the constant volume friction angles, ϕ_{cv}', are quite consistent, falling in the range ϕ_{cv}' = 37° to 39° with maximum contractive strains, ε_{vol} = 0.13 to 0.14%.

There is significant variation in the stresses and strains observed at peak in the three tests. The APSR specimen reaches peak strength at ε_{yy} = 2.0%, approximately half the value observed in the DSC where ε_{yy} = 4.0 to 4.9%. Since the DSC is stress controlled, Bekenstein (1981) and Wong (1985) do not report any post-peak strain

---

[15]The standard DSC uses a 10cm cubical specimen (Arthur et al., 1972).

softening. The peak friction angles range from $\phi_p' = 47^o$ to 53^o with peak dilation rates observed at or near failure in all three tests, D_{max} = -0.53 to -0.79.

The difference in the stiffness near peak for the APSR cell and the DSC specimens may be due to the fact that the APSR cell imposes an active rather than a passive plane strain condition. The volumetric behavior in all of these tests is less dilative than in Deterling's tests and agrees more closely with the APSR cell results. This supports Oda's results which indicate that shearing in the isotropic plane results in less dilative behavior.

4.5. Conclusions

This chapter presents results from an extensive series of proof tests to demonstrate the reliability of APSR cell tests on unreinforced Ticino sand. The test series includes: 1) evaluation of the pressure control systems, 2) evaluation of the influence of boundary friction on the stress distribution in the specimen, and 3) refinement of controls for active plane strain shearing. Plane strain test results for dense (D_r = 75%) and loose (D_r = 31%) Ticino sand are presented and compared to sand data from other shear devices.

The evaluation of the boundary condition controls (tests APSR 1-6) demonstrates that the control systems can maintain the confining air pressure, σ_c, to a tolerance of ±0.15 kPa and the positions of the loading platforms to within ±0.005mm of a target value. Specimens are sheared under pressure control (the loading platform pressures are matched to within 1 kPa) to ensure uniform boundary stresses.

A series of tests were performed to evaluate boundary resistance in the APSR cell, in which the force required to translate the specimen with no relative displacement between the loading platforms was measured. The measured resistance is nearly

independent of confining stress level and is explained by the cohesion of the grease (c_g ≈ 1.4 kPa) on the specimen boundaries. The measured cohesion compares closely with grease strengths observed by Seah (1990) in the Directional Shear Cell.

The most extensive set of tests refined the active plane strain control systems. The cell is capable of maintaining the intermediate principal strain, $\varepsilon_2 \leq 0.02\%$ up to failure, while simultaneously measuring the corresponding intermediate principal stress. Comparison of APSR tests with passive control, inaccurate active control, and 'true' plane strain (Fig. 4.15) shows that the sidewall control has a significant impact on the measured response of the soil. Tests with inaccurate active control exhibited increased dilatancy, stiffness and peak strength, mobilized at much smaller axial strains than in the true plane strain tests. The stress-strain and volumetric response for the passive and true plane strain conditions are in fairly close agreement.

A series of five 'true' plane strain tests ($\varepsilon_2 \leq 0.02\%$) was performed on dense and loose Ticino sand specimens. The dense specimens prepared with the APSR raining apparatus have an average density, $\gamma_d = 1.63 \pm 0.009$ g/cm^3 ($D_r \approx 78\%$). The externally measured stress-strain response for the three dense specimens (Fig. 4.17) is highly repeatable. At failure, $\varepsilon_{yy} = 1.7$ to 1.8% and $\phi'_p = 52^\circ$ to 53°. The secant modulus for the three tests, $E_{50} = 18{,}100$ to 19,100 kPa. The intermediate principal stress ratio, b, is generally in the range of 0.30 to 0.47 throughout shear, with b = 0.44 to 0.47 at failure. The volumetric response of the specimens is also highly repeatable. For the two loose specimens, $\gamma_d = 1.48 \pm 0.02$ g/cm^3 ($D_r \approx 31\%$). The stress-strain and volumetric response for the loose specimens is not as repeatable as for the dense sand (Fig. 4.19). The loose specimens have a much lower stiffness ($E_{50} = 6100$ to 8300 kPa), peak strength ($\phi'_p = 44^\circ$), and intermediate stress ratio ($b_f = 0.35$ to 0.41) than dense specimens, with higher strains at failure, $\varepsilon_{yy} = 3.0$ to 4.5%.

Internal soil strains are measured by radiography over two zones in the APSR cell (the 'near field' and 'far field'; Fig. 4.20). The average strains over each zone and the local strain distributions are computed using a multiple linear regression technique. The measurements indicate that, although the strains within each zone are fairly uniform, the strain magnitudes tend to increase with distance from the rear wall of the cell, particularly near failure (i.e., although the cell imposes uniform stresses through the waterbags, the resulting soil strains are non-uniform across the width of the specimen). Comparison of the internal and external strain measurements (Fig. 4.22) shows: 1) the externally measured shear stress-strain behavior matches closely the behavior observed in the far field radiographs, while the near field internal response is much stiffer; 2) the near and far field measurements follow the same strain history, although the near field exhibits much smaller axial and lateral strains at the same applied stress ratio; and 3) the internally measured volumetric behavior is much more dilative than the external measurements indicate.

The inconsistencies between the internal and external measurements of the soil response can be attributed to the cohesion of the grease acting along the plane strain faces of the specimen, which causes: 1) a reduction of the major principal stress, σ_1, towards the center of the specimen, and 2) an increase in the minor principal stress, σ_3, with increasing distance from the free face of the specimen. Both of these effects cause a decrease in the apparent stress ratio, R, at points away from the specimen boundary. When the internal stresses are corrected for the grease resistance (Fig. 4.32), the external and internal measurements of the shear stress-strain behavior are in excellent agreement (Fig. 4.33). The internal measurements of volumetric vs. axial strain reflect true volumetric behavior at a point within the specimen and are therefore used to estimate the volumetric response of the soil.

The plane strain shear behavior of dense Ticino sand measured in the APSR cell compares reasonably well with trends reported for other sands in the literature. The peak friction angle and soil stiffness are functions of the intermediate principal stress as well as the confining pressure and density. Volumetric strains are significantly smaller than observed at comparable stress ratios in triaxial tests. This result agrees with trends observed by other researchers, and can be attributed to the increased confinement in plane strain compression. Plane strain shearing in the isotropic plane of the APSR cell also reduces the tendency for dilation. Comparison to data for plane strain shearing of dense sand in other devices shows that the initial stiffness and volumetric behavior of the APSR specimens falls within the range observed by other researchers. The axial strain at peak is substantially lower in the APSR cell than for DSC specimens sheared in the isotropic plane, but the volumetric responses are in good agreement.

1. Evaluation of Pressure Control and Specimen Setup Procedures

APSR 1-4: Added waterbags to measure directly σ_1 (Test 3)

APSR 5: First use of raining apparatus

APSR 6: First reliable control of air pressure (σ_3)

2. Evaluation of Lubrication

APSR 7: Lubrication tests at various σ_3, R-value = 4

APSR 8: Lubrication tests with multiple strokes, σ_3 = 31 kPa, R-value = 4

APSR 9: Modified specimen mold to allow lubrication tests at R = 1

3. Plane Strain Shear Tests

(a) Passive Plane Strain Control

APSR 10: First successful shear test with radiography

APSR 11: Leaky specimen membrane caused premature failure

APSR 12: Second successful shear test

APSR 13: Specimen membrane ruptured - premature failure

(b) Refinement of Active Plane Strain Control (Unreinforced Specimens)

APSR 15-17: Large jumps in plane strain walls, poor plane strain control

APSR 18: Good plane strain control, but erratic b-values

APSR 19,20: Well-controlled plane strain shear tests

(c) Refinement of Active Plane Strain Control (Reinforced Specimens)

APSR 21: Sand specimen with two-ply steel reinforcement (0.25 mm thick)
Unable to maintain plane strain condition with independent feedback control

APSR 22,23: First tests with reinforcement position feedback control. Sidewalls controlled by computer to maintain constant b-value.

APSR 24-30: Experimented with sidewall geometry to improve plane strain control

APSR 31-33: Monitored sidewall motions with independent reference frame

APSR 34-35: Well-controlled plane strain tests with improved sidewall geometry and external reference frame for measuring and maintaining plane strain condition.

Note: APSR 1-4 used Leighton Buzzard sand
APSR 5-9 used Ottawa sand
All other tests used Ticino sand

Table 4.1: Summary of APSR Cell Proof Tests

Test No.	Geometry of Inner Sidewalls		Sidewall Control Method	ϕ_p	R_{peak}	b-values	ε_2(%)
	Top Wall	Bottom Wall					
21	1/16" Alum.	1/16" Alum.	Displacement feedback	54°	9.5	0.25-0.45	+1.5
22	1/16" Alum.	1/16" Alum.	Constant b-value	55°	9.8	0.43-0.45	+1.6
23	1/16" Alum.	1/16" Alum.	Constant b-value	55°	10.0	0.64-0.66	±0.3
24	1/16" Alum.	1/16" Alum.	Computer displacement	56°	10.4	0.3-1.1	+1.5
25	1/16" Alum.	3/4" Lexan	Displacement feedback	Early Failure		0.33-0.60	+0.5
26	1/4" Plexi.	3/4" Lexan	Displ feedback (bottom) Computer Control (top)	52°	8.4	0.20-0.85	±1
27	1/4" Alum.	3/4" Lexan	Computer Control	52°	8.4	0.46-0.50	+1.5
28	1/4" Alum. Reduced Area	3/4" Lexan	Displ. feedback (top) Passive control (bottom)	54°	9.2	0.47-0.97	+2.5
29	1/4" Alum. Reduced area	3/4" Lexan Reduced area	Displacement feedback	Early Failure		0.45-0.76	+1.7
30	1/4" Alum. Reduced area	3/4" Lexan Reduced area	Constant b-value	σ_c = 3.5 psi		0.58-0.61	+1.3
31	1/4" Alum. Reduced area	1/4" Alum. Reduced area	Constant b-value	54°	9.6	0.58-0.61	+1.0
32	1/4" Alum. Reduced area	1/4" Alum. Reduced area	Constant b-value Ext. Monitoring Frame	54°	9.6	0.58-0.61	+1.0
33	1/4" Alum. Reduced area	1/4" Alum. Reduced area	Constant b-value Ext. monitoring frame	55°	9.8	0.45-0.50	±0.4
34	1/4" Alum. Reduced area	1/4" Alum. Reduced area	Displacement feedback External reference frame	44°	5.6	0.21-0.43	±0.01
35	1/4" Alum. Reduced area	1/4" Alum. Reduced area	Displacement feedback External reference frame	52°	8.2	0.42-0.56	±0.01

Notes: 1. All tests have e = 0.63±0.02 and 0.010" steel reinforcement, except APSR 34 which was unreinforced, loose Ticino sand with e = 0.80.

2. σ_c = 31 kPa, except for APSR 30 in which σ_c = 24 kPa due to faulty air control.

3. Positive values of ε_2 correspond to outward sidewall displacements (soil expansion).

Table 4.2: Summary of Plane Strain Conditions for APSR 21 through 35

Test Condition[1]	Test No.	E_{50} (kPa)	At Zero Dilation							At Failure						
			R	ϕ'	$\frac{\sqrt{J_2}}{\sigma_{oct}}$[2]	ε_a (%)	$\varepsilon_{vol.}$[3] (%)	ε_2 (%)	b	R	ϕ'	$\frac{\sqrt{J_2}}{\sigma_{oct}}$	ε_a (%)	$\varepsilon_{vol.}$ (%)	ε_2 (%)	b
P	10	15,100	6.4	47°	-	1.42	0.53	-	-	8.2	51°	-	2.3	0.39	-	-
P	12	16,300	7.1	49°	-	1.47	0.52	-	-	8.7	53°	-	2.3	0.31	-	-
A	15	32,700	7.1	49°	-	0.78	0.17	-0.1	-	9.6	52°	-	1.2	0.07	1.5	-
A	16	54,600	7.4	50°	0.77	0.50	0.32	-1.0	0.44	8.2	51°	0.85	1.0	0.29	-0.7	0.38
A	18	65,000	7.1	49°	0.74	0.50	0.16	0.0	0.38	8.4	51°	0.86	1.2	0.10	0.3	0.39
A	19	47,200	6.4	47°	0.80	0.67	0.22	-0.1	0.42	10.0	55°	0.85	1.5	0.0	-0.1	0.43
A	20	34,000	6.3	47°	0.81	0.63	0.23	0.0	0.37	10.8	56°	0.86	1.5	0.0	0.05	0.43
A, ε_2	36	18,800	6.5	47°	0.77	1.13	0.34	0.00	0.42	8.2	52°	0.80	1.7	0.28	-0.02	0.47
A, ε_2	38	18,100	7.4	50°	0.79	1.20	0.45	0.00	0.43	9.1	53°	0.83	1.7	0.36	0.00	0.44
A, ε_2	45	19,100	7.1	49°	0.79	1.19	0.54	0.00	0.42	8.8	53°	0.82	1.8	0.50	-0.01	0.44

1. Key for test conditions:

   P = Passive plane strain control

   A = Active plane strain control

   ε_2 = Measured out-of-plane strain (ε_2) within ±0.02% throughout shear (ε_2 positive in compression).

2. $J_2 = \frac{1}{6}[(\sigma_1 - \sigma_2)^2 + (\sigma_2 - \sigma_3)^2 + (\sigma_3 - \sigma_1)^2]$ is the second invariant of the deviatoric stress tensor.

   $\sigma_{oct} = \frac{1}{3}(\sigma_1 + \sigma_2 + \sigma_3)$ is the mean stress.

3. The volumetric strain, ε_{vol}, is based only on the external axial and lateral displacement measurements, since the amount of out-of-plane strain, ε_2, is not precisely known.

Table 4.3: Externally Measured Shear Behavior from APSR Cell Tests on Unreinforced Dense Ticino Sand

Property	Symbol	Value	Source
USCS Designation[1]:		SP (< 2% fines)	Larson
Coefficient of Uniformity[2]	C_u	1.5	Larson
Specific Gravity of Solids:	G_s	2.67	Franco (1989)
Dry Densities:	γ_{max} γ_{min}	1.70 g/cm^3 1.38 g/cm^3	Franco (1989)
Void Ratios:	e_{max} e_{min}	0.93 0.57	
Constant Volume Friction Angle	ϕ'_{cv}	32°	Franco (1989)

Notes: 1. USCS = Unified Soil Classification System

2. The coefficient of uniformity is defined as $\frac{D_{60}}{D_{10}}$, where D_{60} is the soil diameter at which 60% of the soil is finer by mass and D_{10} the diameter at which 10% of the soil is finer by mass.

Table 4.4: Properties of Ticino Sand

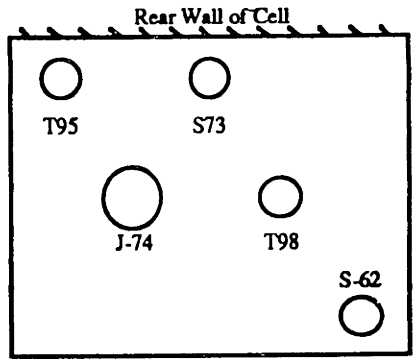

Tare Positions

Tare No.	Tare Ht. (cm)	Tare+ Glass (g)	Vol. (mL)	Tare + Sand (g)	Sand Wt. (g)	Density (g/cc)	e	D_r (%)
S-62	3.5	169	84	307	138	1.64	0.628	82
S-73	3.5	169	84	306	137	1.63	0.638	78
J-74	2.7	179	116	369	190	1.64	0.628	81
T98	5.4	174	132	391	217	1.64	0.628	82
T95	5.4	174	132	388	214	1.62	0.648	75

Table 4.5: Uniformity of Dense Ticino Sand Prepared with the APSR Raining Apparatus

Test No.	Specimen Wt. (kg)	Density[1] (g/cc)	D_r (%)
APSR 39	62.575	1.61	73
APSR 41	62.852	1.62	75
APSR 43	62.649	1.61	73
APSR 45	62.683	1.62	74
APSR 48	63.252	1.63	78
APSR 49	63.327	1.63	79

Note: The specimen volume for all tests was 38.8 liters

Table 4.6: Relative Densities of Dense Ticino Sand Specimens

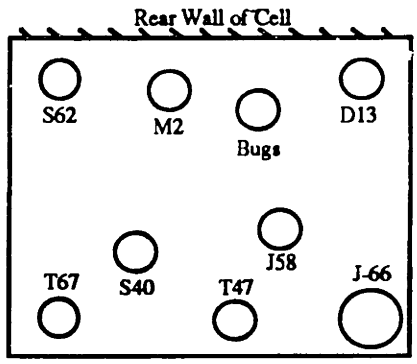

Tare Positions

Tare No.	Tare Ht. (cm)	Tare Wt (g)	Vol. (mL)	Tare + Sand (g)	Sand Wt. (g)	Density (g/cc)	e	D_r (%)
T-47	5.4	62	132	254	192	1.45	0.841	22
T-67	5.4	62	132	256	194	1.47	0.816	28
J-66	2.7	67	114	233	166	1.46	0.829	25
J-58	2.2	55	43	120	65	1.51	0.768	41
D13	2.2	55	45	121	66	1.47	0.816	28
S-40	3.4	57	84	182	125	1.49	0.792	34
Bugs	2.2	55	45	121	66	1.47	0.816	28
M2	2.2	56	43	121	65	1.51	0.768	41
S62	3.4	57	84	181	124	1.48	0.804	31

Table 4.7: Uniformity of Loose Ticino Sand Prepared with the APSR Raining Apparatus

Test No.	Specimen Wt. (kg)	Density[1] (g/cc)	D_r (%)
APSR 37	58.099	1.50	37
APSR 44	57.525	1.48	32
APSR 46	56.632	1.46	25
APSR 47	56.384	1.45	23

Note: The specimen volume for all tests was 38.8 liters

Table 4.8: Relative Densities of Loose Ticino Sand Specimens

Test No.	D_r (%)	E_{50} (kPa)	At maximum shear stress						
			q (kPa)	R	ϕ'	b	$\frac{\sqrt{J_2}}{\sigma_{oct}}$	ε_a (%)	$\varepsilon_{vol.}$ (%)
36	75	18,800	112	8.2	52°	0.47	0.80	1.7	0.28
38	75	18,100	125	9.1	53°	0.44	0.83	1.7	0.36
45	74	19,100	121	8.8	53°	0.44	0.82	1.9	0.50
34	28	6100	71	5.6	44°	0.41	0.73	4.5	1.2
37	36	8300	72	5.6	44°	0.35	0.78	3.0	0.50

Note: σ_c = 31 kPa for all tests.

Table 4.9: Shear Properties for Dense and Loose Ticino Sand in the APSR Cell

X-Ray No.	R	Axial Strains, ε_{yy} (%)							Lateral Strains, ε_{xx} (%)						
		Near Field			Far Field			Ext.	Near Field			Far Field			Ext.
		Mean	S.D.	C.O.V.	Mean	S.D.	C.O.V.	DCDT	Mean	S.D.	C.O.V.	Mean	S.D.	C.O.V.	DCDT
2	3.33	0.16	0.12	0.75	0.30	0.12	0.40	0.29	-0.08	0.16	2.0	-0.16	0.20	1.2	-0.10
3	5.56	0.39	0.15	0.38	0.74	0.12	0.16	0.77	-0.35	0.15	0.43	-0.63	0.18	0.29	-0.35
4	7.78	0.59	0.14	0.24	1.46	0.12	0.08	1.38	-0.42	0.14	0.33	-1.68	0.23	0.14	-0.86
5 Post Peak	8.67	0.71	0.15	0.21	2.01	0.17	0.08	2.18	-0.57	0.17	0.30	-2.51	0.31	0.12	-1.79

Notes: 1. Dense Ticino Sand, D_r = 74%

2. Mean and standard deviations for near and far field X-rays are based on multiple linear regression analysis

3. The coefficient of variation, C.O.V. = S.D./mean.

Table 4.10: Summary of Internal vs. External Strain Measurements in Test APSR 45

X-Ray No.	R	Axial Strains, ε_{yy} (%)							Lateral Strains, ε_{xx} (%)						
		Near Field			Far Field			Ext.	Near Field			Far Field			Ext.
		Mean	S.D.	C.O.V.	Mean	S.D.	C.O.V.	DCDT	Mean	S.D.	C.O.V.	Mean	S.D.	C.O.V.	DCDT
2	2.67	0.37	0.10	0.27	0.41	0.11	0.27	0.40	-0.22	0.15	0.68	-0.16	0.19	1.2	-0.31
3	4.00	0.95	0.15	0.16	1.26	0.14	0.11	1.27	-0.47	0.15	0.32	-0.97	0.19	0.20	-0.87
4	5.33	1.52	0.22	0.14	2.82	0.31	0.11	2.54	-0.93	0.25	0.27	-3.17	0.33	0.10	-2.11
5	5.84	1.95	0.29	0.15	4.63	0.48	0.10	3.74	-1.38	0.37	0.27	-5.39	0.51	0.09	-3.43

Notes: 1. Loose Ticino Sand, D_r = 37%

2. Mean and standard deviations for near and far field X-rays are based on multiple linear regression analysis

3. The coefficient of variation, C.O.V. = S.D./mean.

Table 4.11: Summary of Internal vs. External Strain Measurements in Test APSR 37

Apparatus	Source	Sand	D_r (%)	Preparation Method	σ_3 (kPa)	Plane of Shearing[1]	Plane Strain Control Method
APSR Cell	Larson, 1992	Ticino	75 28-36	Multiple Sieve Pluviation	31	I	Active displace-ment control
Plane Strain Apparatus	Oda et al., 1978	Toyoura	90	Slow funnel deposition	49	A	Passive sidewalls
Plane Strain Apparatus	Marachi et al., 1981	Monterey	90 60 27	Vibratory compaction	70	A	Passive sidewalls
True Triaxial Apparatus	Deterling, 1984	Leighton Buzzard	94 47	• Slow sprinkling • Dry pluviation	20	A	Pressure control
Directional Shear Cell	Bekenstein, 1981	Leighton Buzzard	87 17	• Slow sprinkling • Dry pluviation	13.8	I, A	Passive sidewalls
Directional Shear Cell	Wong, 1985	Leighton Buzzard	90 20	• Slow sprinkling • Dry pluviation	14	I, A	Passive sidewalls

Notes: 1. I = shearing in plane normal to deposition direction ('isotropic plane')
A = shearing in plane parallel to direction of deposition (anisotropic plane)

Table 4.12: Comparison of Several Plane Strain Shear Devices

Test No.	$\sigma_{c,max}$ (kPa)	σ_c (kPa)	E_{50} (kPa)	At Peak				
				R	ϕ'	$\frac{\sqrt{J_2}}{\sigma_{oct}}$	ε_a (%)	$\varepsilon_{vol.}$ (%)
3	98	31	32,300	5.38	43.4	1.03	5.69	-4.77
5	98	31	12,300	5.56	44.0	1.04	3.62	-2.55
7	98	31	19,700	5.77	44.8	1.06	4.72	-3.87
4	31	31	64,600	5.95	45.4	1.08	2.94	-2.83
6	31	31	21,600	6.03	45.7	1.08	3.65	-2.55

Note: All tests have $D_r \sim 93\%$

Table 4.13: Shear Behavior from Triaxial Tests on Dense Ticino Sand (Chauhan, 1991)

Source	D_r (%)	E_{50} (kPa)	Zero Dilation Rate			Peak			
			ϕ'_{cv}	ε_{yy} (%)	ε_{vol} (%)	ϕ'_p	ε_{yy} (%)	ε_{vol} (%)	D_{max}[1]
APSR 45	74	19,100	39°	0.50	0.14	53°	2.0	-0.50	-0.53
Bekenstein, 1981	87	8100	37°	0.40	0.13	52°	4.0	-	-0.6
Wong, 1985	90	8800	-	-	-	49°	4.9	-	-0.79

Note: 1. $D_{max} = \frac{d\varepsilon_{vol}}{d\varepsilon_{yy}}$

Table 4.14: Comparison of Plane Strain Shear Behavior for Isotropic Specimens

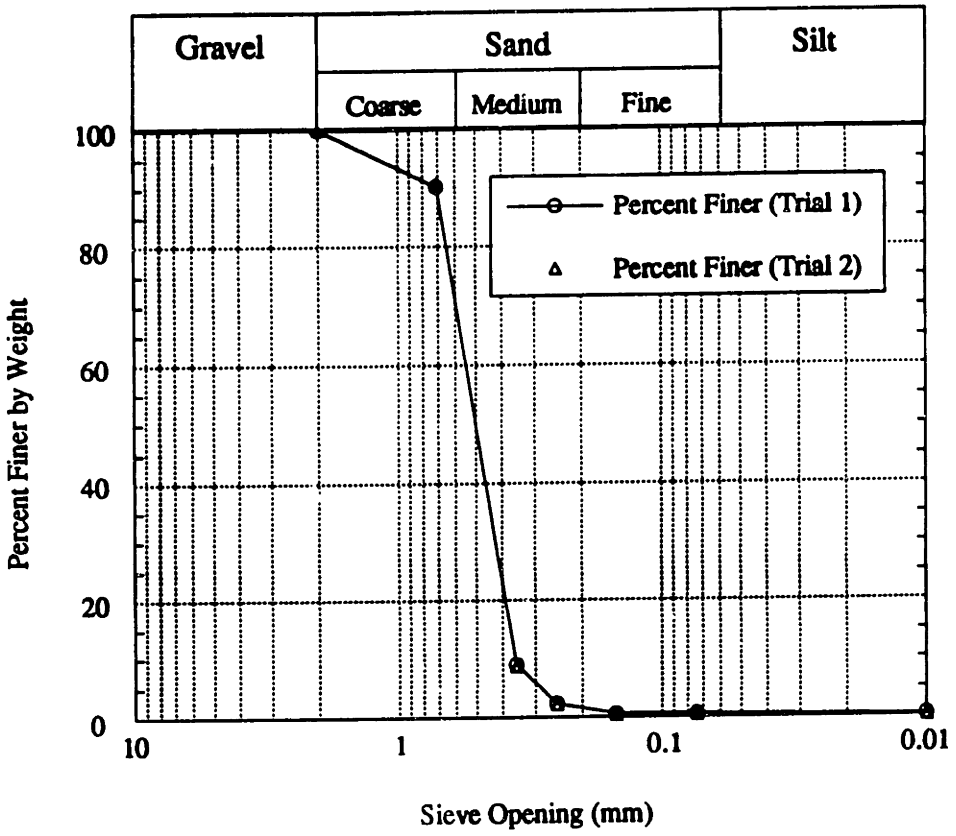

Figure 4.1: Grain Size Distribution for Ticino Sand

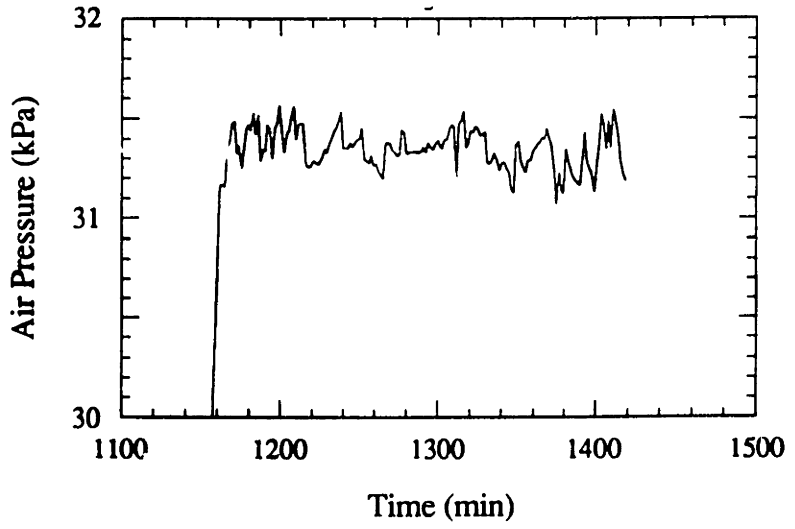

(a) Stability of confining air pressure

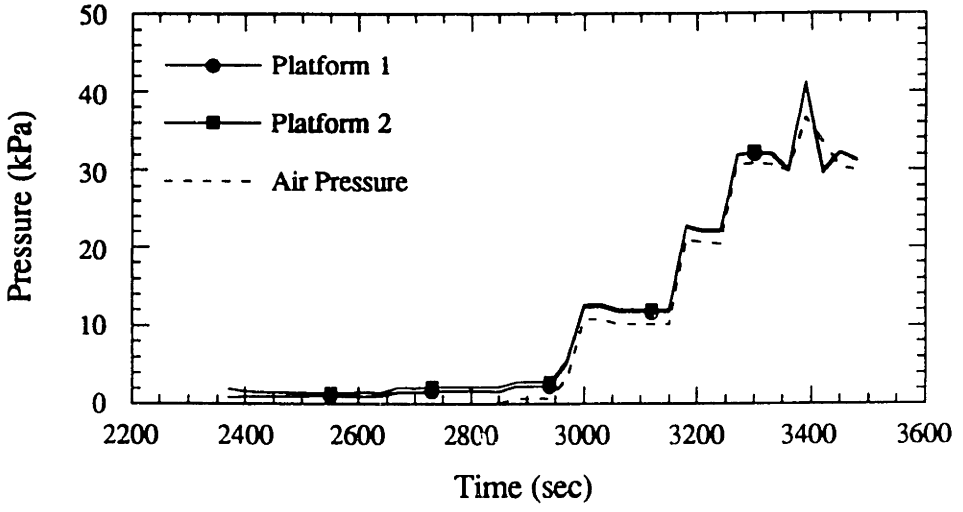

(b) Air and waterbag pressures, APSR 9

Figure 4.2: Reliability of Air Pressure Control in the APSR Cell

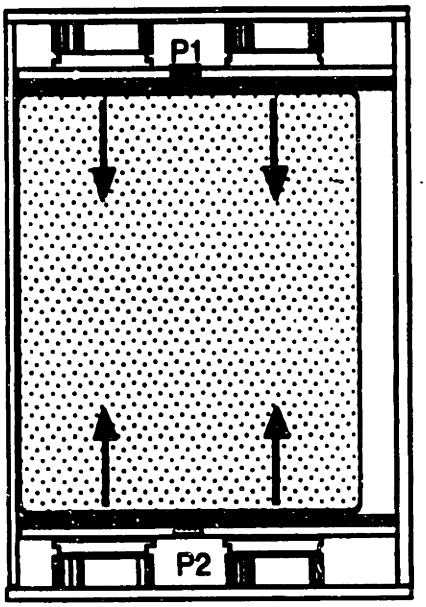

(a) Compress the specimen by Δ/2.

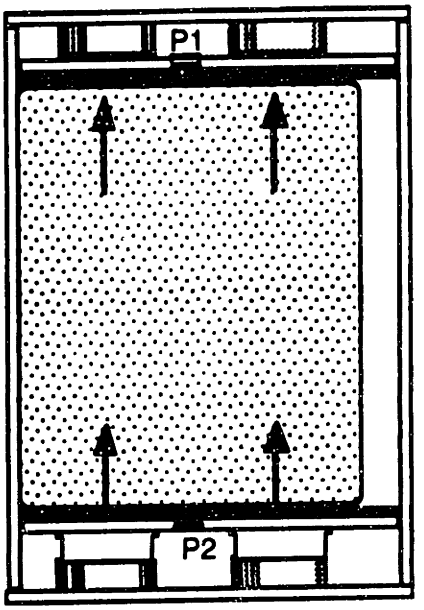

(b) Translate the specimen by Δ/2 in direction of platform 1.

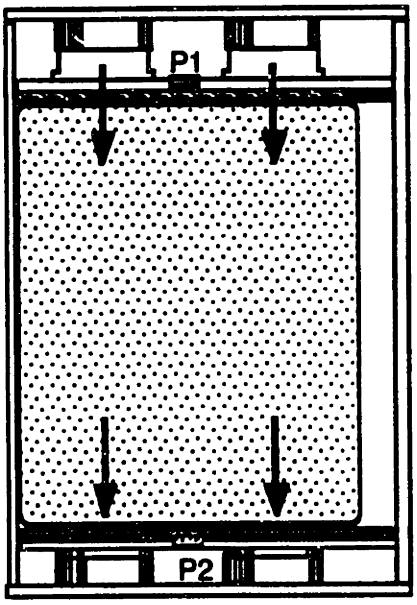

(c) Translate the specimen by Δ in the direction of platform 2.

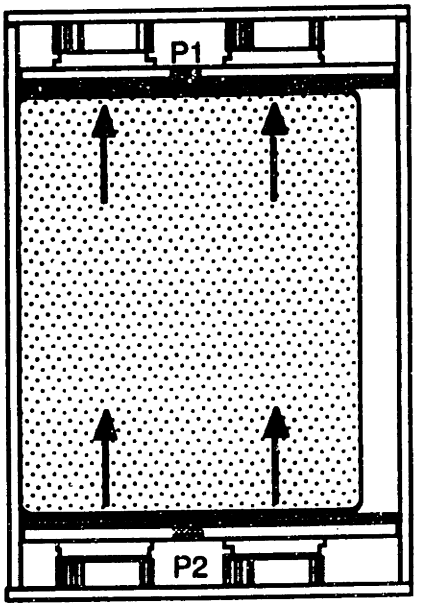

(d) Return the specimen to its central position.

Figure 4.3: Procedure for Evaluating Boundary Resistance in the APSR Cell

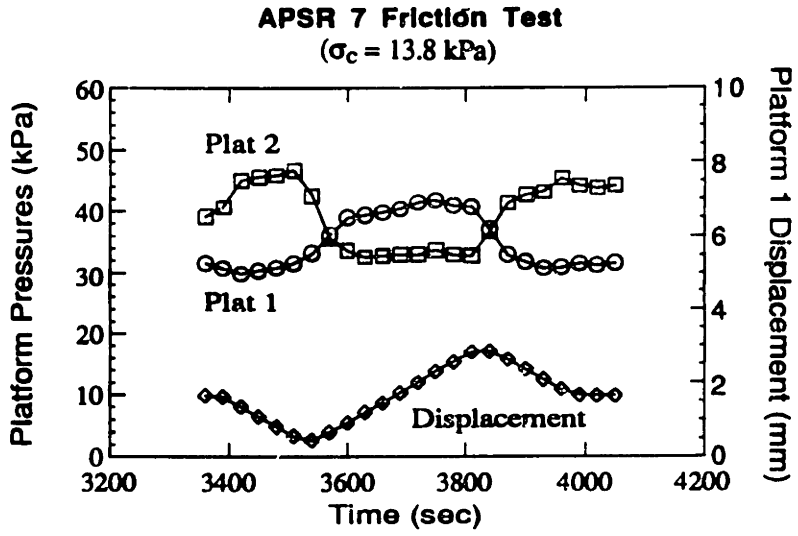

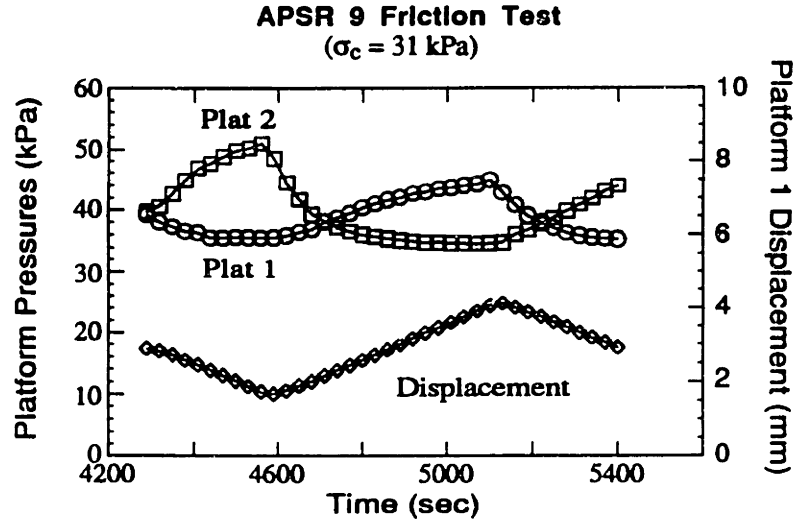

Calculation:

Area of platforms = 0.152 m x 0.457 m = 0.0695 m^2

Average pressure difference[1] = 12.4 kPa

Friction force = 12.4 kPa x 0.0695 m^2 = 0.861 kN

Area over which friction acts = 0.62 m^2

Apparent cohesion of grease, $\bar{c}$ = 0.861 kN / 0.62 m^2 = 1.4 kPa

[1] Average based on 7 translation cycles, σ_c = 14 to 41 kPa

Figure 4.4: Results of Boundary Resistance Measurements

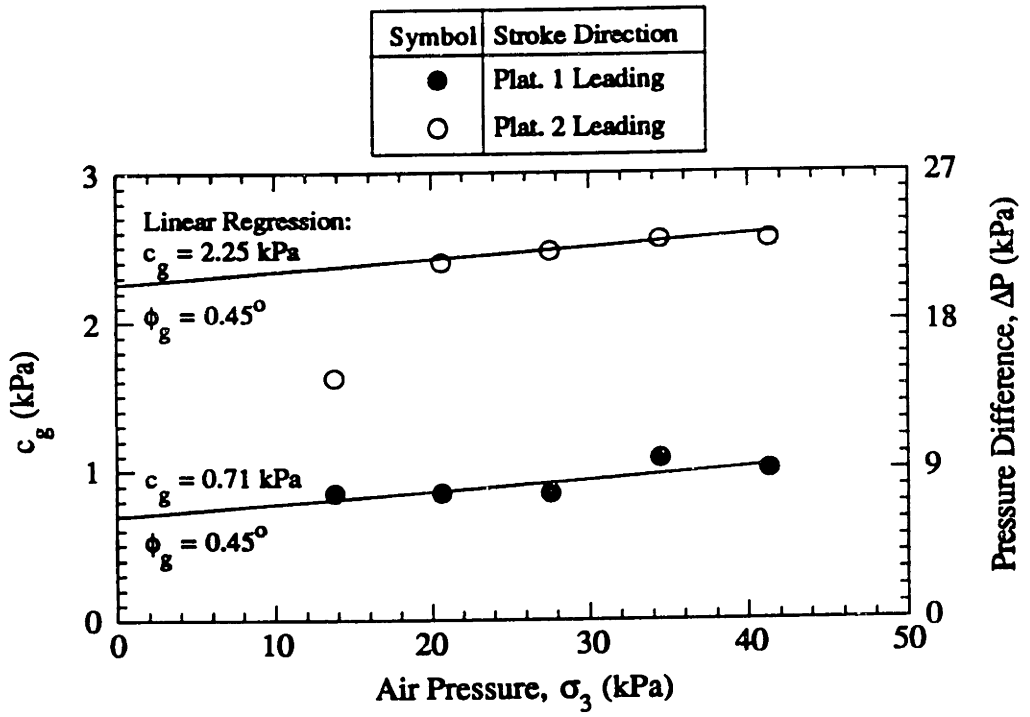

Figure 4.5: Pressure Difference in the Waterbags at Various Confining Pressures During Translation Test (APSR 7)

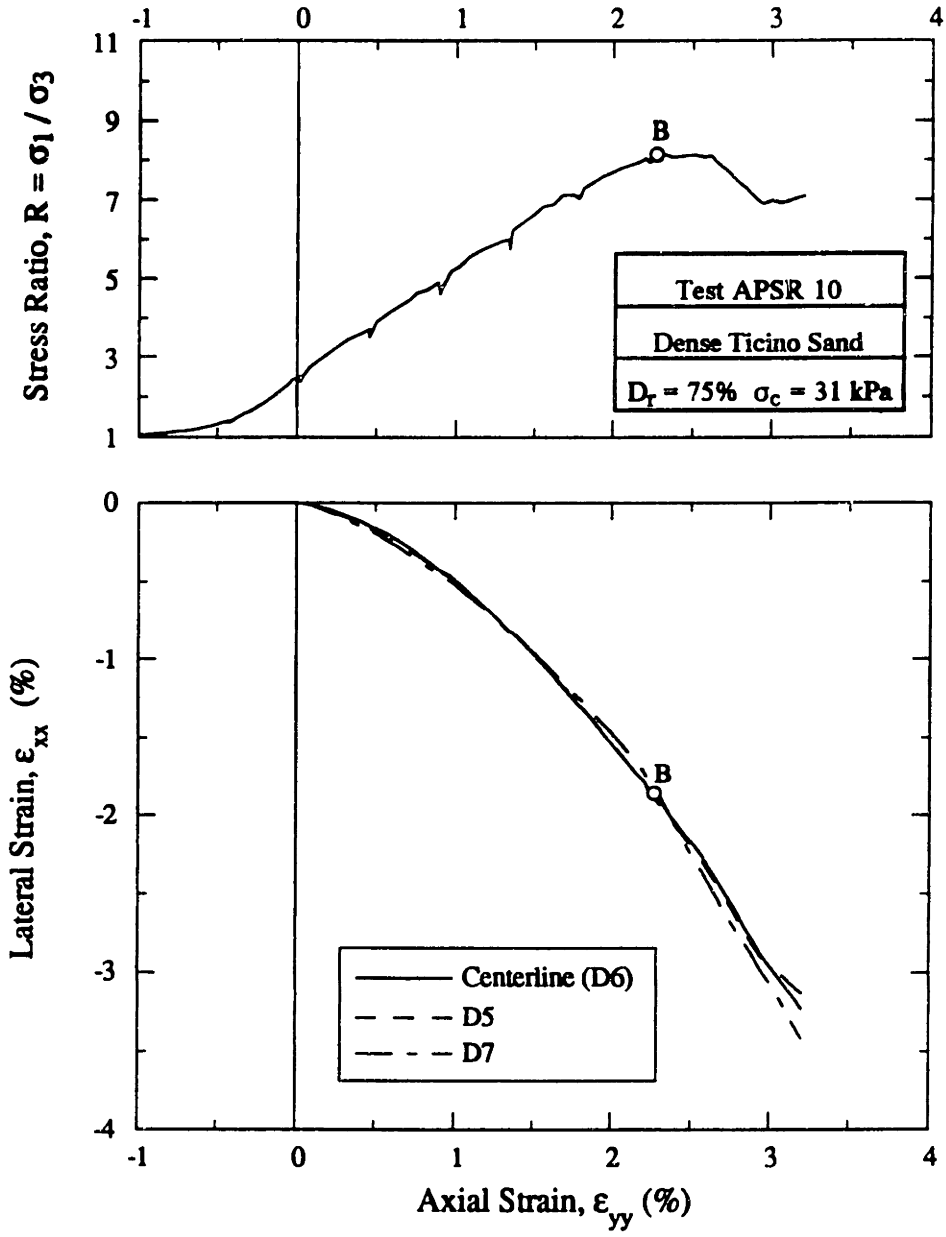

Figure 4.6: Externally Measured Shear Behavior in APSR 10

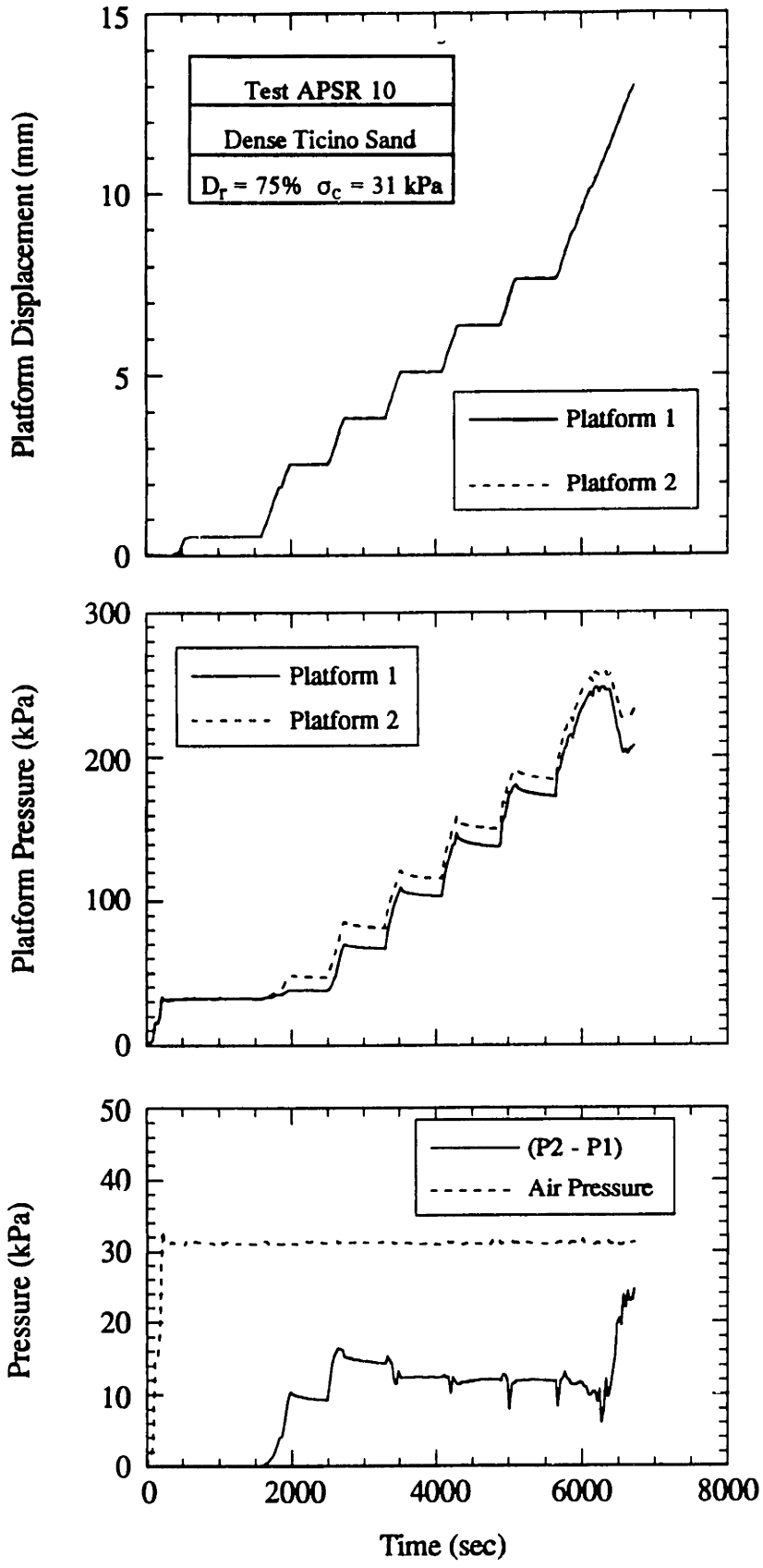

Figure 4.7: Platform Displacements and Pressures in a Displacement Controlled Test

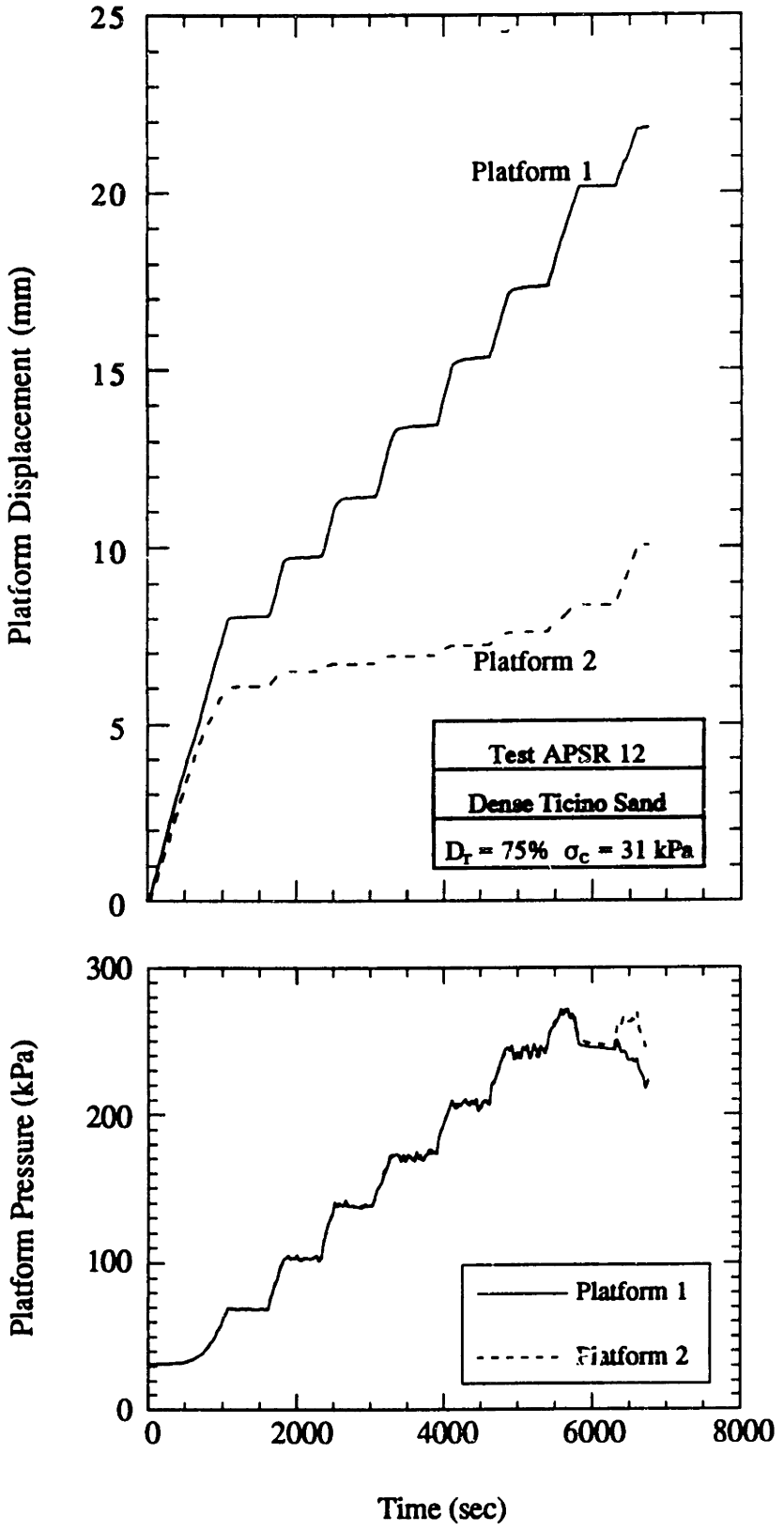

Figure 4.8: Platform Displacements and Pressures Using Boundary Pressure Control

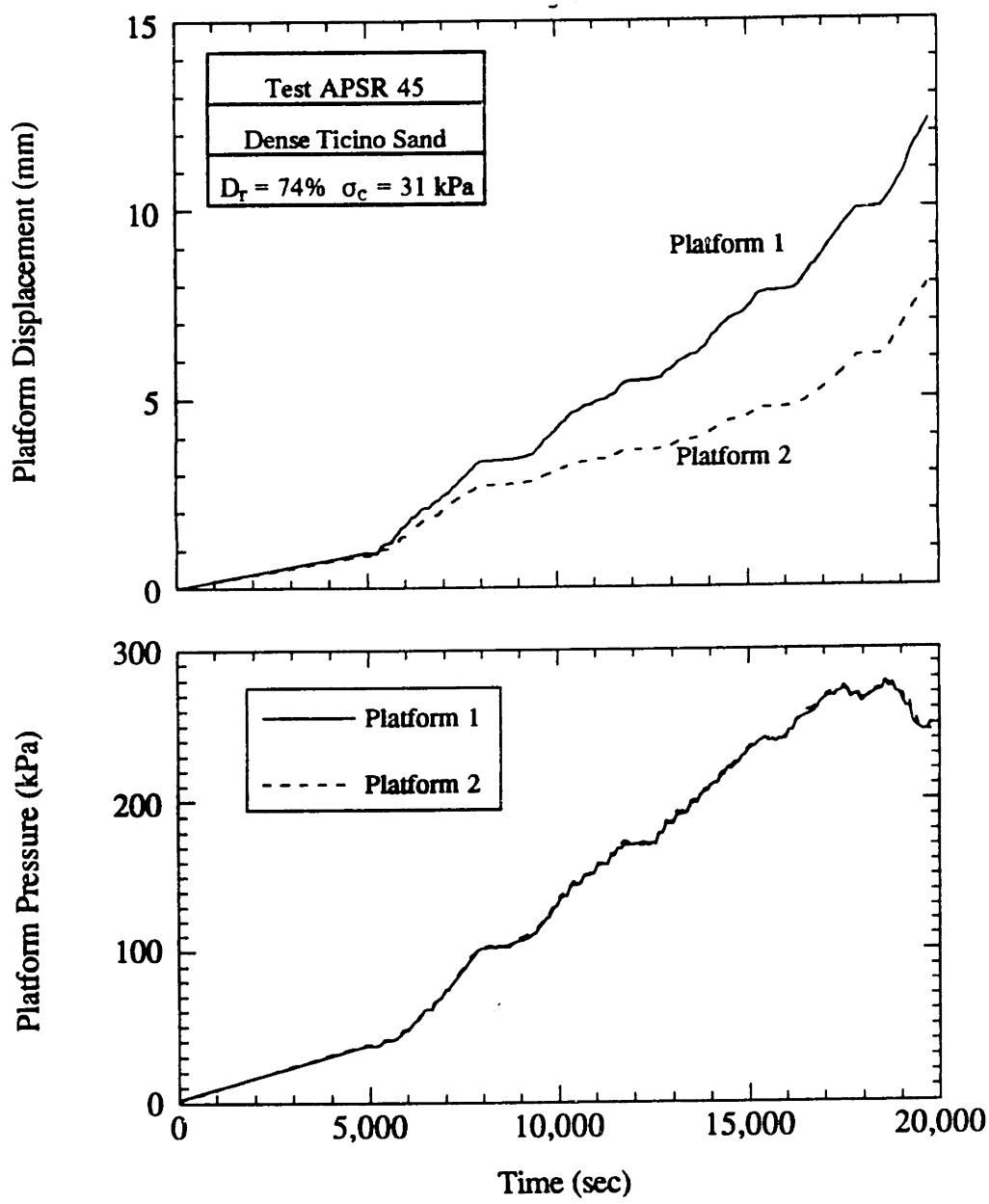

Figure 4.9: Platform Displacements and Pressures Using Refined Pressure Control

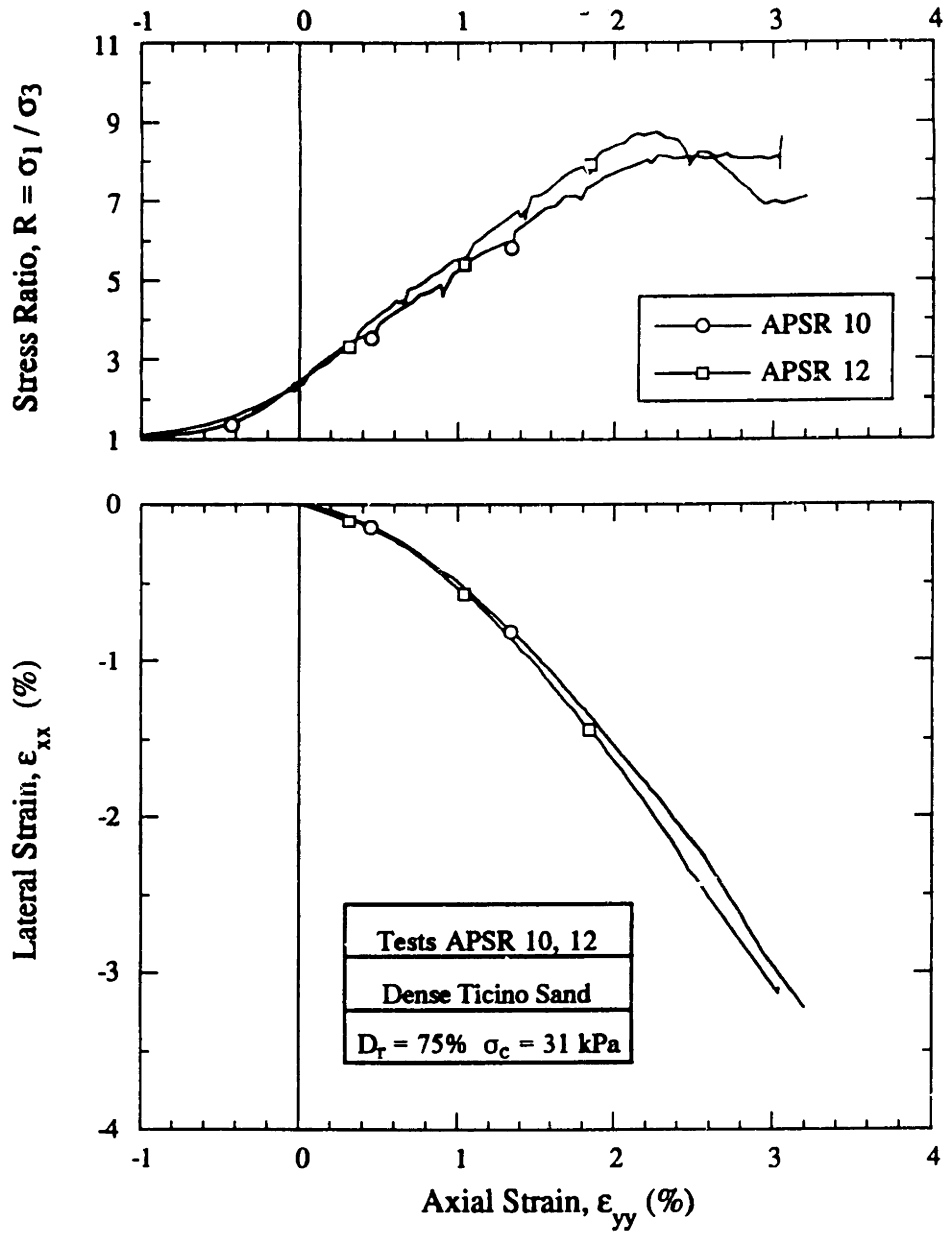

Figure 4.10: Externally Measured Shear Behavior in APSR 10 and 12

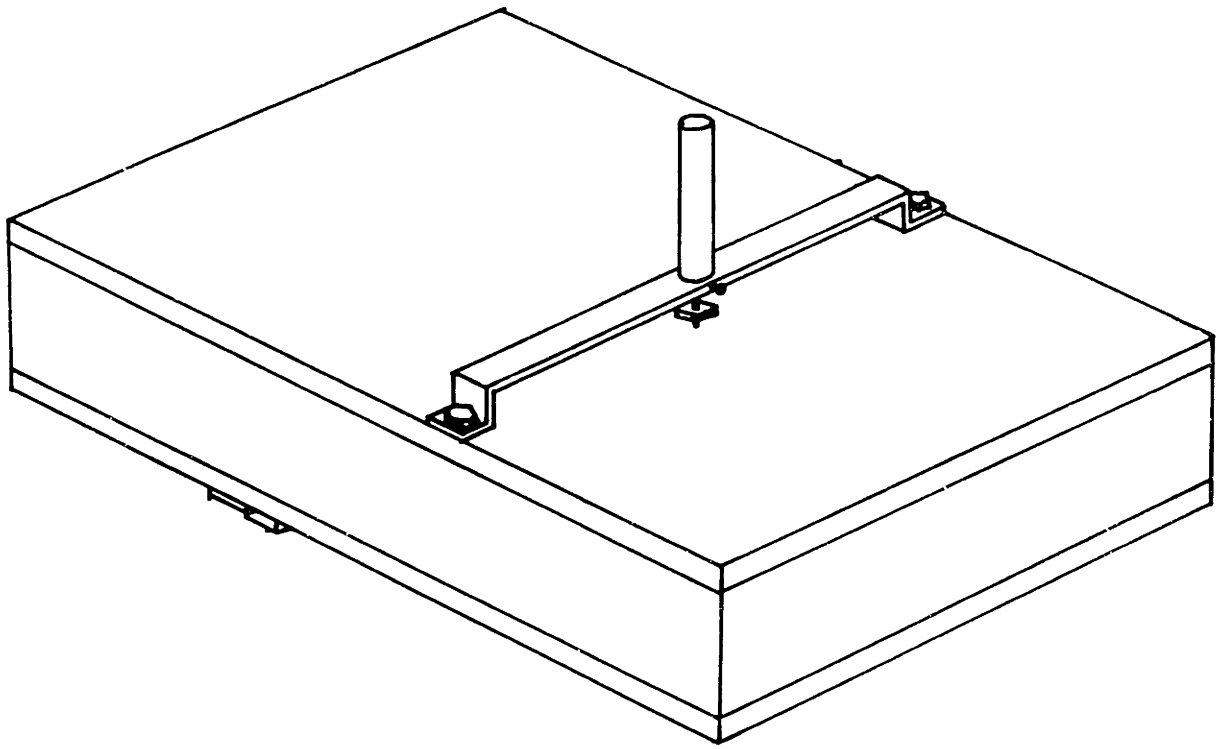

Figure 4.11: Original Clamping Mechanism for the Sidewall LVDTs

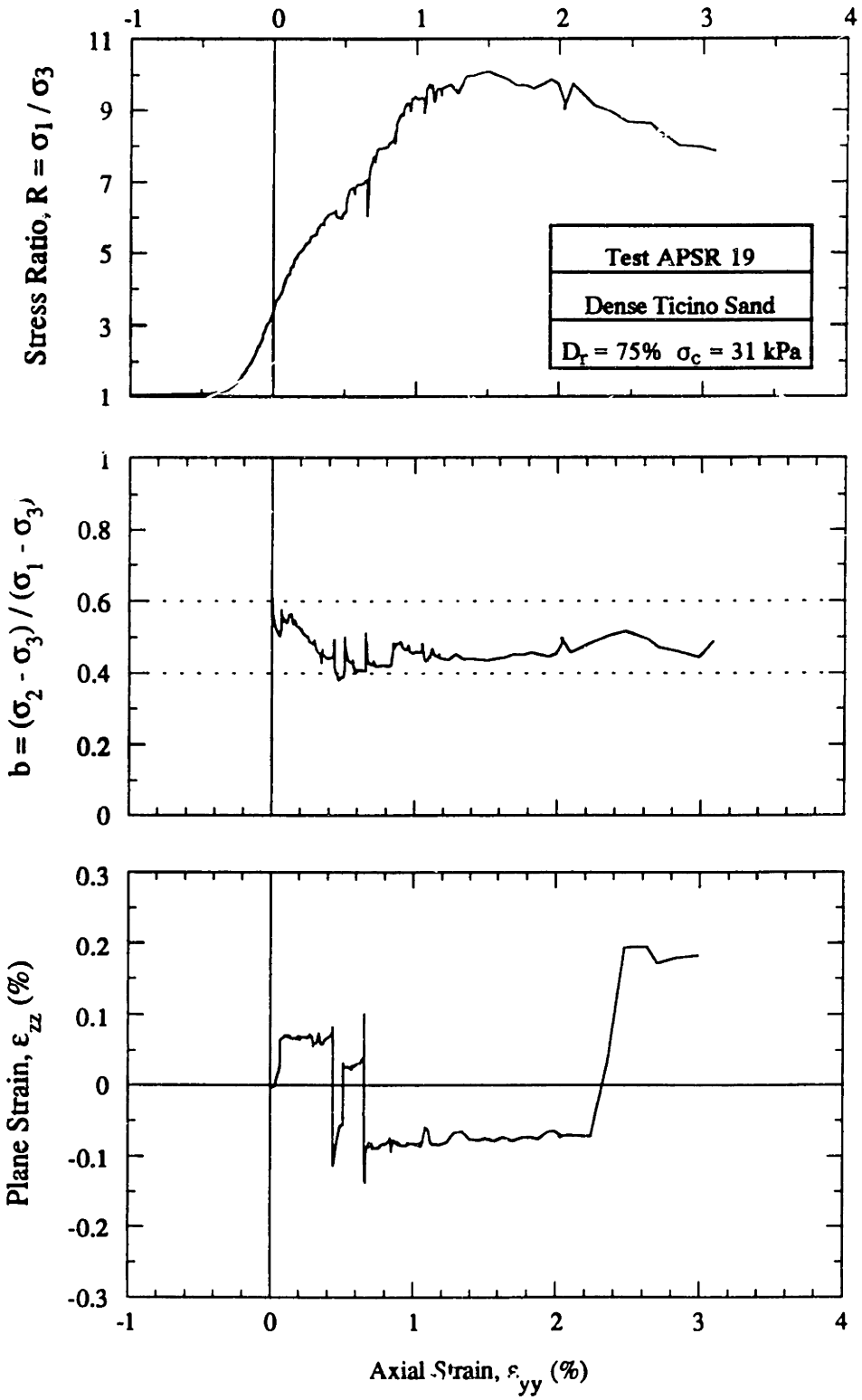

Figure 4.12: Performance of the Original Active Plane Strain Control System

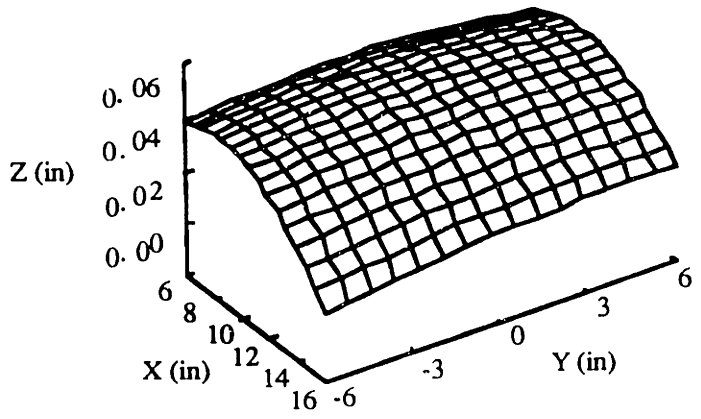

APSR 26

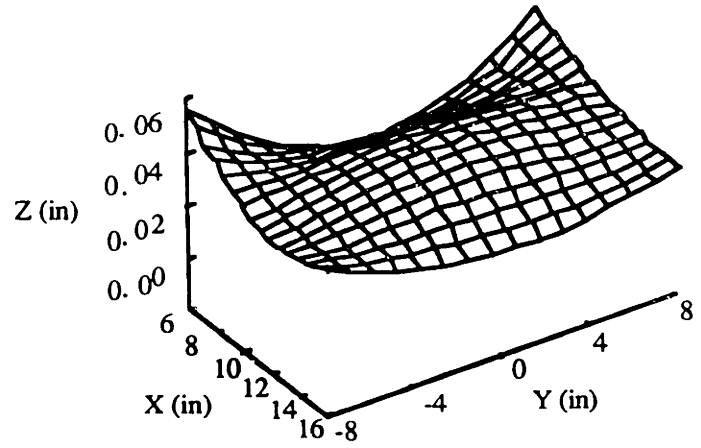

APSR 27

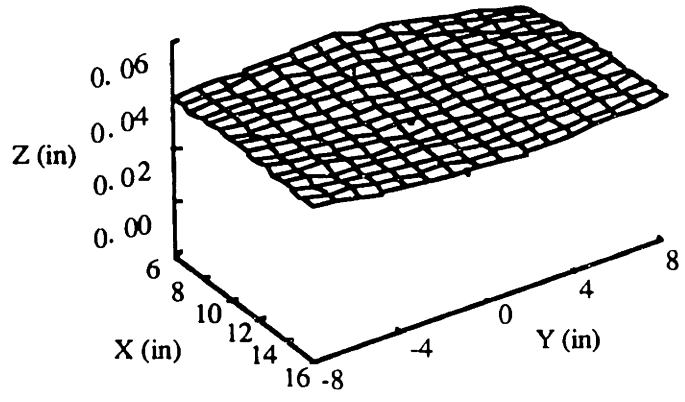

APSR 28

Figure 4.13: Final Specimen Surfaces for APSR 26-28

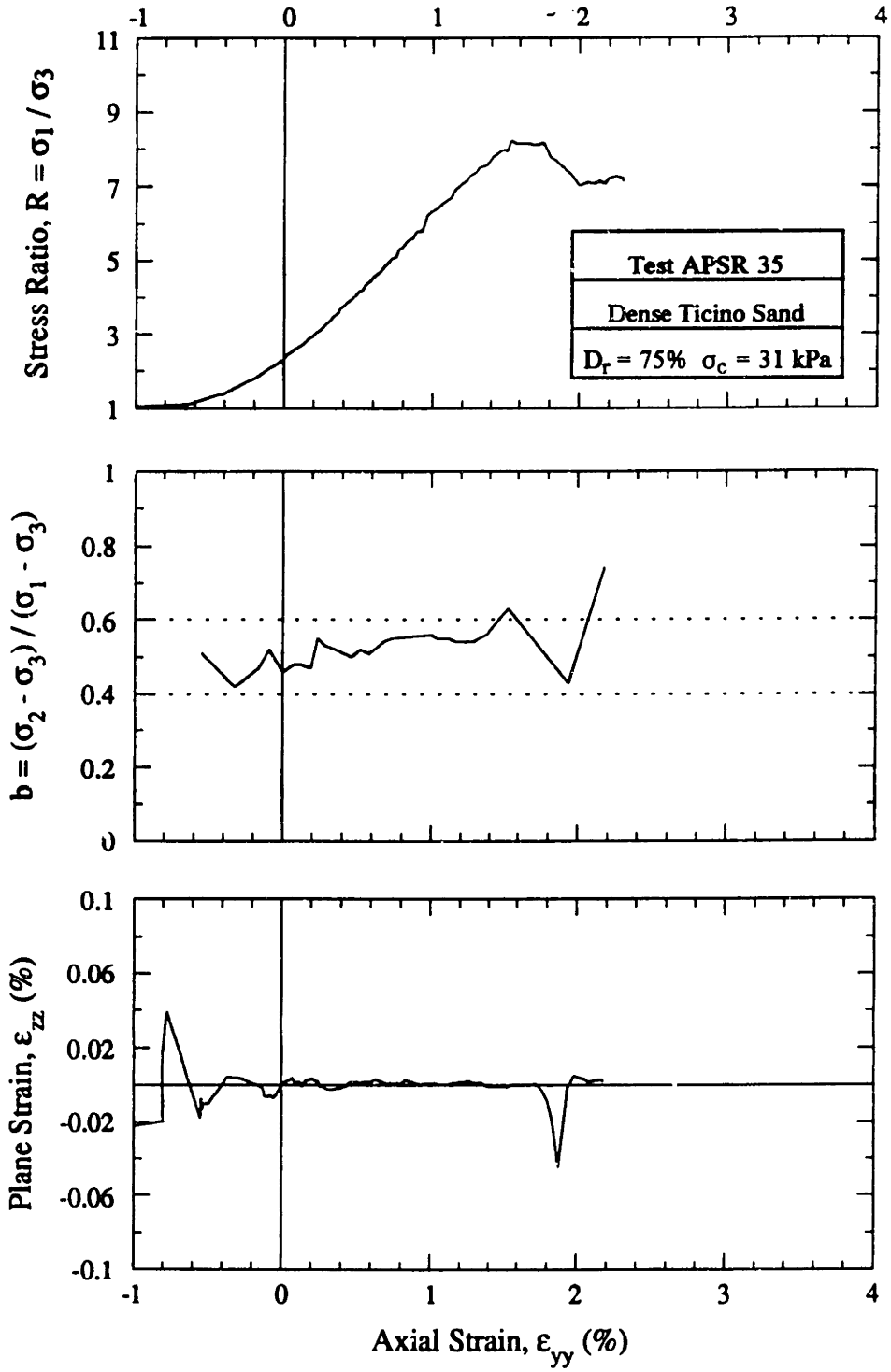

Figure 4.14: Performance of the Refined Active Plane Strain Control System

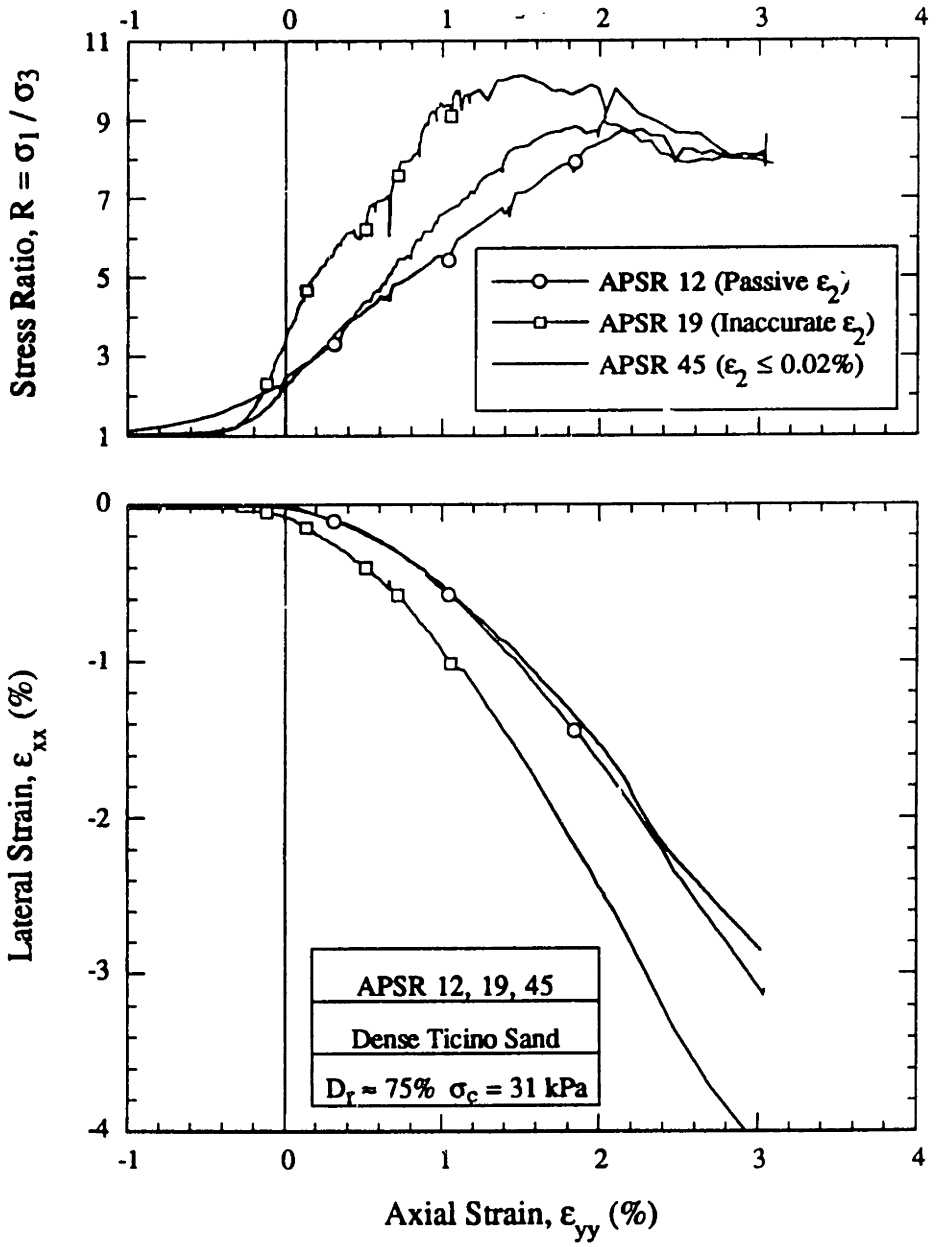

Figure 4.15: Influence of the Plane Strain Condition on the Shear Behavior of Dense Ticino Sand

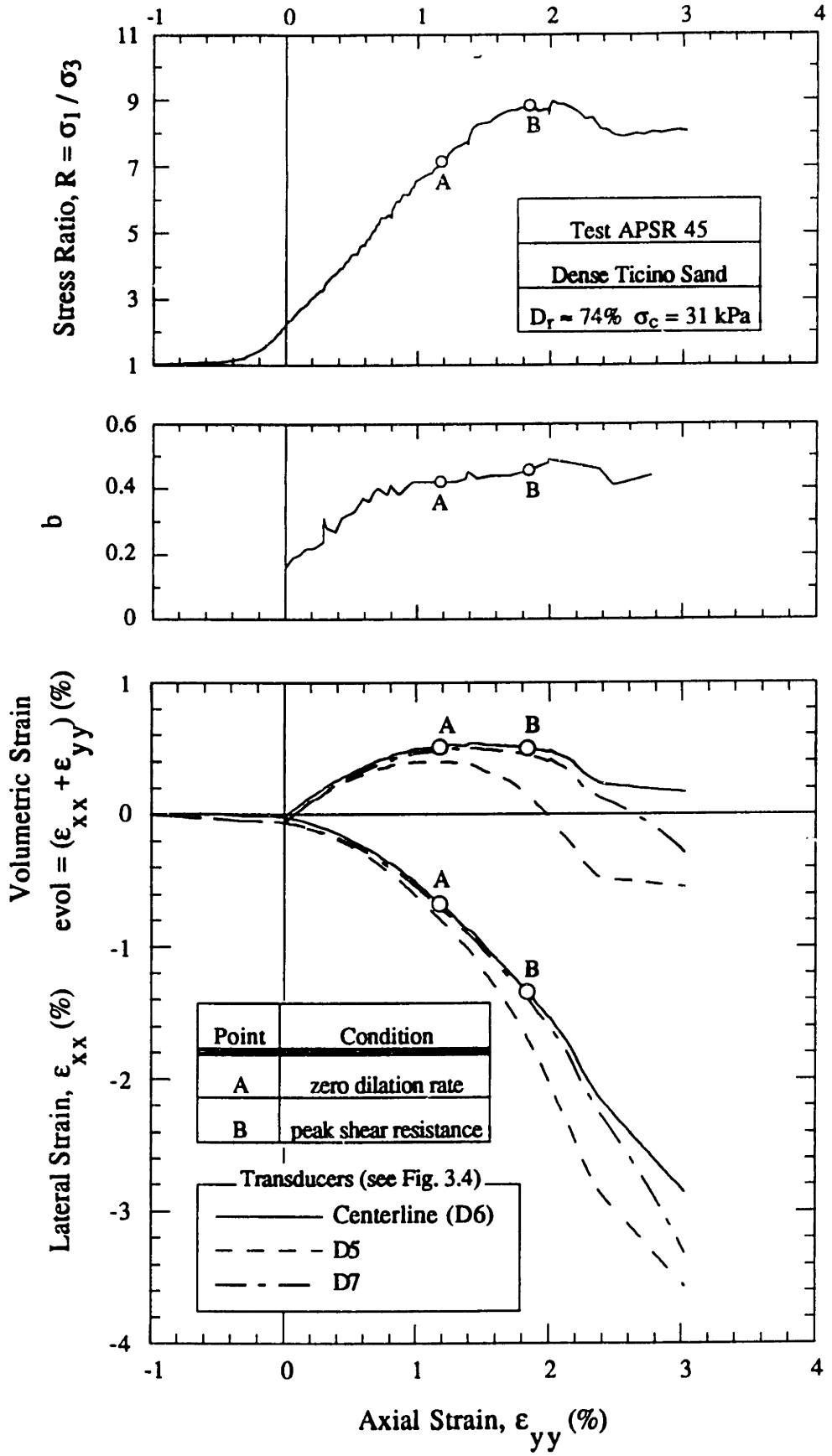

Figure 4.16: Externally Measured Shear Behavior for APSR 45

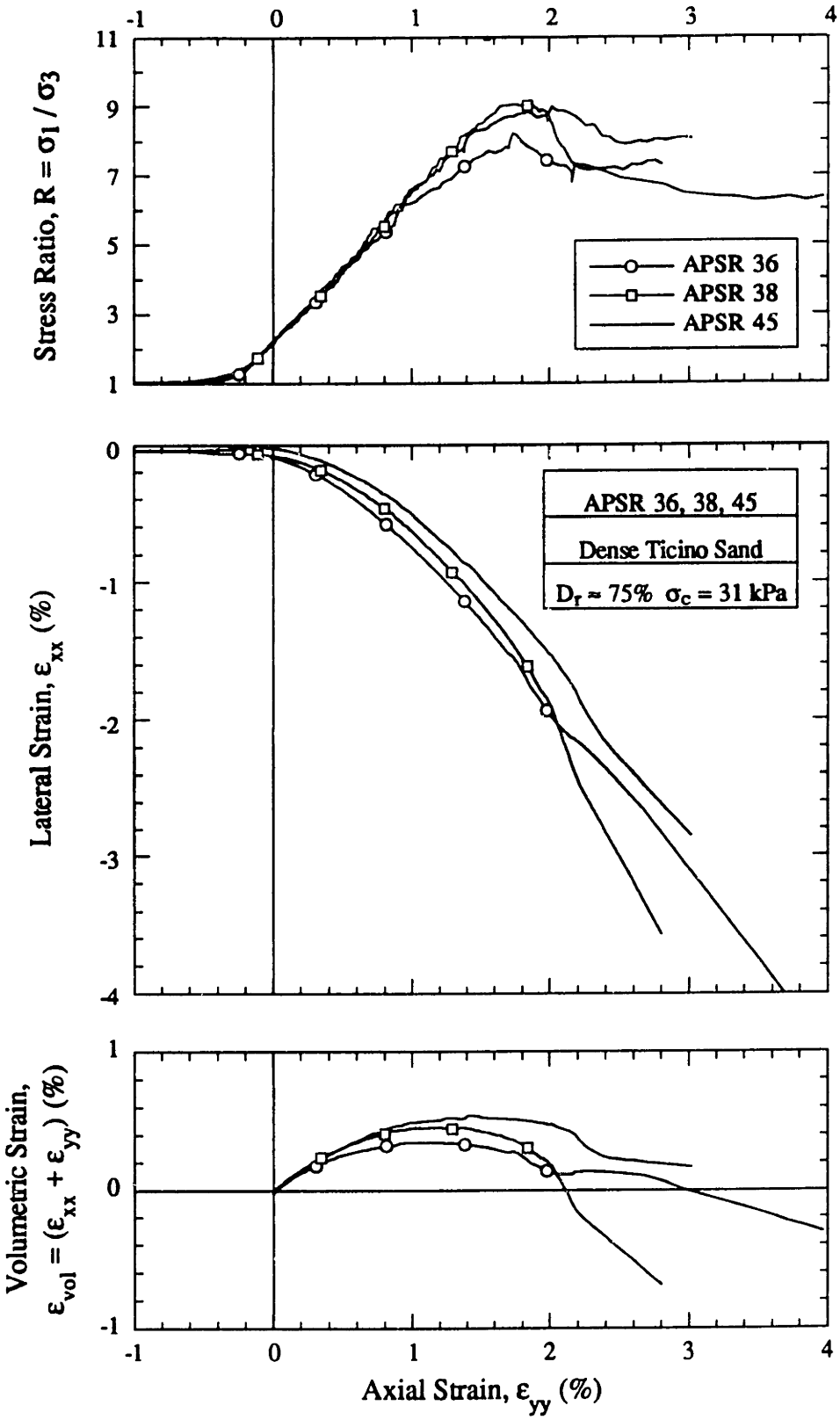

Note: Lateral strains measured at centerline of specimens by transducer D6 (Fig. 3.4).

Figure 4.17: Repeatability of Externally Measured Shear Behavior

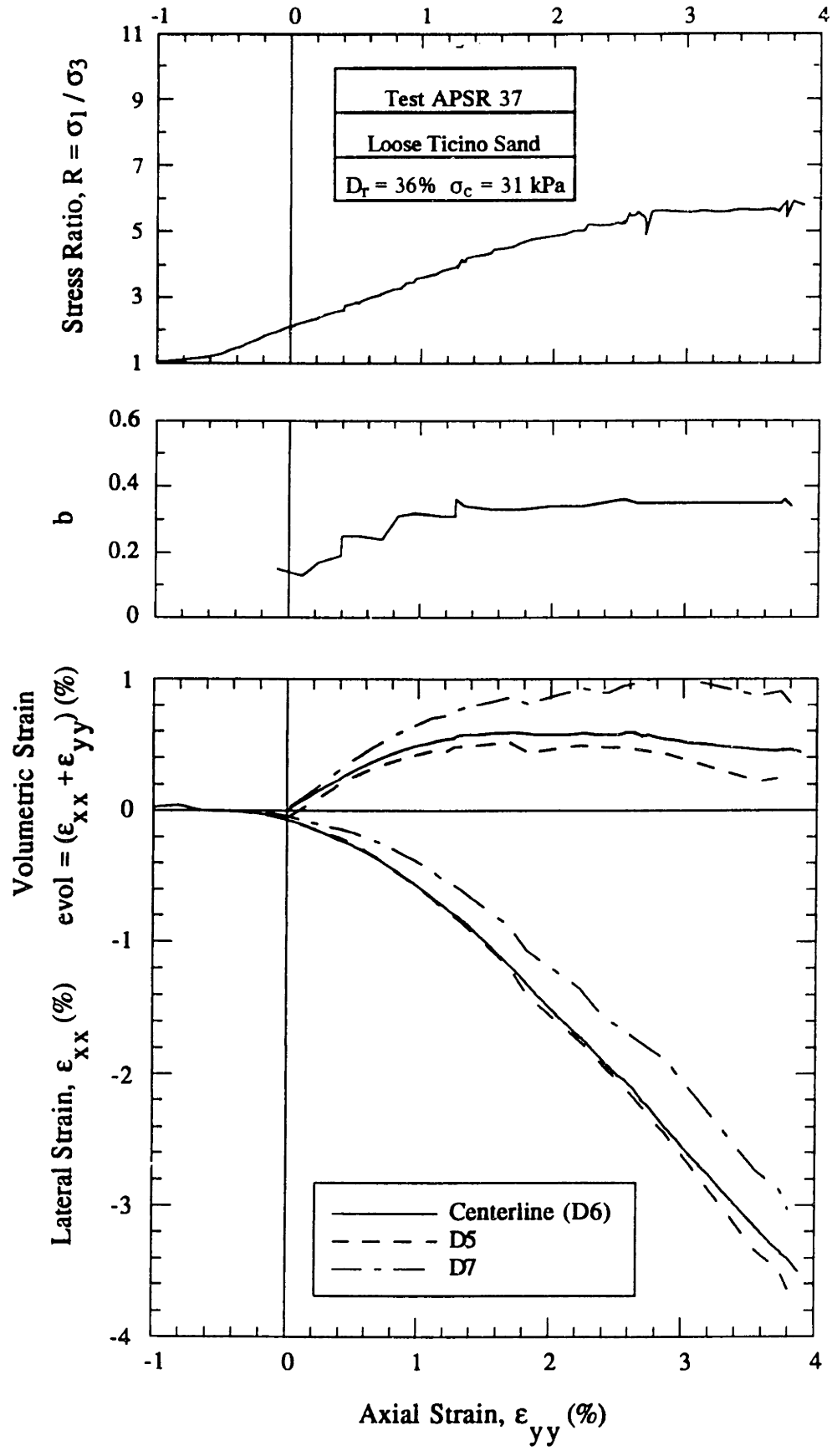

Figure 4.18: Externally Measured Shear Behavior of Loose Ticino Sand

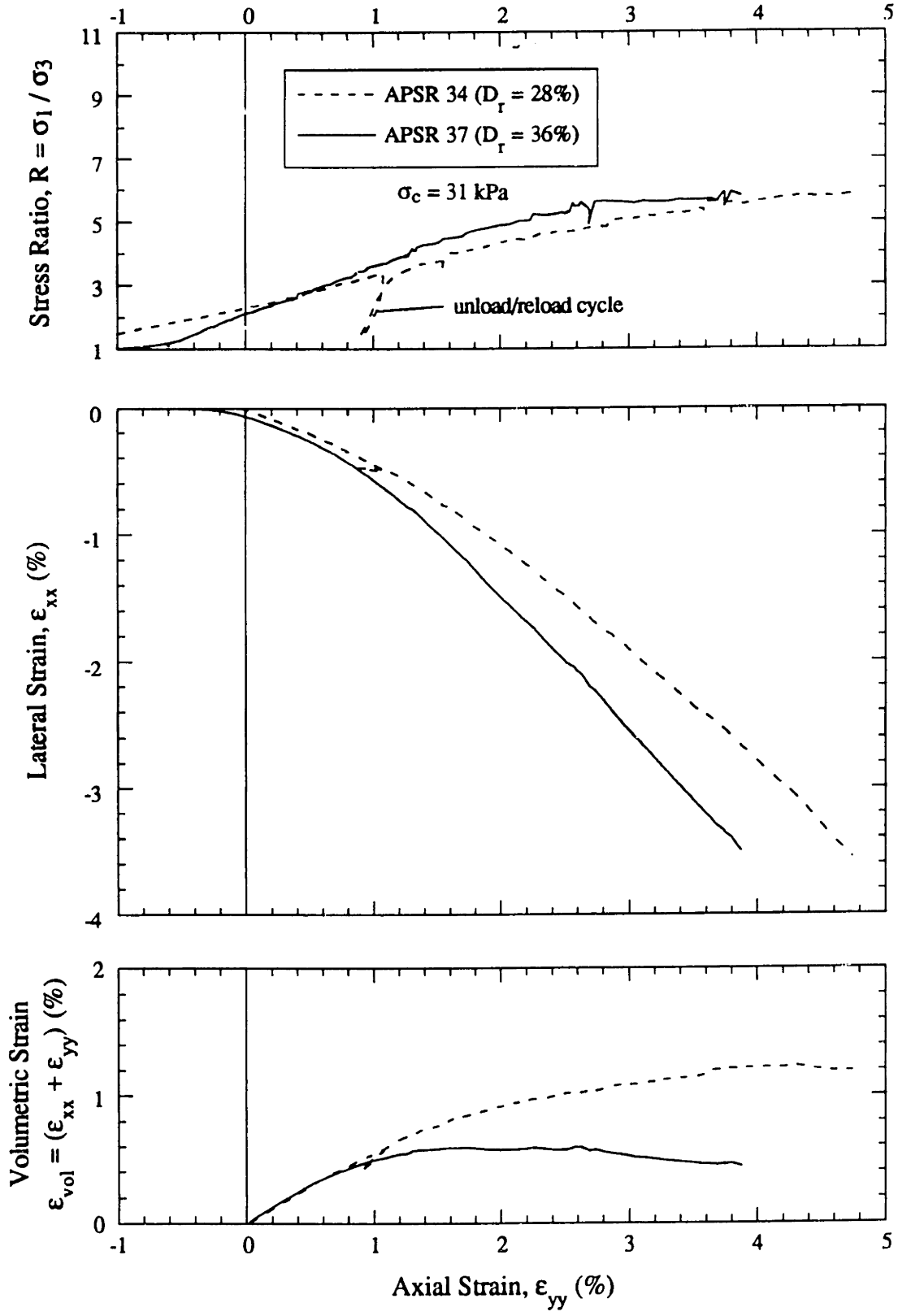

Note: Lateral strains measured at centerline of specimens by transducer D6 (Fig. 3.4).

Figure 4.19: Repeatability of Externally Measured Shear Behavior for Loose Ticino Sand

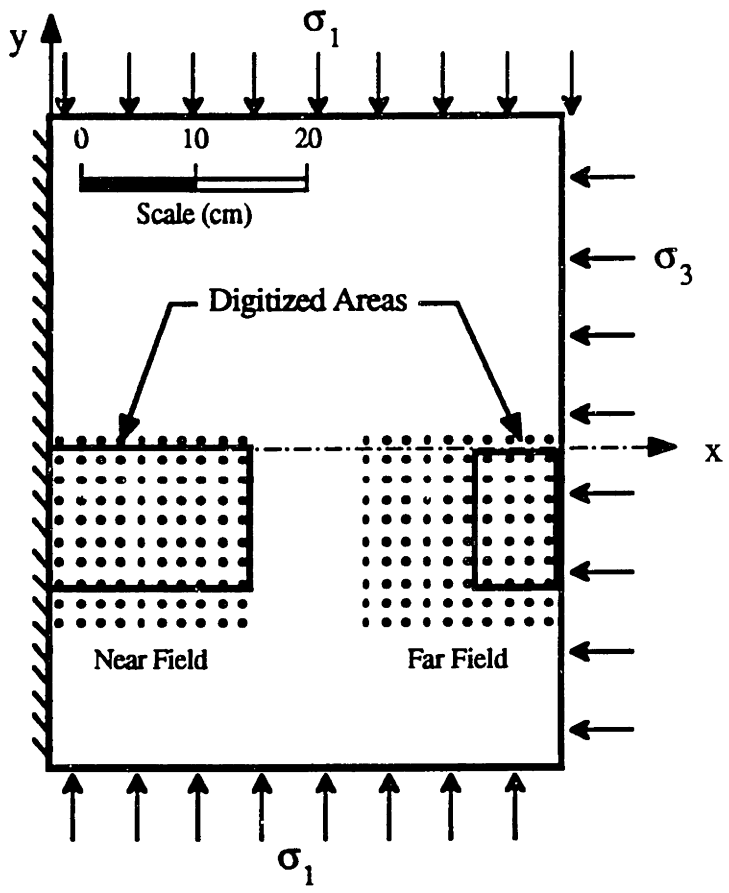

Near and far fields: 100 markers spaced on a 2.0cm grid

Test APSR 45			
X-ray No.	σ_1 (kPa)	σ_3 (kPa)	R
1	31	31	1.0
2	103	31	3.3
3	172	31	5.5
4	241	31	7.8
5 (post peak)	269	31	8.7

Figure 4.20: Configuration of the Tungsten Carbide Markers for Radiographic Strain Measurements in the APSR Cell

Figure 4.21: Photograph of the Sidewall Position Reference Frame

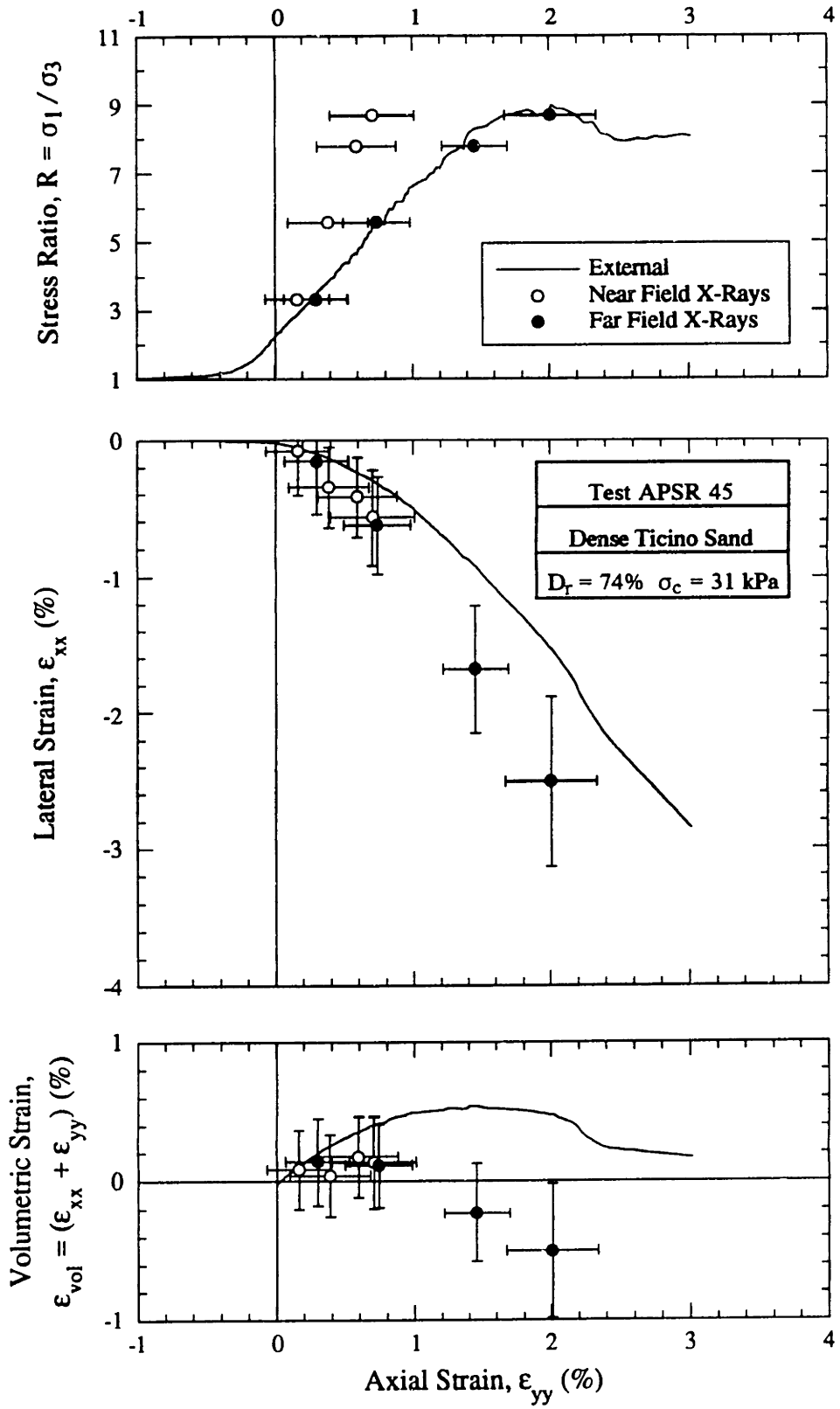

Note: External lateral strain measurements based on centerline DCDT, D6 (Fig. 3.4).

Figure 4.22: Comparison of External and Internal Measurements of Shear Behavior

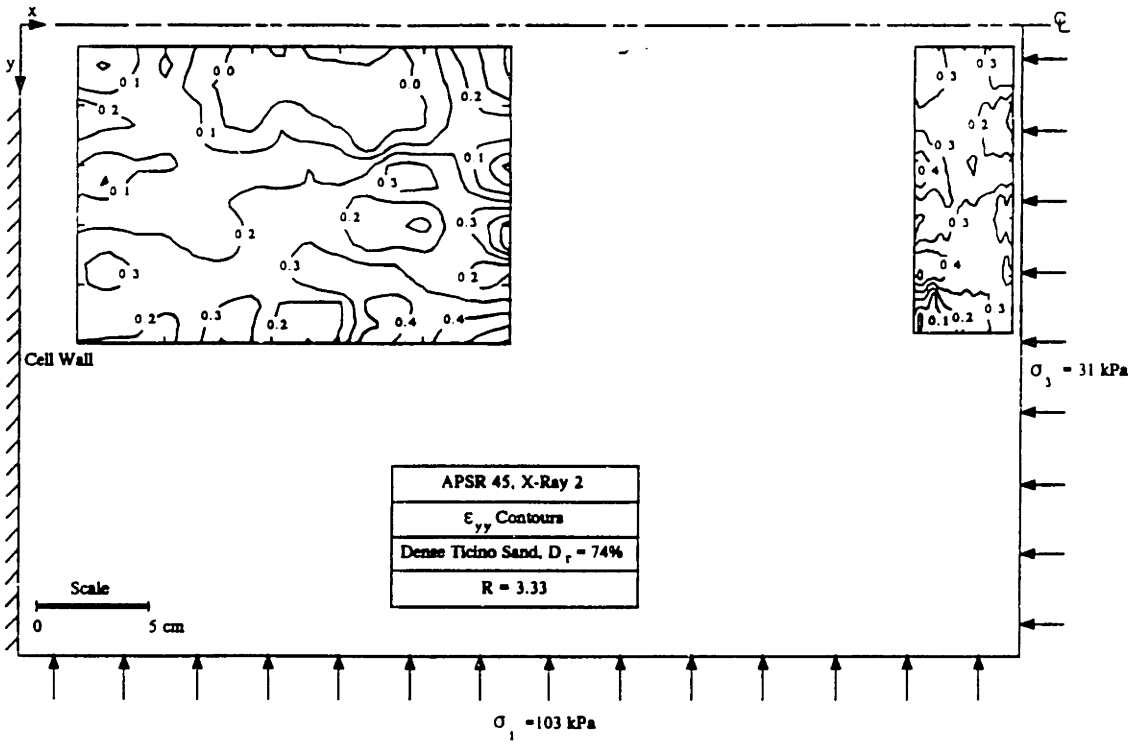

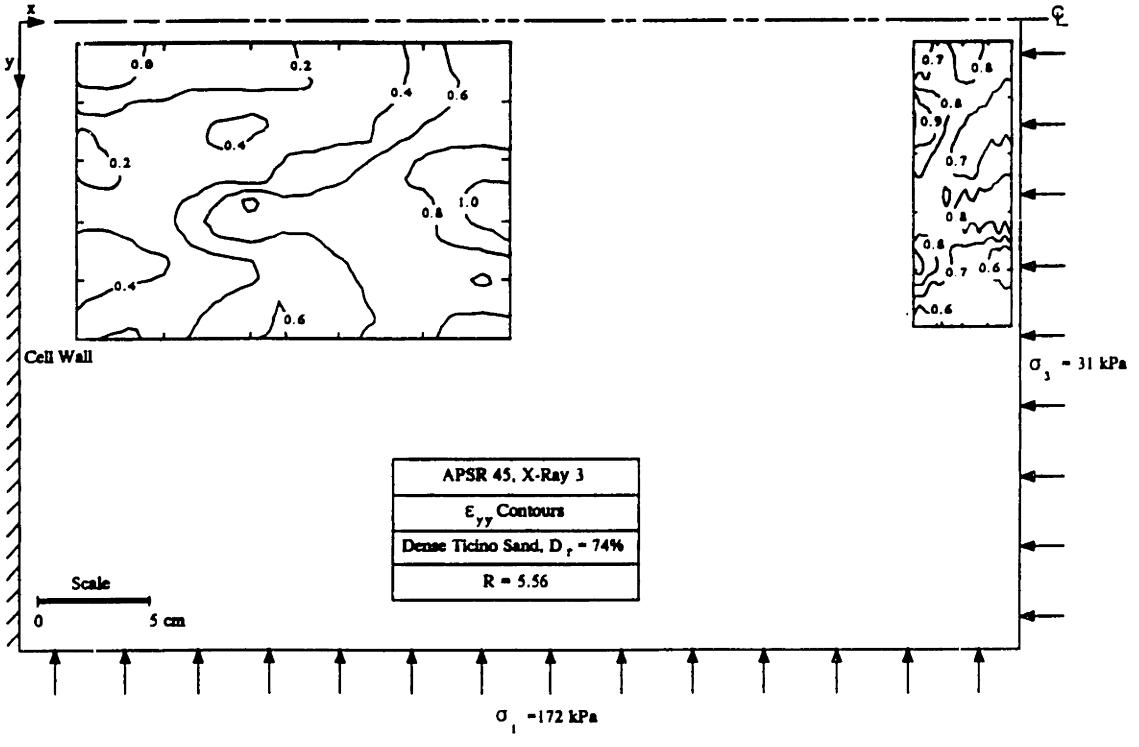

Figure 4.23: Axial Strain Contours, APSR 45, R = 3.33 and 5.56

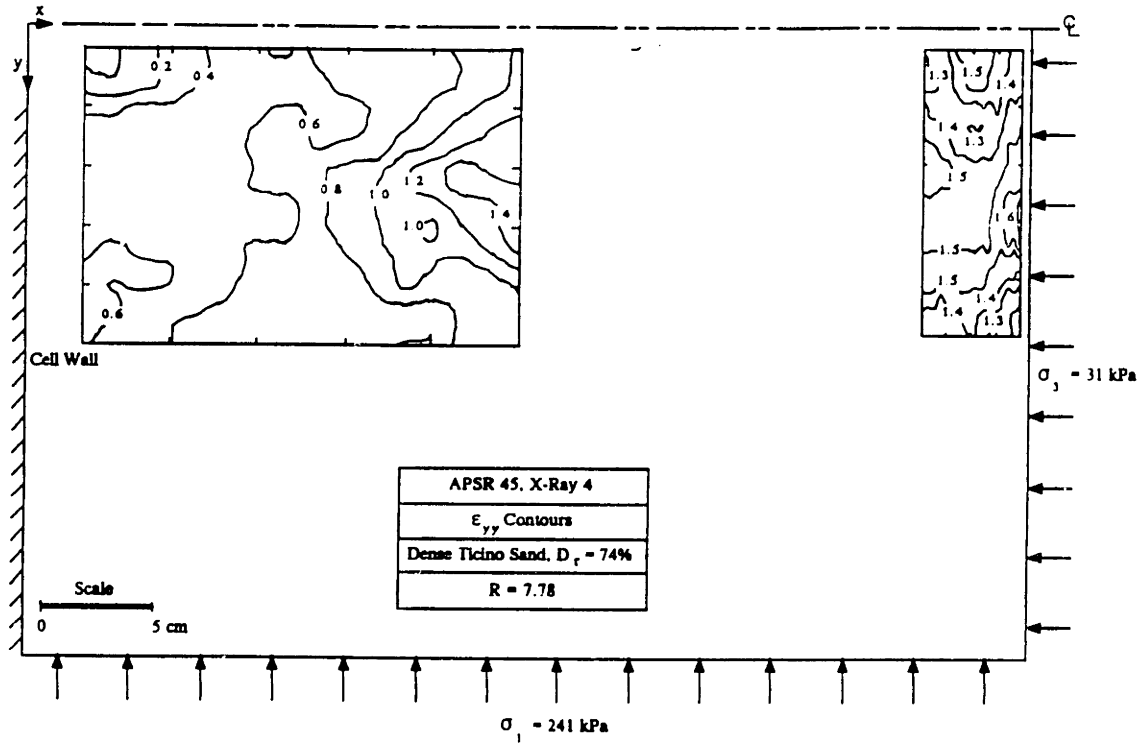

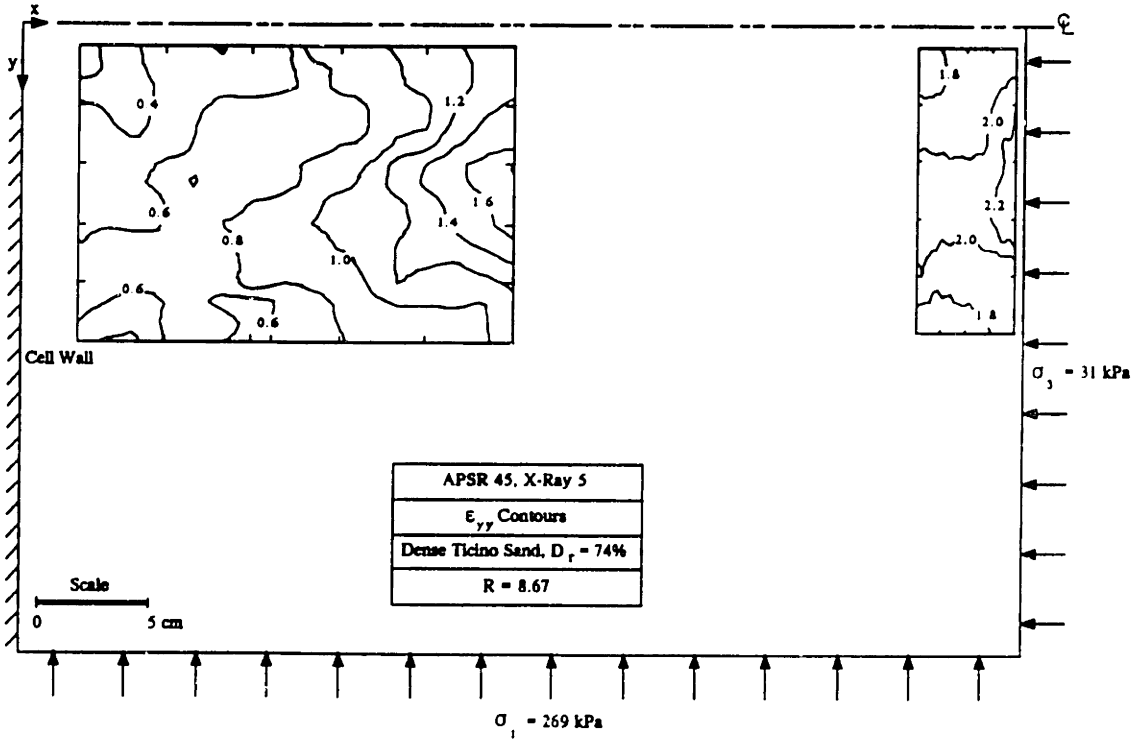

Figure 4.24: Axial Strain Contours, APSR 45, R = 7.78 and 8.67

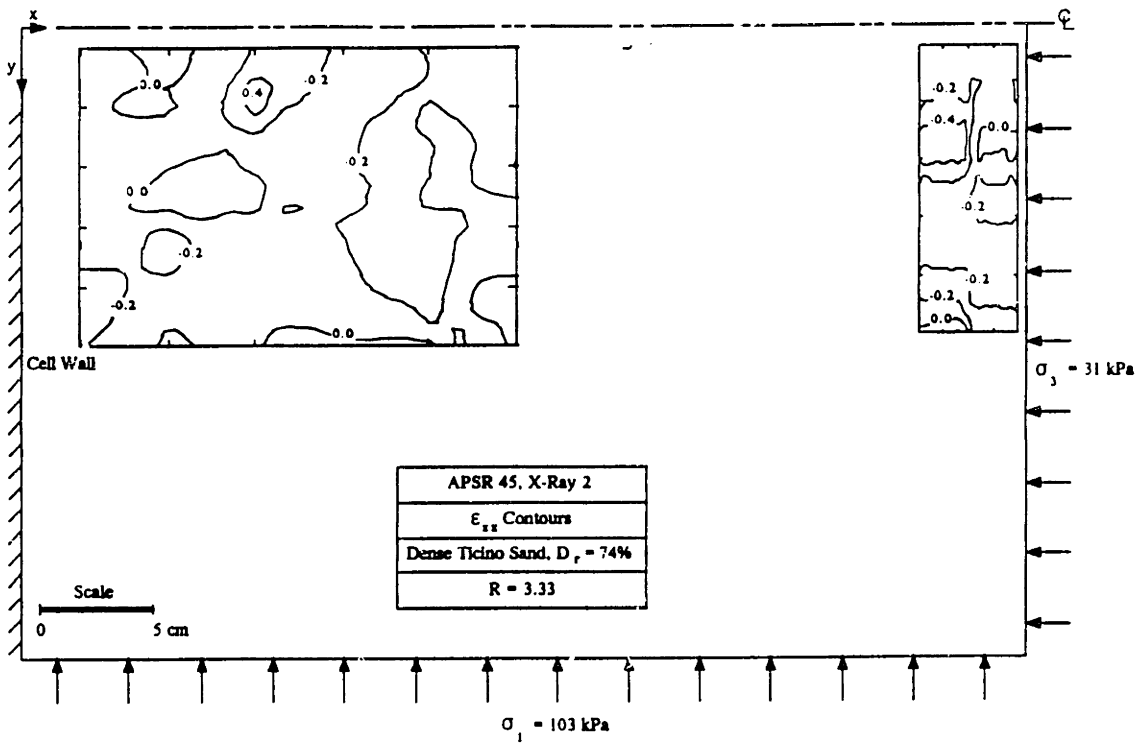

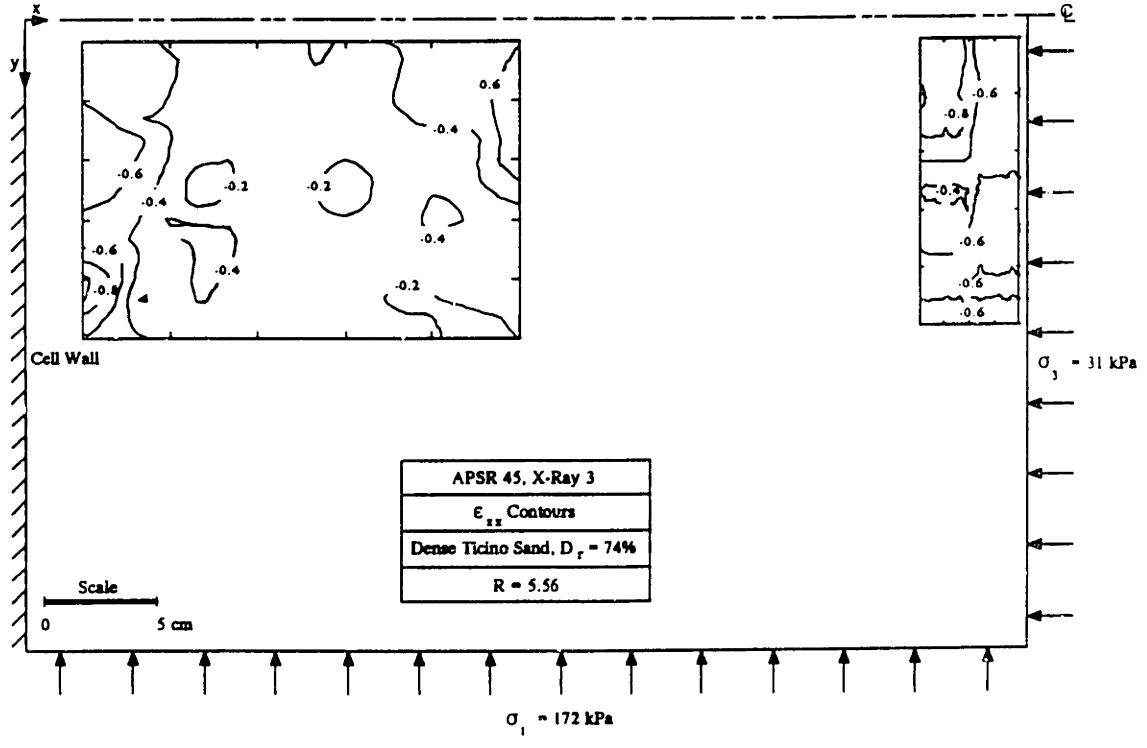

Figure 4.25: Lateral Strain Contours, APSR 45, R = 3.33 and 5.56

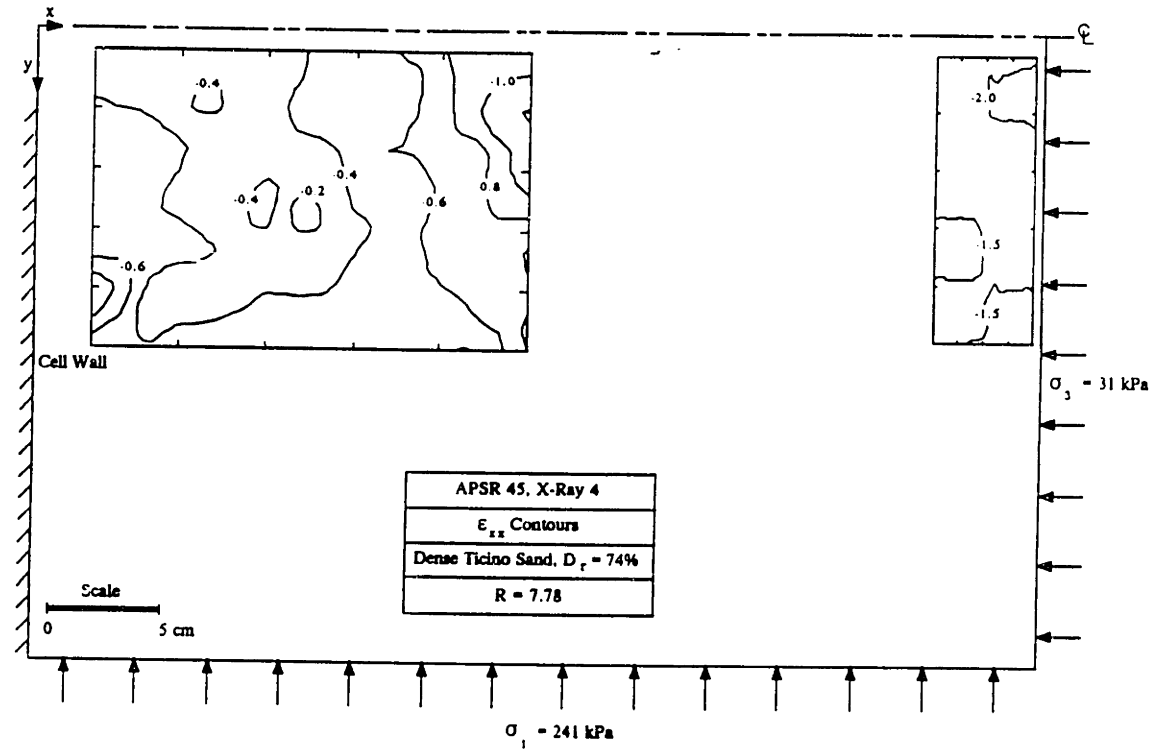

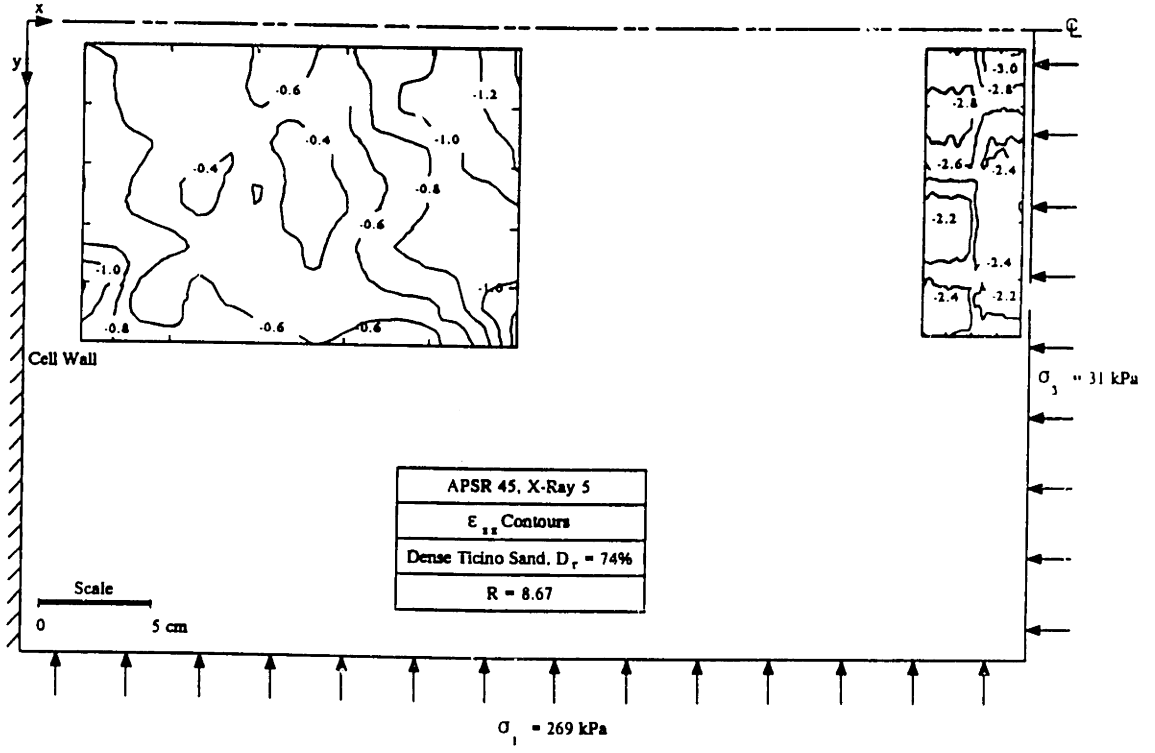

Figure 4.26: Lateral Strain Contours, APSR 45, R = 7.78 and 8.67

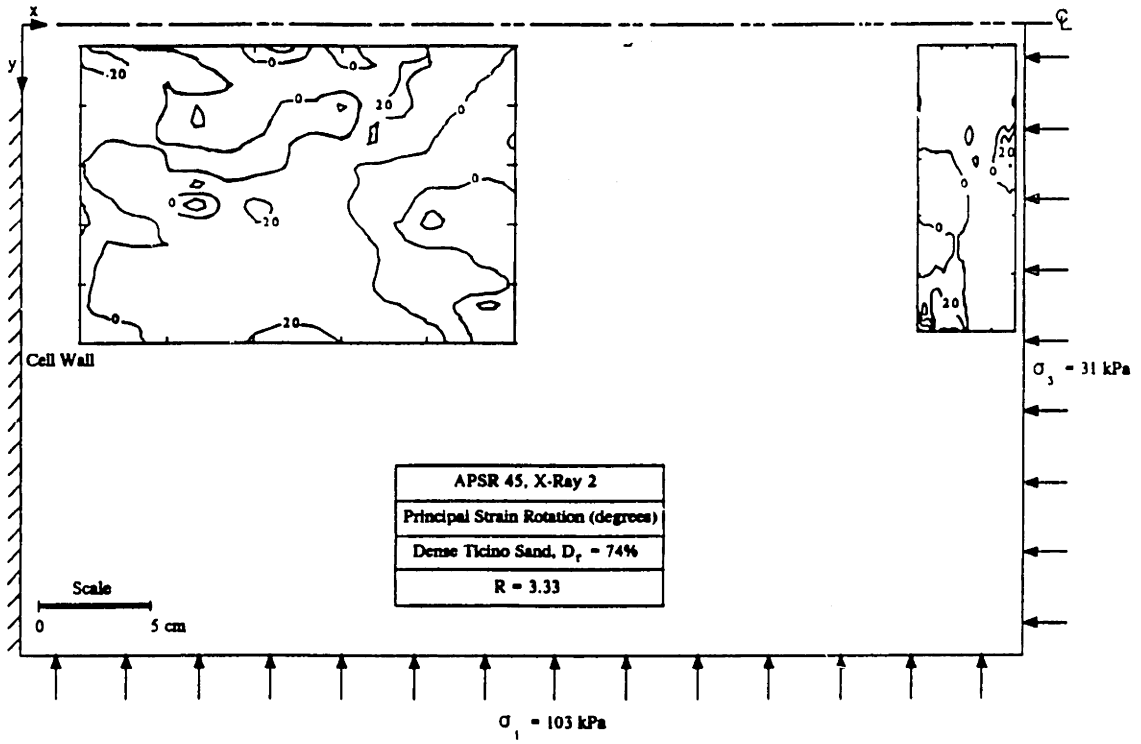

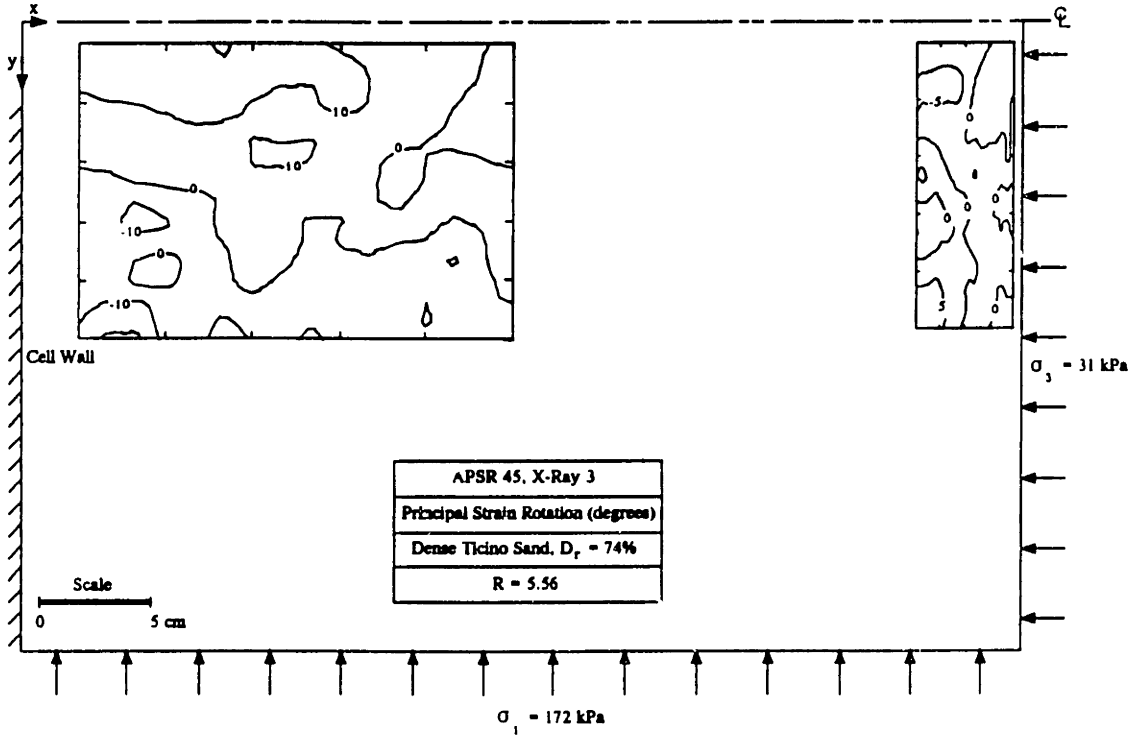

Figure 4.27: Principal Strain Rotations, APSR 45, R = 3.33 and 5.56

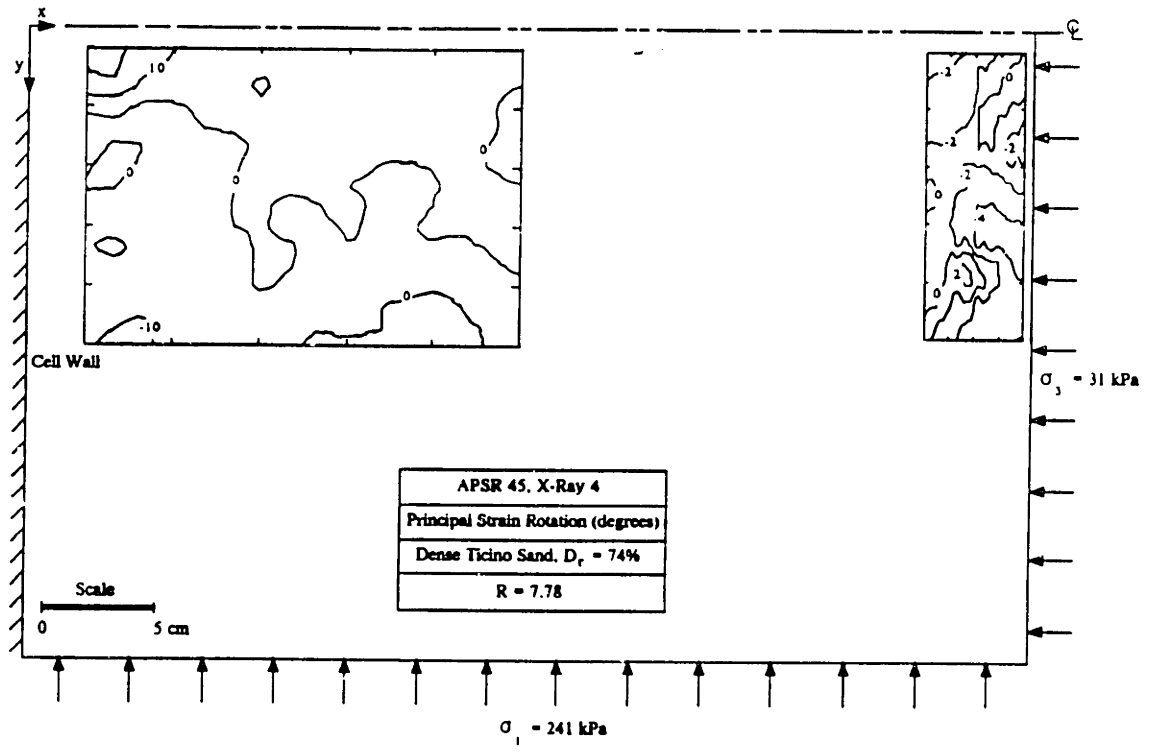

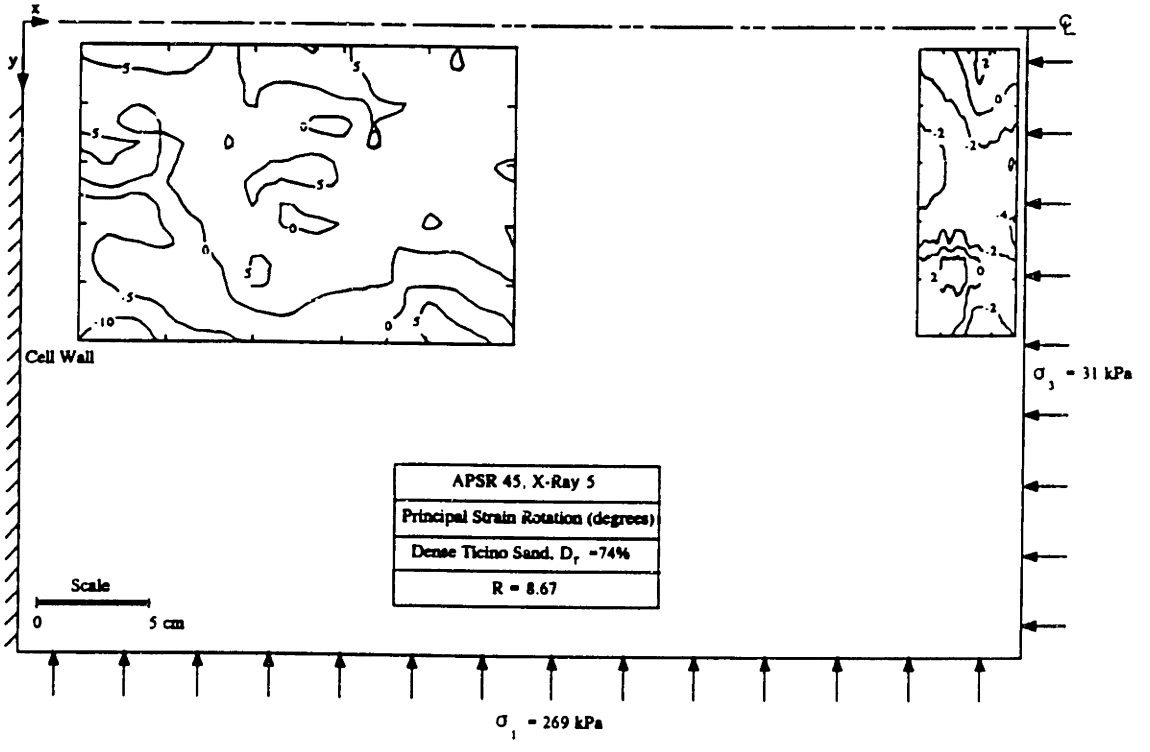

Figure 4.28: Principal Strain Rotations, APSR 45, R = 7.78 and 8.67

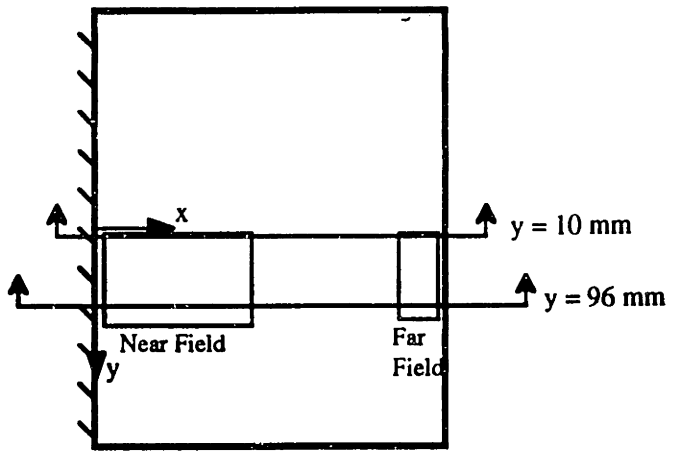

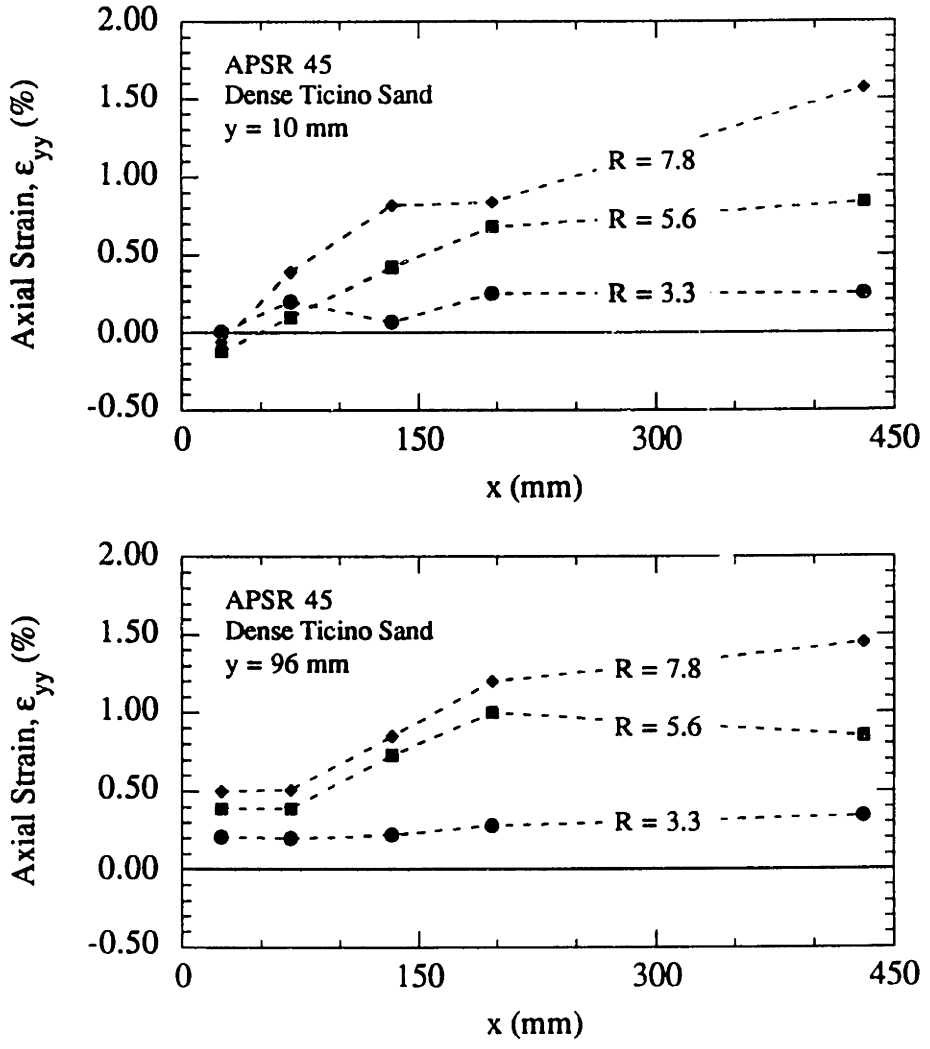

Figure 4.29: Axial Strain Distribution Profiles, APSR 45

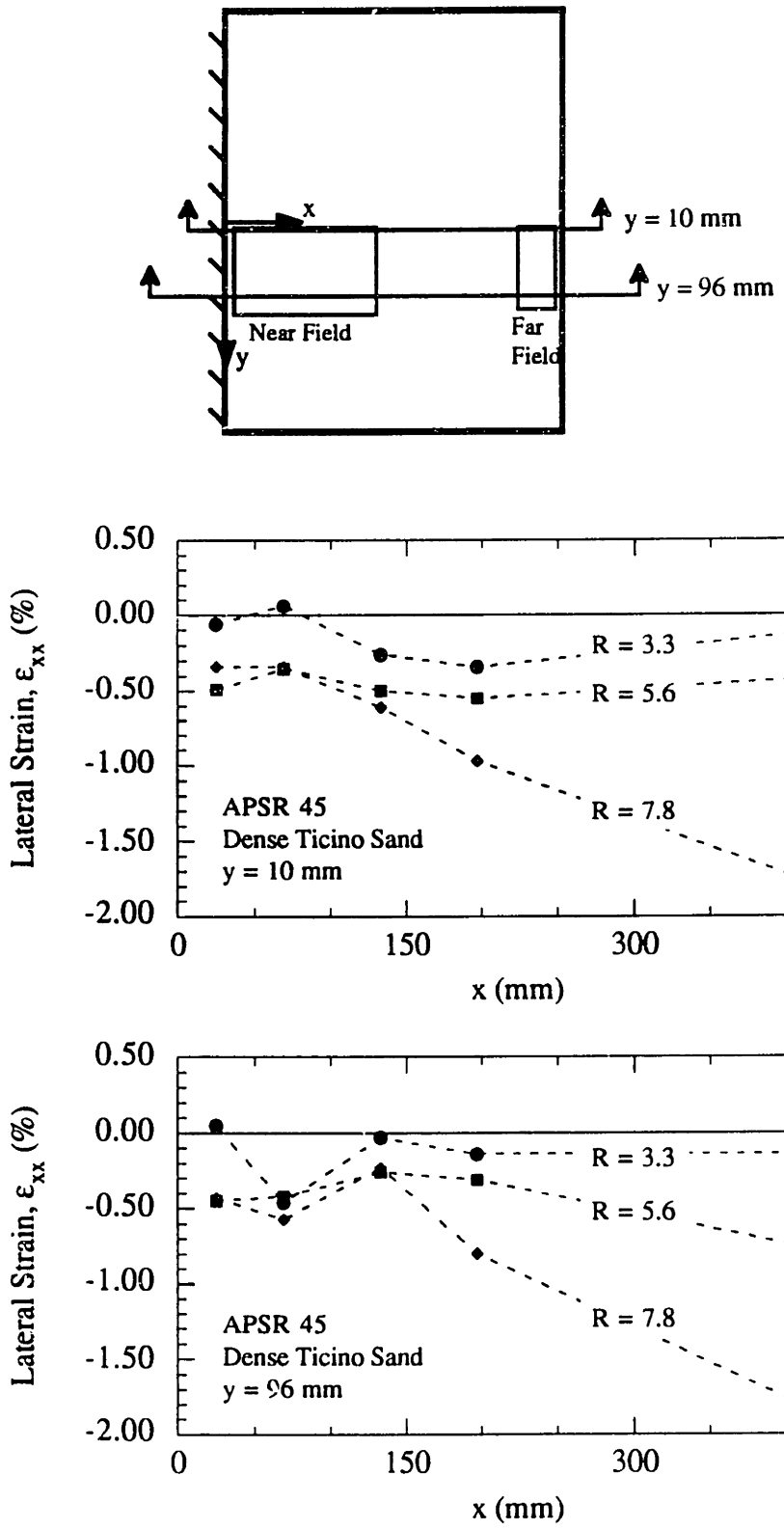

Figure 4.30: Lateral Strain Distribution Profiles, APSR 45

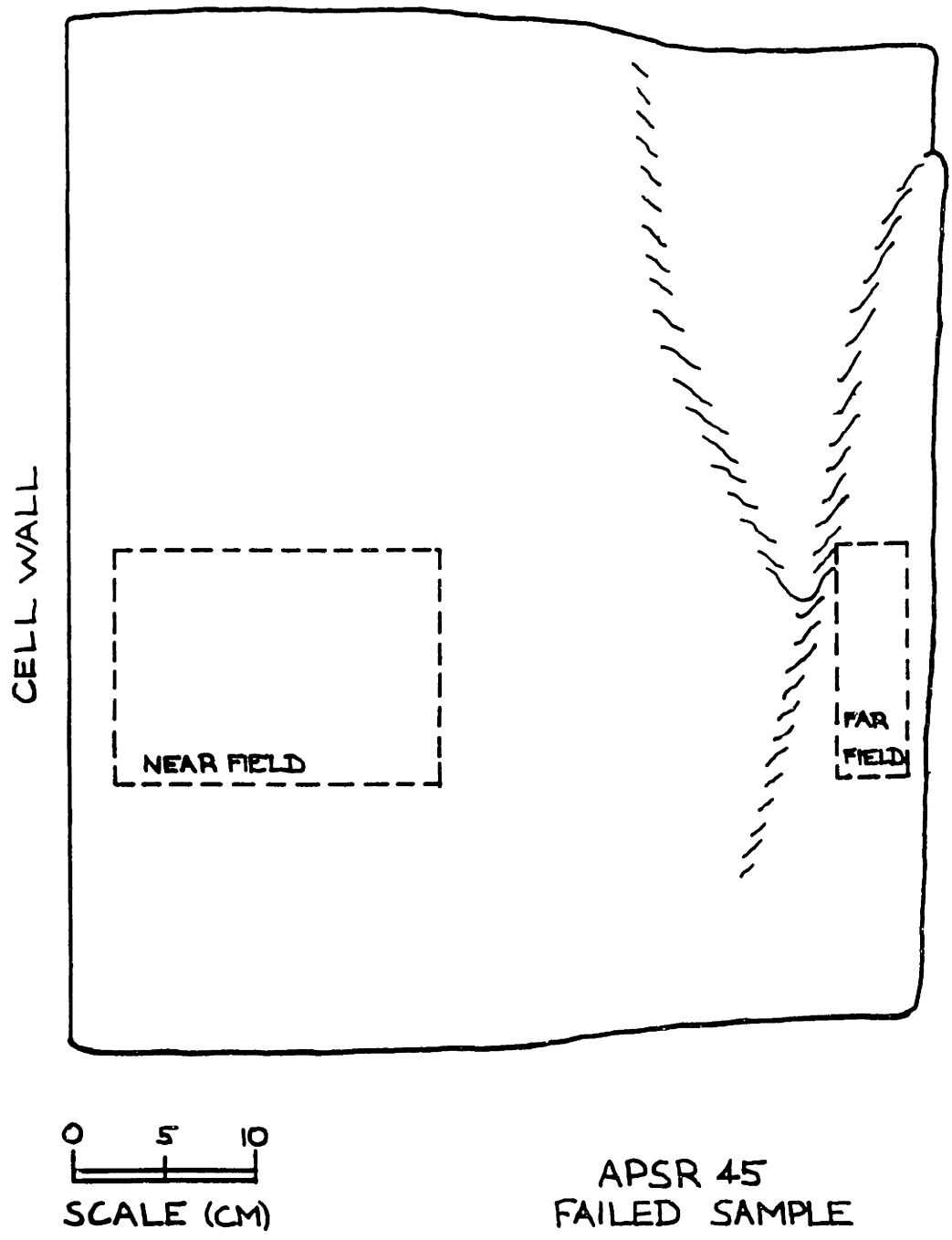

Figure 4.31: Failed Sample, APSR 45 (Dense Ticino Sand)

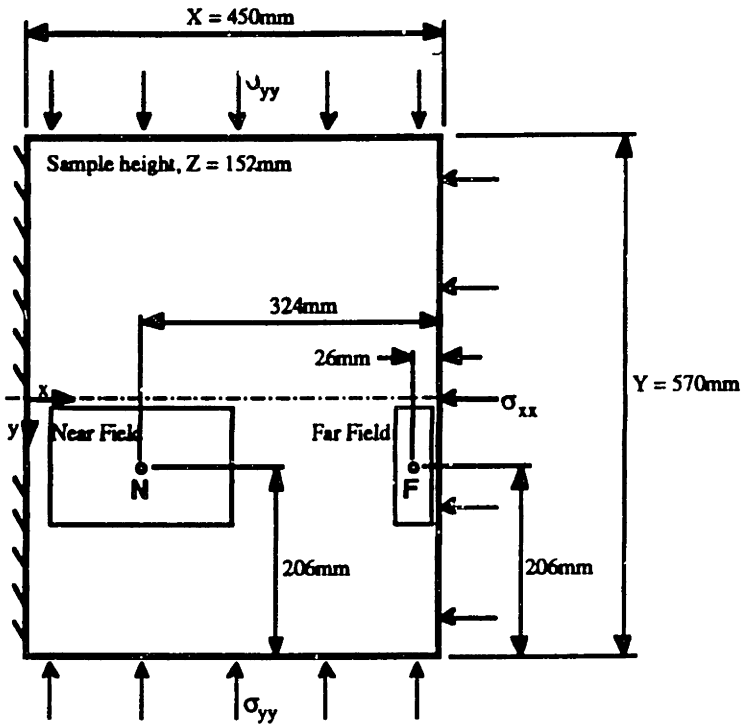

Correction for Sidewall Grease Resistance:

Shear strength of grease = c_g

$$\Delta\sigma_3 = -c_g \frac{2}{Z}(X - x)$$

$$\Delta\sigma_1 = -c_g \frac{2}{Z}(Y - y)$$

Magnitude of c_g (after Seah, 1990):

$$c_g = 0.025\ \sigma_n$$

where $\sigma_n = \sigma_2 = b(\sigma_1 - \sigma_3) + \sigma_3$

	Applied Stresses						Near Field (N)			Far Field (F)		
R_{ext}	σ_1 kPa	σ_2 kPa	σ_3 kPa	c_g kPa	$\Delta\sigma_1$ kPa	$\hat{\sigma}_1$ kPa	$\Delta\sigma_3$ kPa	$\hat{\sigma}_3$ kPa	$\hat{R}$	$\Delta\sigma_3$ kPa	$\hat{\sigma}_3$ kPa	$\hat{R}$
3.33	103	50	31	1.3	-3.5	99	5.5	37	2.68	0.4	31	3.19
5.56	172	87	31	2.2	-6.0	166	9.4	40	4.15	0.8	32	5.19
7.78	241	123	31	3.1	-8.4	233	13.2	44	5.30	1.1	32	7.52
8.67	269	145	31	3.6	-9.8	259	15.3	46	5.63	1.2	32	8.09

Note: $\hat{\sigma}_1$, $\hat{\sigma}_3$, and $\hat{R}$ are the corrected stresses.

Stress corrections for average points in the near and far fields

Figure 4.32: Sidewall Grease Resistance Correction to Estimate Internal Stresses

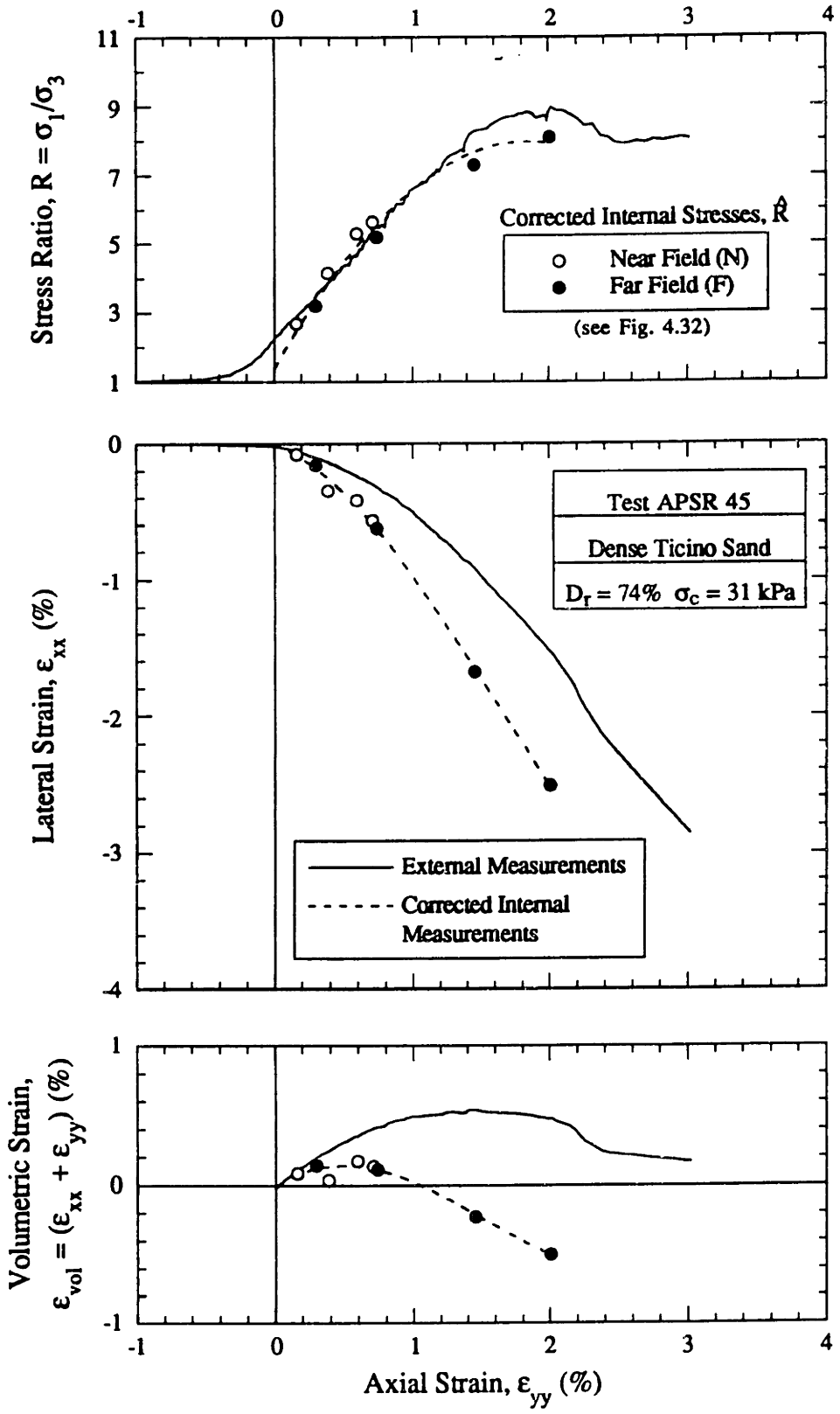

Figure 4.33: Comparison of External and Corrected Internal Measurements for Dense Ticino Sand

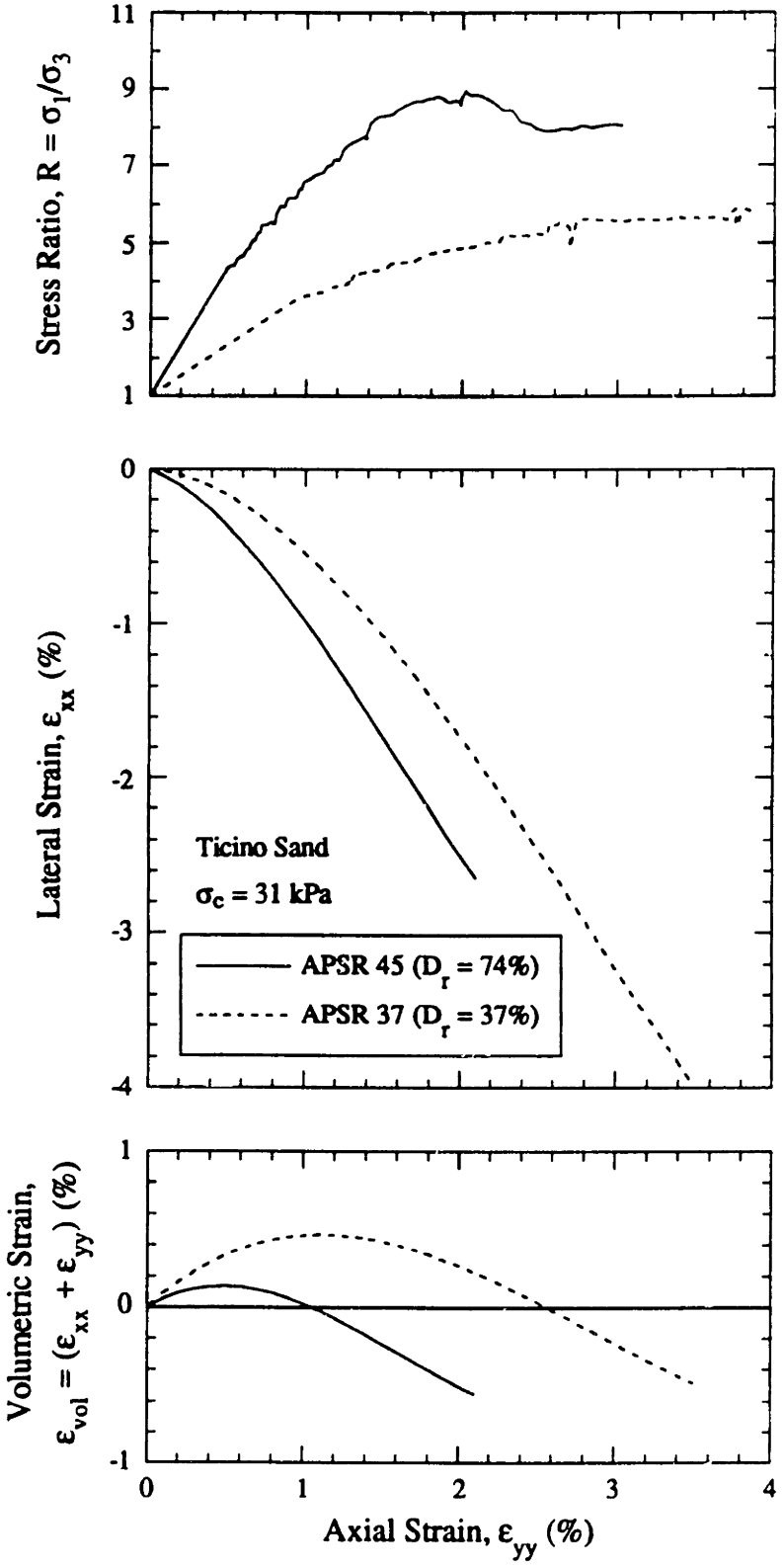

At peak shear stress	Dense	Loose
R_{max}	8.98	5.64
ϕ'_p	53°	44°
ε_{yy}	2.0%	3.5%
ε_{vol}	-0.5%	-0.5%
D_{max}	-0.53	-0.47
E_{50}: (kPa)	19,100	8300

At zero dilation rate	Dense	Loose
R	4.35	3.70
ϕ'	39°	35°
ε_{yy}	0.50%	1.1%
ε_{vol}	0.14%	0.46%

Figure 4.34: Estimated Plane Strain Shear Behavior of Ticino Sand

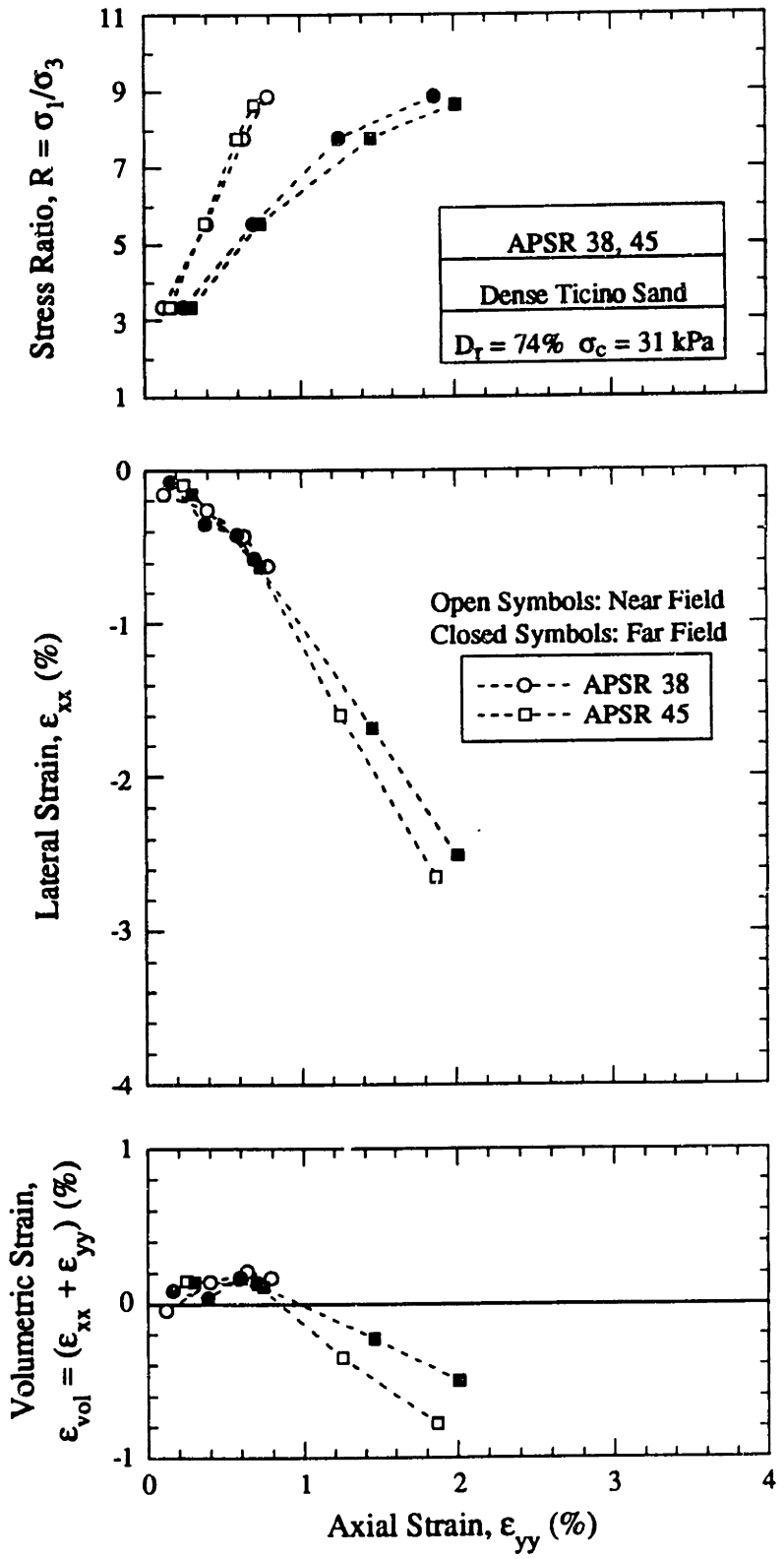

Figure 4.35: Repeatability of Internally Measured Shear Behavior for Dense Ticino Sand in the APSR Cell

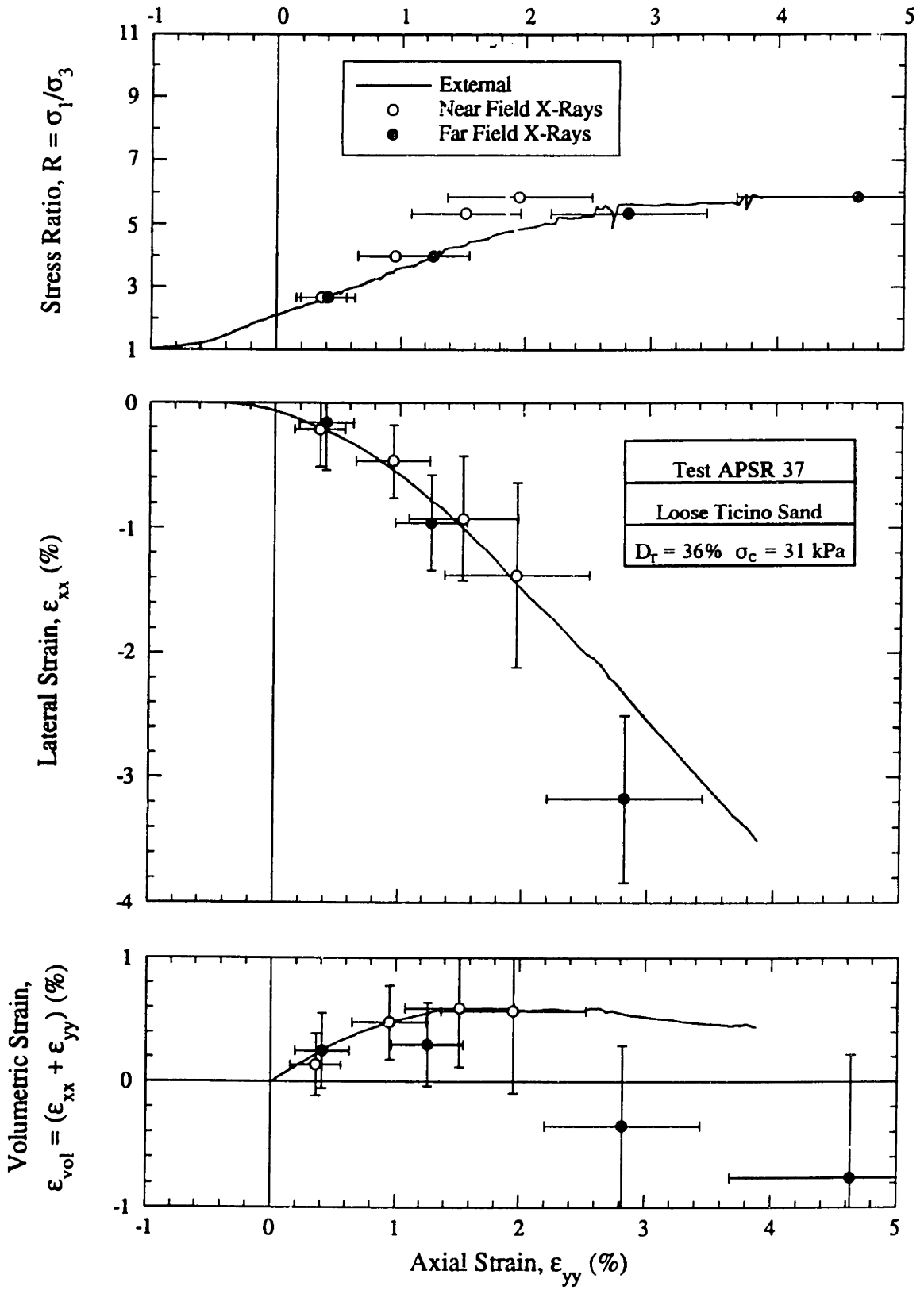

Note: External lateral strain measurements based on centerline DCDT, D6 (Fig. 3.4).

Figure 4.36: Comparison of External and Internal Measurements of Shear Behavior for Loose Ticino Sand

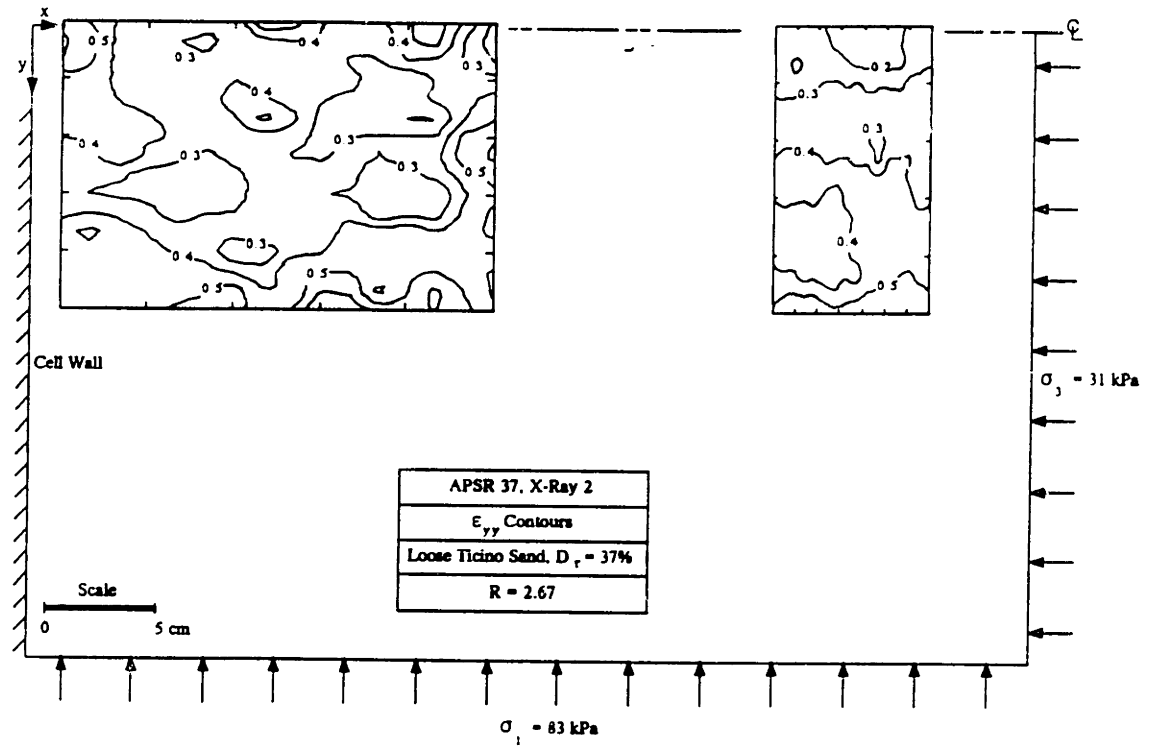

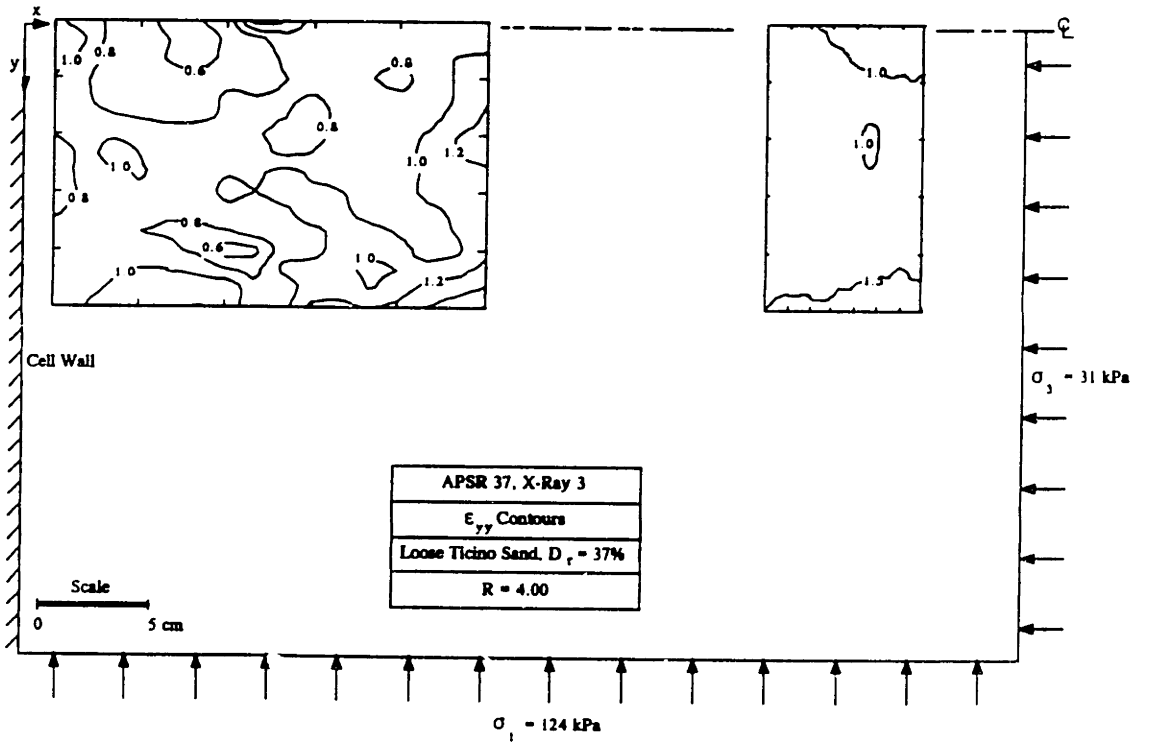

Figure 4.37: Axial Strain Contours, APSR 37, R = 2.67 and 4.00

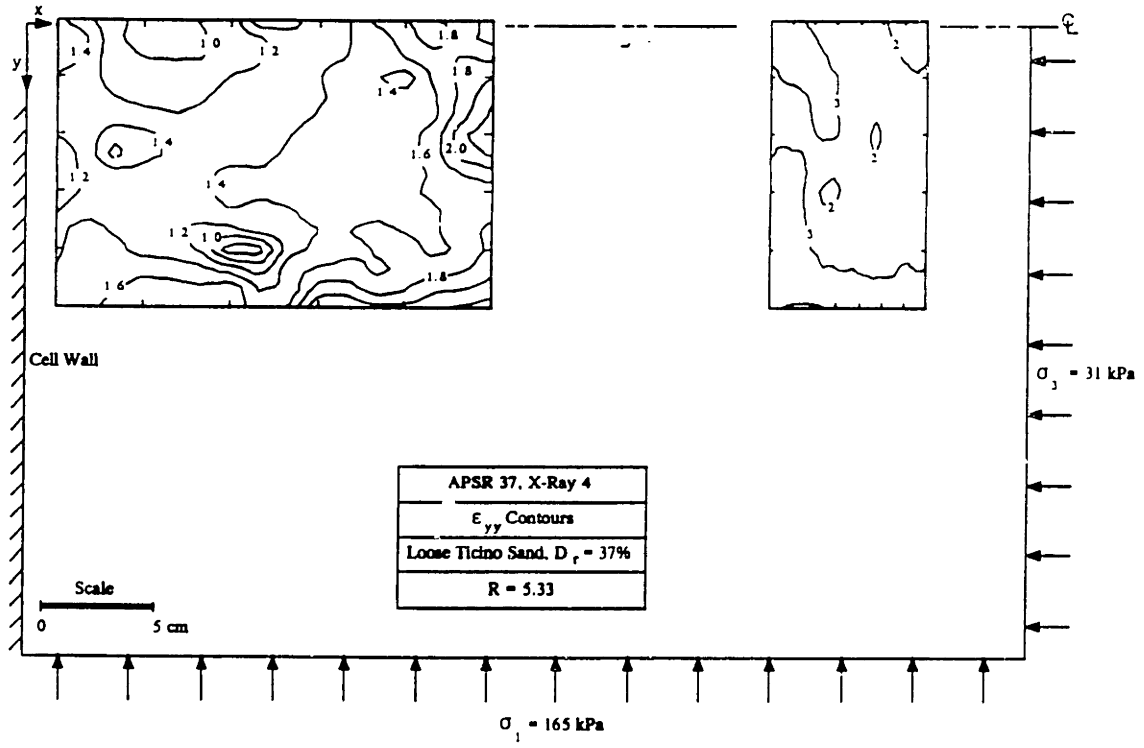

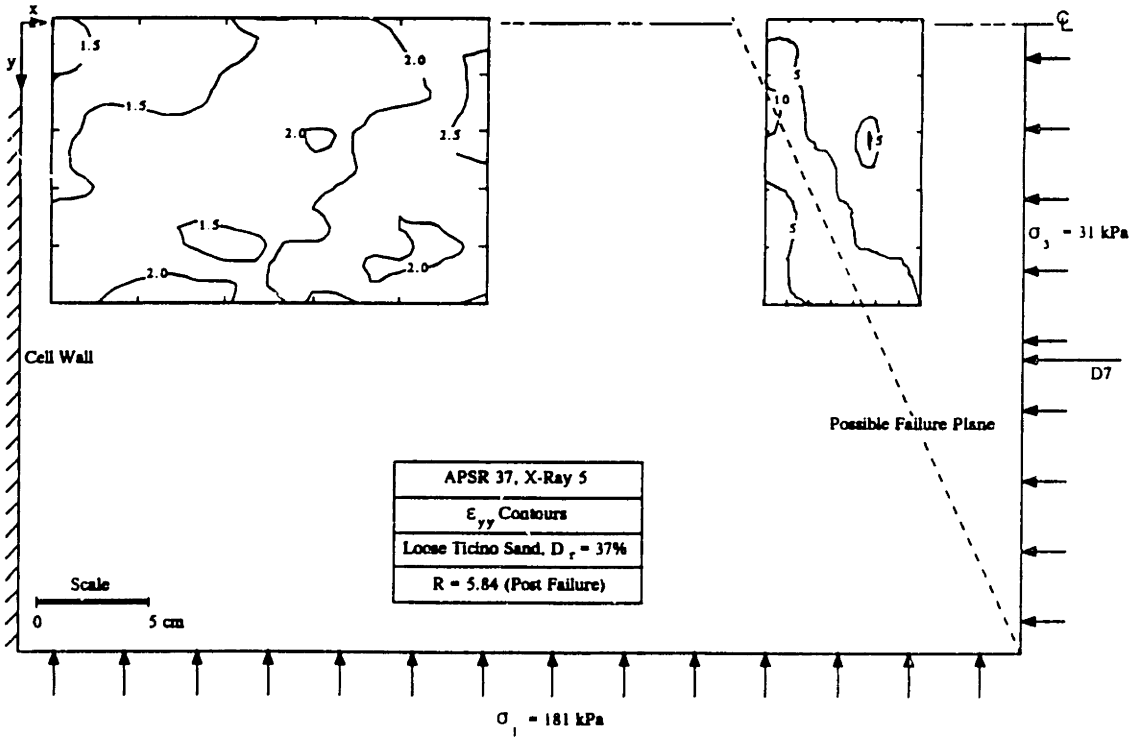

Figure 4.38: Axial Strain Contours, APSR 37, R = 5.33 and 5.84

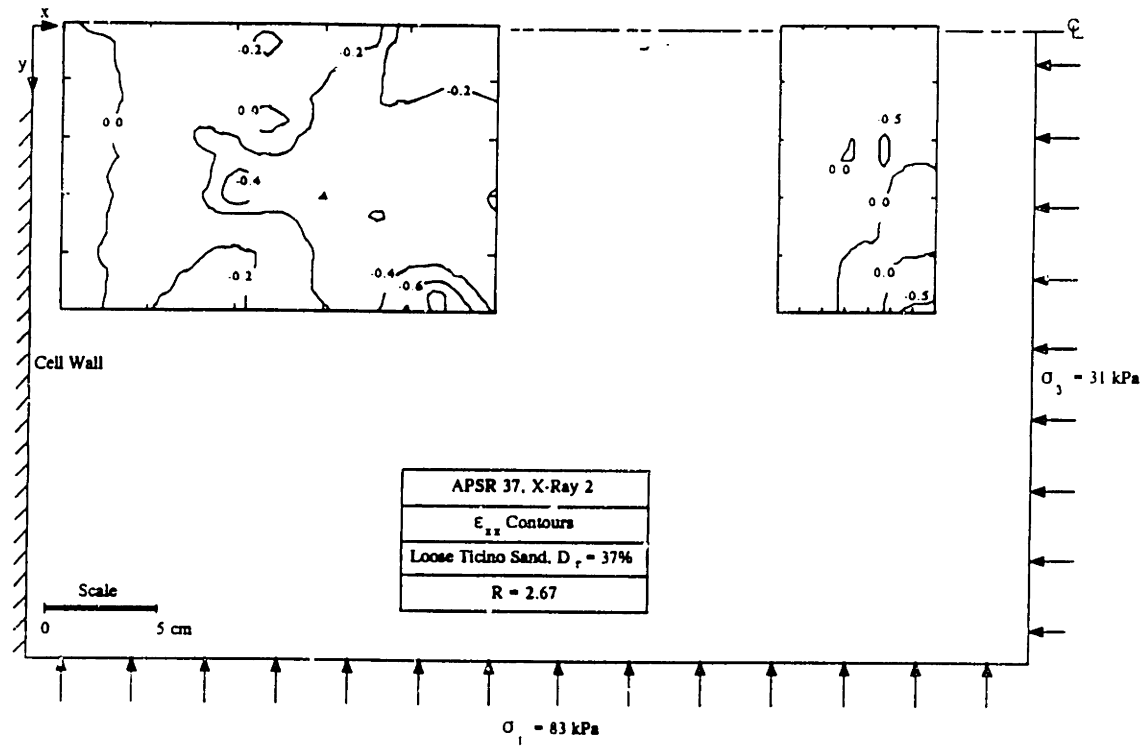

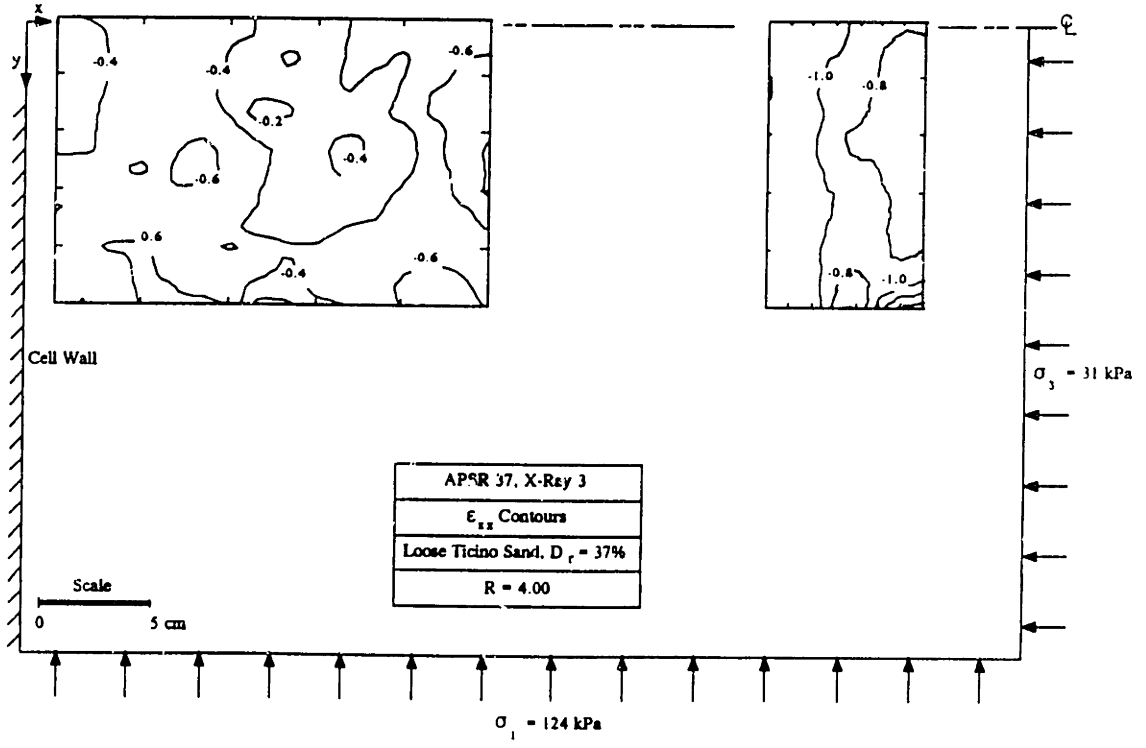

Figure 4.39: Lateral Strain Contours, APSR 37, R = 2.67 and 4.00

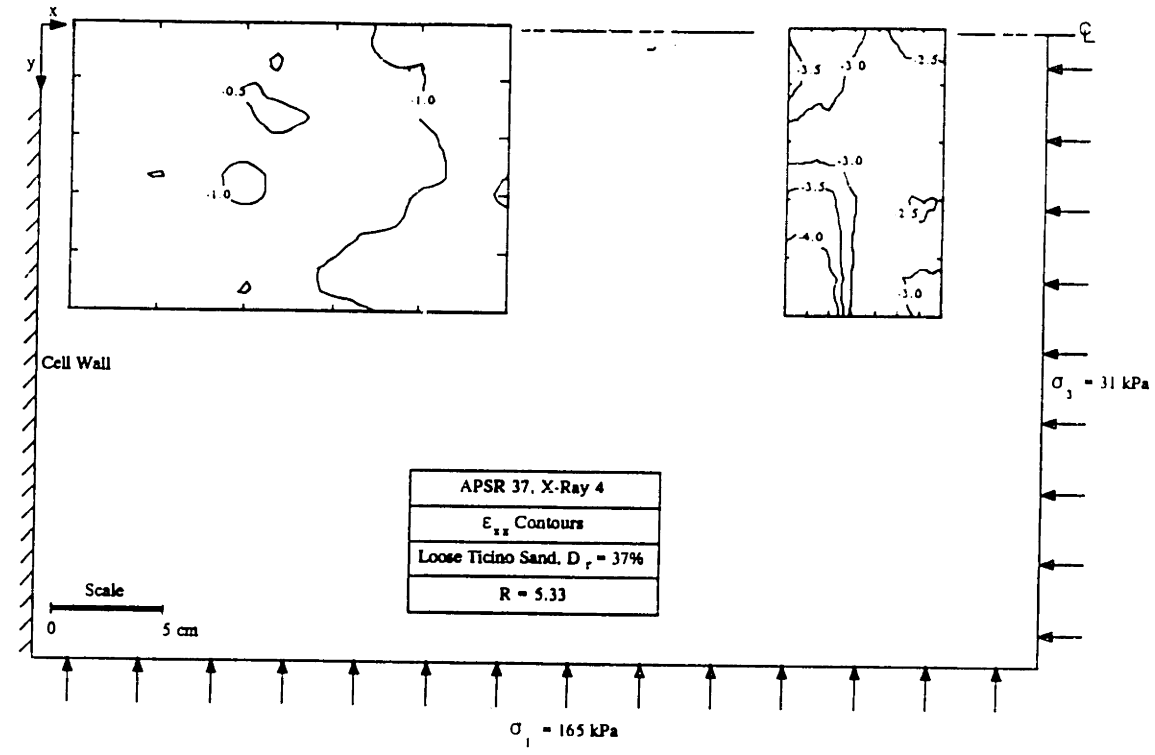

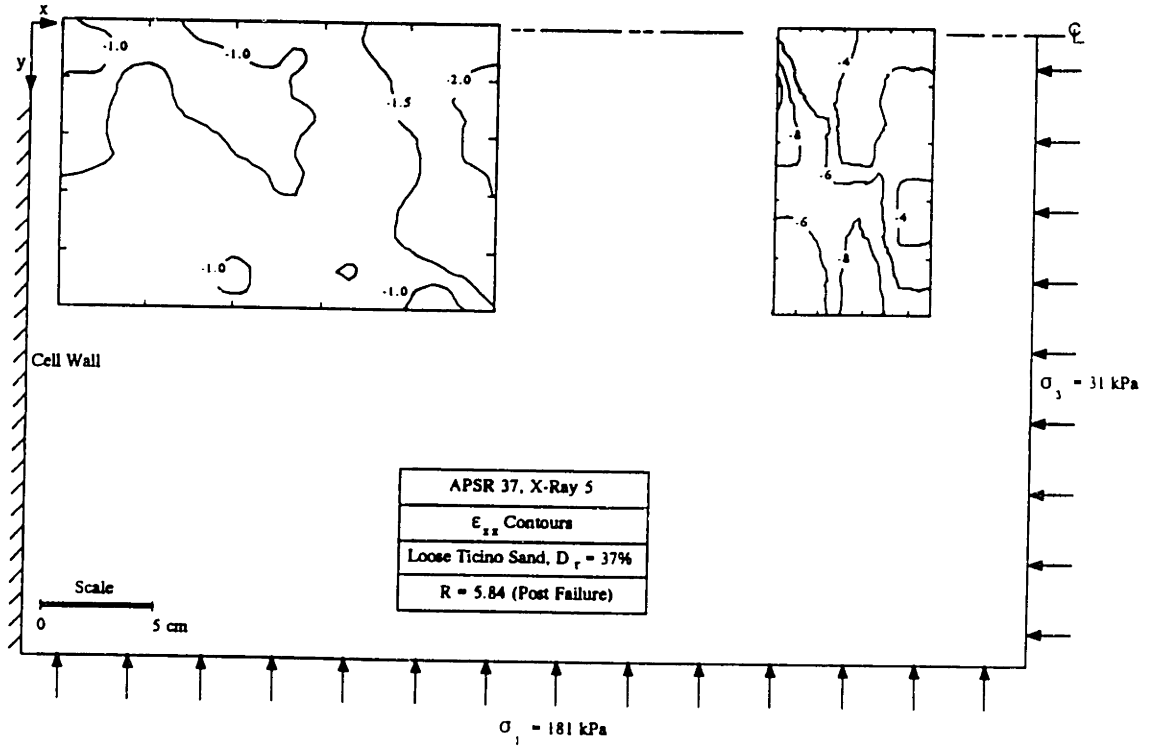

Figure 4.40: Lateral Strain Contours, APSR 37, R = 5.33 and 5.84

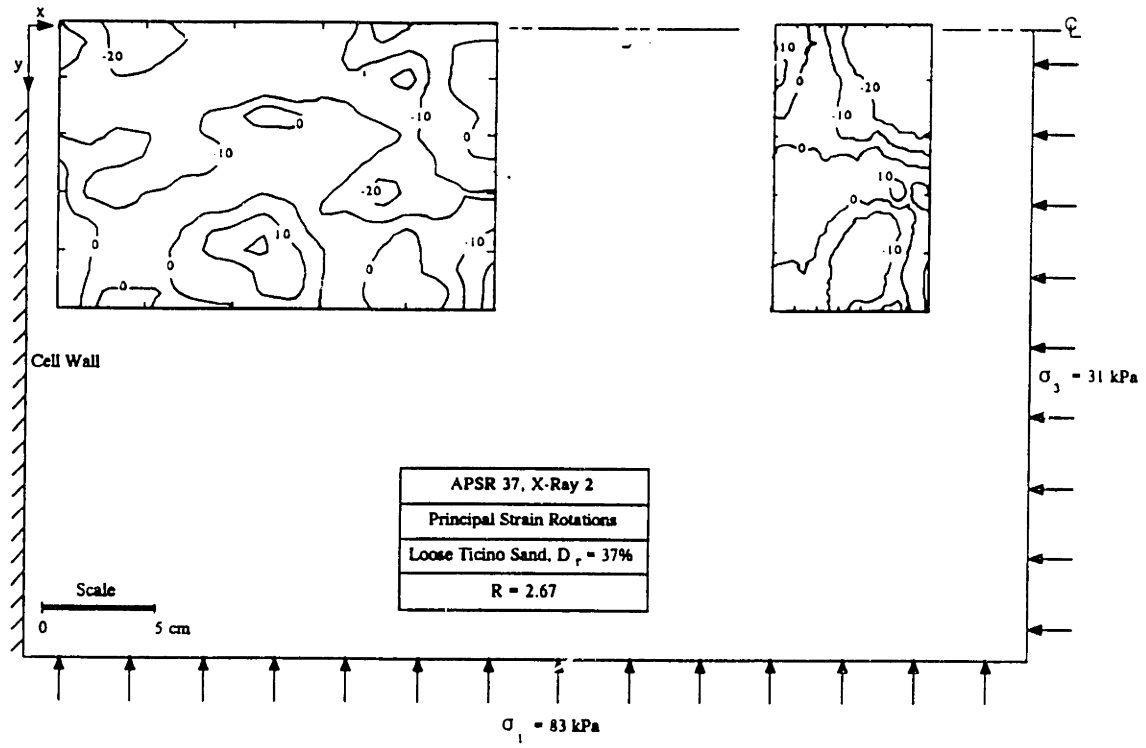

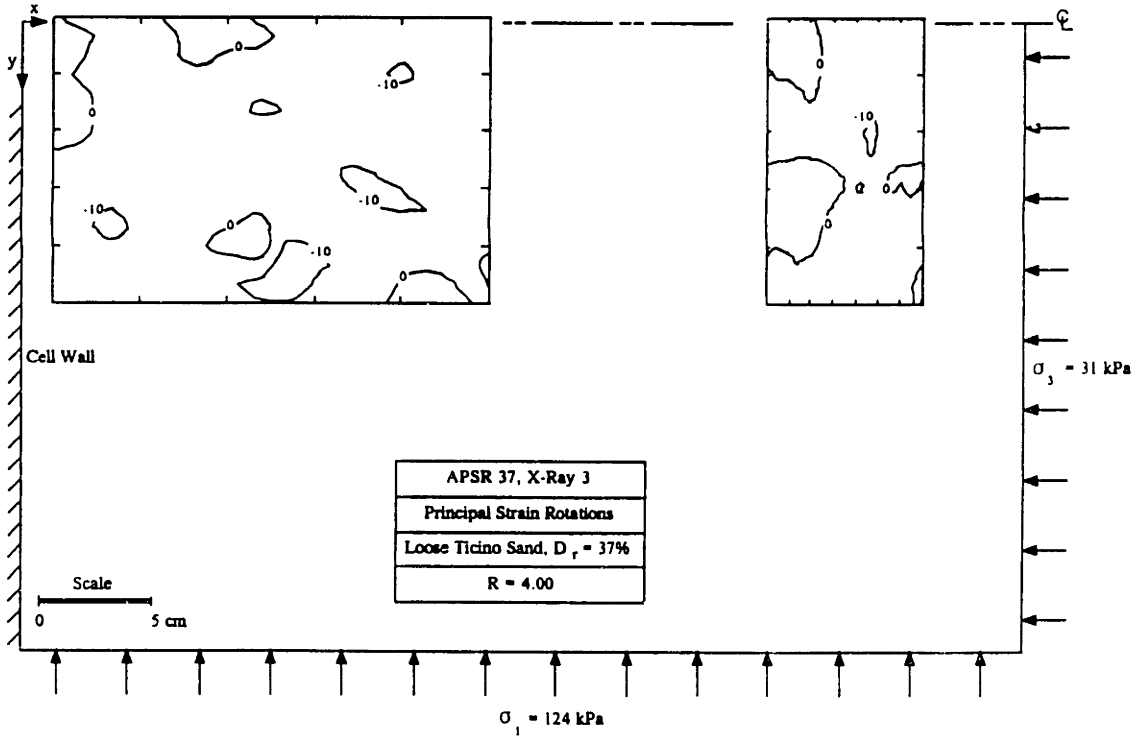

Figure 4.41: Principal Strain Rotations, APSR 37, R = 2.67 and 4.00

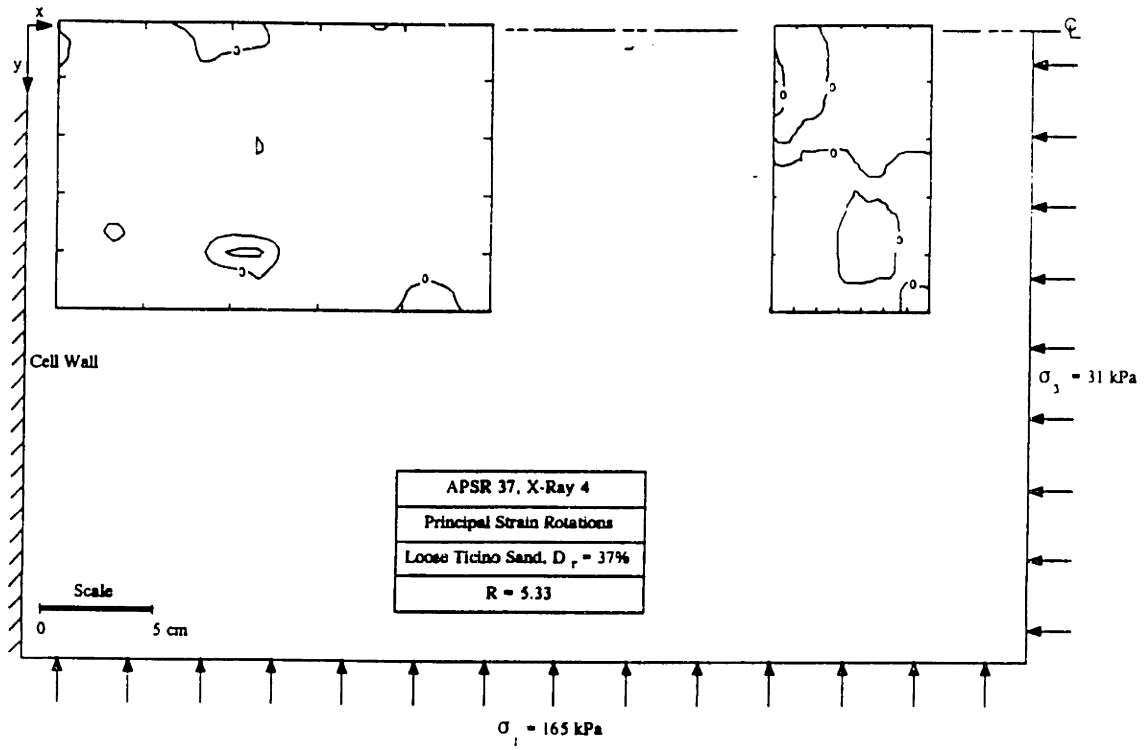

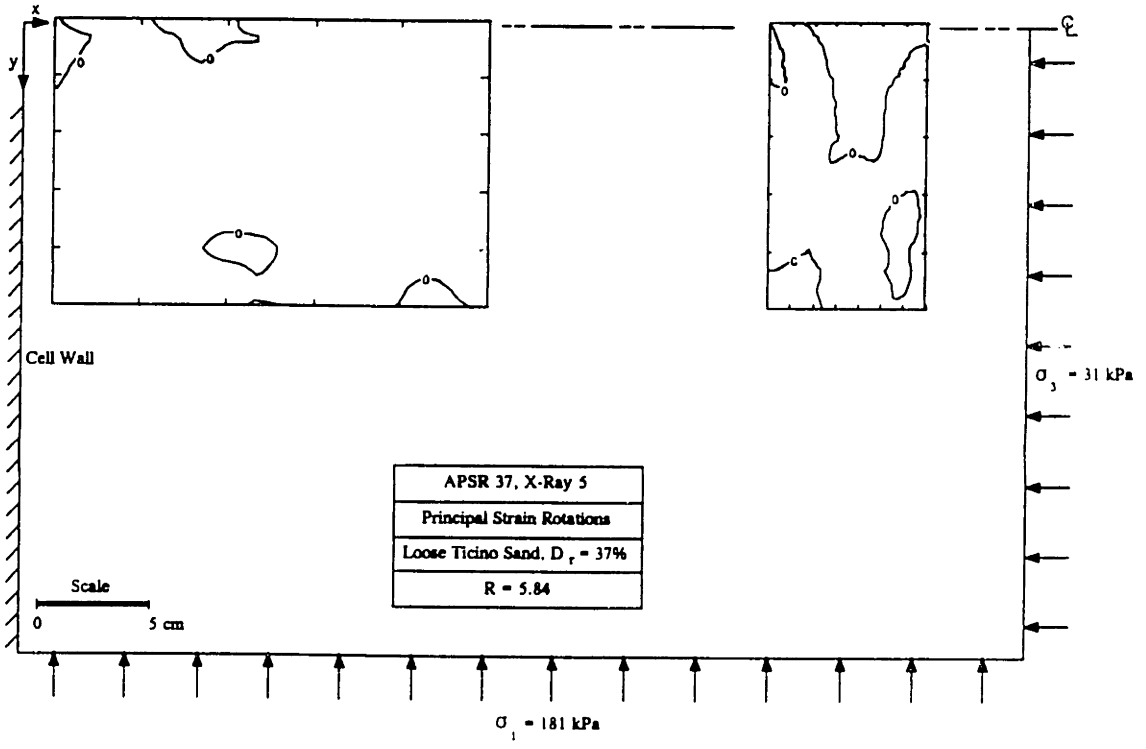

Figure 4.42: Principal Strain Rotations, APSR 37, R = 5.33 and 5.84

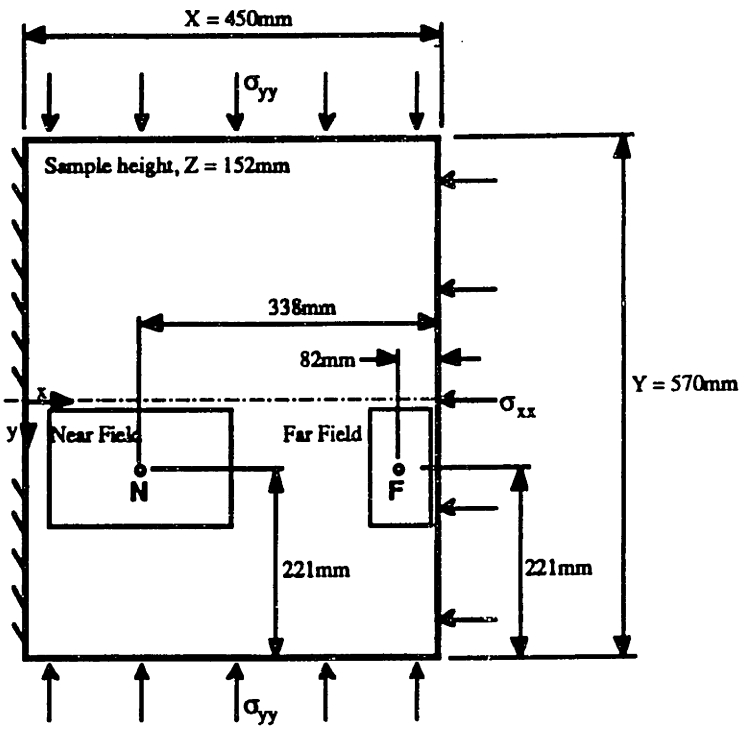

Correction for Sidewall Grease Resistance:

Shear strength of grease = c_g

$$\Delta\sigma_3 = -c_g \frac{2}{Z}(X - x)$$

$$\Delta\sigma_1 = -c_g \frac{2}{Z}(Y - y)$$

Magnitude of c_g (after Seah, 1990):

$$c_g = 0.025\ \sigma_n$$

where $\sigma_n = \sigma_2 = b(\sigma_1 - \sigma_3) + \sigma_3$

	Applied Stresses						Near Field (N)			Far Field (F)		
R_{ext}	σ_1 kPa	σ_2 kPa	σ_3 kPa	c_g kPa	$\Delta\sigma_1$ kPa	$\hat{\sigma}_1$ kPa	$\Delta\sigma_3$ kPa	$\hat{\sigma}_3$ kPa	$\hat{R}$	$\Delta\sigma_3$ kPa	$\hat{\sigma}_3$ kPa	$\hat{R}$
2.67	83	42	31	1.0	-2.9	80	4.4	35	2.3	1.1	32	2.5
4.00	124	62	31	1.6	-4.7	119	7.1	38	3.1	1.7	33	3.6
5.33	165	79	31	2.0	-5.8	159	8.9	40	4.0	2.2	33	4.8
5.84	181	83	31	2.1	-6.1	175	9.3	40	4.4	2.3	33	5.3

Note: $\hat{\sigma}_1$, $\hat{\sigma}_3$, and $\hat{R}$ are the corrected stresses.

Stress corrections for average points in the near and far fields

Figure 4.43: Sidewall Grease Resistance Correction to Estimate Internal Stresses in Loose Ticino Sand

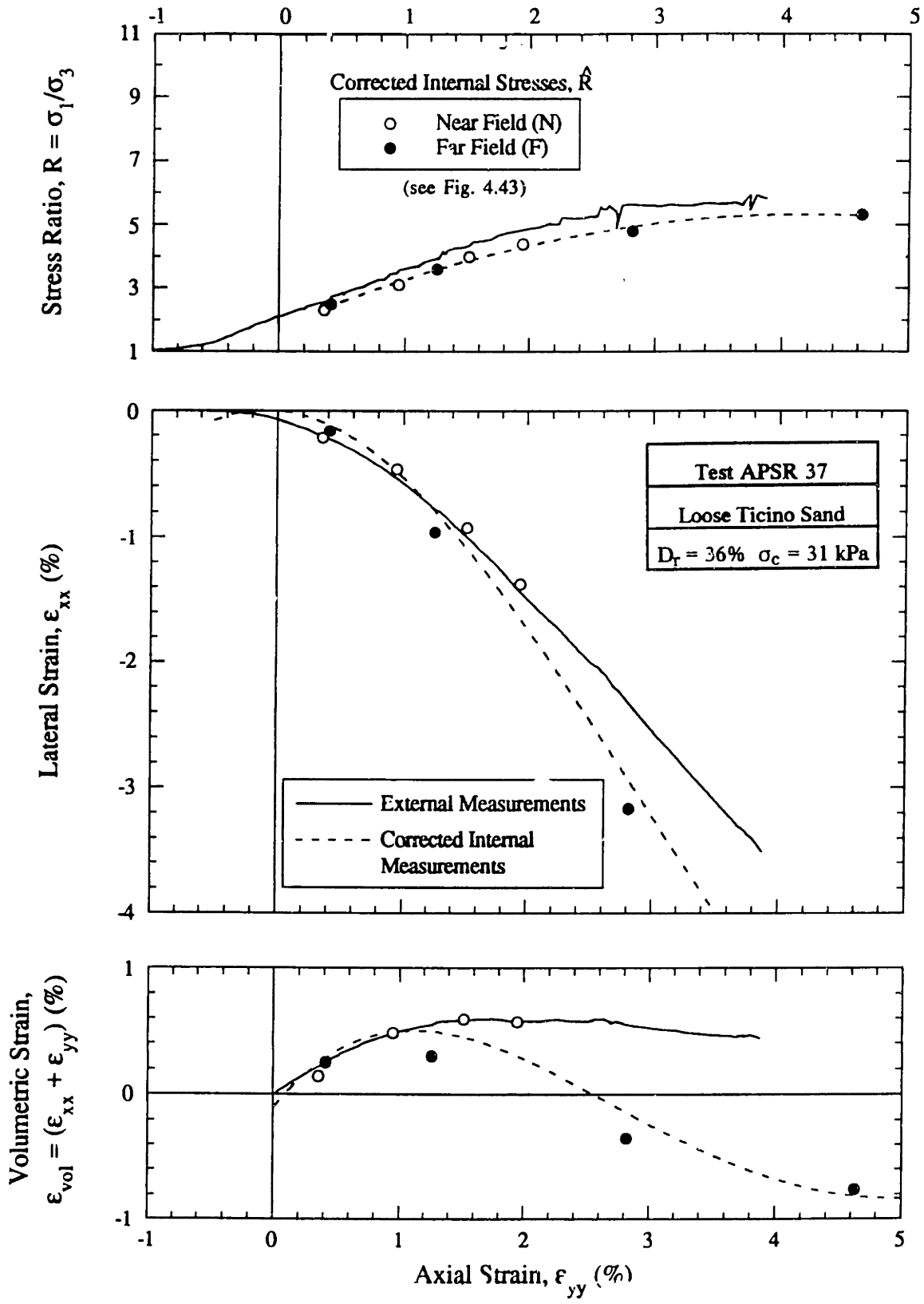

Figure 4.44: Comparison of External and Corrected Internal Measurements for Loose Ticino Sand

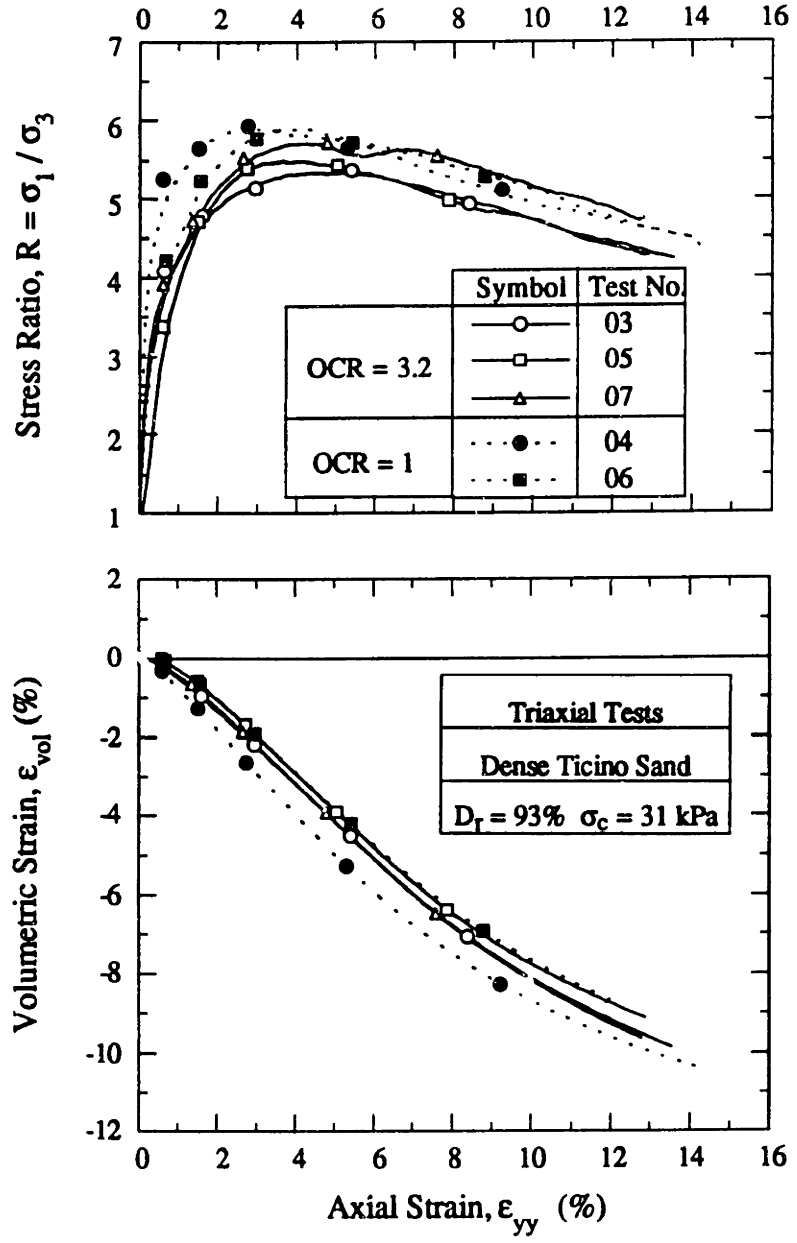

Figure 4.45: Shear Behavior from Triaxial Compression Tests on Dense Ticino Sand

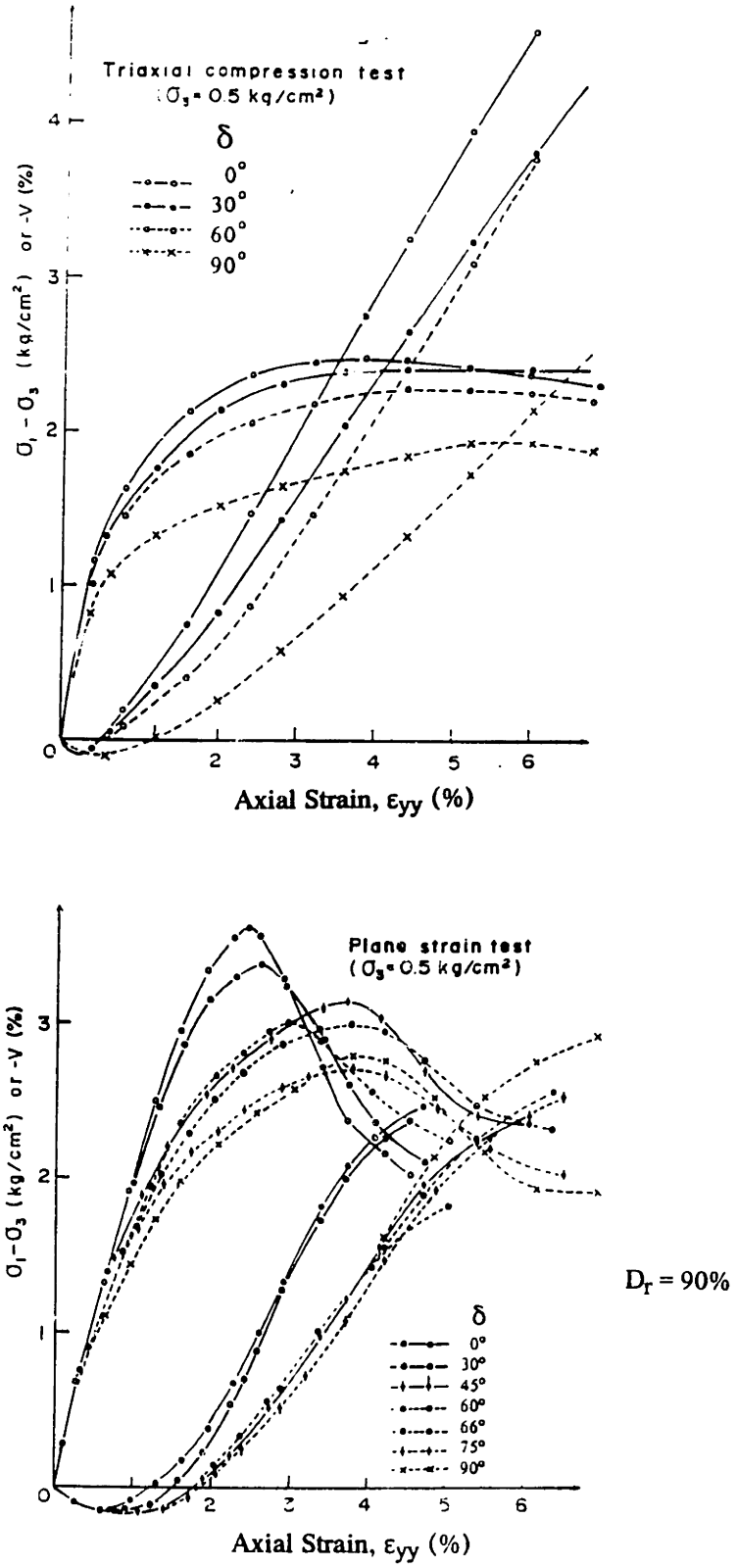

Figure 4.46: Influence of Tilting Angle, δ, on the Behavior of Dense Toyoura Sand (after Oda et al., 1978)

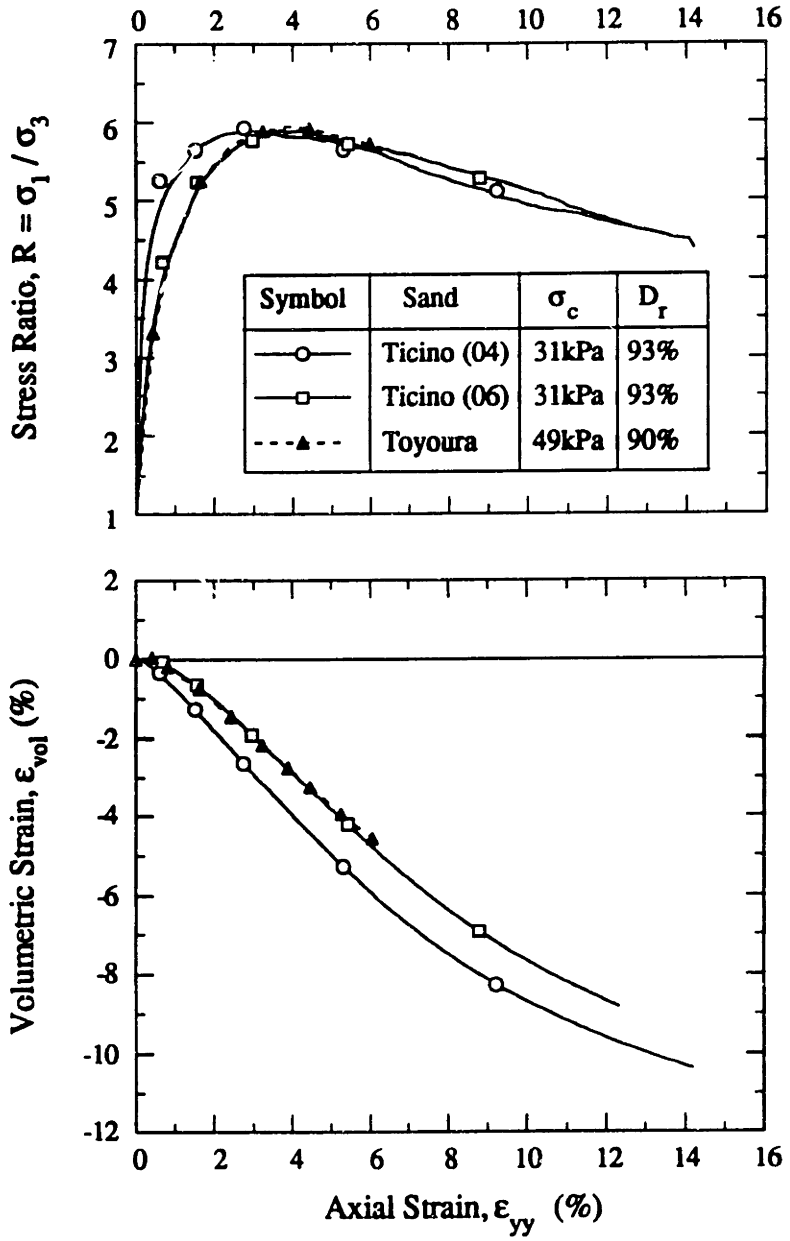

Figure 4.47: Triaxial Shear Behavior for Dense Ticino and Toyoura Sand (Vertical Samples, $\delta = 0^{o}$)

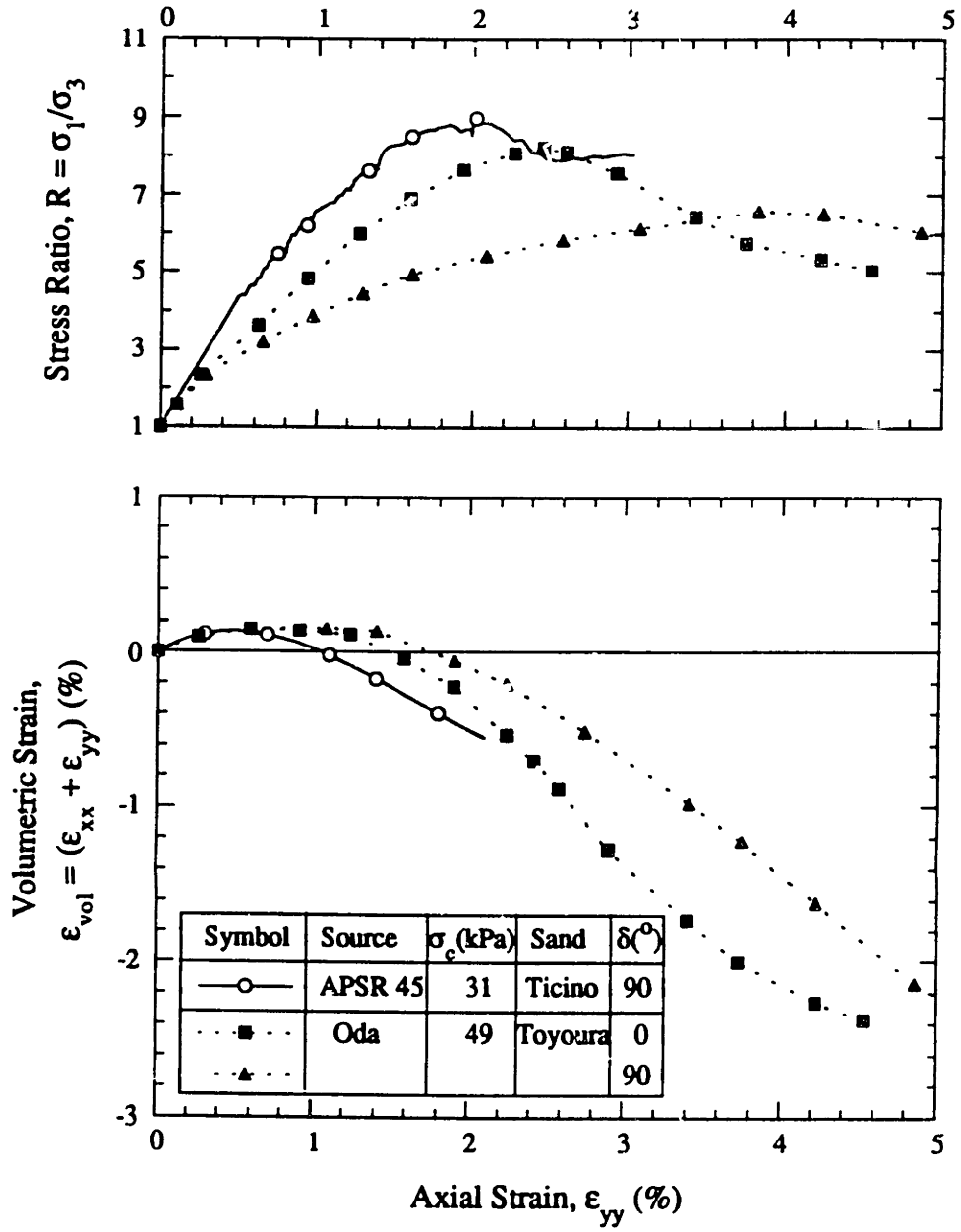

Figure 4.48: Plane Strain Shear Behavior for Dense Ticino and Toyoura Sand

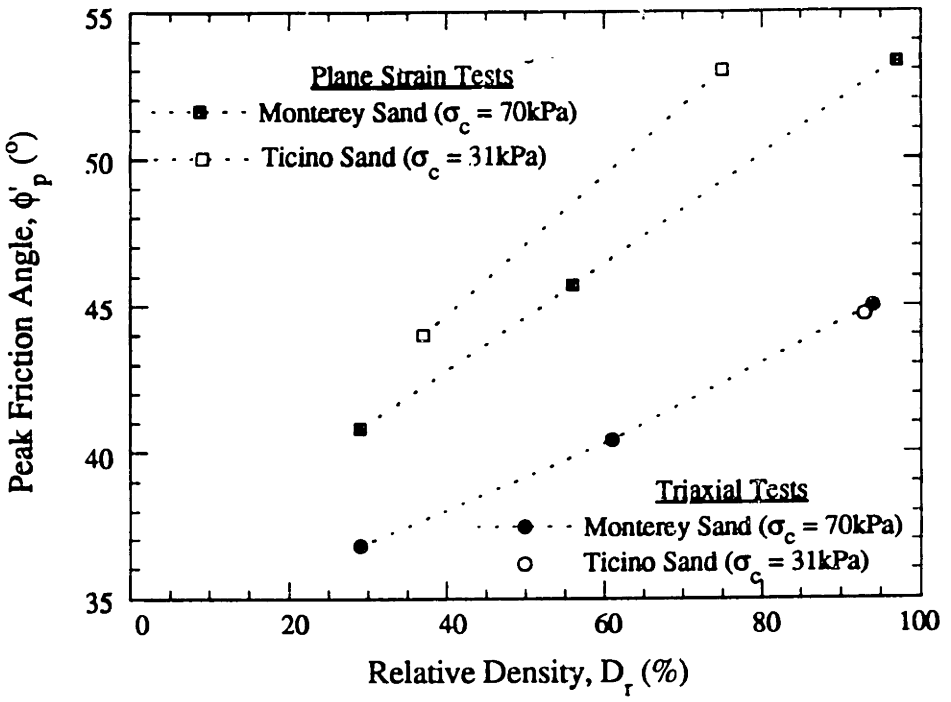

(a) Comparison of peak friction angles for triaxial and plane strain compression tests

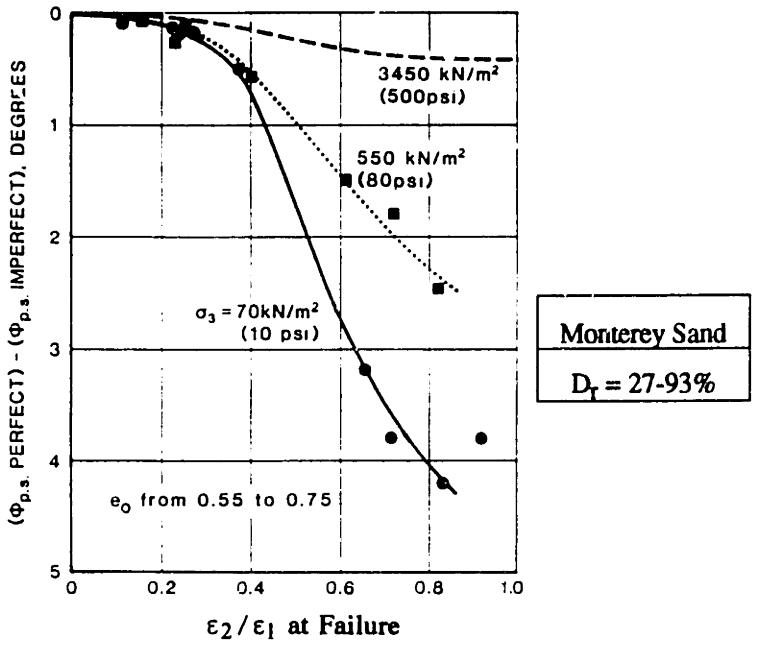

(b) Effect of intermediate principal strain on peak friction angle

Figure 4.49: Results from Plane Strain Compression Tests on Monterey Sand (after Marachi et al., 1981)

Symbol	Source	Sand	σ_3 (kPa)	D_r (%)	δ (°)
- - -◆- - -	Deterling, 1984	Leighton Buzzard	20	94	0
- - -■- - -	Oda et al., 1978	Toyoura	49	90	0
—○—	Chauhan, 1991	Ticino	31	93	0

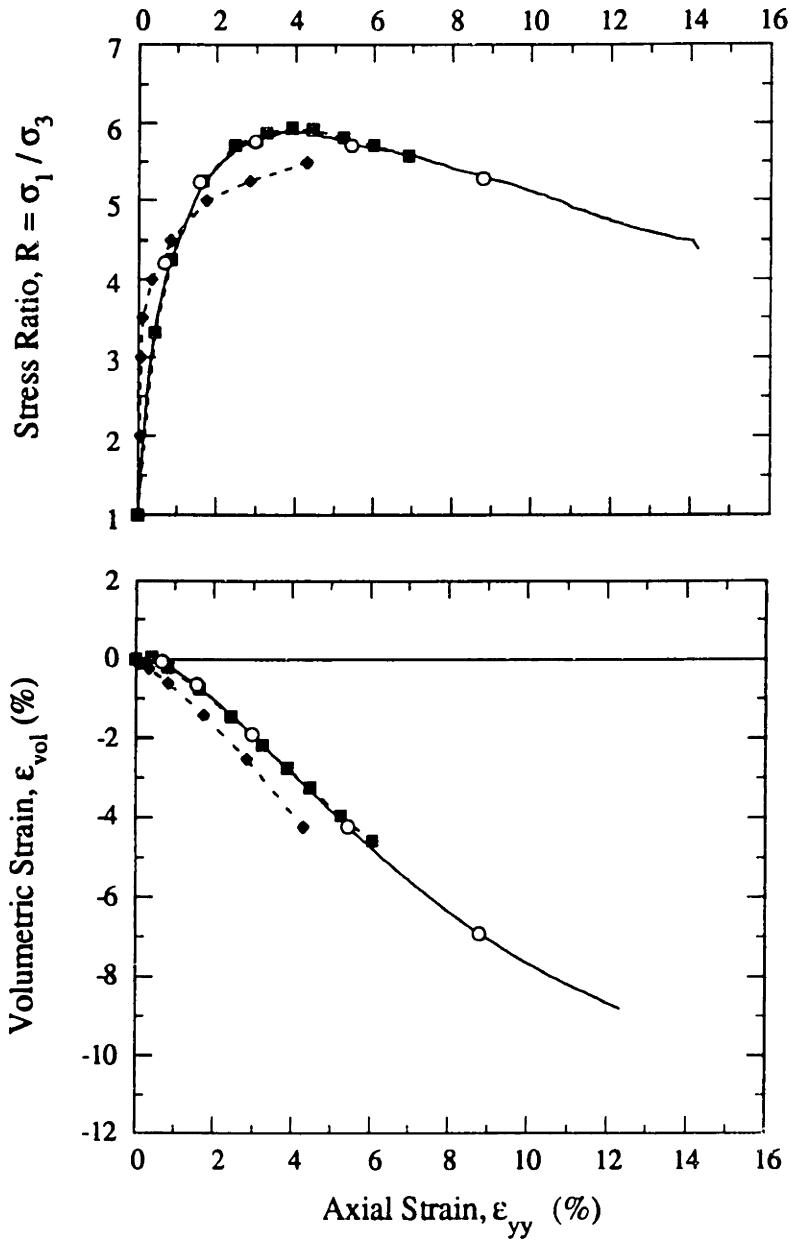

Figure 4.50: Triaxial Compression Shear Behavior of Dense Toyoura, Leighton Buzzard, and Ticino Sand

Symbol	Source	Sand	σ_3 (kPa)	D_r (%)	δ (°)
- - ◆ - -	Deterling, 1984	Leighton Buzzard	20	94	0
- - ■ - -	Oda et al., 1978	Toyoura	49	90	0
—○—	APSR 45	Ticino	31	74	90

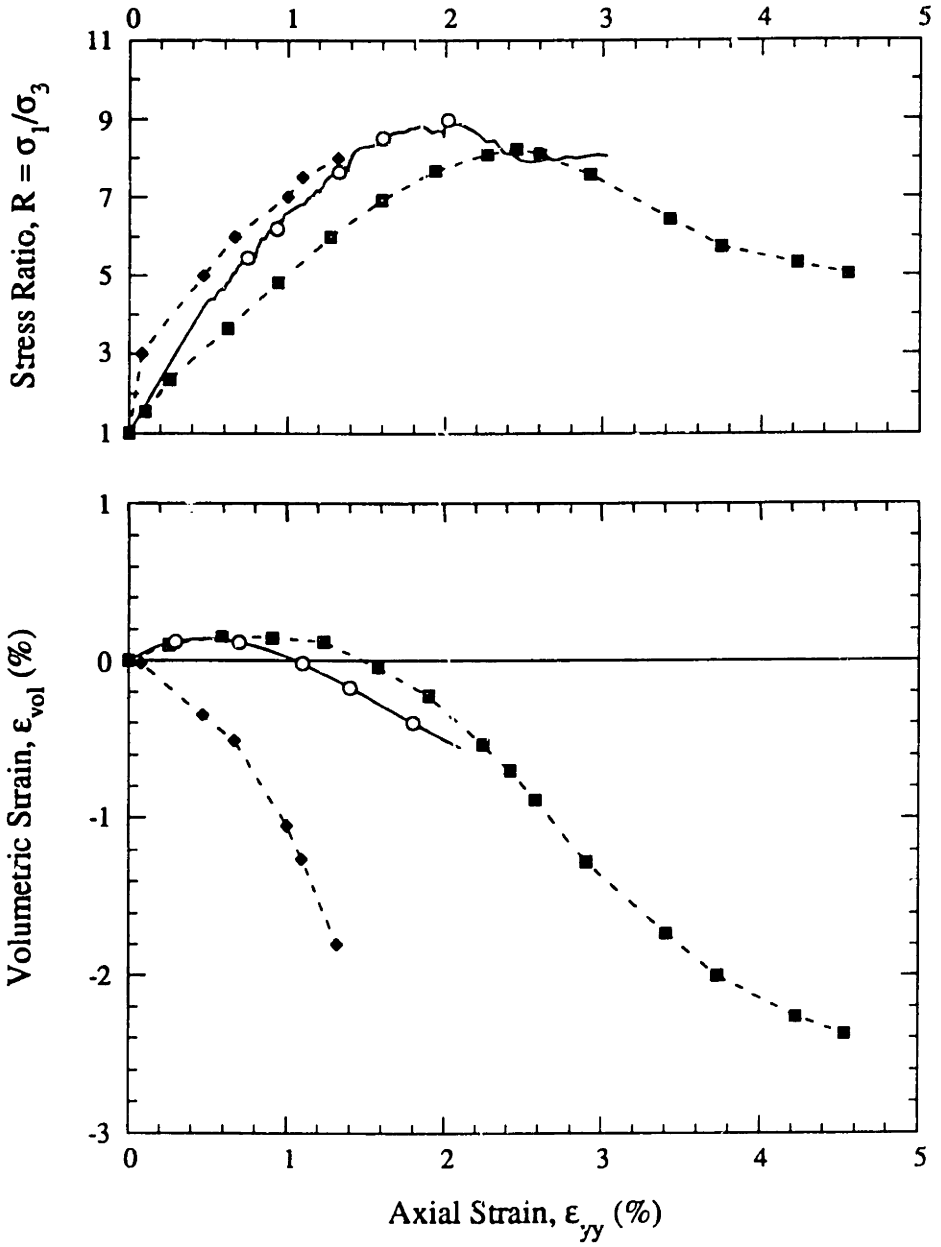

Figure 4.51: Plane Strain Shear Behavior of Dense Toyoura, Leighton Buzzard, and Ticino Sand

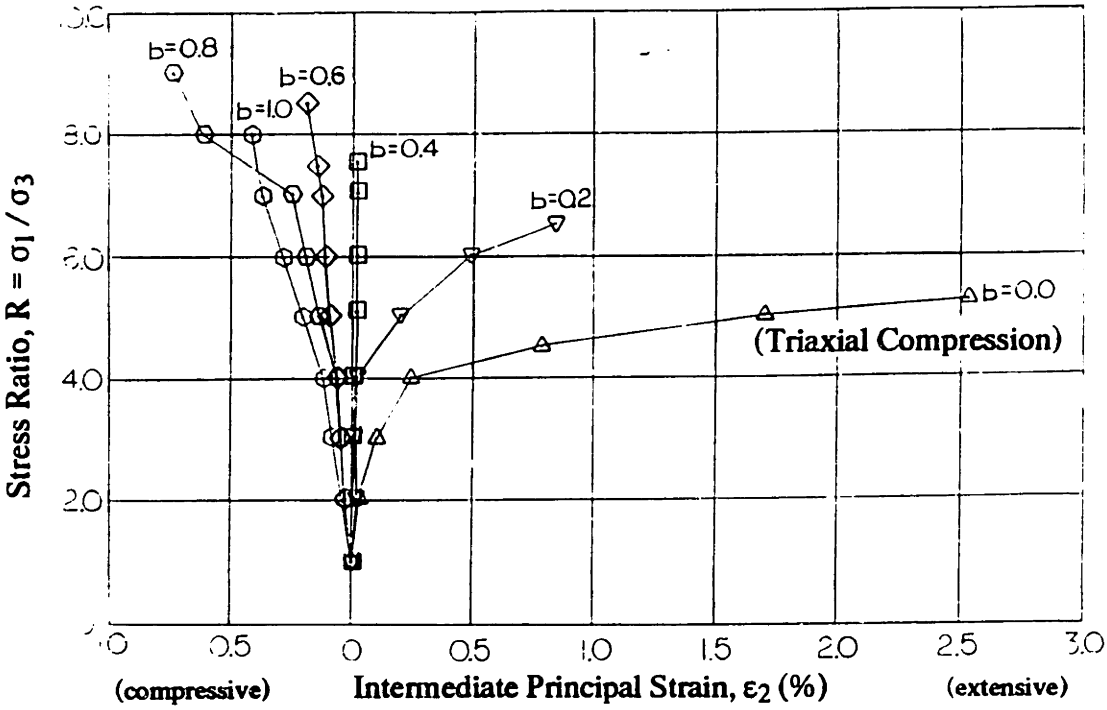

(a) Dense Leighton Buzzard sand (D_r = 94%)

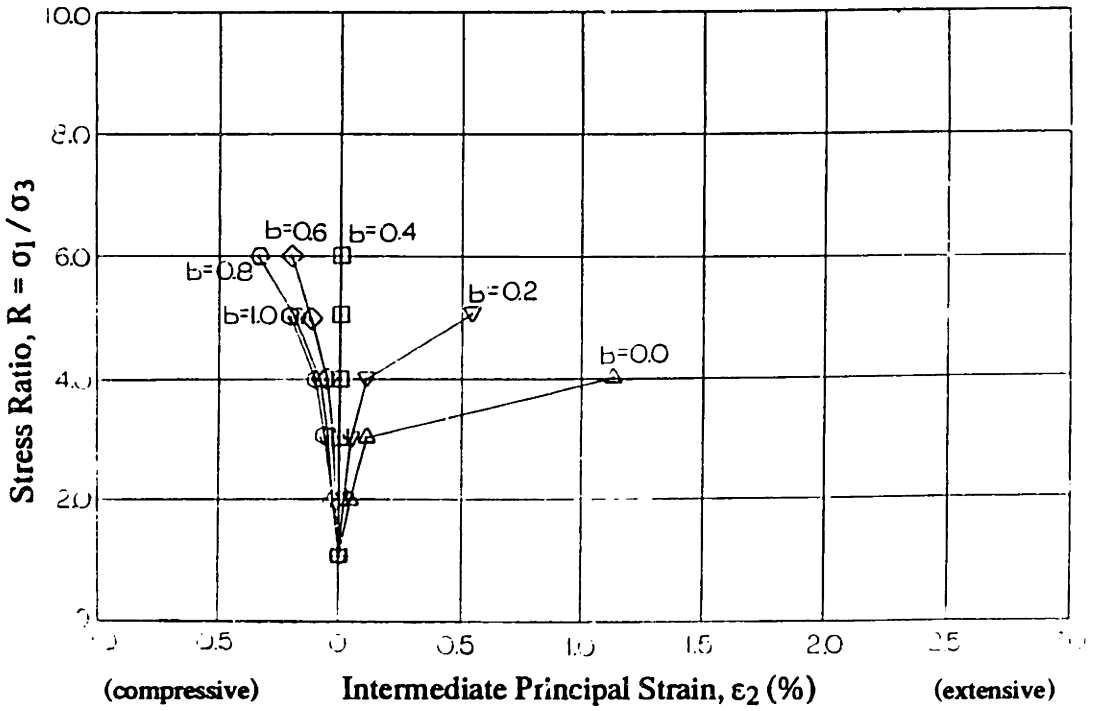

(b) Loose Leighton Buzzard sand (D_r = 47%)

Figure 4.52: Influence of b on the Intermediate Principal Strain in the True Triaxial Apparatus (after Deterling, 1984)

Source	Sand	σ_c (kPa)	D_r (%)
Deterling, 1984	Leighton Buzzard	20	94
Davoudzadeh, 1982	Leighton Buzzard	30	90
Templeton, 1977	Leighton Buzzard	30	90
Oda et al., 1978	Toyoura	49	90
Larson	Ticino	31	74
Chauhan, 1991	Ticino	31	93

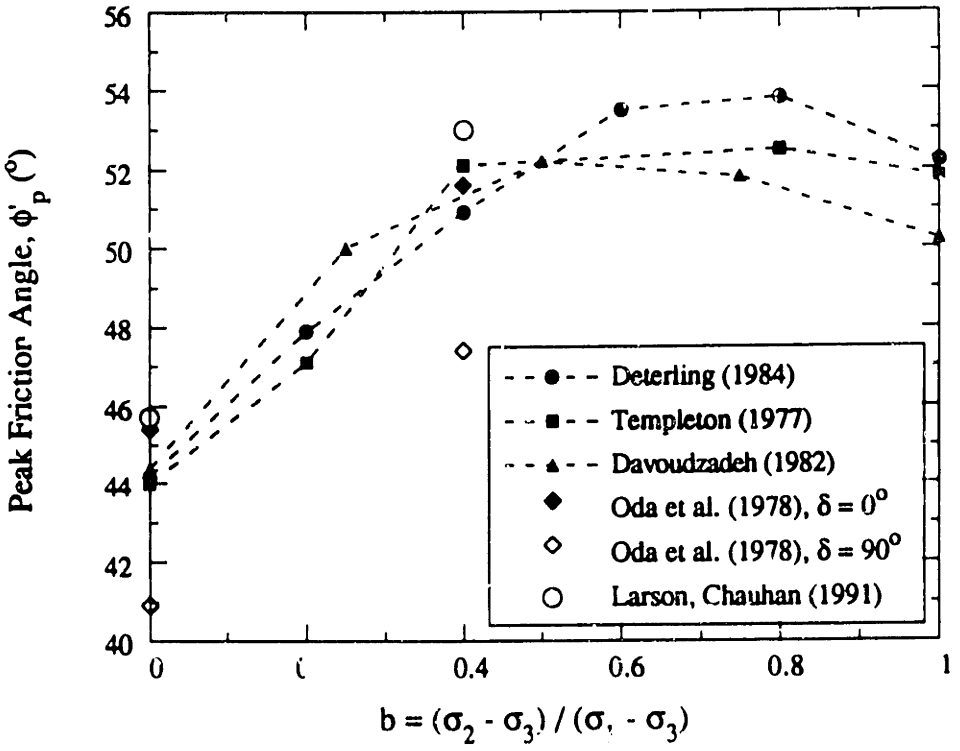

Figure 4.53: Influence of b-value on Peak Friction Angle (after Deterling, 1984)

Source	Sand	σ_c (kPa)	D_r (%)
APSR 45	Ticino	31	74
Bekenstein, 1981	Leighton Buzzard	13.8	87
Wong, 1985	Leighton Buzzard	14	90

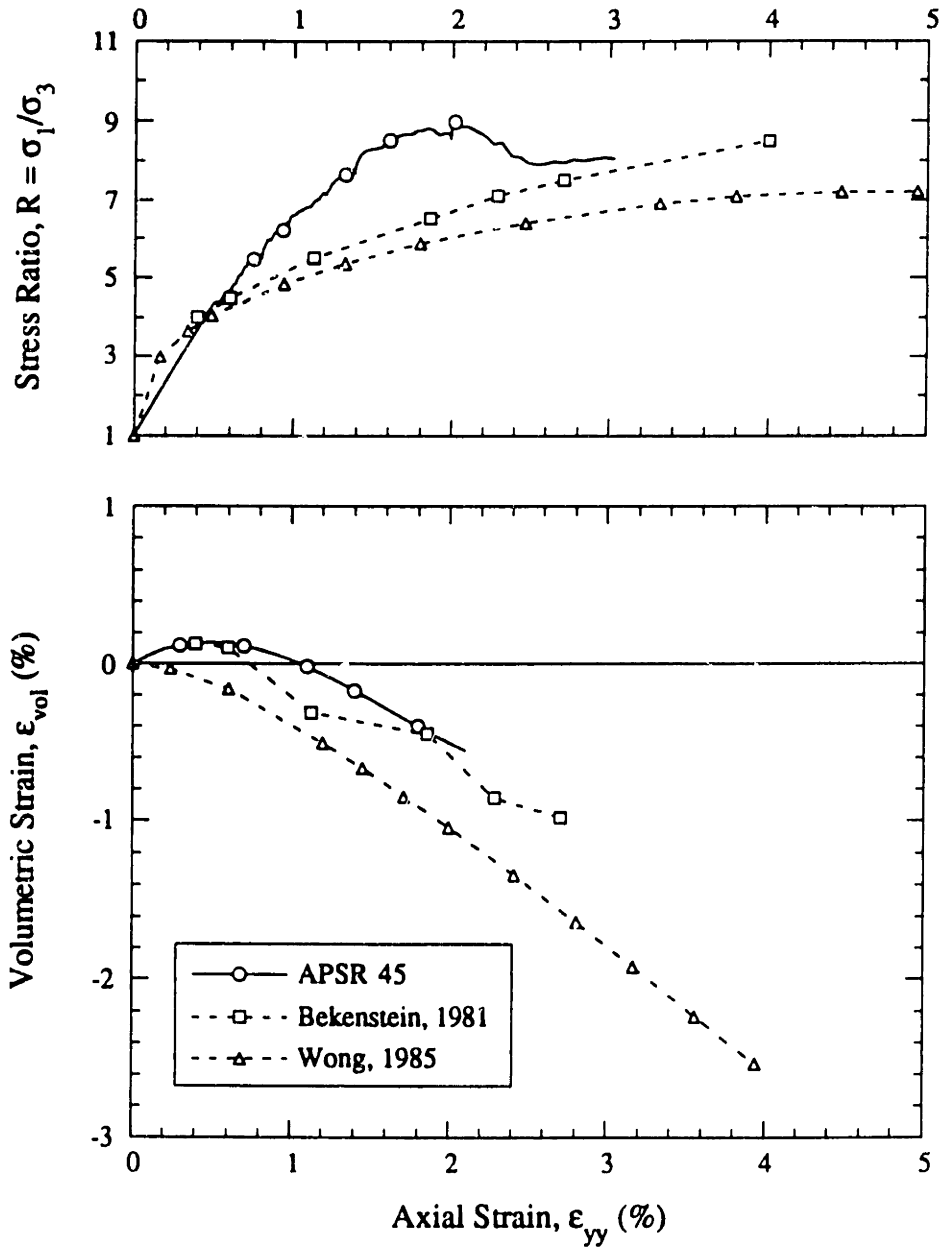

Figure 4.54: Comparison of Plane Strain Tests on Dense Sand Specimens Sheared in the Isotropic Plane

Chapter 5: APSR Tests on Steel-Reinforced Sand

5.1. Introduction

The APSR cell models the unit plane strain element shown in Figure 5.1. The design uses the symmetry and well defined boundary conditions along the x=0 plane (Fig. 5.1) in order to measure the maximum tensile force at the center of a planar inclusion of half-length, L/2, as the surrounding soil deforms in a plane strain compression mode of shearing with uniform principal boundary tractions, σ_1 and σ_3. In principle, the design parameters enable load transfer measurements for a wide range of potential reinforcing materials (including woven and non-woven geotextiles, polymer strips and grids) with $L/2 \leq 450$mm, subject to major principal stress levels, $\sigma_1 \leq 400$ kPa, and axial soil strains, $\varepsilon_{yy} \leq 10\%$ (Fig. 5.1).

This chapter documents the experimental procedures and describes the measurements of load transfer for tests on dry Ticino sand reinforced with steel sheet inclusions. Comprehensive measurements of load transfer are reported for a 'base-case' geometry (section 5.3) consisting of an instrumented inclusion of length, L/2 = 36cm,[1] sheared in dense Ticino sand ($D_r \approx 75\%$) at a confining pressure, $\sigma_3 = 31$ kPa (Fig. 5.2). In addition to measurements of tensile stresses in the reinforcement, the base case tests are

---

[1]This length was chosen to give clearance between the tip of the inclusion and the free face of the specimen in order to avoid possible non-uniformities at the boundary.

used to evaluate the repeatability of load transfer measurements in the APSR cell and the effects of the inclusion on a) boundary measurements of stress-strain behavior for the composite reinforced soil element, and b) internal soil strain fields from radiographic measurement. The experimental program (Table 5.1) focuses on the effects of inclusion length (9cm $\leq L/2 \leq$ 36cm) and sand density (D_r = 30 and 75%) on measurements of load transfer for specimens sheared at a fixed confining pressure, σ_3 = 31 kPa.

5.2. Reinforced Specimen Preparation

5.2.1. Steel Sheet Reinforcements

Steel sheet was selected as the reinforcing material for the first APSR tests for three main reasons: a) it exhibits linear elastic properties over the stress range of interest in APSR tests, b) it is relatively easy to bond strain gauges to steel sheet in order to measure local strains in the inclusion, and c) no special handling procedures or grip design are required. The inclusions are made from a 15.2cm wide roll of 0.127mm thick shim stock[2] and consist of two sheets bonded together with a flexible adhesive. Curvature of the shim stock sheet is counteracted by bonding the sheets back-to-back in order to produce a flat inclusion. Strain gauges are mounted on the inside face of one of the sheets, such that the gauges and electrical leads are protected from abrasion by the surrounding sand. Figure 5.3 shows the geometry and instrumentation of the inclusion used in the base case tests. The length of the sheet includes the embedment (36cm) plus 5.7cm at each end to attach grips for the uniaxial tension test and an additional 2 cm

[2]The shim stock has a thickness tolerance of 10%.

corresponding to the clearance between the grips and the rear wall of the cell (Fig. 5.10). The inclusion contains four BLH SR-4 bonded resistance strain gauges (gauge number FAE-50-35 S13 EL), each 12.7mm long with a nominal resistance of 350 Ω, spaced at 7.6cm intervals. Black (1990) gives full details of the procedure used to make the inclusions:

1. The inside surface of one of the steel sheets is cleaned with emery cloth and acetone to remove rust or surface contamination. Two perpendicular lines are etched onto the steel surface with a stylus (often a nail) to mark the centerpoint where the gauge will be mounted. The gauges are attached to the steel with BLH EPY-150 strain gauge epoxy. The epoxy layer is as thin as possible to minimize its effect on the strains transmitted to the gauge.
2. Each gauge has two short wires for connection to a voltage source. A piece of insulating tape is placed under the strain gauge leads to prevent them from short-circuiting against the steel surface. Two insulated wires (30 gauge) are soldered to the strain gauge and run along the length of the reinforcement to an amphenol connector (Fig. 5.3). When the connections are completed, the exposed leads are covered with insulating tape. The wires must be placed carefully near the end of the inclusion so they are not damaged when drilling holes for the grips.
3. After the gauges and connecting wires are in place and the epoxy has thoroughly cured, the two steel sheets are bonded together with 3M Rubber and Vinyl Adhesive.[3] This is a contact adhesive that sprays onto the inside

---

[3]High modulus adhesives, such as 5 minute epoxy, were tried initially but these cracked easily in bending. The cracks allowed air to pass through the inclusion to the outside of the cell so the

surfaces of both steel sheets. After the adhesive dries, the two surfaces are brought together to form a permanent bond.

4. The hole pattern for the grips is then drilled with a 3/8" drill bit.

5.2.1.1. Strain Gauge Theory

Bonded resistance strain gauges consist of a thin coil of metallic foil whose resistance varies linearly with strain. The coil is mounted on an insulated backing called the carrier matrix, which attaches to the steel surface using an appropriate strain gauge epoxy. The gauges are manufactured with an average "Gauge Factor" (GF), expressing the change in resistance of the gauge for a given amount of strain:

$$GF = \frac{\Delta R/R}{\Delta L/L} \tag{5.1}$$

where: ΔR = change in resistance due to an applied strain
R = unstrained resistance of the strain gauge
$\Delta L/L$ = applied strain.

The actual value of GF for a given strain gauge is typically within ±2% of the values quoted by the manufacturer. The gauges used in this research have factors, GF ≈ 2.0.

A wheatstone bridge circuit (Fig. 5.3) is used to provide a sensitive voltage response to the small changes in resistance across a strain gauge. The circuit consists of three nominally equal resistors (R1, R2, and R_D), while the strain gauge, which forms the fourth arm of the bridge circuit, is a variable resistor. There is an initial voltage difference across the bridge (points 1 and 2), which varies with changes in the strain

---

surrounding sand could not hold the necessary vacuum for test setup. The rubber and vinyl adhesive provides a tight but flexible bond that prevents air flow between the steel sheets.

gauge resistance. If all the resistors had identical resistance to the unstrained gauge, the initial voltage would be zero. There is always a slight discrepancy, however, such that the initial voltage is small but non-zero. The relationship between the bridge circuit output voltage and the strain in the gauge can be expressed as:

$$\varepsilon_{gauge} = \frac{-4V_r}{GF(1 + 2V_r)} \tag{5.2}$$

where the voltage ratio, $V_r = \left(\frac{V_{out}}{V_{in}}\right)_{strained} - \left(\frac{V_{out}}{V_{in}}\right)_{unstrained}$

Figure 5.4 shows the hardware that measures and records the inclusion strains. A junction box houses four separate wheatstone bridge circuits, each containing three 350 Ω resistors. The strain gauges connect to these circuits with a set of lines that run from the strain gauge amphenol connectors through a set of banana plug connectors in the side of the junction box. The box also has a connection for an input voltage source, typically 2.5V. The wheatstone bridge output signals travel through a twenty-five pin connector in the side of the junction box, then along a cable to the central data acquisition system described in section 3.3.1.5. The system reads the bridge output to ±5μV.

5.2.1.2. In-Isolation Tests on Steel Inclusions

A tensile test of each inclusion ensures that all strain gauges respond accurately to an applied load. A set of grips bolts onto each end of the steel inclusion. A 1.5mm thick rubber pad between the grips and the steel surface increases the amount of load that the grips can transfer to the inclusion. They attach easily to an Instron tensile testing machine by means of a custom built chuck (Fig. 5.5a). A 1.3cm diameter hardened steel pin holds the grips in the chuck. The chuck threads into an 8.9 kN (2000 lb) load

cell which measures the tensile force applied to the steel inclusion. The load cell in turn threads into the Instron machine.

Figure 5.5b shows the change in the wheatstone bridge output for four inclusion strain gauges as a function of the load measured by the 2000 lb load cell for the base case geometry (Fig. 5.2). The voltage curves are all fairly linear and exhibit very little noise, indicating that each gauge is well insulated and functioning properly. The maximum change in output voltage is approximately 550 to 700μV at the peak load of 4.8 kN.

Figure 5.6 shows the gauge output using the strain gauge equation (5.2) as a function of stress in the steel inclusion. The stress is computed by dividing the applied load by the cross-sectional area of the inclusion ($38.7mm^2$). Linear regression analyses of the curves yield the apparent Young's moduli shown in each plot. The modulus values range from 209 to 261 GPa, and are 1% to 26% higher than the reference modulus of the steel, E = 207 GPa (Popov, 1976). There are two reasons for the discrepancy. One is that the thickness of the shim stock varies between 0.228 and 0.254 mm, a tolerance of about 10%. The other is that the shim stock comes in a tightly coiled roll, which causes a small amount of permanent curvature. For the inclusion results in Figure 5.6, the gauges are bonded to the convex side of the shim stock. When loaded in the Instron machine, the inclusion straightens out and the gauges undergo bending strains in addition to the applied tensile strain, causing a net strain that is lower than expected. This observation was verified by tension tests on inclusions in which the gauges were mounted on the concave side of the shim. The apparent moduli were 9 to 13% lower

than expected for this case[4] (Fig. 5.7). In both tests, the error is a maximum in gauge 1 and a minimum in gauge 3 toward the center of the inclusion.

The data from the tension tests reveal two deviations from the ideal stress-strain response for steel: 1) the measured curves are not perfectly linear, and 2) the curves are not identical for all four gauges. Curvature in the steel accounts for the non-linearity of the measured response. The differences in the four curves for a given inclusion may be due to non-uniform curvature over the length of the steel sheet, misalignment of the gauges, or variations in gauge factors and steel thickness.

There are three ways to compute inclusion loads from the strain gauge output for steel-reinforced tests in the APSR cell.

1. Use the in-isolation stress-strain curves to determine the load acting at each gauge.
2. Use the best-fit linear regression lines from the in-isolation test.
3. Use the theoretical value based on the gauge factors for each gauge.

These methods are evaluated in the next section for interpreting the tensile forces in the base case tests (L/2 = 36cm).

After the uniaxial tension test, the dummy end of each inclusion (Fig. 5.3) is trimmed and the steel is cut to a width of 13.3cm. The APSR specimens are 15.2cm wide (z-direction, Fig. 3.2), and thus, the inclusion has a clearance of approximately 1cm to the

---

[4]The average modulus computed from the results in Figures 5.6 and 5.7 is $\bar{E}$ = 209±31 GPa (i.e. COV = 14.7%). The value of $\bar{E}$ is within 1.0% of the reference modulus of the steel.

sidewalls (Fig. 5.2) which prevents the sharp edge of the steel from damaging the specimen membrane.

5.2.2. Specimen Membrane Preparation and Installation

Figure 5.8 illustrates the preparation of a specimen membrane for an APSR test. Prior to assembly, the centerline of one of the side flaps is marked to indicate where the steel inclusion will be inserted. Then the membrane is glued and leak checked according to the procedure in section 3.2.6.3. A 13.3cm long slit is cut along the centerline of the side flap with a clearance of 0.9cm from the lower edge of the membrane so that the final position of the inclusion will be equidistant from the plane strain faces of the APSR cell.

A rubber collar, made of 0.25mm thick dental dam (Fig. 5.8b), is fitted around the steel inclusion and seals the inclusion to the specimen membrane. The seam between the collar and the inclusion is sealed using a bead of RTV (Fig. 5.8c) spread evenly across the rubber and steel surfaces. After the bead dries (at least 2 hours), the process is repeated on the reverse side with an overlap at the ends of the slit. The integrity of the seam is checked by visual inspection, using backlighting to highlight flaws in the RTV beads. The seam is resealed if light passes through the bead of RTV.

The collar is then bonded to the specimen membrane with latex adhesive. This is accomplished by fitting the membrane over a slotted wooden frame (Fig. 5.8d). A thin coat of latex adhesive is applied in a 2cm wide band around the inclusion opening in the membrane and on the corresponding surface of the rubber. The two surfaces are then bonded on contact after the adhesive has dried (about 10 minutes). Prior to mating of the collar and membrane, two small dabs of RTV are placed on the inside surface of the collar at the ends of the slit to minimize the potential for air leaks. Additional RTV can

be used to seal any wrinkles between the membrane and collar before it is installed in the APSR cell.

Setting up the membrane inside the specimen mold follows essentially the same procedure described in section 3.2.6.2 (for the unreinforced tests). The rear wall of the cell is fitted with the two wedges that form the entry slot through which the reinforcement passes (Fig. 3.8). The rear wall panels and the floor of the cell are lubricated as described in section 3.2.6.2. The membrane and inclusion sit on the floor of the cell, with the inclusion protruding out through the slot in the rear wall (Fig. 5.9a). The specimen mold is inserted into the cell around the membrane (Fig. 5.9b), and the membrane is then pressed against the sides of the mold (Fig. 5.9c). The steel reinforcement is propped clear of the floor by a small (9mm high) piece of rubber block to prevent the sharp edge from rupturing the specimen membrane. The rest of the specimen preparation procedure is identical to that for the unreinforced soil, section 3.2.6.2.

5.2.3. Reinforcement Position Control

Chapter 3 described the need to prevent movement of the inclusion with respect to the rear wall of the cell. This boundary condition is necessary for the external load cell to reflect accurately the maximum tensile force at the center of an inclusion of equivalent length, L (Fig. 5.1). Figure 5.10 illustrates successive refinements of the mechanism used for referencing the position of the reinforcement.

The first APSR base case tests (APSR 22 to 33) used the system in Figure 5.10a. A set of spacer blocks held the proximity sensor fixed to the rear wall of the cell. The target was a piece of steel sheet metal with a pointed tip that passed through a small hole in the reinforcement. The target was bent at the point where it clamped to the cell wall. The

bend gave it a natural spring tension that pushed the pointed end against the leading edge of the reinforcement pin-hole, preventing any lash back in the system. The target thereby registered any motion in the reinforcement relative to the back wall of the cell. Unfortunately, in these early tests the external load cell often picked up very little load. The source of the problem became apparent in test APSR 28, where the feedback loop alternately loaded and unloaded the inclusion without warning between an upper and lower load limit. The control problems were due to the curvature of the surface of the sheet metal target, which gave the proximity sensor an ambiguous reading. At certain points an increase in the inclusion load increased this curvature, which led to unreliable control.

The control problems were greatly reduced by implementing the reference system shown in Figure 5.10b. A 3.2mm thick steel plate replaced the sheet metal target. The surface of this new target was rigid and flat so that the proximity sensor gave a more reliable reading. The target was hinged at one end, and had a pin glued into the other end. A hook connected the end of the pin to a hole in the inclusion. A spring, mounted between the rear wall and the target, maintained tension in the hook. This system referenced the inclusion at a position closer to the rear surface of the sand specimen than the previous one, reducing potential errors due to elongation of the steel between points A and B in Figure 5.10a.

This system was used in tests APSR 35 and 39. Although the load readings appeared to be reasonable for APSR 35, the load cell measured very little load in APSR 39. One explanation for the problem was that compression of the rubber and grease against the inside of the rear cell wall was causing an outward movement of the rear boundary of the specimen, reducing the tensile force in the inclusion at point A.

The final version of the mechanism (Fig. 5.10c) was implemented to eliminate errors associated with compression of the grease and rubber on the inside of the rear wall. The new system references the inclusion position directly to the rear surface of the specimen. The target is a small steel square, approximately 2 x 2cm, with a thickness of 3mm. A shaft passes from this target to a similar steel square that rests inside the specimen. If the specimen compresses the grease on the rear wall of the cell, the target moves outward to compensate for this motion. The proximity sensor is mounted rigidly in the hinged plexiglas linkage, so it references point B directly to the target at the rear boundary of the specimen. Section 5.3.1 shows that this new system can generate slightly higher inclusion load measurements for stress ratios, $R \leq 3.2$ (test 35 vs. 41; Fig. 5.11). However, the most reliable test data show little difference in the performance of referencing systems 2 and 3 (test 35 vs. test 60, Fig. 5.11).

The steel target is installed through the specimen membrane after the mold is positioned (i.e., following Fig. 5.9c). The shaft of the target passes through a pinhole in the specimen membrane. The rubber membrane closes itself around the shaft so the specimen still holds a reliable vacuum. The steel target threads onto the end of the shaft inside the mold. The sand is rained into the mold and the membrane sealed following the same procedure described in section 3.2.6.3.

5.2.4. Additional Preparation Procedures

Most of the APSR tests are conducted in the MIT Geotechnical X-Ray facility so that internal soil strains can be measured using radiography. The doorway into the X-ray room is 80cm wide. Because of this size restriction, the support arch and reinforcement clamping mechanism (Fig. 3.8) must be assembled after the APSR cell has been wheeled into the X-ray room. The final stage of the test set-up is to connect the strain

gauge junction box to a power supply source and to the amphenol connectors from the inclusion. The transducer extension lines from the control cart are linked to the transducers on the cell (Fig. 3.5), and the specimen is ready for shearing.

5.3. Results from Base Case Reinforced Tests

5.3.1. Tensile Stress in the Reinforcement

5.3.1.1. External Load Cell Measurements

The key feature of the APSR cell is the measurement of the tensile load in the reinforcement at the rear wall, a location equivalent to the centerline of an inclusion with half-length, L/2 (Figs. 5.1, 5.2). The tensile load is measured directly by an external load cell as described in section 3.3.1.4 (Fig. 3.10). Figure 5.11a compares measurements of this 'centerline load'[5] as functions of the applied stress ratio, $R = \sigma_1 / \sigma_3$, for three tests, APSR 35, 41, and 60 (Table 5.1) performed using the base case geometry (Fig. 5.2). Test 35 uses position control mechanism 2 (referenced to the external surface of the cell wall; Fig. 5.10b), while tests 41 and 60 use system 3 (Fig. 5.10c) which references the inclusion position to the steel target embedded at the rear boundary of the sand specimen.

The tests show the same characteristic features. During the initial phase of the test ($R < 1.4$) the inclusion is in compression. Tensile loads are transferred to the reinforcement as the surrounding soil is sheared. The tensile loads increase monotonically with the level of applied stress for stress ratios up to $R \approx 8$ ($\phi' = 51^{\circ}$), corresponding to the

---

[5]Figure 5.11 reports the load per unit width of the reinforcement.

peak shear resistance measured externally in the soil. There is excellent agreement in the tensile loads measured in tests APSR 35 and 60. This result suggests that there is little improvement in measurement accuracy for the two position control mechanisms used in these tests (i.e., grease compression is probably a negligible factor). The data from these tests show that centerline loads are well described as a linear function of the applied stress ratio, R. Table 5.2 summarizes results from linear regression analyses which show regression coefficients $r \geq 0.997$ for tests APSR 35 and 60.

The data from test APSR 41 are in good agreement with results from the other two tests for $R \leq 2$ and $R \geq 6$. However, at intermediate stress ratios ($2 \leq R \leq 6$) higher tensile loads are measured, and the data are more reliably characterized by a bilinear relation (with a change in gradient at R = 3.3, cf. Table 5.2). Although there are many factors which can affect the measurements of load transfer (e.g., curvature in the steel or misalignment of the loading yoke, Fig. 3.10), it has proved very difficult to identify which of these factors contribute to the behavior found in test 41. Overall, the data in Figure 5.11a show that repeatable measurements of load-transfer can be obtained in the APSR cell. However, the data from test 41 suggest the need for further refinement of the referencing mechanism.

5.3.1.2. Strain Gauge Measurements

Strain gauges sandwiched inside the inclusion (Figs. 5.3, 5.12a) measure the local strains at four locations in the base case geometry. Figure 5.12b shows the net output voltage, $\Delta V = (V - V_0)$ from the strain gauges[6] in test APSR 35 as a function of time, t. The reference voltage, V_0, is the strain gauge output after the soil is rained into the cell

---

[6]The gage strain is a function of $(V - V_0)$ rather than of the absolute magnitude of the output.

but before the vacuum is applied. The range of the output voltage is very small ($\Delta V \leq 300\mu V$). However, there is very little noise in the output and the data are fairly smooth and well defined. The in-soil confinement does not appear to impair the reliability of the gauges.

At time t = 0 (Fig. 5.12b), the soil was under a vacuum ($\sigma_v \approx 90$ kPa), and $\Delta V = -15$ to -23 μV for all four gauges, indicating that the inclusion was in compression due to the vacuum pressure. The reinforcement was clamped to the support arch while the vacuum was on the specimen. For t = 0 to 20 mins, the air pressure in the cell was increased to $\sigma_3 = 31$ kPa. This increase in compressive force is measured by gauges 2, 3, and 4.[7] At time t = 20 mins, the vacuum was released from the specimen and the four gauges show a steady increase in net voltage with the applied stress ratio, R, on the soil boundaries (Fig. 5.12b) up to failure of the specimen at t = 180 mins. For $t \geq 80$ mins, the four gauges show qualitatively identical trends, with the highest tensile load in gauge 1 (nearest to the rear wall of the cell). All four gauges reach a peak value simultaneously. This behavior indicates that the strains in the inclusion are a direct function of the stress ratio applied to the surrounding soil, and of distance from the end of the inclusion.

In order to compute the inclusion loads from the strain gauge readings, a "zero value" must be selected which represents the strain gauge output at zero tensile load. The point of zero load in the inclusion corresponds to the R-value at which $F_R = 0$ (from the external load cell). Figure 5.13 shows the initial portions of the centerline load-stress ratio measurements (after Fig. 5.11a) from three base case tests. The reference stress

---

[7]A slight decrease in the compression in gauge 1 may reflect the restraining action of the clamp.

ratios, R_o (at zero tension) range from R_o = 1.3 (APSR 35) to R_o = 1.6 (APSR 60). Strain gauge readings at R_o are taken as the zero values (V_{out} unstrained; eqn. 5.2).

A calibration factor is necessary to convert the strain gauge output signal to the tensile strain and elastic stresses in the reinforcement. Figure 5.14 compares the three methods of computing the tensile loads per unit width of reinforcement (kN/m) using:

1. the gauge factor (GF = 2.08) and reference tensile modulus for steel, E = 207 GPa,
2. the "apparent modulus" based on a linear regression analysis of the uniaxial tension test data for each gauge (ranging from E = 207 to 261 GPa; Fig. 5.6), and
3. the actual load vs. wheatstone bridge response for each gauge (Fig. 5.5).

The results for gauge 1 show that these three methods can generate large differences in the apparent loads in the reinforcement. The lowest tensile loads are obtained using the gauge factor and average modulus method. Results using uniaxial (in-isolation) tension data involve uncertainties associated with measured 'offset stress'[8] recorded in Figures 5.5 and 5.6. This offset value is controlled by the curvature of the sheet reinforcement. For steel reinforcement in the APSR cell it is probably more reliable to interpret the data using the gauge factor (for which the manufacturer's estimated error is ±2%) together with the elastic modulus of the steel.

Figure 5.13b shows the load distribution in the reinforcement at an applied stress ratio, R = 6, and compares strain gauge data estimated from the gauge factor and linear regression methods. The results obtained using the gauge factor show a smooth build

---

[8]i.e., the apparent stress at $\Delta V = 0$ (Fig. 5.5) or $\varepsilon_g = 0$ (Fig. 5.6).

up of tensile stress within the reinforcement which tie in closely with the external load cell measurement. In contrast, when the strain gauge data are reduced using linear regression, the largest tensile load occurs at gauge 1 and exceeds the external load cell measurement. The load distribution is significantly less smooth in this second case. In all subsequent tests, the tensile loads are computed from strain gauge data using the gauge factor and average Young's modulus for steel.

Figure 5.11b compares the tensile load distribution measured in tests APSR 35 and 41 at R = 6.[9] The strain gauge measurements from these two tests differ by less than 10%. The results show the excellent repeatability of load transfer measurements which can be achieved in the APSR cell.

Figure 5.15 summarizes the load transfer measurements in APSR 35 as a function of the stress ratio applied to the soil ($R = \sigma_1 / \sigma_3$). The load at each point along the inclusion can be described as a linear function of R. Table 5.2 summarizes the linear regression analyses for the external load cell and strain gauges over the range of $1.4 < R < 8.0$ (where $R_o = 1.4$ and R = 8 occurs at failure) and shows regression coefficients, $r \geq 0.995$, at all locations. Figure 5.15b shows the tensile load distribution in the reinforcement for R = 4, 6, and 8. The tensile loads build to a maximum at the centerline of the inclusion. The gradient of load is highest near the tip of the inclusion, decreasing to a minimum at the point where the inclusion exits the cell.

---

[9]Note: Gauge 2 short circuited in test 41.

5.3.2. Externally Measured Shear Behavior

Figure 5.16 shows a comparison of the external (boundary) measurements for three base case tests: APSR 35, 39, and 41. All three tests reached a peak stress ratio, R = 8.2 to 9.2 at an axial strain, $\varepsilon_{yy} \approx 1.6\%$. The secant moduli, E_{50} = 12,000 to 20,000 kPa. There is excellent agreement in the lateral strains measured in the three tests at all axial strain levels.

Figure 5.17 compares the boundary measurements for a base-case test (APSR 35) with an unreinforced test on dense Ticino sand (APSR 45). The two curves match one another closely up to an axial strain of 1.5%, at which point the reinforced test reaches a peak stress ratio, R = 8.22. The secant moduli, $E_{50} \approx$ 18,000 kPa for both tests. There is a slight discrepancy in the lateral strains from the two tests immediately prior to failure in the reinforced specimen, with the reinforced case showing slightly more dilation. Based on this comparison, however, it appears that the external measurements for reinforced soil are within the zone of reproducibility of the unreinforced tests.

Figure 5.18 shows sketches of specimens with and without inclusions after failure. The general pattern of failure is the same, with a failure wedge forming close to the free face of the specimen. Small differences between the two are probably due to test variability. The failure of the specimen is not affected significantly by the presence of the inclusion, especially since failure occurs through the unreinforced zone.

5.3.3. Internal Soil Strains

One of the effects of the reinforcement is to alter the strain fields within the soil. The following paragraphs describe the soil strains based on X-ray measurements for base

case test APSR 41 and compares results with an unreinforced test (APSR 45) in order to provide some insight on the mechanics of the soil-reinforcement interaction.

5.3.3.1. Strain Distributions

Figure 5.19a, b, c, and d shows the lateral and axial strain contours, within the near and far field radiograph windows, for the reinforced and unreinforced tests at R = 5.56 at which the maximum inclusion load, F_R= 14.6 kN/m (Fig. 5.11). In the unreinforced case, ε_{xx} varies from -0.2 to -0.8%[10] in a uniform fashion across both the near and far field portions of the specimen. In the reinforced test, ε_{xx} is approximately zero over most of the near field X-Ray. The far field shows lateral strain contours concentrated around the tip of the inclusion. Thus, the inclusion has a substantial impact on the distribution of lateral strains within the specimen. The restraining action extends to y = ±14cm from the inclusion near the rear wall of the cell.

The axial strains, ε_{yy}, for the unreinforced case (Fig. 5.19d) vary between 0.5 and 1% over most of the specimen, dropping off near the rear wall of the cell. For the reinforced case (Fig. 5.19c), the inclusion increases the uniformity of the axial strains in the near field, and decreases the magnitude of the strains over most of the X-ray window. The far field axial strains are approximately the same for both cases.

Figure 5.20a shows the lateral strain distribution across the specimen in a place adjacent to the inclusion in the same tests. For the unreinforced test, $\varepsilon_{xx} \approx$ -0.5% and is uniform across the specimen. In contrast, the reinforcement suppresses the tensile strains close

---

[10] Negative lateral strain corresponds to lateral expansion, in accordance with standard soil mechanics convention.

to the rear wall but amplifies the strains in the far field. There is a sharp strain gradient near the tip of the inclusion, and a very low gradient near the rear wall of the cell where the lateral strains $|\varepsilon_{xx}| \leq 0.1\%$. These results are consistent with the measurements of load transfer described in the previous section. The axial strain (ε_{yy}) profile along the inclusion is shown in Figure 5.20b. For the unreinforced test, $\varepsilon_{yy} \approx 0$ near the rear wall of the cell and increases towards the free face of the specimen. This gradient is due to the increased confinement caused by the grease resistance as described in section 4.3.4. For test 41, the reinforcement suppresses the axial strains over much of the inclusion length, but approaches the unreinforced condition close to the free face of the specimen. Finally, the measurements of the maximum shear strain, $\gamma_{max} = (\varepsilon_1 - \varepsilon_3)$ (Fig. 5.20c), show most clearly the concentration of shear strains which occur in the vicinity of the tip of the inclusion.

Strain contours in the soil near failure (R = 8.4 and 8.7 in tests APSR 41 and 45 respectively) are shown in Figure 5.21. The lateral strains in the unreinforced soil (Fig. 5.21b) concentrate in the far field due to the formation of the failure plane and range from ε_{xx} = -2.2 to -3.2% (compared to ε_{xx} = -0.4 to -1.2% in the near field). The reinforcement continues to suppress the lateral strains in the near field (Fig. 5.21a), however, large tensile strains occur at the tip of the inclusion where it intersects the failure plane shown in Figure 5.18.

The axial strains, ε_{yy}, are 20 to 40% less for the reinforced specimen (Fig. 5.21c vs. 5.21d) in the near field but are similar in magnitude to the unreinforced data in the far field. The presence of the inclusion does not affect the axial strain field as dramatically as it does the lateral strain field.

5.3.3.2. Global Strain Analysis

Table 5.3 compares results of the global strain analyses for the reinforced base case test APSR 41 with the unreinforced behavior (APSR 45). The axial strain measurements have standard deviations between 0.10 to 0.15% for both tests. The mean values of axial strain in the near field are 41 to 47% lower in the reinforced test than those observed at the same R values in the unreinforced test. The far field axial strains are 57 to 75% lower.

The average lateral strains in the reinforced test are nearly zero in the near field (ε_{xx} = -0.08 to -0.12%), and increase to approximately 0.5% in the far field. The strains do not change measurably with increasing R for $R \geq 5.56$. In the unreinforced test, the average lateral strains increase steadily with increasing R. The standard deviations of the lateral strain measurements are between 0.14 and 0.17% in the near field for both tests. The far field standard deviations are higher, varying between 0.18 and 0.31%, but are consistent for both tests.

Figure 5.22 compares the strain measurements in test APSR 41 with behavior of the unreinforced sand (interpreted from test APSR 45). The results show clearly the reduction in lateral tensile strain in the near field due to the reinforcement, such that there is a net compression of the soil in the near field ($\varepsilon_{vol} > 0$; Fig. 5.22b). The far field strains in the reinforced test correspond more closely to the behavior of unreinforced sand and exhibit greater dilation at the same axial strain level. Overall,

these results illustrate the important non-homogeneities in the local strain (and stress) field within the reinforced sand specimen due to the load transfer in the inclusion.[11]

5.4. Influence of Sand Density on Load Transfer

Section 4.3.2.2 reports the effects of density on the stress-strain behavior of unreinforced Ticino sand (measured in the APSR cell) for specimens deposited at $D_r \approx$ 30 and 75% (loose and dense specimens, respectively) and sheared at a confining pressure, σ_3 = 31 kPa. The comparisons show that the loosely deposited specimens ($D_r \approx$ 30%): 1) have a lower secant modulus (typically the stiffness is reduced by a factor of 3 at a given shear stress level); 2) have a lower shear strength (R = 5.6 vs. R = 8.7 for dense sand); and 3) exhibit much smaller lateral tensile strain during shearing at a given stress level (i.e., less tendency for dilation). This section presents similar comparisons for the load transfer in loose and dense specimens of Ticino sand.

Figure 5.23a compares the centerline tensile loads measured for inclusions of half-length, L/2 = 36cm in loose and dense Ticino sand (tests APSR 46 and 35, respectively) as functions of the applied stress ratio, R. The tensile loads measured for the loose specimen are typically 20-25% lower than those found in the dense, base case test (APSR 35) at a given stress ratio. The load transfer for the loose specimen is well characterized as a linear function of R, with an offset stress ratio, R_o = 1.8 (zero tensile load) and regression coefficient, r = 0.997. Differences in the tensile loads for the loose and dense specimens can be summarized by the offset stress ratio (R_o = 1.4 and 1.8,

---

[11] Although the boundary measurements in these same tests are not affected by the inclusion (Fig. 5.17).

respectively) and by the slope of the load transfer gradient (dF_R/dR = 3.27 and 2.87, respectively). The tensile load distribution within the inclusion is obtained from strain gauge measurements using the offset stress ratio, R_o, gauge factor, GF, and average elastic modulus for the steel sheet, as described in section 5.2.1. Figure 5.23b compares the load distribution in the loose[12] and dense specimens at a stress ratio, R = 4.0. These data are consistent with the centerline measurements and show that the tensile loads in the loose specimen are approximately 40% smaller than those obtained for dense Ticino sand.

Figure 5.24 compares the boundary measurements for reinforced (APSR 46) and unreinforced (APSR 37) tests on loose Ticino sand. The shear stress-axial strain behavior for the two tests are identical up to ε_{yy} = 3%. However, the reinforced specimen exhibits a higher shear resistance and fails at R ≈ 7.2 ($\phi' \approx 49^o$) compared to R = 5.6 for the unreinforced specimen (Fig. 5.24a). The lateral strain curves (Fig. 5.24b) match each other at small axial strains ($\varepsilon_{yy} < 0.2\%$). As shearing continues, the reinforced specimen exhibits lower lateral tensile strains at a given level of axial strain (or shear stress). At the point where the deviatoric stress curves diverge, the lateral strain in the reinforced specimen is 20% less than for the unreinforced case.

Overall, the inclusion has little effect on the boundary shear stress-axial strain measurements, but a noticeable effect on the externally measured lateral strains at the centerline of the specimen. At a stress ratio, R = 5.6, the lateral strain in the reinforced test was -1.9%, as opposed to -2.4% for the unreinforced sand. The presence of the

---

[12]There are only three data points from the loose test because gauges 1 and 2 shorted out. The full length inclusion had been used in six tests. Due to repeated unload/reload cycles, the strain gauge wires may have ruptured the electrical tape that protected them from the surrounding steel.

reinforcement has a greater effect on lateral strains in the loose specimen than it did on the dense specimen discussed earlier (cf. Fig. 5.17).

Figure 5.25 compares the failure surfaces for the loose sand with and without the inclusion. No failure surfaces were observed in the unreinforced specimen, while the reinforced test produced many intersecting failure planes. It should be noted that the reinforced specimen was subjected to higher shear stress (R = 7.2 vs. 5.6) and axial strain levels (ε_{yy} = 6.3 vs. 3.9%) than the unreinforced test. The most prominent failure planes in the reinforced test barely overlap the tip of the inclusion and extend farther back into the specimen than in the base case tests for dense sand (Fig. 5.18). The presence of several failure planes in the loose specimen differ significantly from the single predominant slip surface observed in the tests with dense Ticino sand.

5.5. Influence of Reinforcement Length on Load Transfer

One of the key design objectives of the APSR cell is the capability for measuring the centerline tensile loads for inclusions of different lengths. These measurements can then provide a basis for understanding the inclusion length effect on load transfer. This section describes the results of tests performed on inclusions with half lengths, L/2 = 9cm to 36cm, in dense and loose Ticino sand ($D_r \approx 75\%$ and 30%, respectively; Table 5.1).

Figure 5.26a summarizes the centerline tensile loads, measured by the external load cell, for steel sheet inclusions with L/2 = 9, 18, 27, and 36cm in dense Ticino sand. The centerline tensile load in the shortest of these inclusions (L/2 = 9cm) is approximately 33±5% of that reported previously for the base case geometry (L/2 =

36cm). This result emphasizes the importance of inclusion length on load transfer behavior measured in small scale laboratory tests. Although there is some non-linearity in the data (notably in test APSR 64, L/2 = 18cm), the centerline tensile loads can be described approximately by linear functions of the stress ratio, R, for $R \leq 8$.

Table 5.4 summarizes the linear regression analyses for these tests which show offset stress ratios, R_o = 1.3 to 1.6 and load transfer gradients (dF_R/dR) which decrease from 3.56 at L/2 = 36cm to 0.94 at L/2 = 9cm. The regression coefficients, $r \geq 0.99$ for all tests except APSR 64 ($r = 0.975$), and confirm that the linear relation is adequate for characterizing the load transfer behavior.

Tests performed in loose Ticino sand ($D_r \approx 30\%$) at L/2 = 18cm and 36cm (Fig. 5.26b) show qualitatively similar trends. The accumulation of centerline loads is approximately linear for $R \leq 6$ (Table 5.4). At R = 6, the tensile force in the 36cm inclusion, F_R = 12.0 kN/m (approximately 80% of the load developed for the same length in dense sand), while 18cm reinforcement carries F_R = 4.53 kN/m (equivalent to 57% of the load for the same geometry in dense sand).

Figure 5.27 compares the contours of the strain components ε_{xx} and ε_{yy} at R = 4.0 in loose Ticino sand for a specimen with an 18cm steel inclusion and an unreinforced specimen. In the unreinforced test, the strain fields are relatively uniform across the specimen. In contrast, the short reinforcement (L/2 = 18cm) suppresses the lateral and axial strains in the near field but amplifies the shear strains close to the tip of the inclusion.[13] These results confirm that the mechanism of load transfer is similar for

---

[13]These results are qualitatively similar to those shown in Figure 5.20 for the base case tests on inclusions of length L/2 = 36cm.

inclusions of different lengths in the APSR cell. The volume of soil affected by the inclusion is a function of its length. Previous results have shown that boundary measurements of the stress-strain response are not affected significantly for inclusion of length, L/2 = 36cm. Thus, the external stress-strain behavior for the shorter inclusions (L/2 = 9 to 27cm) is practically identical to measurements for the unreinforced sand reported in Chapter 4.

5.6. Conclusions

This chapter describes measurements of load transfer in the APSR cell for linearly elastic steel sheet inclusions in dry Ticino sand. The main focus of this work is the refinement of test instrumentation and procedure to achieve reliable and repeatable measurements of the centerline tensile loads (i.e., the force in the inclusions at the rear wall) in the APSR cell using an external load cell. The chapter also documents the measurement of tensile loads from strain gauges within the reinforcing inclusion.

Comprehensive interpretation of APSR tests for the 'base case' geometry, comprising an inclusion of length L/2 = 36cm sheared in dense Ticino sand (D_r = 75%) at a confining stress, σ_3 = 31 kPa, shows the following:

1. Reliable and repeatable measurements of centerline tensile loads requires very precise referencing and position control at the exit point from the APSR cell. The position control mechanisms described in this chapter (Fig. 5.10b and c) achieve reliable measurements for steel sheet inclusions. However, further refinement is recommended to develop a more robust measuring system.
2. Local measurements of reinforcement stresses are difficult to interpret due to uncertainties in the 'zero strain' readings. For steel sheet reinforcements,

tensile forces are estimated by using: a) external load cell measurements to determine the point of zero longitudinal strain in the reinforcement, b) the gauge factors to compute local strains, and c) the known elastic modulus of steel to compute the elastic stresses.

3. Radiographic measurements of soil strains within the APSR cell provide insight into the mechanisms of load transfer. The data show that the steel sheet reinforcement suppresses lateral and axial strains in the soil adjacent to the inclusion. However, there is a significant amplification of the shear strain levels close to the tip of the inclusion.
4. The presence of the reinforcement has only a secondary effect on the external (boundary) measurements of stress-strain-strength behavior for the composite soil element. This behavior is due primarily to the small volume fraction of the soil specimen affected by the reinforcement in the APSR cell.

A series of APSR tests (Table 5.1) was performed to study the influence of sand density and inclusion length on the load transfer for steel sheet inclusions sheared in Ticino sand at a confining stress, $\sigma_3 = 31$ kPa. In all of these tests, the load transfer can be characterized by a linear relationship between the tensile load and the stress ratio, $R = \sigma_1 / \sigma_3$, applied on the soil specimen. For stress ratios $R < R_o$ (where R_o is the 'offset stress ratio'), the inclusion undergoes compression, while for $R > R_o$, the accumulation of tensile load, F_R, can be expressed by a constant transfer gradient dF_R/dR. The results show the following:

1. Reinforcement tensile loads in loose Ticino sand ($D_r \approx 30\%$) are 20 to 50% lower than those measured at the same stress ratio and geometry for dense sand specimens ($D_r \approx 75\%$).

2. The centerline tensile load increases significantly with the length of the inclusion. Loads measured for a 9cm inclusion were less than 30% of the magnitude of those obtained for a 36cm inclusion. These length-scale effects represent an important capability of the APSR cell and are essential for understanding reinforcement stresses in field situations as shown in Chapter 6.

Test No.	Relative Density (%)		Inclusion Length (cm)				Test Geometry		
	Dense	Loose	Full	3/4	1/2	1/4	No. Strain Gauges	1 or 2 ply	Referencing System[2]
APSR 35	75		36				4	2	2
APSR 39	73		36				4	2	2
APSR 41	75		36				3	2	3
APSR 60	75		36				-	1	3
APSR 62	75			27			-	1	3
APSR 43	73				18		-	2	3
APSR 64	75				18		-	1	3
APSR 44		32			18		-	2	3
APSR 46		25	35				2	2	3
APSR 47		23				9	-	2	3
APSR 65	75					9	-	1	3
APSR 48	78					10	-	2	3

Notes: 1. All inclusions were 0.25mm thick steel sheet, 13.3cm wide.

2. See Figure 5.10

Table 5.1: Summary of APSR Tests with Steel Inclusions

Strain Gauge	Distance from Centerline (cm)	APSR 35		APSR 41		APSR 60	
		Slope F_R/R (kN/m)	Least Squares Coefficient, r	Slope F_R/R (kN/m)	Least Squares Coefficient, r	Slope F_R/R (kN/m)	Least Squares Coefficient, r
Load Cell	0	3.27	0.9954	3.30	0.988	3.56	0.998
SG1	5.5	3.18	0.9971	3.35	0.988	-	-
SG2	13.1	3.09	0.9974	-	-	-	-
SG3	20.8	2.58	0.9989	2.40	0.996	-	-
SG4	28.4	1.82	0.9988	1.68	0.994	-	-

Table 5.2: Linear Regression Analyses of Tensile Loads in Inclusions as Functions of the Applied Stress Ratio for the Base-Case Test Geometry

R	Axial Strain, ε_{yy} (%)								Lateral Strain, ε_{xx} (%)							
	Unreinforced (APSR 45)				36 cm Steel (APSR 41)				Unreinforced (APSR 45)				36 cm Steel (APSR 41)			
	Near Field		Far Field		Near Field		Far Field		Near Field		Far Field		Near Field		Far Field	
	Mean	S.D.	Mean	S.D.	Mean	S.D.	Mean	S.D.	Mean	S.D.	Mean	S.D.	Mean	S.D.	Mean	S.D.
3.33	0.16	0.12	0.30	0.12	-	-	-	-	-0.08	0.16	-0.16	0.20	-	-	-	-
5.56	0.39	0.15	0.74	0.12	0.23	0.10	0.32	0.14	-0.35	0.15	-0.63	0.18	-0.08	0.16	-0.48	0.23
7.78	0.59	0.14	1.46	0.12	0.31	0.11	0.36	0.14	-0.42	0.14	-1.68	0.23	-0.12	0.15	-0.49	0.23
Post Failure	0.71	0.15	2.01	0.17	0.42	0.11	0.55	0.15	-0.57	0.17	-2.51	0.31	-0.11	0.16	-0.50	0.26

Table 5.3: Comparison of Internally Measured Strains for a Reinforced and Unreinforced Test with Dense Ticino Sand

Test No.	Inclusion Length (cm)	Relative Density D_r	Externally Measured Tensile Force		
			R_o	Slope L/R (kN/m)	Least Squares Coefficient, r
35	36	75%	1.3	3.27	0.995
41	36	75%	1.3	3.30	0.988
60	36	75%	1.6	3.56	0.998
62	27	75%	1.6	2.67	0.992
64	18	75%	1.4	1.42	0.975
65	9	75%	1.6	0.94	0.989
46	35	25%	1.8	2.87	0.997
44	18	32%	1.8	0.88	0.970

Table 5.4: Linear Regression Anlayses of Externally Measured Inclusion Loads vs. Applied Stress Ratio

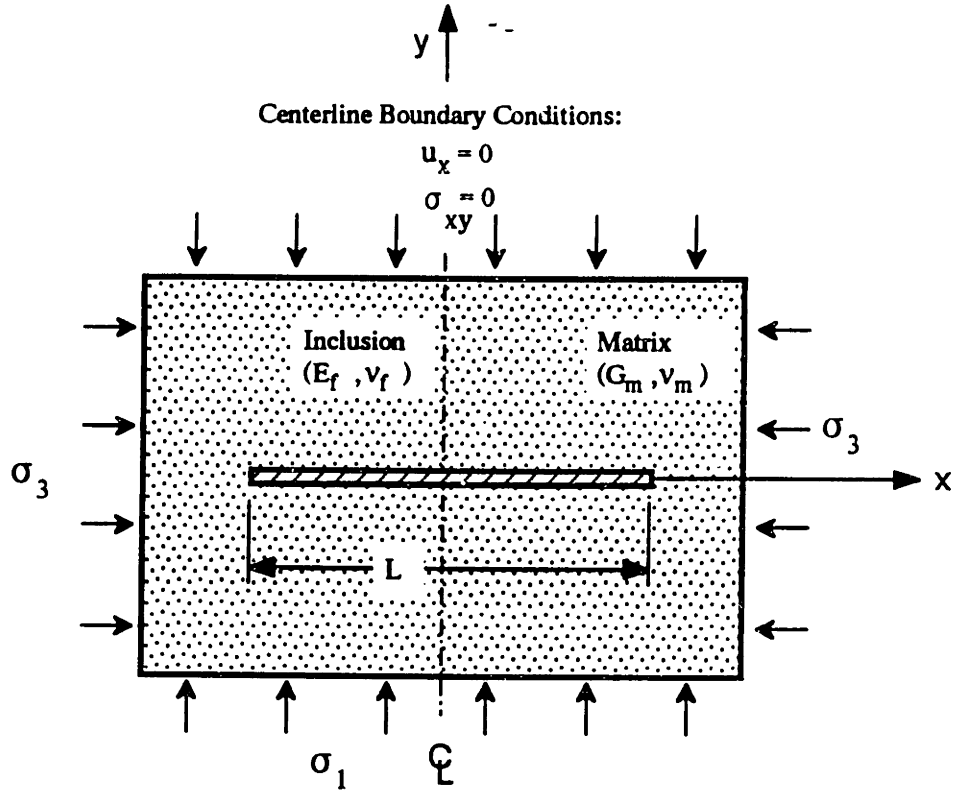

Figure 5.1: Ideal Reinforced Block

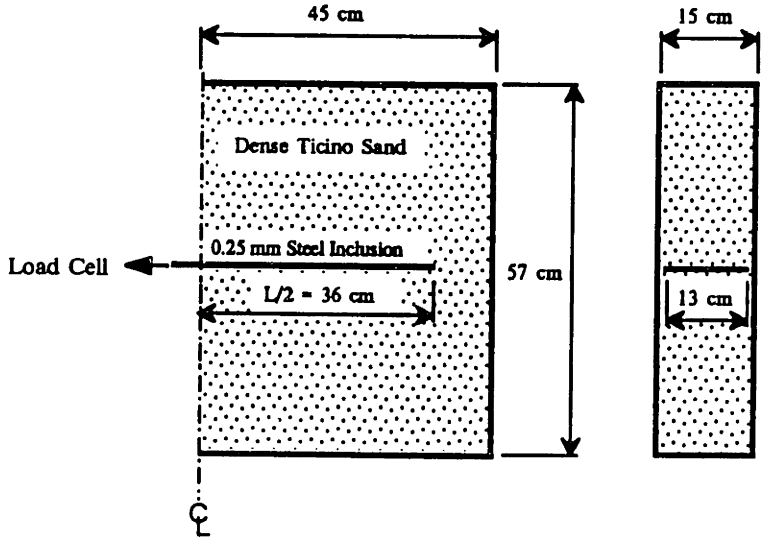

Figure 5.2: Base-Case Geometry

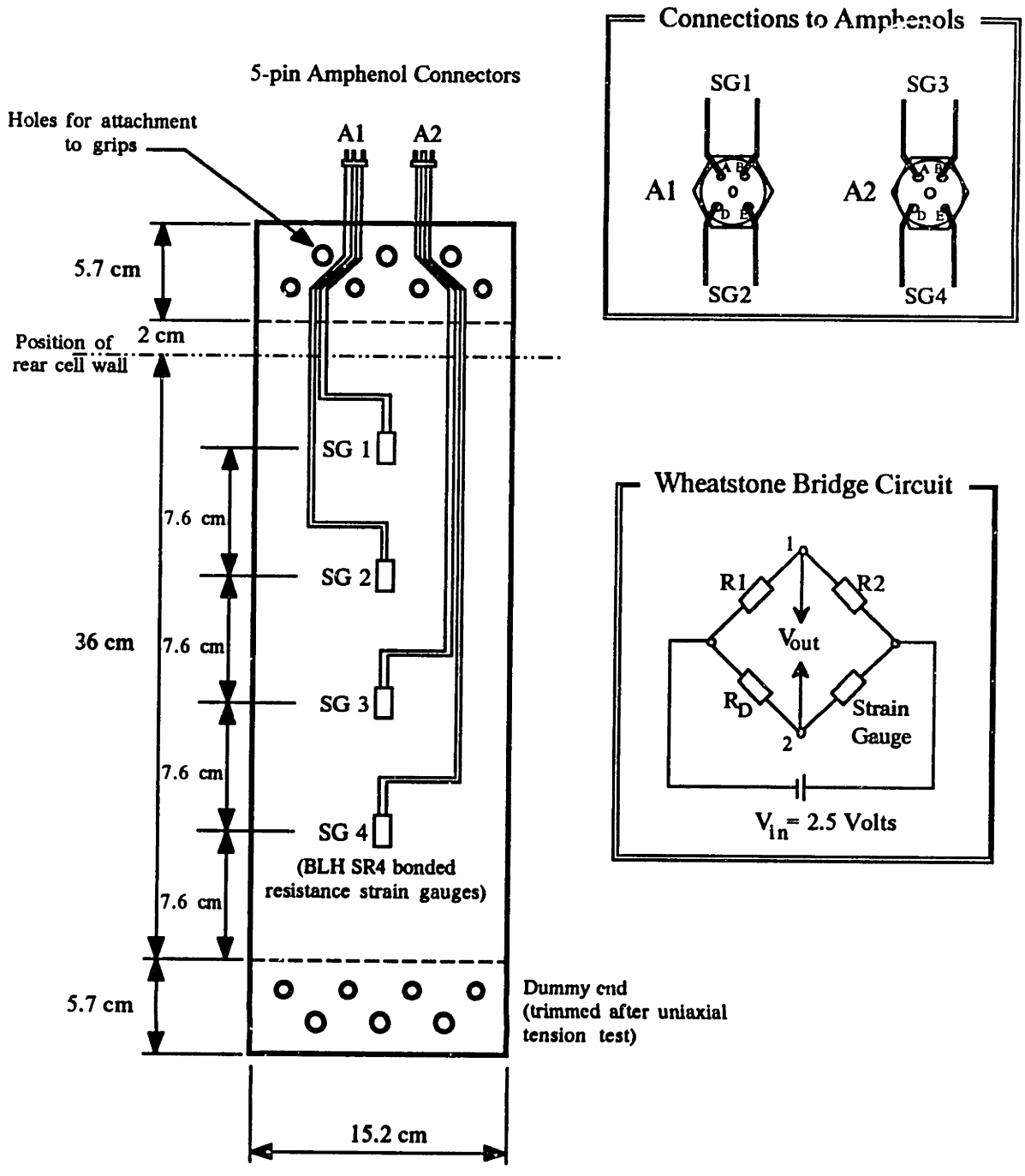

Figure 5.3: Schematic of the Instrumented Steel Inclusion for the Base Case Tests

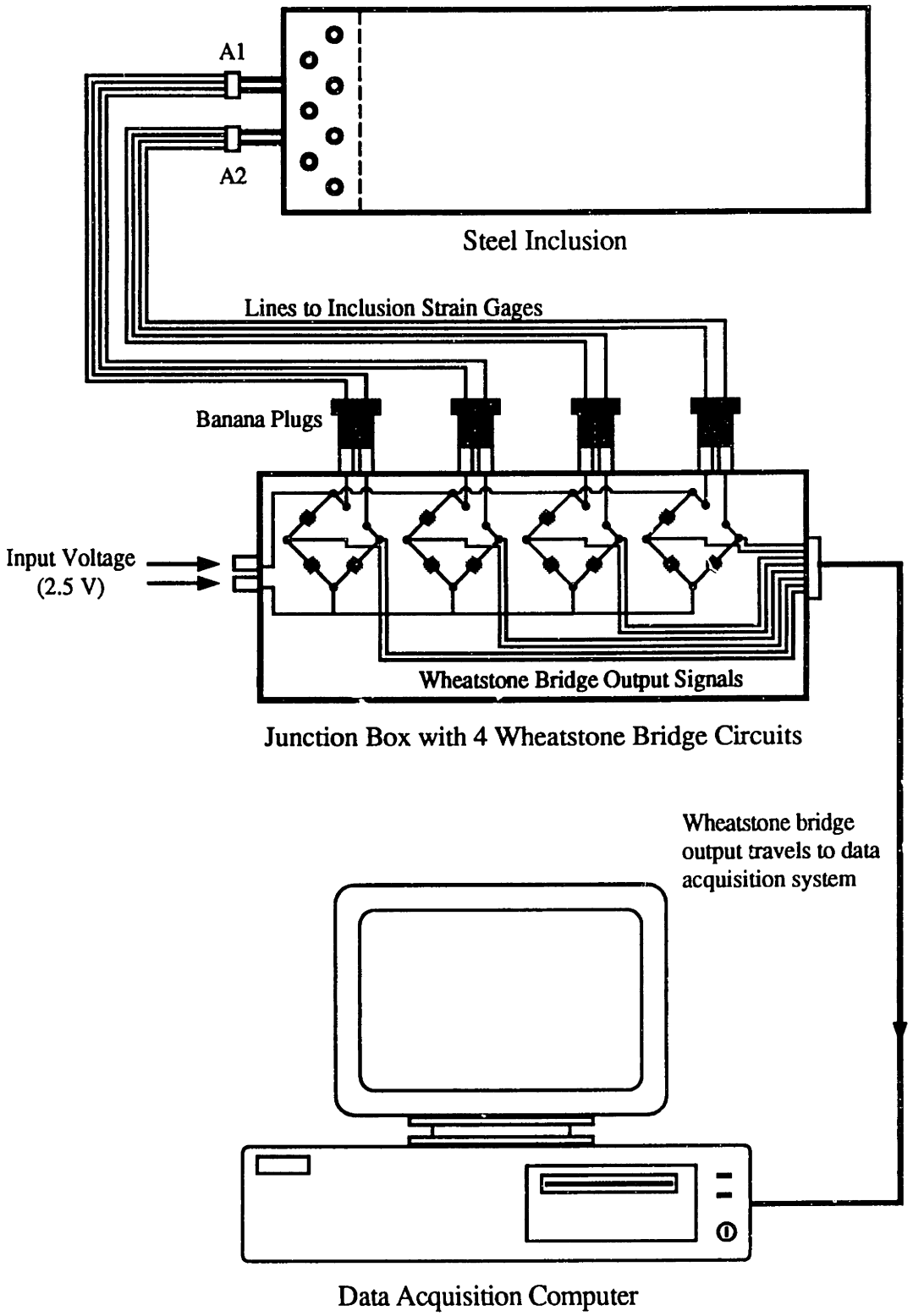

Figure 5.4: Hardware to Measure and Record Inclusion Strains

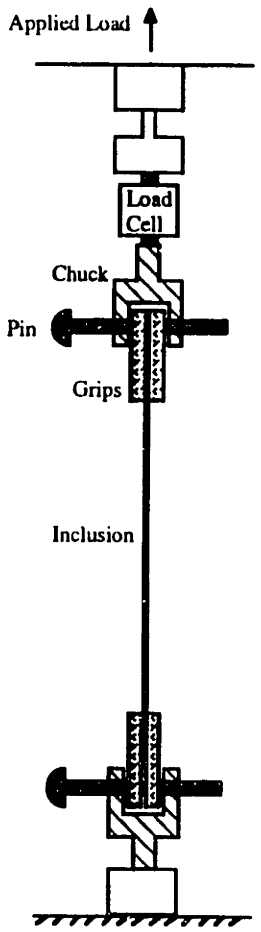

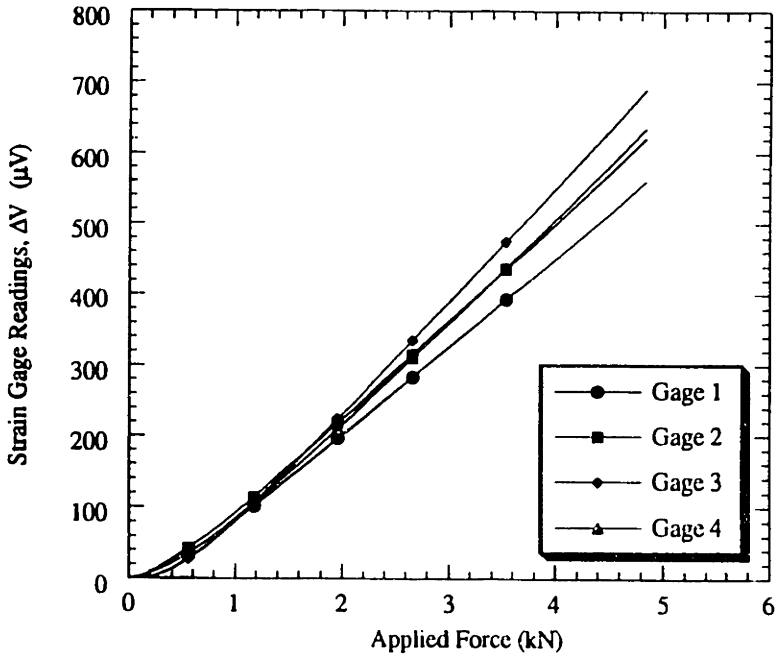

(a) In-isolation test schematic

(b) Wheatstone bridge output during in-isolation test

Figure 5.5: In-isolation Test of an Instrumented Steel Inclusion

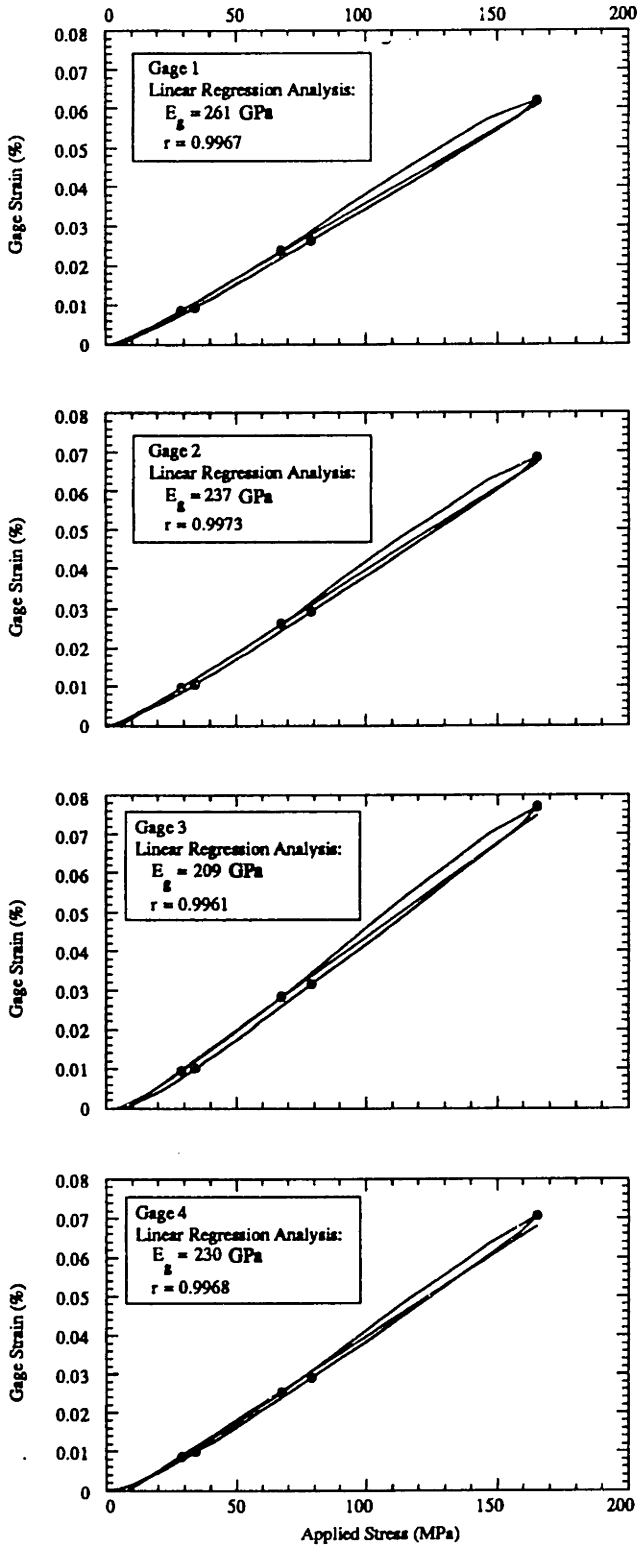

Figure 5.6: Strain Gage Readings vs. Applied Load for Inclusions with Gages Mounted on Convex Steel Surface

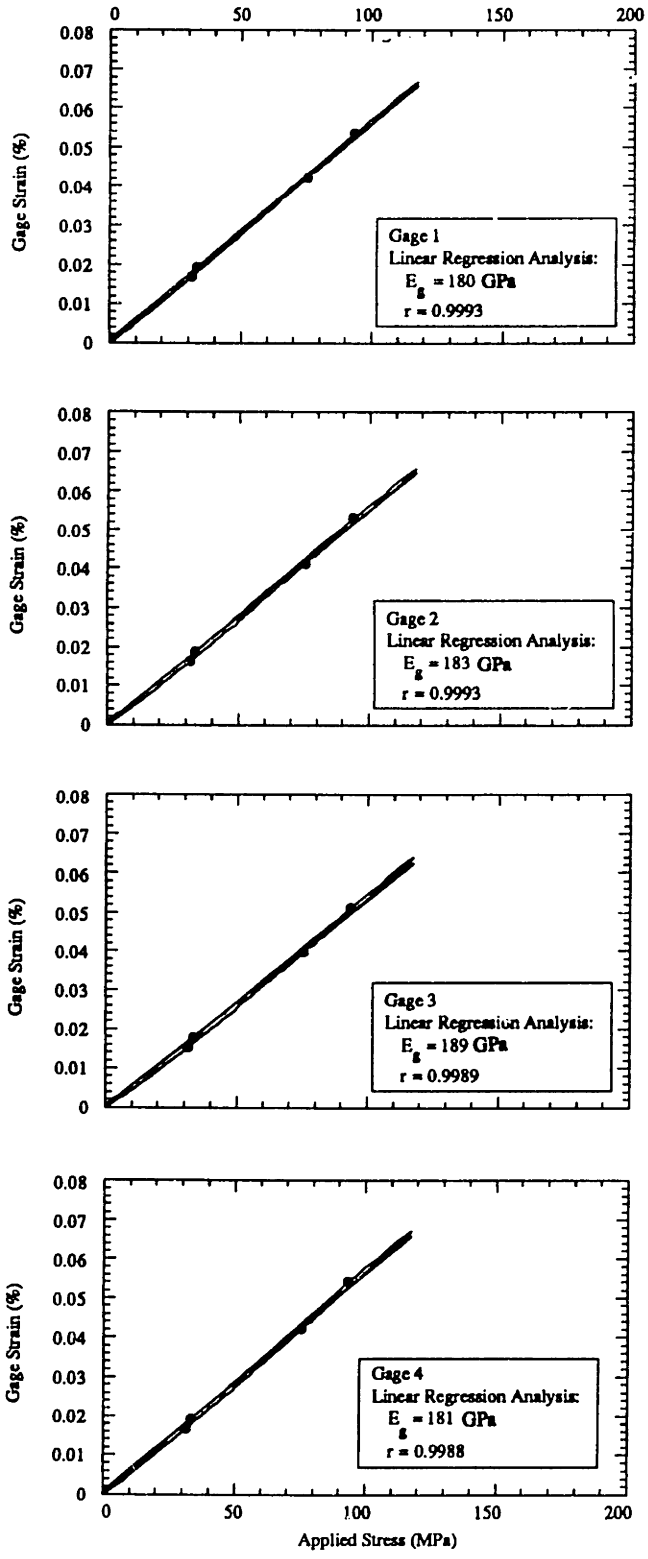

Figure 5.7: Strain Gage Readings vs. Applied Load for Inclusions with Gages Mounted on Concave Steel Surface

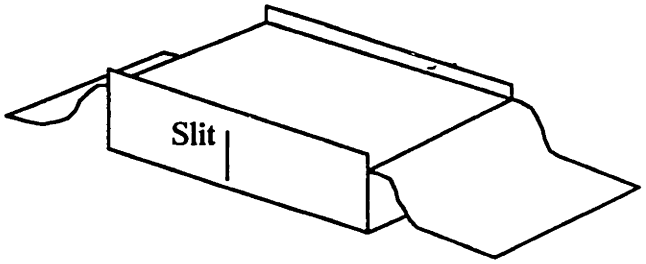

(a) Make a slit in the specimen membrane

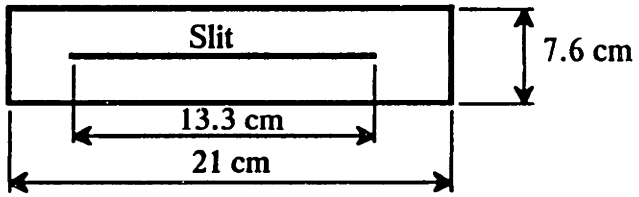

(b) Cut a rubber collar from 0.25 mm thick dental dam

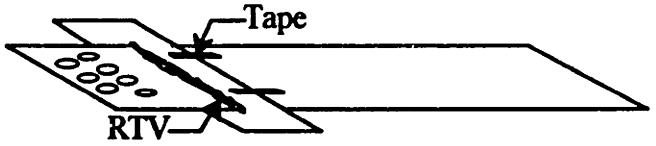

(c) Seal rubber collar to inclusion with RTV (repeat on reverse side)

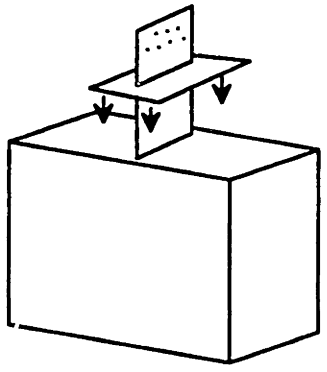

(d) Apply latex adhesive to collar and specimen membrane, and bond the two together

Figure 5.8: Specimen Membrane Preparation for Reinforced Tests

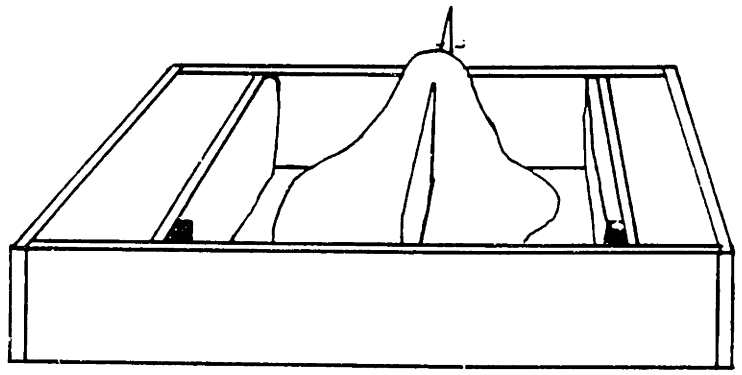

(a) Membrane and inclusion inside cell

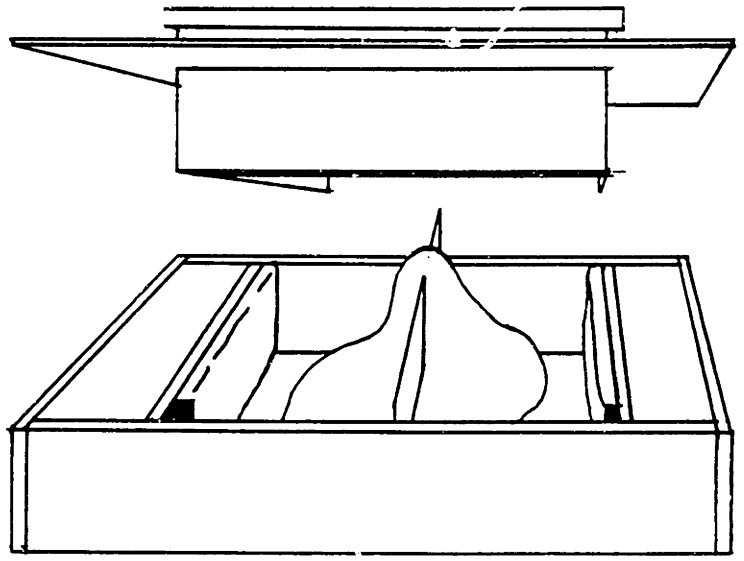

(b) Insertion of specimen mold

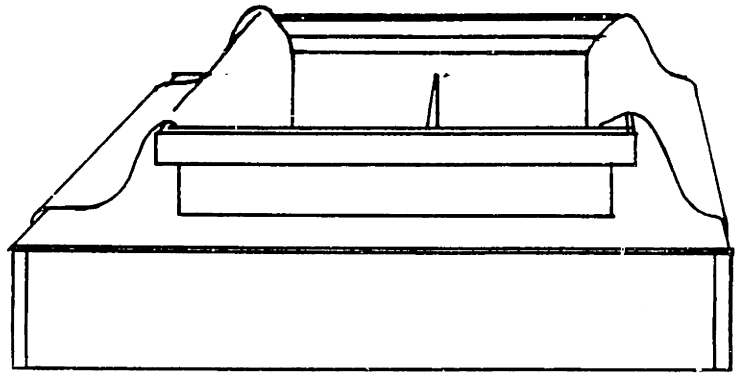

(c) Specimen membrane in place

Figure 5.9: Specimen Membrane Installation

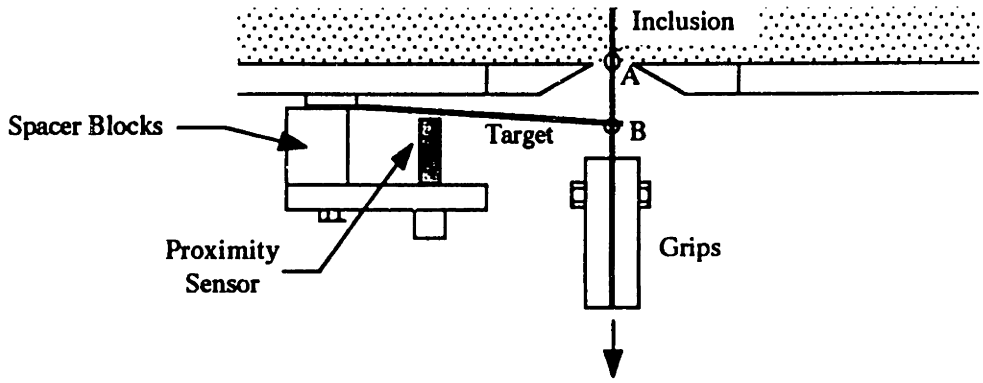

(a) External cell wall position control mechanism, system 1

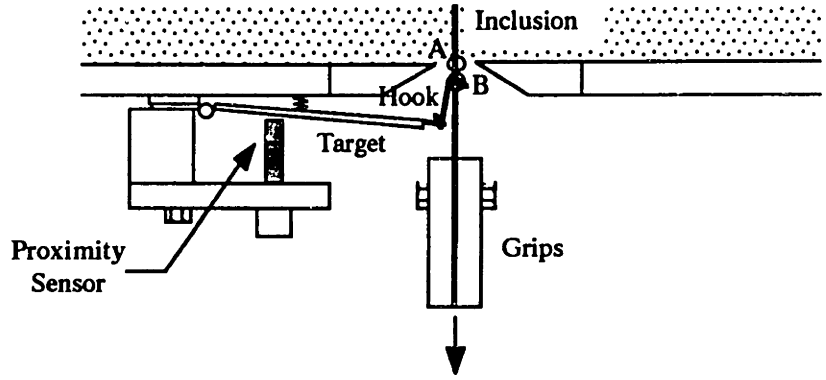

(b) Improved external cell wall position control mechanism, system 2

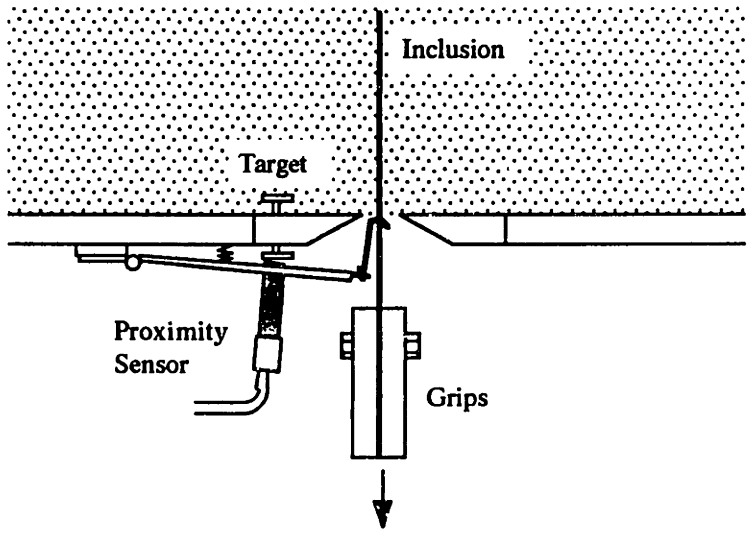

(c) Internally referenced position control mechanism, system 3

Figure 5.10: Methods for Referencing the Inclusion Position

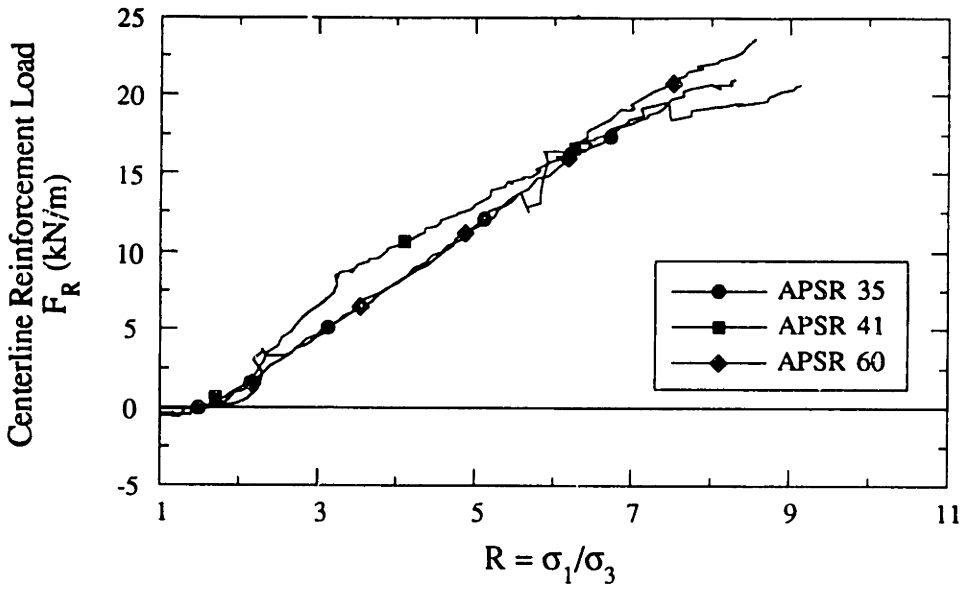

(a) Centerline loads (external load cell)

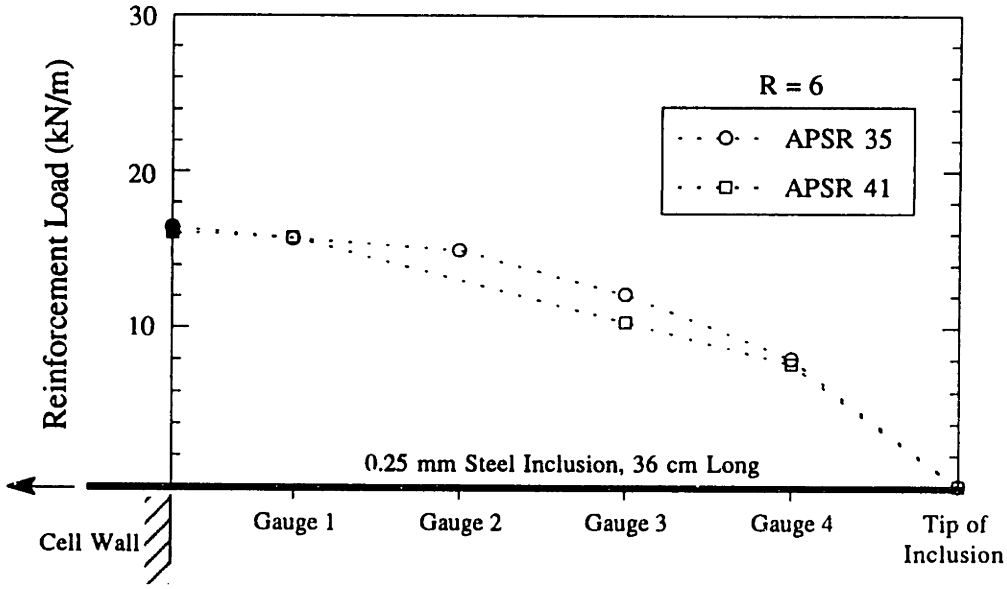

(b) Load distribution (external load cell and strain gauges)

Figure 5.11: Comparison of Load Pickup Measurements for Base-Case Tests in Dense Ticino Sand

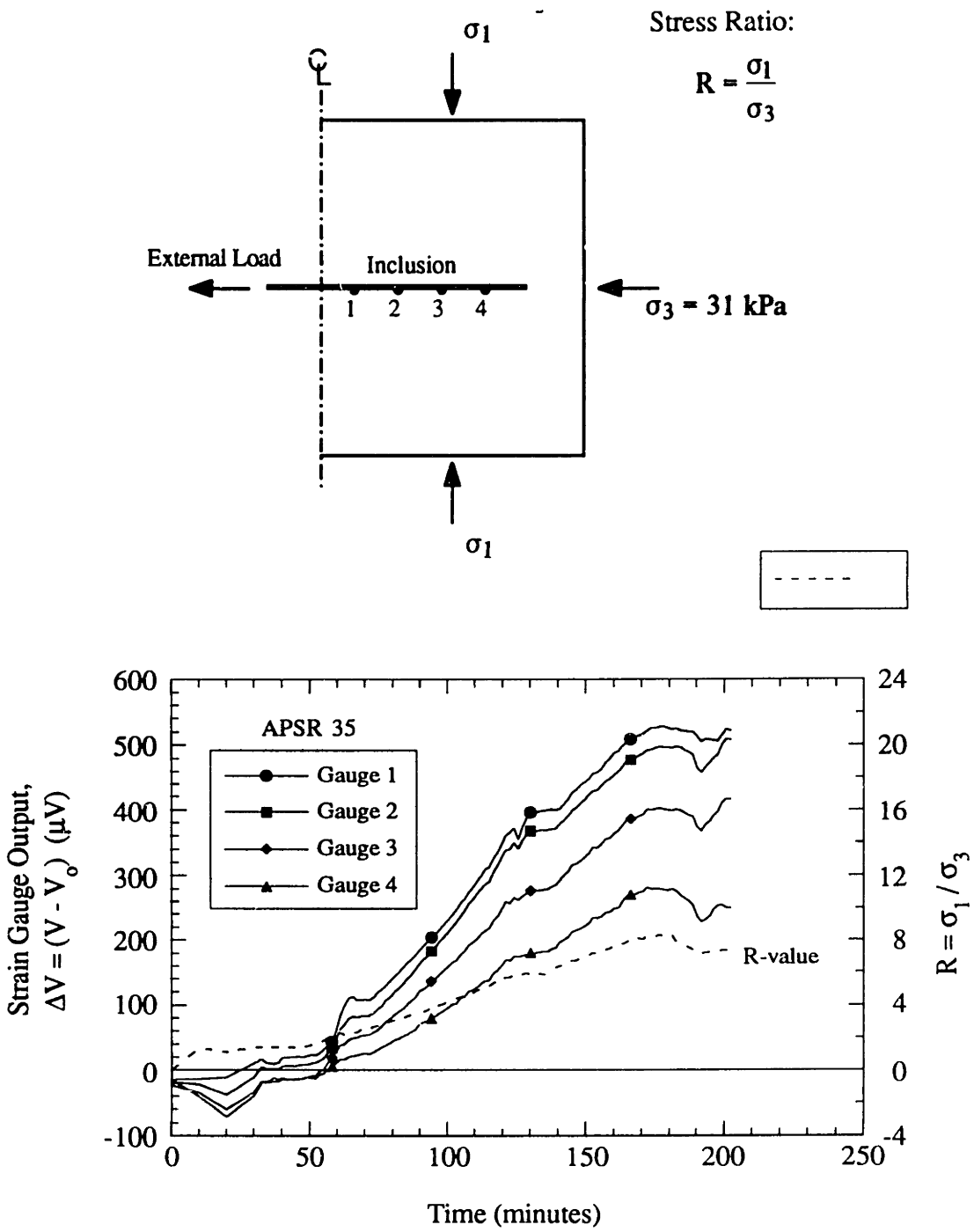

Figure 5.12: Strain Gage Output during Shear, APSR 35
Dense Ticino Sand, 36 cm Steel Reinforcement

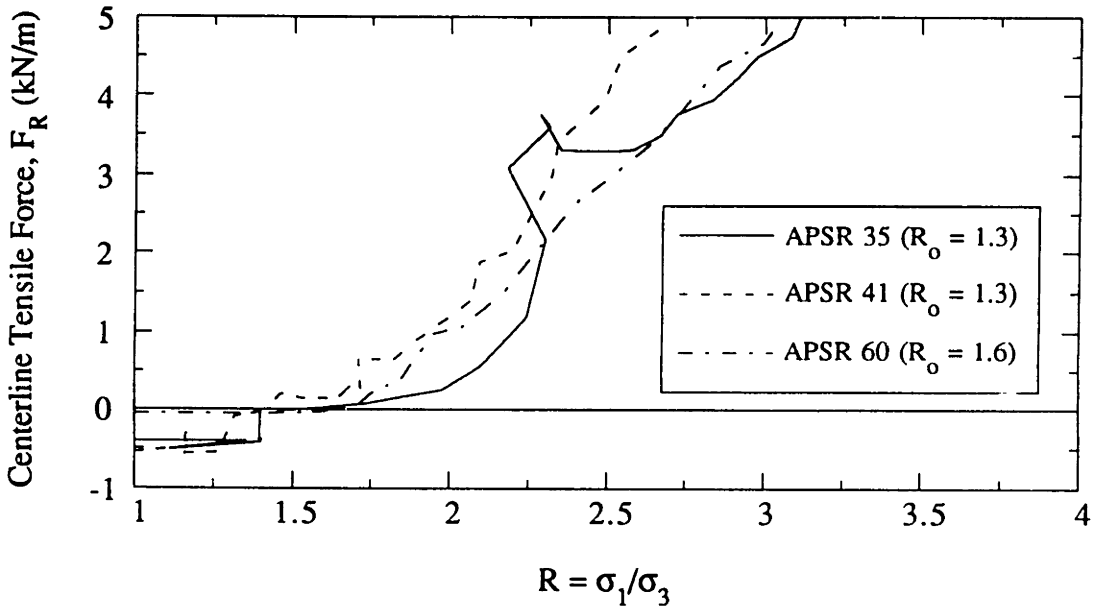

Figure 5.13: Initial Load Pickup for Base-Case Tests

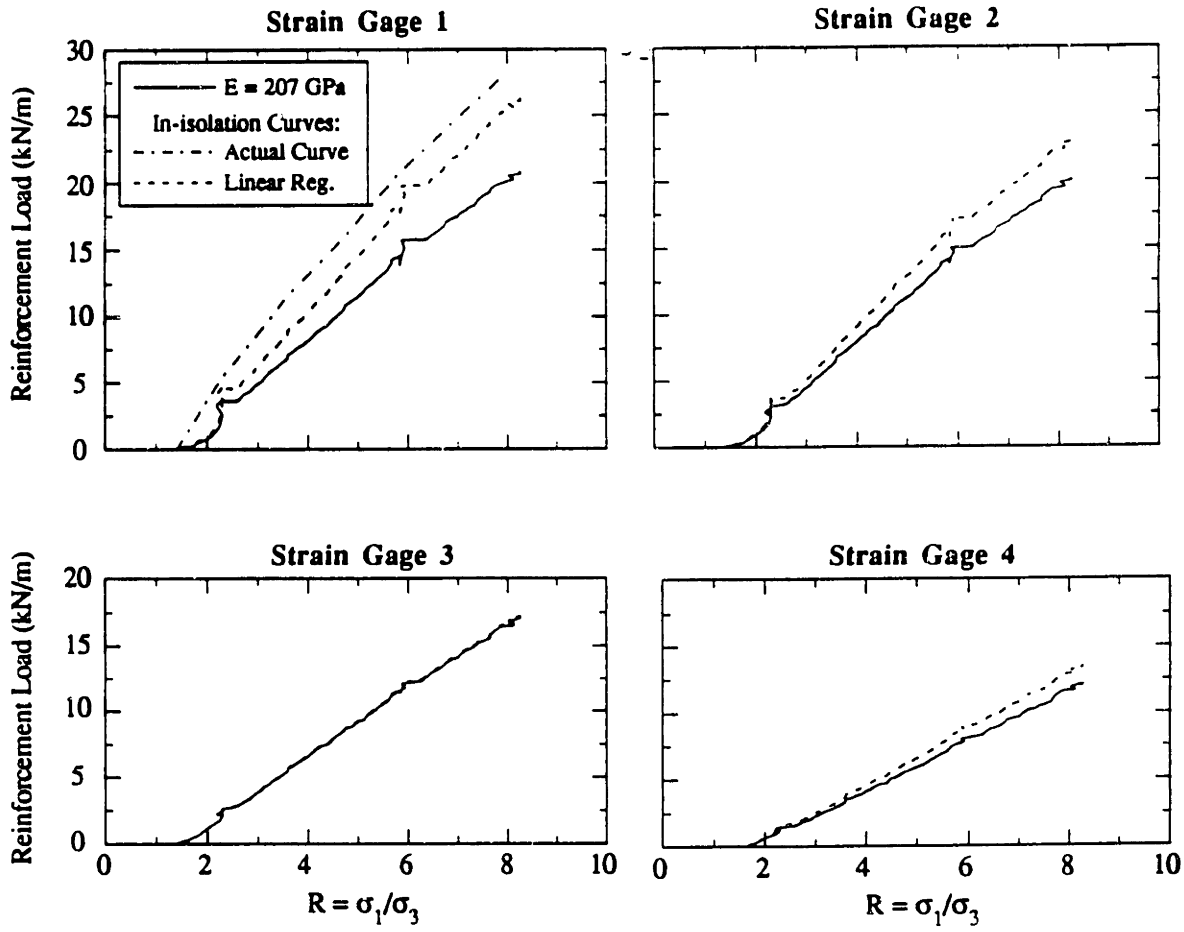

(a) Response from individual strain gauges

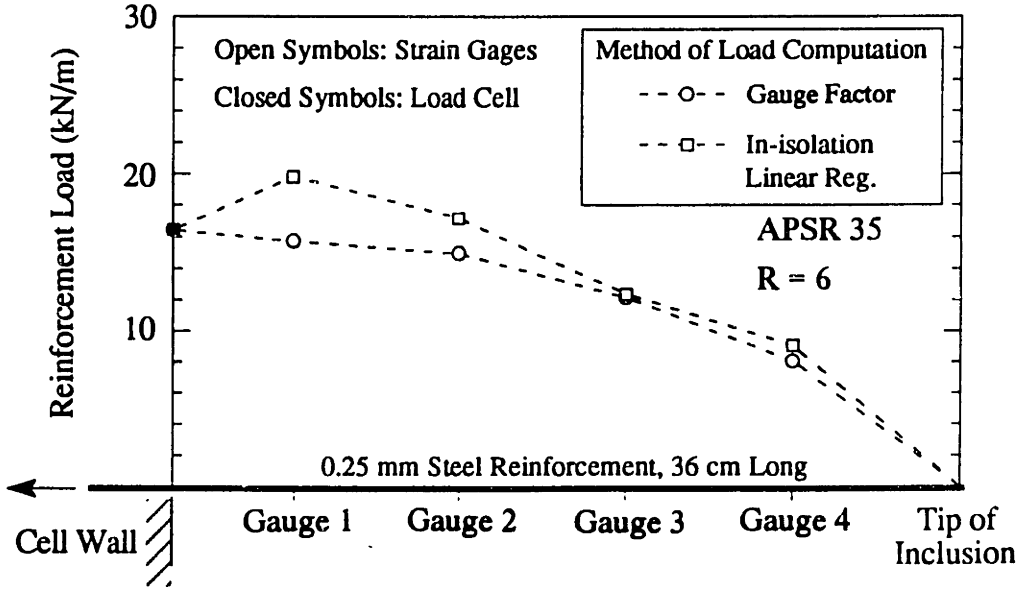

(b) Load distribution

Figure 5.14: Comparison of Reinforcement Tensile Force Calculations

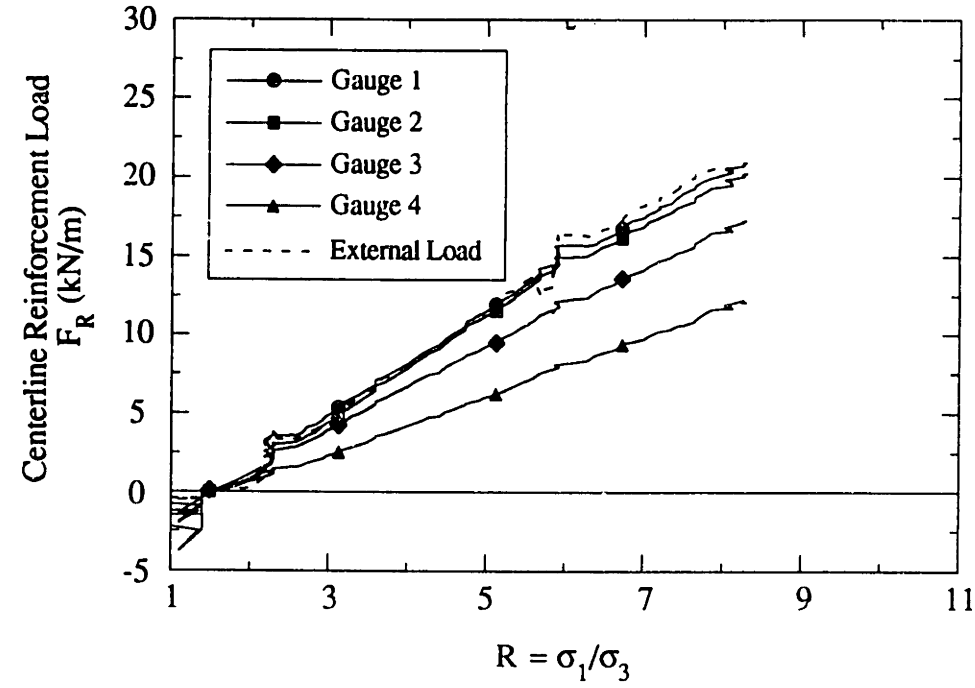

(a) Centerline loads (external load cell)

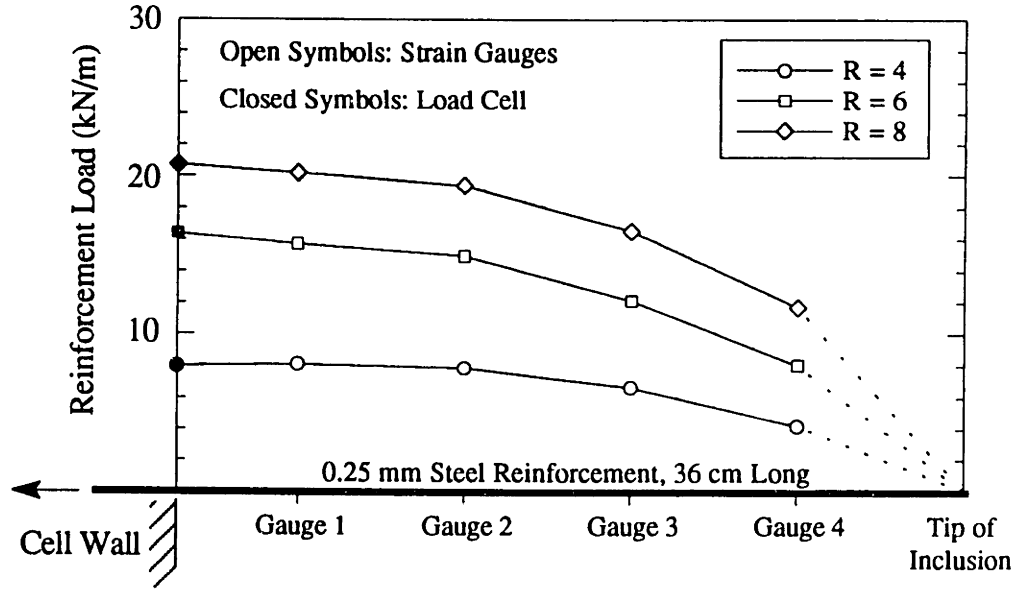

(b) Load distribution (external load cell and strain gauges)

Figure 5.15: Load Pickup in Inclusion for Base-Case Test APSR 35

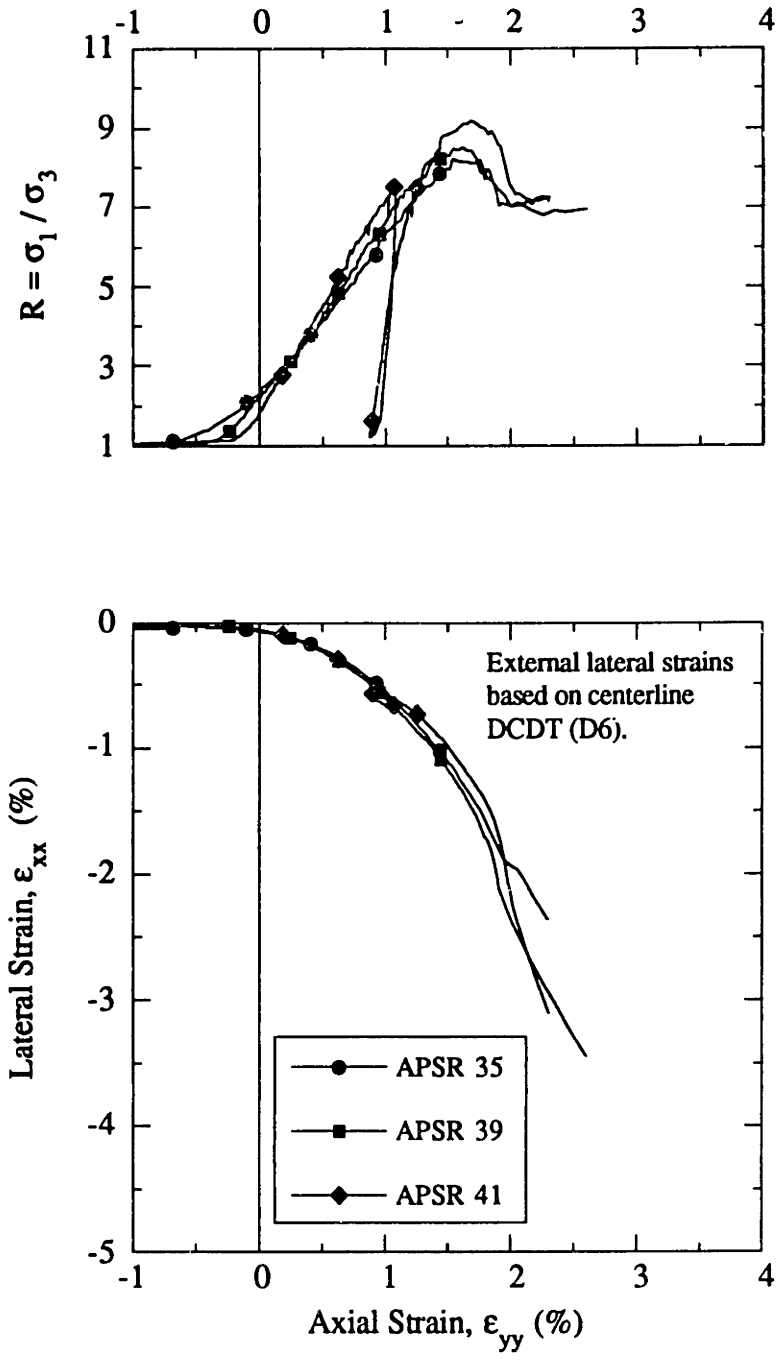

Figure 5.16: Externally Measured Shear Behavior from Three Base Case Tests

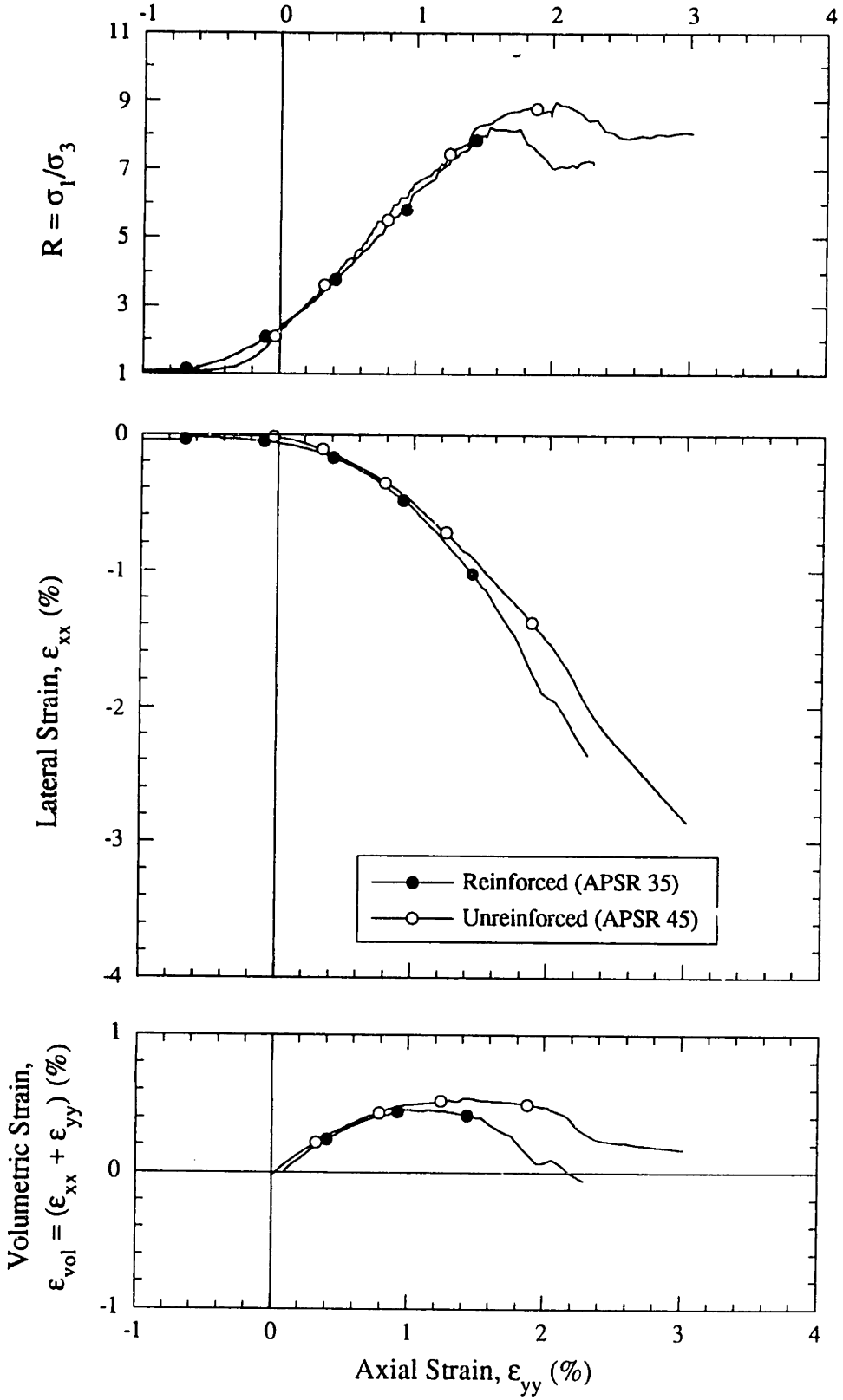

Note: Lateral strains measured at centerline of specimens by transducer D6 (Fig. 3.4)

Figure 5.17: Comparison of Externally Measured Shear Behavior for a Base-Case and Unreinforced Test

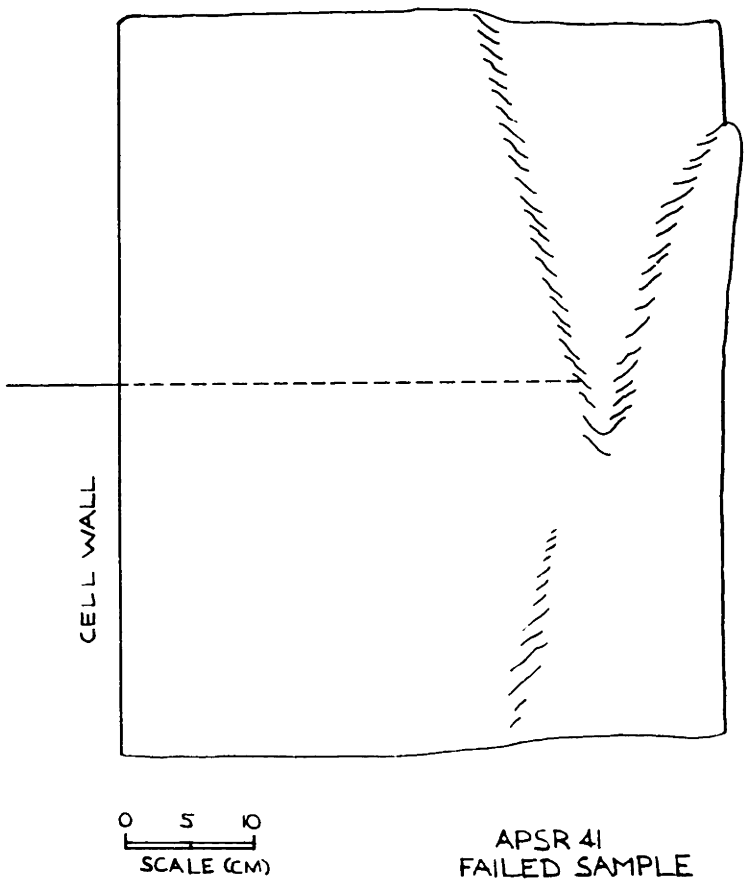

(a) Specimen with a 36cm steel inclusion

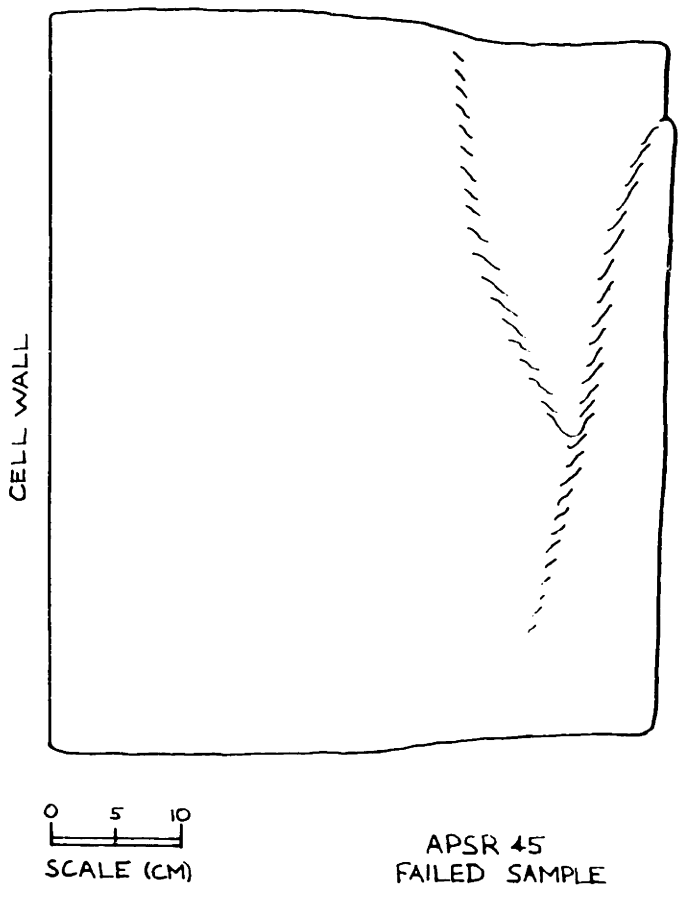

(b) Unreinforced specimen

Figure 5.18: Failure Surfaces in Dense Ticino Sand Specimens

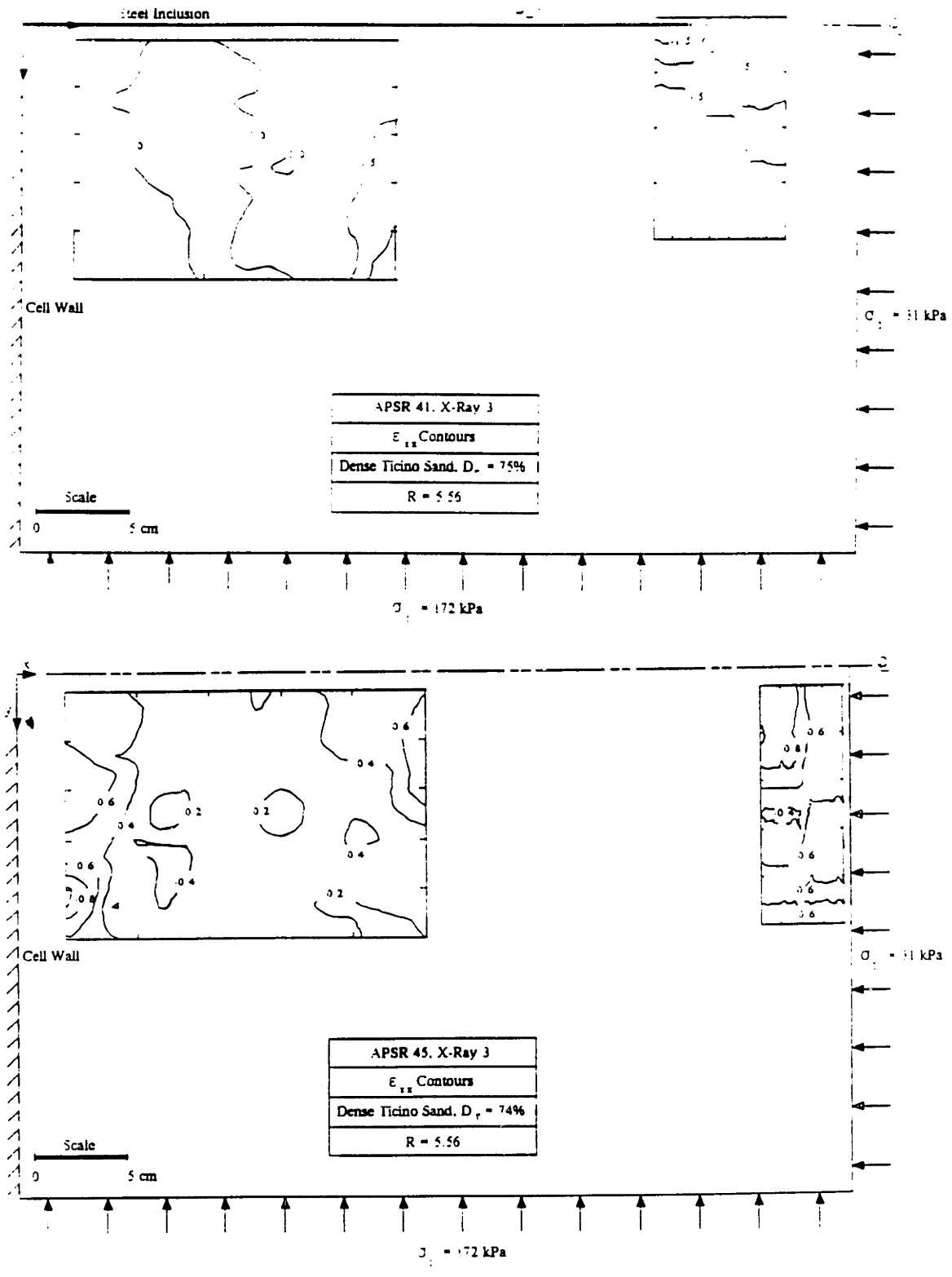

Figure 5.19a, b: Strain Contours for a Base-Case and Unreinforced Test on Dense Ticino Sand

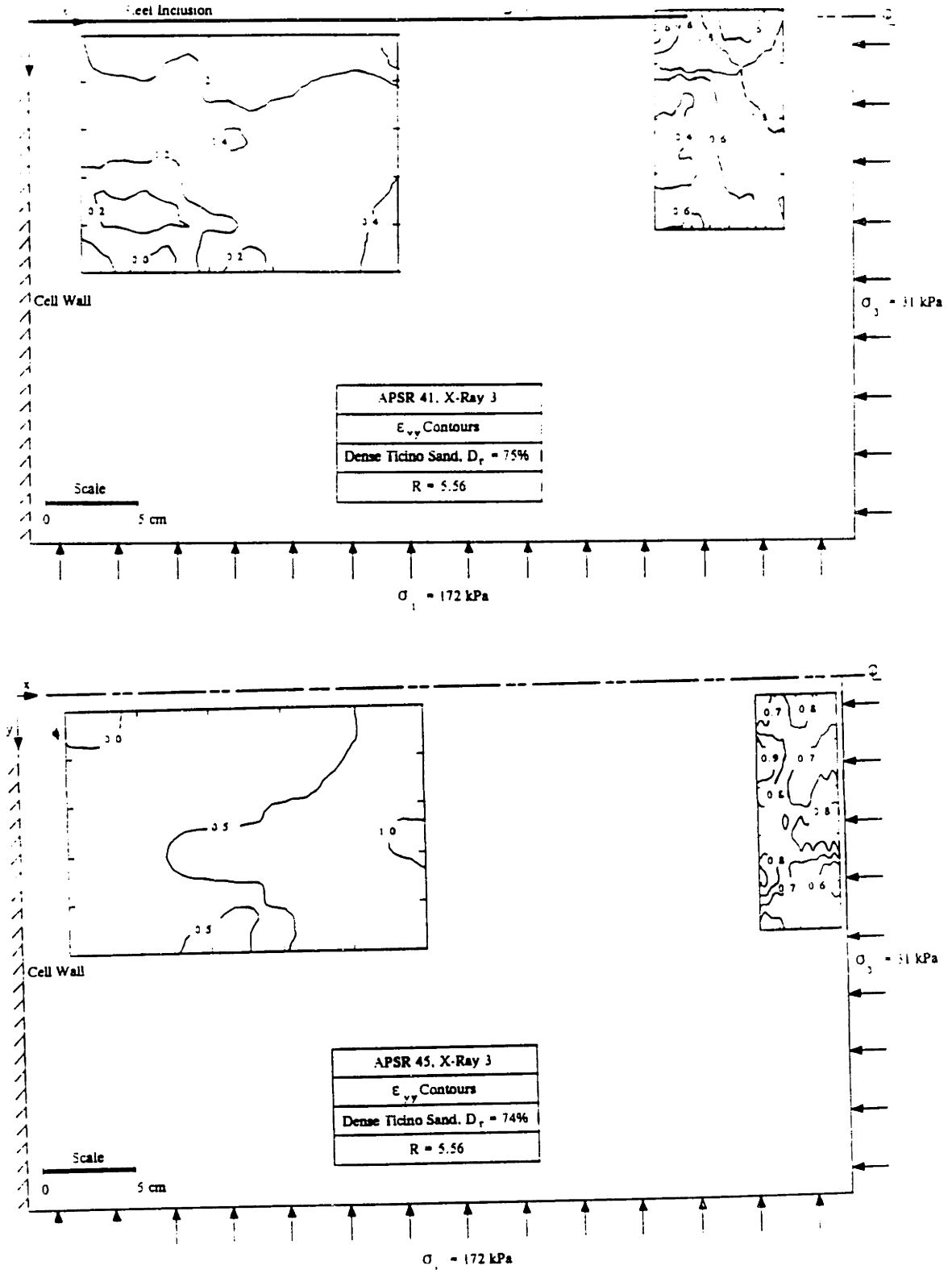

Figure 5.19c, d: Strain Contours for a Base-Case and Unreinforced Test on Dense Ticino Sand

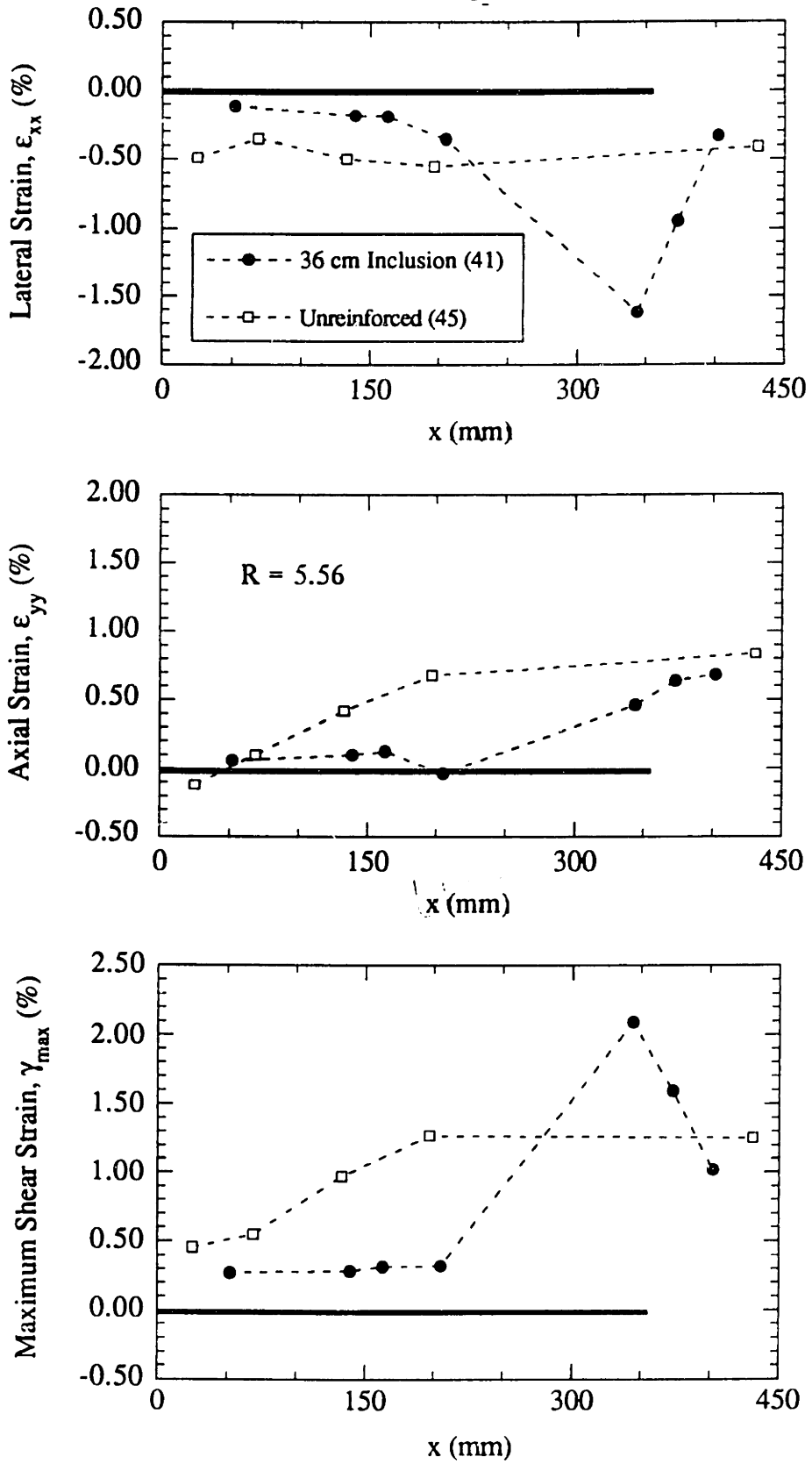

Figure 5.20: Strain Profiles Along Inclusion Interface in Dense Ticino Sand

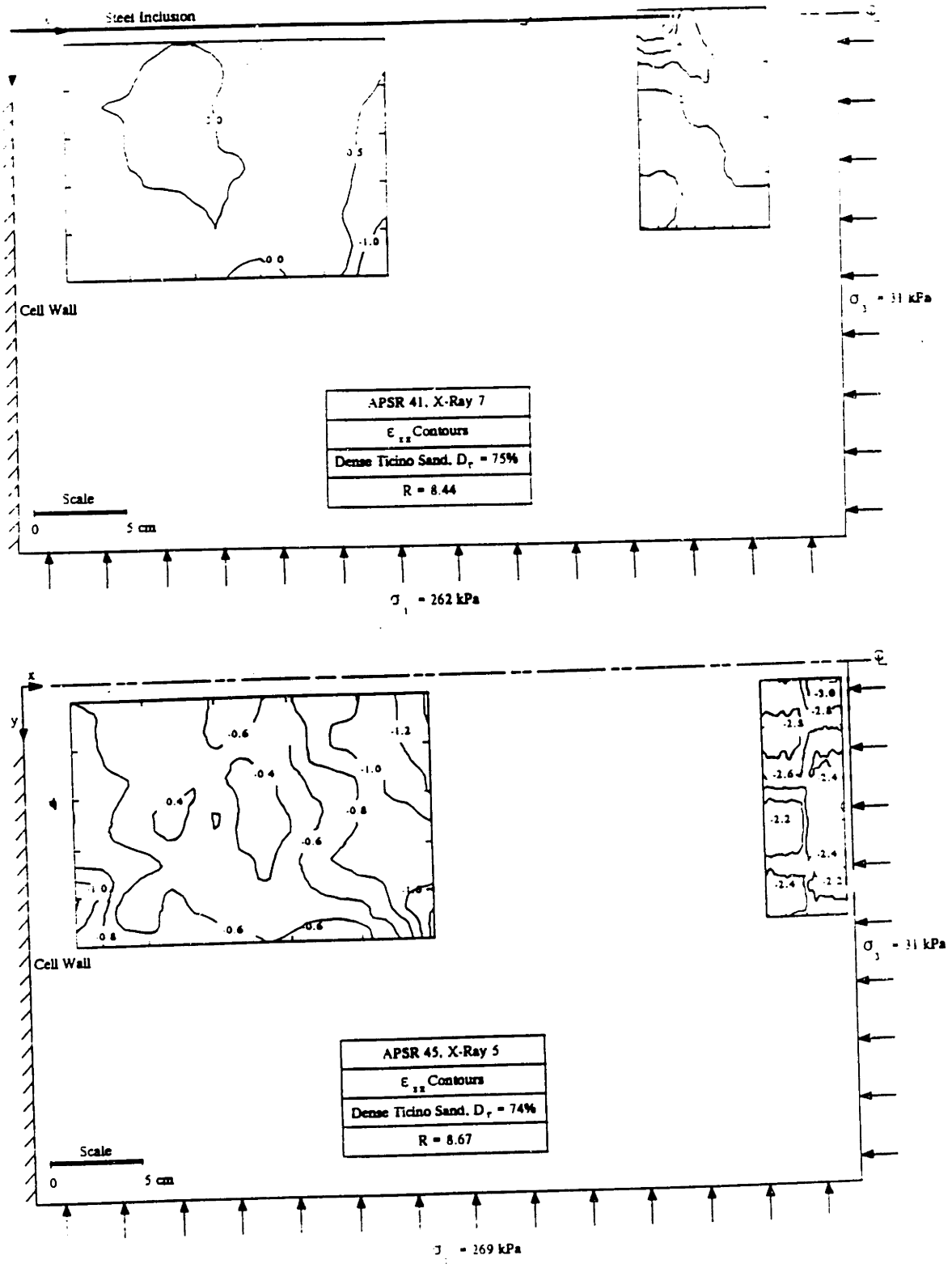

Figure 5.21a, b: Strain Contours for a Base-Case and Unreinforced Test on Dense Ticino Sand at Failure

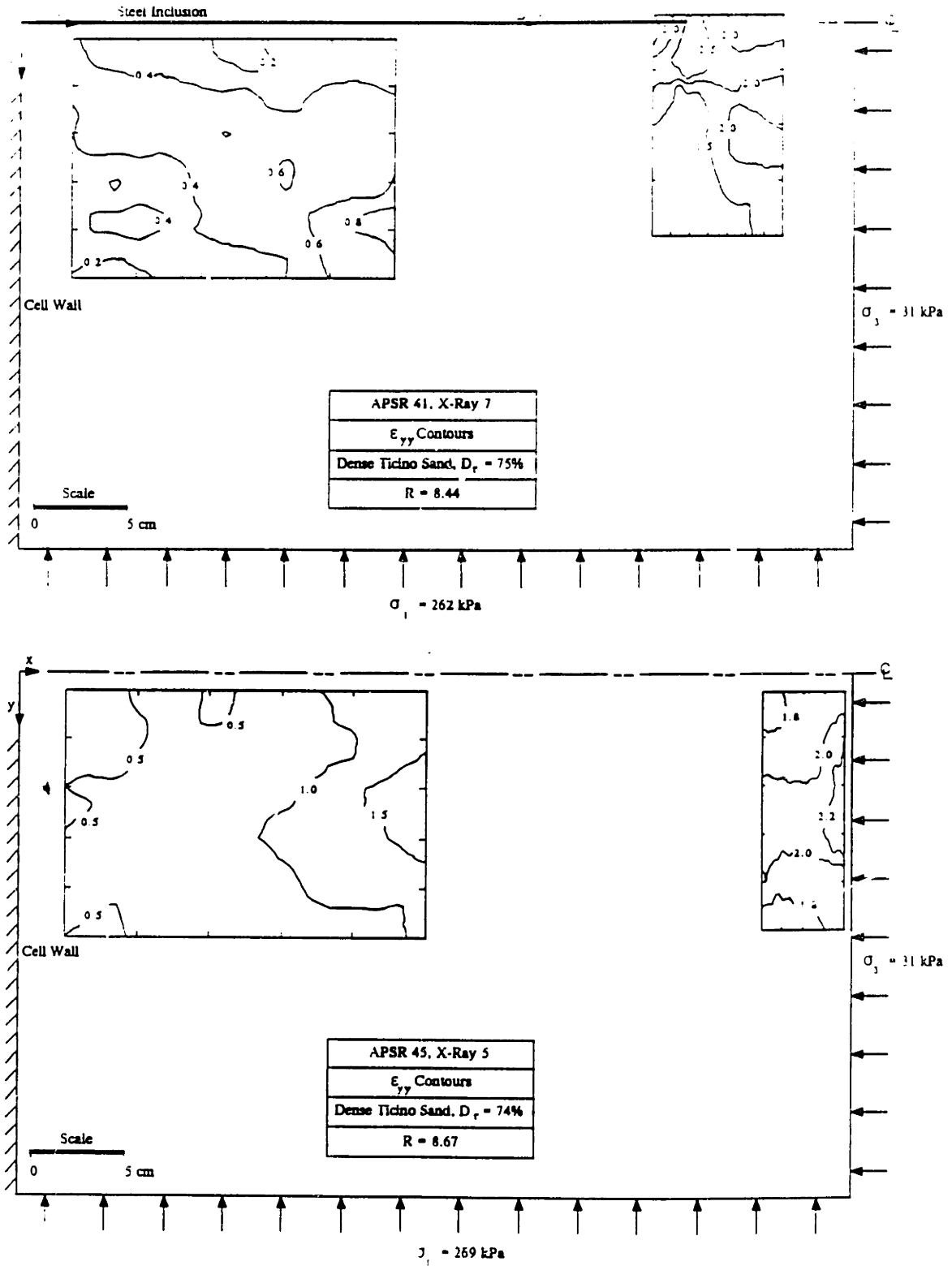

Figure 5.21c, d: Strain Contours for a Base-Case and Unreinforced Test on Dense Ticino Sand at Failure

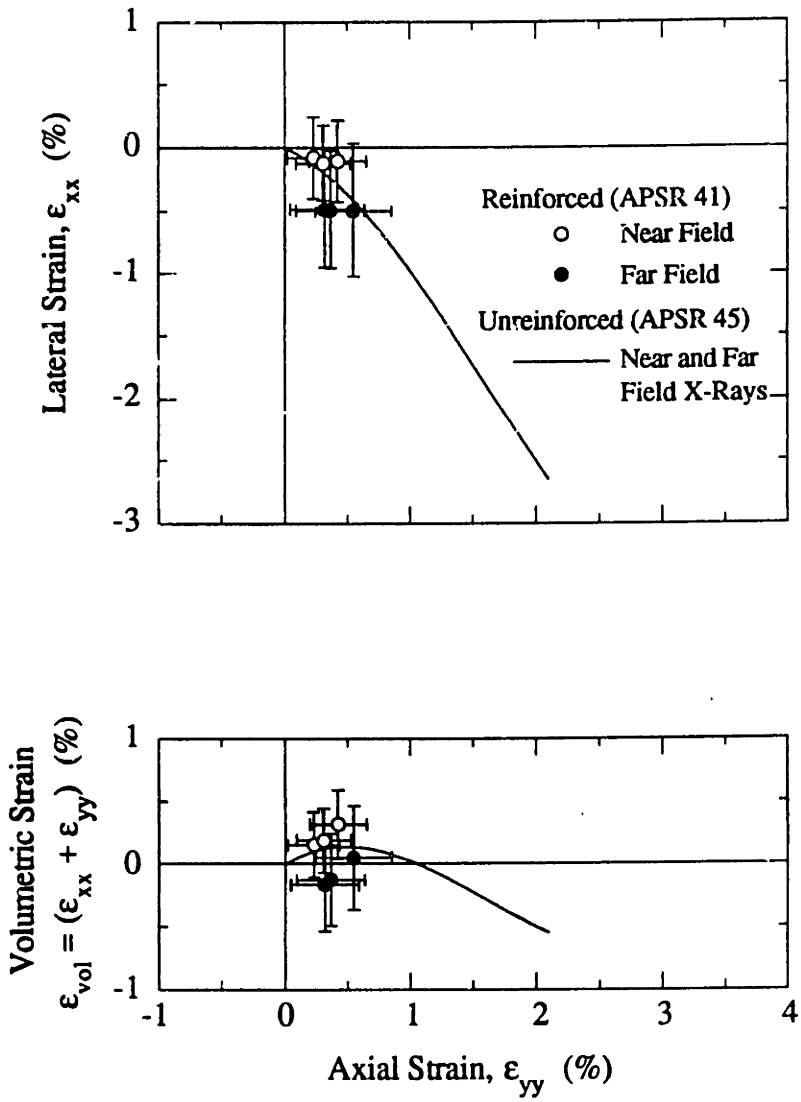

Figure 5.22: Comparison of Internal Soil Strain Responses for Dense Ticino Sand with and without a 36cm Steel Inclusion

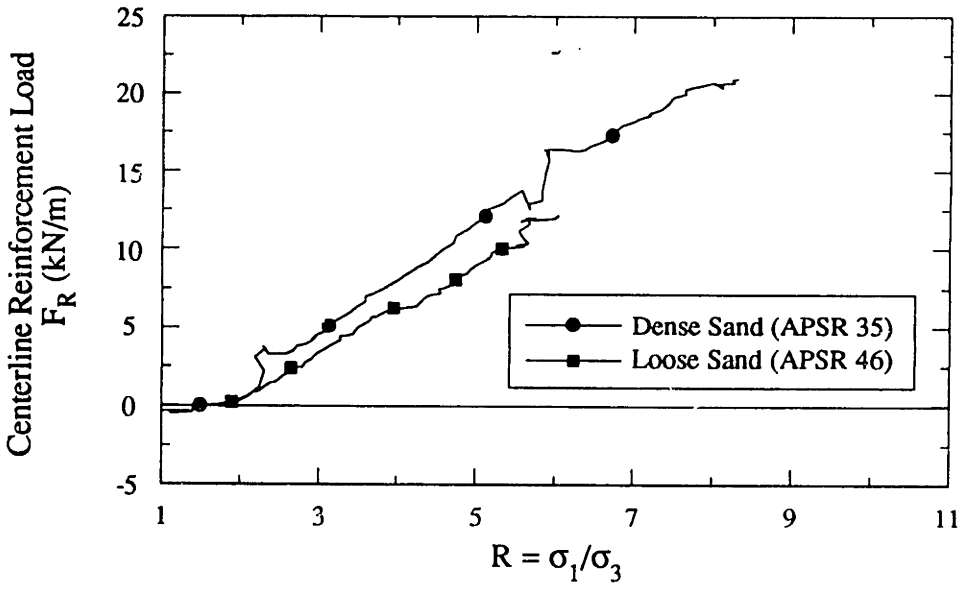

(a) Centerline loads (external load cell)

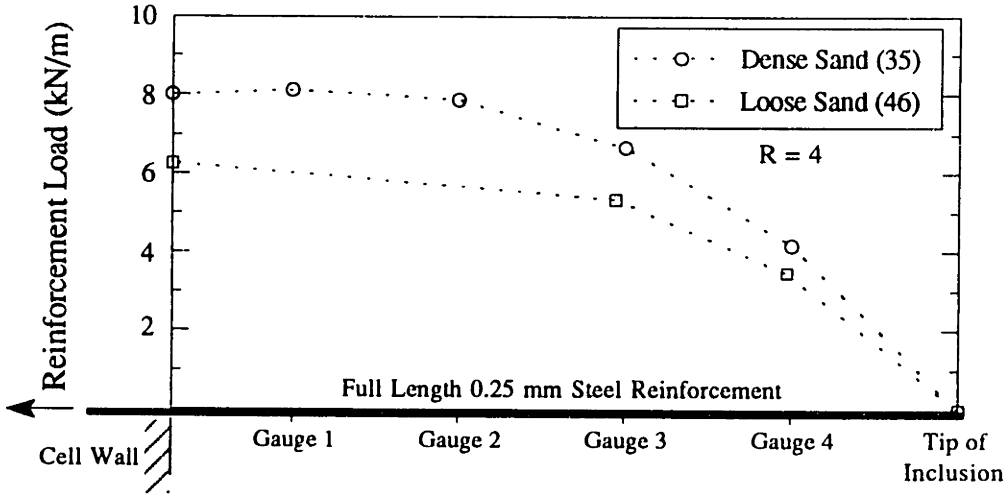

(b) Load distribution (external load cell and strain gauges)

Figure 5.23: Comparison of Load Measurements from Full Length Inclusions in Dense and Loose Ticino Sand

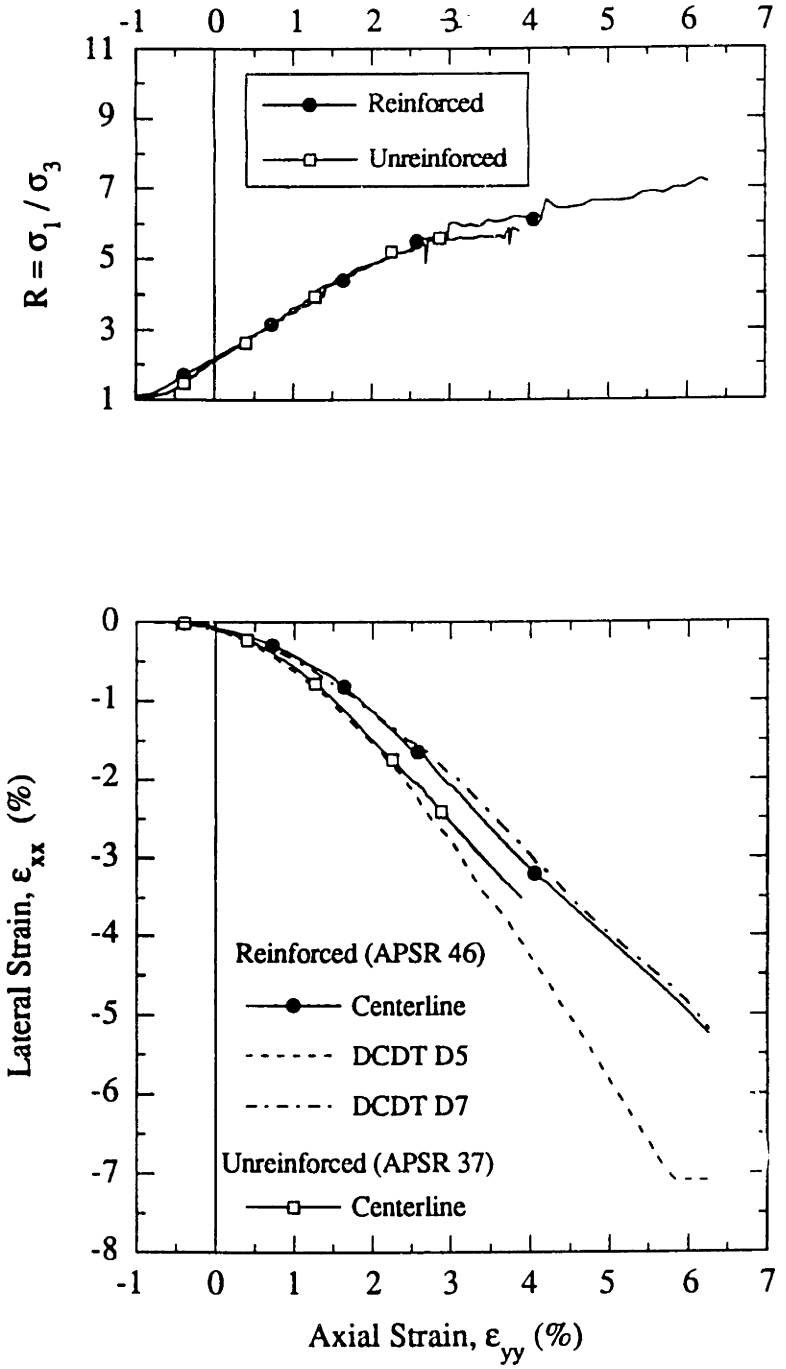

Figure 5.24: Externally Measured Shear Behavior of Loose Ticino Sand with and without a 36cm Steel Inclusion

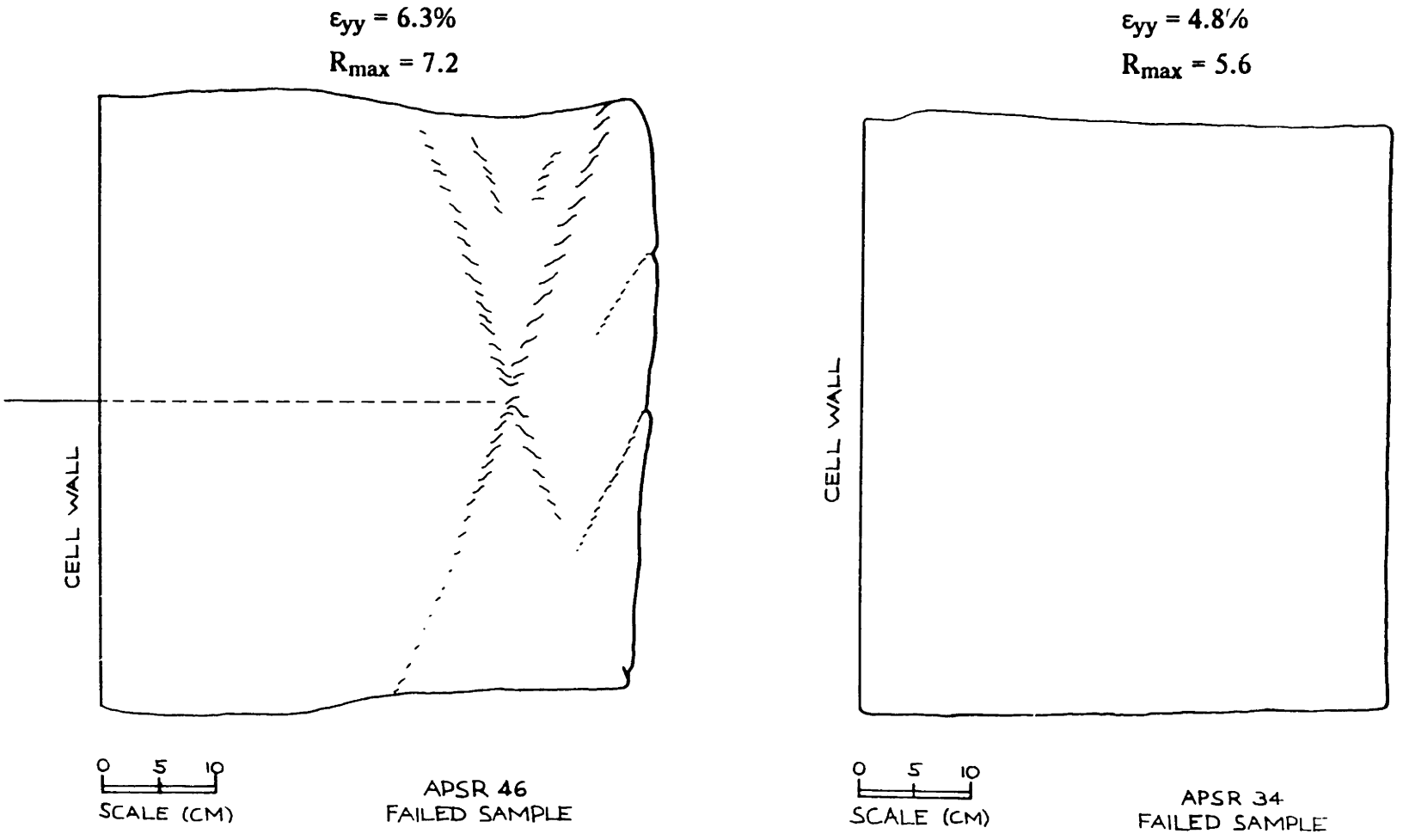

(a) Specimen with a 36cm steel inclusion

(b) Unreinforced specimen

Figure 5.25: Failure Surfaces in Loose Ticino Sand Specimens

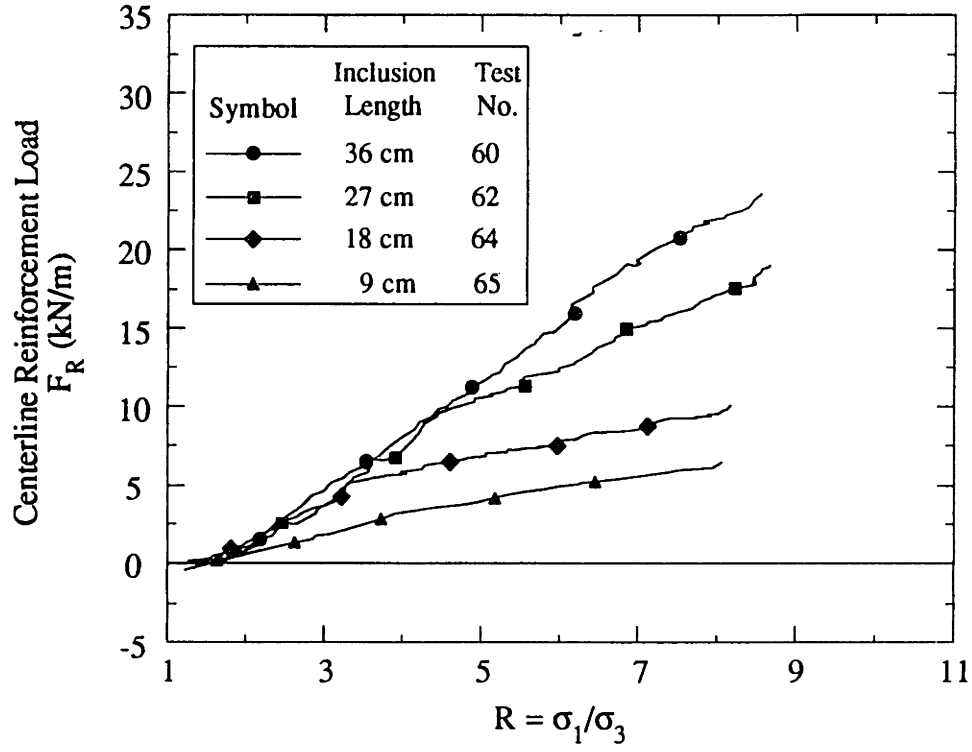

(a) Dense Ticino sand

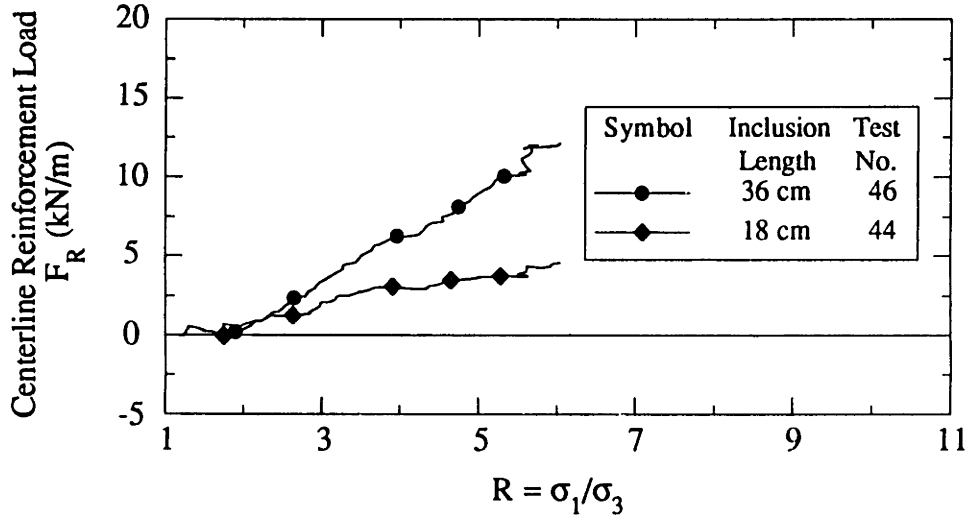

(b) Loose Ticino sand

Figure 5.26: Effect of Inclusion Length on Centerline Tensile Loads

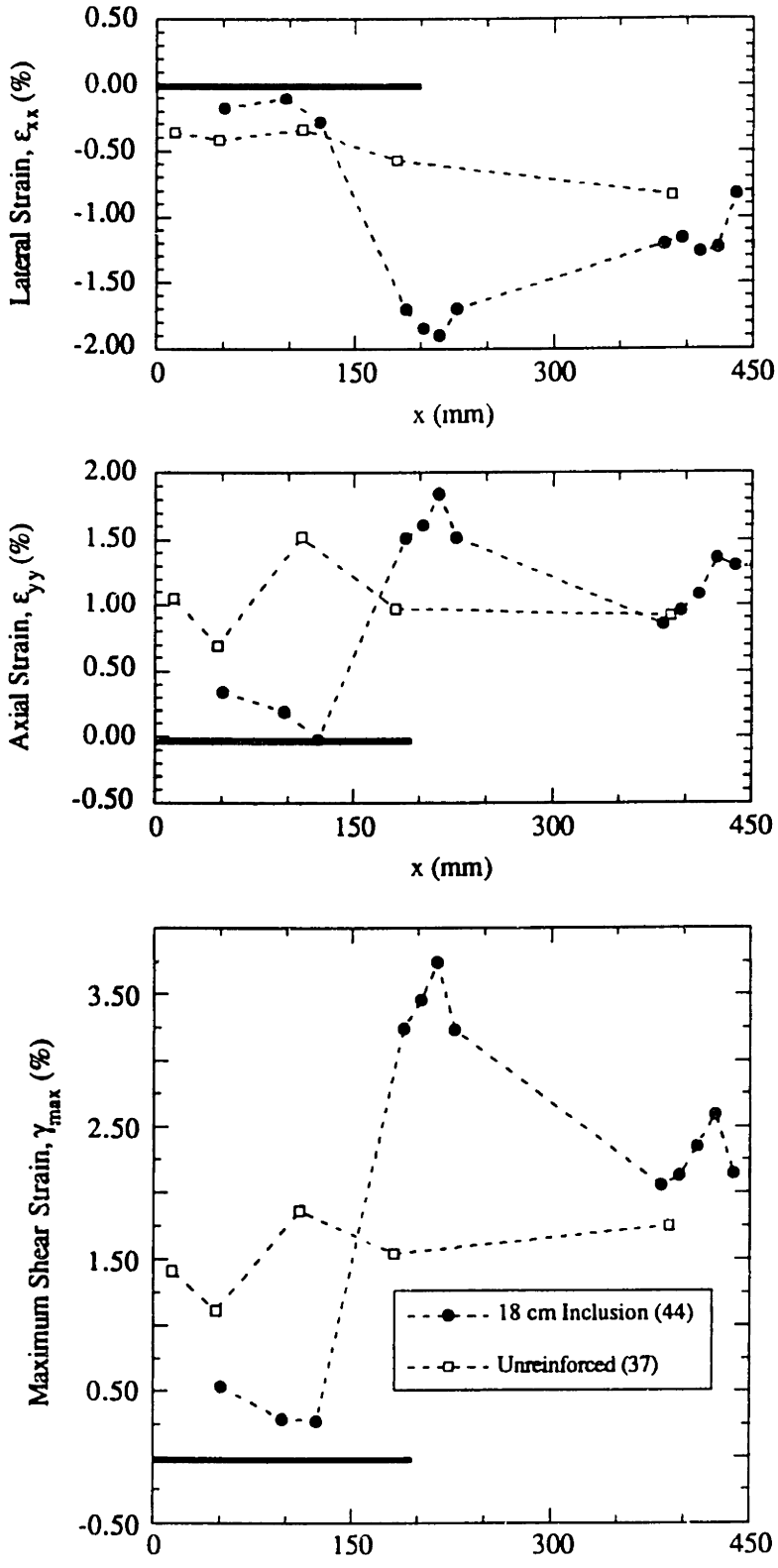

Figure 5.27: Strain Profiles Along Inclusion in Loose Ticino Sand

Chapter 6: Interpretation of APSR Results

6.1. Introduction

The APSR cell simulates the behavior of the composite plane strain element shown in Figure 6.1. The element comprises a planar inclusion of thickness, f, and length, L, embedded in a soil mass of overall height, m + f. The inclusion is oriented parallel to the minor, external principal stress (σ_3). For thin inclusions (m >> f), the dimension, m, corresponds to the typical inclusion spacing in a reinforced soil mass. Tensile stresses develop in the inclusion as the surrounding soil is sheared by increasing the major principal stress, σ_1 (at constant confining stress, σ_3). Even for this simplified geometry, complete analytical solutions are difficult to achieve. Abramento and Whittle (1992) have developed approximate analytical solutions for predicting and interpreting the load transfer measurements in the APSR cell based on techniques of shear lag analysis (Cox, 1952; Kuhn, 1956). Their solutions assume that the soil and reinforcement behave as linear, isotropic and elastic materials linked through a frictional interface. The analyses express the tensile stress in the reinforcement as closed form functions of the constituent material properties and inclusion geometry. The proposed formulation provides a simple and direct method for interpreting APSR data without recourse to more comprehensive numerical analyses (e.g., finite element methods).

This chapter summarizes briefly the shear lag analysis proposed by Abramento and Whittle (1992) and describes typical results which illustrate load transfer for different ranges of soil and reinforcement properties. The shear lag predictions are then

compared with load transfer data from APSR tests on Ticino sand reinforced with elastic, steel sheet inclusions.

6.2. Overview of the Shear Lag Analysis

This section summarizes the shear lag analysis developed by Abramento and Whittle (1992) for estimating tensile stresses in a single planar reinforcement due to shearing of the surrounding soil matrix. The analysis expresses reinforcement stresses as closed form functions of the inclusion geometry, elastic properties of the constituent materials (soil and reinforcement), and the interface friction between the two, and therefore provides physical insight into the mechanism of load transfer in reinforced soils.

The essence of the shear lag analysis (Cox, 1952; Kuhn, 1956) is to assume a simplified deformation field within the soil matrix, such that the tensile stresses in the inclusion, σ^f_{xx}, can be solved from equilibrium considerations:

$$\frac{d\sigma^f_{xx}}{dx} = \frac{2}{f}\sigma^i_{xy} = \alpha\,(u - v) \qquad (6.1)$$

where f is the inclusion thickness, σ^i_{xy} are the shear tractions at the soil-inclusion interface, and u, v are axial displacements at the same location, for situations with and without the inclusion.

The proposed analysis makes the following assumptions:

1. The soil matrix and reinforcement behave as linear, isotropic, and elastic materials, characterized by properties G_m, ν_m and E_f, ν_f, respectively.
2. The soil matrix and reinforcing inclusion are linked through a frictional interface, characterized by interface friction angle δ.

3. There is no axial stress acting at the ends of the inclusion, since the inclusion is thin and is not physically bonded to the soil matrix.
4. The axial stresses in the soil matrix and in the inclusion are functions of the x ordinate only.

Based on assumption 4, the horizontal stresses in the inclusion and the soil can be related by:

$$\bar{\sigma}^m_{xx} = \sigma^m_{xx} = a\,\sigma^f_{xx} + \sigma_3\,(1 + a) \tag{6.2}$$

and hence,

$$\frac{d\sigma^m_{xx}}{dx} = a\,\frac{d\sigma^f_{xx}}{dx} \tag{6.2a}$$

where $a = \frac{f}{m}$, the inclusion ratio.

The sign convention (Fig. 6.1) for the above equation is that compressive stresses are positive in the soil matrix, while the inclusion stress, σ^f_{xx}, is positive in tension. Neglecting body forces, the equilibrium equations in the soil matrix and the inclusion are:

$$\frac{\partial\sigma^m_{xx}}{\partial x} + \frac{\partial\sigma^m_{xy}}{\partial y} = 0 \tag{6.3a}$$

$$\frac{\partial\sigma^m_{xy}}{\partial x} + \frac{\partial\sigma^m_{yy}}{\partial y} = 0 \tag{6.3b}$$

$$\frac{d\sigma^f_{xx}}{dx} - \frac{2}{f}\,\sigma^i_{xy} = 0 \tag{6.3c}$$

with the boundary conditions:

$$\text{for } x = 0, L \text{ and } \left| y - \frac{f}{2} \right| \le \frac{m}{2} \quad : \quad \sigma^m_{xx} = \sigma_3 \tag{6.4a}$$

$$\text{for } 0 \le x \le L \text{ and } \left| y - \frac{f}{2} \right| = 0 \quad : \quad \sigma^m_{xy} = \sigma^i_{xy} \text{ and } \sigma^m_{yy} = \sigma^i_{yy} \tag{6.4b}$$

$$\text{for } 0 \le x \le L \text{ and } \left| y - \frac{f}{2} \right| = \frac{m}{2} \quad : \quad \sigma^m_{xy} = 0 \text{ and } \sigma^m_{yy} = \sigma_1 \tag{6.4c}$$

Equations 6.2, 6.3, and 6.4 can be used to determine distributions of the shear and normal stress components in the soil matrix as functions of the boundary tractions:

$$\sigma^m_{xy} = \sigma^i_{xy}\left[1 - a \left(\frac{2\,y}{f} - 1 \right) \right] \tag{6.5a}$$

$$\sigma^m_{yy} = \sigma^i_{yy} + \frac{4}{m}(\sigma_1 - \sigma^i_{yy})\left[-\frac{1}{m} y^2 + (1 + a)\, y - \frac{f}{2}\left(1 + \frac{a}{2} \right) \right] \tag{6.5b}$$

Equilibrium conditions, expressed by equations 6.2 through 6.4, lead to the following expression which relates the interface tractions to the axial stress in the inclusion:

$$\sigma^i_{yy} = \sigma_1 + \frac{m}{4}\frac{d\sigma^i_{xy}}{dx} = \sigma_1 + \frac{mf}{8}\frac{d^2\sigma^f_{xx}}{dx^2} \tag{6.6}$$

In order to apply the shear lag formulation, it is necessary to relate the stresses and strains in the direction of the inclusion. This is achieved by decoupling the normal and shear stresses within the soil matrix. Decoupling divides the soil matrix into two zones:

1. an inner "shear spring" layer of lateral dimension $\bar{m}$, adjacent to the inclusion, in which only shear stresses occur, and
2. an outer layer having the same lateral dimension as the physical model (i.e., m/2), which transmits normal stresses acting in the x and y directions.

The shear lag analysis uses the following assumptions to obtain average stresses in the inner and outer zones:

1. For the inner layer, the shear stresses are equated with the interface shear tractions (i.e., $\bar{\sigma}^m_{xy} = \sigma^i_{xy}$). The dimension $\bar{m}$ is determined by equating the

elastic shear strain energy in the physical (real) and decoupled models (after Budiansky et al., 1986) from which $\bar{m} = m/3$.

2. The stress parallel to the inclusion, $\bar{\sigma}^m_{xx}$, is the same in the decoupled system as it is in the real system, while the average normal stress, $\bar{\sigma}^m_{yy}$, is obtained by considering statically equivalent forces in the two systems:

$$\bar{\sigma}^m_{yy} = \frac{2}{3}\sigma_1 + \frac{1}{3}\sigma^i_{yy} \tag{6.7}$$

Shear stresses in the inner layer relate the interface tractions to axial displacements in the soil matrix, u_x, as follows:

$$\sigma^i_{xy} = \bar{\sigma}^m_{xy} = G_m \frac{du_x}{dy} = -G_m \frac{2}{\bar{m}}\left(u^{\bar{m}}_x - u^i_x\right) \tag{6.8}$$

where u^i_x and $u^{\bar{m}}_x$ are the axial displacements at the soil-inclusion and inner-outer zone, respectively.

Equation 6.8 is the shear lag approximation for the solution to equation 6.1. The strains in the x direction at the interfaces between the inclusion-soil and inner-outer soil zones are:

$$\varepsilon^{\bar{m}}_{xx} = \frac{du^{\bar{m}}_x}{dx} = \frac{1+\nu_m}{E_m}\left[\left(1-\nu_m\right)\sigma^m_{xx} - \nu_m\bar{\sigma}^m_{yy}\right] \tag{6.9a}$$

$$\varepsilon^i_{xx} = \frac{du^i_x}{dx} = \frac{1+\nu_f}{E_f}\left[-\left(1-\nu_f\right)\sigma^f_{xx} - \nu_f\,\sigma^i_{yy}\right] \tag{6.9b}$$

Combination of equations 6.2, 6.6, 6.7, and 6.9 yields a differential equation which characterizes the axial stress in the inclusion:

$$\frac{d^2\sigma^f_{xx}}{dx^2} - K_1\,\sigma^f_{xx} + K_2\,\sigma = 0 \tag{6.10}$$

where $K_2\,\sigma = K_2^1\,\sigma_1 + K_2^3\,\sigma_3$ (6.10a)

K_1, K_2^1, and K_2^3 are constants, defined in terms of the material properties and geometry of the soil matrix and the inclusion:

$$K_1 = \frac{6}{m\ f} \frac{\left[(1 - \nu_m)\ a + 2\ \frac{G_m}{E_f}\ (1 + \nu_f)\ (1 - \nu_f)\right]}{\left[\ 1 + \frac{1}{4}\nu_m - \frac{3}{2}\ \frac{G_m}{E_f}\ (1 + \nu_f)\ \nu_f\right]} \tag{6.11a}$$

$$K_2^1 = \frac{6}{m\ f} \frac{\left[\nu_m - 2\ \frac{G_m}{E_f}\ (1 + \nu_f)\ \nu_f\right]}{\left[\ 1 + \frac{1}{4}\nu_m - \frac{3}{2}\ \frac{G_m}{E_f}\ (1 + \nu_f)\ \nu_f\right]} \tag{6.11b}$$

$$K_2^3 = -\frac{6}{m\ f} \frac{\left[(1 - \nu_m)\ (1 + a)\right]}{\left[\ 1 + \frac{1}{4}\nu_m - \frac{3}{2}\ \frac{G_m}{E_f}\ (1 + \nu_f)\ \nu_f\right]} \tag{6.11c}$$

The tensile stress in the inclusion reaches a maximum at the centerline due to symmetry and hence, the boundary conditions can be written:

$$\text{for } x = 0, L : \qquad \sigma_{xx}^f = 0 \tag{6.12a}$$

$$\text{for } x = L/2 : \qquad \frac{d\sigma_{xx}^f}{dx} = 0 \tag{6.12b}$$

Using these boundary conditions (eqn. 6.12) to solve equation 6.10 provides the general expression for the axial stress in the reinforcement as a linear function of the applied stresses, σ_1, σ_3:

$$\sigma_{xx}^f = \frac{K_2\ \sigma}{K_1}\left[\ 1 - \frac{\cosh \sqrt{K_1}\left(\frac{L}{2} - x\right)}{\cosh \sqrt{K_1}\ \frac{L}{2}}\right] \tag{6.13}$$

The maximum axial stress at the centerline of the inclusion ($x = L/2$) is:

$$\sigma_{max}^f = \frac{K_2\ \sigma}{K_1}\left[1 - \text{sech}\ \sqrt{K_1}\ \frac{L}{2}\right] \tag{6.13a}$$

For a very long inclusion, where $L/2 \rightarrow \infty$, the maximum inclusion load is:

$$\sigma_{xx}^{f}(\infty) = \sigma_{\infty}^{f} = \frac{K_2\,\sigma}{K_1} \qquad (6.13b)$$

This equation shows that the maximum tensile stress in a long inclusion is controlled by three factors: 1) the shear stress mobilized in the soil matrix, σ_1/σ_3; 2) the relative stiffness of the inclusion and soil, E_f/G_m; and 3) the volume ratio of the reinforcement, a=f/m.

Figure 6.2 summarizes the 'maximum load transfer ratio', $\sigma_{max}^{f}/\sigma_{\infty}^{f}$, as a function of the inclusion half-length, L/2, and the stiffness ratio, E_f/G_m, for an inclusion with typical thickness, f = 1mm, and spacing, m = 0.5m. The results show that the 'pick-up length' necessary to achieve maximum load transfer (i.e., $\sigma_{max}^{f} \approx \sigma_{\infty}^{f}$) increases significantly with the stiffness ratio. For a relatively inextensible reinforcement such as steel ($E_f/G_m \approx 10^4$, Fig. 6.2), the maximum load transfer occurs for inclusions with half-lengths $L/2 \geq 1.5$m, while more extensible materials ($E_f/G_m=10^2$, Fig. 6.2) achieve similar conditions for $L/2 \approx 0.4$m.

Figure 6.3 illustrates the distribution of the tensile stress, σ_{xx}^{f}, normalized by the major principal stress, σ_1, for typical material properties, spacing and thickness of the reinforcement (Fig. 6.3). The results for inclusions with half-lengths, L/2 = 0.25, 0.5 and 1.5m, at an external stress ratio, $\sigma_1/\sigma_3 = 6$ (Fig. 6.3a), show that there are two distinct regions which characterize the soil-reinforcement interaction:

I) the zone close to the tip of the inclusion, in which the tensile stress accumulates due to shear stresses acting along the soil-reinforcement interface; and

II) the zone of constant axial inclusion stress (i.e., $\sigma_{xx}^{f} \rightarrow \sigma_{\infty}^{f}$).

These two regions are fully developed for 'long' inclusions (e.g., L/2 = 1.5m; Fig. 6.3a). For 'short' inclusions (L/2 = 0.25, 0.5m; Fig. 6.3a), the maximum load transfer is not achieved, and the shear lag parameter, K_1 (Eqn. 6.11a) controls the distribution of tensile stresses in zone I.

Figure 6.3b shows the load transfer for a short inclusion with half-length, L/2 = 0.5m, as a function of the applied stress ratio, $R = \sigma_1 / \sigma_3$, in the soil matrix. For a soil matrix with linear, isotropic properties, the ratio $\sigma_1 / \sigma_3 = (1 - \nu_m) / \nu_m = 1/K_0$ (i.e., for ν_m = 0.3, $1/K_0 = 2.3$; Fig. 6.3b) corresponds to one-dimensional deformation of the unreinforced soil matrix (i.e., $\varepsilon_{xx} = 0$). Tensile stresses only develop in the reinforcement when $\sigma_1 / \sigma_3 > 1/K_0$. There are two important limitations on the interpretation of results in Figure 6.3b:

1. For drained shearing of dry, cohesionless soils (e.g., good quality granular fills), the shear strength is most commonly described by a Mohr-Coulomb failure criterion with friction angle, $\phi = \sin^{-1} (\sigma_1-\sigma_3)/(\sigma_1+\sigma_3)$. Ladd et al. (1977) report $35^0 \leq \phi_{ps} \leq 57^0$ ($3.7 \leq \sigma_1/\sigma_3 \leq 11.7$) for typical sands sheared in plane strain compression. Thus, local failure will initiate in the matrix (at locations close to the tip of the inclusion) when the stress ratio mobilizes the frictional strength of the soil.
2. The linear, isotropic model of soil behavior does not describe accurately the volumetric response of cohesionless soils in drained shearing at high stress ratios. Extensive observations show that sands dilate when the mobilized friction exceeds a threshold value, $\phi_{cv} = 35^0$ to 45^0 ($\sigma_1/\sigma_3 = 3.7$ to 5.8) (Bolton, 1986). The practical implication of this behavior is that the proposed analysis will tend to underestimate both the lateral strains in the

soil matrix and the tensile stresses in the reinforcement (especially for $\sigma_1/\sigma_3 > 6$).

The preceding results assume that there is no slip between the soil matrix and the planar reinforcement. The results in Figure 6.3c show the effects of the interface friction angle, δ, on the load transfer for an inclusion of half-length, L/2 = 0.5m, at a stress ratio, $\sigma_1/\sigma_3 = 6$. For the selected material properties and geometry, interface slippage has very little influence on tensile stresses in the reinforcement for $\delta \geq 17^0$ ($\mu = \tan \delta \geq 0.3$). However, there are significant reductions in load transfer when the friction ratio is artificially low ($\mu = 0.1$, $\delta = 7^0$). Further studies (Abramento and Whittle, 1992) also show that, for practical values of interface friction, $\delta = 10^o$ -30^o, interface slippage has little effect on the expected load transfer for a wide range of constituent material properties and inclusion geometries.

6.3. Comparison of APSR Test Results and Shear Lag Predictions

The shear lag analysis provides a framework for predicting and interpreting the tensile loads measured in the APSR cell. Input parameters for the approximate shear lag analysis include the elastic properties for describing the shear behavior of the unreinforced sand (G_m, ν_m). The steel reinforcement is an elastic material with known elastic constants, $E_f = 2.07 \times 10^8$ kPa and $\nu_f = 0.2$. These properties, together with the known geometry of the APSR cell, enable shear lag predictions of the tensile loads as a function of inclusion length and applied stress ratio.

Figure 6.4 illustrates a set of elastic approximations to the unreinforced dense sand behavior in the APSR cell (test APSR 45). The parameters, α and β, in the figure were

derived as follows. For plane strain compression of an elastic soil, the strain components, ε_{xx} and ε_{yy}, can be expressed by:

$$\varepsilon_{xx} = \frac{1 + \nu_m}{E_m} [(1 - \nu_m)\sigma_{xx} - \nu_m \sigma_{yy}] \tag{6.14a}$$

$$\varepsilon_{yy} = \frac{1 + \nu_m}{E_m} [(1 - \nu_m)\sigma_{yy} - \nu_m \sigma_{xx}] \tag{6.14b}$$

From equation 6.14b, the axial stress, σ_{yy}, is a linear function of ε_{yy} for a constant confining stress (σ_{xx}):

$$\sigma_{yy} = \frac{E_m \varepsilon_{yy}}{(1 - \nu_m^2)} + \frac{\nu_m \sigma_{xx}}{(1 - \nu_m)} \tag{6.15}$$

The secant slope of the stress-strain response at 50% of the failure stress (Fig. 6.4a) can then be obtained as:

$$\alpha = \frac{\Delta(\sigma_{yy} - \sigma_{xx})}{\Delta\varepsilon_{yy}} = \frac{2G_m}{1 - \nu_m} = 19.2 \text{ MPa} \tag{6.16}$$

where G_m is the elastic shear modulus, $G_m = \frac{E_m}{2(1 + \nu_m)}$.

For an elastic material in plane strain compression, the lateral strain, ε_{xx}, is a linear function of ε_{yy}. The slope of the idealized relationship between ε_{xx} and ε_{yy} is the derivative of equation 6.14a with respect to ε_{yy}:

$$\beta = \frac{\Delta\varepsilon_{xx}}{\Delta\varepsilon_{yy}} = \frac{-\nu_m}{1 - \nu_m} \tag{6.17}$$

The shear lag analysis is fairly sensitive to the value of ν_m, and hence, two values are used to make predictions of load transfer (Fig. 6.4b):

1. The initial value, based on the initial slope of the lateral strain curve.

2. The value based on passing a line from the origin through the point of zero dilation rate on the lateral strain curve.

For slopes, β = -0.486 and -0.729 (Fig. 6.4b), the corresponding values of ν_m = 0.33 and 0.42, respectively.

Substituting back into equation 6.16 gives G_m = 5600 to 6400 kPa. The shear lag analysis is not very sensitive to the value of soil modulus, particularly for the case of a steel inclusion where the stiffness ratio, $E_f/G_m \approx 35{,}000$ (cf. Fig. 6.2). The following comparisons assume G_m = 6000 kPa.

From the elastic approximation, shear lag predictions were made of the expected tensile loads in a 36cm steel inclusion in the APSR cell. Table 6.1 shows the elastic and geometric properties used in these predictions, along with the resulting shear lag parameters.

Figure 6.5a compares shear lag predictions with the centerline tensile loads measured in the base case test APSR 35 (L/2 = 36cm, t = 0.25mm). The plot shows the sensitivity of the analysis to the value of the Poisson's ratio, ν_m. Decreasing ν_m has two effects on the load-stress ratio relationship: 1) the slope of the load vs. R line decreases, and 2) the offset stress ratio, R_o, increases. The value ν_m = 0.42, based on the zero dilation condition, substantially overpredicts the tensile force at the centerline of the inclusion at all R values. Predictions based on the initial Poisson's ratio show good correlation with

the externally measured tensile force in the inclusion. The measured inclusion loads generally fall between the shear lag predictions for $\nu_m = 0.33$ to 0.35.[1]

Figure 6.5b compares the predicted tensile force distribution along the length of the inclusion to the actual measured loads from APSR 35 at two stress ratios, R = 3 and 6, using $\nu_m = 0.35$. The predicted and measured results are quite close at both R-values. At R = 3, the shear lag analysis slightly underpredicts the inclusion loads measured by the four strain gauges. The maximum error occurs at gauge 3, where the measured load is 18% higher than predicted. At R = 6, the maximum error of 13% occurs in gauge 4.

Figure 6.6 presents the measured stress-strain response of (unreinforced) loose Ticino sand from APSR 37, along with the range of proposed elastic approximations (summarized in Table 6.2). The measured behavior is less linear than for the dense sand, so there is a wider spread between the values of the slope, β, through the lateral strain curve at the origin and at the point of zero dilation rate. Equation 6.17 gives corresponding Poisson's ratios of $\nu_m = 0.16$ (initial response) and $\nu_m = 0.37$ (at the point of zero dilation rate). The straight line through the stress-strain curve at the point halfway to failure has slope $\alpha = 8334$ kPa. The corresponding range of shear moduli is $G_m = 2600$ to 3500 kPa. The shear lag predictions for loose sand use $G_m = 3000$ kPa ($E_f/G_m = 69{,}000$).

Figure 6.7a compares the predicted and measured maximum tensile force in the inclusion. For the loose sand, using the initial Poisson's ratio greatly underpredicts the measured inclusion force, while the Poisson's ratio based on the point of zero dilation

---

[1]Note that for an elastic soil, $K_o = \frac{\nu_m}{1 - \nu_m}$. Thus, for dense Ticino sand, matching occurs for K_o = 0.49 to 0.54.

rate, $\nu_m = 0.37$, gives better correlation. The measured relationship between the inclusion force and applied stress ratio from APSR 46 is closely approximated by the shear lag analysis for $\nu_m = 0.31$. For this case, the predicted offset stress ratio, R_o, is slightly higher than the observed value ($R_o = 1.8$), while the load transfer gradient is also slightly larger than measured. The plot of predicted vs. measured inclusion load distribution in Figure 6.7b again demonstrates that the form of the distribution predicted by the shear lag analysis is reasonable.

Figure 6.8 compares the shear lag predictions with APSR measurements of centerline stresses for inclusions with half-lengths, L/2 = 9 to 36cm. The predictions assume the elastic parameters listed in Tables 6.1 and 6.2 for dense and loose sand, respectively. The results for dense sand (Fig. 6.8a) show that, although the shear lag analysis is in good agreement with the data for L/2 = 36cm, it underpredicts significantly the measurements for short inclusions (L/2 = 9cm). However, the overall framework is in reasonable agreement with the APSR data. The most significant discrepancy is the non-linearity measured in short inclusions for $R \leq 4$ (particularly in the test with L/2 = 18cm). There is generally better agreement between the predicted and measured inclusion loads at R = 8 than at R = 4. Differences between the predicted and measured results may be due to several factors, including the following:

1) Soil behavior is not well represented as a linear elastic material.
2) Soil stresses are not perfectly uniform within the APSR specimen due to boundary friction described in section 4.2.2.

There is a better correlation between the predicted and measured load transfer for the loose sand than for the dense sand (Fig. 6.8b). For the two tests shown in Figure 6.8b, the shear lag analysis underpredicts the measured loads at low R values and slightly

overpredicts them for $R \geq 5$. The analysis describes accurately the effect of inclusion length on the load transfer measured in the loose Ticino sand.

Figure 6.9 presents the centerline tensile load at a stress ratio, R = 6, as a function of the inclusion length. The plot demonstrates the use of the shear lag analysis for predicting loads in a very long inclusion based on APSR test data. The first step is to perform tests on inclusions of different lengths in the APSR cell in order to evaluate input parameters for the shear lag analysis. Equation 6.13b then gives an estimate of the maximum tensile force for long reinforcements. For the relatively inextensible elastic steel sheet reinforcements described in this thesis, the shear lag analysis shows that the tensile load measured in the APSR cell (L/2 = 36cm) is approximately 50% of the load that would occur in a long inclusion in the field. Full load transfer occurs for inclusions of half-length $L/2 \geq 1.50$m for both loose and dense Ticino sand at $\sigma_3 = 31$ kPa.

6.4. Conclusions

This chapter summarizes the shear lag analysis developed by Abramento and Whittle (1992). The analysis provides simple closed form expressions for the tensile stresses in a planar reinforcement, based on known properties of the soil and reinforcement. The proposed analysis assumes that the soil matrix and the reinforcement behave as isotropic, linear-elastic materials, linked through a frictional interface. The analysis provides a framework for interpreting APSR measurements described in Chapter 5. Elastic input properties (G_m, ν_m) were obtained for dense and loose Ticino sand from unreinforced tests in the APSR cell. Using these properties and known elastic constants for the steel sheet reinforcement, shear lag predictions were made of the inclusion loads measured in the APSR tests.

Predictions made for tests with a 36cm steel inclusion show that the analysis is sensitive to the value of Poisson's ratio of the soil, ν_m. For dense sand, predictions of the maximum inclusion load made using $E_f/G_m = 35{,}000$ and $\nu_m = 0.35$ match closely the externally measured inclusion loads in the APSR cell at all R-values. The analysis also predicts the measured load distribution along the length of the inclusion quite well. For loose sand, the measured relationship between the inclusion tensile load and applied stress ratio is closely approximated by the shear lag analysis with $E_f/G_m = 69{,}000$ and $\nu_m = 0.31$.

The shear lag analysis underpredicts the centerline tensile loads for short inclusions in dense sand (i.e., for $L/2 < 36$cm). However, there is better agreement between the predicted and measured load transfer for tests in loose sand. The shear lag analysis predicts reliably the gradient of the linear load transfer function for both the 18 and 36cm steel inclusions in loose sand.

The shear lag analysis shows that the tensile force measured in APSR tests with $L/2 =$ 36cm steel sheet reinforcements represents approximately half the load transferred to a long inclusion ($L/2 \geq 1.5$m) for both dense and loose Ticino sand.

The comparisons described in this chapter demonstrate the use of shear lag analysis for predicting and interpreting load transfer in the APSR tests. The analysis provides physical insight into the constituent properties controlling load transfer, and gives reasonable agreement with measured data for elastic steel sheet inclusions. Further refinement of the analysis should consider the non-linear and dilative behavior of sand during shearing.

Elastic Properties for the Sand and Reinforcement			
Property	Sand		Reinforcement
Modulus	G_m = 6000 kPa		$E_f = 2.07 \times 10^8$ kPa
Poisson's ratio	ν_m = 0.33 to 0.42		ν_f = 0.2
Lateral dimension	m = 0.57 m		$f = 2.54 \times 10^{-4}$ m
Length			L/2 = 0.36 m
Resulting Shear Lag Parameters			
	ν_m = 0.33	ν_m = 0.35	ν_m = 0.42
K_1	13.561	13.159	11.781
K_2^1	12,633	13,337	15,751
K_2^3	-25,662	-24,781	-21,762

Table 6.1: Input Parameters for Shear Lag Predictions of Load Pickup in Dense Ticino Sand

Elastic Properties for the Sand and Reinforcement			
Property	Sand		Reinforcement
Modulus	G_m = 3000 kPa		$E_f = 2.07 \times 10^8$ kPa
Poisson's ratio	ν_m = 0.16 to 0.37		ν_f = 0.2
Lateral dimension	m = 0.57 m		$f = 2.54 \times 10^{-4}$ m
Length			L/2 = 0.35 m
Resulting Shear Lag Parameters			
	ν_m = 0.16	ν_m = 0.31	ν_m = 0.37
K_1	16.025	12.896	11.705
K_2^1	6375.5	11,923	14,035
K_2^3	-33,488	-26,550	-23,909

Table 6.2: Input Parameters for Shear Lag Predictions of Load Pickup in Loose Ticino Sand

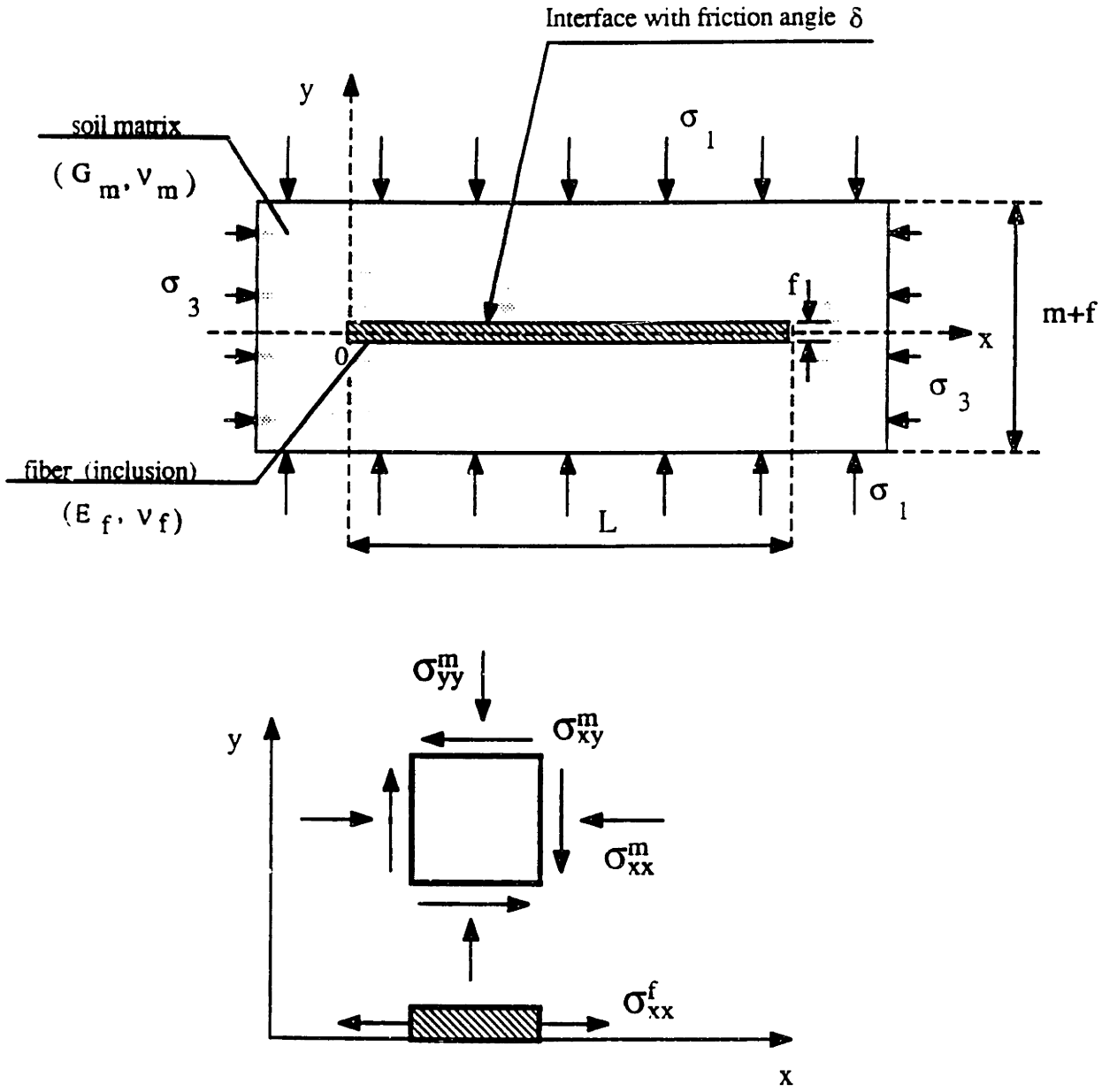

Positive Stress Convention in Soil

Figure 6.1: Ideal Reinforced Soil Element Modelled by the Shear Lag Analysis (After Abramento and Whittle, 1992)

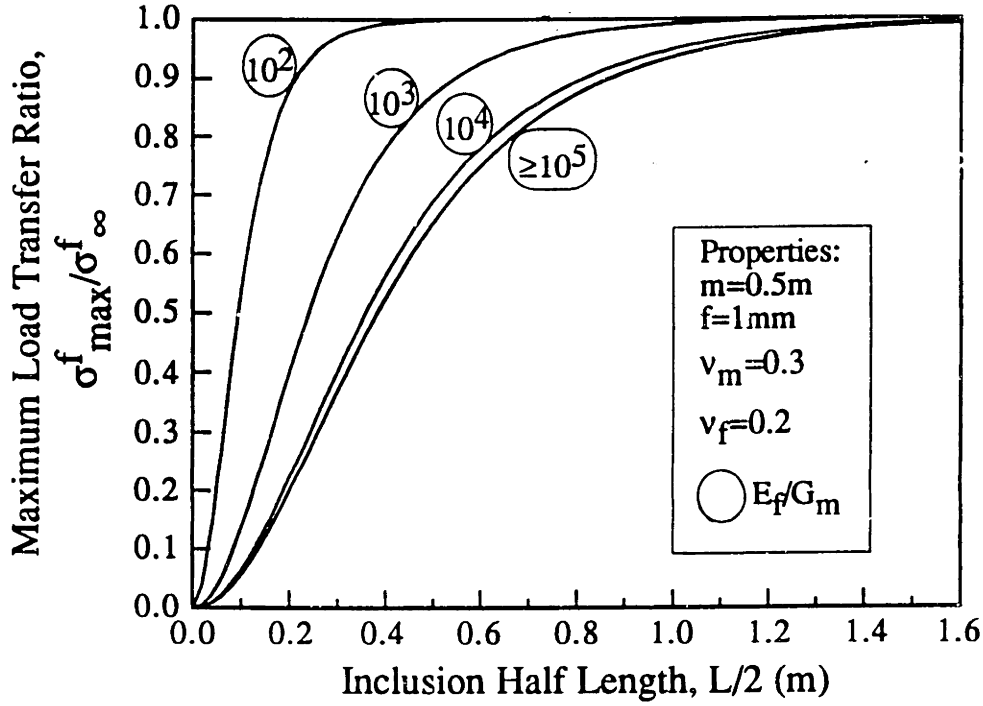

Figure 6.2: Effect of Inclusion Length and Stiffness on Maximum Load Transfer Ratio

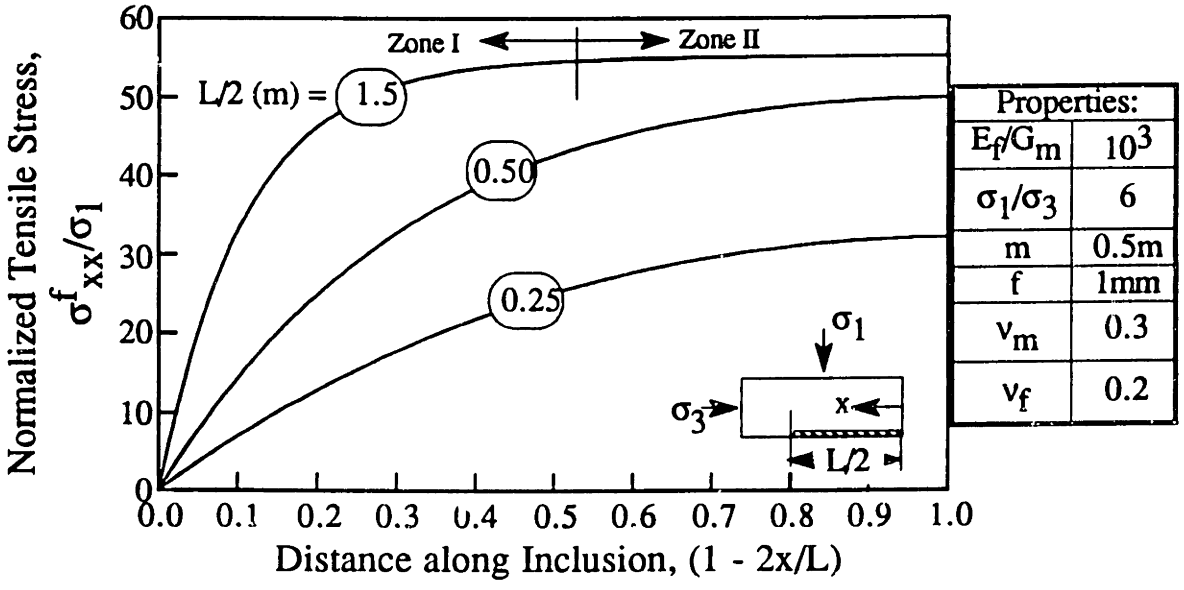

a) Effect of inclusion length

Figure 6.3: Distribution of Tensile Stresses in a Planar Reinforcement

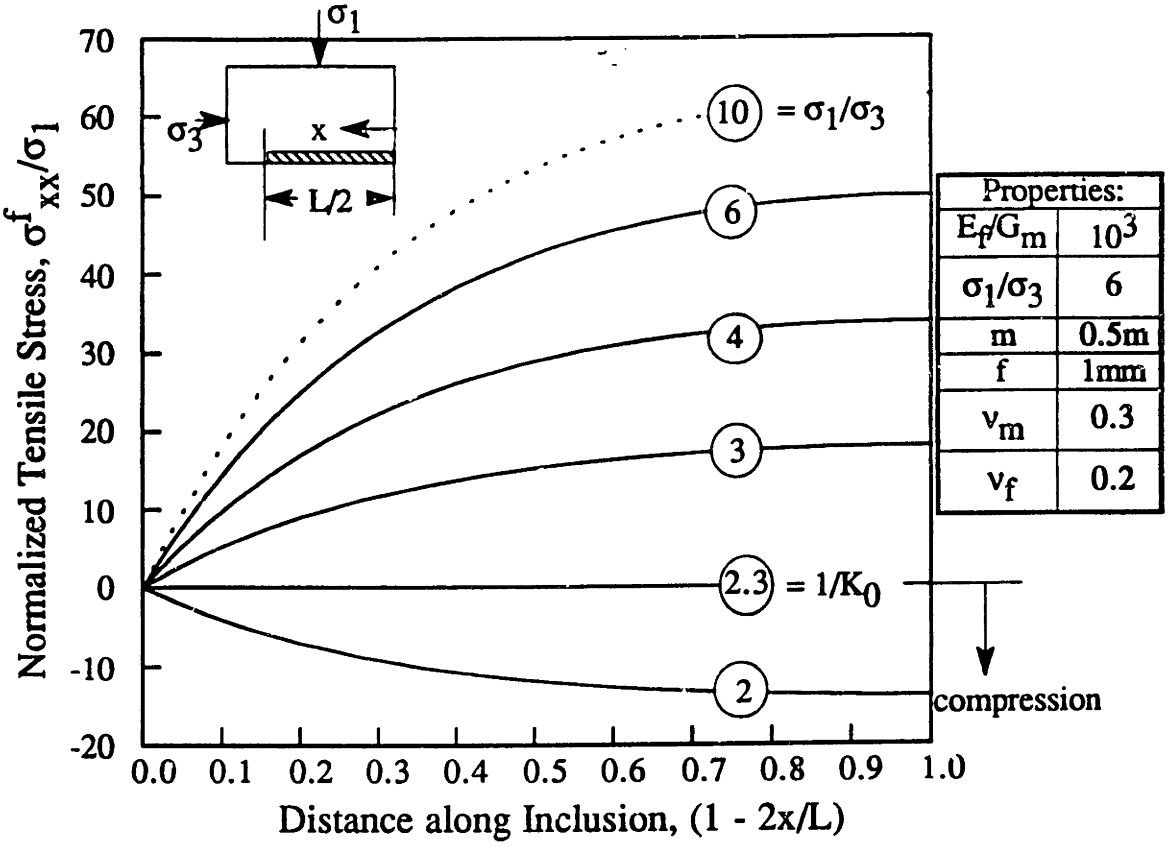

(b) Load transfer due to shearing of the soil

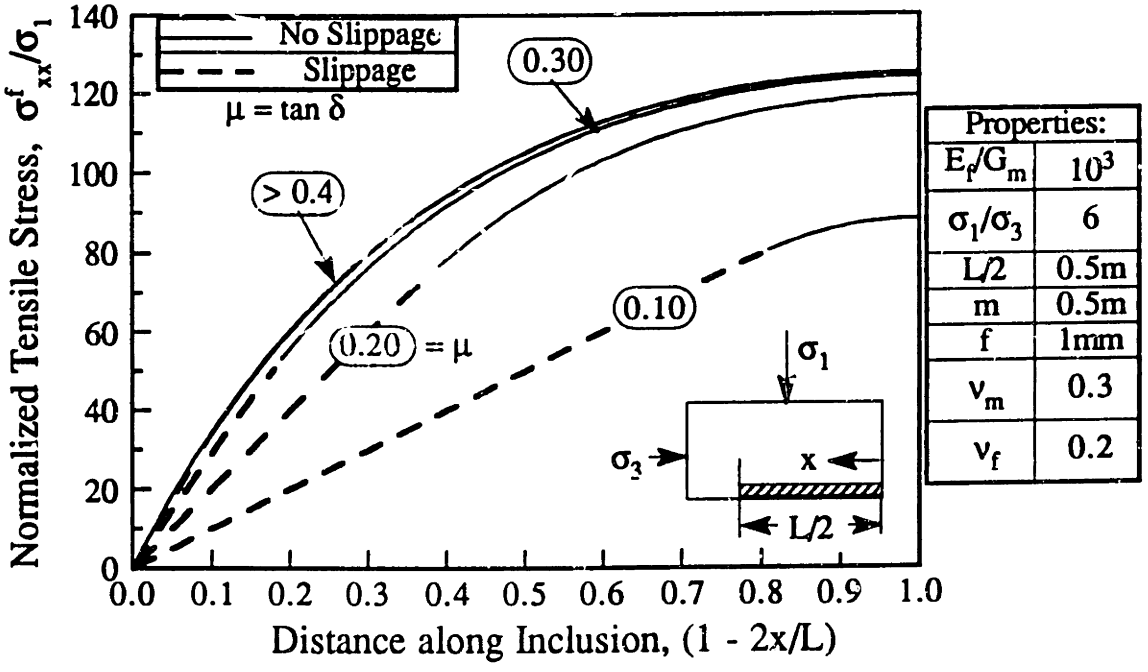

(c) Effects of interface friction

Figure 6.3 (cont'd): Distribution of Tensile Stresses in a Planar Reinforcement

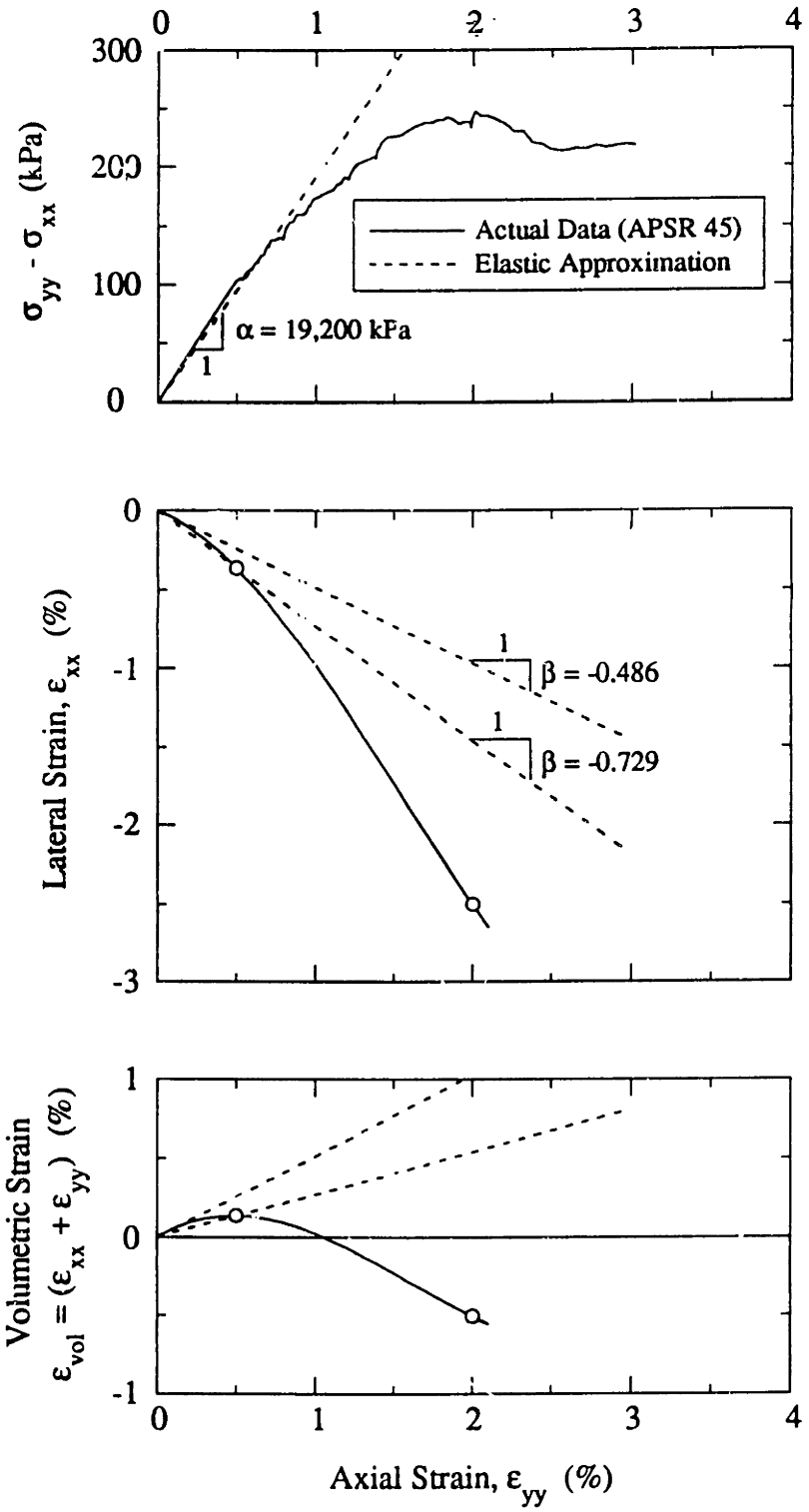

Figure 6.4: Elastic Approximations to Plane Strain Behavior of Dense Ticino Sand

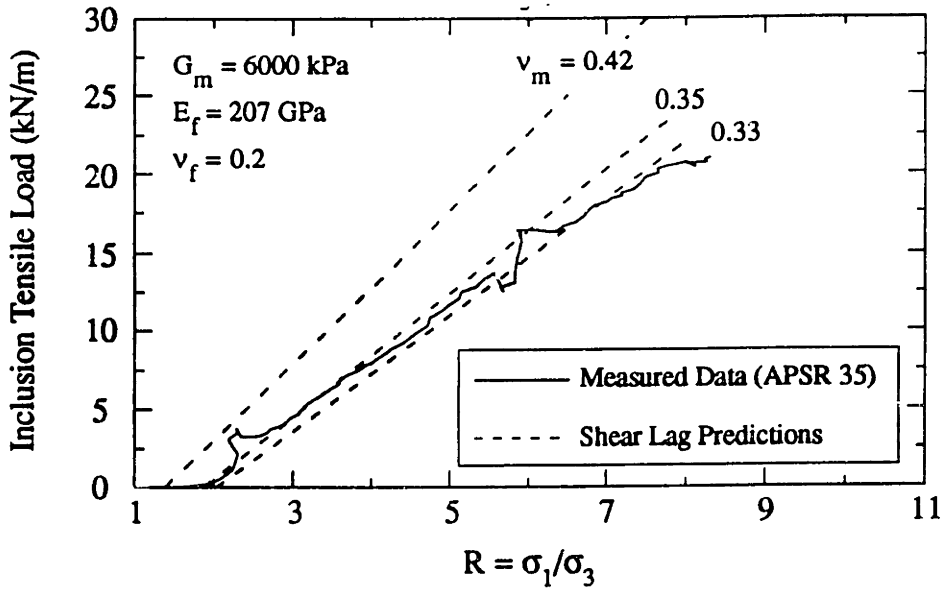

(a) Predicted vs. measured tensile load at inclusion centerline

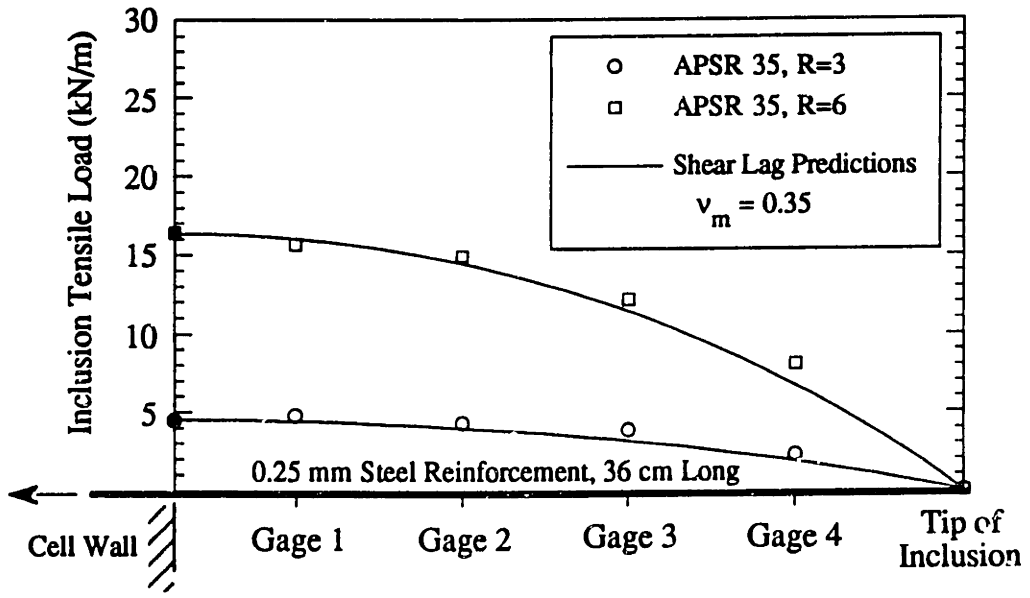

(b) Predicted vs. measured inclusion load distribution

Figure 6.5: Comparison of Shear Lag Predictions of Inclusion Tensile Loads to Measured Data for a Base-Case Test

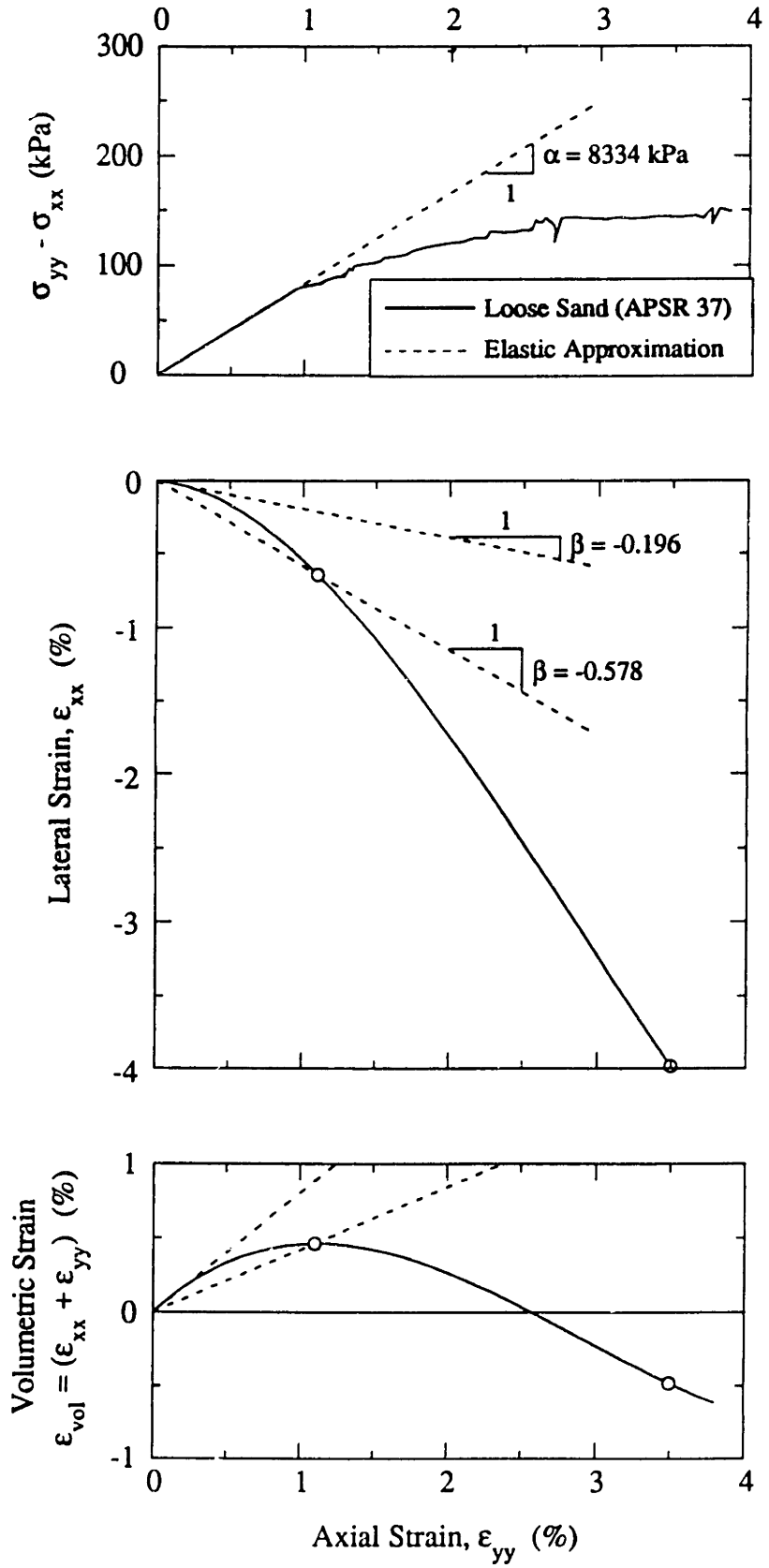

Figure 6.6: Elastic Approximations to Plane Strain Behavior of Loose Ticino Sand

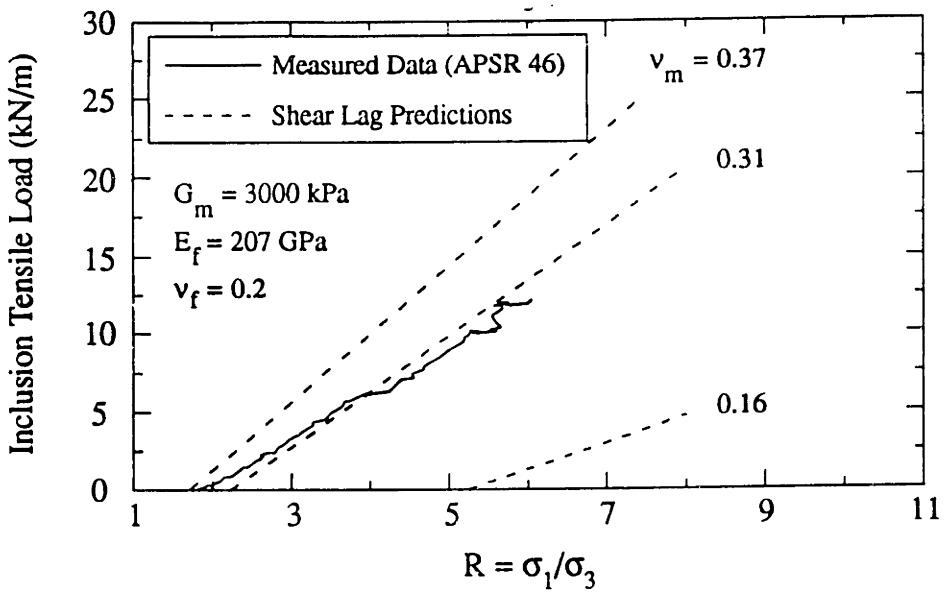

(a) Predicted vs. measured tensile load at inclusion centerline

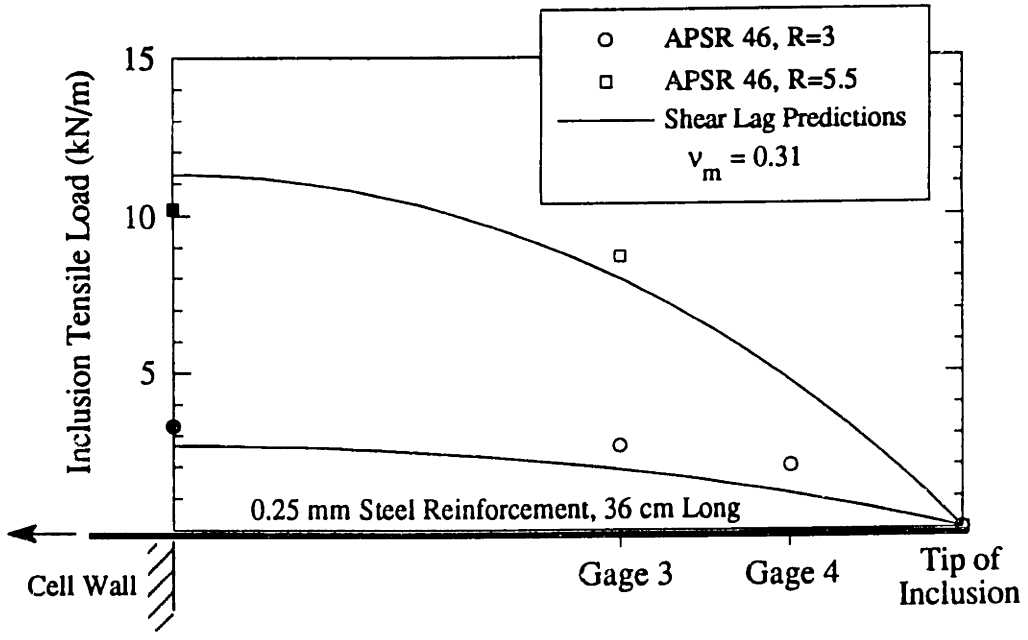

(b) Predicted vs. measured inclusion load distribution

Figure 6.7: Comparison of Shear Lag Predictions of Inclusion Tensile Loads to Measured Data for Loose Sand

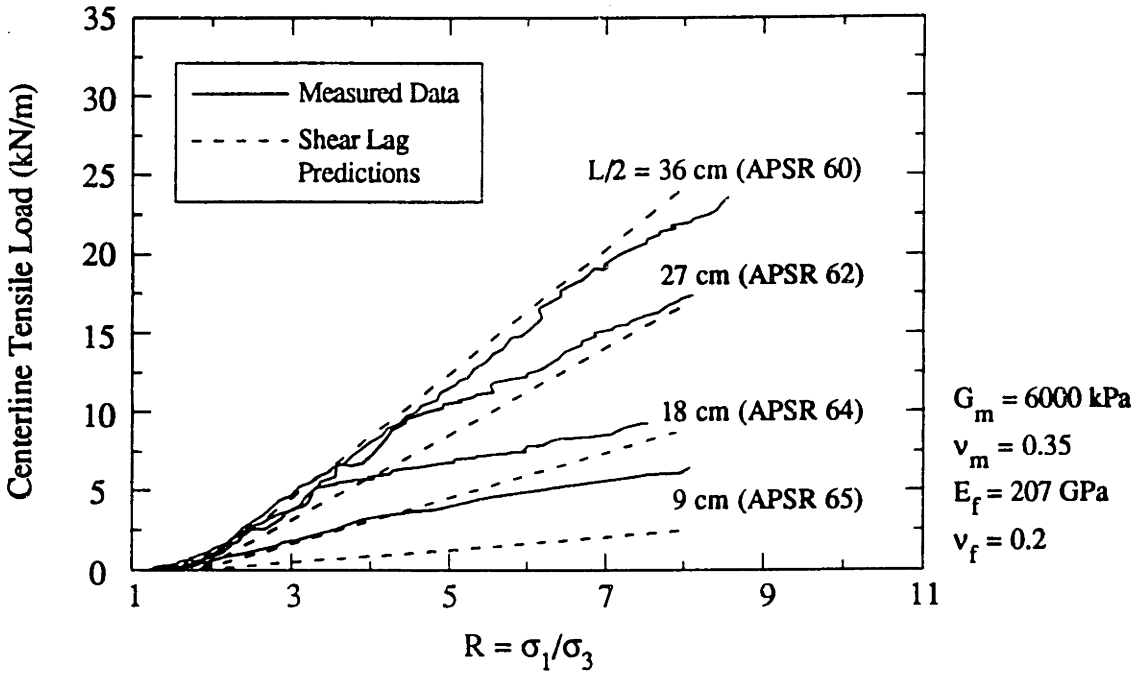

(a) Predicted vs. measured tensile load at inclusion centerline for dense sand

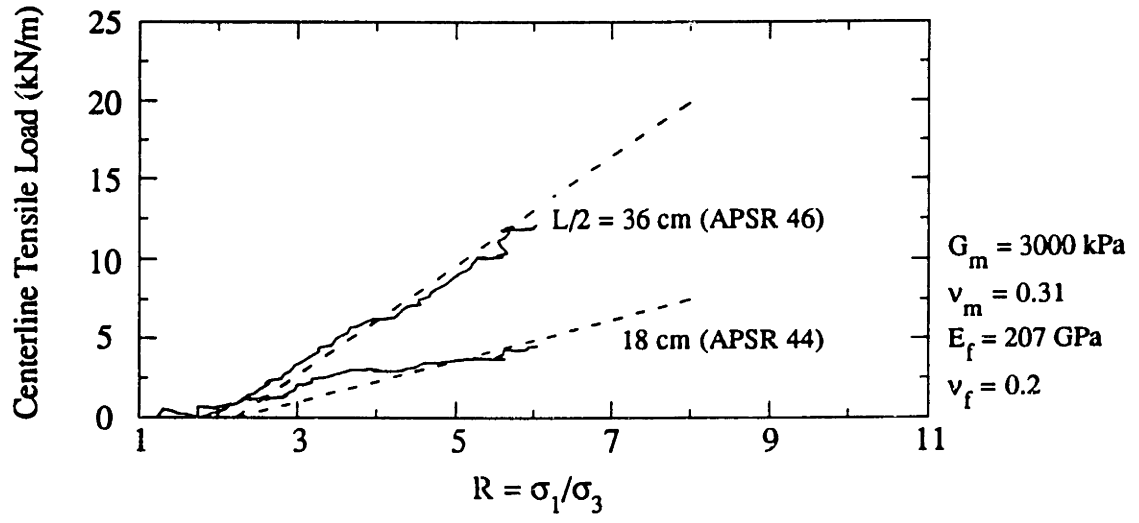

(b) Predicted vs. measured tensile load at inclusion centerline for loose sand

Figure 6.8: Shear Lag Predictions vs. Measured Inclusion Tensile Loads for Inclusions of Different Lengths

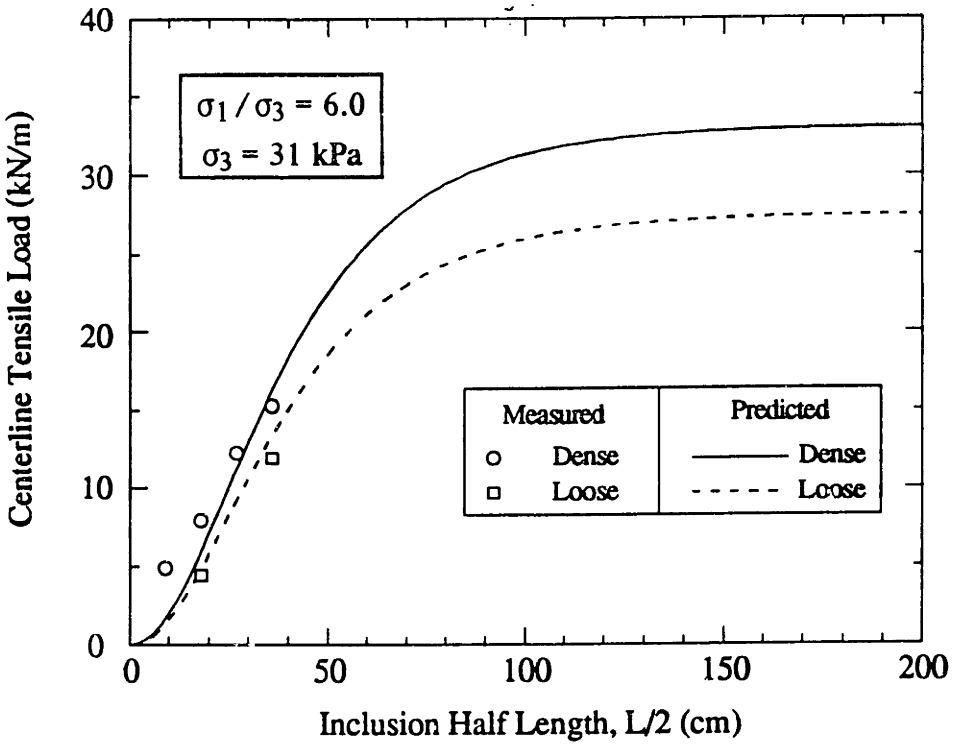

Figure 6.9: Predicted vs. Measured Maximum Tensile Force in Inclusion at R = 6.0

Chapter 7: Conclusions

7.1. Summary

This thesis describes the design, development and application of a new laboratory device, the Automated Plane Strain Reinforcement (APSR) cell, for investigating load transfer in reinforced soil. A literature review of existing laboratory measurements of soil-reinforcement interaction was performed to identify the design requirements for the APSR cell. Previous laboratory investigations are grouped in three main categories according to the level at which they provide insight into soil-reinforcement load transfer mechanisms:

1. Tests of the deformation and shear strength properties of reinforced soil composites, interpreted using homogenization methods (see Table 2.1), which provide no direct measurements of soil-reinforcement load transfer.
2. Tests of soil-reinforcement 'bond' resistance (i.e. interface shear and pullout tests, Fig. 2.13) used for limit equilibrium stability analyses, which consider only conditions at failure.
3. Detailed observations of mechanisms of soil-reinforcement interaction from local measurements of deformations, stresses, and strains in the soil and reinforcement, primarily in direct shear box inclusion tests.

Existing laboratory tests are generally not well suited for estimating load transfer characteristics in reinforced soil, especially at working (i.e. non-failure) load levels. Limitations include: a) lack of direct measurement of loads carried by the reinforcing

materials, b) inability to scale results to prototype field situations, and c) non-uniformity of stresses and strains within the soil.

The APSR cell is designed to overcome these limitations. The device simulates the mechanical interaction that occurs in a reinforced soil element (Fig. 3.1) at working load levels under realistic and interpretable boundary conditions. The APSR cell measures directly the tensile force transferred to a planar reinforcing inclusion due to plane strain shearing of the surrounding soil mass. The cell corresponds to one-half of the unit element (Fig. 3.2) containing an inclusion of length, L/2. The rear wall of the cell, which represents the midplane of the reinforced soil element, is rigid and lubricated to minimize friction, thus modelling the boundary conditions in the ideal element along that plane. The key design feature of the cell is that the inclusion is clamped externally to a load cell (Fig. 3.3) which measures the force in the reinforcement at a location equivalent to the centerline of an inclusion with length, L. An hydraulic piston controls the position of the reinforcement such that there is no displacement of the inclusion at the reference entry point.

The APSR soil specimen is 570mm high by 450mm wide by 152mm deep, and can contain a reinforcing inclusion up to 450mm long. The cell applies a confining stress, $\sigma_3 \leq 50$ kPa, against the specimen using pressurized air and imposes the major principal stress, σ_1, by moving two end platforms into the specimen. Waterbags on top of the platforms provide uniform boundary pressures. The cell imposes axial strains up to 10% on the specimen. The plane strain sidewalls (Figs. 3.9, 3.16) have an unique active control system which ensures $\epsilon_{zz} \leq 0.02\%$ throughout shear. Uniform specimens of dry sand are prepared using a custom-built raining apparatus, which deposits the sand along either the z- or y-axis (Fig. 3.2). This thesis presents data for sand

specimens deposited normal to the plane of shearing and hence, exhibit isotropic properties in the APSR tests.

External instrumentation in the cell (Fig. 3.4) includes displacement transducers to measure movements of the specimen boundaries and pressure transducers to measure directly the applied major, minor, and intermediate principal stresses. Radiography provides a record of internal soil displacements. The APSR cell is fully automated with eight closed feedback control loops for the displacements of the platform and arch jacks, the positions of the plane strain sidewalls, and the confining air pressure.

A series of 33 proof tests were performed in order to: 1) debug the control systems, 2) evaluate the reliability of the boundary conditions imposed by the APSR cell, 3) refine the active plane strain control, and 4) evaluate the uniformity of sand specimens prepared with the APSR raining apparatus. After completing the proof test program, five 'true' plane strain tests were performed on unreinforced dense ($D_r \approx 75\%$) and loose ($D_r \approx 31\%$) Ticino sand in the isotropic plane to provide detailed external and radiographic measurements of the large scale plane-strain shear behavior in the cell. The observed behavior from these tests are compared with data from other shear devices in section 4.4.

A set of fifteen tests were performed to examine the effects of sand placement density and inclusion length on load transfer between soil and elastic steel sheet reinforcements. Four 'base-case' tests (dense Ticino sand with a 36cm steel inclusion, 0.25mm thick, oriented parallel to the minor principal stress direction) were performed to determine the repeatability of load transfer measurements in the cell. In two of these tests, a two-ply, elastic, steel sheet instrumented with four strain gauges was used to determine the load distribution within the inclusion. Radiography was used in most of the tests to measure

local strains within the soil. Additional tests were performed on dense specimens with steel sheets of lengths 27, 18, and 9cm and for loose specimens reinforced with inclusions of lengths 36 and 18cm. The data from these tests were compared with analytical predictions based on a new shear lag analysis developed by Abramento and Whittle (1992), which assumes linear, elastic properties for the soil and reinforcing materials.

7.2. Conclusions Based on APSR Cell Results

7.2.1. Proof Test Series

Chapter 4 presents results from an extensive series of proof tests which demonstrate the reliability of APSR cell tests on unreinforced Ticino sand. The evaluation of the boundary condition controls (tests APSR 1-6) demonstrates that the control systems can maintain the confining air pressure, σ_c, to a tolerance of ± 0.15 kPa and the positions of the loading platforms to within ± 0.005mm of a target value. A series of lubrication tests, performed to determine boundary friction in the cell, measured the force required to translate the specimen with no relative displacement between the loading platforms. The measured resistance was found to be nearly independent of confining stress level and is explained by cohesive resistance of the grease ($c_g \approx 1.4$ kPa) on the specimen boundaries. This result is in good agreement with the grease cohesion measured by Seah (1990) in the Directional Shear Cell (DSC).

Comparison of APSR tests with different levels of plane strain control, including passive control, inaccurate active control, and 'true' plane strain (Fig. 4.15), shows that the sidewall control has a significant impact on the measured response of the soil. Tests with inaccurate active control exhibited increased dilatancy, stiffness and peak

strength, mobilized at much smaller axial strains than in the true plane strain tests. The stress-strain and volumetric response for the passive and true plane strain conditions are in fairly close agreement.

A series of five 'true' plane strain tests ($\varepsilon_2 \leq 0.02\%$) was performed on dense and loose Ticino sand specimens sheared in the isotropic plane. The dense specimens, prepared with the APSR raining apparatus, have an average density, $\gamma_d = 1.62$ g/cm^3 ($D_r \approx 75\%$). The externally measured stress-strain response for the three dense specimens (Fig. 4.17) is highly repeatable. At failure, $\varepsilon_{yy} = 1.7$ to 1.8% and $\phi'_p = 52^\circ$ to 53°. The secant modulus for the three tests, $E_{50} = 18.1$ to 19.1 MPa at a confining pressure, $\sigma_3 = 31$ kPa. The intermediate principal stress ratio, $b = 0.30$ to 0.47 throughout shear ($b_f = 0.44$ to 0.47 at failure). Loose specimens prepared in the APSR cell were less repeatable with formation densities, $\gamma_d = 1.45$ to 1.50 g/cm^3 ($D_r = 23$ to 37%). The loose specimens have a much lower stiffness ($E_{50} = 6.1$ to 8.3 MPa at $\sigma_3 =$ 31 kPa), peak strength ($\phi'_p = 44^\circ$), and intermediate stress ratio ($b_f = 0.35$ to 0.41) than dense specimens, with higher strains at failure ($\varepsilon_{yy} = 3.5$ to 4.5%).

Internal soil strains are measured by radiography over two zones in the APSR cell (the 'near field' and 'far field'; Fig. 4.20). The measurements indicate that, although the strains within each zone are fairly uniform, the strain magnitudes tend to increase with distance from the rear wall of the cell, particularly near failure. The internal strain response can be attributed to the cohesion of the grease acting along the plane strain faces of the specimen, which causes: 1) a reduction of the major principal stress, σ_1, towards the center of the specimen, and 2) an increase in the minor principal stress, σ_3, with increasing distance from the free face of the specimen. Both of these effects cause a decrease in the apparent stress ratio, R, at points away from the specimen boundary. When the internal stresses are corrected for the grease resistance (Fig. 4.32), the

external and internal measurements of the shear stress-strain behavior are in excellent agreement (Fig. 4.33). The internal measurements of volumetric strain reflect the true strain response at a point within the specimen and are therefore used to estimate the global volumetric behavior of the soil.

The plane strain shear behavior of dense Ticino sand measured in the APSR cell compares reasonably well with trends reported for other sands in the literature. The peak friction angle and soil stiffness are functions of the intermediate principal stress as well as the confining pressure and density. Volumetric strains are significantly smaller than observed at comparable stress ratios in triaxial tests. This result agrees with trends observed by other researchers, and can be attributed to the increased confinement in plane strain compression. Plane strain shearing in the isotropic plane of the APSR cell also reduces the tendency for dilation. Comparison to data for plane strain shearing of dense sand in other devices shows that the initial stiffness and volumetric behavior of the APSR specimens falls within the range observed by other researchers. The axial strain at peak is substantially lower in the APSR cell than for DSC specimens sheared in the isotropic plane, but the volumetric responses are in good agreement.

7.2.2. Steel-Reinforced Tests

Comprehensive load transfer measurements have been obtained for a 'base case' geometry comprising an inclusion of length L/2 = 36cm sheared in dense Ticino sand (D_r = 75%) at a confining stress, σ_3 = 31 kPa. These results demonstrate that reliable and repeatable measurements of centerline tensile loads requires very precise referencing and inclusion position control at the exit point from the APSR cell. The position control mechanisms described in Chapter 5 (Fig. 5.10b and c) achieve reliable

measurements for steel sheet inclusions. However, further refinement is recommended to develop a more robust measuring system.

A series of APSR tests (Table 5.1) was performed to study the influence of sand density and inclusion length on the load transfer for steel sheet inclusions sheared in Ticino sand at a confining stress, $\sigma_3 = 31$ kPa. In all of these tests, the load transfer can be characterized by a linear relationship between the tensile load and the stress ratio, $R = \sigma_1 / \sigma_3$, applied on the soil specimen. For stress ratios $R < R_o$ (where R_o is the 'offset stress ratio'), the inclusion undergoes compression, while for $R > R_o$, the accumulation of tensile load, F_R, can be expressed by a constant transfer gradient dF_R/dR. The results show the following:

1. Reinforcement tensile loads in loose Ticino sand ($D_r \approx 30\%$) are 20 to 50% lower than those measured at the same stress ratio and geometry for dense sand specimens ($D_r \approx 75\%$).
2. The centerline tensile load increases significantly with the length of the inclusion. Loads measured for a 9cm inclusion were less than 30% of the magnitude of those obtained for a 36cm inclusion. These length-scale effects represent an important capability of the APSR cell and are essential for understanding reinforcement stresses in field situations.

Radiographic measurements of soil strains within the APSR cell provide insight into the mechanisms of load transfer. The data show that the steel sheet reinforcement suppresses lateral and axial strains in the soil adjacent to the inclusion. However, there is a significant amplification of the shear strain levels close to the tip of the inclusion. The presence of the reinforcement has only a secondary effect on the external (boundary) measurements of stress-strain-strength behavior for the composite soil

element, due primarily to the small volume fraction of the soil specimen affected by the reinforcement.

7.2.3. Comparison of Results with Shear Lag Predictions

The method of shear lag analysis provides a useful framework for interpreting APSR measurements described in Chapter 5. Elastic input properties (G_m, ν_m) were obtained for dense and loose Ticino sand from unreinforced tests in the APSR cell. Using these properties and known elastic constants for the steel sheet reinforcement, shear lag predictions were made of the inclusion loads measured in the APSR tests.

Predictions for tests with a 36cm steel inclusion show that the analysis is sensitive to the value of Poisson's ratio of the soil, ν_m. For dense sand, the predictions of the maximum tensile load were made using $E_f/G_m = 35{,}000$ and $\nu_m = 0.35$, and match closely the externally measured inclusion loads in the APSR cell at all R-values. The analysis also gives good agreement with the measured load distribution along the length of the inclusion. For loose sand, the measured relationship between the inclusion tensile load and applied stress ratio is closely approximated by the shear lag analysis with $E_f/G_m = 69{,}000$ and $\nu_m = 0.31$. The shear lag analysis underpredicts the centerline tensile loads for short inclusions in dense sand (especially for $L/2 = 9$cm). However, there is better agreement between the predicted and measured load transfer for tests in loose sand. The shear lag analysis predicts reliably the gradient of the linear load transfer function for both the 18 and 36cm steel inclusions in loose sand.

The analyses show that the tensile force measured in APSR tests with $L/2 = 36$cm steel sheet reinforcements represents approximately half the load that would be transferred to a long inclusion ($L/2 \geq 1.5$m) for both dense and loose Ticino sand.

7.3. Recommendations

There are several equipment modifications which could be made to improve the performance of the APSR cell. Although the measurements of centerline inclusion force presented in this thesis appear to be accurate, the current referencing systems are prone to malfunctions. A more robust system should be developed to improve the reliability of the position control. The current design of the APSR cell uses a system of passive lubrication in order to minimize the sidewall shear resistance. However, detailed interpretation of internal strains within the soil specimens have shown that the confining stress distribution within the soil is noticeably affected by the boundary resistance caused by the grease. Potential improvements include the use of active lubrication systems such as pressurized oil or air bearings. The system for radiographing the APSR specimen should be modified to permit radiography of the entire specimen area and hence, provide more complete information on the internal strain distributions. The current interpretation of the radiographic measurements is very labor intensive. Improved digitizing techniques, such as automated digital X-ray sensing screens, would greatly reduce the time required to analyze this information.

Additional instrumentation can be added to the current system in order to improve measurements of local stresses acting within both the soil and reinforcement. Earth pressure cells along the rear wall of the cell and along the reinforcement can provide direct measurements of the effects of load transfer on internal soil stresses. Direct measurements of internal reinforcement tensile loads are also desirable, and would eliminate uncertainties associated with strain gauge measurements.

The proof tests described in Chapter 4 provide reasonable estimates of the stress-strain and volumetric response of Ticino sand sheared in the isotropic plane. Several

additional unreinforced tests could be performed, however, to provide a more detailed study of plane strain shear behavior, particularly at different confining pressures. Tests on widely-graded sands (which have a greater range of possible void ratios than poorly-graded Ticino sand) would provide more insight into the effects of relative density on shear behavior. Tests can also be performed on unreinforced sand deposited in the y-direction (Fig. 3.2) to study the effects of soil anisotropy on plane strain shear behavior, thus permitting a more detailed comparison with research in the Directional Shear Cell.

Several factors that may have a significant impact on load transfer have not yet been investigated in the APSR cell, including inclusion spacing, surface properties, stiffness, and rate dependence of inclusion materials. Adding spacer blocks on top of the platform jacks would provide the ability to test soil specimens of different lengths (in the y-direction; Fig. 3.2). This modification will affect the load transfer for a given inclusion length (cf. Abramento and Whittle, 1992), and will also change the failure mechanisms that occur in the soil mass.

Interface friction is often regarded as an important attribute for reinforcing materials. Tests should be conducted in the APSR cell to evaluate the importance of surface roughness on the load transfer at non-failure loads for some candidate reinforcing materials (e.g., roughened steel and polymer sheets). More comprehensive tests should be conducted to compare the load transfer characteristics for different classes of geosynthetic reinforcing materials, including geogrids, woven and non-woven geotextiles. Geosynthetic materials will present many new experimental difficulties and challenges. Special designs will be required for the inclusion grips, entry slot and position control mechanism, while new procedures will be required for conformable fabric materials. Many geosynthetic materials exhibit non-linear and time dependent

properties which will affect: a) the selection of instrumentation to measure load distribution, and b) the types of tests performed in the APSR cell (e.g., creep and relaxation tests).

References

Abramento, M., and Whittle, A.J. (1992), "Shear Lag Analysis of a Planar Soil Reinforcement in Plane Strain Compression," paper submitted to the Journal of Geotechnical Engineering, ASCE.

Al-Hussaini, M., and Perry, E.B. (1978), "Field Experiment of Reinforced Earth Wall," Proc. Symposium on Earth Reinforcement, ASCE, Pittsburgh, pp. 127-156.

Andersen, G.R. (1991), Physical Mechanisms Controlling the Strength and Deformation Behavior of Frozen Sand, Ph.D. Thesis, Massachusetts Institute of Technology, Cambridge, MA.

Andrawes, K.Z., McGown, A., and Al-Hasani, M.M. (1978), "Alteration of soil behaviour by the inclusion of materials with different properties," Ground Engineering, pp. 35-42.

Andrawes, K.Z., McGown, A., Wilson-Fahmy, R.F., and Mashhour, M.M. (1982), "The Finite Element Method of Analysis Applied to Soil-Geotextile Systems," Second International Conference of Geotextiles, Las Vegas, pp. 695 - 700.

Arthur, J.R.F. (1988), "Cubical Devices: Versatility and Constraints," Advanced Triaxial Testing of Soil and Rock, ASTM STP 977, R.T. Donaghe, R.C. Chaney, and M.L. Silver, Eds., American Society for Testing and Materials, Philadelphia, pp. 743-765.

Arthur, J.R.F., and Menzies, B.K. (1972), "Inherent anisotropy in a sand," Géotechnique, v. 22, n. 1, pp. 115-128.

Baldi, G., et al. (1985), "Laboratory validation of in-situ tests," AGI Jubilee Volume, Proc. 11th ICSMFE, San Francisco, CA.

Basset, R.H., and Last, N.C. (1978), "Reinforcing Earth Below Footings and Embankments," Symposium on Earth Reinforcment, Pittsburgh, PA, pp. 202-231.

Bekenstein, S. (1981), Directional Shear Tests on Leighton Buzzard Sand, S.M. Thesis, Massachusetts Institute of Technology, Cambridge, MA.

Bishop, A.W. (1966), "The strength of soils as engineering material," Géotechnique, v. 16, n. 2, pp. 89-130.

Black, D.S. (1990), "Geosynthetic Reinforcement of Soil Masses: In-Isolation Testing of Reinforcement Strips," Report on summer intern program, Department of Civil Engineering, MIT.

Bolton, M.D. (1986), "The strength and dilatancy of sands," Géotechnique, v. 36, n. 1, pp. 65-79.

Bolton, M.D., Choudhury, S.P., and Pang, P.L.R. (1978), "Reinforced Earth Walls: A Centrifugal Model Study," Proc. Symposium on Earth Reinforcement, ASCE, Pittsburgh, pp. 252-281.

Bolton, M.D., and Pang, P.L.R. (1982), "Collapse limit states of reinforced earth retaining walls," Géotechnique, v. 32, n. 4, pp. 349-367.

Bonaparte, R., and Schmertmann, G.R. (1987), "Reinforcement Extensibility in Reinforced Soil Wall Design," The Application of Polymeric Reinforcement in Soil Retaining Structures, P.M. Jarret and A. McGown (eds.), Kluwer Academic Publishers, pp. 409-458.

Broms, B.B. (1977), "Polyester Fabric as Reinforcement in Soil," Proceedings of the International Conference on the Use of Fabrics in Geotechnics, Paris, v. 1, pp. 129-135.

Budiansky, B., Hutchinson, J.W., and Evans, A.G. (1986), "Matrix Fracture in Fiber-Reinforced Ceramics," Journal of the Mechanics of Physical Solids, v. 34, n. 2, pp. 167-189.

Butterfield, R., Harkness, R.M., and Andrawes, K.Z. (1970), "A stereo-photogrammetric method for measuring displacement fields," Géotechnique, v. 20, n. 3, pp. 308-314.

Chalaturnyk, R., Chan, D.H.K., and Scott, J.D. (1988), "Finite Element Analysis of Reinforced Soil," The Application of Polymeric Reinforcement in Soil Retaining Structures, P.M. Jarret and A. McGown (eds.), Kluwer Academic Publishers, pp. 557-560.

Chang, J.C., Hannon, J.B., and Forsyth, R.A. (1977), "Pull-out Resistance and Interaction of Earth Reinforcement and Soil," Transport Research Record No. 640, Washington, D.C.

Chauhan, S. (1991), Personal communication

Chen, L.S. (1948), "An Investigation of Stress-Strain and Strength Characteristics of Cohesionless Soils by Triaxial Compression Tests," Proc. Second International Conference on Soil Mechanics and Foundation Engineering, v. 5, p. 35.

Christie, I. F. (1982), "Economic and Technical Aspects of Embankments Reinforced with Fabric," Proc. Second International Conference on Geotextiles, Las Vegas, pp. 659-664.

Cornforth, D.H. (1964), "Some experiments on the influence of strain conditions on the strength of sand," Géotechnique, v. 24, n. 2, pp. 143-167.

Cox, H.L. (1952), "The elasticity and strength of paper and other fibrous materials," British Journal of Applied Physics, v. 3, pp. 72-79.

Dash, U. (1978), "Design and Field Testing of a Reinforced Earth Wall," Proc. Symposium on Earth Reinforcement, ASCE, Pittsburgh, pp. 334-357.

Davoudzadeh, F. (1982), Response of Sand to Three Independently Controlled Principal Stresses, Ph.D. Thesis, Dept. of Civil and Municipal Engineering, UCL, London, England.

deBuhan, P., Mangiavacchi, R., Nova, R., Pellegrini, G., and Salençon, J. (1989), "Yield design of reinforced earth walls by a homogenization method," Géotechnique, v. 39, n. 2, pp. 189-201.

Degautte, G., and Mathieu, G. (1986), "Experimental Research of Friction between Soil and Geomembranes or Geotextiles Using a 30 x 30 cm Shearbox", Proc. Third International Conference on Geotextiles, Vienna, Austria, v. 4, pp. 1251-1256.

Delmas, P., Gourc, J.P., and Giroud, J.P. (1979), "Analyse Experimental de l'Interaction Mecanique Sol-Geotextile," Proc. International Conference on Soil Reinforcement, Paris, v. 1, pp. 29-34.

Deterling, P.A. (1984), Behavior of Sand Stressed under Three Independently Controlled Principal Stresses, S.M. Thesis, Massachusetts Institute of Technology, Cambridge, MA.

Draper, N., and Smith, H. (1981), Applied Regression Analysis, John Wiley & Sons, New York.

Dyer, M.R. (1985), Observation of the Stress Distribution in Crushed Glass with Applications to Soil Reinforcement, Ph.D. Thesis, University of Oxford.

Dyer, M.R., and Milligan, G.W.E. (1984), "A photoelastic investigation of the interaction of a cohesionless soil with reinforcement placed at different orientations," Proc. Int. Conf. on Insitu Soil and Rock Reinforcement, Paris, pp. 257-262.

Formazin, J., and Batereau, C. (1985), "The shear strength behavior of certain materials on the surface of geotextiles," Proceedings of the 11th ICSMFE, San Francisco, v. 3, pp. 1773-1775.

Franco, C. (1989), Caratteristiche Sforzi-Deformazioni-Resistenza Delle Sabbie, Ph.D. Thesis, Politecnico di Torino, Torino, Italy.

Fukushima, S., Mochizuki, Y., and Kagawa, K. (1988), "Strength characteristic of reinforced sand in large scale triaxial compression test," International Geotechnical Symposium on Theory and Practice of Earth Reinforcement, Fukuoka, Japan, A.A. Balkema, pp. 93-98.

Germaine, J.T. (1982), Development of the Directional Shear Cell for Measuring Cross Anisotropic Clay Properties, Ph.D. Thesis, Massachusetts Institute of Technology, Cambridge, MA.

Gourc, J.P., Ratel, A., and Delmas, P. (1986), "Design of Fabric Retaining Walls: The Displacements Method," Proc. Third International Conference on Geotextiles, Vienna, v. 3, pp. 1067-1072.

Gray, D.H., and Al-Refeai, T. (1986), "Behavior of Fabric- versus Fiber-Reinforced Sand," Journal of Geotechnical Engineering, ASCE, v. 112, n. 8, pp. 804-820.

Gray, D.H., Athanasopoulos, G., and Ohashi, H. (1982), "Internal/External Fabric Reinforcement of Sand," Proc. Second International Conference on Geotextiles, Las Vegas, pp. 611-616.

Gray, D.H., and Ohashi, H. (1983), "Mechanics of Fiber Reinforcement in Sand," Journal of Geotechnical Engineering, ASCE, v. 109, n. 3, pp. 335-353.

Green, G.E., and Reades, D.W. (1975), "Boundary conditions, anisotropy and sample shape effects on the stress-strain behaviour of sand in triaxial compression and plane strain," Géotechnique, v. 25, n. 2, pp. 333-356.

Guilloux, A., Schlosser, F., and Long, N.T. (1979), "Etude du Frottement Sable-Armature en Laboratoire," Proc. International Conference on Soil Reinforcement, Paris, v. 1, pp. 35-40.

Harrison, W.J. and Gerrard, C.M. (1972), "Elastic Theory Applied to Reinforced Earth," Journal of the Soil Mechanics and Foundation Engineering Division, ASCE, v. 98, n. 12, pp. 1325-1344.

Hausmann, M.R. (1976), "Strength of reinforced soil," Proceedings, 8th Australian Road Research Board Conference, Perth, Australia.

Hausmann, M.R., and Lee, I.K. (1976), "Strength Characteristics of Reinforced Soil," International Symposium on New Horizons in Construction Materials, Lehigh University, v. 1, pp. 165-176.

Hausmann, M.R., and Vagneron, J.M. (1977), "Analysis of soil-fabric interaction," C. R. Coll. Int. Sols Textiles, Paris, pp. 139-144.

Hayashi, S., Ochiai, H., Yoshimoto, A., Sato, K., and Kitamura, T. (1988), "Functions and effects of reinforcing materials in earth reinforcement," International Geotechnical Symposium on Theory and Practice of Earth Reinforcement, Fukuoka, Japan, pp. 99-104.

Hill, R. (1963), "Elastic Properties of Reinforced Solids: Some Theoretical Principles," Journal of the Mechanics and Physics of Solids, v. 11, pp. 357-372.

Holister, G.S., and Thomas, C. (1969), Fibre Reinforced Materials, Elsevier, London.

Holtz, R.D., Tobin, W.R., and Burke, W.W. (1982), "Creep Characteristics and Stress-Strain Behavior of a Geotextile-Reinforced Sand," Second International Conference on Geotextiles, Las Vegas, pp. 805-809.

Houlsby, G.T., and Jewell, R.A. (1988), "Analysis of unreinforced and reinforced embankments on soft clays by plasticity theory," Numerical Methods in Geomechanics, Innsbruck, A.A. Balkema, Rotterdam, pp. 1443-1448.

Ingold, T.S. (1982), "Some Observations on the Laboratory Measurement of Soil-Geotextile Bond," Geotechnical Testing Journal, GTJODJ, v. 5, n. 3/4, pp. 57-67.

Ingold, T.S. (1984), "A laboratory investigation of soil-geotextile friction," Ground Engineering, v. 17, n. 11, pp. 21-28.

Ingold, T.S., and Templeman, J.E. (1979), "The comparative performance of polymer net reinforcement," Proceedings of the International Conference on Soil Reinforcement, Paris, v. 1, pp. 65-70.

Jewell, R.A. (1980), Some effects of reinforcement on the mechanical behaviour of soils, Ph.D. Thesis, University of Cambridge.

Jewell, R. A. (1985), "Limit equilibrium analysis of reinforced soil walls," Proc. 11th ICSMFE, San Francisco, v.3, pp. 1705-1708.

Jewell, R.A. (1990), "Strength and Deformation in Reinforced Soil Design," Proc. Fourth International Conference on Geotextiles, Geomembranes, and Related Products, The Hague, 79 p.

Jewell, R.A., and Wroth, C.P. (1987), "Direct shear tests on reinforced sand," Géotechnique, v. 37, n. 1, pp. 53-68.

Jewell, R.A. (1988), "Reinforced Soil Wall Analysis and Behaviour," The Application of Polymeric Reinforcement in Soil Retaining Structures, P.M. Jarret and A. McGown (eds.), Kluwer Academic Publishers, pp. 365-408.

Jewell, R.A., Milligan, G.W.E., Sarsby, R.W., and Dubois, D. (1985), "Interaction Between Soils and Geogrids," Polymer Grid Reinforcement, Thomas Telford, London, pp. 18-30.

John, N.W.M. (1987), Geotextiles, Chapman and Hall, New York.

Juran, I., and Christopher, B. (1989), "Laboratory Model Study on Geosynthetic Reinforced Soil Retaining Walls," Journal of Geotechnical Engineering, ASCE, v. 115, n. 7, pp. 905-926.

Juran, I., Guermazi, A., Chen, C.L., and Ider, M.H. (1988a), "Modelling and Simulation of Load Transfer in Reinforced Soils: Part 1," International Journal for Numerical and Analytical Methods in Geomechanics, v. 12, pp. 141-155.

Juran, I., Guermazi, A., Chen, C.L., and Ider, M.H. (1988b), "Numerical Analysis of the Response of Reinforced Soils to Direct Shearing: Part 2," International Journal for Numerical and Analytical Methods in Geomechanics, v. 12, pp. 157-171.

Kelly, A. (1986), Strong Solids, Clarendon Press, Oxford

Kim, O. Y. (1987), Triaxial Extension Testing of Hollow Cylinder Type Sample of Reinforced Sand, Research Report, Dept. of Civil Engineering, University of California, Davis.

Koerner, R.M. (1986), Designing with Geosynthetics, Prentice-Hall, Englewood Cliffs, NJ.

Koerner, R.M., Hwo, B.L., and Wayne, M.H. (1987), "Soft soil stabilization using geosynthetics," Geotextiles and Geomembranes, v. 6, pp. 33-51.

Koerner, R.M., and Wayne, M.H. (1990), "Geomembrane Anchorage Behavior Using a Large-Scale Pullout Apparatus," Geomembranes: Identification and Performance Testing, Chapman and Hall, New York.

Koivumaki, O. (1983), "Friction Between Sand and Metal," Proc. Eighth European Conference on Soil Mechanics and Foundation Engineering, Helsinki, v. 2, pp. 517-520.

Kuhn, P. (1956), Stresses in Aircraft and Shell Structures, McGraw-Hill, New York, 1956.

Ladd, C.C., Foott, R., Ishihara, K., Schlosser, F., and Poulos, H.G. (1977), "Stress-Deformation and Strength Characteristics," Proceedings of the Ninth International Conference on Soil Mechanics and Foundation Engineering, Tokyo, pp. 421-494.

Lam, W.K., and Tatsuoka, F. (1988), "Effects of Initial Anisotropic Fabric and σ_2 on Strength and Deformation Characteristics of Sand," Soils and Foundations, v. 28, n. 1, pp. 89-106.

Lee, K.L. (1978), "Mechanisms, Analysis, and Design of Reinforced Earth: State-of-the-Art Report," Proc. Symposium on Earth Reinforcement, ASCE, Pittsburgh, pp. 62-76.

LeFlaive, E., and McGown, A. (1988), "The Purpose of Materials Evaluation and Recommendations for Materials Testing," The Application of Polymeric Reinforcement in Soil Retaining Structures, P.M. Jarret and A. McGown (eds.), Kluwer Academic Publishers, pp. 343-355.

Leshchinsky, D., and Reinschmidt, A.J. (1985), "Stability of Membrand Reinforced Slopes," Journal of Geotechnical Engineering, ASCE, v. 111, n. 11, pp. 1285-1300.

Leshchinsky, D., and Volk, J.C. (1985), "Stability of geotextile retained earth railroad embankments," Geotextiles and Geomembranes, v.3, pp. 105-128.

Long, N.T., Guegan, Y., and Legeay, G. (1972), "La Terre Armée au Triaxial," Rapport de Recherche du Laboratoire Central des Ponts et Chaussées, n. 17.

Marachi, N.D., Duncan, J.M., Chan, C.K., and Seed, H.B. (1981), "Plane-Strain Testing of Sand," Laboratory Shear Strength of Soil, ASTM STP 740, R.N. Young and F.C. Townsend, Eds., American Society for Testing and Materials, pp. 294-302.

McGown, A., and Andrawes, K.Z. (1977), "The influences of non-woven fabric inclusions on the stress-strain behaviour of a soil mass," C. R. Coll. Int. Sols Textiles, Paris, pp. 161-165.

McGown, A., Andrawes, K.Z., and Al-Hasani, M.M. (1978), "Effect of inclusion properties on the behaviour of sand," Géotechnique, v. 28, n. 3, pp. 327-346.

McGown, A., Andrawes, K.Z., Hytiris, N., and Mercer, F.B. (1985), "Soil Strengthening Using Randomly Distributed Mesh Elements," Proc. Eleventh ICSMFE, San Francisco, v. 3, pp. 1735-38.

McGown, A., Andrawes, K.Z., and Kabir, M.H. (1982), "Load-Extension Testing of Geotextiles Confined In-Soil," Proc. Second International Conference on Geotextiles, Las Vegas, pp. 793-798.

McGown, A., Andrawes, K.Z., and Yeo, K.C. (1985), "The load-strain-time behaviour of Tensar geogrids," Polymer Grid Reinforcement, Thomas Telford Ltd., London, pp. 11-17.

Mitchell, J. K., and Schlosser, F. (1979), "General Report," International Conference on Soil Reinforcement, Paris, v. 3, pp. 25-62.

Miura, S., and Toki, S. (1983), "A Sample Preparation Method and Its Effect on Static and Cyclic Deformation-Strength Properties of Sand," Soils and Foundations, v. 22, n. 1, pp. 61-77.

Miyamori, T., Iwai, S., and Makiuchi, K. (1986), "Frictional Characteristics of Non-Woven Fabrics," Proc. Third International Conference on Geotextiles, Vienna, v. 3, pp. 701-706.

National Research Council (1989), Geotechnology: Its Impact on Economic Growth, the Environment and National Security, National Academy Press, Washington, D.C.

Oda, M. (1972), "Initial Fabrics and Their Relations to Mechanical Properties of Granular Material," Soils and Foundations, v. 12, n. 1, pp. 17-36.

Oda, M. (1981), "Anisotropic Strength of Cohesionless Sands," JGED, ASCE, v. 107, n. GT9, pp. 1219-1231.

Oda, M., Koishikawa, I., and Higuchi, T. (1978), "Experimental Study of Anisiotropic Shear Strength of Sand by Plane Strain Test," Soils and Foundations, v. 18, n. 1, pp. 25-38.

Ohiai (1992), Personal communication.

Palmeira, E.M. (1981), Utilization of Geotextile Reinforcement as a Reinforcement for Access Roads on Soft Ground, MSc Thesis, Coppe/Federal University of Rio de Janeiro, Brazil.

Palmeira, E.M. (1987), The Study of Soil-Reinforcement Interaction by means of Large Scale Laboratory Tests, Ph.D. Thesis, University of Oxford.

Palmeira, E.M., and Milligan, G.W.E. (1989), "Large scale direct shear tests of reinforced soils," Soils and Foundations, v. 29, n. 1, pp. 18-30.

Palmeira, E.M., and Milligan, G.W.E. (1989), "Scale and other factors affecting the results of pull-out tests of grids buried in sand," Géotechnique, v. 39, n. 3, pp. 511-524.

Perrier, H., Blivet, J.C., and Khay, M. (1986), "Stabilisation de Talus par Reinforcement tout Textile: Ouvrage Experimental et Reel," Proc. Third International Conference on Geotextiles, Vienna, v. 2, pp. 313-318.

Popov, E.P. (1976), Mechanics of Materials, Prentice Hall, London.

Potyondy, J.G. (1961), "Skin Friction Between Cohesive Granular Soils and Construction Materials," Géotechnique, v. 11, n. 4, pp. 339-353.

Rad, N.S., and Tumay, M.T. (1987), "Factors Affectin Sand Specimen Preparation by Raining," Geotechnical Testing Journal, GTJODJ, v. 10, n. 1, pp. 31-37.

Richards, E.A., and Scott, J.D. (1985), "Soil-Geotextile Frictional Properties," Proceedings of the Second Canadian Conference on Geotextiles, pp. 13-24.

Roark, R.J., and Young, W.C. (1975), Formulas for Stress and Strain, Fifth edition, McGraw-Hill, pp. 385-404.

Romstad, K.M., Herrman, L.R., and Shen, C.K. (1976), "Integrated Study of Reinforced Earth - 1: Theoretical Formulation," Journal of the Geotechnical Engineering Division, ASCE, v. 102, n. GT5, pp. 457-471.

Rowe, P.W. (1962), "The Stress-Dilatancy Relation for Static Equilibrium of an Assembly of Particles in Contact," Proceedings of the Royal Society of London, v. A269, pp. 500-527.

Rowe, P.W. (1969), "The relation between the shear strength of sands in triaxial compression, plane strain and direct shear," Géotechnique, v. 19, n. 1, pp. 75-86.

Rowe, R.K., and Ho, S.K. (1988), "Application of Finite Element Techniques to the Analysis of Reinforced Soil Walls," The Application of Polymeric Reinforcement in Soil Retaining Structures, P.M. Jarret and A. McGown (eds.), Kluwer Academic Publishers, pp. 541-553.

Rowe, R.K., Ho, S.K., and Fisher, D.G. (1985), "Determination of Soil-Geotextile Interface Strength Properties," Proceedings of the Second Canadian Symposium on Geotextiles and Geomembranes, Edmonton, Canada, pp. 25-34.

Sawicki, A. (1983), "Plastic Limit Behavior of Reinforced Earth," Journal of the Geotechnical Engineering Division, ASCE, v. 109, n. 7, pp. 1000-1005.

Schlosser, F., and Elias, V. (1978), "Friction in Reinforced Earth," Proceedings of the ASCE Symposium on Earth Reinforcement, Pittsburgh, PA, pp. 735-762.

Schlosser, F., and Guilloux, A. (1979), "Friction Between Soil and Strips in Reinforced Earth Structures," Proceedings of the First International Conference on Soil Reinforcement, Paris, pp. 151-156.

Schlosser, F., and Long, N.T. (1972), "Comportement de la terre armée dans les ouvrages de souténement," Proceedings of the Fifth European Conference on Soil Mechanics and Foundation Engineering, Madrid, v. 1, pp. 299-306.

Schlosser, F. and Long, N. T. (1974), "Recent Results in French Research on Reinforced Earth," Journal of the Construction Division, ASCE, v. 100, n. CO3, pp. 223-237.

Schwab, E.F., Prengl, O., and Broms, B.B. (1977), "Deformation Behavior of Reinforced Sand at Model Tests Measured by the X-ray Technique," Proceedings of the First International Conference on the Use of Fabrics in Geotechnics, v. 1, pp. 105-112.

Seah, T.H. (1990), Anisotropy of Resedimented Boston Blue Clay, Ph.D. Thesis, Massachusetts Institute of Technology, Cambridge, MA.

Sheahan, T. C. (1991), An Experimental Study of the Time-Dependent Undrained Shear Behavior of Resedimented Clay Using Automated Stress Path Triaxial Equipment, Sc.D. Thesis, Massachusetts Institute of Technology, Cambridge, MA.

Shen, C. K., Kim, O. Y., Li, X. S., and Sohn, J. (1988), "Soil Reinforcement Interaction Determined by Extension Test," Theory and Practice of Earth Reinforcement, A.A. Balkema, Rotterdam, pp. 165-170.

Shen, C.K., Mitchell, J.K., deNatale, J.S., and Romstad, K.M. (1979), "Laboratory Testing and Model Studies of Friction in Reinforced Earth," Proc. International Conference on Soil Reinforcement, Paris, v. 1, pp. 169-174.

Shewbridge, S.E., and Sitar, N. (1989), "Deformation Characteristics of Reinforced Sand in Direct Shear," Journal of Geotechnical Engineering, ASCE, v. 115, n. 8, pp. 1134-1147.

Sweeney, B.P. (1987), Liquefaction Evaluation Using a Miniature Cone Penetrometer and a Large Scale Calibration Chamber, Ph.D. Thesis, Stanford University.

Tatsuoka, F., Sakamoto, M., Kawamura, T., and Fukushima, S. (1986), "Strength and Deformation Characteristics of Sand in Plnae Strain Compression at Extremely Low Pressures," Soils and Foundations, v. 26, n. 1, pp. 65-84.

Transportation Research Board (1985), "Research Problem Statements: Research in Engineering Fabrics," TRB Circular No. 291.

Uesugi, M., and Kishida, H. (1986a), "Influential Factors of Friction Between Steel and Dry Sands," Soils and Foundations, v. 26, n. 2, pp. 33-46.

Uesugi, M., and Kishida, H. (1986b), "Frictional Resistance at Yield Between Dry Sand and Mild Steel," Soils and Foundations, v. 26, n. 4, pp. 139-149.

Vidal, H. (1966), "La Terre Armée," Annales de l'Institut Techniques des Batîments et des Travaux Publiques, Paris, pp. 888-938.

Wakabayashi, T. (1957), "Photoelastic method for determination of stress in powdered mass," Proc. 7th Japanese National Conference on Applied Mechanics, pp. 153-158.

Werner, R.J. (1990), The Influence of Load History on the Response of Arctic Silt to Undrained Cyclic and Monotonic Direct Simple Shear, S.M. Thesis, Massachusetts Institute of Technology, Cambridge, MA.

Westergaard, H.M. (1938), "A Problem of Elasticity Suggested by a Problem in Soil Mechanics," Mechanics of Solids, Timoshenko 60th Anniversary Volume, MacMillan & Co., New York, N.Y.

Whittle, A.J., Larson, D.G., and Abramento, M. (1991), "Annual Technical Report on Geosynthetic Reinforcement of Soil Masses," Research Report, Department of Civil Engineering, Massachusetts Institute of Technology.

Wong, R.K.S. (1985), "Sand Subjected to Cyclic Principal Stress Rotations," Ph.D. Thesis, University College London.

Wrigley, N.E. (1987), "Durability and long-term performance of Tensar polymer grids for soil reinforcement," Materials Science and Technology, v. 3, n. 3, pp. 161-170.

Yang, Z. (1972), Strength and Deformation Characteristics of Reinforced Sand, Ph.D. Thesis, Unversity of California, Los Angeles.

Appendix A. APSR Control Software

A.1. Introduction

This appendix describes the program APSR.BAS which controls the air pressure, sidewall pressures and platform positions in the APSR cell. The first section describes the features of the program. This is followed by a more detailed user's guide to the program's menu options, then a listing of the program code.

The program reads the transducers shown in Figure 3.4. APSR.BAS seeks to match these transducer signals to target values set by the user. When a test is in progress, the program sends voltage pulses to five motors and an air pressure regulator which control the three principal stresses. After a set of pulses has been sent, the program checks the platform positions and the principal stresses and sends another set of pulses as needed to reach the desired target values (see the flowchart, Fig. 3.23). This loop repeats throughout the testing process.

The program reads transducer voltages through an analog-to-digital (A/D) conversion card contained in the computer. Without this card the program will not function. The transducer signals are fed to this card through a 25 pin connector which attaches to the back of the computer. APSR.BAS sends output voltages to the motor controllers and the air regulator through a digital-to-analog conversion card[1]. The voltages pass to a

[1] The card is manufactured by Strawberry Tree, Inc.

terminal strip outside the computer. The motors and the air regulator connect to the appropriate channels on the terminal strip.

A.1.1. Program Start-Up

This section describes the hardware setup required to run the APSR control program.

Four files must be in the computer directory. These are: APSR.BAS, APSR.BAT, ZEROS.BAS, and ZEROS.BAT.

The four platform piston motor controllers must be turned on and set to "External Signal". The voltage output lines on the Strawberry Tree terminal panel must be connected to the "External Signal" plugs on the motor control panels and to the Fairchild air regulator. The motors must be plugged in to their respective controllers through the "Signal to Motor" plug.

The output air line from the Fairchild regulator must be attached to the cell. There should be no major leaks in the cell.

The transducers shown in Figure 3.4 must be connected to the A/D cards as shown in Table A.1. Transducer signals feed into the A/D cards through 25 pin connectors. When all the connections have been made, type ZEROS to record the initial readings of all the transducers. ZEROS.BAS creates a file called ZEROS that stores these initial readings. APSR.BAS uses these readings to compute total displacements and pressures. Type APSR to run the APSR control program.

A.1.2. Menu Commands

There are seven menu commands (Fig. 3.22) that may be selected at any time while the APSR program is active. To select a command, use the up and down arrow keys to

highlight the desired function and press [RETURN]. While a command is in progress, the menu system is inactive. Program control returns to the menu after the command has been completed or halted by the user. The following paragraphs give a summary of menu choices. More detailed information on each item is given in the next section.

Air Pressure: Sets the target air pressure (confining pressure) inside the cell, in units of pounds per square inch (psi). Acceptable input is any value between 0 and 7.

Set Mode: Determines whether to operate the major principal stress platforms under displacement or stress control. Acceptable input is a single character, either "D" (for displacement control), "S" (for stress control), or "R". Selecting "R" will cause the program to return the platforms to their starting positions.

Target: Sets either a target pressure (in psi) or a target position (in inches) for the major principal stress platforms, depending on whether the SetMode command is set for stress or displacement control.

Set Scale: Sets the speed at which to run the motors that control the platform pistons. Acceptable input is any number between 0 and 100, corresponding to a percentage of the full scale motor output.

B Ctrl: Determines how the sidewalls are controlled. Acceptable input is a single character. "B" causes the program to match the pressures in the sidewalls to a target b-value, "D" causes the program to maintain zero sidewall displacements, and "Q" turns off computer control of the sidewalls.

RUN: Causes the program to read the incoming transducer signals and activates computer control of the motors and the air pressure using all of the currently selected settings. Pressing "S" stops computer controlled testing and reactivates the main menu.

Set-Up: Enables modification of testing parameters such as the time length of each motor step, the error amplification factor for sidewall control, calibration factors of the transducers, and current input voltage.

A.2. Descriptions of Menu Commands

A.2.1. Air Pressure

This command prompts the user for a target air pressure (in psi). Any value between 0 and 7 psi is acceptable. The program then adjusts the Fairchild pressure regulator until the actual air pressure matches the target air pressure to within a user-specified tolerance (the default tolerance is 0.05 psi).

A.2.1.1. Method of Air Pressure Adjustment

The Fairchild voltage-pneumatic transducer is a pressure regulator which scales its output pressure according to a signal voltage between 0 and 10V. The APSR program controls the voltage that is sent to the Fairchild through output line 5 (see Table A.1). If the output voltage has not been previously set by the user, the program selects a first guess according to the calibration curve of the Fairchild regulator:

$$V = (T - 1.098)/0.709$$

where V is the output voltage that will be sent to the Fairchild, and T is the target air pressure (in psi).

The program then checks the actual air pressure in the APSR cell and fine tunes the output voltage to the Fairchild until the actual pressure matches the target pressure. Control then returns to the menu system. To fine tune the pressure the program changes the voltage to the Fairchild by 0.02V, re-checks the actual air pressure, then changes the output voltage again until the proper pressure is achieved. The output voltage is recorded in the POUTV variable, which is displayed in the upper right corner of the computer screen. Pressing "S" halts this control loop and returns program control to the main menu.

A.2.1.2. Possible Errors

The routine that is executed by the Air Pressure command has two safety checks. If the output voltage exceeds 8V, the program will beep and pause after each voltage increment, signalling that the voltage is approaching its maximum allowable value of 9V. If the POUTV variable reaches 9V, the control loop terminates. This may occur for two reasons:

1) The APSR cell is not sealed adequately, and the Fairchild cannot keep up with the high air flow demand.
2) The supply pressure to the Fairchild regulator is too low.

A.2.2. Set Mode

This command determines whether to run the major principal stress platforms under displacement or stress control. Acceptable input is a single character, either "D" (for displacement control), "S" (for stress control), or "R" (for reset). Once one of these

letters is entered, program control returns to the main menu and the active mode ([D] or [S]) is displayed on the menu.

A.2.2.1. Displacement Control

This option resets the initial positions of the platforms to their current positions. This new initial position is used for computing and displaying the current axial strain and for referencing target displacements. When the test is running under displacement control, the program matches both platform displacements.

A.2.2.2. Stress Control

Under stress control, the program steps the platforms so that the pressures in both pressure bags match each other. This can result in one platform moving more than the other, so the displacement rates of the two platforms may no longer be the same.

A.2.2.3. Reset

The reset option causes the program to return the platforms to their starting positions (i.e., the positions they were at when the program was first activated) when the RUN command is activated. This option resets the reference initial positions of the four platform LVDTs to their value at the start of the test. It sets the target displacement for zero inches, and changes the test mode to displacement control.

A.2.3. Target

Target prompts for either a target pressure (in psi) or a target position (in inches) for the major principal stress platforms, depending on whether the SetMode command is set for stress or displacement control. Once an acceptable value is entered, control returns to the menu system. The current target is displayed in the upper right corner of

the screen. The target displacement is measured from the last time the SetMode command was set to displacement control.

A.2.4. Set Scale

The Set Scale command sets the speed at which to run the four motors controlling the platform pistons. Acceptable input is any number between 0 and 100, corresponding to the percentage of the full scale motor output. When the test is running, the program will use this percentage to step the motors for a fixed time increment (approximately 0.75 sec). Larger values result in larger motor steps during each time increment.

A.2.5. B Ctrl

This command sets the type of sidewall control that will be used during testing. Acceptable input is a single character. "B" causes the program to match the pressures in the sidewalls to a target b-value, "D" causes the program to maintain zero sidewall displacements, and "Q" turns off computer control of the sidewalls.

A.2.5.1. Testing without computer control

The default value for the B Ctrl feature is "Q". In this case the program reads and displays the sidewall displacements and pressures, but doesn't send any signals to the sidewall motors. This mode should be used if the sidewalls are run under independent feedback control.

A.2.5.2 B-value control

When the mode is set to "B", the program prompts for a desired b-value. Any value between 0 and 1 is valid. For plane strain conditions, use a value of 0.4 to 0.5. During testing (i.e. when the RUN command is executed), the program will compute

the existing b-value from the average pressure in the two water bags (σ_1), the pressure in the top sidewall (σ_2), and the air pressure (σ_3). To match the target b-value, the program sends a scaled voltage pulse to the two sidewall controllers. The size of the pulse is a function of the amount of error between the actual and the target b-value. The program continues to send pulses to the sidewall motors until either 1) they reach the target b-value or 2) the sidewall pressure is within 0.15 psi of the necessary value to achieve the target b-value.

A.2.5.3. Zero displacement control

If the sidewall control is set to "D", APSR.BAS adjusts the sidewall pressures to keep the measured intermediate principal strain, ε_2, nearly zero. When the displacement option is selected, the program records the positions of the sidewall LVDTs. During the RUN cycle, the program checks the positions of the sidewall LVDTs and adds their total displacement from the initial position. It sends a voltage pulse (proportional to the measured error) to the sidewall motors. The control loop continues until the walls return to their initial positions.

A.2.6. RUN

The RUN command activates computer controlled testing. In RUN mode, the program reads the incoming transducer signals and controls the motors and the air pressure using all of the current settings and targets. To stop computer controlled testing and return to the main menu, press "S".

The RUN command cycles through a continuous feedback loop to reach and maintain the targets set by the user. This cycle is illustrated in Figure 3.23. First the program checks and adjusts the air pressure until it matches the target value. Then it adjusts the

sidewalls until they achieve either their target b-value or zero displacement, depending on how the sidewall control is set. Between each voltage pulse to the sidewalls, the program rechecks and adjusts the air pressure when necessary. The final step in the cycle is to adjust the two platform positions. Between each voltage pulse sent to the platform motors, the program rechecks and adjusts the sidewall pressures and the air pressure.

A.2.6.1. Air Pressure Control

The RUN command uses the same method for controlling the air pressure as the AIR PRESSURE command described earlier. The program checks the actual air pressure. If it has deviated from the target, the program increments the voltage to the Fairchild pressure regulator by 0.02 volts. This cycle continues until the air pressure is at its target value.

A.2.6.2. Sidewall Control

Sidewall control is described under the B CTRL command. During the RUN cycle, the program checks the displacements and pressures in the two sidewalls. If they have deviated from the target values, the program sends a voltage pulse of fixed duration to the sidewall motors. The size of this pulse is proportional to the amount of error. The duration of the pulse and the error amplification factor can be set with the SET UP menu command.

A.2.6.3. Platform Control

The RUN cycle steps the platforms to match either a target pressure or a target displacement set with the TARGET menu command. Before a step, the program

checks the readings of the four LVDTs that measure the platform positions and the two pressure transducers on the water bags.

Under displacement control, the program checks if both platforms have reached the target displacement. If not, it determines if one has moved more than the other. If both platforms are the same distance from the target value, the program moves both platforms by one step. If one has moved more than the other, the program will only move the platform that is farthest from the target value.

In a stress controlled cycle, the program checks the measured pressures in the two platform water bags. If the pressures are approximately equal, the program steps both platforms. Otherwise it only steps the platform with the pressure that is farthest from the target value.

To move a platform, the program computes if one side of the platform has moved more than the other (i.e. the platform is tipping). If both displacements are approximately equal, it sends a voltage pulse to both motors controlling that platform. Otherwise it only sends a pulse to the motor controlling the jack on the trailing side of the platform.

A.2.7. Set Up

The Set Up command is used to change some of the key variables of APSR.BAS. The command replaces the main computer screen with a Set Up menu containing the current values of these variables. To change a value, use the arrow keys to move to the desired variable. Type in the new value and hit [Return]. When all required changes are done, type "M" to return to the main screen. The meanings of the variables in the Set Up menu are explained below.

Calib. Factor	Sets the calibration factors for the four platform LVDTs.
BTARGET	The target B-value used to set the sidewall pressures.
Input Voltage	The input voltage being sent to the transducers monitored by APSR.BAS.
Stress Tol.	The tolerance used to match measured stresses to target values, which determines if the sidewall pressures and the platform pressures are close enough to their target value.

A.3. Program Code

```
10 'Program APSR.BAS
15 'Last Update: 9/24/91
20 'Written by: Doug Larson
25 ' Menu driven program to control the APSR Cell
26 ' This version controls the B-Value and displacement in the sidewalls
28 ' Define Constants
29 '
30 'Strawberry Tree set-up
35 STCARD% = 6960  'Memory address of Strawberry Tree card
40 LOBIT0% = 255  'Low bit for 2048, the number to signal 0 V output.
45 HIBIT0% = 7    'Hi bit for 2048
50 STOPALL%= 208  'Tells the card to send output to all the motors
51              ' (Channels (bits) 1-4 and 6 set to 0, the rest to 1).
59  FGD = 15 : BGD = 9
60 CLS
61  'PADJ is a flag to indicate that the air pressure has never been set
62 PRINT "Are you restarting a test already in progress? (Y/N): ";
63 INPUT ANS$
64 IF ANS$ = "Y" OR ANS$ = "y" THEN PADJ = 1 : GOTO 70
```

```
65 IF ANS$ = "N" OR AI 'S$ = "n" THEN PADJ = 0 ELSE GOTO 60
70 INTTIME = 21 'Integration time of A/D converter
80 AD1170 = 768 'Address of the AD1170
90 INTBIT = 13 'Set bit precision of AD1170
100 AD1170KEY = 0
110 GRNDCHANNEL = 7 : VINCHANNEL = 6
120 SCALE = .9   'Fraction of full scale to be sent to motors
130 INC% = 700    'Amount of time to run the motors per increment
135 MCODE$ = "O"   'Code to indicate mode of platform motion  ("O" = opposite)
140 MINHEIGHT = -1!
150 MAXHEIGHT = 1!
160 FIRSTEP = 0 : STARGET=0 : BVALUE=.45
170 MAXPRESS = 8! : PTARGET = 0   'Set maximum and default air pressures
190 NUMTRANS = 4 : TOL = .0007 : TARGET = 0!
200 PINC= .02 : PTOL= .05 . STOL=.15 'Voltage increment and pressure tolerance
210 PCF = -1.2405   'CF of pressure transducer #DO9483 in psi/mV/V
220 STROKE = .1   'Stroke of friction test (in inches)
230 DIM MLABEL$(7), MVAL(7)
240 DIM X2(8), Y2(8), MVAL2(8,5), MLABEL2$(8)  'Set up menu arrays
250 RUNMODE$ = "D"
255 COUNT = 0
260 '
265 'Declare the variables used to control the sidewall pressures
270 SSCALE = .95   'Determines the full scale speed of the motors
275 BTARGET = .65 : BTOL = .01
280 EAMP = 50   'Error amplification used for the sidewall motors
290 SIDEWALLS% = 0  'Flag to determine whether sidewall control is active
295 BCTRL$ = "Q"
300 'This code lets the user set POUTV.
310 '  POUTV is the output voltage to the Fairchild air regulator.
320 '  If PADJ = 1, the following steps will be executed.
330  IF PADJ=0 THEN GOTO 400
340     PRINT "Enter the value of POUTV: ";
350     INPUT POUTV
355     WHILE POUTV>9 OR POUTV<0
```

```
356       LOCATE 2,1 : PRINT "ENTER POUTV BETWEEN 0 AND 9: ";
357       INPUT POUTV
358     WEND
360     PRINT "Enter target air pressure: ";
370     INPUT PTARGET
373     WHILE PTARGET>7 OR PTARGET<0
374       LOCATE 2,1 : PRINT "ENTER PTARGET BETWEEN 0 AND 7 PSI: ";
375       INPUT PTARGET
376     WEND
380     CLS
390 '
400 ' Set up both AD1170
410 OUT AD1170, 69 : WAIT AD1170,1,1  'set default calib. time to 167 ms
420 OUT AD1170+1, INTBIT  'Load data format into second bit slot
430 OUT AD1170,48 : WAIT AD1170,1,1  'Lock in the data format loaded
440 AD1170=AD1170+32
450 IF AD1170<801 THEN GOTO 410
460 AD1170=768
580 GOSUB 2000 'StopMotors
585 'If running APSR2, do not zero the output pressure!
590 IF PADJ = 0 THEN GOSUB 2100  'ZeroPressure
600 '
700 '
720 ' Set Height of rise and calibration factor
730 DIM NEWINIT(4), PRESSURE(4)
740 DIM POSITION(6), CF(12), VOLTAGE(12), DELTA(4)
750 DIM INIVOLT(10), DELTVOLT(10)  'Stores voltage values for press. trans.
760 CF(0) = -1.3406 : CF(1) = -1.2778 : VIN = 6!
770 CF(2) = -1.3136 : CF(3) = -1.2858
780 CF(4) = -1.2405 : CF(5) =  4.9948 : CF(6) =  4.987 'psi/mV/Vin
784 ' CF(7) is for DO2169 (top wall) and CF(8) for DO2170
785 CF(7) = 4.9282: CF(8) = 4.9898  'Calib. factors for sidewall pressures
786 '
788 CF(9) = -1.2551 : CF(10) = -1.4406  'Calib. factors for sidewall DCDTs
790 GOSUB 1200  'Subroutine ReadZeros
```

```
800 ' Determine initial positions of DCDTs
820 GOSUB 3000 'Subroutine FindPositions
825 ' Set the initial platform positions
830   NEWINIT(0) = POSITION(0)
840   NEWINIT(1) = NEWINIT(0)   'Insures that the platforms are level
850   NEWINIT(2) = POSITION(2)
860   NEWINIT(3) = NEWINIT(2)
920 '
940 AVG = 0
980 GOSUB 10000 'Menu system
990 END
999 '
1000 'Subroutine ADREAD
1010  'Reads a channel on the A/D Converter
1015  'Channels 0-6 are on card 1 (address 800), and channels 7-10
1016  '  are on card 2 (address 768)
1020  CH = CHANNEL
1030  IF CH > 6 THEN AD1170=768 ELSE AD1170=800
1040  IF CH > 6 THEN CH = CH-7
1050  OUT AD1170+8, CH
1060  OUT AD1170,INTTIME: WAIT AD1170,1,1
1070  OUT AD1170+8,15
1080  LOWBYTE=INP(AD1170+1) : MIDBYTE=INP(AD1170+2) : HIBYTE =
INP(AD1170+3)
1090  CTS = LOWBYTE+256*MIDBYTE+65536!*HIBYTE
1100  VTS = (CTS*10/2^(INTBIT+7)-5)
1110 RETURN
1120 '
1200 'Subroutine ReadZeros
1210 '  Reads the zero values for the four DCDTs and the five
1220 '  pressure transducers from an external data file
1230 '  called "ZEROS".
1240  OPEN "I", 2, "ZEROS"
1250  FOR I = 0 TO 8
1260    INPUT #2, INIVOLT(I)
```

```
1270   NEXT I
1280   CLOSE #2
1290   GOSUB 1500    'Sets the sidewall zeros
1300 RETURN
1310 '
1500 'Subroutine ResetSidewalls
1510 '  Resets the zero position for plane strain control
1520 '  of the sidewalls
1530   FOR I = 10 TO 11
1540     CHANNEL = I-1
1550     GOSUB 1000  'Read the A/D converter to see current position
1590     INIVOLT(CHANNEL) = VTS
1600   NEXT I
1610   GOSUB 2700    'Prints current sidewall motion and strain
1620 RETURN
1630 '
2000 'Subroutine STOPMOTORS
2010  OUT STCARD%, LOBIT0%    'Tell the card to send zero volts
2020  OUT STCARD%+1, HIBIT0%
2030  OUT STCARD%+2, STOPALL%  'Sends zero volts to all four motors.
2040  OUT STCARD%+2, 255       'Close registers on card.
2060 RETURN
2070 '
2100 'Subroutine ZeroPressure
2110  OUT STCARD%, 0          'Tell the card to send zero volts
2120  OUT STCARD%+1, 0
2130  OUT STCARD%+2, 239       'Sends zero volts to channel 5 only
2140  OUT STCARD%+2, 255       'Close registers on card.
2160 RETURN
2170 '
2500 'Subroutine SendVoltages
2510 '  Sends specified outputs to the Strawberry Tree card
2520 '  The low bits in MOTORBIT% represent the channels that will
2530 '     receive the voltage specified by the value of LOBIT% and
2540 '      HIBIT%.
```

```
2560     OUT STCARD%, LOBIT%
2570     OUT STCARD%+1, HIBIT%
2580     OUT STCARD%+2, MOTORBITS%
2590     OUT STCARD%+2, 255        'Clear the output registers
2600 '
2610 RETURN
2620 '
2700 'Subroutine SidewallPositions
2710 '  Computes and prints the sidewall motions and total
2720 '  out-of-plane strain.
2730   FOR I = 10 TO 11
2740     CHANNEL = I-1
2750     GOSUB 1000
2760     'Print the voltage reading for each sidewall DCDT
2770     LOCATE 17, 10+(I-6)*10 : COLOR 15,8
2780     PRINT USING "+#.####"; VTS;
2790     'Calculate DCDT positions
2800     POSITION(I-6) = (VTS-INIVOLT(CHANNEL))*CF(CHANNEL)/VIN
2810     LOCATE 18,10+(I-6)*10 : COLOR 15,4
2820     PRINT USING "+#.####"; POSITION(I-6);
2830   NEXT I
2840   'Find amount of out-of-plane strain
2850   E2 = 100*(POSITION(4)+POSITION(5))/6!
2860   COLOR FGD, BGD : LOCATE 19,60 : PRINT "E2 = ";
2870   PRINT USING "+##.##"; E2; : PRINT " %";
2880 RETURN
2890 '
3000 'Subroutine FindPositions
3010   FOR I = 1 TO 4
3020     CHANNEL = I-1
3030     GOSUB 1000  'ADREAD reads AD Converter
3040     VOLTAGE(CHANNEL) = VTS
3050     LOCATE 17, 10+(I-1)*10 : COLOR 15,8
3060     PRINT USING "+#.####"; VOLTAGE(CHANNEL)
3070     ' Calculate DCDT positions
```

```
3090    POSITION(CHANNEL)=(VOLTAGE(CHANNEL)-
INIVOLT(CHANNEL))*CF(CHANNEL)/VIN
3120  NEXT I
3125  GOSUB 2700    'Print sidewall positions
3130 RETURN
3140 '
3200 'Subroutine FindBagPressures
3210 '  Computes the water pressures in the platform bags
3220  FOR I = 0 TO 1
3230    CHANNEL = 5+I
3240    GOSUB 1000  'ADREAD reads A/D Converter
3250    VOLTAGE(CHANNEL) = VTS
3253    LOCATE 21, (CHANNEL*10)-30 : COLOR 15,8
3256    PRINT USING "+##.##"; 1000*VOLTAGE(CHANNEL);
3260    PRESSURE(I)=1000*(VOLTAGE(CHANNEL)-
INIVOLT(CHANNEL))*CF(CHANNEL)/VIN
3270    LOCATE 22, (CHANNEL*10)-30 : COLOR 15,4
3280    PRINT USING "+##.##"; PRESSURE(I);
3290  NEXT I
3300  FOR I = 2 TO 3
3310    CHANNEL = 5+I
3320    GOSUB 1000  'ADREAD reads A/D Converter
3330    VOLTAGE(CHANNEL) = VTS
3333    LOCATE 21, 20+(I*10) : COLOR 15,8
3336    PRINT USING "+##.##"; 1000*VOLTAGE(CHANNEL);
3340    PRESSURE(I)=1000*(VOLTAGE(CHANNEL)-
INIVOLT(CHANNEL))*CF(CHANNEL)/VIN
3350    LOCATE 22, 20+(I*10) : COLOR 15,4
3360    PRINT USING "+##.##"; PRESSURE(I); : COLOR FGD, BGD
3370  NEXT I
3380 RETURN
3390 '
3500 'Subroutine to compute average platform position since starting
3505 '  displacement control
3510  AVG = (POSITION(0)-NEWINIT(0)+POSITION(1)-NEWINIT(1))/2
```

```
3515   AV1 = (POSITION(0)+POSITION(1))/2
3520 RETURN
3530 '
3600 'Subroutine to compute avg position of platform 2
3610   AVG2 = (POSITION(2) - NEWINIT(2) + POSITION(3) - NEWINIT(3))/2
3615   AV2 = (POSITION(2)+POSITION(3))/2
3620 RETURN
3630 '
4000 'Subroutine STEP
4010 '  Causes the motors on one platform to move one increment
4030   DELTA1 = DELTA(MNUM-1) : DELTA2 = DELTA(MNUM)
4040   MOTION = 0
4043   IF DELTA1 < DELTA2 - TOL THEN MOTION=1
4045   IF DELTA1 > DELTA2 + TOL THEN MOTION=2
4050   VOLTBITS! = 2048*(1+SCALE*FLAG)
4052   HIBIT% = INT(VOLTBITS!/256)
4054   LOBIT% = INT(VOLTBITS!-HIBIT%*256)
4070   IF MOTION = 0 THEN GOTO 4080 ELSE GOTO 4120
4080     LOCATE 1, 1 : COLOR FGD,BGD : PRINT "MOTION = 0, FLAG = "
FLAG
4082     COLOR 14,14 : LOCATE 2,MNUM*5+2 : PRINT "M"MNUM+1;
4084     LOCATE 2,(MNUM-1)*5+2: PRINT "M"MNUM; : COLOR FGD,BGD
4090     MOTORBITS% = 255 - 2^(MNUM-1) - 2^MNUM  'Sends signal to both
motors.
4100     GOTO 4190  'Skip to timer sequence
4110 'If Motor 2 is ahead of motor 1, then execute these lines
4120   IF MOTION = 1 THEN GOTO 4122 ELSE GOTO 4150
4122     IF FLAG<>1 THEN GOTO 4128
4124       COLOR 14,14 : LOCATE 2,(MNUM-1)*5+2 : PRINT "M"MNUM;
4126       GOTO 4133
4128       COLOR 14,14 : LOCATE 2,(MNUM)*5+2 : PRINT "M"MNUM+1;
4133     LOCATE 1, 1 : COLOR FGD,BGD : PRINT "MOTION = 1, FLAG = "
FLAG
4140     IF FLAG=1 THEN MOTORBITS%=255-2^(MNUM-1) ELSE
MOTORBITS%=255-2^MNUM
```

```
4145    GOTO 4190 'Send signal to motors
4150 'If Motor 1 is ahead of motor 2 then do the next two lines
4152    IF FLAG=1 THEN GOTO 4158
4154      COLOR 14,14 : LOCATE 2,(MNUM-1)*5+2 : PRINT "M"MNUM;
4156      GOTO 4163
4158      COLOR 14,14 : LOCATE 2,(MNUM)*5+2 : PRINT "M"MNUM+1;
4163    LOCATE 1, 1 : COLOR FGD,BGD : PRINT "MOTION = 2, FLAG = "
FLAG
4170    IF FLAG=1 THEN MOTORBITS%=255-2^(MNUM) ELSE
MOTORBITS%=255-2^(MNUM-1)
4175    GOTO 4190 'Send signal to motors
4180 '
4190  'Send output to Strawberry Tree Card
4200    OUT STCARD%, LOBIT%
4210    OUT STCARD%+1, HIBIT%
4220    OUT STCARD%+2, MOTORBITS%
4230    OUT STCARD%+2, 255      'Clear the output registers
4280 '
4290  'Timing sequence
4300  FOR N = 1 TO INC%  'Times the motor pulse
4310  NEXT N
4330  GOSUB 2000 'Stop all motors
4340  COLOR FGD,BGD : LOCATE 2,2 : PRINT "M-1  M-2  M-3  M-4  ";
4350 RETURN
4360 '
4500 'Subroutine FindMotion
4510 'Determines which pistons need to be advanced on each platform
4520  GOSUB 5000 'Find the piston displacements
4530  MOTION = 0 'Default setting - all pistons can advance
4535  'Check platform 1 for tipping
4540  IF DELTA(0) < DELTA(1) - TOL THEN MOTION = 1  'Advance piston 1
only
4550  IF DELTA(0) > DELTA(1) + TOL THEN MOTION = 2  'Advance piston 2
only
4555  'Check platform 2 for tipping
```

```
4560   IF DELTA(2) < DELTA(3) - TOL THEN MOTION = 3   'Advance piston 3
only
4570   IF DELTA(2) > DELTA(_) + TOL THEN MOTION = 4   'Advance piston 4
only
4580 RETURN
4990 '
5000 'Subroutine RelPosition
5010 '  Prints the total motion the DCDTs have undergone
5020   FOR K = 1 TO NUMTRANS
5030     DELTA(K-1) = POSITION(K-1) - NEWINIT(K-1)
5040     LOCATE 18, 10+(K-1)*10 : COLOR 15,4
5060     PRINT USING "+#.####"; POSITION(K-1)
5070   NEXT K
5080 RETURN
5090 '
5200 'Subroutine PrintB
5210 '  Computes and prints the current b-value
5220   GOSUB 3200   'Compute and display current pressures
5225   'Read, print, and adjust air pressure if necessary
5230     IF PTARGET > .1 THEN GOSUB 37000 ELSE GOSUB 36200
5240   AVGPRESS = (PRESSURE(0)+PRESSURE(1))/2   'Average platform
pressures
5245   IF (AVGPRESS-AIRPRESSURE) < .001 THEN BVALUE = 0
5247   IF (AVGPRESS-AIRPRESSURE) < .001 THEN GOTO 5280
5250   RVALUE = AVGPRESS/AIRPRESSURE
5260   BVALUE = (PRESSURE(2)-AIRPRESSURE)/(AVGPRESS-
AIRPRESSURE)
5280   COLOR FGD,BGD : LOCATE 21,60 : PRINT "BVALUE = ";
5285   IF BVALUE>1.5 THEN PRINT "> 1.5 ";
5290   IF BVALUE>=0! AND BVALUE<=1.5 THEN PRINT USING "#.##   ";
BVALUE
5295   IF BVALUE<0! THEN PRINT "< 0   ";
5300 RETURN
5310 '
5500 'Subroutine b-value
```

```
5510 ' Computes and displays current pressures and corrects b-value
5520 ' if necessary.
5525 COLOR FGD,BGD : LOCATE 22,60 : PRINT SPACE$(20)
5530 GOSUB 5200 'Compute and display current pressures
5533 'IF BVALUE > 1.05 THEN BEEP
5534 IF BVALUE > 1.05 THEN RETURN
5535 'Do not adjust b-value if sidewalls are deactivated
5540 IF SIDEWALLS% = 0 THEN RETURN
5545 'Do not adjust if air pressure has not been set
5550 IF PTARGET < .1 THEN RETURN
5555 'No adjustment if platforms are not in contact with sample
5560 IF RVALUE < 1.2 THEN RETURN
5570 GOSUB 7000 'Determine if sidewalls need to be moved
5580 'The SIDEFLAG% variable determines if walls need to be moved.
5590 'IF SIDEFLAG% = 0, then the walls are within the specified
5600 ' B-value or displacement tolerance.
5610 LOCATE 22,60 : COLOR FGD, BGD : PRINT "BVOLTS = ";
5620 IF SIDEFLAG% = 0 THEN PRINT " NONE" SPACE$(3);
5630 IF SIDEFLAG% = 0 THEN RETURN
5640 LOCATE 22,70 : PRINT USING "+##.##"; BVOLTS!;
5690 ' Compute the bit output to the Strawberry Tree card...
5700 BBITS! = 2048*(1+BVOLTS!/5!)
5710 HIBIT% = INT(BBITS!/256)
5720 LOBIT% = INT(BBITS!-HIBIT%*256)
5730 MOTORBITS% = 223 'Sends signal to channel 6 only
5740 GOSUB 2500 'Sends signal to the motor
5750 'Timing sequence
5760 FOR N = 1 TO INC%
5770 NEXT N
5775 GOSUB 2000 'Stop all motors
5790 '
5800 ' Allow the user to interupt the b-value correction
5810 ' cycle if it is taking too long...
5815 IF A$ = "S" OR A$ = "s" THEN RETURN
5820 A$ = INKEY$
```

```
5830   IF A$ = "S" OR A$ = "s" THEN RETURN
5840   'Return to the top of the b-value correction loop
5850   GOTO 5530
5860 RETURN
5870 '
6000 'Subroutine to set up display
6005   COLOR FGD, BGD
6010   FOR J = 1 TO NUMTRANS
6020     LOCATE 16, 10+(J-1)*10: PRINT "DCDT " J
6030   NEXT J
6040   LOCATE 17, 2: PRINT "Volts:";
6050   LOCATE 18, 1: PRINT "Inches:";
6060   LOCATE 20, 10 : PRINT "AIR";
6070   LOCATE 20, 20 : PRINT "PLAT 1";
6080   LOCATE 20, 30 : PRINT "PLAT 2";
6090   LOCATE 20, 1: PRINT "Press.:";
6100   LOCATE 20, 40 : PRINT "TOP WALL";
6110   LOCATE 20, 50 : PRINT "BOT. WALL";
6120   LOCATE 21, 3  : PRINT "VOLTS:";
6130   LOCATE 22, 3  : PRINT "psi:";
6140   LOCATE 16, 50 : PRINT "TOP SIDE";
6150   LOCATE 16, 60 : PRINT "BOT SIDE";
6160 RETURN
6170 '
7000 'Subroutine SideError
7010 '  This subroutine decides whether the pressure in the
7020 '  sidewalls needs to be changed.
7030 '  * If no change is needed, the SIDEFLAG% variable is set to
7040 '  zero and the subroutine ends.
7050 '  * If a change is needed, this routine computes the output voltage
7060 '  to be sent to the sidewall motors and stores it in variable
7070 '  BVOLTS!.
7080   SIDEFLAG% = 0
7090   IF BCTRL$ = "d" OR BCTRL$ = "D" THEN GOTO 7300
7095   IF BCTRL$ = "s" OR BCTRL$ = "S" THEN GOTO 7400
```

```
7100    'Execute these steps if the sidewalls are being controlled
7110    ' by the target B-value
7120    IF BVALUE > BTARGET-BTOL AND BVALUE < BTARGET+BTOL
THEN RETURN
7130    ' Compute the error in the sidewall pressures
7140    ' If it is within the pressure tolerance, then RETURN
7150    PERROR = BTARGET*(AVGPRESS-AIRPRESSURE)+AIRPRESSURE-
PRESSURE(2)
7160    IF ABS(PERROR) < STOL THEN RETURN
7170    ' Compute the error in the b-value and scale output to motors
7180    ' accordingly. As the b-value approaches the target value,
7190    ' the motors will slow down.
7200    BERROR = BTARGET-BVALUE
7210    BVOLTS! = EAMP*BERROR
7220    IF BVOLTS! > 4.999 THEN BVOLTS! = 4.999
7230    IF BVOLTS! < -4.999 THEN BVOLTS! = -4.999
7240    'Set the SIDEFLAG% variable to indicate that BVOLTS! has
7250    ' been updated.
7260    SIDEFLAG% = 1
7270    RETURN
7280  'If the sidewalls are under displacement control, execute these
7290   'steps.
7300    GOSUB 2700  'Compute the sidewall positions
7310    IF ABS(E2) < BTOL*2 THEN RETURN
7320    BVOLTS! = -2*E2*EAMP
7330    IF BVOLTS! > 4.999 THEN BVOLTS! = 4.999
7340    IF BVOLTS! < -4.999 THEN BVOLTS! = -4.999
7350    'Set the SIDEFLAG% variable to indicate that BVOLTS! has
7360    ' been updated.
7370    SIDEFLAG% = 1
7380    RETURN
7390  'If bottom sidewall is being run to match pressure in top
7400  '  top sidewall, then run these steps...
7410    DELTAP = .4   'Desired pressure difference between sidewalls.
7420    PERROR = PRESSURE(3) - (PRESSURE(2)+DELTAP)
```

```
7430     IF ABS(PERROR)<STOL THEN RETURN
7440     BVOLTS! = -1*EAMP*PERROR
7450     IF BVOLTS! > 4.999 THEN BVOLTS! = 4.999
7460     IF BVOLTS! < -4.999 THEN BVOLTS! = -4.999
7470     'Set the SIDEFLAG% variable to indicate that BVOLTS! has
7480     '  been updated.
7490     SIDEFLAG% = 1
7500     RETURN
7510 RETURN
7520 '
9990 '
10000 'Subroutine Main Menu
10010 '
10015 FGD = 15 : BGD = 9 : MFGD = 15 : MBGD = 12  'Set menu colors
10020 COLOR FGD,BGD: CLS
10030 CHOICE = 0 : NUMCHOICE = 7  'Sets the total number of main menu choices
10035 TOPITEM = 4 : LEFTITEM = 3  'X and Y coords for first menu item
10040 MV$ = ""
10060 HEADING$ = "Main Menu"
10080 LOCATE 2, (80 - LEN(HEADING$))/2
10100 COLOR 14,8 : PRINT HEADING$
10110 MLABEL$(0) = "  Set Up  "
10120 MLABEL$(1) = "  Target  "
10130 MLABEL$(2) = "   RUN    "
10140 MLABEL$(3) = "Set Scale "
10150 MLABEL$(4) = "Air Press."
10160 IF RUNMODE$ = "D" OR RUNMODE$ = "d" THEN MLABEL$(5) =
"SetMode[D]"
10170 IF RUNMODE$ = "S" OR RUNMODE$ = "s" THEN MLABEL$(5) =
"SetMode[S]"
10180 MLABEL$(6) = "B Ctrl [" + BCTRL$ + "]"
10190 'IF BCTRL$ = "B" OR BCTRL$ = "b" THEN MLABEL$(6) = "B Ctrl [B]"
10200 GOSUB 10360 'Print Menu choices
10205 GOSUB 6000 'Prints DCDT column headings
10210 GOSUB 3000 'Prints out current DCDT Voltages
```

```
10211  GOSUB 36200  'Prints current air pressure
10212 GOSUB 3200 'Prints current bag pressures
10215 GOSUB 5000 'Prints current total DCDT movement
10220 GOSUB 10600 'Activate Cursor Keys
10225 PROMPT$ = "Press [E] to exit program"
10230 LOCATE 23, (80-LEN(PROMPT$))/2 : COLOR 15,9 : PRINT PROMPT$;
10240 B$ = INKEY$
10260 ' Check to see if input is valid
10280 IF (B$="E" OR B$="e") THEN GOTO 10320
10300 IF (B$ = CHR$(13)) THEN GOSUB 11120
10310 GOTO 10240   'Return to top of loop
10320 COLOR 14,9
10330 CLS
10335 SYSTEM   'Return to DOS
10340 END
10350 '
10360 'Subroutine to print out Menu choices
10400   COLOR 8,7
10420   LOCATE TOPITEM,LEFTITEM: PRINT MLABEL$(0)
10430   COLOR MFGD,MBGD
10440   FOR K = 1 TO NUMCHOICE-1
10460     LOCATE TOPITEM+K, LEFTITEM : PRINT MLABEL$(K)
10480   NEXT K
10490   LOCATE TOPITEM+2, 45: COLOR FGD,BGD
10500   IF RUNMODE$ = "D" OR RUNMODE$ = "d" THEN GOTO 10505
10502     PRINT "TARGET PRESSURE: ";: PRINT USING "+##.##"; STARGET;
10503     PRINT SPACE$(3)
10504     GOTO 10510
10505   PRINT "TARGET POSITION: "; TARGET;
10510   LOCATE TOPITEM, 45 : PRINT "Motor Output: ";
10515   PRINT USING "+##.##"; 100*SCALE; : PRINT " %" SPACE$(2)
10520   LOCATE TOPITEM+4, 45 : PRINT "TARGET AIR PRESS.: ";
10530   PRINT USING "+##.##"; PTARGET; : PRINT " psi" SPACE$(2)
10535   GOSUB 12000  'Print POUTV variable
10540   GOSUB 36200  'Print air pressure
```

```
10560 RETURN 'End of Subroutine
10580 '
10600 'Subroutine to activate cursor keys
10620   ON KEY(11) GOSUB 10720 'Cursor up
10640   ON KEY(14) GOSUB 10920 'Cursor down
10660   KEY(11) ON: KEY(14) ON
10680 RETURN
10700 '
10720 'Subroutine to move cursor up
10740   LOCATE TOPITEM+CHOICE, LEFTITEM : COLOR MFGD,MBGD  'Erase
old cursor
10760   PRINT MLABEL$(CHOICE)
10780   CHOICE = CHOICE - 1
10800   IF CHOICE=-1 THEN CHOICE=NUMCHOICE-1
10820   LOCATE TOPITEM+CHOICE, LEFTITEM : COLOR 8,7
10840   PRINT MLABEL$(CHOICE) 'Prints new cursor
10860   MV$ = ""
10880 RETURN
10900 '
10920 'Subroutine to move cursor down
10940   LOCATE TOPITEM+CHOICE, LEFTITEM: COLOR MFGD,MBGD  'Erase
old cursor
10960   PRINT MLABEL$(CHOICE)
10980   CHOICE = CHOICE + 1
11000   IF CHOICE=NUMCHOICE THEN CHOICE=0
11020   LOCATE TOPITEM+CHOICE, LEFTITEM : COLOR 8,7
11040   PRINT MLABEL$(CHOICE) 'Prints new cursor
11060   MV$ = ""
11080 RETURN
11100 '
11120 'Subroutine Dispatch
11140 '  Takes keyboard input and acts appropriately
11160   ON CHOICE+1 GOSUB 15000, 18500, 19000, 33000, 35000, 18700,
22000
11170 '  SUB 15000 = SetDefaults
```

```
11180 '  SUB 18500 = SetMotion
11190 '  SUB 19000 = RunTest
11200 '  SUB 33000 = SetScale      (Sets the output to the motors)
11210 '  SUB 35000 = SetPressure   (Sets the target air pressure)
11220 '  SUB 18700 = SetRunMode    (Sets stress or displacement control)
11230 '  SUB 22000 = SideWallControl
11320 RETURN
11340 '
12000 'Subroutine PrintPOUTV
12010 '  Prints the value of the POUTV variable in the upper right
12020 '  corner of the screen.  POUTV is the voltage that is being sent
12030 '  to the Fairchild air regulator.
12040   LOCATE 2, 65 : COLOR FGD, BGD
12050   PRINT "POUTV = ";
12060   PRINT USING "+#.##"; POUTV
12070 RETURN
12080 '
13000 'Subroutine SideWallControl
13010 RETURN
13020 '
15000 'Subroutine SetDefaults
15020 '  Allows user to specify default variable values
15025   KEY(11) OFF: KEY(14) OFF   'Turn off main menu cursor
15040   NUMCHOICE = 8              'Sets the number of menu choices
15060   FGD = 15 : BGD = 12  'Sets foreground and background colors
15080   YCHOICE = 0 : XCHOICE = 0  'Cursor position variables
15120   XDELT = 10         'Offset between CF headings
15140   MV$ = ""
15160   HEADING$ = "SET UP MENU"
15180   COLOR FGD, BGD: CLS     'Fills screen with new color scheme
15200   LOCATE 2, (80 - LEN(HEADING$))/2
15220   COLOR 15,9: PRINT HEADING$
15240   MLABEL2$(0) = "CALIB. FACTOR: ": X2(0) = 20 : Y2(0) = 5
15245   MLABEL2$(1) = "BTARGET     : " : X2(1) = 35 : Y2(1) = 7
15250   MLABEL2$(2) = "INPUT VOLTAGE: ": X2(2) = 35 : Y2(2) = 9
```

```
15255  MLABEL2$(3) = "STRESS TOLERANCE" : X2(3) = 35 : Y2(3) = 12
15260  MLABEL2$(4) = "OUTPUT (% F.S.):  ": X2(4) = 35 : Y2(4) = 14
15270  MLABEL2$(5) = "SIDES ON? (0=OFF):": X2(5) = 35 : Y2(5) = 16
15280  MLABEL2$(6) = "B TOLERANCE (<1):": X2(6) = 35 : Y2(6) = 18
15290  MLABEL2$(7) = "ERROR AMP FACTOR: ": X2(7) = 35 : Y2(7) = 20
15300  ' Set array variable to current default values
15310  MVAL2(0,0) = CF(0) : MVAL2(0,1) = CF(1)
15320  MVAL2(0,2) = CF(2) : MVAL2(0,3) = CF(3)
15325  MVAL2(0,4) = PCF
15327  MVAL2(1,0) = BTARGET
15330  MVAL2(2,0) = VIN
15335  MVAL2(3,0) = STOL
15340  MVAL2(4,0) = SSCALE
15350  MVAL2(5,0) = SIDEWALLS%
15360  MVAL2(6,0) = BTOL
15370  MVAL2(7,0) = EAMP
15380  GOSUB 15500    'InitScreen
15390  GOSUB 16000    'Activate UpDown
15395  GOSUB 16400    'Activate LeftRight
15400  GOSUB 17000    'GetInput
15410  GOSUB 18200    'SetValues
15412  KEY(11) OFF : KEY(12) OFF : KEY(13) OFF : KEY(14) OFF
15420  GOSUB 10000    'Return to Main Menu
15430 RETURN
15440 '
15500 'Subroutine InitScreen
15510 '  Draws the screen for the set-up menu
15520  PROMPT$ = "Press [M] to return to main menu"
15530  COLOR FGD, BGD
15540  FOR I = 1 TO NUMTRANS      'Prints DCDT headings
15550    LOCATE Y2(0)-1, (X2(0)+(I-1)*XDELT)
15560    PRINT "DCDT " I;
15570  NEXT I
15575  LOCATE Y2(0)-1, (X2(0)+4*XDELT) : PRINT "AIR PRESS.";
15580  'Print labels for input boxes
```

```
15590  FOR I = 1 TO NUMCHOICE
15600    LOCATE Y2(I-1), (X2(I-1) - (LEN(MLABEL2$(I-1))+1))
15610    PRINT MLABEL2$(I-1)
15620  NEXT I
15630  'Print motor control heading
15640  LOCATE Y2(3)-1, (X2(0) - (LEN(MLABEL2$(1)) + 1))
15650  PRINT "MOTOR CONTROL: ";
15660  'Print prompt at bottom of screen
15670  COLOR 15, 9
15680  LOCATE 22, (80 - LEN(PROMPT$))/2 : PRINT PROMPT$;
15690  'Print variable values
15700  COLOR 8,7       'Change to black on white
15710  LOCATE Y2(0), X2(0) : PRINT USING "+#.####"; MVAL2(0,0)
15720  COLOR 15,8      'Print the other values in white on black
15730  FOR I = 1 TO NUMTRANS   'Prints the calibration factors
15740    LOCATE Y2(0), X2(0)+I*XDELT
15750    PRINT USING "+#.####"; MVAL2(0,I)
15760  NEXT I
15770  FOR I = 1 TO NUMCHOICE-1   'Print the values of the other variables
15780    LOCATE Y2(I), X2(I)
15785    IF I = 5 THEN GOTO 15795  'INC has to be printed as an int.
15790    PRINT USING "+#.####"; MVAL2(I, 0);
15792    GOTO 15800
15795    PRINT USING "+###   "; MVAL2(I, 0)
15800  NEXT I
15810 RETURN
15820 '
16000 'Subroutine Activate UpDown
16010  ON KEY(11) GOSUB 16100  'Cursor Up
16020  ON KEY(14) GOSUB 16250  'Cursor Down
16030  KEY(11) ON : KEY(14) ON
16040 RETURN
16050 '
16100 'Subroutine MoveUp
16110 '  Moves the cursor up
```

```
16120  LOCATE Y2(YCHOICE), X2(YCHOICE)+XDELT*XCHOICE   'Erase old
cursor
16130  COLOR 15,8
16131  IF YCHOICE = 5 THEN GOTO 16136   ' print INC variable as an int.
16133    PRINT USING "+#.####"; MVAL2(YCHOICE, XCHOICE)
16135    GOTO 16140
16136  PRINT USING "+###   "; MVAL2(YCHOICE, XCHOICE)
16140  IF YCHOICE = 0 THEN GOSUB 16700   'Turn left-right keys off
16150  YCHOICE = YCHOICE - 1
16160  IF YCHOICE = -1 THEN YCHOICE = NUMCHOICE - 1
16170  LOCATE Y2(YCHOICE), X2(YCHOICE) : COLOR 8,7   'Print new cursor
16175  IF YCHOICE = 5 THEN GOTO 16185   'INC has to be printed as an int.
16180  PRINT USING "+#.####"; MVAL2(YCHOICE, 0);
16182  GOTO 16190
16185  PRINT USING "+###   "; MVAL2(YCHOICE, XCHOICE)
16190  MV$ = ""
16200  IF YCHOICE = 0 THEN GOSUB 16400   'Turn left-right keys on
16210 RETURN
16220 '
16250 'Subroutine MoveDown
16260 '  Moves the cursor down
16270  LOCATE Y2(YCHOICE), X2(YCHOICE)+XDELT*XCHOICE   'Erase old
cursor
16280  COLOR 15,8
16281  IF YCHOICE = 5 THEN GOTO 16286   ' print INC variable as an int.
16283    PRINT USING "+#.####"; MVAL2(YCHOICE, XCHOICE)
16285    GOTO 16290
16286  PRINT USING "+###   "; MVAL2(YCHOICE, XCHOICE)
16290  IF YCHOICE = 0 THEN GOSUB 16700   'Turn left-right keys off
16300  YCHOICE = YCHOICE + 1
16310  IF YCHOICE = NUMCHOICE THEN YCHOICE = 0
16320  LOCATE Y2(YCHOICE), X2(YCHOICE) : COLOR 8,7   'Print new cursor
16325  IF YCHOICE = 5 THEN GOTO 16335   'INC has to be printed as an int.
16330  PRINT USING "+#.####"; MVAL2(YCHOICE, 0);
16332  GOTO 16340
```

```
16335   PRINT USING "+###   "; MVAL2(YCHOICE, XCHOICE)
16340   MV$ = ""
16350   IF YCHOICE = 0 THEN GOSUB 16400   'Turn left-right keys on
16360 RETURN
16370 '
16400 ' Subroutine LRKeysON
16410 '   Turns on the left-right cursor keys
16420   ON KEY(12) GOSUB 16470   'Move cursor left
16430   ON KEY(13) GOSUB 16590   'Move cursor right
16440   KEY(12) ON : KEY(13) ON
16450 RETURN
16460 '
16470 'Subroutine CursorLeft
16480 '   Moves the cursor left
16490   LOCATE Y2(YCHOICE), X2(YCHOICE)+XDELT*XCHOICE   'Erase old
cursor
16500   COLOR 15,8: PRINT USING "+#.####"; MVAL2(YCHOICE, XCHOICE)
16510   XCHOICE = XCHOICE - 1
16520   IF XCHOICE = -1 THEN XCHOICE = NUMTRANS
16530   LOCATE Y2(YCHOICE), X2(YCHOICE)+XDELT*XCHOICE : COLOR
8,7
16540   PRINT USING "+#.####"; MVAL2(YCHOICE, XCHOICE);
16550   MV$ = ""
16560 RETURN
16580 '
16590 'Subroutine CursorRight
16600 '   Moves the cursor right
16610   LOCATE Y2(YCHOICE), X2(YCHOICE)+XDELT*XCHOICE   'Erase old
cursor
16620   COLOR 15,8: PRINT USING "+#.####"; MVAL2(YCHOICE, XCHOICE)
16630   XCHOICE = XCHOICE + 1
16640   IF XCHOICE = NUMTRANS+1 THEN XCHOICE = 0
16650   LOCATE Y2(YCHOICE), X2(YCHOICE)+XDELT*XCHOICE : COLOR
8,7
16660   PRINT USING "+#.####"; MVAL2(YCHOICE, XCHOICE);
```

```
16670   MV$ = ""
16680 RETURN
16690 '
16700 'Subroutine LRKeysOff
16710 '   Turns off the left-right cursor keys
16720    KEY(12) OFF : KEY(13) OFF
16730    XCHOICE = 0
16740 RETURN
16750 '
17000 'Subroutine GetInput
17010 '  This subroutine continues to accept user input until
17020 '    until [M] or [m] is pressed to return to main menu.
17030  A$ = INKEY$       'Check user input
17040   'Check to see if input is valid
17050  IF (A$>="0" AND A$<="9") OR (A$=".") OR (A$="-") OR (A$=CHR$(13))
OR (A$=CHR$(8)) THEN GOSUB 17100
17060   'Exit if user presses [M] or [m]
17070   IF (A$ <> "M") AND (A$ <> "m") THEN GOTO 17030
17080 RETURN
17090 '
17100 'Subroutine AddInput
17110   'Takes keyboard input and updates variables
17120  IF A$ <> CHR$(13) THEN GOTO 17142
17130    GOSUB 17300                  'If the user hits [Return]...
17140   GOTO 17200
17142  IF A$ <> CHR$(8) THEN GOTO 17150
17143    MV$ = MID$(MV$, 1, LEN(MV$)-1)   'Backspace erases last character
17144    GOTO 17160
17150  MV$ = MV$ + A$
17160  LOCATE Y2(YCHOICE), X2(YCHOICE)+XDELT*XCHOICE
17170  COLOR 8,7 : PRINT USING "\    \"; MV$
17200 RETURN
17300 'Subroutine UpdateValue
17305   IF MV$ = "" THEN GOTO 17370
17310 '  Takes the current MV$ and updates MVAL(YCHOICE, XCHOICE)
```

```
17320   GOSUB 17400 'Check user input
17330   IF CHECK = -1 THEN GOTO 17370   'Won't update value if bogus
17340    MVAL2(YCHOICE,XCHOICE) = VAL(MV$)
17350    LOCATE Y2(YCHOICE), X2(YCHOICE)+XDELT*XCHOICE : COLOR
8,7
17355   IF YCHOICE = 5 THEN GOTO 17362  'Print INC variable as an int.
17360     PRINT USING "+#.####"; MVAL2(YCHOICE,XCHOICE)  'Print new
cursor
17361     GOTO 17365
17362   PRINT USING "+###   "; MVAL2(YCHOICE,XCHOICE)
17365   MV$ = ""
17370   RETURN
17380 '
17400 'Subroutine CheckInput (Still to be coded)
17410 '  Checks user's numerical input
17420   CHECK = 1
17430 RETURN
17440 '
17500 'Subroutine GetInput
17510 '  This subroutine continues to accept user input until
17520 '    until [M] or [m] is pressed to return to main menu.
17530 RETURN
17540 '
18200 'Subroutine SetValues
18210 '  Sets the variables to the values entered by the user during
18220 '    during the GetInput subroutine.
18230   CF(0) = MVAL2(0,0) : CF(1) = MVAL2(0,1)
18240   CF(2) = MVAL2(0,2) : CF(3) = MVAL2(0,3)
18245   PCF = MVAL2(0,4)
18247   BTARGET = MVAL2(1,0)
18250   VIN = MVAL2(2,0)
18255   STOL = MVAL2(3,0)
18260   SSCALE = MVAL2(4,0)
18270   SIDEWALLS% = MVAL2(5,0)
18280   BTOL = MVAL2(6,0)
```

```
18290   EAMP = MVAL2(7,0)
18300 RETURN
18310 '
18500 'Subroutine SetMotion
18510 ' Allows user to set desired platform motion
18515   KEY(11) OFF : KEY(14) OFF  'Turn off cursor keys
18520   LMARG = 15 'Sets the left location of the prompts
18530   LOCATE 23, 1: COLOR 15,12: PRINT "Subroutine SetMotion";
18540   COLOR FGD,BGD: PRINT SPACE$(5);
18545   IF RUNMODE$= "S" OR RUNMODE$ = "s" THEN GOSUB 21000 ELSE
GOSUB 18550
18547 RETURN
18548 'Subroutine SetTargetHeight
18550   LOCATE TOPITEM+2,LMARG: COLOR 8, 10: PRINT "Target Height: ";
18560   INPUT TARGET
18570   IF TARGET >= 0 AND TARGET <= .95 THEN GOTO 18610
18580     LOCATE TOPITEM+3, LMARG : PRINT "Invalid Input";
18590     COLOR FGD,BGD: LOCATE TOPITEM+2,LMARG: PRINT
SPACE$(23);
18600     GOTO 18550
18610   COLOR FGD, BGD : LOCATE TOPITEM+2, LMARG: PRINT
SPACE$(23);
18620   LOCATE TOPITEM+3, LMARG: PRINT SPACE$(23);
18630   LOCATE TOPITEM+2, 45: COLOR FGD,BGD
18635   PRINT "TARGET POSITION: " TARGET;
18640   PRINT SPACE$(10);
18645   LOCATE 23,1 : PRINT SPACE$(22)
18650   GOSUB 10600  'Reactivate cursor keys
18660 RETURN
18670 '
18700 'Subroutine SetMode
18710 ' Allows user to set RunMode for either stress or displacement control
18715   KEY(11) OFF : KEY(14) OFF  'Turn off cursor keys
18720   LMARG = 15 'Sets the left location of the prompts
18730   LOCATE 23, 1: COLOR 15,12: PRINT "Subroutine SetRunMode";
```

```
18740   COLOR FGD,BGD: PRINT SPACE$(5);
18745   OLD$ = RUNMODE$
18750   LOCATE TOPITEM+CHOICE*2,LMARG: COLOR 8,10:PRINT "Run
Mode (S/D): ";
18760   INPUT RUNMODE$
18761   IF RUNMODE$ = "d" THEN RUNMODE$ = "D"
18762   IF RUNMODE$ = "s" THEN RUNMODE$ = "S"
18763   IF RUNMODE$ = "r" THEN RUNMODE$ = "R"
18770   IF RUNMODE$="D" OR RUNMODE$="S" OR RUNMODE$="R" THEN
GOTO 18810
18780     LOCATE TOPITEM+CHOICE*2 + 1, LMARG : PRINT "Invalid Input";
18790     COLOR FGD,BGD: LOCATE TOPITEM+CHOICE*2,LMARG: PRINT
SPACE$(23);
18800     GOTO 18750
18810   COLOR FGD, BGD : LOCATE TOPITEM+CHOICE*2, LMARG: PRINT
SPACE$(23);
18820   LOCATE TOPITEM+CHOICE*2+1, LMARG: PRINT SPACE$(23);
18825   IF (OLD$ = "S") AND (RUNMODE$ = "D") THEN GOSUB 18900
18827   IF RUNMODE$ = "R" THEN GOSUB 19700
18830   IF RUNMODE$="D" OR RUNMODE$ = "R" THEN MLABEL$(CHOICE)
= "SetMode[D]"
18835   IF RUNMODE$= "S" THEN MLABEL$(CHOICE) = "SetMode[S]"
18838   LOCATE TOPITEM+2, 45: COLOR FGD,BGD
18839   IF RUNMODE$ = "D" OR RUNMODE$ = "R" THEN GOTO 18842
18840     PRINT "TARGET PRESSURE: "; STARGET; : PRINT SPACE$(5)
18841     GOTO 18845
18842   PRINT "TARGET POSITION: "; TARGET; : PRINT SPACE$(5)
18845   LOCATE 23,1 : PRINT SPACE$(22)
18847   LOCATE TOPITEM+CHOICE, LEFTITEM : COLOR 8,7
18848   PRINT MLABEL$(CHOICE) 'Prints new cursor
18850   GOSUB 10600   'Reactivate cursor keys
18860 RETURN
18870 '
18900 'Subroutine ResetStartPos
18910   GOSUB 3000   'Find current DCDT positions
```

```
18920   NEWINIT(0) = POSITION(0)
18930   NEWINIT(1) = NEWINIT(0)
18940   NEWINIT(2) = POSITION(2)
18950   NEWINIT(3) = NEWINIT(2)
18960 RETURN
18970 '
19000 'Subroutine RunTest
19010 ' Runs a test based on user specified motion
19015   A$ = ""     'Initialize the cancellation string
19020   LOCATE 23, 1: COLOR 15,12: PRINT "Subroutine RunTest";
19030   LOCATE 23, 25 :PRINT "PRESS [S] OR [s] TO STOP";
19040   COLOR 15,9: PRINT SPACE$(5);
19050   KEY(11) OFF: KEY(14) OFF 'Turns off arrow keys
19060   COLOR 15, 8 'Set color to white on black
19062   GOSUB 3000    'Find current DCDT readings
19064   GOSUB 5000    'Print total DCDT motions
19066   GOSUB 3200 'Prints current bag pressures
19070   IF RUNMODE$ = "S" OR RUNMODE$ = "s" THEN GOSUB 20000 ELSE
GOSUB 19080
19072 RETURN
19073 '
19078 'Subroutine DisplacementControl
19080   GOSUB 3500 'Subroutine to compute average platform position
19090   GOSUB 3600 'Subroutine to compute avg position of platform 2
19091   START1 = AVG  'Records initial position of platform 1 for this run
19092   START2 = AVG2 'Records init. position of pltfm 2 form this run
19095   '
19100   ' This loop causes the platforms to rise until the target is
19120   '   reached or the user presses "S" to stop
19140   '
19160   IF AVG>TARGET-TOL AND AVG < TARGET+TOL THEN GOTO 19210
19200     GOSUB 30000 'Steps the motors to adjust position
19210   'Read, print, and adjust current air pressure if necessary
19215   IF PTARGET > .1 THEN GOSUB 37000 ELSE GOSUB 36200
19220   GOSUB 5500 'Prints current bag pressures and corrects b value
```

```
19230   GOSUB 3000 'Find the new DCDT positions
19240     GOSUB 3500 : GOSUB 3600 'Compute new average position
19250     LOCATE 12,45: PRINT "Current Strain: ";
19251     PRINT USING "+##.###"; 100*(AVG+AVG2)/22.5;
19252     PRINT " %";
19255   GOSUB 5000  'Print new DCDT positions (in inches)
19260   'Check for user input to stop run
19270   IF A$ = 's" OR A$ = "S" THEN GOTO 19360
19280   A$ = INKEY$
19300   IF A$ = "s" OR A$ = "S" THEN GOTO 19360
19320   'Return to top of loop
19340   GOTO 19160
19360 GOSUB 19500 'Subroutine to stop running
19380 RETURN
19400 '
19500 'Subroutine EndRun
19510 '  Ends execution of run routine and returns screen to normal
19515    A$ = ""  'Clear the variable that tells the run routine to stop
19520    GOSUB 10600  'Activate menu cursor keys
19540    LOCATE 23, 25: COLOR 15,9 : PRINT SPACE$(30)  'Erase prompt
19550    LOCATE 1,1:PRINT SPACE$(25):LOCATE 2,1:PRINT SPACE$(25)
19560    LOCATE 12,45: PRINT SPACE$(30)  'Erase current position
19570    LOCATE 23, 1: PRINT SPACE$(23)   'Erase choice indicator
19580    LOCATE 23, (80 - LEN(PROMPT$))/2 : PRINT PROMPT$;
19590    LOCATE 21, 60 : PRINT SPACE$(20) 'Erase b-value
19600    LOCATE 22, 60 : PRINT SPACE$(20) 'Erase BVOLTS
19610 RETURN
19620 '
19700 'Subroutine Reset
19710 '  Called from SetRunMode
19720   FOR I = 1 TO 4
19730     NEWINIT(I-1) = .001
19740   NEXT I
19750   RUNMODE$ = "D"
19770 RETURN
```

```
19780 '
20000 'Subroutine StressControl
20010 '  Called from RunTest, used to run a stress controlled test
20020  'Top of loop that runs until user hits a key
20030    LEAD=0
20040    IF PRESSURE(1)>PRESSURE(0)+STOL THEN LEAD=2
20050    IF PRESSURE(1)<PRESSURE(0)-STOL THEN LEAD=1
20060  IF PRESSURE(0)>STARGET-STOL AND
PRESSURE(0)<STARGET+STOL AND LEAD = 0 THEN GOTO 20300
20070    'Check which platform has the higher pressure
20080    IF PRESSURE(0)<STARGET THEN FLAG=1 ELSE FLAG=-1
20090    'Execute STEP algorithm
20100    IF LEAD <> 0 THEN GOTO 20170
20110      'Move both platforms 1 step
20120      GOSUB 31400 'Subroutine StepBoth
20160      GOTO 20300  'Execute the rest of the loop
20170    IF LEAD <> 1 THEN GOTO 20230
20180      'If platforms are advancing and platform 1 is in the lead
20190      '  then move platform 2 only.  If retreating, move platform 1
20200      IF FLAG = 1 THEN MNUM = 3 ELSE MNUM = 1
20210      GOSUB 4000
20220      GOTO 20300
20230    IF LEAD <> 2 THEN PRINT "ERROR: invalid LEAD variable (Stress)"
20240      IF FLAG= 1 THEN MNUM = 1 ELSE MNUM = 3
20250      GOSUB 4000
20260      GOTO 20300
20270    'End of STEP execution phase
20280    '
20300    'Read, print, and adjust air pressure if necessary
20310    IF PTARGET > .1 THEN GOSUB 37000 ELSE GOSUB 36200
20315  GOSUB 20500   'Plays a tone if target has been reached
20320    GOSUB 5500  'Find new pressures
20330    GOSUB 3000  'Find new DCDT positions
20340    GOSUB 5000  'Print new DCDT positions
20350    GOSUB 3500 : GOSUB 3600 'Compute new average position
```

```
20360     LOCATE 12,45: PRINT "Current Strain: ";
20370     PRINT USING "+##.###"; 100*(AVG+AVG2)/22.5;
20375     PRINT " %";
20380     'Check for user input to stop run
20385     IF A$ = "S" OR A$ = "s" THEN GOTO 20430
20390     A$ = INKEY$
20400     IF A$ = "S" OR A$ = "s" THEN GOTO 20430
20410     'Return to top of loop
20420     GOTO 20020
20430   GOSUB 19500   'Subroutine EndRun
20440 RETURN
20450 '
20500 'SUBROUTINE BEEP
20510   'Sounds a tone if the target pressure has been reached
20515   IF PRESSURE(0)>STARGET-STOL AND
PRESSURE(0)<STARGET+STOL AND LEAD = 0 THEN GOTO 20520 ELSE
RETURN
20520   COUNT = COUNT + 1
20530   IF COUNT < 0 THEN COUNT = 0
20540   IF COUNT < 4 THEN RETURN
20550   IF COUNT >=4 THEN COUNT = 0
20560   PLAY "N15 L16"
20570 RETURN
20580 '
21000 'Subroutine SetTargetPressure
21010   COLOR FGD, BGD : LOCATE TOPITEM+2, LMARG: PRINT
SPACE$(23);
21020   LOCATE TOPITEM+3, LMARG: PRINT SPACE$(23);
21030   LOCATE TOPITEM+2, 45: COLOR FGD,BGD
21050   LOCATE TOPITEM+2,LMARG: COLOR 8, 10: PRINT "Target Press.: ";
21060   INPUT STARGET
21070   IF STARGET >= 0 AND STARGET <= 60 THEN GOTO 21110
21080     LOCATE TOPITEM+3, LMARG : PRINT "Invalid Input";
21090     COLOR FGD,BGD: LOCATE TOPITEM+2,LMARG: PRINT
SPACE$(23);
```

```
21100     GOTO 21050
21110   COLOR FGD, BGD : LOCATE TOPITEM+2, LMARG: PRINT
SPACE$(23);
21120   LOCATE TOPITEM+3, LMARG: PRINT SPACE$(23);
21130   LOCATE TOPITEM+2, 45: COLOR FGD,BGD
21135     PRINT "TARGET PRESSURE: ";: PRINT USING "+##.##"; STARGET;
21140     PRINT SPACE$(3)
21145   LOCATE 23,1 : PRINT SPACE$(22)
21150   GOSUB 10600   'Reactivate cursor keys
21160 RETURN
21170 '
22000 'Subroutine SideWallMode
22010 '   Allows the user to select either target B-value or
22020 '   zero displacement sidewall control
22030   KEY(11) OFF : KEY(14) OFF  'Turn off cursor keys
22040   LMARG = 15 'Sets the left location of the prompts
22050   LOCATE 23, 1: COLOR 15,12: PRINT "Subroutine SideWallMode";
22060   COLOR FGD,BGD: PRINT SPACE$(2);
22070   LOCATE TOPITEM+CHOICE,LMARG: COLOR 8,10:PRINT "B Mode
(B/D/S/Q): ";
22080   INPUT BCTRL$
22090   IF BCTRL$ = "d" THEN BCTRL$ = "D"
22095   IF BCTRL$ = "s" THEN BCTRL$ = "S"
22100   IF BCTRL$ = "b" THEN BCTRL$ = "B"
22110   IF BCTRL$ = "q" THEN BCTRL$ = "Q"
22120   IF BCTRL$="D" OR BCTRL$="B" OR BCTRL$ = "S" OR BCTRL$="Q"
THEN GOTO 22160
22130     LOCATE TOPITEM+CHOICE + 1, LMARG : PRINT "Invalid Input";
22140     COLOR FGD,BGD: LOCATE TOPITEM+CHOICE,LMARG: PRINT
SPACE$(23);
22150     GOTO 22070
22160   COLOR FGD, BGD : LOCATE TOPITEM+CHOICE, LMARG: PRINT
SPACE$(23);
22170   LOCATE TOPITEM+CHOICE+1, LMARG: PRINT SPACE$(23);
22175   'Activate the sidewalls
```

```
22180   SIDEWALLS% = 1
22190   IF BCTRL$ = "D" THEN GOSUB 1500   'Re-zero sidewalls
22200   IF BCTRL$ = "B" THEN GOSUB 22500  'Get target b-value
22210   IF BCTRL$ = "Q" THEN SIDEWALLS% = 0  'Turn off sidewalls
22220   MLABEL$(CHOICE) = "B Ctrl [" + BCTRL$ + "]"
22230   LOCATE 23,1 : PRINT SPACE$(24)
22240   LOCATE TOPITEM+CHOICE, LEFTITEM : COLOR 8,7
22250   PRINT MLABEL$(CHOICE); 'Prints new cursor
22260   GOSUB 10600  'Reactivate cursor keys
22270 RETURN
22280 '
22500 'Subroutine SetB-value
22510 '  Prompts the user for a target b-value
22520   LOCATE TOPITEM+CHOICE,LMARG : COLOR 8,10
22530   PRINT "TARGET B: ";
22540   INPUT BTARGET
22550   IF BTARGET < 1 AND BTARGET > 0 THEN GOTO 22590
22560     LOCATE TOPITEM+CHOICE + 1, LMARG : PRINT "Invalid Input";
22570     COLOR FGD,BGD: LOCATE TOPITEM+CHOICE,LMARG: PRINT
SPACE$(23);
22580     GOTO 22520
22590   COLOR FGD, BGD : LOCATE TOPITEM+CHOICE, LMARG: PRINT
SPACE$(23);
22600   LOCATE TOPITEM+CHOICE+1, LMARG: PRINT SPACE$(23);
22610 RETURN
22620 '
24000 'Subroutine Define ISMCODE
24020     L = 0
24030     IF MCODE$ = "o" OR MCODE$ = "O" THEN L = 1
24040     IF MCODE$ = "m" OR MCODE$ = "M" THEN L = 1
24050     IF MCODE$ = "1" OR MCODE$ = "2" THEN L = 1
24080 RETURN
25000 'Subroutine Rel. Motion
25020 '  Determines how to move platforms relative to each other
25040   LOCATE 23, 1: COLOR 15,12: PRINT "Subroutine Rel. Motion"
```

```
25060   COLOR 15,9: PRINT SPACE$(8);
25070   YPROM = 8 + CHOICE*2    'Y coordinate of the menu selection
25080   LMARG = 15 : PFGD = 15 : PBGD = 11   'Set prompt colors
25100   ' Draw the input prompt next to the menu choice
25110   LOCATE YPROM, LMARG : COLOR PFGD, PBGD
25120   PRINT "Platform Code: ";
25122   MCODE$ = INKEY$
25130   IF MCODE$ = "" GOTO 25122
25135   PRINT MCODE$;
25137   GOSUB 24000
25140   IF L=1 THEN GOTO 25200
25150     LOCATE YPROM+1, LMARG: PRINT "Invalid Input"
25160     COLOR FGD, BGD : LOCATE YPROM, LMARG : PRINT SPACE$(23)
25170     GOTO 25100
25200   COLOR FGD, BGD : LOCATE YPROM+1, LMARG : PRINT SPACE$(23)
25210   LOCATE YPROM, LMARG : PRINT SPACE$(23)
25215   ' Print the new MCODE$ value
25220   LOCATE 8, 45: COLOR FGD,BGD : PRINT "Platform Code: " MCODE$;
25230   '  Erase the Subroutine indicator
25240   LOCATE 23, 1 : COLOR FGD, BGD : PRINT SPACE$(23)
25250   RETURN
25260 '
30000 'Subroutine MovePlatforms
30010 '  Steps the platforms
30020   GOSUB 3500   'Compute average motion of platform 1
30030   GOSUB 3600   'Compute average motion of platform 2
30055   ' Determine direction of platform travel
30056   IF AVG < TARGET THEN FLAG = 1 ELSE FLAG = -1
30060   'If platforms are to move in opposite directions, execute
30065   '  the MoveOpposite subroutine
30070   IF MCODE$ = "O" OR MCODE$ = "o" THEN GOSUB 31000
30080   'If platforms are to move in the same directions, execute
30090   '  the MoveTogether subroutine
30100   IF MCODE$ = "M" OR MCODE$ = "m" THEN GOSUB 32000
30300 RETURN
```

```
30310 '
31000 'Subroutine MoveOpposite
31010 ' Moves the platforms 1 step in opposite directions
31030  LEAD = 0 'Variable to determine if one platform is ahead of the other
31040  IF AVG2 > AVG + TOL THEN LEAD = 2
31050  IF AVG2 < AVG - TOL THEN LEAD = 1
31100  ' Execute the STEP algorithm to match platform motions
31120  IF LEAD <> 0 THEN GOTO 31190
31130    'Move both platforms by one step
31140    GOSUB 31400  'Subroutine StepBoth
31180    GOTO 31300    'Exit the MovePlatforms algorithm
31190  IF LEAD <> 1 THEN GOTO 31250
31200    'If platforms are advancing and platform 1 is in the lead, then
31210    'move platform 2 only. If retreating, move platform 1 only.
31220    IF FLAG = 1 THEN MNUM = 3 ELSE MNUM = 1
31230    GOSUB 4000    'Call the STEP algorithm
31240    GOTO 31300    'Exit this subroutine
31250  IF LEAD <> 2 THEN PRINT "ERROR: invalid LEAD variable"
31260    'If platforms are advancing and platform 1 is in the lead, then
31270    'move platform 2 only. If retreating, move platform 1 only.
31280    IF FLAG = 1 THEN MNUM = 1 ELSE MNUM = 3
31290    GOSUB 4000    'STEP algorithm
31300 RETURN
31310 '
31400 'Subroutine StepBoth
31410 ' Moves both of the platforms one step. It alternates which
31420 ' platform is stepped first, hence the FIRSTEP variable.
31450  IF FIRSTEP = 1 THEN GOTO 31550
31500    MNUM = 1     'Specifies platform 1 in the STEP algorithm
31510    GOSUB 4000   'STEP algorithm
31520    MNUM = 3     'Specifies platform 2 in the STEP algorithm
31530    GOSUB 4000
31535    FIRSTEP = 1  'Switch the FIRSTEP variable
31540    GOTO 31650   'Exit the subroutine
31545  'Moves platform number 2 first...
```

```
31550     MNUM = 3      'Specifies platform 2 in the STEP algorithm
31560     GOSUB 4000    'STEP algorithm
31570     MNUM = 1      'Specifies platform 1 in the STEP algorithm
31580     GOSUB 4000
31590     FIRSTEP = 0   'Switch the FIRSTEP variable
31650 RETURN
32000 'Subroutine MoveParallel
32010 ' Moves the platforms one step in the same direction
32020  ' Determine if either platform is ahead of the other
32030  '  in terms of total displacement from the starting position
32035  LOCATE 1,50:PRINT "MoveParallel";
32040  LEAD = 0
32050  IF STARTPOS - AVG > AVG2 - STARTPOS + TOL THEN LEAD = 1
32060  IF STARTPOS - AVG < AVG2 - STARTPOS - TOL THEN LEAD = 2
32064  IF FLAG = 1 AND LEAD = 1 THEN LEAD = 2 ELSE GOTO 32068
32066  GOTO 32070
32068  IF FLAG = 1 AND LEAD = 2 THEN LEAD = 1
32070  ' Move the platforms by one step
32080  GOSUB 4500   'Subroutine FindMotion
32090  IF LEAD <> 0 THEN GOTO 32400  'Skip to LEAD = 1 sequence
32100    IF MOTION <> 0 THEN GOTO 32300  'Skip to individ. motion sequence
32110      'Step all four motors at once...
32120      VOLTBITS! = 2048*(1+SCALE*FLAG)
32130      HIBIT% = INT(VOLTBITS!/256)
32140      LOBIT% = INT(VOLTBITS!-HIBIT%*256)
32150      MOTORBITS% = 252
32160      GOSUB 2500  'Subroutine SendVolts sends output to motors 1 and 2
32170      'Send Voltages to Platform 2 motors (motors 3 and 4)...
32180      VOLTBITS! = 2048*(1+SCALE*FLAG)
32190      HIBIT% = INT(VOLTBITS!/256)
32200      LOBIT% = INT(VOLTBITS!-HIBIT%*256)
32210      MOTORBITS% = 252
32220      GOSUB 2500  'Subroutine SendVolts sends output to motors 1 and 2
32230      LEAVE MOTORS RUNNING WITH THE FOLLOWING FOR LOOP
32240      FOR I = 1 TO 500
```

```
32250         NEXT I
32260       GOSUB 2000   'Stop Motors
32270       CALL AM1(A%(0), B%(0), C$)
32290       GOTO 32900     'Exit subroutine
32300     'Sequence to move both platforms individually.  This is
32310     'necessary if one of the platforms is tipping.
32320     'Execute the STEP algorithm to match platform motions
32330     'Move both platforms by one step
32335     LOCATE 2,50:PRINT "LEAD = ";LEAD;
32340     MNUM = 1      'Specifies platform 1 in the STEP algorithm
32350     GOSUB 4000    'STEP algorithm
32360     MNUM = 3      'Specifies platform 2 in the STEP algorithm
32370     FLAG = -1*FLAG 'Moves platform 1 in the opposite stroke direction
32380     GOSUB 4000
32390     GOTO 32900    'Exit the MoveParallel algorithm
32400   'If platform one is in the lead, execute the following...
32410   IF LEAD <> 1 THEN GOTO 32600
32420     'If platforms are advancing and platform 1 is in the lead, then
32430     'move platform 2 only.  If retreating, move platform 1 only.
32435     LOCATE 2,50:PRINT "LEAD = ";LEAD;
32440     'IF FLAG = 1 THEN MNUM = 3 ELSE MNUM = 1
32445     ' Move platform 2 in opposite piston stroke direction
32450     MNUM = 3 : FLAG = -1*FLAG
32480     GOSUB 4000    'Call the STEP algorithm
32490     GOTO 32900    'Exit this subroutine
32590   'If platform two is in the lead ...
32600   IF LEAD <> 2 THEN PRINT "ERROR: invalid LEAD variable"
32610     'If platforms are advancing and platform 2 is in the lead, then
32620     'move platform 1 only.  If retreating, move platform 2 only.
32625     LOCATE 2,50:PRINT "LEAD = ";LEAD;
32630     'IF FLAG = 1 THEN MNUM = 3 ELSE MNUM = 1
32640     'IF MNUM = 3 THEN FLAG = -1*FLAG
32650     MNUM = 1
32660     GOSUB 4000    'STEP algorithm
32900   LOCATE 1,50:COLOR FGD,BGD:PRINT SPACE$(14);
```

```
32905   LOCATE 2,50:COLOR FGD,BGD:PRINT SPACE$(14);
32910 RETURN
32920 '
33000 'Subroutine SetSpeed
33010 '  Sets the voltage that will be sent to the four motors
33020 '  during a step. The variable affected is SCALE, which
33030 '  expresses the voltage as a fraction of full scale output.
33040 '
33050 '  Turn off cursor control keys
33060   KEY(11) OFF : KEY(14) OFF
33070 '  Set location of input prompt
33080   QY = TOPITEM + (CHOICE)*2
33090   QX = LEFTITEM + 15
33100 '  Set prompt colors
33110   PFGD = 8 : PBGD = 10
33120 '  Print the prompt for user input
33130   LOCATE QY, QX : COLOR PFGD, PBGD
33140   PRINT "Percent output (0-99): ";
33150   INPUT SCALE
33160   SCALE = SCALE/100
33170 '
33180 '  Check the input
33190   IF SCALE > 0 AND SCALE < .999 THEN GOTO 33250
33200     LOCATE QY+1, QX : PRINT "INVALID INPUT";
33210     'Erase the invalid input line
33220     COLOR FGD, BGD : LOCATE QY, QX : PRINT SPACE$(30);
33230     GOTO 33120
33240 '
33250 '  Erase the prompts
33260   COLOR FGD, BGD : LOCATE QY, QX : PRINT SPACE$(30)
33264   LOCATE TOPITEM, 45 : PRINT "Motor Output: ";
33265   PRINT USING "+##.##"; 100*SCALE; : PRINT " %" SPACE$(2)
33270   LOCATE QY+1, QX : PRINT SPACE$(15);
33280 '  Reactivate cursor keys
33290   GOSUB 10600
```

```
33300 RETURN
33310 '
34990 '
35000 'Subroutine SetPressure
35010 '  Gets a target value for the air pressure
35020 '  Output line 5 will go to the Fairchild pressure controller
35025   A$ = ""     'Turns off the cancellation string
35030   AIRCHANNEL = 5  'Strawberry Tree channel controlling pressure
35040   'Set location of input prompt
35050   QY = TOPITEM + (CHOICE)*2
35060   QX = LEFTITEM + 15
35070   'Turn off cursor control keys
35080   KEY(11) OFF : KEY(14) OFF
35090   'Set prompt colors
35100   PFGD = 8 : PBGD = 10
35110   'Print the prompt for user input
35120   LOCATE QY, QX : COLOR PFGD, PBGD
35130   PRINT "Target Pressure (psi): ";
35140   INPUT PTARGET
35150   IF PTARGET > 0 AND PTARGET < MAXPRESS THEN GOTO 35200
35160     LOCATE QY+1, QX : PRINT "INVALID INPUT";
35165     'Erase the invalid input line
35170     COLOR FGD, BGD : LOCATE QY, QX : PRINT SPACE$(30);
35180     GOTO 35110
35190   'Erase all prompts
35200   COLOR FGD, BGD : LOCATE QY, QX : PRINT SPACE$(30)
35210   LOCATE QY+1, QX : PRINT SPACE$(20)
35220   LOCATE TOPITEM + 4, 45 : PRINT "TARGET AIR PRESS.: ";
35230   PRINT USING "#.##"; PTARGET; : PRINT " psi" SPACE$(5)
35240   'Adjust Fairchild until air pressure is correct
35250   GOSUB 37000  'Subroutine FixPressure
35260   'Activate cursor keys again
35270   GOSUB 10600
35280 RETURN
35290 '
```

```
36000 'Subroutine ReadPressure
36010 '  Reads the pressure transducer
36020   CHANNEL = 4     'Assumes pressure is on input line 5
36030   GOSUB 1000      'ADREAD reads A/D converter
36040   MILVOLTS = VTS*1000
36050   AIRPRESSURE = (MILVOLTS-1000*INIVOLT(4))*PCF/VIN
36060   LOCATE 21,10 : COLOR 15,8
36070   PRINT USING "+##.##"; MILVOLTS
36080   LOCATE 22,10 : COLOR 15,4
36090   PRINT USING "+##.##"; AIRPRESSURE
36100 RETURN
36110 '
36200 'Subroutine ShowPressure
36210 '  Prints the value of the air pressure to the screen
36220   GOSUB 36000   'Subroutine ReadPressure
36230   AY = TOPITEM + 5 : AX = 45
36240   LOCATE AY, AX : COLOR 15, 8 : PRINT "Act. Pressure = ";
36245   IF AIRPRESSURE > 20 OR AIRPRESSURE < -1 THEN GOTO 36255
36250   PRINT USING "#.##"; AIRPRESSURE;
36251   GOTO 36260
36255   PRINT "> 20";
36260   PRINT " psi";
36265   COLOR FGD, BGD : PRINT SPACE$(2)
36270 RETURN
36280 '
37000 'Subroutine FixPressure
37010 '  Adjusts voltage to Fairchild until AIRPRESSURE = PTARGET
37020   GOSUB 36200  'Finds and prints the current AIRPRESSURE
37030   'Check if pressure has been "roughly" tuned based on
37040   '  calibration factor of Fairchild transducer
37050   IF PADJ = 0 THEN GOTO 37060 ELSE GOTO 37170
37060     'Check if selected pressure is within the linear range
37070     '  of the Fairchild
37080     IF PTARGET > 2.4 THEN GOTO 37110
37090       POUTV = 0
```

```
37100       GOTO 37160
37110     'If PTARGET is within the linear range, then compute the
37120     ' approximate required output voltage
37130     POUTV = (PTARGET - 1.098)/.709     '(Pressure given in psi)
37140     ' Slope of linear regression = 0.709 psi/volt
37150     ' Intercept = 1.098 psi
37160     PADJ = 1  'Signals that POUTV has been coarsely adjusted
37165     GOSUB 38000  'Send the computed voltage to the Fairchild
37170   'Fine-tune the air pressure to match target pressure
37180   WHILE AIRPRESSURE < (PTARGET - PTOL) OR AIRPRESSURE >
(PTARGET + PTOL)
37190     'Incrementallly adjust output voltage until the proper
37200     'pressure is achieved
37210     IF AIRPRESSURE < (PTARGET - PTOL) THEN GOTO 37240
37220       POUTV = POUTV - PINC
37230       GOTO 37270
37240     'If AIRPRESSURE < (PTARGET + PTOL)
37250       POUTV = POUTV + PINC
37270     'Check to see that POUTV is within legal limits
37271     IF POUTV>8 THEN GOTO 37272 ELSE GOTO 37280
37272     LOCATE QY+1, QX : PRINT "WAITING FOR PRESSURE TO
EQUALIZE";
37273     FOR I6 = 1 TO 5000
37274     NEXT I6
37275     COLOR FGD, BGD: LOCATE QY+1, QX : PRINT SPACE$(35)
37280     IF POUTV < 9 AND POUTV > 0 THEN GOTO 37350
37290       BEEP
37300       IF POUTV > 9 THEN POUTV = 9
37310       IF POUTV < 0 THEN POUTV = 0
37320       GOSUB 12000 'Prints the value of POUTV on the screen
37340       RETURN  'Exit while loop
37350     GOSUB 38000  'Send new voltage to Fairchild
37360     FOR I5 = 1 TO 100
37370     NEXT I5
37380     GOSUB 36200  'Read and display current air pressure
```

```
37390   IF A$ = "s" OR A$ = "S" THEN RETURN
37400   A$ = INKEY$
37410   IF A$ = "s" OR A$ = "S" THEN RETURN
37420  WEND
37430 RETURN
37440 '
38000 'Subroutine SendVoltage
38010 '  Sends the output voltage specified by the POUTV variable to
38020 '  line 5 of the Strawberry Tree terminal panel
38030 '  This routine assumes the card has been set for 0-10 volts output
38035   GOSUB 12000  'Prints the value of POUTV on the screen.
38040   VBITS! = (POUTV/10)*4095
38045   HIBIT% = INT(VBITS!/256)
38050   LOBIT% = INT(VBITS!-HIBIT%*256)
38055   MOTORBITS% = 239  'Only channel 5 will be active
38060   GOSUB 2500       'Subroutine SendVolts, which activates S.T. card.
38070   FOR N = 1 TO 500
38080   NEXT N
38090 RETURN
38100 '
39990 '
40000 'Subroutine FrictionTest
40001 '******** THIS SUBROUTINE IS NOW INACTIVE **************
40002 'To use it, add another menu item that calls this subroutine.
40010 '  Moves the platforms in the same direction to measure
40020 '  the membrane friction against the sidewalls of the
40030 '  APSR cell. This routine moves the platforms by the amount
40040 '  set by the stroke variable in one direction, then returns
40050 '  the platforms to their position at the start of this routine.
40060 '
40065   IF RUNMODE$ = "S" THEN RETURN
40070   LOCATE 23,1 : COLOR 15,12 : PRINT "Subroutine FrictionTest";
40080   LOCATE 23,25 : PRINT "PRESS [S] OR [s] TO STOP";
40090   COLOR 15, 9: PRINT SPACE$(5);
40100   KEY(11) OFF : KEY(14) OFF      'Turn off the arrow keys
```

```
40110  COLOR 15,8
40112  'Store the present value of the user input TARGET position
40113  T1 = TARGET
40115  MCODE$ = "M" : LOCATE TOPITEM,45 : COLOR FGD, BGD
40116  PRINT "Platform Code: " MCODE$;
40120  GOSUB 3000  'Find current DCDT positions
40130  GOSUB 5000  'Print DCDT motions
40135  GOSUB 3200   'Print out current platform pressures
40140  GOSUB 3500 : GOSUB 3600  'Find avg motion of platforms
40160  STARTPOS = AVG
40163  ' Check if the friction test can be performed at current position
40165  IF AV1 < STROKE/2 + .01 OR AV2 < STROKE/2 + .01 THEN GOTO
40800
40170  TARGET = AVG - STROKE/2
40180  COLOR FGD, BGD : LOCATE TOPITEM+2, 45
40190  PRINT "TARGET POSITION: "; : PRINT USING "+#.###"; TARGET;
40200  '
40210  ' The STROKE loop moves the platforms in the same direction until
40220  ' stroke is reached or the user presses [S]
40230  '
40240  GOSUB 41000   'Subroutine STROKE to move pistons to new TARGET
40250  '
40350 'Move platforms to START position + 1/2 STROKE
40360  TARGET = STARTPOS + STROKE/2
40370  COLOR FGD, BGD : LOCATE TOPITEM+2, 45
40380  PRINT "TARGET POSITION: "; : PRINT USING "+#.###"; TARGET;
40400  GOSUB 41000   'Subroutine STROKE to move pistons to new TARGET
40450 'Move platforms to START position
40460  TARGET = STARTPOS
40470  COLOR FGD, BGD : LOCATE TOPITEM+2, 45
40480  PRINT "TARGET POSITION: "; : PRINT USING "+#.###"; TARGET;
40500  GOSUB 41000   'Subroutine STROKE to move pistons to new TARGET
40800  MCODE$ = "O" : LOCATE TOPITEM,45 : COLOR FGD, BGD
40810  PRINT "Platform Code: " MCODE$;
40820  TARGET = T1
```

```
40830   COLOR FGD, BGD : LOCATE TOPITEM+2, 45
40840   PRINT "TARGET POSITION: "; : PRINT USING "+#.####"; TARGET;
40850   GOSUB 19500 'Subroutine EndRun     Cleans up the window
40860 RETURN
40870 '
40990 '
41000 'Subroutine STROKE
41010 '  Moves the platforms until TARGET is reached
41030   IF AVG > TARGET - TOL AND AVG<TARGET+TOL THEN RETURN
41040     GOSUB 30000   'Subroutine MovePlatforms
41045     GOSUB 37000   'Subroutine FixPressure
41050     GOSUB 3000    'Find new DCDT positions
41060     GOSUB 3500 : GOSUB 3600 'Compute new avg platform positions
41070     LOCATE 12,45 : PRINT "Current Position: ";
41080     PRINT USING "+#.####"; AVG,
41085     GOSUB 3200    'Print out platform pressures
41090     GOSUB 5000    'Print new DCDT positions
41100     'Check for user interrupt
41110     A$ = INKEY$
41120     IF A$ = "S" OR A$ = "s" THEN RETURN     'Exit Subroutine
41130     GOTO 41030   'Return to top of loop
```

Analog-to-Digital Conversion Card Connections

APSR Channel	Transducer	Quantity Measured	A/D Connection	
			Card No.	Pin No.
1	D 1	Piston 1 displacement	1	1,2
3	D 3	Piston 3 displacement	1	5,6
5	P 3	Air pressure	1	9,10
6	D 2	Piston 2 displacement	1	3,4
7	P 1	Platform 1 pressure	1	11,12
8	P 2	Platform 2 pressure	1	13,14
9	D 10	Top sidewall displacement	2	5,6
10	D 11	Bottom sidewall displacement	2	7,8
12	D 4	Piston 4 displacement	1	7,8
1A	P 4	Top sidewall pressure	2	1,2
2A	P 5	Bottom sidewall pressure	2	3,4

Note: 1. See Figure 3.4 for transducer layout.

Digital-to-Analog Conversion Card Connections

Strawberry Tree Output Channel	Device Receiving Voltage	Quantity Controlled
1	Motor 1	Piston 1 displacement
2	Motor 2	Piston 2 displacement
3	Motor 3	Piston 3 displacement
4	Motor 4	Piston 4 displacement
5	Fairchild Air Reg.	Air pressure
6	Motors 5 and/or 6	Sidewall displacements/pressures

Table A.1: Connections to the A/D and D/A Cards

Appendix B: Interpretation of Internal Soil Strains

B.1. Introduction

This appendix describes the technique used to find internal soil strains in the APSR Cell. Included are an overview of the equipment used for digitizing X-rays of APSR specimens and instructions for using the strain reduction computer software that has been developed for the APSR project.

Soil strains in the APSR cell are measured using an X-ray technique that is similar to one developed by Arthur (1977) for studying soil strains in the directional shear cell (DSC). Tungsten-carbide balls (2.4mm diameter) are placed at mid-height within an APSR sand specimen, spaced uniformly on a 2cm grid. The specimen is X-rayed to determine the positions of the tungsten balls immediately prior to shearing and at several points during shearing. After the X-rays films are developed, the positions of the balls on the films are digitized using the program POINTS. The STRAIN computer program reduces the digitized coordinate data to determine average and local strains within the soil using a technique of locally weighted multiple linear regression (Seah, 1990). A number of commercially available software packages can generate contour maps of the local strain fields from the output of STRAIN.

B.2. Digitizing X-Rays

This section explains how to set up and run the equipment used to digitize the positions of the tungsten carbide balls on a series of X-ray films, and how to use the computer program POINTS for recording digitized data. Figure 3.18 shows a schematic of this equipment.

B.2.1. Digitizing Components

The main components of the digitizing system are the optical comparator, the Sony Digital Position Readout System, and the personal computer to store data. The optical comparator consists of a light source, a moving platform (or stage) on which to mount the X-ray film, and a viewing screen which displays a magnified image (20x) of the X-ray film. The moving platform is equipped with adjustment screws for fine motion control in the X and Y directions to allow precise positioning of the X-ray image on the viewing screen. Two Sony Magnescales measure the X and Y position of the platform to a precision of 2 μm. A cable connects each of these Magnescales to the Digital Position Readout System, which displays coordinate measurements in either inches or millimeters.

The Digital Position Readout System (DPRS) has an RS232 communication port on its rear panel. A standard 25-pin connector connects the DPRS to the serial port on the personal computer. Data is sent to the computer in the form of an 18 character "word" whenever the user presses either the foot pedal or the [PRT] button on the DPRS. The first 9 bytes contain the X coordinate at the time the [PRT] button was pressed; the second 9 bytes contain the Y coordinate.

B.2.2. Program POINTS

B.2.2.1. Introduction

A computer program called POINTS was developed to record coordinate data for a series of X-Ray films with a regularly spaced grid of markers. POINTS will accept a rectangular array of points of any dimension up to 15x15. It is written in BASIC, and must be started before digitizing can begin. The program consists of two parts. The first part stores coordinate data in a disk file. The second part corrects the coordinates from the first film for rigid body rotation, then for the remaining films it computes the displacements of the tungsten balls from their initial positions. This displacement data is stored in a second file. The program STRAIN can then be used to compute global and local strains from this output.

B.2.2.2. Digitizing with POINTS

A disk containing the program POINTS.BAS must be in the computer's disk drive. To start the program, type GWBASIC A:POINTS.BAS. An introductory screen will appear; press [RETURN] to continue with the main program. The program will then ask for a filename to store the data. Any 8 character name without an extension[1] is allowed. The program will then ask for the number of points (i.e. the number of marker images) in the X and Y directions (15 or less). The next requested input is for the "f" factor. This is used by the program STRAIN to determine the minimum number of points to be considered when performing a local strain analysis (see section B.3.1). A number between 0.05 and 0.2 will work for a 10x10 array of points. A larger "f" factor

[1] An extension is a period followed by zero to three characters (i.e. filename.ext).

should be used for smaller arrays (e.g. 0.2 to 0.3 for a 4x4 array). The "f" factor must be large enough such that (f)(N) ≥ 2, where N is the total number of points on a film.

POINTS then displays an instruction screen explaining how to digitize the first X-ray film. The film must be located so that the marker point in the front left corner of the stage is at the center of the comparator screen. Zero the digitizer at this point by pressing the red X and Y buttons on the DPRS. Points are generally entered by rows from left to right, with rows incremented from front to back. Hit [Return] to go on to the film entry screen.

The film entry screen displays an array of points corresponding to the field of points on the X-ray film. The program asks for a film number; any integer is acceptable. The coordinates on the DPRS should start at 0,0 with the first point. Press the foot pedal or the [PRT] button to register this first point. The second point on the computer screen will start to blink, indicating that the program is waiting for that point to be entered. Move the stage on the comparator until the corresponding point on the X-ray film is in the center of the viewing screen. Press the foot pedal to register this point. The array indices and measured coordinates of the last point entered will be displayed on the computer screen. Continue in this way until all the points on the film have been entered. To correct a mistake, use the left or right arrow keys to move to the point that needs to be re-entered. These keys can also be used to check the coordinates that have been recorded for any point on the screen.

After all the points on a film have been entered, press the F1 key to store the coordinates in the disk file. The program will display a new film entry screen. Place the next film on the stage, zero the DPRS on the front left point, and repeat the digitizing

procedure for each film as described above. Once all the films have been entered, press [RETURN] at the film number prompt to terminate the program.

B.2.2.3. Marker Displacement Computations

Program POINTS automatically converts the digitized coordinate data into a set of u,v displacements after the user specifies that all the films have been entered. The displacement field data is stored in a file called "filename.SF", where "filename" is the name that was specified at the start of the digitizing session. This file consists of two parts: the first part stores the coordinates of the first film, corrected for rigid body rotation. The second part contains the x and y displacements (u, v) of each point on the remaining films, referenced to the first film. Figure B.1 shows the layout of the files produced by POINTS.

The program corrects for rigid body rotation of the first film by averaging a ray through the first row of points. If no rigid body motion occurred, the y coordinates of all these points would be zero. The angle of the ray corresponds to the amount of rotation. The program converts the coordinates of all the points on the first film to polar notation, rotates them so that the base line of points lies along the X-axis, then converts back to Cartesian coordinates. These coordinates are stored in the first part of the new output file. The program then computes the displacements of the points on each succeeding film from their corrected position on the first film. These values are stored in the second part of the output file.

B.3. Strain Field Computation: Program STRAIN

B.3.1. Background theory

The strain analysis used in this research is based on the work of Seah (1990) at MIT. The method uses multiple linear regression (Draper and Smith, 1981) to estimate strains from a displacement field. For a global analysis, the strains are averaged over the entire field of interest by fitting a plane through the calculated strains at each known displacement point. In the local analysis, a uniform grid is defined over the displacement field. At each node on this grid the nearest known displacement points are used to compute the average strains at that node. The greater the number of known displacement points taken into account at each grid node, the smoother the fit from one grid point to the next. The local analysis is like fitting a plane through the first to the i^{th} nearest known strain at each nodal point. The following summary of the analysis is taken from Seah (1990).

An infinitesimal displacement field with displacements (u_i, v_i) at the Cartesian coordinates (x_i, y_i) can be written:

In the x-direction: $$u_i = b_{11} + b_{12}x_i + b_{13}y_i + \varepsilon_{1i} \quad \text{(B.1)}$$

In the y-direction: $$v_i = b_{21} + b_{22}x_i + b_{23}y_i + \varepsilon_{2i} \quad \text{(B.2)}$$

where the coefficients b are constants which are related to the components of strains and rotations. ε_{1i} and ε_{2i} are error terms that are normally distributed random variables with means of zero and standard deviations $\sigma_{1\varepsilon}$ and $\sigma_{2\varepsilon}$, respectively.

The displacement matrix, $\underline{U}$, can be written:

$$\underline{U} \equiv \begin{bmatrix} u_1 & v_1 \\ u_2 & v_2 \\ \vdots & \vdots \\ u_i & v_i \\ \vdots & \vdots \\ u_n & v_n \end{bmatrix} \tag{B.3}$$

where n is the number of data points.

The displacements in the matrix form can then be expressed as:

$$\underline{U} = \underline{H}\,\underline{b} + \underline{\varepsilon} \tag{B.4}$$

where $\underline{H} = \begin{bmatrix} 1 & x_1 & y_1 \\ 1 & x_2 & y_2 \\ \vdots & \vdots & \vdots \\ 1 & x_i & y_i \\ \vdots & \vdots & \vdots \\ 1 & x_n & y_n \end{bmatrix}$, $\underline{b} = \begin{bmatrix} b_{11} & b_{21} \\ b_{12} & b_{22} \\ b_{13} & b_{23} \end{bmatrix}$ and $\underline{\varepsilon} = \begin{bmatrix} \varepsilon_{11} & \varepsilon_{21} \\ \varepsilon_{12} & \varepsilon_{22} \\ \vdots & \vdots \\ \varepsilon_{1i} & \varepsilon_{2i} \\ \vdots & \vdots \\ \varepsilon_{1n} & \varepsilon_{2n} \end{bmatrix}$.

The weight matrix is given by:

$$\underline{W} = \text{diag}\,(w_i) = \begin{bmatrix} w_1 & & & & \\ & w_2 & & & \\ & & \ddots & & \\ & & & w_i & \\ & & & & \ddots \\ & & & & & w_n \end{bmatrix} \tag{B.5}$$

This weight matrix is introduced so that the different types of analyses (global and local) can be expressed using the same set of equations but with different weights.

The quantity, $\hat{\underline{b}}$, is defined as the least square estimate of $\underline{b}$ for which $(\underline{U} - \underline{H}\,\hat{\underline{b}})^T \underline{W} (\underline{U} - \underline{H}\,\hat{\underline{b}})$ is a minimum, and it is given by:

$$\hat{\underline{b}} = (\underline{H}^T \underline{W}\,\underline{H})^{-1}\,\underline{H}^T \underline{W}\,\underline{U} \tag{B.6}$$

$\hat{\underline{b}}$ is determined from eqn. B.6, and, as shown below, the strains are the products of this $\hat{\underline{b}}$ matrix.

The estimated displacements are given by:

$$\hat{u}_i = \hat{b}_{11} + \hat{b}_{12}\, x_i + \hat{b}_{13}\, y_i \tag{B.7}$$

$$\hat{v}_i = \hat{b}_{21} + \hat{b}_{22}\, x_i + \hat{b}_{23}\, y_i \tag{B.8}$$

The infinitesimal strains are determined from the derivatives of displacements from eqns B.1 and B.2:

The axial strain in the x-direction,

$$\varepsilon_{xx} = \frac{\partial u}{\partial x} = \hat{b}_{12} \tag{B.9}$$

The axial strain in the y-direction,

$$\varepsilon_{yy} = \frac{\partial v}{\partial x} = \hat{b}_{23} \tag{B.10}$$

The shear strain,

$$\varepsilon_{xy} = \varepsilon_{yx} = \frac{\partial u}{\partial y} + \frac{\partial v}{\partial x} = \frac{1}{2}(\hat{b}_{13} + \hat{b}_{22}) \tag{B.11}$$

The maximum shear strain,

$$\gamma_{max} = \sqrt{[(\varepsilon_{xx} - \varepsilon_{yy})^2 + 4\, \varepsilon_{xy}^2]}$$

$$\gamma_{max} = \sqrt{[(\hat{b}_{12} - \hat{b}_{23})^2 + (\hat{b}_{13} + \hat{b}_{22})^2]} \tag{B.12}$$

For plane strain shearing, the volumetric strain can be expressed as:

$$\varepsilon_{vol} = \varepsilon_{xx} + \varepsilon_{yy} = \hat{b}_{12} + \hat{b}_{23} \tag{B.13}$$

The major and minor principal strains, ε_1 and ε_3, are:

$$\varepsilon_1 = \frac{1}{2}(\varepsilon_{vol} + \gamma_{max})$$

$$\varepsilon_1 = \frac{1}{2}\left\{(\hat{b}_{12} + \hat{b}_{23}) + \sqrt{[(\hat{b}_{12} - \hat{b}_{23})^2 + (\hat{b}_{13} + \hat{b}_{22})^2]}\right\} \tag{B.14}$$

$$\varepsilon_3 = \frac{1}{2}(\varepsilon_{vol} - \gamma_{max})$$

$$\varepsilon_1 = \frac{1}{2}\left\{(\hat{b}_{12} + \hat{b}_{23}) - \sqrt{[(\hat{b}_{12} - \hat{b}_{23})^2 + (\hat{b}_{13} + \hat{b}_{22})^2]}\right\} \tag{B.15}$$

The rigid body rotation, ω, is:

$$\omega = \frac{\partial v}{\partial x} - \frac{\partial u}{\partial y} = \frac{1}{2}(\hat{b}_{22} - \hat{b}_{13}) \tag{B.16}$$

The major principal strain direction relative to the y-axis, ξ, is given by:

$$\xi = \frac{1}{2}\tan^{-1}\left[\frac{2\,\varepsilon_{xy}}{\varepsilon_{xx} - \varepsilon_{yy}}\right] = \frac{1}{2}\tan^{-1}\left[\frac{\hat{b}_{13} + \hat{b}_{22}}{\hat{b}_{12} - \hat{b}_{23}}\right] \tag{B.17}$$

In the global strain analysis, the average strains are calculated using multiple linear regression, with the weight, w_i, at the *i* th data point equal to 1. Therefore, the weight matrix, $\underline{W}$, is the identity matrix (eqn. B.5), and the average strains are computed from eqs B.4 to B.17. The associated variances of the average strains have to be known in order to evaluate the uniformity of the specimen. Assuming that the model in eqn. B.6 is correct, the variance matrix of $\hat{\underline{b}}$ is:

$$\underline{\Sigma}_{\hat{b}} = \sigma_\varepsilon^2 (\underline{H}^T \underline{W}\, \underline{H})^{-1} \tag{B.18}$$

where σ_ε^2 is a measure of the scatter of the population about the regression line. An unbiased estimator of σ_ε^2 is given by:

$$s^2 = \frac{(\underline{U} - \underline{H}\,\hat{\underline{b}})^T\,\underline{W}\,(\underline{U} - \underline{H}\,\hat{\underline{b}})}{\text{tr}\,\underline{W} - \text{tr}\,[(\underline{H}^T\,\underline{W}\,\underline{H})^{-1}\,\underline{H}^T\,\underline{W}^2\,\underline{H}]}$$

$$s^2 = \begin{bmatrix} \sigma_{1\varepsilon}^2 & 0 \\ 0 & \sigma_{2\varepsilon}^2 \end{bmatrix} \qquad \text{(B.19)}$$

The variance matrix in the x-direction is:

$$\underline{\Sigma}_1 = \sigma_{1\varepsilon}^2\,(\underline{H}^T\,\underline{W}\,\underline{H})^{-1}$$

$$\underline{\Sigma}_1 = \begin{bmatrix} \Sigma_{111} & \Sigma_{112} & \Sigma_{113} \\ \Sigma_{121} & \Sigma_{122} & \Sigma_{123} \\ \Sigma_{131} & \Sigma_{132} & \Sigma_{133} \end{bmatrix} \qquad \text{(B.20)}$$

and the variance matrix in the y-direction is:

$$\underline{\Sigma}_2 = \sigma_{2\varepsilon}^2\,(\underline{H}^T\,\underline{W}\,\underline{H})^{-1}$$

$$\underline{\Sigma}_2 = \begin{bmatrix} \Sigma_{211} & \Sigma_{212} & \Sigma_{213} \\ \Sigma_{221} & \Sigma_{222} & \Sigma_{223} \\ \Sigma_{231} & \Sigma_{232} & \Sigma_{233} \end{bmatrix} \qquad \text{(B.21)}$$

The derivative of $\underline{U}$ from eqn. B.4 can be expressed as:

$$\underline{U}' = \underline{H}'\,\underline{b}$$

Combining eqns B.9 to B.11 yields the strain components:

$$\underline{S} = \begin{bmatrix} \varepsilon_{xx} \\ \varepsilon_{yy} \\ \varepsilon_{xy} \end{bmatrix} = \begin{bmatrix} 1 & 0 & 0 & 0 \\ 0 & 0 & 0 & 1 \\ 0 & 0.5 & 0.5 & 0 \end{bmatrix} \begin{bmatrix} \hat{b}_{11} \\ \hat{b}_{13} \\ \hat{b}_{22} \\ \hat{b}_{23} \end{bmatrix} \tag{B.22}$$

Rewriting eqn. B.22 gives $\underline{S} = \underline{G}\,\underline{B}$, where $\underline{G}$ is referred to as the transformation matrix. The variance matrix of strain is:

$$\underline{\Sigma}_s = \underline{G}\,\underline{\Sigma}\,\underline{G}^T$$

The variance matrix, $\underline{\Sigma}$, is determined from eqns B.20 and B.21:

$$\underline{\Sigma}_s = \begin{bmatrix} \Sigma_{122} & 0 & \frac{1}{2}\Sigma_{123} \\ 0 & \Sigma_{233} & \frac{1}{2}\Sigma_{223} \\ \frac{1}{2}\Sigma_{132} & \Sigma_{232} & \frac{1}{4}(\Sigma_{133} + \Sigma_{222}) \end{bmatrix} \tag{B.23}$$

The variances of ε_{xx}, ε_{yy},and ε_{xy} are the product of the variance matrix given in eqn. B.23:

$$\mathrm{Var}(\varepsilon_{xx}) = \Sigma_{122} \tag{B.24}$$

$$\mathrm{Var}(\varepsilon_{yy}) = \Sigma_{233} \tag{B.25}$$

$$\mathrm{Var}(\varepsilon_{xy}) = \frac{1}{4}(\Sigma_{133} + \Sigma_{222}) \tag{B.26}$$

The variances associated with the principal strains and the maximum shear strains can be determined using Taylor Series expansion. The first-order approximation to the variance of ε is:

$$\mathrm{Var}(\varepsilon) \cong \sum_i \sum_j (\underline{\Sigma}_s)_{ij}\, D(\varepsilon)_i\, D(\varepsilon)_j \tag{B.27}$$

where i, j = 1, 2, 3, and

$$D_1 = \left.\frac{\partial \varepsilon}{\partial \varepsilon_{xx}}\right|_m , \qquad D_2 = \left.\frac{\partial \varepsilon}{\partial \varepsilon_{yy}}\right|_m , \text{ and } \quad D_3 = \left.\frac{\partial \varepsilon}{\partial \varepsilon_{xy}}\right|_m .$$

The terms D_1, D_2, and D_3 are evaluated at ε_{xx}, ε_{yy}, and ε_{xy}. The strain, ε, is replaced by the principal strains (ε_1 and ε_3) and the maximum shear strain, γ_{max}. The variances of the angles are determined using eqns. B.23 and B.27. The major principal strain direction is calculated with ε being replaced by the angle ξ (in radians). The resulting variance is:

$$\text{Var}(\xi) \cong \sum_i \sum_j (\underline{\Sigma}_s)_{ij} D(\xi)_i D(\xi)_j \qquad \text{(B.28)}$$

The rigid body rotation is given by:

$$\text{Var}(\omega) = \frac{1}{4}(\Sigma_{133} + \Sigma_{222}) \qquad \text{(B.29)}$$

The variances of each parameter shown above are the population variances of the estimates.

In the local strain analysis, a non-linear weighting function is used to compute strains based on a 'window' of known displacements points nearest a point of interest. The weighting function, W, has the following properties:

$W(z) > 0$ for $|z| < 1$;

$W(-z) = W(z)$;

$W(z)$ is a non-increasing function for $z \geq 0$;

$W(z) = 0$ for $|z| \geq 1$.

The weighting function used in program STRAIN is a 'tricube' function, expressed by:

$$W(z) = (1 - |z|^3)^3 \qquad (B.30)$$

The procedure centers W to z_i with a value of 1 at that position and scales it so that the point at which W first becomes zero is at the *r* th nearest neighbor of z_i. The distance between this point and z_i is h times the average distance between two adjacent points. The larger the r value selected, the more data points will be used in the strain calculation and the smoother the fit will be. The f factor specified in program POINTS is the ratio of r to the total number of data points.

B.3.2. Running the program

The program STRAIN.FOR is based on a program developed by Seah (1990), but with several modifications. STRAIN.FOR will work for displacement fields of any dimension, mxn. It allows the user to specify the number of nearest neighbors, r, to be used in the local strain analysis. Because the strain analysis requires extensive matrix calculations, STRAIN requires a math coprocessing chip. If such a chip is not present, the program will not function.

STRAIN takes the output file from POINTS and processes it to compute global and local strain fields. To run the program, two files must be present: the STRAIN.EXE program file and a file called R1. R1 is an input file that contains displacement field data generated by the program POINTS.

B.4. Program Listings

B.4.1. Program POINTS.BAS

```
10 'PROGRAM POINTS.BAS
20 'Written 9/1/90
25 'Last Update: 3/11/91
30 'By: Douglas Larson
40 '    MIT Geotechnical Laboratories
50 '
60 'Explanation screen
70 COLOR 14,9
80 CLS
90 LOCATE 8,30
100 PRINT "Program POINTS"
110 LOCATE 11, 1
120 PRINT "This program reads data from a Sony Digital Position Readout"
130 PRINT "System and writes it to a data file.  The points to be entered"
140 PRINT "must be in a rectangular array of any dimension up to 15x15"
150 PRINT "points.  This program was written to digitize X-Rays for the"
160 PRINT "APSR project sponsored by the ARO."
170 LOCATE 23, 25: COLOR 15,8 : PRINT "Hit any key to continue..."
180 A$ = INKEY$
190 IF A$ = "" THEN GOTO 180
200 '
210 'Initial data entry screen
220 COLOR 14,9 : CLS
230 PRINT "Enter filename to store data: ";
240 INPUT FILE$
250 PRINT
251 PRINT "Are you reducing an existing data file to find u,v displacements?"
252 PRINT "Enter Y or N: ";
```

```
255 A$ = INKEY$
256 IF A$ = "" THEN GOTO 255
257 IF A$ = "Y" OR A$ = "y" THEN GOTO 560
258 CLS
260 INPUT "Number of points in X direction: ", MAXX
270 INPUT "Number of points in Y direction: ", MAXY
280 LOCATE 12,1
290 PRINT "Filename = "; FILE$
300 PRINT "Max x = "; MAXX
310 PRINT "Max y = "; MAXY
320 LOCATE 17,23 : COLOR 15,8 : PRINT "Type [c] to continue"
330 LOCATE 18,23 : COLOR 15,8 : PRINT "Type [r] to re-enter"
340 A$ = INKEY$
350 IF A$ = "C" THEN A$ = "c"
360 IF A$ = "R" THEN A$ = "r"
370 IF A$ <> "c" AND A$ <> "r" THEN GOTO 340
380 IF A$ = "r" THEN GOTO 210
390 '
400 'Open the data file for writing...
410 PRINT
420 PRINT "Are you adding to an existing file [y/n] : ";
422 ADD$ = INKEY$
423 IF ADD$ = "" THEN GOTO 422
430 IF (ADD$ = "Y" OR ADD$ = "y") THEN ADD$ = "A" ELSE ADD$ = "O"
440 OPEN ADD$, #2, FILE$
445 IF ADD$ = "A" THEN GOTO 470
450 PRINT #2, "FILE: "; FILE$
460 WRITE #2, MAXX, MAXY
462 'The FFACTOR variable determines the minimum number of points
463 '  to be considered at each node when doing a local strain
464 '  analysis (see T.H. Seah thesis for explanation).
465 PRINT "Enter the desired f factor (0 < f < 1): ";
466 INPUT FFACTOR
467 IF FFACTOR <= 0 OR FFACTOR >= 1 THEN GOTO 465
468 WRITE #2, FFACTOR
```

```
470 COLOR 14,9 : CLS
480 ' Film data entry screen...
490 '   Dimension necessary variables
500 DIM COORDS!(15,15,2)  'Array to hold coordinate values
510 OPEN "COM1:1200" AS #1
520 '
530 GOSUB 2000  'Subroutine to print instructions on the screen
540 GOSUB 950   'Subroutine to initialize film entry screen
550 CLOSE #1 : CLOSE #2  'Close file and shut down serial port
560 GOSUB 20000  'Subroutine to make a displacement file
570 GOSUB 5000  'Subroutine to end execution
575 SYSTEM
580 END
590 '
950 'Subroutine FilmEntry
960 '  Allows the user to digitize the points on a single film
970 '  Set up the screen...
980    COLOR 15,9 : CLS  'Clear the screen
984 '  Write all data so far to the file and flush the buffer...
985 CLOSE #2
990 OPEN "A", #2, FILE$
1000 '   Print a field which shows the array of points to be entered.
1010 COLOR 15, 8
1020 FOR I = 1 TO MAXX
1030   FOR J = 1 TO MAXY
1040     LOCATE J*2, 40-MAXX+I*2 : PRINT CHR$(1)
1045     FOR K = 0 TO 1                'Erase the COORDS! array
1046       COORDS!(I-1, J-1, K) = 0!
1047     NEXT K
1050   NEXT J
1060 NEXT I
1070 '   Prompt user for film number
1080 LOCATE 21,20 : PRINT "Hit enter to terminate";
1090 LOCATE 20, 20 : INPUT; "Enter film number: "; NUM$
1100 IF NUM$ = CHR$(13) OR NUM$ = "" THEN RETURN
```

```
1110 PRINT #2, NUM$
1120 COLOR 14,9 : LOCATE 20,20 : PRINT SPACE$(55)
1130 COLOR 14,9 : LOCATE 21,20 : PRINT SPACE$(55)
1140 LOCATE 23, 30 : PRINT "Entering film "; NUM$
1150 LOCATE 20, 20
1160 PRINT "Step on pedal to register points.";
1170 LOCATE 21, 20
1180 PRINT "Use arrow keys to re-enter points.";
1185 LOCATE 22,20 : PRINT "Hit [F1] to go on to next film";
1190 '
1195 CURSX = 0 : CURSY = 0   'Sets the current cursor position
1200 'Activate screen for user input
1210 GOSUB 10000
1230 ' Return to top of loop to enter a new film
1240 GOTO 980
2000 'Subroutine FilmInstructions
2010 '   Displays the instructions for how to enter film data
2020   LOCATE 3, 30 : PRINT "Film Entry Instructions"
2030   LOCATE 6, 1
2040   PRINT "Input marker coordinates as follows:"
2050   PRINT "   1) Locate first marker at front-left corner of stage"
2060   PRINT "   2) Zero the digitizer at this marker"
2070   PRINT "   3) Enter points by rows (left to right)"
2080   PRINT "   4) Increment the rows front to back"
2090   LOCATE 15, 30 : COLOR 15, 8 : PRINT "Hit any key to continue...";
2100   A$ = INKEY$
2110   IF A$ = "" THEN GOTO 2100
2120 RETURN
2130 '
5000 'Subroutine EndRun
5010   'Prints a farewell message, clears the
5020   '   screen, and ends execution of the program
5050   COLOR 14, 9 : CLS
5060   LOCATE 12,1
5070   PRINT "Closing down program POINTS.  The data points you entered are
```

```
5080   PRINT "stored in file "; FILE$; ". To compute strain fields from the"
5090   PRINT "points, run the FORTRAN program called STRAIN.EXE."
5100   LOCATE 22, 30 : PRINT "Hit any key..."
5110   A$ = INKEY$
5120   IF A$ = "" THEN GOTO 5110
5130   CLS
5140 RETURN
5150 '
10000 'Subroutine DataEntry
10010 '  Allows user to enter digitized points
10020   HOME$ = ""  'Variable to indicate if user is done entering points
10030   GOSUB 11000  'Subroutine TurnOnKeys
10040   WHILE HOME$ = ""
10060   WEND
10070   GOSUB 12000     'Subroutine TurnOffKeys
10080   GOSUB 15000     'Subroutine WriteData
10090 RETURN
10100 '
11000 'Subroutine TurnOnKeys
11010 '  Activate the left, right, and home keys
11020   ON KEY(12) GOSUB 11100
11030   ON KEY(13) GOSUB 11400
11040   ON KEY(1) GOSUB 11700
11045   ON COM(1) GOSUB 13000
11050   KEY(12) ON : KEY(13) ON : KEY(1) ON : COM(1) ON
11060 RETURN
11070 '
11100 'Subroutine CursorLeft
11110 '  Moves the point cursor one space to the left
11120   NEWX = CURSX-1
11130   NEWY = CURSY
11140   IF NEWX <> -1 THEN GOTO 11180
11150     NEWX = MAXX-1
11160     NEWY = NEWY-1
11170     IF NEWY = -1 THEN NEWY = MAXY-1
```

```
11180  'Erase the cursor at the old cursor location
11190  GOSUB 16000
11200  'Draw a cursor at the new position
11210  CURSX = NEWX
11220  CURSY = NEWY
11225  GOSUB 11850 'Prints the coordinates for this point on the screen
11230  GOSUB 16500
11240 RETURN
11250 '
11400 'Subroutine CursorRight
11410 '  Moves the point cursor one space to the right
11420  NEWX = CURSX+1
11430  NEWY = CURSY
11440  IF NEWX <> MAXX THEN GOTO 11480
11450    NEWX = 0
11460    NEWY = NEWY+1
11470    IF NEWY = MAXY THEN NEWY = 0
11480  'Erase the cursor at the old cursor location
11490  GOSUB 16000
11500  CURSX = NEWX
11510  CURSY = NEWY
11515  GOSUB 11850 'Print coordinates of this point on the screen
11520  'Draw a cursor at the new position
11530  GOSUB 16500
11540 RETURN
11550 '
11700 'Subroutine F1
11710 '  Terminates data entry for the current film by setting the
11720 '  HOME$ variable equal to a non-null value
11730  LOCATE 1,1
11740  COLOR 14,8
11750  INPUT; "TERMINATE ENTRY"; ANS$
11760  IF ANS$ = "y" OR ANS$ = "Y" THEN HOME$ = "END"
11770  COLOR 14,9
11780  LOCATE 1,1 : PRINT SPACE$(25)
```

```
11790 RETURN
11800 '
11850 'Subroutine WriteCoords
11860   'Display the coordinates that were entered for this point
11870   LOCATE 2,60 : PRINT SPACE$(20) : LOCATE 3, 60 : PRINT SPACE$(20)
11880   COLOR 14,9 : LOCATE 2,60 : PRINT "POINT " CURSX ", " CURSY;
11890   LOCATE 3, 60
11900   PRINT USING "+##.####"; COORDS!(CURSX,CURSY,0);
11910   PRINT ", ";
11920   PRINT USING "+##.####"; COORDS!(CURSX, CURSY, 1);
11930 RETURN
11940 '
12000 'Subroutine TurnOffKeys
12010 '  Turns off cursor keys
12020   KEY(12) OFF
12030   KEY(13) OFF
12040   KEY(1) OFF
12050 RETURN
12060 '
13000 'Subroutine GetAPoint
13010 '  Reads a point from the digitizer and increments the cursor
13020 '     position up by one.
13030 '  Read incoming input from the digitizer
13040    INPUT #1, X$
13050   W$ = ""
13060   V$ = ""
13070   W$ = MID$(X$, 4, 9)
13080   W = VAL(W$)
13090   V$ = MID$(X$, 16, 9)
13100   V = VAL(V$)
13110 '  Add new input to the array variable
13120   COORDS!(CURSX, CURSY, 0) = V
13130   COORDS!(CURSX, CURSY, 1) = W
13140 'Update screen, increment cursor position by one.
13150   GOSUB 11400 'Moves cursor one space to the right
```

```
13160   COLOR 14, 9 : LOCATE 2,1 : PRINT "Last point entered:
13165   LOCATE 3, 1 : PRINT SPACE$(20)
13170   LOCATE 3,1 : COLOR 14, 10
13180   PRINT USING "+##.####"; V;
13190   PRINT ", ";
13200   PRINT USING "+##.####"; W;
13210   COLOR 14, 9
13220 RETURN
13230 '
15000 'Subroutine WriteData
15010 '  Writes the data from the COORDS! array to the data file.
15020   FOR J = 0 TO MAXY-1
15030     FOR I = 0 TO MAXX-1
15040       WRITE #2, COORDS!(I,J,0), COORDS!(I,J,1)
15050     NEXT I
15060   NEXT J
15070 RETURN
15080 '
16000 'Subroutine EraseCursor
16010 '  Draws a steady, filled in smiley face to appear at the
16020 '  cursx, cursy position if the COORDS! array has been filled.
16030 '  Otherwise the routine draws an empty face.
16040   SCREENX = 40-MAXX+(1+CURSX)*2  'Screen position of the x cursor
16050   SCREENY = (MAXY-CURSY)*2  'Screen position of the Y cursor
16060   IF CURSX = 0 AND CURSY = 0 THEN GOTO 16200  'Filled in face
16070   'Draw an empty face if slot hasn't been filled
16080   IF COORDS!(CURSX, CURSY, 0) = 0 AND
COORDS!(CURSX,CURSY,1) = 0 THEN GOTO 16100
16090   GOTO 16200
16100   'Draw an empty face
16110  LOCATE SCREENY, SCREENX : COLOR 15,8
16120  PRINT CHR$(1)
16130  GOTO 16240
16140 '
16200   'Draw a full face
```

```
16210   LOCATE SCREENY, SCREENX : COLOR 15,8
16220   PRINT CHR$(2)
16230 '
16240   COLOR 15,9
16250   RETURN
16260 '
16500 'Subroutine DrawCursor
16510 '  Draws a blinking smiley face at the cursx, cursy position.
16520   SCREENX = 40-MAXX+(1+CURSX)*2  'Screen position of the x cursor
16530   SCREENY = (MAXY-CURSY)*2  'Screen position of the Y cursor
16540   IF CURSX = 0 AND CURSY = 0 THEN GOTO 16620  'Filled in face
16550   'Draw an empty face if slot hasn't been filled
16560   IF COORDS!(CURSX, CURSY, 0) = 0 AND
COORDS!(CURSX,CURSY,1) = 0 THEN GOTO 16580
16570   GOTO 16620
16580   'Draw an empty face
16590   LOCATE SCREENY, SCREENX : COLOR 31,8
16600   PRINT CHR$(1)
16610   GOTO 16660
16620   'Draw a full face
16630   LOCATE SCREENY, SCREENX : COLOR 31,8
16640   PRINT CHR$(2)
16650 '
16660   COLOR 14,9
16670 RETURN
16680 '
20000 'Subroutine CONVERT
20020 '  Makes a file with the x,y coordinates of the first film (corrected
20030 '  for rotation), and the u,v displacements of the other films.
20040 '
20070   'Re-open the digitized points file to read in the necessary data.
20080   OPEN "I", #1, FILE$
20090   'Get past first two lines
20100   INPUT #1, HEAD$
20110   INPUT #1, MAXX, MAXY
```

```
20115   INPUT #1, FFACTOR
20120   LOCATE 20,1 : PRINT "MAXX = "; MAXX;
20130   LOCATE 21,1 : PRINT "MAXY = "; MAXY;
20140   'Array variable:
20150   '  XX stores x coordinates
20160   '  YY stores y coordinates
20170   '  U and V store displacements of points from initial positions
20180   DIM XX(3000), YY(3000), U(250), V(250), AP(30)
20190   'Open the file to store converted output
20200   OFILE$ = FILE$ + ".SF"
20210   OPEN "O", #2, OFILE$
20220   'Print header lines to output file
20230   PRINT #2, "File: "; OFILE$
20240   WRITE #2, MAXX, MAXY
20245    WRITE #2, FFACTOR
20250   GOSUB 21000   'Read in x,y coordinates for each film
20260   GOSUB 22000   'Make rotation correction for first film
20270   GOSUB 23000   'Compute u,v displacements for remaining films
20280   CLOSE #1 : CLOSE #2
20290 RETURN
20300 '
21000 'Subroutine ReadXY
21010 '  Reads the point coordinates for all the films into the
21020 '  XX and YY arrays.
21030 '
21040    COUNT = 0
21050    IF EOF(1) THEN RETURN
21060    INPUT #1, AP(COUNT)   'Reads in the film number
21070    FOR PNUM = 1 TO MAXX*MAXY     'Enters each data point
21080      INDEX = COUNT*MAXX*MAXY+PNUM
21090      INPUT #1, XX(INDEX), YY(INDEX)
21100    NEXT PNUM
21110    COUNT = COUNT + 1
21120    GOTO 21050
21130 RETURN
```

```
21140 '
22000 'Subroutine Rotate
22010 '  Makes a rotation correction of the X,Y coordinates for the
22020 '  first film. The algorithm computes a ray through the
22030 '  line of points where y should be zero. It then rotates
22040 '  the entire set so this ray lies on the x-axis.
22050 '
22060   Z = 0 : X = 0 : Y = 0
22065   PI = 3.14159265#
22070   'Average a ray through the base points
22080   FOR N = 2 TO MAXX
22090     X = XX(N)+X
22100     Y = YY(N)+Y
22110   NEXT N
22120   Z = ATN(Y/X)
22130   LOCATE 22,1 : PRINT "Z = " Z;
22140   WRITE #2, XX(1), YY(1)
22150   FOR N = 2 TO MAXX*MAXY
22160     A = 0
22170     IF XX(N)<=0 THEN A = PI
22180     IF YY(N)<=0 THEN A = 2*PI
22190     'Make sure XX(N) is not zero to avoid division error
22200     IF XX(N) = 0! THEN XX(N) = .00001
22210     A = ATN(YY(N)/XX(N))+A
22220     B = A - Z
22230     R = SQR(XX(N)*XX(N) + YY(N)*YY(N))
22240     XX(N) = R*COS(B)
22250     YY(N) = R*SIN(B)
22260     WRITE #2, XX(N), YY(N)
22270   NEXT N
22280 RETURN
22290 '
23000 'Subroutine UV
23010 '  Converts x and y coordinates to u,v displacements
23020   'Compute number of points in each film
```

```
23030   NUMP = MAXX*MAXY
23040   FOR N = 1 TO CCUNT - 1
23050     WRITE #2, AP(N)
23060     FOR I = 1 TO NUMP
23070       U = XX(NUMP*N+I) - XX(I)
23080       V = YY(NUMP*N+I) - YY(I)
23090       WRITE #2, U, V
23100     NEXT I
23110   NEXT N
23120   'Add an end of file marker (999)
23130   X = 999 : WRITE #2, X
23140 RETURN
23150 '
```

B.4.2. Program STRAIN.FOR

```
C   Program STRAIN.FOR
C     Program to compute strains from displacement data
C
C   Written by: T.H. Seah
C   Modified by: D. Larson
C   Last Update: Sept 11, 1990
C
C
      DIMENSION X(2,10,10),U(2,10,10),W(10,10),G(2,20,20)
     DIMENSION A(3,3),AA(3,3),B(2,3),C(3,3)
      DIMENSION BH(2,3),SIG(2,3,3),SS(2),Y(2,10,10)
      DIMENSION GU(2,20,20),TD(3),D(3),DD(2,3),SIGG(3,3),SP(2),E(5)
    CHARACTER*10 JUNK
C
C   The unit 8 file is created with Program POINTS.BAS
     OPEN ( unit=8, file='R1')
C
C   Output Files :
     OPEN ( unit=7, file='R2')
     OPEN ( unit=10, file='R3')
    open ( unit=12, file='R3.DAT')
    open ( unit=13, file='Rd.DAT')
C
C   This program computes global strains for the entire strain
C     field area and four sub-areas.  It also computes local
C     strains at each point of a 19x19 grid through the entire
C     strain field area.
C
C   READ THE DATA
C   Get past file heading
    READ (8,5) JUNK
```

```
 5  FORMAT (A10)
C    Read in the number of points in the X and Y directions
     READ (8,*) MAXX, MAXY
C    Read in the minimum number of points for local strain analysis
     READ (8,*) FFACTOR
C
     H=0.0
     DO 10 I=1,MAXX
      READ (8,*) (X(1,I,J),X(2,I,J),J=1,MAXY)
 10  CONTINUE
 56  I0=0
     NP=0
C    The LINE variable tells which sub-area is currently being
C      processed.  It is used in Subroutine DG
     LINE = 0
C    Variable AP holds the film number of the field of points being
C      considered
     READ (8,*) AP
C
C    The displacement data file ends with 999.  Check to see if end
C      of file has been reached.
     IF (AP.EQ.999) GOTO 55
C
C    Read in a set of displacements
     DO 24 I=1,MAXX
      READ(8,*) (U(1,I,J),U(2,I,J),J=1,MAXY)
 24  CONTINUE
 57  I0=I0+1
 77  IF (I0.EQ.1) CALL DG(LINE,X,X0,Y0,NX,NY,DX,DY,MAXX,MAXY)
     IF (I0.GE.2) CALL DL(X,X0,Y0,NX,NY,DX,DY,F,R0,MAXX,MAXY)
     NN=0
C
C    READ THE LOCAL GRID
C
     R1 = FFACTOR*MAXX*MAXY
```

```
C
      IF (I0.GE.2) CALL GRID (X0,Y0,NX,NY,DX,DY,G)
  58  IF (I0.EQ.1) CALL GLOBAL(X0,Y0,DX,DY,G)
      DO 30 MX=1,NX
      DO 40 MY=1,NY
      NN=NN+1
      IF (I0.GE.2) CALL W1(X,G,R1,MX,MY,W,MAXX,MAXY)
      IF (I0.EQ.1) CALL W2(X,G,W,MAXX,MAXY)
      CALL FIT (A,B,C,W,U,X,MAXX,MAXY)
      CALL AINV (A,AA)
      CALL STRAIN (AA,B,BH,SS,W,U,SIG,A,C,X,MAXX,MAXY)
      CALL
DEV(GU,BH,G,WW,SW,SIG,E,EV,SV,GAM,SG,SP,THETA,ST,MX,MY)
      IF (I0.GE.2) CALL PRVL (WW,GU,G,E,GAM,THETA,MX,MY)
C
  40  CONTINUE
  30  CONTINUE
      FF=0.0
      IF (I0.EQ.1) FF=ABS(WW)
      IF (FF.GE.0.005) CALL CONV(WW,X,U,MAXX,MAXY)
      IF (FF.GE.0.005) GOTO 58
      IF (I0.EQ.1) THEN
       CALL PRVG(WW,SW,G,E,SIG,GAM,SG,SP,THETA,ST,MX,MY,EV,SV)
      NP=NP+1
      ENDIF
      IF (I0.EQ.1.AND.NP.EQ.5) GOTO 57
      IF (I0.EQ.1.AND.(LINE+1)*2.GE.MAXX+2) GOTO 57
      IF (I0.EQ.1.AND.(LINE+1)*2.GE.MAXY+2) GOTO 57
      IF (I0.GE.2) GOTO 56
      IF (I0.EQ.1) GOTO 77
  55  CLOSE (7)
      CLOSE (8)
      CLOSE (10)
      CLOSE (12)
      CLOSE (13)
```

```
      STOP
      END
C
C     ***********************************************
      SUBROUTINE DG(LINE,X,X0,Y0,NX,NY,DX,DY,MAXX,MAXY)
C     Computes the parameters for the five area calculations
      DIMENSION X(2,10,10)
      LINE = LINE+1
C     Compute average spacing between points in X and Y directions
      DELTX = X(1,MAXX,MAXY)/(MAXX-1)
      DELTY = X(2,MAXX,MAXY)/(MAXY-1)
C     Compute area calculation parameters
      X0 = (LINE-1.5)*DELTX
      Y0 = (LINE-1.5)*DELTY
      NX = 1
      NY = 1
      DX = (MAXX+2-LINE*2)*DELTX
      DY = (MAXY+2-LINE*2)*DELTY
      RETURN
      END
C
C     ***********************************************
      SUBROUTINE DL(X,X0,Y0,NX,NY,DX,DY,F,R0,MAXX,MAXY)
C     Divide the displacement field into a 19x19 grid
      DIMENSION X(2,10,10)
      X0 = 0
      Y0 = 0
      NX = 19
      NY = 19
      DX = X(1,MAXX,MAXY)/19
      DY = X(2,MAXX,MAXY)/19
      F = 2
      R0 = (X(1,MAXX,MAXY)+X(2,MAXX,MAXY))/18
      RETURN
      END
```

```
C
C   ***********************************************
      SUBROUTINE W1(X,G,R1,MX,MY,W,MAXX,MAXY)
      DIMENSION X(2,10,10),G(2,20,20),W(10,10)
      NH=0
C     Zero the W matrix
      DO 42 I=1,10
      DO 43 J=1,10
      W(I,J) = 0.0
   43 CONTINUE
   42 CONTINUE
  231 N=0
      NH=NH+1
      DO 50 I=1,MAXX
      DO 60 J=1,MAXY
      R=SQRT((X(1,I,J)-G(1,MX,MY))**2+(X(2,I,J)-G(2,MX,MY))**2)
      IF (R.GT.NH) GOTO 60
      W(I,J)=(1-R*R*R/NH/NH/NH)**3
      N=N+1
   60 CONTINUE
   50 CONTINUE
      IF (N.LT.R1) GOTO 231
      RETURN
      END
C
C   ***********************************************
      SUBROUTINE GLOBAL(X0,Y0,DX,DY,G)
      DIMENSION G(2,20,20)
      G(1,1,1)=X0
      G(2,1,1)=Y0
      G(1,2,2)=X0+DX
      G(2,2,2)=Y0+DY
      RETURN
      END
C
```

```
C     ********************************************
      SUBROUTINE W2(X,G,W,MAXX,MAXY)
      DIMENSION X(2,10,10),G(2,20,20),W(10,10)
C     Zero the W matrix
      DO 51 I=1,10
      DO 52 J=1,10
      W(I,J) = 0.0
   52 CONTINUE
   51 CONTINUE
C     Fill in the W matrix
      DO 62 I=1,MAXX
      DO 64 J=1,MAXY
        IF (X(1,I,J).GE.G(1,1,1).AND.X(1,I,J).LE.G(1,2,2).AND.X(2,I,J)
     *.GE.G(2,1,1).AND.X(2,I,J).LE.G(2,2,2)) W(I,J)=1.0
   64 CONTINUE
   62 CONTINUE
      RETURN
      END
C
C     ********************************************
      SUBROUTINE GRID (X0,Y0,NX,NY,DX,DY,G)
      DIMENSION G(2,20,20)
      DO 80 II=1,NY
      DO 90 JJ=1,NX
      G(1,JJ,II)=DX*(FLOAT(JJ)-1)+X0
      G(2,JJ,II)=DY*(FLOAT(II)-1)+Y0
   90 CONTINUE
   80 CONTINUE
      RETURN
      END
C
C     ********************************************
      SUBROUTINE FIT (A,B,C,W,U,X,MAXX,MAXY)
      DIMENSION X(2,10,10),U(2,10,10),W(10,10)
      DIMENSION A(3,3),B(2,3),C(3,3)
```

```
      DO 100 II=1,3
      DO 110 LL=1,3
      A(II,LL)=0.0
      C(II,LL)=0.0
  110 CONTINUE
      DO 120 LL=1,2
      B(LL,II)=0.0
  120 CONTINUE
  100 CONTINUE
      DO 130 II=1,MAXX
      DO 140 LL=1,MAXY
      A(1,1)=W(II,LL)+A(1,1)
      A(1,2)=W(II,LL)*X(1,II,LL)+A(1,2)
      A(1,3)=W(II,LL)*X(2,II,LL)+A(1,3)
      A(2,1)=A(1,2)
      A(2,2)=W(II,LL)*X(1,II,LL)*X(1,II,LL)+A(2,2)
      A(2,3)=W(II,LL)*X(1,II,LL)*X(2,II,LL)+A(2,3)
      A(3,1)=A(1,3)
      A(3,2)=A(2,3)
      A(3,3)=W(II,LL)*X(2,II,LL)*X(2,II,LL)+A(3,3)
      B(1,1)=W(II,LL)*U(1,II,LL)+B(1,1)
      B(1,2)=W(II,LL)*U(1,II,LL)*X(1,II,LL)+B(1,2)
      B(1,3)=W(II,LL)*U(1,II,LL)*X(2,II,LL)+B(1,3)
      B(2,1)=W(II,LL)*U(2,II,LL)+B(2,1)
      B(2,2)=W(II,LL)*U(2,II,LL)*X(1,II,LL)+B(2,2)
      B(2,3)=W(II,LL)*U(2,II,LL)*X(2,II,LL)+B(2,3)
      C(1,1)=W(II,LL)*W(II,LL)+C(1,1)
      C(1,2)=W(II,LL)*W(II,LL)*X(1,II,LL)+C(1,2)
      C(1,3)=W(II,LL)*W(II,LL)*X(2,II,LL)+C(1,3)
      C(2,1)=C(1,2)
      C(2,2)=W(II,LL)*W(II,LL)*X(1,II,LL)*X(1,II,LL)+C(2,2)
      C(2,3)=W(II,LL)*W(II,LL)*X(1,II,LL)*X(2,II,LL)+C(2,3)
      C(3,1)=C(1,3)
      C(3,2)=C(2,3)
      C(3,3)=W(II,LL)*W(II,LL)*X(2,II,LL)*X(2,II,LL)+C(3,3)
```

```
 140 CONTINUE
 130 CONTINUE
     RETURN
     END
C
C    ********************************************
C    INVERT THE A MATRIX
C
     SUBROUTINE AINV (A,AA)
     DIMENSION AA(3,3),A(3,3)
     DA=A(1,1)*(A(2,2)*A(3,3)-A(2,3)*A(3,2))-A(1,2)*(A(2,1)*A(
     *3,3)-A(2,3)*A(3,1))+A(1,3)*(A(2,1)*A(3,2)-A(2,2)*A(3,1))
     AA(1,1)=(A(2,2)*A(3,3)-A(3,2)*A(2,3))/DA
     AA(2,1)=(A(3,1)*A(2,3)-A(2,1)*A(3,3))/DA
     AA(3,1)=(A(2,1)*A(3,2)-A(2,2)*A(3,1))/DA
     AA(1,2)=(A(1,3)*A(3,2)-A(1,2)*A(3,3))/DA
     AA(2,2)=(A(1,1)*A(3,3)-A(1,3)*A(3,1))/DA
     AA(3,2)=(A(1,2)*A(3,1)-A(1,1)*A(3,2))/DA
     AA(1,3)=(A(1,2)*A(2,3)-A(2,2)*A(1,3))/DA
     AA(2,3)=(A(1,3)*A(2,1)-A(1,1)*A(2,3))/DA
     AA(3,3)=(A(1,1)*A(2,2)-A(1,2)*A(2,1))/DA
     RETURN
     END
C
C    ********************************************
      SUBROUTINE STRAIN (AA,B,BH,SS,W,U,SIG,A,C,X,MAXX,MAXY)
      DIMENSION BH(2,3),SIG(2,3,3),SS(2)
      DIMENSION X(2,10,10),U(2,10,10),W(10,10)
      DIMENSION A(3,3),AA(3,3),B(2,3),C(3,3)
     DO 200 KK=1,2
     DO 210 II=1,3
      BH(KK,II)=0.0
     DO 220 JJ=1,3
      BH(KK,II)=AA(II,JJ)*B(KK,JJ)+BH(KK,II)
 220 CONTINUE
```

```
 210 CONTINUE
 200 CONTINUE
     P=0.0
C
     DO 226 KK=1,3
     DO 227 LL=1,3
     P=AA(KK,LL)*C(KK,LL)+P
 227  CONTINUE
 226  CONTINUE
     DO 225 KK=1,2
     SS(KK)=0.0
     DO 230 II=1,MAXX
     DO 240 JJ=1,MAXY
       SX=BH(KK,1)+BH(KK,2)*X(1,II,JJ)+BH(KK,3)*X(2,II,JJ)
       SS(KK)=W(II,JJ)*(U(KK,II,JJ)-(BH(KK,1)+BH(KK,2)*X(1,II,JJ)
     *+BH(KK,3)*X(2,II,JJ)))**2+SS(KK)
 240  CONTINUE
 230  CONTINUE
     IF (P.EQ.A(1,1)) THEN P = P+0.00001
     SS(KK)=SS(KK)/(A(1,1)-P)
     DO 250 KA=1,3
     DO 260 LA=1,3
     SIG(KK,KA,LA)=SS(KK)*AA(KA,LA)
 260  CONTINUE
 250  CONTINUE
 225  CONTINUE
     RETURN
     END
C
C    ******************************************
     SUBROUTINE DEV(GU,BH,G,WW,SW,SIG,E,EV,SV,
     *GAM,SG,SP,THETA,ST,MX,MY)
     DIMENSION GU(2,20,20),TD(3),D(3),DD(2,3),SIGG(3,3),SP(2),E(5)
     DIMENSION BH(2,3),SIG(2,3,3),SS(2),G(2,20,20)
C
```

```
C    TRANSLATE
C
     DO 300 KK=1,2

GU(KK,MX,MY)=BH(KK,1)+BH(KK,2)*G(1,MX,MY)+BH(KK,3)*G(2,MX,MY
)
 300  CONTINUE
C
C    RIGID BODY ROTATION
C
      WW=.5*(BH(2,2)-BH(1,3))
      SW=.25*(SIG(1,3,3)+SIG(2,2,2))
C
     E(1)=BH(1,2)
     E(2)=BH(2,3)
      E(3)=.5*(BH(1,3)+BH(2,2))
     EV=E(1)+E(2)
      SV=SIG(1,2,2)+SIG(2,3,3)
     GAM=SQRT((E(1)-E(2))*(E(1)-E(2))+4*E(3)*E(3))
     IF (GAM.EQ.0.0) GAM=0.000001
     D(1)=(E(1)-E(2))/GAM
     D(2)=-D(1)
     D(3)=4*E(3)/GAM
      SIGG(1,1)=SIG(1,2,2)
      SIGG(1,2)=0
      SIGG(1,3)=0.5*SIG(1,2,3)
      SIGG(2,1)=0
      SIGG(2,2)=SIG(2,3,3)
      SIGG(2,3)=.5*SIG(2,2,3)
      SIGG(3,1)=SIGG(1,3)
      SIGG(3,2)=SIGG(2,3)
      SIGG(3,3)=.25*(SIG(1,3,3)+SIG(2,2,2))
     SG=0.0
     DO 400 KK=1,3
     DO 410 LL=1,3
```

```
      SG=SIGG(LL,KK)*D(LL)*D(KK)+SG
  410 CONTINUE
  400 CONTINUE
C
C     CALCULATING THE PRINCIPLE STRAINS
C
      DD(1,1)=.5*(1+D(1))
      DD(1,2)=.5*(1-D(1))
      DD(1,3)=.5*D(3)
      DD(2,1)=.5*(1-D(1))
      DD(2,2)=.5*(1+D(1))
      DD(2,3)=.5*D(3)
      DO 500 II=1,2
      SP(II)=0.0
      DO 510 KK=1,3
      DO 520 LL=1,3
      SP(II)=SIGG(LL,KK)*DD(II,KK)*DD(II,LL)+SP(II)
  520 CONTINUE
  510 CONTINUE
  500 CONTINUE
      E(4)=.5*(E(1)+E(2)+GAM)
      E(5)=.5*(E(1)+E(2)-GAM)
C
C
      EE=E(1)-E(2)
      IF (EE.EQ.0.0) EE=0.00001
      T=2*E(3)/EE
      THETA=.5*ATAN(T)*180/3.141592
      TD(1)=.5*T/EE/(1+T*T)
      TD(2)=-TD(1)
      TD(3)=1/EE/(1+T*T)
      ST=0.0
      DO 600 KK=1,3
      DO 610 LL=1,3
      ST=SIGG(LL,KK)*TD(LL)*TD(KK)+ST
```

```
 610 CONTINUE
 600 CONTINUE
     RETURN
     END
C
C    ********************************************
     SUBROUTINE PRVL(WW,GU,G,E,GAM,THETA,MX,MY)
      DIMENSION GU(2,20,20),E(5),G(2,20,20)
     G1=G(1,MX,MY)+GU(1,MX,MY)
     G2=G(2,MX,MY)+GU(2,MX,MY)
     GG=GAM*100
     theta=-theta
     WRITE(10,2)
G(1,MX,MY),G(2,MX,MY),WW,E(4),E(5),GAM,THETA,G1,G2
  2   FORMAT (1X,2(1X,F10.6),4(1X,F8.6),3(1X,F10.6))
     WRITE(12,332) G(1,MX,MY),G(2,MX,MY),gg
  332 FORMAT (1X,2(1X,F10.6),1X,F8.5)
     WRITE(13,333) g(1,MX,MY),g(2,MX,MY),theta
  333 FORMAT (1X,2(1X,F10.6),1X,F10.5)
     RETURN
     END
C
C    ********************************************
     SUBROUTINE
PRVG(WW,SW,G,E,SIG,GAM,SG,SP,THETA,ST,MX,MY,EV,SV)
      DIMENSION G(2,20,20),SIG(2,3,3),SP(2),E(5)

      SIG(1,2,2)=SQRT(SIG(1,2,2))
      SIG(2,3,3)=SQRT(SIG(2,3,3))
     SW=SQRT(SW)
     SP(1)=SQRT(SP(1))
     SP(2)=SQRT(SP(2))
     SG=SQRT(SG)
     SV=SQRT(SV)
     ST=SQRT(ST)*180/3.141592
```

```
      WRITE (7,1) G(1,MX,MY),G(2,MX,MY),WW,SW,E(1),SIG(1,2,2),E(2),
     *SIG(2,3,3),E(3),SW,E(4),SP(1),E(5),SP(2),GAM,SG,EV,SV,THETA,ST
    1  FORMAT (1X,2(1X,F10.6),16(1X,F8.6),2(1X,F10.6))
      RETURN
      END
C
C     ********************************************
      SUBROUTINE CONV (WW,X,U,MAXX,MAXY)
      DIMENSION X(2,10,10),U(2,10,10),Y(2,10,10)
      AN=-ASIN(WW)
      DO 33 I=1,MAXX
      DO 44 J=1,MAXY
       Y(1,I,J)=X(1,I,J)+U(1,I,J)
       Y(2,I,J)=X(2,I,J)+U(2,I,J)
       R=SQRT(Y(1,I,J)*Y(1,I,J)+Y(2,I,J)*Y(2,I,J))
      IF (Y(1,I,J).EQ.0.0) THETA=3.141592/2
      IF (Y(1,I,J).EQ.0.0) GOTO 66
      THETA=0
       IF (Y(1,I,J).LT.0.0) THETA=3.141592
       IF (Y(2,I,J).LE.0.0) THETA=3.141592*2
       IF (Y(1,I,J).GT.0.0.AND.Y(2,I,J).GT.0.0) THETA=0
      THETA=ATAN(Y(2,I,J)/Y(1,I,J))+THETA
   66 ALFA=THETA+AN
      U(1,I,J)=R*COS(ALFA)-X(1,I,J)
      U(2,I,J)=R*SIN(ALFA)-X(2,I,J)
   44 CONTINUE
   33 CONTINUE
      RETURN
      END
```

Filename	Filename.SF
File: Filename	File: Filename
m, n	m, n
f factor	f factor
Film No.	Film No.
X_1, Y_1	X_1, Y_1
X_2, Y_2	X_2, Y_2
.	.
.	.
.	.
X_m, Y_n	X_m, Y_n
Film No.	Film No.
X_1, Y_1	u_1, v_1
X_2, Y_2	u_2, v_2
.	.
.	.
.	.
X_m, Y_n	u_m, v_n
Film No.	Film No.
.	.
.	.
.	.

Figure B.1: Output Files Created by Program POINTS.BAS

Appendix C: Transducer Data Reduction

This appendix describes the methods used to compute boundary stresses and displacements of the APSR specimens based on the transducer readings recorded by the MIT Geotechnical Data Acquisition System. These calculations form the basis for most of the APSR data plots presented in this thesis. The last section of this appendix describes the Lotus 123 spreadsheets used to make the stress, displacement and force calculations.

C.1. Transducer Calibration

The transducers that measure the boundary stresses and displacements are listed in Table 3.2. Each of these transducers has a "calibration factor" which is used to convert the transducer output voltages to engineering units. The calibration factors for the LVDTs were obtained by inserting each LVDT into a stationary collar with its core extension resting on a hand operated micrometer that has a 2.54cm stroke. The micrometer reads displacements to a precision of 2μm. The LVDT is excited with a 6V input signal and allowed to warm up for at least 30 minutes. An initial reading of the output voltage is then taken, and the micrometer adjusted so that the extension rod moves by a known amount. The new output voltage is recorded. Readings are taken at five intervals over the micrometer's range, and this process is repeated for two unload/reload cycles to evaluate the hysteresis of the transducer. The LVDT output voltages are plotted against the extension rod displacements. The calibration factor, CF, is given by the expression:

$$CF = \frac{V_{in}}{m} \qquad (C.1)$$

where V_{in} is the input voltage supplied to the transducer, and m is the slope of the best fit line through the displacement vs. output signal data points.

The above expression for the calibration factor assumes that the response of the transducer is directly proportional to the supplied input voltage. All of the transducers used in the APSR cell were calibrated at the same input voltage that is used during testing (6V).

The pressure transducers are calibrated in the same way. Each transducer is excited with a 6V input and allowed to warm up for 30 minutes. It is then subjected to at least five pressure increments using a custom built calibration machine over two unload/reload cycles.

C.2. Boundary Stress Computation

The data reduction computations rely on the transducer calibration factors to determine the boundary stresses. The computations require a "zero" reading for each transducer, which is the transducer output signal corresponding to the condition where the transducer is subjected to zero gage pressure. The zeros for the waterbag and air pressure transducers are obtained by recording the data acquisition readings before any pressures are applied in the APSR cell. The zeros for the sidewall pressure transducers are obtained by connecting them to a tube in which the water is exposed to atmospheric pressure.

The pressures measured by the transducers throughout a test are then calculated using the formula:

$$P = \frac{(V - V_0)\ CF}{V_{in}} \qquad (C.2)$$

where: V is the transducer output signal,

V_0 is the transducer zero,

CF is the transducer calibration factor, and

V_{in} is the input voltage.

C.3. Boundary Displacement Computation

The lateral displacements are measured by transducers D5, D6, and D7 (Fig. 3.4). The zero values for these transducers are taken when their plexiglas feet are against the specimen membrane while the specimen is under a vacuum pressure prior to shearing. During shear, the front face of the specimen moves into the air void and the LVDT readings change. The amount of lateral displacement is computed using eqn. C.2. The average lateral strain, ε_{xx}, across the specimen is computed by dividing the lateral specimen displacement by the lateral specimen dimension (45cm).

The definition of the zero values for the platform and waterbag LVDTs are not as straightforward as for the lateral LVDTs. The zero values for the waterbag LVDTs (D8 and D9, Fig. 3.4) are adjusted so that the boundary measured axial strain and the internal axial strains (based on radiographic analysis) coincide for the stress level at which the first X-ray strain measurement is taken. The boundary measured axial strain is computed by adding the two waterbag displacements and dividing the total by the axial dimension of the specimen (57cm).

In test APSR 33, an external reference frame was constructed around the cell to check for outward movement of the end plates which would, in turn, cause outward movement of the platform and waterbag LVDTs. Dial gages mounted to this external

reference frame showed that the end plates only moved outward by a maximum of 0.13mm, implying very little error in the axial boundary displacements measured by the waterbag LVDTs. The total error in measured axial strain at failure is approximately 0.02% for this amount of outward movement.

C.4. Lotus Spreadsheets

The central data acquisition computer records voltages in a format compatible with the Lotus 123 spreadsheet program. The data reduction process for APSR tests has been largely automated with the use of two template spreadsheets. These spreadsheets are programmed to retrieve the raw data taken during a test, convert it to engineering units, and generate a series of data plots. The names of the two template spreadsheets are APSRTEMP.WK3 and LOADTEMP.WK3.

APSRTEMP.WK3 reduces the data and generates plots for the boundary stresses and displacements. The plots it creates include deviatoric stress ($q = (\sigma_1 - \sigma_3)/2$), lateral strain ($\varepsilon_{xx}$), and volumetric strain ($\varepsilon_{xx} + \varepsilon_{yy}$) vs. axial strain ($\varepsilon_{yy}$). LOADTEMP.WK3 processes the reinforcement force measurements from the strain gauges and the load cell. It produces plots of reinforcement loads vs. R and vs. axial strain in the specimen.

The layout of both spreadsheets is fairly straightforward. At the top of the sheet is the background information for each test, such as the test operator, test number, and date performed. Immediately under this are several rows of transducer information, which includes the transducer number, channel, calibration factor, and transducer zero. Each transducer has its own column. The next series of rows is the raw test data retrieved from the MIT Geotechnical Data Acquisition System, one row for each set of

transducer readings. Below the rows of raw data are the reduced data, with column headings to indicate the information and units for that column.

Because of the large amount of data collected for each test, it is impractical to provide a comprehensive appendix with all of the transducer readings. Anyone interested in obtaining APSR data on disk should write to:

Prof. A. J. Whittle, Room 1-370
Department of Civil Engineering
Massachusetts Institute of Technology
Cambridge, MA 02139